Understanding Extraneous Argon in Silicic Volcanic Products Using $^{40}Ar/^{39}Ar$ Laserprobe Geochronology

Thesis

UNRESTRICTED

Understanding Extraneous Argon in Silicic Volcanic Products using $^{40}Ar/^{39}Ar$ Laserprobe Geochronology

A thesis presented in fulfilment of the degree of Doctor of Philosophy by

Camilla M. Wilkinson

B.Sc., University of Greenwich (2004)

Department of Environment, Earth & Ecosystems
The Open University

February 2013

Date of Submission: 7 February 2013
Date of Submission: 7 February 2013
Date of Award: 20 May 2013

Acknowledgments

Thank you to my supervisors Dr Sarah Sherlock, Prof. Simon Kelley, Dr Bruce Charlier and Prof. Colin Wilson for their help, guidance, and patience over the past three (…and a bit!) years. Thank you to Dr Olivier Bachmann, who allowed the use of his samples, and who was extremely helpful when I needed additional locality information! Thank you to my examiners Dr Stephen Blake, and Prof. Nicolas Arnaud for their detailed comments and suggestions. NERC studentship (NE/F020066/1) is acknowledged for supporting this research.

Endless thanks must go to the members of the Ar-Ar lab, past and present, including Dr Alison Halton; Dr Stephanie Flude and Dr James Schwanethal, who were always on hand to help me with the instruments and answer all my questions. I am going to miss MAP-2 – you were the best mass spectrometer a girl could ask for! Dr Clare Warren and Dr Felix Hanke are thanked for introducing me to the delights of DIFFARG and Ar diffusion modelling. Thank you to the team of people who accompanied me on the Yellowstone fieldwork trip, in particular Prof. Wilson who drove me from Idaho to California (via Nevada), and got me to appreciate the complexities of the Bishop Tuff.

Michelle Higgins and Kay Green are acknowledged for their help with preparing my sections and polished blocks, and John Watson, who helped me with XRF preparation and analysis. I am very grateful to Andy Lloyd for poster printing, and to Liz Lomas (the keeper of the keys) for explaining to me for the hundredth time how to fill in the expenses claim form! Electron microprobe data in this thesis would not have been possible without the help and guidance of Dr Andy Tindle and Dr Susanne Schwenzer. Special thanks must also go to ARTHUR, who photographs thin sections beautifully, and Dr Sam Hammond

for her help (…and health and safety know how) with sample preparation involving HF and a stopwatch.

Finally, I would like to thank my friends, who supported me in my efforts to complete this work and always 'appeared' to be interested whenever I talked about rocks! Most importantly I would like to thank my parents and little sister for their continued love and support - thank you for always believing in me, and for inspiring me to nurture my desire to learn.

Abstract

The Ar-Ar dating technique is one of the most widely applied geochronological techniques to products of silicic volcanism, which represent geologically instantaneous events, and have been used to calibrate the geological timescale, correlate stratigraphy and biostratigraphy over large areas, and assess the impact of explosive volcanic eruptions. Recent advances (e.g., improved instrument precision and recalibration of the K-Ar decay scheme), are now making it possible to obtain increasingly precise and accurate ages for young volcanic eruptions, K-poor minerals, and even discrete parts of single crystals. These advances have highlighted the realisation that relatively small levels of Ar contamination (e.g., extraneous Ar, either excess ($^{40}Ar_E$), or inherited Ar), previously assumed to be minor, may now have a considerable effect on the accuracy of ages determined using the Ar-Ar technique.

To assess the issue of extraneous Ar, this study applied the Ar-Ar technique to a range of minerals (including sanidine, plagioclase and biotite), and glass separated from the products of large-volume silicic magma systems, which have undergone repeated cycles of crystallisation and rejuvenation. The *in situ* Ar-Ar laserprobe technique was applied to dacite of the Fish Canyon magmatic system (erupted at ~ 28 Ma; Colorado, USA), and the single-grain fusion Ar-Ar laser melting technique was applied to rhyolitic pumice (from explosive ignimbrite and ash fall, and effusive dome building events) of the Yellowstone Plateau Volcanic Field (≤ 2.1 Ma; Idaho, Wyoming, USA), and the Bishop Tuff (erupted at ~ 0.76 Ma; California, USA).

The *in situ* study revealed variable $^{40}Ar_E$ contamination of feldspar (i.e., hosted in fluid and melt inclusions in plagioclase and sanidine), and biotite (incorporated $^{40}Ar_E$ due to having a relatively high Ar mineral/fluid partition coefficient), resulting in an age range of 25.07 ±

1.86 to 61.46 ± 10.11 Ma. Single-grain fusion experiments revealed that in some cases the source of extraneous Ar was identifiable as partially re-set xenocrysts contaminating systems immediately prior to, and/or during eruption. In other cases, in particular some Yellowstone rhyolite domes, persistent recycling of material (crystal mixes including phenocrysts and antecrysts imparting an inherited Ar component), has resulted in a spread to older ages. This signal of inheritance is also seen in U-Pb zircon ages, but this is less evident or absent in Ar-Ar ages of co-existing glass. Ar diffusion modelling and Ar-Ar data in this study suggests sanidine is more likely to yield an eruption age. The use of sanidine feldspar, instead of anorthoclase and/or plagioclase feldspar is therefore strongly recommended. Biotite, which has shown to incorporate the largest proportion of $^{40}Ar_E$, should be used with caution, and successful dating of a glass phase can be a useful geochronological tool.

Despite extraneous Ar contamination, the Ar-Ar dating technique can be successfully applied to the products of silicic volcanism. This work has provided the opportunity to determine new Ar-Ar eruption ages (Green Canyon Flow dome at 1.29 ± 0.01 Ma; Sheridan Reservoir dome at 2.04 ± 0.03 Ma, and Snake River Butte dome at 2.15 ± 0.01 Ma), for rhyolite domes of the Yellowstone Plateau Volcanic Field previously only dated using the K-Ar technique. Finally, dating multiple phases (e.g., feldspar (sanidine); glass, and where possible zircon) is strongly recommended in order to identify cases of subtle contamination which will have a negative impact on our ability to obtain an accurate eruption age.

Contents

Index of Figures

Chapter 1

Chapter 2

Chapter 3

Chapter 4

Appendices

Index of Tables

Chapter 2

Chapter 3

Chapter 4

Appendices

Chapter 1. Introduction to the Study.

1.1 Introduction

The precise and accurate measurement of geological time is vital for understanding Earth's history. Geological tools of stratigraphy and palaeontology provide precise methods of measuring relative age, but are not able to give an accurate estimate of the absolute age of geological events of interest. Various geochronological techniques can be employed to numerically calibrate the geological timescale (e.g., Ar-Ar; K-Ar; U-Pb; Fission track; Rb-Sr and ^{14}C), and therefore provide an independent absolute age for various geological events. Application of radioisotopic dating techniques (e.g., U-Pb, U-Th, Ar-Ar, K-Ar, Rb-Sr) to minerals (e.g., feldspars, mica, zircon) and glass, separated from volcanic rocks (e.g., pumice, lava flows, ignimbrite flows, tephra and ash horizons), have been previously used to determine the timing of eruption (e.g., K-Ar and Ar-Ar, Deino *et al.*, 1990; Renne *et al.*, 1992; 1997; Gansecki *et al.*, 1998), differentiate between multiple magmatic events (e.g., U-Th, Lowenstern *et al.*, 2000; Rb-Sr, Christensen and DePaolo, 1993) and constrain magma generation and storage times (e.g., Charlier *et al.*, 2005; 2007; Bachmann *et al.*, 2007; Reid and Coath, 2000; Simon *et al.*, 2008).

Advances in the Ar-Ar technique (e.g., increased instrument precision and development of *in situ* methods), are making it possible to date increasingly younger volcanic eruptions, K-poor minerals and even discrete parts of single crystals. This is also making it possible to identify relatively small levels of contamination (e.g., extraneous Ar, either excess ($^{40}Ar_E$), or inherited Ar). Much of Ar-Ar dating assumes that such issues are minor; however instrumental precision has now approached the level that allows events to be dated to the nearest 5,000 years (e.g., Storey *et al.*, 2012). Therefore if one or several dated samples are

contaminated it can lead to erroneous conclusions, such as assigning an age to a volcanic eruption that is too old and at odds with field relations, or inferring several eruptions have taken place. This study investigates the occurrences of extraneous Ar in large-volume silicic volcanic systems and the impact even relatively small levels of contamination can have on the accuracy of Ar-Ar determined apparent ages. This chapter provides a brief introduction to the application of the Ar geochronometer to material from silicic volcanic systems, an explanation of the Ar-Ar technique and the problem of extraneous Ar contamination, as well as the main study aims and objectives.

1.2 Ar-Ar Geochronology: The importance of dating silicic volcanic products

The Ar-Ar dating technique is one of the most widely applied geochronological methods. It is based upon the decay of a naturally occurring isotope of potassium (K), ^{40}K to isotopes of radiogenic Ar ($^{40}Ar^*$) at a known rate. Silicic volcanic systems (e.g., Yellowstone), produce a range of lithologies from explosively erupted ignimbrites to effusively erupted lava flows and domes (e.g., Christiansen, 2001), and previous work has demonstrated the successful application of the Ar-Ar technique to products of silicic volcanism, which are often K- and crystal-rich. The dating of minerals from volcanic deposits are generally used to define the age of volcanic eruptions (e.g., McDougall, 1985; Turbeville and Self, 1988; Spell *et al.*, 1990; Gansecki *et al.*, 1996; 1998; Deino *et al.*, 2004; 2008), as well as providing an understanding of eruptive cycles (e.g., Lanphere *et al.*, 2002), the rates of magma chamber processes, and the overall magmatic evolution of a particular volcanic system (e.g., Bachmann *et al.*, 2007). Ar-Ar geochronology has been used to investigate the source and timing of xenocrystic contamination (e.g., van den Bogaard *et al.*, 1989; Deino and Potts, 1992; Gansecki *et al.*, 1996; 1998; Singer *et al.*, 1998; Gardner *et al.*, 2002), and $^{40}Ar_E$ contamination of volcanic minerals and glass (e.g., Renne *et al.*, 1997;

Esser *et al.*, 1997; Winick *et al.*, 2001; Kelley, 2002; Thomas *et al.*, 2003; Hora *et al.*, 2010; Clay *et al.*, 2011).

Deposits from large ash-forming eruptions provide chronostratigraphic markers that represent geologically instantaneous events. Volcanic tuff and tephra layers are routinely used to calibrate the geological timescale (e.g., Hess and Lippolt, 1986; Kuiper *et al.*, 2008; Rivera *et al.*, 2011; Storey *et al.*, 2012), and date paleomagnetic events, such as polarity reversals (e.g., Izett and Obradovich, 1994; Deino *et al.*, 2002; Lanphere *et al.*, 2002; Ellis *et al.*, 2012). They are used to correlate stratigraphy and biostratigraphy over large areas (e.g., Odin *et al.*, 1995), place an age against early humanoid tools (e.g., Semaw *et al.*, 1997) and hominid activities (e.g., Deino and Potts, 1992; Storey *et al.*, 2012), and assess the impact of explosive volcanic eruptions by correlating distal tephra layers with ignimbrite eruptions (e.g., Pringle *et al.*, 1992; Ton-That *et al.*, 2001). In addition, volcanic minerals are used as primary and secondary standards in Ar-Ar geochronology, because a relatively simple history (i.e., rapidly cooled) is assumed. For example, sanidine of the Fish Canyon Tuff and Taylor Creek Tuff are two of the most extensively used interlaboratory standards for Ar-Ar dating (e.g., Renne *et al.*, 1994; 1998; Villeneuve *et al.*, 2000; Dazé *et al.*, 2003; Jourdan and Renne, 2007; Renne *et al.*, 2010; 2011; Rivera *et al.*, 2011).

1.2.1 Products of silicic volcanism: materials useful for Ar-Ar dating

In principle any K-bearing mineral can be used for Ar-Ar dating, and volcanic minerals commonly used include feldspars (alkali feldspar, plagioclase); feldspathoids (leucite, nepheline); mica (biotite); amphibole and whole rock. In addition, the use of volcanic glass is steadily increasing. Members of the alkali feldspar series ($NaAlSi_3O_8$ - $KAlSi_3O_8$; sanidine-anorthoclase-high albite), generally have high K contents (up to 14 %). High temperature alkali feldspars, in particular sanidine, are readily used in Ar-Ar

geochronology because they generally yield ages that are interpreted in terms of the timing of volcanism, although contamination of phenocryst populations with $^{40}Ar_E$ has previously been noted (e.g., Renne *et al.*, 1997).

Plagioclase feldspars (Na end member albite, and Ca end member anorthite) contain relatively low K contents (e.g., < 0.1 to ~ 1 %), although this depends on the composition of the host rock (McDougall and Harrison, 1999). Plagioclase is commonly used for dating basaltic igneous rocks where it is often the only K-bearing phase available (e.g., Renne *et al.*, 1992), although their low K contents does mean that the incorporation of $^{40}Ar_E$ (e.g., Layer and Gardner, 2001) can cause significant increases to Ar-Ar apparent age determinations. Fresh and unaltered biotite usually contains 7 to 8 % K (McDougall and Harrison, 1999), and can be readily separated from crushed whole rock samples (e.g., Bachmann *et al.*, 2007b), although it can alter readily (e.g., Hildreth and Wilson, 2007), and incorporate $^{40}Ar_E$ (e.g., Thomas *et al.*, 2003; Hora *et al.*, 2010).

In circumstances where obtaining Ar-Ar ages from more conventional K-bearing phases has not been possible (either not available or have been disturbed), or where there is an absence of a truly phenocrystic population of crystals (i.e., when a mixture of phenocrysts, antecrysts and/or xenocrysts exists), volcanic glass can be utilised as an alternative K-bearing material for dating. Although inconsistent glass ages have been shown to be due to K and/or Ar mobility (e.g., Cerling *et al.*, 1985), owing to the inability of glass to retain elements as well as crystalline minerals, the use of separated glass can be critical in filling gaps in chronological information (e.g., Morgan *et al.*, 2009), or $^{40}Ar_E$ behaviour in volcanic systems (e.g., Clay *et al.*, 2011).

1.3 The Ar-Ar dating method

1.3.1 Introduction

The $^{40}Ar^*/^{39}Ar_K$ ratio is determined by measuring *in situ* produced radiogenic $^{40}Ar^*$ from the decay of ^{40}K, which has a half-life of 1.250 (± 0.002) × 10^9 years, and $^{39}Ar_K$ from ^{39}K, produced via fast neutron bombardment, whereby a nuclear reaction is produced between a neutron and the ^{39}K nucleus to produce particles of ^{39}Ar plus the emission of a proton during sample irradiation. The ratio is measured in a single isotopic analysis, unlike the K-Ar technique where K and Ar are measured on two separate sample aliquots. The $^{40}Ar^*/^{39}Ar_K$ is proportional to the $^{40}Ar^*/^{40}K$ ratio in the sample and therefore is proportional to the age. This is because the $^{39}Ar_K$ present following irradiation depends on the amount of ^{39}K present and the $^{39}K/^{40}K$ ratio is assumed to be constant in nature (McDougall and Harrison 1999). Ar-Ar ages are calculated relative to a standard of known age, which is irradiated together with the unknown. The standard acts as a fluence (neutron flux) monitor (discussed further in Appendix section A1), allowing the indirect determination of the integrated neutron flux (responsible for converting $^{39}Ar_K$ from ^{39}K) the unknown receives during sample irradiation. This allows the age of the unknown to be calculated by comparison with the known $^{40}Ar^*/^{39}Ar_K$ of the fluence monitor standard (McDougall and Harrison 1999).

In order to apply a geochronological tool, assumptions are required to be made in order to determine an age (McDougall and Harrison, 1999). The Ar-Ar technique makes the following assumptions: (1) ^{40}K parent nuclide decays at a constant rate, independent of any changes in pressure or temperature; (2) Measured radiogenic component (daughter product $^{40}Ar^*$) has been produced by *in situ* decay of ^{40}K; (3) The $^{40}K/K$ ratio is constant (in the case of Ar-Ar dating it is the $^{40}K/^{39}K$ ratio = 0.000125); (4) It is assumed that the

rock/mineral has remained a closed system since the event being dated (e.g., volcanic eruption) and that there has been no loss or gain of K or ^{40}Ar (other than from the radioactive decay of ^{40}K). (5) Various corrections are made, in particular correcting for non-radiogenic (atmospheric) Ar contamination and the production of interfering isotopes of Ar, via nuclear reactions, other than the production of $^{39}Ar_K$ during sample irradiation (e.g., ^{36}Ar and ^{39}Ar produced from Ca). ^{40}Ar is present in the atmosphere, therefore to correct for contaminating atmospheric Ar contained within the sample or contributed from the vacuum system in which gas extraction takes place, it is assumed that all of the ^{36}Ar measured is of atmospheric origin. Data can yield ^{36}Ar isotope measurements at instrument blank level; therefore there is no measurable ^{36}Ar to make a correction. Making the correction in this case can result in an age with larger errors than a zero measurement and mean error, and therefore non-atmospheric corrected data can be considered. If applying the ^{36}Ar correction to data that yields negative ^{36}Ar values (propagated through the age equation), can result in slightly older ages, therefore in this case it is appropriate to consider uncorrected data, while enhancing the errors appropriately using the variation seen in the blanks (discussed further in section 5.4.4).

It is important to correct for the decay of ^{37}Ar ($\lambda_{37} = 0.01974778292$ day $^{-1}$), between irradiation and conducting the experiment, as this value can be used as a proxy for Ca content of a sample or mineral (e.g., aid identification of plagioclase). Likewise, the decay of ^{39}Ar ($\lambda_{39} = 7.055 \times 10^{-6}$ day^{-1}), must also be corrected for as the value of $^{39}Ar_K$ is used to provide an estimate of the actual K-content of the unknown sample. ^{36}Ar and ^{39}Ar are produced from calcium (^{40}Ca and ^{42}Ca respectively), during sample irradiation. The effects of this can be significant when the technique is applied to minerals with low K/Ca ratios (e.g., plagioclase feldspar). Therefore, it is important this basic correction is made because atmospheric ^{40}Ar is corrected for by means of the ^{36}Ar measured, and any ^{36}Ar produced from ^{40}Ca will lead to overcorrection for atmospheric ^{40}Ar, resulting in low apparent ages.

It is also necessary to correct for reactor induced ^{40}Ar from ^{40}K present in the sample, which can in some cases be quite significant. Although cadmium shielding of samples during sample irradiation can reduce the effects of this reaction, failure to make this correction, especially to young samples, which have a low $^{40}Ar/^{39}Ar$ ratio, will result in older apparent ages. For a detailed explanation of the history and development of the Ar-Ar technique see McDougall and Harrison (1999), and references therein. An explanation of the $^{40}Ar/^{39}Ar$ age equation, current ^{40}K decay constants, sample preparation techniques, mass spectrometry, data reduction and corrections is given in Appendix section A1.

1.3.2 Volume diffusion of Ar

Dodson (1973) used the term 'closure temperature' to describe the relationship between the diffusivity of a daughter element ($^{40}Ar^*$), where by the mineral is an open system to volume diffusion, and the closure temperature of that element in a particular mineral. Figure 1.1 illustrates the concept of the closure temperature where there is little retention of Ar at the start, and fast volume diffusion of Ar at high temperatures. As the temperature decreases with time there will be some accumulation (but not complete retention), and as the mineral is cooled further $^{40}Ar^*$ will be retained in the mineral, which is now a closed system. The diffusion of any species in a solid mineral, controlled by temperature and the diffusion coefficient D, is defined by equation (1.1), where D_0 is the diffusion coefficient of the particular mineral involved, E the activation energy of the diffusion process, R the gas constant and T the temperature. Equation (1.2) is an expression used to calculate the closure temperature of a particular mineral phase, where A = geometry of the grain (i.e., 55 for a sphere which is used to represent feldspar, and 27 for a cylinder used to represent biotite) and a = grain radius (McDougall and Harrison, 1999).

$$D = D_0 e^{(-\frac{E}{RT})} \quad (1.1)$$

$$\frac{E}{RT_c} = ln\left[\frac{ART_c^2 D_0}{a^2 E \frac{\partial T}{\partial t}}\right] \quad (1.2)$$

The Ar-Ar geochronometer, when applied to a range of volcanic minerals including alkali-feldspars (e.g., sanidine), plagioclase, amphibole and biotite record ages after the mineral has cooled through ~ 500 °C (e.g., 300 to 350 °C for biotite, and ~ 250 °C for K-feldspar; McDougall and Harrison, 1999). In the case of volcanic systems, the erupted products go from a high temperature magmatic environment (i.e., one where Ar is free to re-equilibrate among the minerals, inclusions, and grain boundary fluid), to effectively being quenched upon eruption (i.e., where Ar becomes immobile), becoming a closed system to Ar diffusion (McDougall and Harrison, 1999). It is assumed the measured age will therefore reflect the time from which the sample passed through this closure temperature (instantaneous at point of eruption), to the present day. One of the key assumptions made when applying this technique is the radiogenic daughter product measured ($^{40}Ar^*$) was produced by the *in situ* radioactive decay of lattice-hosted ^{40}K. However, the incorporation of extraneous Ar, either in the form of excess Ar ($^{40}Ar_E$) or inherited radiogenic Ar from contamination by older material, such as xenocrysts or antecrysts can elevate Ar-Ar apparent ages.

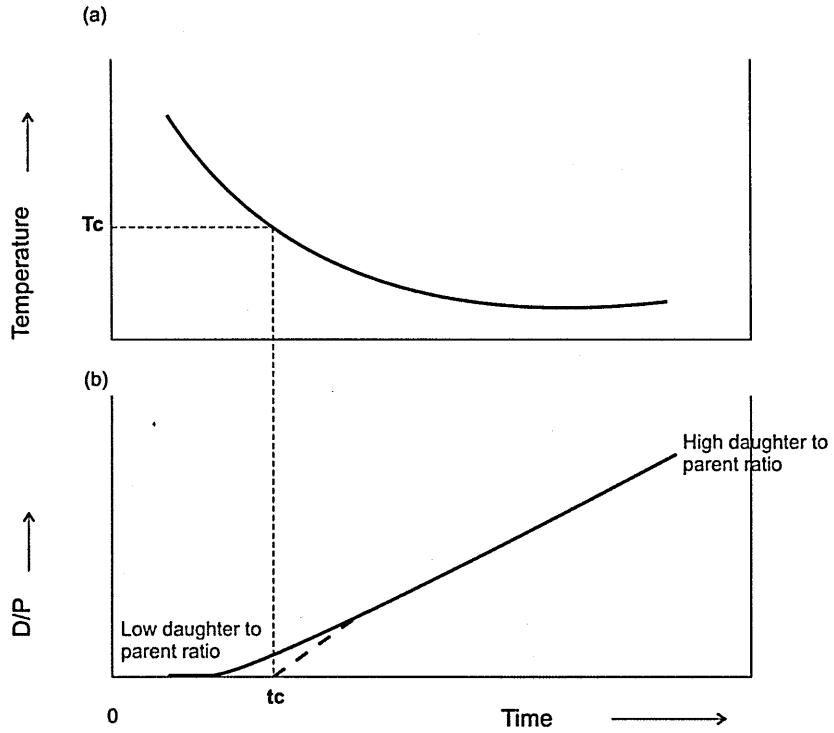

Figure 1.1 Relationship between geochronological closure of a mineral and its cooling history. Graph (a) shows the cooling history of the mineral as it decreases with time. Graph (b) relates to the diffusion coefficient *D* and rate of escape of radiogenic daughter product. The daughter-to-parent ratio (*D/P*; vertical axis) passes from an open state (where *D/P* = 0) through a zone of partial accumulation, until diffusive loss slows and the *D/P* ratio increases. T_c is the closure temperature, which is achieved at time t_c (and therefore t_c = mineral age). Dashed black line represents extrapolation from point of total accumulation back to t_c (redrawn and modified after McDougall and Harrison, 1999).

1.4 Extraneous Ar

Ar is a trace element and is present in all rocks at trace levels. Problems arise if additional Ar (^{40}Ar) is present, because it can be responsible for artificially elevating the $^{40}Ar/^{39}Ar$ ratio and therefore the age (termed 'apparent ages') (Kelley, 2002). Additional ^{40}Ar is commonly referred to as extraneous Ar and includes both excess ($^{40}Ar_E$), and inherited ^{40}Ar. $^{40}Ar_E$ is that component of ^{40}Ar (excluding atmospheric ^{40}Ar), which can be defined as 'Ar incorporated into a mineral during crystallisation, introduced into the mineral lattice by subsequent diffusion or within fluid or melt inclusions within the mineral' (Kelley, 2002). Inherited Ar is defined as ^{40}Ar that has been introduced into a sample by physical

contamination from older material (e.g., detrital grains, soils incorporated into ignimbrite eruptions) or partially re-set minerals (e.g., antecrysts and xenocrysts).

1.4.1 Excess Ar ($^{40}Ar_E$)

The presence of $^{40}Ar_E$ in minerals has been known since the development of the K-Ar dating method, which resulted in difficulties in interpreting K-Ar mineral ages, in particular from plutonic and metamorphic environments (e.g., Boven *et al.*, 2001). $^{40}Ar_E$ contamination of volcanic phenocrysts (e.g., feldspar and biotite) has been identified in various Ar-Ar geochronological studies (e.g., Spell *et al.*, 1990; Villa, 1991; Esser *et al.*, 1997; Renne *et al.*, 1997; Hora *et al.*, 2010). To better understand the effects of $^{40}Ar_E$ on apparent Ar-Ar ages, we need to consider $^{40}Ar_E$ source, transport and sinks. A source could be any K-bearing mineral, host rock or inclusion, its transport involves the inter- and intra-grain movement via diffusion, and a sink could be any mineral or inclusion (not necessarily K-bearing) within range of the transport distance that is able to take up Ar. The distribution of Ar between different phases, because Ar is a trace element and inert, can be discussed in terms of Ar solubility. This is expressed as a solid/melt or solid/liquid partition coefficient (K_D), and the accumulation of $^{40}Ar_E$ can be explained in terms of exchange between phases (including grain boundary fluids/melt) and the accumulation of $^{40}Ar^*$ (Kelley, 2002).

1.4.1.1 Ar solubility in melts, fluids and minerals

Ar solubility and diffusion in silicate liquids has been extensively studied (e.g., Carroll and Stolper, 1993 and references therein), and melts in the compositional range basalts to rhyolites have Ar solubilities in the range 0.05 to 0.1 ppm bar^{-1}, and up to 1.8 ppm bar^{-1} in pure silica melts (Carroll and Stolper, 1993). The solubility of Ar in common melt

compositions is thought to be strongly linked to ionic porosity (ratio of the unit cell volume and the calculated volume of the constituent anions and cations), which in turn is correlated with the silica content of the melt. Therefore the higher the silica content, the higher Ar solubility (e.g., rhyolite has an ionic porosity of 49.5, close to that of pure silica ~ 50.5, and as a result has a higher Ar solubility than basalt). This means when Ar is free to equilibrate between mineral phases and the melt, it will preferentially partition into the melt phase (Kelley, 2002). The solubility of Ar in melts is similar to that of CO_2, which is readily exsolved, suggesting that in well-degassed volcanic systems, Ar will partition into the exsolved gas phase and be lost to the atmosphere instead of remaining in the glass phase (Carroll and Stolper, 1993; Kelley, 2002).

Crystal/melt partition coefficients calculated for Ar and other noble gases made on minerals during crystal growth studies (e.g., clinopyroxene, Chamorro *et al.*, 2002) suggest a highly incompatible behaviour for noble gases during melting and crystallisation processes, and that Ar prefers melt or fluid phases (e.g., circulating hydrothermal fluids). Later studies (e.g., Ar in quartz; Watson and Cherniak, 2003, and olivine; Thomas *et al.*, 2008), suggests that Ar could be moderately to highly compatible in minerals. In general, partition coefficients for mineral/fluid and mineral/melt range 0.01 to 7×10^{-6} for Ar, which suggests $^{40}Ar_E$ will only cause significant problems (other than melt or fluid inclusions trapped in the lattice, section 1.4.1.1) when Ar concentration (i.e., Ar partial pressure; P_{Ar}) in the melt reaches a significant level and causes partitioning of Ar back into the mineral phase (Kelley, 2002).

K-rich minerals, such as mica (e.g., biotite; Hora *et al.*, 2010), and K-feldspar tend to display a higher Ar solubility than relatively K-poor minerals such as plagioclase and clinopyroxene (Kelley, 2002). Sherlock *et al.*, (2008) concluded partitioning of $^{40}Ar_E$ (dissolved in fluids), back into muscovite was responsible for elevated apparent ages.

Interstitial melt or fluids from shallow hydrothermal systems could potentially be a significant source of $^{40}Ar_E$ in magmatic environments, which could partition back into growing crystals. Villa (1991) suggested that magmas erupted in the Roman Volcanic Province (Italy), contained $^{40}Ar_E$ derived either from mantle or shallow hydrothermal sources, which had become trapped in lattice defects in leucite and sanidine phenocrysts.

1.4.1.2 Inclusion hosted $^{40}Ar_E$

Ar contained in fluid and melt inclusions can be a significant source of $^{40}Ar_E$ and can be a particular problem when dating young or low K minerals (e.g., plagioclase and amphiboles). Ar solubility is greater in hydrous fluids relative to melts, and so fluid inclusions can be a significant source of $^{40}Ar_E$ (Kelley, 2002). The release of $^{40}Ar_E$ from fluid inclusions has been correlated with measured Cl/K ratio during the decrepitation of fluid inclusions during sample analysis (e.g., Rama and Hart, 1965; Kelley *et al.*, 1986; Harrison *et al.*, 1994). Melt inclusions are easier to detect (often yellow/brown to black in colour) than fluid inclusions, and although they often contain relatively lower concentrations of $^{40}Ar_E$ can significantly disturb Ar-Ar apparent ages (e.g., Renne *et al.*, 1997; Winick *et al.*, 2001). A detailed study of $^{40}Ar_E$ in zero age anorthoclase from Mount Erebus (Esser *et al.*, 1997) showed that the Ar signal released from melt inclusions on the mineral surface (released at 900 to 1000 °C during stepped heating experiments) could be distinguished from, but Ar liberated from buried melt inclusions were released at the same time as lattice hosted Ar (temperatures ~ 1100 °C). This leads to the mixing of $^{40}Ar_E$ hosted within melt inclusions and lattice hosted $^{40}Ar^*$ resulting in elevated apparent ages (Renne *et al.*, 1997).

1.4.2 Inherited Ar

The effects of contamination by older material such as antecrysts and xenocrysts can be a significant problem when attempting to accurately date volcanic eruptions. Single-grain fusion Ar-Ar geochronology has identified contamination in ignimbrite flows, re-worked distal ash-fall deposits (e.g., Ton-That *et al.*, 2001; Hildreth and Wilson, 2007), as well as post-caldera rhyolitic lavas (e.g., Obradovich, 1992; Gansecki *et al.*, 1996; 1998). The term antecryst (after Charlier *et al.*, 2005), is used to define older crystals (representing an earlier stage of magma chamber development), which have become reincorporated into the erupted magma by remelting and disaggregation of their host rocks (partially or completely solidified). They may be partially reset and retain an older core (and inherited $^{40}Ar^*$ component), but continue to grow along with the main phenocryst population. This can be significant in the case of young and/or low K samples, where ingrowth of radiogenic Ar ($^{40}Ar^*$) is comparatively small and the inherited $^{40}Ar^*$ component starts to dominate the overall $^{40}Ar^*$ measurement resulting in ages that are generally too old.

Mechanisms by which antecrysts and/or xenocrysts may become incorporated and distributed amongst a phenocryst population include the cannibalisation of already crystallised material (magma roof or wall and/or host rocks), and the plucking and scavenging of material during deposition. The incorporation of xenocrystic material (e.g., lithic fragments and crystals), can occur during movement of magma towards the surface (e.g., van den Bogaard *et al.*, 1989; Spell and Harrison, 1993; Gansecki *et al.*, 1996), as well as during eruption, caldera collapse and emplacement (e.g., Nielson *et al.*, 1990; Wilson and Hildreth, 1997). Chen *et al.*, (1996), dated sanidine crystals separated from tephra layers erupted from the Mono Craters, California, USA (5000 to 30,000 years ago), and showed that the tephra layers were heavily contaminated by xenocrystic material incorporated during explosive fragmentation, but inferred the rhyolitic domes of the Mono

Craters showed no significant contamination because xenocrysts would be more likely to be reset in slow cooling rhyolitic flows.

Xenocrystic contamination of juvenile material (e.g., pumice) can also occur. For example, van den Bogaard (1995), identified a distinct xenocryst population in crystals separated from mafic phonolite hosted pumice lapilli of the Laacher See Tephra (12, 900 yr BP). The study indicated that ~ 20 % of crystals were xenocrystic in origin, preserved in explosively erupted and thinly deposited units, which were quickly cooled. Wilson and Hildreth (1997; 1998), have also noted the presence of rare xenoliths inside pumice clasts (e.g., metasediments). Mixed juvenile and xenocrystic feldspar populations in pumice lapilli of the Hutenberg tephra (East Eifel Volcanic Field), were identified by van den Bogaard *et al.*, (1989), and were inferred to represent subsurface material, incorporated prior to eruption and contaminating the magma with xenocrysts.

1.4.3 Diffusion of extraneous Ar

Extraneous Ar, either 'inherited' from antecrysts and/or xenocrysts, or $^{40}Ar_E$ diffused into minerals, can yield older than expected Ar-Ar apparent ages if not sufficiently removed (via diffusion) either prior to or immediately following eruption. When considering the diffusive loss of Ar, it is assumed the movement of Ar is controlled by the concentration of Ar in the grain boundary network, which for open systems is considered to be zero. At high temperatures (e.g., magmatic temperatures > 700 °C), Ar rapidly diffusing out of the grain is lost to the 'infinite reservoir' and efficiently removed. Previous studies have shown that this is not always applicable and $^{40}Ar_E$ induced older ages can result from, (1) insufficient removal of grain boundary Ar by grain boundary fluids (e.g., Warren *et al.*, 2012); (2) the assimilation of $^{40}Ar_E$ hosted in fluids driven through bulk rock (e.g., Sherlock *et al.*, 2008), or (3) late magmatic/early sub-solidus alteration by reaction with $^{40}Ar_E$ hosted in fluid

phases (e.g., Landoll *et al.*, 1989). So therefore the question is - can it be assumed that Ar is lost to an infinite reservoir in a 'mush' magma chamber setting? Such as magma systems hosted in the upper crust, which evolve along cyclic episodes of crystallisation (to a rigid, near-solidus state), followed by reheating and rejuvenation (e.g., Fish Canyon magmatic system; Bachmann and Bergantz, 2003; 2004; Charlier *et al.*, 2007; Bachmann *et al.*, 2002; 2007b; Burgisser and Bergantz, 2011).

It is also assumed that bulk diffusion (lattice diffusion) is the dominant process and that the apparent age (concentration of ^{40}Ar) is a function of K concentration, which is assumed constant and to have a homogeneous distribution within the crystal at all times. Although not specifically applied to volcanic minerals, for crystals which have been slowly cooled, previous work has experimentally demonstrated that 'fast-pathways' will allow Ar to diffuse more rapidly than within the bulk lattice by shortening the effective diffusional radius (i.e., maximum distance over which diffusion occurs before Ar leaves the crystal). Therefore the existence of multiple diffusion pathways (e.g., Lee *et al.*, 1995; Clay *et al.*, 2010 and references therein) or domains (e.g., Lovera, 1989), suggests that assuming volume diffusion may not always be applicable. The process of crystal shattering and dispersal of crystal fragments, common during explosive volcanism (e.g., pre- and post-Fish Canyon Tuff eruptions; Bachmann *et al.*, 2002), may offer a 'fast-pathway' for Ar to escape.

The use of diffusion modelling programmes (e.g., DIFFARG, Wheeler, 1996), combined with experimentally derived diffusion parameters (activation energy; E_a and diffusion coefficient; D_0) for different mineral phases (e.g., Foland *et al.*, 1974; Cassata *et al.*, 2009; Wartho *et al.*, 2012), can provide a way of estimating at what time prior to eruption antecrysts and/or xenocrysts were incorporated in the magma (e.g., Gansecki *et al.*, 1996; 1998; Singer *et al.*, 1998; Gardner *et al.*, 2002). When crystals, already containing a $^{40}Ar^*$

signal, are incorporated into a magma they can diffusively lose their radiogenic Ar. Partial resetting of contaminating antecrysts and/or xenocrysts in the magma prior to eruption can result in anomalous single-crystal Ar-Ar ages, which are scattered and slightly older than the juvenile population (e.g., Spell and Harrison, 1993; Gansecki *et al.*, 1996). The interpretation of Ar-Ar ages can be complicated by not knowing exactly what is being analysed (i.e., phenocryst, antecryst, xenocryst or $^{40}Ar_E$), and therefore what geological process, if any, is being recorded.

1.5 Study Aims and Objectives

The main aim of this study was to identify the presence of extraneous Ar ($^{40}Ar_E$ hosted in melt, fluid or mineral inclusions and sources of inherited Ar) within mineral phases and glass separated from the products of both explosive and effusive silicic volcanism, and to identify the impact extraneous Ar contamination has on Ar-Ar age determinations. The study focuses on obtaining both inter- and intra-grain Ar-Ar age information from young volcanic minerals, where extraneous Ar can dominate the overall $^{40}Ar^*$ budget.
Specifically the objectives are:

(1) Develop techniques and methods in identifying extraneous Ar

Ar extraction techniques: Apply a range of Ar extraction techniques (i.e., *in situ* and single-grain fusion) to single crystals separated from juvenile material (pumice) and whole rock ignimbrite, in order to identify possible age variations caused by extraneous Ar.

Compare new Ar-Ar ages with those previously determined by independent techniques: Use pre-existing geochronological data (e.g., K-Ar, Ar-Ar, and U-Pb) where

available to identify possible sources of contamination and determine the source of extraneous Ar contamination (e.g., $^{40}Ar_E$ or inherited Ar).

Mineral phase: Investigate the geochronological information obtained from multiple phases (e.g., co-existing feldspar, biotite and glass), and seek to identify those phases most affected by extraneous Ar contamination.

(2) Evaluate the nature of extraneous Ar in silicic magma systems

Distribution of extraneous Ar: Investigate the distribution of $^{40}Ar_E$ and inherited Ar within the magma chamber and how this impacts on our current understanding of the 'mush' magma chamber setting.

Ar diffusion: Investigate cases of subtle contamination and determine whether $^{40}Ar_E$ or inherited Ar is the cause (i.e., conducting diffusion modelling experiments), and identify geological processes that may be responsible.

Suitable phases for Ar-Ar dating: Use geochronological information to assess how suitable volcanic minerals and glass, separated from silicic volcanic samples, are for precise and accurate Ar-Ar dating.

1.6 Layout of the Thesis

- **Chapter 1** provides an introduction to the study (how and why minerals from silicic volcanic products are routinely used in Ar-Ar geochronology), and the main aims and objectives. The Ar-Ar technique is introduced in terms of its application to volcanic minerals and the problem of extraneous Ar. Further information of the Ar-Ar technique (i.e., sample preparation, Ar extraction, Ar-Ar age calculations), and general methods (i.e., Electron microprobe, X-Ray Fluorescence, DIFFARG modelling program) used in this study are covered in Appendix section A1.

- **Chapter 2** presents a study of the Fish Canyon Magmatic System, USA, detailing previous geochronology, petrology and geochemistry and a new Ar-Ar dataset derived from applying the UV and IR *in situ* laserprobe technique. These new data are discussed in the context of previously reported Ar-Ar and U-Pb ages and the behaviour of extraneous Ar in an archetypal 'mushy' magma chamber.

- **Chapter 3** details previous geochronology, petrology and geochemistry of multiple tuffs and domes of the Yellowstone Plateau Volcanic Field, USA. This chapter discusses a new extensive Ar-Ar (IR laserprobe) single-grain fusion dataset in the context of previous work (K-Ar, Ar-Ar and U-Pb). Ar diffusion modelling is used to determine the nature of extraneous Ar contamination (i.e., $^{40}Ar_E$ or inherited), and how this relates to magma chamber processes. This chapter also details the effects of different sample preparations on Ar-Ar data.

- **Chapter 4** presents a new Ar-Ar (IR laserprobe) single-grain fusion dataset for the Bishop Tuff, Long Valley Caldera, California, USA. Ar-Ar age determinations have been made on crystals separated from juvenile material (pumice) of both

plinian air fall and ignimbrite flow deposits in an attempt to map extraneous Ar contamination throughout the course of a single eruption. This chapter also outlines the challenges faced when dating young volcanic samples, K-poor minerals and the effects of possible alteration on Ar-Ar determined ages.

- **Chapter 5** provides a synthesis of Chapters 2, 3 and 4 and considers extraneous Ar in the context of the causes (e.g., diffusion and solubility of Ar in various mineral phases, geological processes) of extraneous Ar contamination, the affects this contamination has on Ar-Ar ages obtained from silicic volcanic products, and a strategy (including some recommendations) to facilitate future work. This chapter also highlights the key achievements of the study (including new Ar-Ar ages, which will replace outdated K-Ar ages), in relation to the original aims and objectives set, the concluding statements drawn from chapters 2 to 4, and finally outlines avenues for further work.

Chapter 2. Application of Ar-Ar dating to minerals of the Fish Canyon magmatic system: a UV and IR *in situ* approach.

2.1 Introduction

The eruptive products of the Fish Canyon magmatic system in the San Juan volcanic field (south-western Colorado, USA) comprise the Pagosa Peak Dacite (PPD), the Fish Canyon Tuff (FCT) and the Nutras Creek Dacite (NCD), and were emplaced at ~ 28 Ma. It has been the focus of mineralogical studies (e.g., Whitney and Stormer, 1985; Bachmann *et al.*, 2002; 2007); geochronological studies (e.g., Dazé *et al.*, 2003 and references there in; Spell and McDougal, 2003; Bachmann *et al.*, 2007b; Renne *et al.*, 2010; 2011; Rivera *et al.*, 2011 and references therein), and shallow magmatic processes and magma chamber evolution (e.g., Lipman *et al.*, 1997; Bachmann and Bergantz, 2003; 2008; Bachmann *et al.*, 2005; 2007; Charlier *et al.*, 2007; Lipman and McIntosh, 2008).

This study investigates the FCT, PPD and NCD for the presence of extraneous Ar (excess and inherited), using *in situ* laser extraction techniques (both ultraviolet and infrared laser systems). Contamination has been identified in the eruptive products of similar systems such as Toba (e.g., Chesner, 1998; Gardner *et al.*, 2002; Thomas *et al.*, 2003) using single grain, and bulk Ar-Ar techniques. The ultraviolet (UV) *in situ* laserprobe method in particular, has been effective in extracting Ar from transparent minerals, such as K-feldspar (e.g., Kelley *et al.*, 1994; Wartho *et al.*, 1999), and in providing detailed age patterns at the single-grain scale, which may have otherwise gone undetected (e.g., Reddy *et al.*, 1999; 2001; Boven *et al.*, 2001; Sherlock and Kelley, 2002; Sherlock *et al.*, 1999;

2005; 2008). The UV laser can be used to detect fine-scale variation in age or apparent age in minerals. Minerals can preserve age variation caused by pockets of $^{40}Ar_E$, resulting in geologically meaningless ages, or the presence of inherited Ar, which could date a previous stage of magma chamber crystallisation.

To date, there has been no study which has investigated minerals of the Fish Canyon magmatic system using the *in situ* laserprobe technique. This study has utilised both the UV and infrared (IR) laser extraction systems to investigate age variations at both an inter- and intra-grain level. These two techniques have their advantages and disadvantages, for example the user has better control over analysis position using a UV laser, which also couples well with clear/transparent minerals (e.g., feldspars), however locating crystals which are large enough to allow sufficient material to be ablated, thus releasing measurable Ar gas (UV laser removes *ca.* 10 μm of the mineral surface), can be difficult. In comparison, the IR laser approach, which couples poorly with transparent minerals does allow for more gas to be released (by melting of the sample rather than ablation), but can cause heating of the area surrounding the laser pit. The overall aim of this study is to apply a range of *in situ* laser probe techniques (UV laser ablation and IR laser spot analysis) to minerals of the Fish Canyon magmatic system in order to test the applicability of these methods to material < 30 Ma, and to identify the presence of extraneous Ar ($^{40}Ar_E$ hosted in melt, fluid or mineral inclusions and/or inherited Ar) within crystals.

2.2 Background

2.2.1 Laser-based extraction techniques

The application of laser probe technology to Ar-Ar geochronology greatly enhanced the technique by allowing the direct investigation of small multigrain samples, single crystals

and/or spatially distinct parts of crystals (McDougall and Harrison, 1999). One key advantage of laser probe extraction is the precision, due to the narrow beam of the laser, which can be achieved by permitting the release of Ar from a relatively small amount of sample material (compared with bulk furnace heating experiments). Ar-Ar laser probe dating by total fusion (either by complete melting of the mineral grain in one heating step, or by heating over a number of steps to release the Ar incrementally) is useful for assessing the gross inter-grain age variations and the presence (or absence) of extraneous Ar. However, these approaches are indiscriminate in terms of what is actually sampled within the mineral (e.g., inclusions), and multiple Ar components (including any contamination) can be homogenised resulting in the loss of valuable information. These data, where possible, should therefore be used in conjunction with another technique that can resolve the differences within single grains.

In situ laser extraction is a useful tool for investigating $^{40}Ar_E$ distributions within minerals, and can provide information about the relationship between $^{40}Ar_E$ diffusion through the mineral lattice and its incorporation into melt, fluid and solid inclusions within minerals (Kelley, 2002). The UV laser system uses short high-energy pulses to extract Ar from small areas of sample without considerable heating of the surrounding area. Laser pulses can also be achieved using continuous wave lasers (e.g., infrared laser) fitted with a shuttering system (McDougall and Harrison, 1999). This study has utilised both the UV and infrared (IR) laser extraction systems to investigate age variations at both an inter- and intra-grain level.

2.2.1.1 UV laser extraction

Previous work has demonstrated the advantages of the UV laser system and the absorbance of the UV wavelength by all natural mineral species, including transparent minerals such as feldspars (e.g., Kelley *et al.*, 1994). Boven *et al.*, (2001) released Ar from spatially discrete parts of individual plagioclase crystals to illustrate the correlation between age variation and heterogeneous $^{40}Ar_E$ contained within inclusions. Reddy *et al.*, (1999; 2001) combined UV *in situ* ages with microstructural studies (e.g., high resolution SEM) to investigate controls (e.g., deformation-induced microstructures) on the distribution of apparent Ar-Ar ages at the intra-grain level, and a study by Sherlock *et al.*, (2008) used UV *in situ* analysis to reveal complex patterns detailing periodic assimilation of $^{40}Ar_E$ during slate formation, which was not detected by incremental heating or total fusion methods. The UV *in situ* method has also been used to investigate $^{40}Ar_E$ contamination in high-pressure metamorphic rocks (e.g., Sherlock and Arnaud, 1999; Sherlock *et al.*, 1999; Sherlock and Kelley, 2002; Warren *et al.*, 2011), K-feldspar overgrowths (e.g., Sherlock *et al.*, 2005), as well as Ar diffusion in gem quality orthoclase (e.g., Arnaud and Kelley, 1997; Wartho *et al.*, 1999).

2.2.1.2 IR laser extraction

In comparison to the UV laser method, the application of the IR *in situ* method has limited applicability to minerals that have low absorption (colourless minerals e.g., feldspars) of the IR wavelength (McDougall and Harrison, 1999), although it may be possible, if a large enough area can be targeted, to release enough Ar gas for a successful measurement. However, the heating of, and Ar loss, from surrounding areas should also be considered, as melting of more susceptible minerals or groundmass outside the physical extent of the laser spot may lead to erroneous Ar-Ar ages. Experimental work has showed that dark

inclusions or adjacent minerals may melt at distances of up to 0.5 mm from the laser spot in a feldspar grain (e.g., Kelley *et al.*, 1994).

2.2.2 Sample size

The amount of sample required for a successful Ar-Ar age measurement at an appropriate level of precision depends upon a number of factors, including the age and potassium content of the sample. The *in situ* technique has previously been applied to samples ranging in age from ~ 50 Ma (e.g., Putlitz *et al.*, 2005) to over 400 Ma (e.g., Sherlock *et al.*, 2005), so therefore the challenge here is to apply the *in situ* technique to samples < 30 Ma. To date younger and/or low potassium samples, larger areas of mineral must be melted or ablated. Preliminary experiments at the start of this study showed that single spots (~ 120 μm) would not release sufficient radiogenic Ar ($^{40}Ar^*$) and ^{39}Ar (nucleogenic Ar), and therefore larger areas (rastering UV laser) or multiple spots (IR laser) would be required.

2.2.3 High-sensitivity, high-resolution mass spectrometer: the Nu Instruments Noblesse

To ensure the detection of small $^{40}Ar^*$ component over a background signal of atmospheric Ar derived from the sample itself, or from the blank of the extraction system, a sensitive mass spectrometer should be used to measure Ar isotopes. For this study the UV laser probe system has been coupled with the Nu Instruments Noblesse mass spectrometer, which has a low volume extraction line (minimises the internal volume contributions to blank level), and is fitted with detectors for measuring very small ion beams (high-sensitivity of 1.13×10^{-15} cc per count on ^{40}Ar).

Using an instrument with suitable sensitivity is extremely important, especially with regards to the ^{36}Ar measurement, which is essentially considered to be of atmospheric origin. Corrections are made for contaminating atmospheric Ar contained within the sample or contributed from the vacuum system in which the gas is extracted from the sample. Therefore, elevated ^{36}Ar measurements will magnify that part of the ^{40}Ar signal which is atmospheric in composition and lead to over-correction, which can have a detrimental effect on young and/or K-poor samples where only a small quantity of accumulated $^{40}Ar^*$ is present. This is particularly relevant to the minerals of the Fish Canyon magmatic system, which yield ages ~ 28 Ma, and both K-rich (i.e., sanidine) and K-poor (i.e., plagioclase) have previously been dated. In addition, this instrument is also capable of mass resolving measured isotopes of Ar as well as resolving interfering peaks (e.g., hydrocarbons), which may have a similar mass to Ar isotopes of interest (e.g., C^3, H or ^{35}Cl can interfere with ^{36}Ar).

2.3 Geological setting

2.3.1 Fish Canyon magmatic system

The San Juan region (south-western Colorado, USA) contains the largest erosional remnant of the mid-Tertiary volcanic field, which once formed continuous cover across much of the Colorado Rocky Mountains and into northern New Mexico (Fig. 2.1a). Numerous large-volume ignimbrite eruptions and associated caldera collapse occurred within the San Juan region of which the Fish Canyon magmatic system is one of nine major ash-flow tuffs and related lavas. Scattered intermediate-composition volcanic centres (dominantly andesite, lesser dacite and minor rhyolite), erupted lava flows and volcaniclastic breccia in the San Juan region (starting ca. 35 to 34 Ma), followed by large crystal rich dacite ignimbrite eruptions from northern (e.g., Saguache Creek Tuff; ~ 32 Ma), and south eastern clusters

(e.g., Platoro caldera complex; 30 to 28 Ma) (Bachmann, 2001; Lipman and McIntosh, 2008). The Fish Canyon magmatic system produced in rapid succession, three compositionally identical units, which were erupted from the La Garita caldera and emplaced ~28 Ma (Fig. 2.1b) (Bachmann, 2001; Bachmann *et al.*, 2007b).

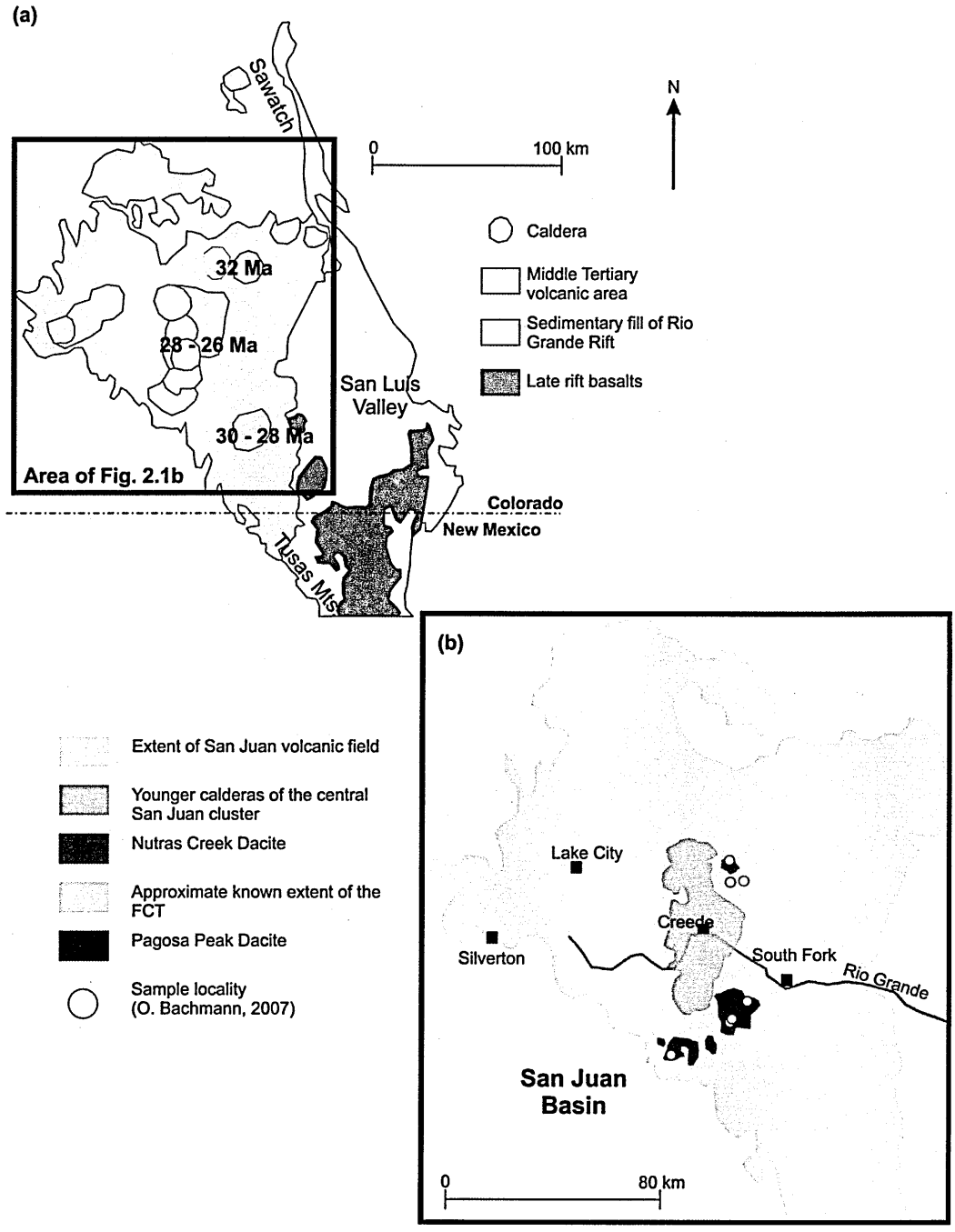

Figure 2.1. (a) Map of Southern Rocky Mountain Volcanic Field, showing ignimbrite calderas and approximate time span active (Ma), inferred original extent of mid-Tertiary volcanic cover and late rift basalts and sedimentary fill of Rio Grande rift zone. Black box indicates area of Fig. 2.1b

(*Fig. 2.1 cont.*) (redrawn and modified after Lipman and McIntosh, 2008); (b) Map showing the preserved extent of the San Juan Volcanic Field and approximate distribution of the eruptive units of the Fish Canyon magmatic system. Sample localities (of O. Bachmann, 2001; 2007), are indicated by yellow circles. (redrawn and modified after Bachmann *et al.*, 2007b).

2.3.2 The Fish Canyon magma body

The Fish Canyon magma (dacitic in bulk composition) is characterised by its high crystal content (~ 40 to 45 %) set in high-silica (~ 76 to 78 % SiO_2) interstitial rhyolitic melt (Lipman *et al.*, 1997; Bachmann *et al.*, 2002; Charlier *et al.*, 2007). This compositional signal can be identified for each eruptive unit of the Fish Canyon magmatic system; the Pagosa Peak Dacite (PPD), the Fish Canyon Tuff (FCT) and the Nutras Creek Dacite (NCD). The Fish Canyon magma chamber is thought to have been weakly heterogeneous but did not erupt material in a systematic fashion, and shows little evidence for the presence of significant pre-eruptive compositional gradients (in contrast to The Bishop Tuff deposits; e.g., Hildreth and Wilson, 2007).

Extensive sampling and analysis of various FCT samples (sample localities cover a wide geographical area), suggests that compositional variation can be explained by syn-eruptive crystal-ash fractionation (Whitney and Stormer, 1985; Bachmann *et al.*, 2002), rather than due to magma mixing and mingling with a more mafic component prior to eruption. Andesite inclusions identified in late erupted intracaldera FCT samples provide evidence for such a process occurring before eruption took place, but the mafic component is not considered significant enough to induce the variability seen (Bachmann *et al.*, 2002).

2.3.2.1 The 'mush' model

Recent work on the Fish Canyon magmatic system hypothesises that it conforms with the 'mush' model scenario, whereby batholith sized magma bodies hosted in the upper crust, evolve along cyclic episodes of magma cooling (to a rigid, near-solidus state), followed by reheating and remelting (Bachmann and Bergantz, 2003; Bachmann *et al.*, 2007b; Burgisser and Bergantz, 2011). The growth of amphibole and biotite occurred at the same time as the generation of new melt by partial remelting of feldspar and quartz (Charlier *et al.*, 2007; Bachmann, 2001; Bachmann *et al.*, 2007b), suggesting rejuvenation of the nearly-solidified crystal mush by progressive reheating from ~ 720 to ~ 760 °C (inferred from Al-zoning profiles in hornblendes) prior to eruption (Charlier *et al.*, 2007; Bachmann *et al.*, 2007b). The lack of obvious thermal or compositional zoning in the deposits, suggests the Fish Canyon magma must have retained a high volatile content within the 'mush' body (Bachmann and Bergantz, 2003).

Processes including 'defrosting' (Mahood, 1990), 'gas sparging' (Bachmann and Bergantz, 2003; 2006), and more recently 'stable front remobilisation' (Burgisser and Bergantz, 2011), have all been suggested to account for the reheating and rejuvenation of the partially solidified crystal mush. The model described by Mahood (1990), suggests portions of magma, which have been "frozen" as a crystallized rind or immobile mush, can be "defrosted" by propagation of a thermal pulse from deeper levels, possibly as a result of mafic intrusions. This remelted material could either erupt soon after formation, or reside in the magma chamber as a liquid for a considerable period of time.

Bachmann and Bergantz (2003), suggested that mafic melt input and associated heat, specifically for the Fish Canyon magmatic system, was minor and that rejuvenation (modelled to occur on a timescale of 150 to 200 kyr) could be better achieved by the

transfer of an exsolved gas phase originating at the base and passing upwards through the silicic crystal mush (Fig. 2.2a). This model also accounts for the addition of a minor mafic component, which would have been required by crystallising hornblende and biotite during reheating, and perhaps not achievable through self-mixing or conduction alone. In contrast a recent model proposed by Burgisser and Bergantz (2011), offers an alternative to the 'gas sparging' mechanism. The 'stable front remobilisation' mechanism (Fig. 2.2b), similar to the 'defrosting' model of Mahood (1990), describes a mobile layer (reheated from below by a fresh magma intrusion), which can then rejuvenate the crystal mush magma body. Rejuvenation can occur by either growth of this mobile layer, until it fills the magma chamber and all pre-existing mush has been remobilised, or by the mobile layer buoyantly ascending into the overlying crystal mush, and causing the mush to be overturned (Burgisser and Bergantz (2011) refer to this process as 'unzipping'). By applying this mechanism specifically to the Fish Canyon, Burgisser and Bergantz (2011) suggest the mushy magma chamber could have been remobilised in < 200 years, compared to 150 to 200 kyr proposed for rejuvenation by 'gas sparging', and that the unzipping process is likely to be repeated until either eruption or solidification of the mush occurs.

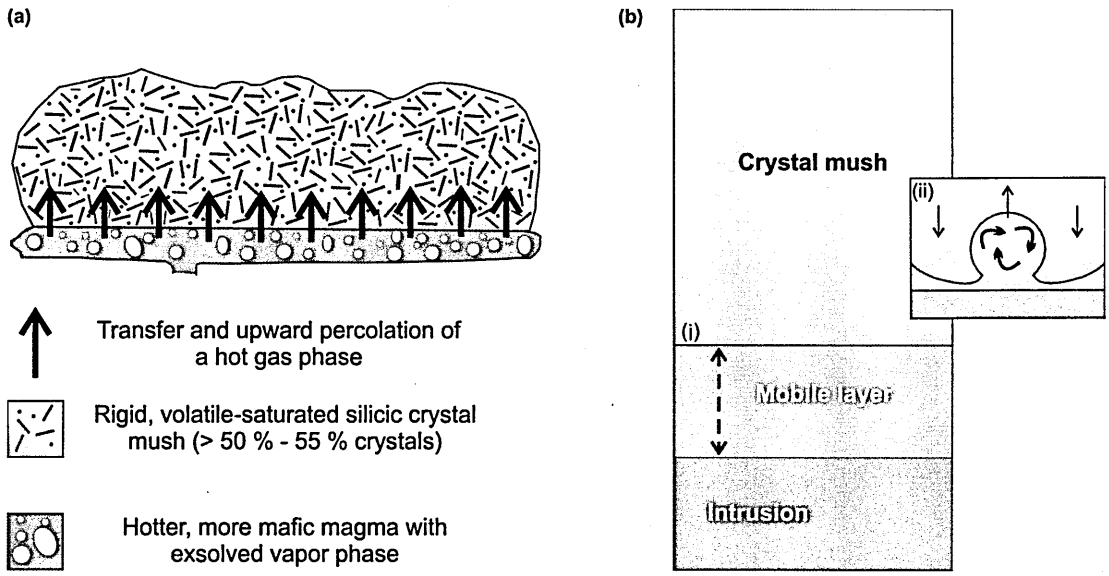

Figure 2.2. Schematic diagrams illustrating the concept of: (a) the 'gas sparging' model of Bachmann and Bergantz (2003). Rejuvenation of the silicic crystal mush occurs as a result of an exsolved vapour phase, sourced from a shallow intrusion of volatile-rich mafic magma, percolating upwards (redrawn after Bachmann and Bergantz, 2003); (b) the 'stable front remobilisation' model of Burgisser and Bergantz (2011). Rejuvenation of the silicic crystal mush occurs as a result of an intrusion heating the base of the mush magma chamber thus creating a mobile layer. Remobilisation of the mush occurs by (i) growth of this mobile layer, and/or (ii) unzipping, whereby the mobile layer buoyantly rises into the mush (redrawn after Burgisser and Bergantz, 2011).

2.3.2.2 The Fish Canyon Tuff

The Fish Canyon tuff, a silicic volcanic unit, emplaced as highly mobile ash-flows, during the collapse of the La Garita caldera, forms the bulk of erupted volume (> 95 %) and covers an estimated ~ 5000 km^3 (Lipman *et al.*, 1997; Bachmann *et al.*, 2002; Bachmann *et al.*, 2007). The predominantly welded ash-flow unit has a basal vitrophyre (< 10 m thickness), which is underlain by plinian and pyroclastic surge deposits (Whitney and Stormer, 1985). The tuff is dacitic in bulk composition, with a highly evolved rhyolitic glass phase and contains a near-solidus mineral assemblage comprising plagioclase, K-feldspar (sanidine), biotite, hornblende, sphene, zircon, allanite and other exotic minor REE-bearing accessory phases (Hurford and Hammerschmidt, 1985; Bachmann *et al.*, 2002; Dazé *et al.*, 2003).

2.3.2.3 The Pagosa Peak Dacite

The voluminous (200 km^3) and less explosive precaldera Pagosa Peak Dacite deposits are preserved around the south-eastern edge of the La Garita caldera and are thought to be the product of low energy pyroclastic fountaining (Lipman *et al.*, 1997; Bachmann *et al.*, 2002). The pumices have a composition similar to that of Fish Canyon magma. In addition to this they also preserve magmatic textures, which have been destroyed in the FCT due to crystal shattering and dispersal upon eruption (Bachmann *et al.*, 2002). Although the PPD is mostly homogeneous, it also contains rare andesite blebs (~ 58 % SiO_2) suggesting mingling occurred with a mafic component prior to eruption (Lipman *et al.*, 1997). The FCT sits directly on top of the dacite and there is no evidence of erosion, soil formation or sediment deposition. The lack of such evidence to support a significant time break suggests there must have been a relatively short time interval between the deposition of the first two units. Fumarolic alteration, and a welded base of the FCT, which might be expected if the PPD was still hot at the time of tuff emplacement, is absent suggesting that a time gap in the order of months, ruling out erosion or soil formation, could be assumed (Bachmann, 2001; Bachmann *et al.*, 2007b).

2.3.2.4 The Nutras Creek Dacite

The Nutras Creek Dacite is a small post-FCT lava flow (< 1 km^3), which overlies the intracaldera tuff on the northern flank of the resurgent dome of the La Garita caldera. It is similar to the PPD, erupting with relatively low energy and containing non-fragmented material of Fish Canyon magma. The length of a time break between the tuff and the NCD could not be ascertained from field relations (Bachmann, 2001; Bachmann *et al.*, 2007b).

2.4 Previous work

2.4.1 Petrology

A detailed petrological study already exists for the minerals of the Fish Canyon magmatic system (e.g., Whitney and Stormer, 1985; Bachmann *et al.*, 2002; 2007b) and the following summary of previous findings focuses on minerals used in this study. Phenocrysts of feldspar (sanidine and plagioclase) and quartz appear to be corroded and contain melt pockets. Resorption textures have been inferred to be due to the melting of the crystal mush rather than eruption induced (Bachmann *et al.*, 2002). In some large sanidine grains melt pockets contain plagioclase inclusions (irregular shaped and sub- to euhedral laths), and more rarely other phases (e.g., biotite). Plagioclase inclusions may be concentrated at the rims of host crystals, resulting in complex Ba zoning (Bachmann *et al.*, 2007b). Euhedral biotite show minor reaction with surrounding melt and inclusions of apatite and plagioclase are common. Due to crystal shattering and dispersal related to magma fragmentation of the FCT, corrosion textures in sanidine and quartz are not so readily seen, although in the late-erupted (intracaldera) units, sanidine is sometimes overgrown by euhedral granophyric rims (Bachmann *et al.*, 2007b).

Interstitial glass in most cases is devitrified except in basal vitrophyres of PPD and FCT where it is preserved. The fine-grained matrix of non-devitrified PPD mostly contains broken phenocrysts, fine crystal dust and angular glass shards. Devitrified samples contain spherulites and large variations in chlorine content of the groundmass due to devitrification (Bachmann *et al.*, 2002). Fine-scale granophyric intergrowths of quartz and sanidine exist as overgrowths around pre-existing feldspar crystals (in particular sanidine; Bachmann *et al.*, 2002), as well as filling open fractures and cracks in crystals in late erupted FC magmatic system material (e.g., NCD) (Lipman *et al.*, 1997; Bachmann *et al.*, 2002).

2.4.2 Geochronology

Determining the primary age of the FCT has been the focus of numerous studies using a range of techniques, for example, fission-track (Cebula *et al.*, 1986 cited in Dazé *et al.*, 2003); U-Pb (e.g., Lanphere and Baadsgaard, 2001; Villeneuve *et al.*, 2000; Schmitz and Bowring, 2001; Min *et al.*, 2001; Bachmann *et al.*, 2007b); Rb-Sr (e.g., Lanphere and Baadsgaard, 200); U/Th-He (e.g., Reiners and Farley, 1999 and Reiners *et al.*, 2002 cited in Spell and McDougal, 2003), and K-Ar (Hurford and Hammerschmidt, 1985). Ages obtained for the various units of the Fish Canyon magmatic system range from 26.78 ± 0.26 to 30.1 ± 0.5 Ma (summarised in Table A5.1a; Appendix section A5).

Various reasons have been suggested to account for the inconsistency that exists between published Ar-Ar ages of FC minerals including: instrument precision and accuracy; preparation of separates resulting in 'purity' issues on a single-grain (e.g., Spell and McDougall, 2003) and bulk separate level (e.g., Dazé *et al.*, 2003), or ^{39}Ar and ^{37}Ar recoil loss (displacement of ^{39}Ar and ^{37}Ar during neutron irradiation; e.g., Jourdan *et al.*, 2007). The age difference that exists between the most precise methods (K-Ar and Ar-Ar eruption ages and U-Pb zircon crystallisation ages) has previously been explained in terms of calibration problems and/or uncertainties in decay constants providing a source of error (Renne *et al.*, 2010; 2011), or the assumption that some mineral phases are more likely to recall multiple pre-eruptive crystallisation episodes and record a complex crystallisation history (e.g., zircon; Charlier *et al.*, 2005), than those used for K-Ar or Ar-Ar dating (e.g., feldspar).

2.4.3 Ar-Ar standards: the Fish Canyon sanidine (FCs) and biotite

Ar-Ar ages are calculated with reference to independent age determinations for standard minerals. The Fish Canyon sanidine (FCs) has been repeatedly used as a interlaboratory standard for Ar-Ar dating (summarised in Table A5.1b), and its age has been extensively researched and reported in the literature (see Cebula *et al.*, 1986; Renne *et al.*, 1998; Lanphere and Baadsgaard, 2001; Schmitz and Bowring, 2001; Spell and McDougall, 2003; Dazé *et al.*, 2003; Kuiper *et al.*, 2004; 2008; Jourdan and Renne, 2007; Renne *et al.*, 2010, Channell *et al.*, 2010; Rivera *et al.*, 2011). Primary age determination (by K-Ar) of the FCT biotite (including standard 79COLE-5) range from ~ 27.15 to ~ 27.9 Ma, and Ar-Ar ages determined by total fusion and incremental heating (including standards 79COLE-5, FCT-3, FCT87 and FCT92) range from ~ 27.35 to ~ 28.25 Ma (Baksi *et al.*, 1996; Lanphere and Baadsgaard, 2001; Dazé *et al.*, 2003 and references therein; Bachmann *et al.*, 2007b; summarised in Table A5.1b). The detailed intercalibration study of Dazé *et al.*, (2003) outlined the limited use of the FCT-3 biotite standard based on uncertainties associated with geological factors, such as inclusions and possible $^{40}Ar_E$ contamination.

A sample needs to meet certain criteria before it can be considered a suitable standard for Ar-Ar dating and the general consensus is that the criterion of homogeneity for standards at the single-crystal level is met by the FCs (McDougall and Harrison, 1999). Ar-Ar age spectra (Renne *et al.*, 1998; Lanphere and Baadsgaard, 2001; Spell and McDougall, 2003; Bachmann *et al.*, 2007b), and total fusion grain-to-grain reproducibility studies (e.g., Baksi *et al.*, 1996; Renne *et al.*, 1998; Jourdan and Renne, 2007), have also been published in support of the FCs homogeneity.

Despite this agreement Bachmann *et al.*, (2002) revealed textural variability of FCT phenocrysts, and multiple sanidine crystals analysed contained numerous mineral

inclusions and internal melt pools. Dazé *et al.*, (2003) also reported grains with heterogeneous potassium distribution. Spell and McDougall (2003) commented on 'minor structure' present in Ar-Ar step-heating results and suggested slightly higher initial ages, followed by some variation during the intermediate temperature steps and a general increase in age with increasing temperature, may be related to $^{40}Ar_E$ hosted by melt-inclusions. In addition Spell and McDougall (2003) noted that total fusion experiments of large sample splits (tens of milligrams) highlighted no significant inhomogeneities, whereas laser fusion of 1 to ~ 50 single crystal grains did.

In recent years the age of FCs has been determined using a number of alternative decay constants, which update the value of 5.543×10^{-10} a^{-1} recommended by Steiger and Jäger (1977). Kuiper *et al.*, (2008) prefer an FCs age of 28.20 ± 0.02 Ma, astronomically tuned to sedimentary cycles in the Messinian Melilla Basin, Morocco, and calculated relative to the total ^{40}K decay constant of 5.463×10^{-10} a^{-1} published by Min *et al.*, (2000). Rivera *et al.*, (2011) independently verified the Kuiper *et al.*, (2008) FCs age with 28.17 ± 0.03 Ma, again using the ^{40}K decay constant of Min *et al.*, (2000). Renne *et al.*, (2010) prefer the age of 28.31 ± 0.04 Ma calculated relative to the total ^{40}K decay constant of 5.549×10^{-10} a^{-1} (Renne *et al.*, 2010), which is slightly older than ages published by Kuiper *et al.*, (2008) and Rivera *et al.*, (2011).

Discussions on the accuracy and precision of the decay constants in conjunction with the dating of the FCT has previously been heavily reviewed (e.g., Renne *et al.*, 1998; Lanphere and Dalrymple, 2000; Min *et al.*, 2000; Villeneuve *et al.*, 2000; Schmitz and Bowring, 2001; Renne *et al.*, 2010; 2011), because decay constant values have multiple appearances in the Ar-Ar age equation, and therefore has an effect on the final age calculated (Renne *et al.*, 1998). New ages presented in this thesis have been calculated using the newly determined ^{40}K decay constant of Renne *et al.*, (2010). Previously determined ages made

by Bachmann *et al.*, (2007b) have been recalculated in this thesis using the new ^{40}K decay constant value so direct comparison can be made between data collected on the same samples.

2.5 Materials and methods

2.5.1 Sample descriptions

Samples used in this study formed part of Dr Olivier Bachmann's collection, which have previously been worked on (e.g., Bachmann, 2001; Bachmann *et al.*, 2007b; Charlier *et al.*, 2007). Table 2.1 summarises the lithology, groundmass and main phenocryst phases present in each sample analysed by both UV and IR *in situ* laser ablation. See Appendix section A2.2 for thin section descriptions and representative thin section and EMP images.

Table 2.1. Lithology, groundmass and main phenocryst descriptions for Fish Canyon polished thick sections used in this study (PPD = Pagosa Peak Dacite; FCT = Fish Canyon Tuff and NCD = Nutras Creek Dacite).

Sample	Formation	Lithology	Assemblage	
			Groundmass	*Main Phenocryst*
BFC83	PPD	Dacite	Silicic rhyolite glass	Plagioclase + Alkali feldspar + biotite
BFC196	PPD	Dacite	Silicic rhyolite glass	Plagioclase + Alkali feldspar + biotite
BFC171	PPD	Dacite	Silicic rhyolite glass	Plagioclase + Alkali feldspar + biotite
PCB 1	PPD	Dacite	Silicic rhyolite glass	Plagioclase + Alkali feldspar
BFC129	FCT	Tuff	Silicic rhyolite glass	Plagioclase + biotite
BFC191	FCT	Tuff	Silicic rhyolite glass	Plagioclase + biotite
BFC115	NCD	Dacite	Silicic rhyolite glass	Plagioclase + Alkali feldspar + biotite

2.5.2 Sample preparation and methods of chemical analysis

Whole rock samples were not available for this study and therefore major and trace element chemistry pertaining to the samples used are not reported here. For XRF data

relating to samples used in this study refer to Bachmann (2001). Electron microprobe (Cameca SX100) analysis of individual feldspar and biotite crystals were carried out to determine the composition of the feldspar (e.g., Ca-rich or K-rich), K content of the biotite, the nature of any inclusions, compositional zonation and evidence of alteration. Average mean probe analyses for each sample are listed in Tables 2.2 to 2.4 (section 2.6.1).

2.5.3 Sample preparation for Ar-Ar analysis

Sample off-cuts acquired from the collection belonging to Dr Olivier Bachmann (see Bachmann, 2001), and previously analysed by Charlier *et al.*, (2007) were used to make polished thick sections (~ 350 μm thickness), which were prepared for Ar-Ar analysis as outlined in Appendix section A1.7.1. Foil wrapped samples were cadmium shielded and irradiated for 16.67 hrs (50 MWH) at McMaster reactor (Canada). Neutron flux was monitored with biotite standard GA15-50, which has an age of 99.769 ± 0.108 Ma calculated relative to the ^{40}Ar decay constant, $5.549 \times 10^{-10} \pm 0.009 \times 10^{-10}$ a^{-1} (Renne *et al.*, 2010).

2.5.4 Analytical methods: Ar-Ar age determinations

To investigate age variations at both the inter- and intra-grain level, polished thick sections (~ 350 μm thickness) have been analysed using two different laser extraction systems: New Wave Instruments 213 nm, pulsed Nd-YAG laser coupled with a Nu Instruments Noblesse noble gas mass spectrometer (used for UV *in situ* analysis), and SPI 1090 nm diode fibre IR laser (with fixed spot size of 50 μm) coupled with a MAP-215-50 noble gas mass spectrometer (used for multiple IR spot analysis) following methods outlined in Appendix section A1.3. The full data set, including average blank levels and calculated *J*-values used for data processing raw data can be found in Appendix section A3. Analyses

corrected for blank levels, ^{37}Ar decay (34.95 ± 0.08 d; Renne *et al.*, 2001), and neutron induced interference reactions. The following correction factors were used: $(^{39}Ar/^{37}Ar)_{Ca}$ = 0.00065 ± 0.00003, $(^{36}Ar/^{37}Ar)_{Ca}$ = 0.000265 ± 0.000001, $(^{40}Ar/^{39}Ar)_{K}$ = 0.0085 ± 0.00004, based on analysis of Ca and K salts. Extracted gases were cleaned by two SAES AP10-N getters (one at 450 °C and one at room temperature), and three SAES AP10 getters (one at 450 °C and two at room temperature) prior to automatic inlet for the New Instruments Noblesse and MAP-215-50 noble gas mass spectrometers respectively (see Appendix section A1.3.3). All reported errors are 2σ unless otherwise stated.

2.6 Results

2.6.1 Sample chemistry: EMP

Mean electron microprobe analysis (EMP) results for individual sanidine, plagioclase and biotite mineral phases for samples of the Fish Canyon magmatic system (BFC83, BFC196, BFC171, PCB 1, BFC129, BFC191 and BFC115) are listed in summary Table 2.2, for full results tables see Appendix section A4.1.2. In addition, several feldspar crystals were selected for rim to core analysis. Data points along the transect that had low totals (deviation > 2 % either way from 100 %) due to uneven sample surface or accidental analysis of micro-inclusions were removed.

2.6.1.1 Pagosa Peak Dacite

Mean silica contents, determined by EMP for feldspar (sanidine and plagioclase), and biotite range 60.52 % to 65.39 %, and 38.77 % to 39.22 % respectively for Pagosa Peak Dacite samples (BFC83, BFC196, BFC171 and PCB 1). Mean K_2O contents for sanidine,

plagioclase and biotite are 12.40 %, 0.95 % and 9.49 % respectively. Feldspar composition is bimodal, and either sanidine (Or_{65} to Or_{77}), or plagioclase (An_{20} to An_{40}; Fig. 2.3).

Table 2.2. Mean electron microprobe (bold, wt. %) analysis of Pagosa Peak Dacite (BFC83; BFC196; BFC171 and PCB 1), Fish Canyon Tuff (BFC129 and BFC191), and Nutras Creek Dacite (BFC115) samples. The standard deviation of the mean is listed below the mean value. Several crystals analysed contained both Ca- and K-rich zones and are not included in the summary below. Examples have instead been displayed in Figure 2.4, and detailed in full in Appendix section A4.1.2.

Sample	Phase	SiO_2	TiO_2	Al_2O_3	FeO	MnO	MgO	CaO	Na_2O	K_2O	BaO	SrO	F	Cl	Total
BFC83	Biotite*	**39.22**	**4.65**	**13.64**	**16.32**	**0.36**	**14.80**	**0.02**	**0.45**	**9.49**	**0.31**	**0.03**	**0.54**	**0.17**	**96.58**
	n = 39	0.22	0.11	0.18	0.18	0.02	0.17	0.01	0.04	0.09	0.13	0.03	0.09	0.01	0.31
BFC83	Sanidine	**65.39**	**0.01**	**18.45**	**0.12**	**0.01**	**0.00**	**0.18**	**2.72**	**12.40**	**0.59**	**0.11**	**0.01**	**0.00**	**99.90**
	n = 30	0.49	0.01	0.17	0.01	0.01	0.00	0.02	0.12	0.22	0.48	0.04	0.03	0.00	0.20
	Plagioclase	**61.16**	**0.01**	**23.80**	**0.24**	**0.00**	**0.01**	**6.20**	**7.40**	**0.95**	**0.05**	**0.15**	**0.02**	**0.00**	**99.95**
	n = 14	0.80	0.01	0.60	0.03	0.00	0.01	0.47	0.28	0.17	0.03	0.06	0.02	0.01	0.33
BFC196	Biotite*	**38.77**	**4.63**	**13.68**	**16.62**	**0.36**	**14.91**	**0.03**	**0.43**	**9.57**	**0.28**	**0.02**	**0.54**	**0.17**	**95.88**
	n = 26	0.28	0.11	0.13	0.23	0.02	0.19	0.03	0.03	0.06	0.06	0.02	0.09	0.01	0.45
	Plagioclase	**60.52**	**0.01**	**24.52**	**0.23**	**0.00**	**0.01**	**6.40**	**7.15**	**0.91**	**0.05**	**0.18**	**0.01**	**0.00**	**99.24**
	n = 11	0.39	0.01	0.26	0.01	0.01	0.01	0.31	0.18	0.07	0.02	0.04	0.01	0.00	0.15
BFC171	Biotite	**39.38**	**4.47**	**13.45**	**16.28**	**0.34**	**14.90**	**0.06**	**0.41**	**9.35**	**0.29**	**0.03**	**0.76**	**0.17**	**96.59**
	n = 15	0.30	0.31	0.43	0.35	0.03	0.17	0.02	0.06	0.34	0.13	0.03	0.20	0.01	0.57
BFC171	Plagioclase	**60.70**	**0.02**	**24.19**	**0.22**	**0.00**	**0.01**	**6.26**	**7.52**	**0.87**	**0.03**	**0.17**	**0.01**	**0.00**	**100.23**
	n = 16	0.61	0.02	0.38	0.02	0.01	0.01	0.43	0.19	0.08	0.02	0.02	0.02	0.00	0.25
PCB 1	Sanidine	**65.19**	**0.02**	**18.68**	**0.12**	**0.00**	**0.00**	**0.34**	**3.34**	**11.26**	**0.89**	**0.14**	**0.02**	**0.00**	**99.84**
	n = 34	0.61	0.02	0.74	0.03	0.00	0.00	0.79	0.73	1.61	0.32	0.03	0.03	0.00	0.20
	Plagioclase	**61.32**	**0.01**	**23.68**	**0.29**	**0.00**	**0.01**	**6.04**	**7.51**	**0.91**	**0.03**	**0.15**	**0.03**	**0.00**	**99.91**
	n = 27	0.93	0.03	0.84	0.36	0.01	0.01	0.64	0.18	0.11	0.02	0.03	0.04	0.00	0.30
BFC129	Biotite	**38.80**	**4.66**	**13.51**	**16.88**	**0.35**	**14.37**	**0.03**	**0.54**	**9.51**	**0.27**	**0.03**	**0.87**	**0.17**	**96.46**
	n = 15	0.18	0.39	0.09	0.24	0.03	0.20	0.01	0.05	0.08	0.09	0.04	0.32	0.01	0.56
BFC129	Plagioclase	**61.00**	**0.02**	**23.97**	**0.22**	**0.00**	**0.01**	**6.07**	**7.54**	**0.95**	**0.03**	**0.16**	**0.02**	**0.00**	**99.71**
	n = 12	0.43	0.03	0.31	0.01	0.00	0.00	0.33	0.15	0.08	0.03	0.03	0.03	0.00	0.31
BFC191	Biotite	**39.20**	**4.55**	**13.56**	**16.52**	**0.32**	**14.76**	**0.03**	**0.48**	**9.52**	**0.37**	**0.02**	**0.49**	**0.17**	**95.86**
	n = 14	0.30	0.28	0.35	0.83	0.03	0.67	0.02	0.06	0.11	0.15	0.03	0.17	0.03	0.76
BFC191	Plagioclase	**60.63**	**0.02**	**24.12**	**0.22**	**0.01**	**0.01**	**6.24**	**7.61**	**0.91**	**0.03**	**0.19**	**0.01**	**0.00**	**99.72**
	n = 14	0.38	0.02	0.26	0.01	0.01	0.01	0.28	0.16	0.06	0.02	0.04	0.02	0.00	0.42
BFC115	Biotite*	**39.11**	**4.29**	**13.51**	**17.52**	**0.36**	**13.99**	**0.03**	**0.44**	**9.52**	**0.29**	**0.02**	**0.76**	**0.17**	**96.81**
	n = 36	0.37	0.26	0.34	0.71	0.05	0.55	0.02	0.06	0.13	0.08	0.02	0.42	0.01	0.70
BFC115	Sanidine	**64.92**	**0.02**	**18.70**	**0.11**	**0.00**	**0.00**	**0.20**	**2.81**	**11.98**	**1.09**	**0.14**	**0.02**	**0.00**	**99.87**
	n = 48	0.29	0.05	0.11	0.01	0.01	0.01	0.04	0.15	0.24	0.29	0.04	0.03	0.00	0.29
	Plagioclase	**60.57**	**0.01**	**24.35**	**0.23**	**0.00**	**0.01**	**6.49**	**7.24**	**0.87**	**0.03**	**0.17**	**0.02**	**0.00**	**100.02**
	n = 25	0.70	0.02	0.44	0.01	0.01	0.01	0.50	0.22	0.08	0.02	0.04	0.03	0.00	0.25

n = number of analyses used to calculate the mean. * = Inclusions of plagioclase and apatite were identified in some biotite grains.

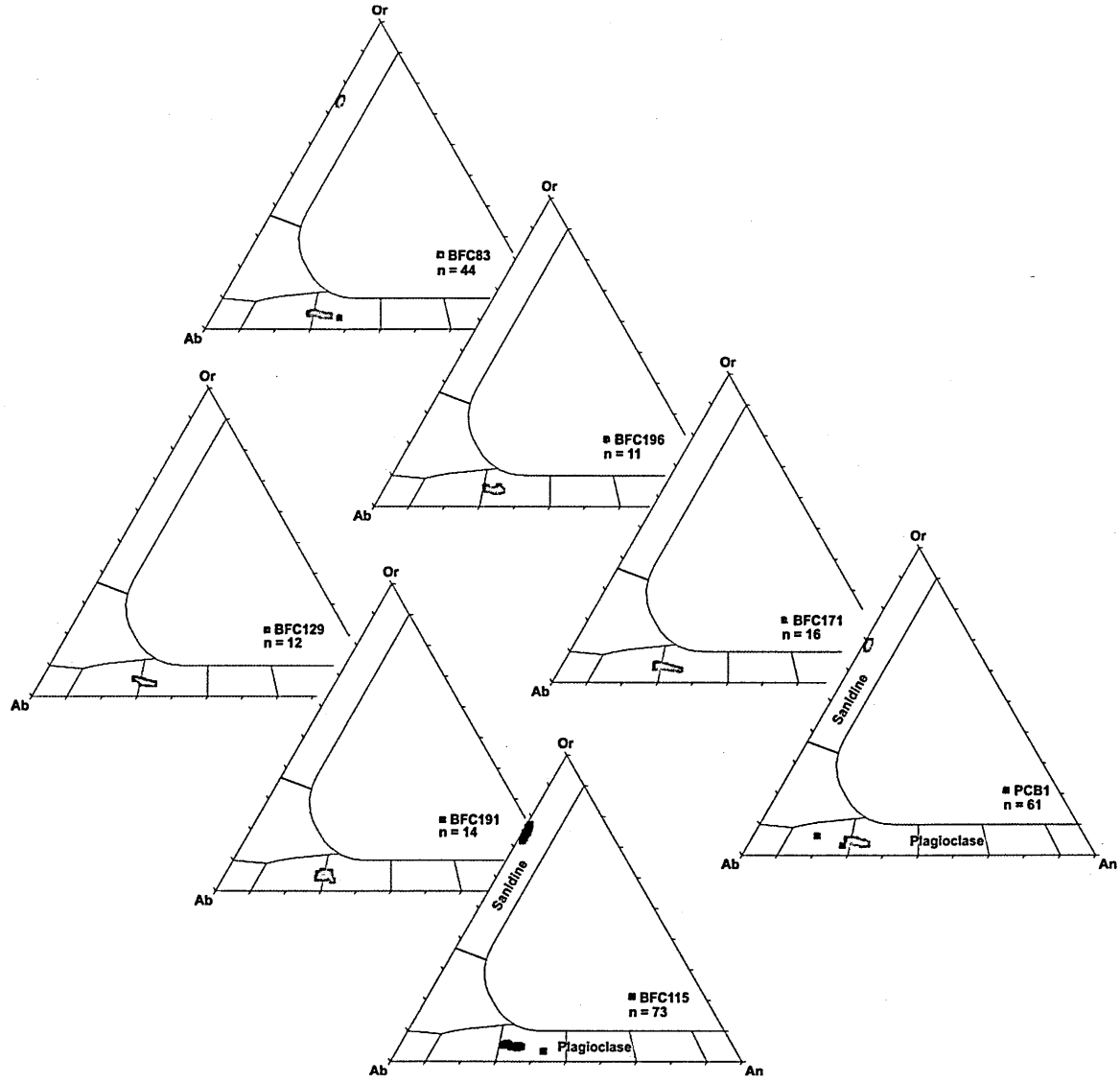

Figure 2.3. An-Or-Ab ternary diagrams showing individual feldspar compositions for the Pagosa Peak Dacite (samples BFC83, BFC196, BFC171 and PCB 1); the Fish Canyon Tuff (samples BFC129 and BFC191), and the Nutras Creek Dacite (sample BFC115).

Several feldspar crystals (Fig. 2.4) show variation in An content along transects illustrating minor variation (Fig. 2.4a); cyclic zonation (Fig. 2.4b); An rich core (up to ~ 30 %; Fig. 2.4c), and a An rich rim (up to ~ 30 %; Fig. 2.4d).

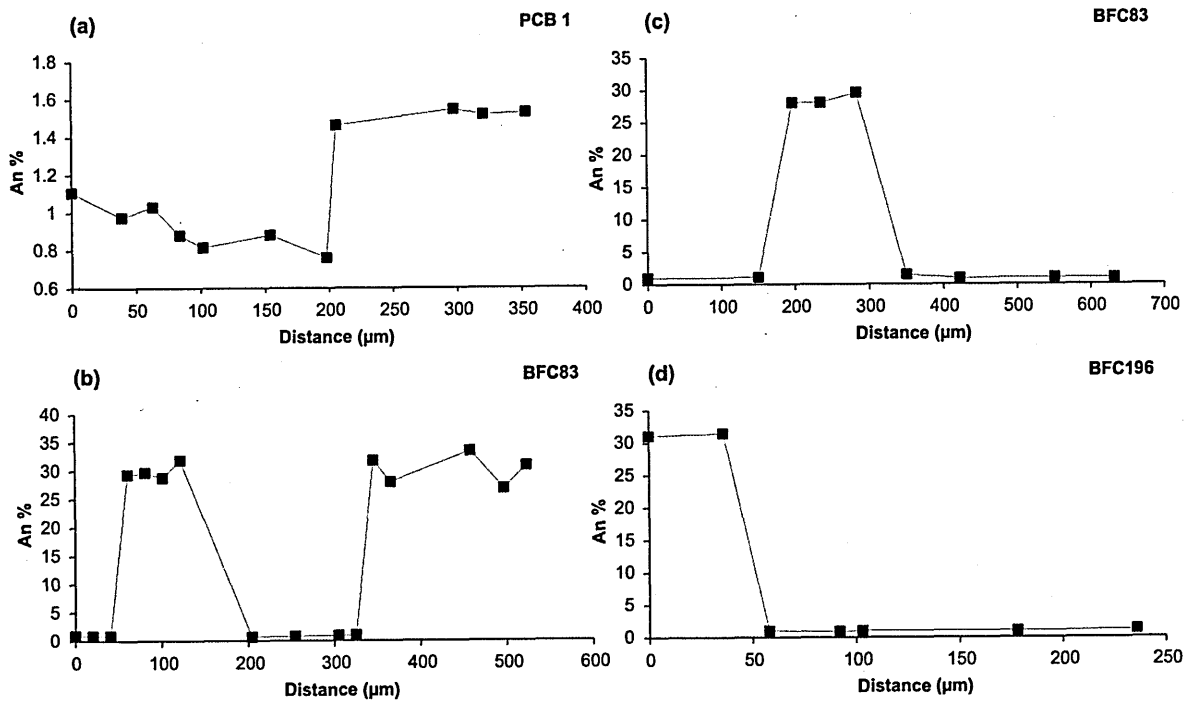

Figure 2.4. Panels (a) to (d) show examples of An content (%) variation across transects from crystal edge to edge, for selected feldspar phenocrysts of the Pagosa Peak Dacite (samples PCB 1, BFC83 and BFC196). Note different scale on X-axis.

2.6.1.2 Fish Canyon Tuff

Mean silica contents, determined by EMP for plagioclase and biotite range 60.63 % to 61.00 %, and 38.80 % to 39.20 % respectively for Fish Canyon Tuff samples (BFC129 and BFC191). Mean K_2O range 9.82 to 10.23 % for biotite. Feldspars are plagioclase in composition (An_{27} to An_{35}; Fig. 2.3), with mean K_2O, CaO and Na_2O contents in the range of 0.91 % to 0.95 %; 6.07 % to 6.66 % and 7.54 % to 7.61 % respectively. Only plagioclase feldspar could be located, and core to rim analysis revealed little variation with regards to K_2O and CaO content.

2.6.1.3 Nutras Creek Dacite

Mean silica contents, determined by EMP for feldspar (sanidine and plagioclase), and biotite are 60.57 % to 64.92 %, and 39.11 % respectively for Nutras Creek Dacite sample

(BFC115). Feldspar compositions are bimodal and either sanidine (Or_{70} to Or_{80}), or plagioclase (An_{30} to An_{43}; Fig. 2.3). Biotites contain a mean K_2O content of 9.52 %.

2.6.2 Ar-Ar *in situ* data

Samples BFC83, BFC196, BFC171, PCB 1, BFC129, BFC191 and BFC115 were analysed by the UV *in situ* method (results ordered by sample and then by mineral phase for each geological unit). Each age has been calculated from gas released by rastering the UV laser over a specifically defined area, and is summarised in Tables 2.3 to 2.5. In addition to obtaining age data by UV *in situ* geochronology, samples BFC83, PCB 1, BFC191 and BFC115 were also analysed using the IR *in situ* laserprobe technique (results ordered by sample for each geological unit). Each age calculated from gas released from multiple IR spots. Ar-Ar age data is summarised in Tables 2.6 to 2.8. Weighted mean ages (± 2σ; MSWD value), inverse isochron analyses and probability density plots have been calculated using Isoplot (K. Ludwig, 2011), and details are discussed in Appendix section A1.6.2.

2.6.2.1 Pagosa Peak Dacite: UV data

Sample BFC83

Sanidine

Ar-Ar UV ages for sanidine range from 27.70 ± 2.89 Ma to 28.48 ± 0.39 Ma. Multiple analyses were carried out on one large crystal (~ 2500 μm in length) (Fig. 2.5; BFC83 – 3), and the ages range 28.13 ± 0.36 to 28.48 ± 0.38 Ma and yielded a weighted mean age of 28.22 ± 0.18 (MSWD = 0.57) where n=5. A single sanidine gave an age of 27.70 ± 2.89 Ma (Fig. 2.5; BFC83 – 2).

Biotite

Biotite UV ages range from 27.94 ± 0.52 to 28.22 ± 0.36 Ma (Fig. 2.5). Two analysis were taken from Biotite #1(Fig. 2.5; BFC83 – 1) yield a weighted mean age of 28.01 ± 0.38 (MSWD = 0.15). There is little variation in $^{36}Ar/^{40}Ar$ and $^{38}Ar/^{39}Ar$ ratios between the two data points; however the older of the two ages from within this single grain is associated with a slightly higher $^{37}Ar/^{39}Ar$ ratio. Biotite #2 yielded an age of 28.81 ± 0.36 Ma (BFC83 - 1; Fig. 2.5).

Plagioclase

For grains too small in size to permit only one analysis, single ages range from 27.02 ± 3.19 to 30.30 ± 3.48 Ma (2σ error) (Fig. 2.5), and $^{37}Ar/^{39}Ar$ values range from 1.03 – 4.06 indicating a high Ca content and therefore the grain is unlikely to be sanidine. Multiple analysis were obtained from Plagioclase #1 with one part of the crystal yielding an age of 28.65 ± 2.96 Ma, which is younger than the second age which was 44.99 ± 1.89 Ma (Fig. 2.5; BFC83 – 1). Both analyses have not been corrected for ^{36}Ar due to measured ^{36}Ar being within error of or less than blank ^{36}Ar level (error doubled to account for lack of ^{36}Ar correction). Two ages were obtained from Plagioclase #2 (Fig. 2.5; BFC83 – 1) and yielded a weighted mean of age of 27.8 ± 2.6 Ma at the 2σ level (n=2; MSWD = 0.63). Plagioclase #4 (Fig. 2.5; BFC83 – 1) yielded two ages that are within uncertainty of each other and gave a weighted mean of 27.4 ± 0.9 Ma (n=2; MSWD = 1.04).

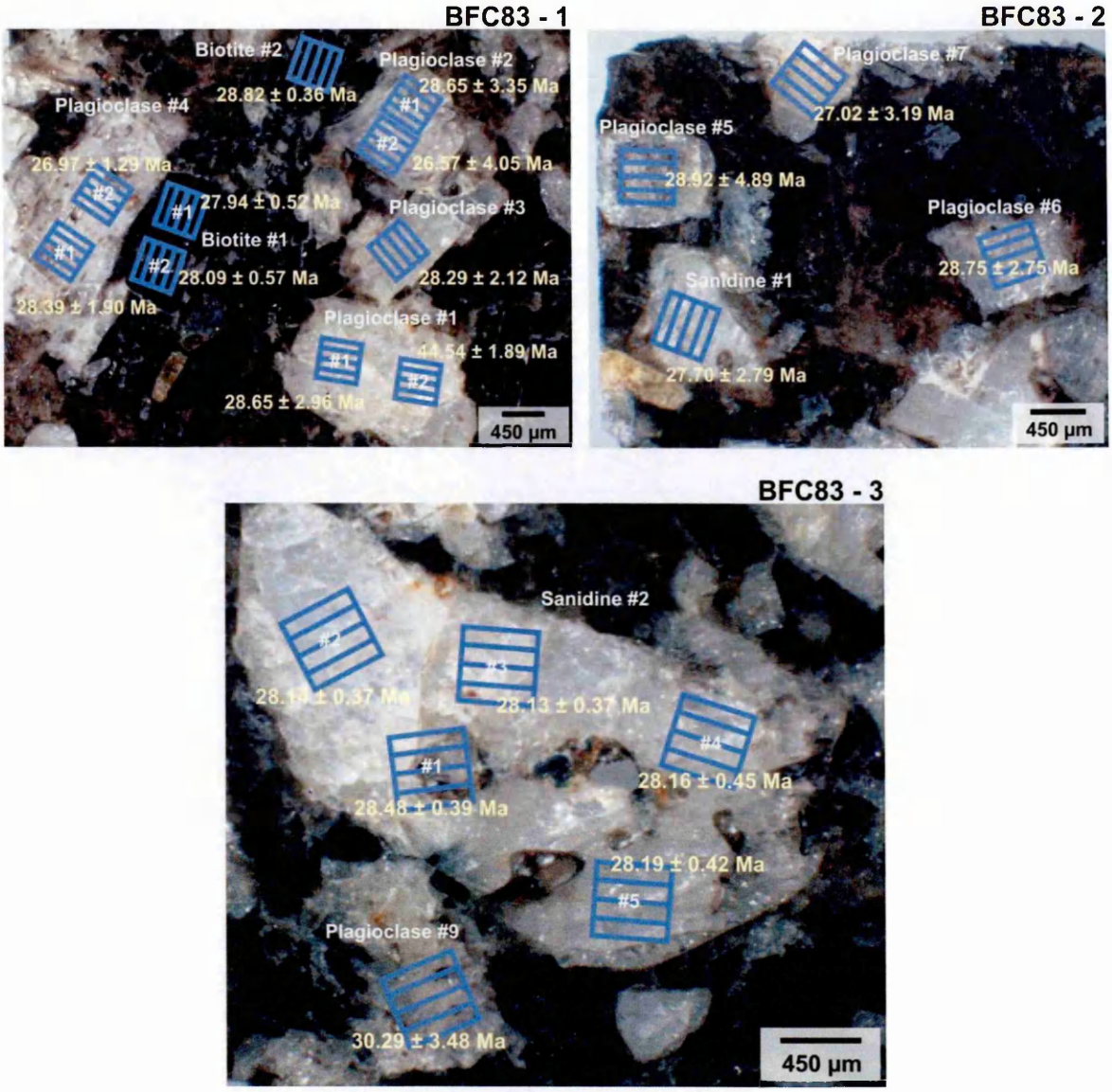

Figure 2.5. Photomicrograph of sample BFC83 (BFC83 – 1, BFC83 – 2 and BFC83 – 3) showing location of UV rasters and corresponding Ar-Ar age (± 2σ). Scale as indicated.

Sample BFC196

Plagioclase

Two ages were obtained from Plagioclase #1 (Fig. 2.6) yielding a weighted mean age of 29.20 ± 1.1 Ma (MSWD = 1.4). A second crystal (Fig. 2.6; Plagioclase #2), large enough to permit multiple analysis, yielded two ages, which yielded a weighted mean age of 28.00 ± 1.9 Ma (MSWD = 0.11). A single plagioclase analysis (Fig. 2.6; plagioclase #3) gave an

age of 28.04 ± 1.12 Ma. Plagioclase analyses tend to have variable $^{39}Ar/^{40}Ar$ and $^{36}Ar/^{40}Ar$ ratios, high $^{40}Ar^*/^{39}Ar$ ratios and low $^{38}Ar/^{39}Ar$ ratios.

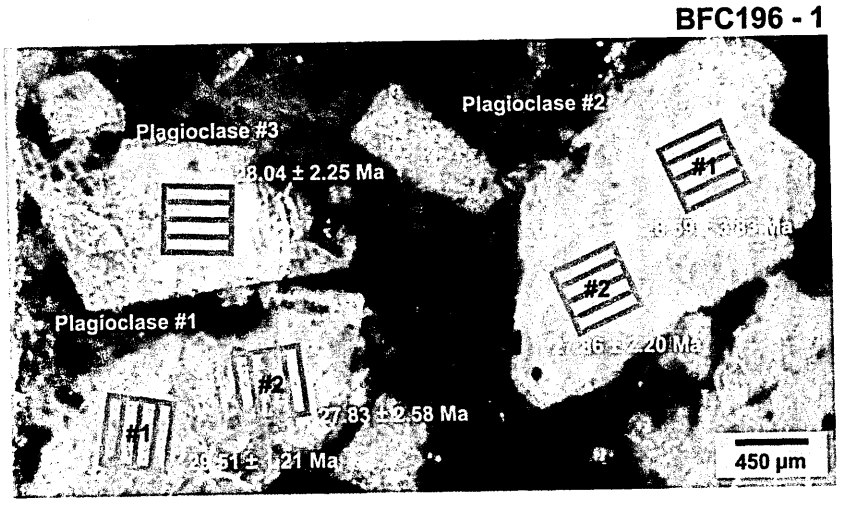

Figure 2.6. Photomicrograph of sample BFC196 (BFC196 – 1) showing location of UV rasters and corresponding Ar-Ar age (± 2σ). Scale as indicated.

Sample BFC171

Plagioclase

Plagioclase #1 (Fig. 2.7) yielded two ages of 26.88 ± 2.72 Ma and 27.88 ± 3.37 Ma with a notably large difference in $^{37}Ar/^{39}Ar$ ratio between two data points (0.1117 ± 0.0002 compared with 2.80 ± 0.01).

Biotite

Single biotite ages range from 28.11 ± 0.47 to 28.34 ± 0.52 Ma and $^{37}Ar/^{39}Ar$ ratios range from 0.0325 ± 0.0003 to 0.1183 ± 0.0003. One biotite (Fig. 2.7) was large enough to allow multiple analysis and yielded ages in the range 27.71 ± 0.41 to 28.26 ± 0.44 Ma and a weighted mean age of 28.00 ± 0.26 (MSWD = 1.8). There is slight variation in $^{37}Ar/^{39}Ar$ between data points (i.e., 0.03 to 0.1).

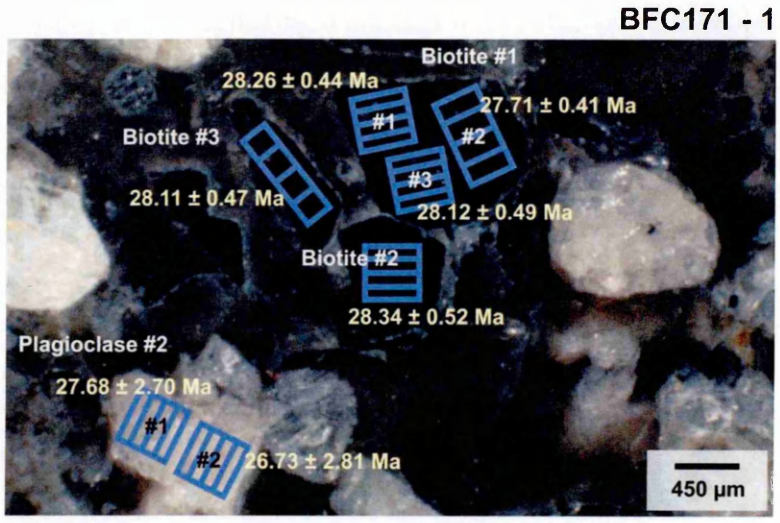

Figure 2.7. Photomicrograph of sample BFC171 (BFC171 – 1) showing location of UV rasters and corresponding Ar-Ar age (± 2σ). Scale as indicated.

Sample PCB 1

A large (~ 9000 µm in length) sanidine (Fig. 2.8) gave two ages of 28.47 ± 0.39 Ma and 28.80 ± 1.44 Ma. The latter age was also associated with a higher Ca content, and had a $^{37}Ar/^{39}Ar$ ratio of ~1.3 compared with ~ 0.01 for the former.

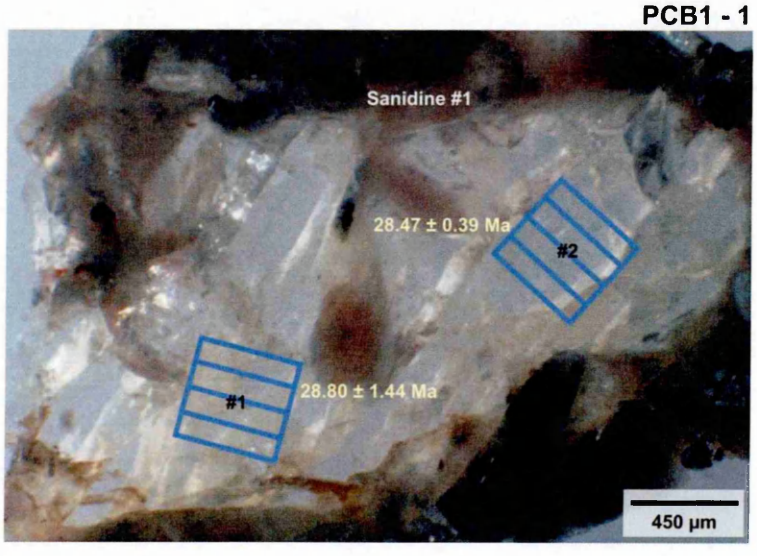

Figure 2.8. Photomicrograph of sample PCB 1 (PCB1 – 1) showing location of UV rasters and corresponding Ar-Ar age (± 2σ). Scale as indicated.

Table 2.3. Summary table of Ar-Ar UV *in situ* age data obtained for Pagosa Peak Dacite minerals. Sample name and *J*-value are given for each sample batch. ^{40}Ar presented as cc x 10^{-10}. Full data set, including instrument blanks and raw data can be found in Appendix section A3.1.1.

Sample #	Phase	Analysis #	^{40}Ar	± 2σ	$^{37}Ar/^{39}Ar$	± 2σ	Age (Ma)	± 2σ (Ma)	% $^{40}Ar^*$
PPD	Dacite								
Irradiation = McM# 60									
J-value = 0.006004802 ± 0.00002966									
BFC83 - 1	Plagioclase #1	Raster #1	0.048	0.00024	3.11	0.04	**28.65** #	**2.96**	100
BFC83 - 1	Plagioclase #1	Raster #2	0.010	0.00016	4.06	0.04	**44.54** #	**1.89**	60
BFC83 - 1	Plagioclase #2	Raster #1	0.004	0.00024	3.03	0.04	**28.65**	**3.35**	95
BFC83 - 1	Plagioclase #2	Raster #2	0.004	0.00024	2.61	0.04	**26.57**	**4.05**	86
BFC83 - 1	Plagioclase #3		0.005	0.00016	2.82	0.03	**28.29** #	**2.12**	100
BFC83 - 1	Plagioclase #4	Raster #1	0.009	0.00016	2.55	0.02	**27.89** #	**1.27**	100
BFC83 - 1	Plagioclase #4	Raster #2	0.015	0.00021	1.03	0.01	**26.97**	**1.29**	100
BFC83 - 1	Biotite #1	Raster #1	0.053	0.00025	0.03	0.00	**27.94**	**0.52**	97
BFC83 - 1	Biotite #1	Raster #2	0.043	0.00022	0.10	0.00	**28.09**	**0.56**	98
BFC83 - 1	Biotite #2		0.110	0.00023	0.01	0.00	**28.82**	**0.36**	98
J value = 0.006034125 ± 0.00002980									
BFC83 - 2	Plagioclase #5		0.006	0.00008	3.56	0.04	**28.92**	**4.89**	77
BFC83 - 2	Plagioclase #6		0.007	0.00008	2.63	0.02	**28.75**	**2.75**	99
BFC83 - 2	Plagioclase #7		0.006	0.00008	2.23	0.02	**27.02**	**3.19**	90
BFC83 - 2	Sanidine #1		0.027	0.00028	0.03	0.03	**27.70**	**2.79**	96
J value = 0.006014577 ± 0.000029701									
BFC83 - 3	Plagioclase #9		0.009	0.00010	2.74	0.03	**30.30**	**3.48**	70
BFC83 - 3	Sanidine #2	Raster #1	0.095	0.00016	0.01	0.00	**28.48**	**0.39**	99
BFC83 - 3	Sanidine #2	Raster #2	0.102	0.00018	0.01	0.00	**28.15**	**0.37**	99
BFC83 - 3	Sanidine #2	Raster #3	0.113	0.00020	0.02	0.00	**28.13**	**0.36**	99
BFC83 - 3	Sanidine #2	Raster #4	0.065	0.00019	0.01	0.00	**28.16**	**0.45**	98
BFC83 - 3	Sanidine #2	Raster #5	0.069	0.00012	0.01	0.00	**28.19**	**0.42**	100
J value = 0.005955932 ± 0.00002942									
BFC196 - 1	Plagioclase #1	Raster #1	0.017	0.00009	2.35	0.02	**29.51**	**1.21**	96
BFC196 - 1	Plagioclase #1	Raster #2	0.009	0.00020	3.05	0.02	**27.83**	**2.58**	85
BFC196 - 1	Plagioclase #2	Raster #1	0.006	0.00006	2.72	0.04	**28.59**	**3.83**	85
BFC196 - 1	Plagioclase #2	Raster #2	0.011	0.00009	1.97	0.03	**27.86**	**2.20**	72
BFC196 - 1	Plagioclase #3		0.012	0.00007	1.53	0.02	**28.04**	**2.25**	79
J value = 0.006043899± 0.00002985									
BFC171 - 1	Biotite #1	Raster #1	0.121	0.00052	0.11	0.00	**28.26**	**0.44**	89
BFC171 - 1	Biotite #1	Raster #2	0.091	0.00019	0.12	0.00	**27.71**	**0.41**	89
BFC171 - 1	Biotite #1	Raster #3	0.077	0.00020	0.03	0.00	**28.11**	**0.49**	93
BFC171 - 1	Biotite #2		0.081	0.00019	0.12	0.00	**28.34**	**0.52**	92
BFC171 - 1	Biotite #3		0.085	0.00019	0.03	0.00	**28.11**	**0.47**	93
BFC171 - 1	Plagioclase #1	Raster #1	0.007	0.00022	4.17	0.04	**27.68**	**2.69**	94
BFC171 - 1	Plagioclase #1	Raster #2	0.006	0.00022	2.76	0.03	**26.73**	**2.81**	97
J value = 0.006089515 ± 0.00003008									
PCB1 - 1	Sanidine #1	Raster #1	0.026	0.00017	1.31	0.01	**28.80**	**1.44**	95
PCB1 - 1	Sanidine #1	Raster #2	0.148	0.00026	0.01	0.00	**28.47**	**0.39**	100

 # = No ^{36}Ar correction applied due to measured ^{36}Ar at blank level or yielded a negative ^{36}Ar value.

2.6.2.2 Fish Canyon Tuff: UV data

Sample BFC129 (intracaldera)

Biotite

Core and rim analysis were taken for each biotite and ages range from 28.61 ± 0.72 to 29.67 ± 0.60 Ma (Fig. 2.9; BFC129 - 1). Biotite #1 has a core age of 29.33 ± 0.37 Ma, and a rim age of 29.03 ± 0.39 Ma. Although the ages are within error of each other at the 2σ level, the core of this grain has a higher $^{36}Ar/^{40}Ar$ and $^{37}Ar/^{39}Ar$ ratio than the rim ($^{38}Ar/^{39}Ar$ ratio are within error of each other). The weighted mean age of both data points is 29.18 ± 0.26 Ma (MSWD = 1.3). Biotite #2 has a core age of 28.63 ± 0.75 Ma and a rim age of 28.61 ± 0.72 Ma, the core has a slightly higher $^{37}Ar/^{39}Ar$ ratio (~ 0.044) than the rim (~ 0.028), whilst core and rim $^{36}Ar/^{40}Ar$ and $^{38}Ar/^{39}Ar$ ratios are within error of each other. Weighted mean age of both data points is 28.62 ± 0.52 Ma (MSWD = 0.002). Biotite #3 has a core age of 29.67 ± 0.60 Ma and a rim age of 29.63 ± 0.64 Ma. In contrast to Biotite #1 and Biotite #2, the rim of this grain has a higher $^{37}Ar/^{39}Ar$ ratio (~ 0.20) than the core (~ 0.06), as well as a higher $^{36}Ar/^{40}Ar$ ratio. A weighted mean age of both data points is 29.65 ± 0.44 Ma (MSWD = 0.009).

Plagioclase

Individual plagioclase crystals from a large mass of multiple inter-grown plagioclase feldspar crystals and quartz were targeted. Plagioclase feldspar age data range 23.27 ± 5.32 to 61.46 ± 10.12 Ma (Fig. 2.9). Plagioclase # 1 gave the highest ages that were obtained (61.46 ± 10.12 Ma and 47.61 ± 6.12 Ma) and were located in a part of the crystal that has a highly mottled appearance due to a high proportion of inclusions (Fig. 2.9; BFC129 – 1). The oldest of these two ages is associated with a lower $^{36}Ar/^{40}Ar$, $^{37}Ar/^{39}Ar$ and $^{38}Ar/^{39}Ar$ ratio compared to the younger of the two ages. Other ages from within this mass were variable. Plagioclase #2 and #3 have high associated errors and gave ages of 26.44 ± 5.32

Ma and 30.82 ± 6.53 Ma respectively. Plagioclase #4 (27.66 ± 1.60 Ma and 29.02 ± 2.29 Ma) had an inclusion rich core, which exhibited a mottled texture and Plagioclase #5 and plagioclase #6 each yielded three ages each (Fig. 2.9; BFC129 – 2) of 31.56 ± 3.66 Ma; 29.82 ± 3.33 Ma and 27.81 ± 2.92 Ma, and 30.46 ± 2.73 Ma; 35.81 ± 5.51 Ma and 28.05 ± 1.73 Ma respectively.

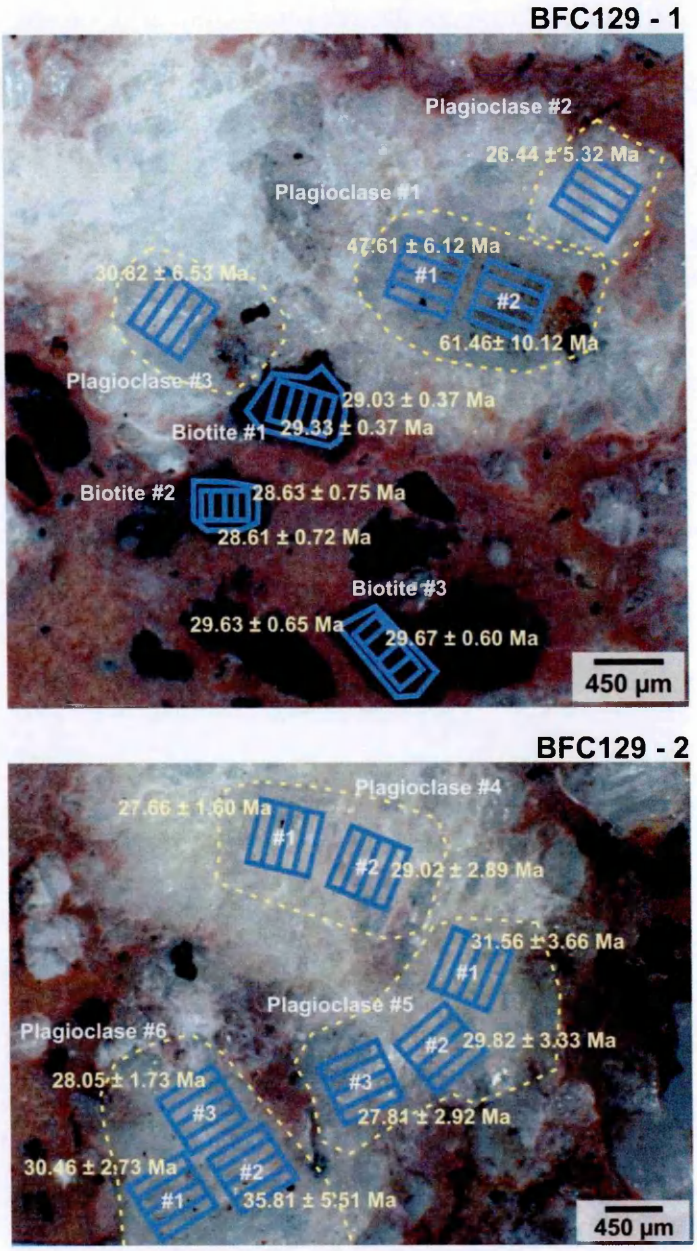

Figure 2.9. Photomicrograph of sample BFC129 (BFC129 – 1 and BFC129 - 2) showing location of UV rasters and corresponding Ar-Ar age (± 2σ). Scale as indicated.

Sample BFC191 (intracaldera)

Biotite

A single biotite (Fig. 2.10) gave an age of 29.46 ± 0.56 Ma, with a $^{37}Ar/^{39}Ar$ ratio of 0.01.

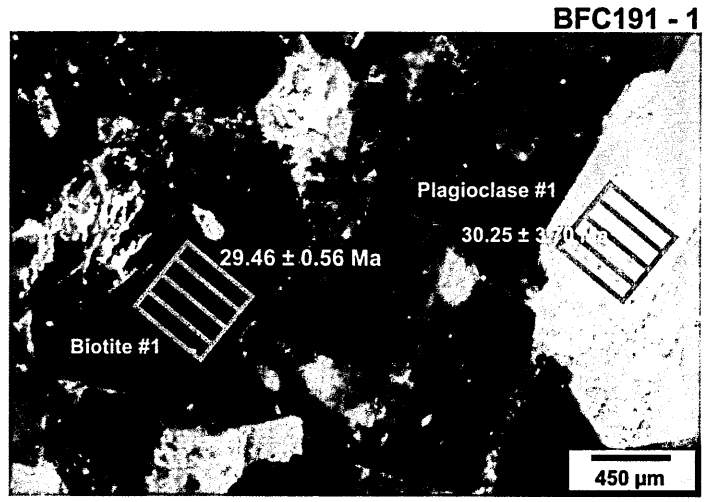

Figure 2.10. Photomicrograph of sample BFC191 (BFC191 – 1) showing location of UV rasters and corresponding Ar-Ar age (± 2σ). Scale as indicated.

Plagioclase

Plagioclase #1 (Fig. 2.10) gave an age of 30.25 ± 3.70 Ma with a ^{36}Ar measurement at blank level. ^{36}Ar corrected and non-corrected ages are within error of each other, so on this occasion both could be used and so the ^{36}Ar corrected age is accepted.

Table 2.4. Summary table of Ar-Ar UV *in situ* age data obtained for Fish Canyon Tuff minerals. Sample name and *J*-value are given for each sample batch. ^{40}Ar presented as cc x 10^{-10}. Full data set, including instrument blanks and raw data can be found in Appendix section A3.1.1.

Sample #	Phase	Analysis #	^{40}Ar	± 2σ	$^{37}Ar/^{39}Ar$	± 2σ	Age (Ma)	± 2σ (Ma)	% $^{40}Ar^*$
FCT	Tuff								
Irradiation = McM# 60									
J-value = 0.006133373 ± 0.00003029									
BFC129 - 1	Biotite #1	Rim line	0.107	0.00017	0.09	0.00	**29.03**	**0.37**	81
BFC129 - 1	Biotite #1	Core raster	0.122	0.00019	0.16	0.00	**29.33**	**0.37**	76
BFC129 - 1	Biotite#2	Rim line	0.057	0.00051	0.03	0.00	**28.61**	**0.72**	77
BFC129 - 1	Biotite#2	Core raster	0.058	0.00050	0.04	0.00	**28.63**	**0.75**	75
BFC129 - 1	Biotite #3	Rim line	0.091	0.00051	0.20	0.00	**29.63**	**0.65**	63
BFC129 - 1	Biotite #3	Core raster	0.118	0.00052	0.06	0.00	**29.67**	**0.60**	56
BFC129 - 1	Plagioclase #1	Raster #1	0.048	0.00019	11.99	0.16	**47.61**	**6.12**	10
BFC129 - 1	Plagioclase #1	Raster #2	0.011	0.00017	9.02	0.17	**61.46**	**10.11**	39
BFC129 - 1	Plagioclase #2		0.007	0.00017	2.72	0.04	**26.44**	**5.32**	45
BFC129 - 1	Plagioclase #3		0.010	0.00041	2.53	0.04	**30.82**	**6.53**	45
J value = 0.006120090± 0.00003023									
BFC129 - 2	Plagioclase #4	Raster #1	0.028	0.00023	2.92	0.02	**27.66**	**1.60**	52
BFC129 - 2	Plagioclase #4	Raster #2	0.013	0.00024	3.01	0.02	**29.02**	**2.29**	94
BFC129 - 2	Plagioclase #5	Raster #1	0.012	0.00026	2.45	0.02	**31.56**	**3.66**	65
BFC129 - 2	Plagioclase #5	Raster #2	0.010	0.00024	3.05	0.03	**29.82**	**3.32**	84
BFC129 - 2	Plagioclase #5	Raster #3	0.013	0.00024	3.77	0.03	**27.81**	**2.92**	71
BFC129 - 2	Plagioclase #6	Raster #1	0.010	0.00027	3.62	0.04	**30.46**	**2.73**	90
BFC129 - 2	Plagioclase #6	Raster #2	0.014	0.00038	2.88	0.03	**35.81**	**5.51**	42
BFC129 - 2	Plagioclase #6	Raster #3	0.026	0.00027	3.03	0.02	**28.05**	**1.73**	47
J value = 0.006151294 ± 0.00003038									
BFC191 - 1	Plagioclase #1		0.013	0.00039	2.41	0.03	**30.25**	**3.68**	99
BFC191 - 1	Biotite #1		0.191	0.00045	0.01	0.00	**29.46**	**0.56**	66

2.6.2.3 Nutras Creek Dacite: UV data

Sample BFC115

Biotite

A single biotite (Fig. 2.11; BFC115 - 1) gave an age of 28.13 ± 0.40 Ma ($^{37}Ar/^{39}Ar$ value of 0.06). Biotite #2 (Fig. 2.11; BFC115 - 2) was large enough (~ 2700 μm in length) to permit four analyses and the ages range from 28.20 ± 5.51 to 35.43 ± 3.56 Ma. $^{37}Ar/^{39}Ar$ ratios are variable and high (3.83 to 8.50), indicating the presence of Ca. Therefore possible analysis of Ca rich inclusions, such as apatite, has taken place.

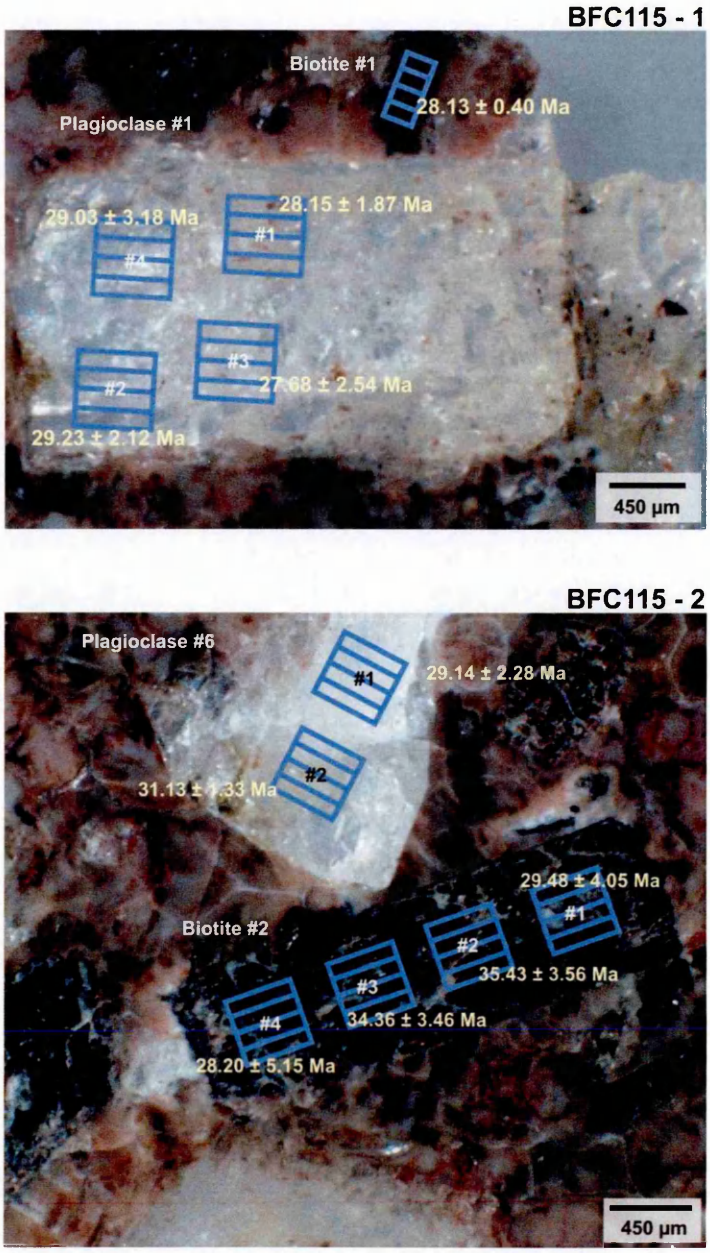

Figure 2.11. Photomicrograph of sample BFC115 (BFC115 – 1 and BFC115 - 2) showing location of UV rasters and corresponding Ar-Ar age (± 2σ). Scale as indicated.

Plagioclase

Plagioclase #1 (Fig. 2.11; BFC115 - 1), yielded four ages, ranging from 27.68 ± 2.54 to 29.23 ± 2.12 Ma. $^{36}Ar/^{40}Ar$ and $^{38}Ar/^{40}Ar$ show little variation but there is minor variation in $^{37}Ar/^{39}Ar$. Both data points from Plagioclase #6 (Fig. 2.11; BFC115 - 2), had ^{36}Ar values at (or very close to) blank level and so ages of 29.14 ± 2.28 Ma and 31.13 ± 1.34 Ma (non ^{36}Ar corrected) have been accepted.

Table 2.5. Summary table of Ar-Ar UV *in situ* age data obtained for Nutras Creek Dacite minerals. Sample name and *J*-value are given for each sample batch. ^{40}Ar presented as cc x 10^{-10}. Full data set, including instrument blanks and raw data can be found in Appendix section A3.1.1.

Sample #	Phase	Analysis #	^{40}Ar	± 2σ	$^{37}Ar/^{39}Ar$	± 2σ	Age (Ma)	± 2σ (Ma)	% $^{40}Ar^*$
NCD	Dacite								
Irradiation = McM# 60									
J-value = 0.006015668 ± 0.00002971									
BFC115 - 1	Plagioclase #1	Raster #1	0.013	0.00018	3.27	0.02	**28.15**	**1.87**	88
BFC115 - 1	Plagioclase #1	Raster #2	0.010	0.00018	3.15	0.03	**29.23**	**2.12**	100
BFC115 - 1	Plagioclase #1	Raster #3	0.008	0.00018	2.29	0.02	**27.68**	**2.54**	91
BFC115 - 1	Plagioclase #1	Raster #4	0.011	0.00078	3.06	0.02	**29.03**	**3.18**	85
BFC115 - 1	Biotite #1		0.080	0.00022	0.06	0.00	**28.13**	**0.40**	98
J value = 0.006008648 ± 0.00002968									
BFC115 - 2	Biotite #2	Core raster #1	0.009	0.00029	8.50	0.08	**29.48**	**4.05**	61
BFC115 - 2	Biotite #2	Core raster #2	0.006	0.00029	7.68	0.09	**35.43**	**3.56**	83
BFC115 - 2	Biotite #2	Core raster #3	0.006	0.00029	6.73	0.07	**34.36** #	**3.44**	88
BFC115 - 2	Biotite #2	Core raster #4	0.005	0.00008	6.76	0.09	**28.20**	**5.15**	70
BFC115 - 2	Plagioclase #6	Raster #1	0.003	0.00009	3.13	0.08	**29.14** #	**2.28**	92
BFC115 - 2	Plagioclase #6	Raster #2	0.005	0.00008	2.41	0.03	**31.13** #	**1.33**	95

 # = No ^{36}Ar correction applied due to measured ^{36}Ar at blank level or yielded a negative ^{36}Ar value.

2.6.2.4 Pagosa Peak Dacite: IR data

Sample BFC83

Sanidine ages range from 27.65 ± 0.39 to 29.08 ± 1.0 Ma (Fig. 2.11). Plagioclase (Fig. 2.12) ages range from 27.12 ± 1.27 to 30.11 ± 1.50 Ma, the majority with a $^{37}Ar/^{39}Ar$ ratio indicating the presence of Ca (range 1.308 ± 0.009 to 1.688 ± 0.007). A single biotite #3 (Fig. 2.12) yielded an age of 27.57 ± 1.18 Ma.

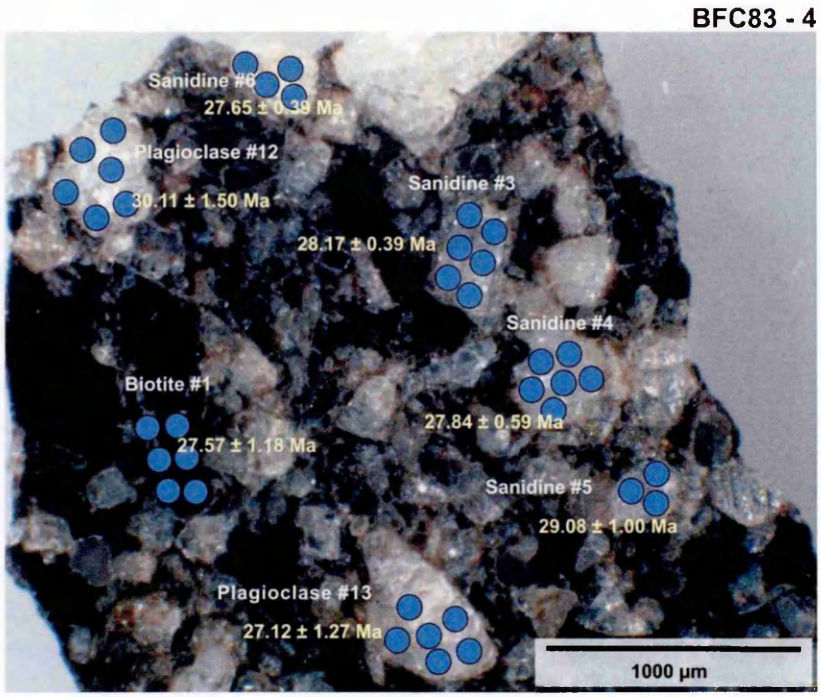

Figure 2.12. Photomicrograph of sample BFC83 (BFC83 – 4) showing location of IR spots and corresponding Ar-Ar age (± 2σ). Scale as indicated.

Sample PCB 1

Ages range from 28.06 ± 0.60 to 36.42 ± 3.37 Ma (2σ error) within a single sanidine crystal (Fig. 2.13). IR spot data that yielded an age of 28.80 ± 0.40 Ma (where spots cover site of previously analysed UV raster) is identical to the age obtained using the UV technique. This demonstrates good agreement between the two techniques. This IR analysis also has a slightly higher $^{37}Ar/^{39}Ar$ ratio compared to the other IR analysis within the same crystal (~ 0.12). This elevated $^{37}Ar/^{39}Ar$ also corresponds to what we see with the UV analysis of the same area within the sanidine grain. A different part of the same grain gave an IR age of 36.42 ± 3.37 Ma but only had a $^{37}Ar/^{39}Ar$ ratio of 0.07 ± 0.01. This elevated age could be due to the high $^{40}Ar^*/^{39}Ar$ ratio of 3.36 ± 0.16. There is variability with regards to $^{38}Ar/^{39}Ar$ ratio, the oldest age of ~ 36 Ma corresponding to the highest $^{38}Ar/^{39}Ar$ ratio. A plagioclase grain, located next to the large sanidine gave an age of 30.86 ± 1.66 Ma.

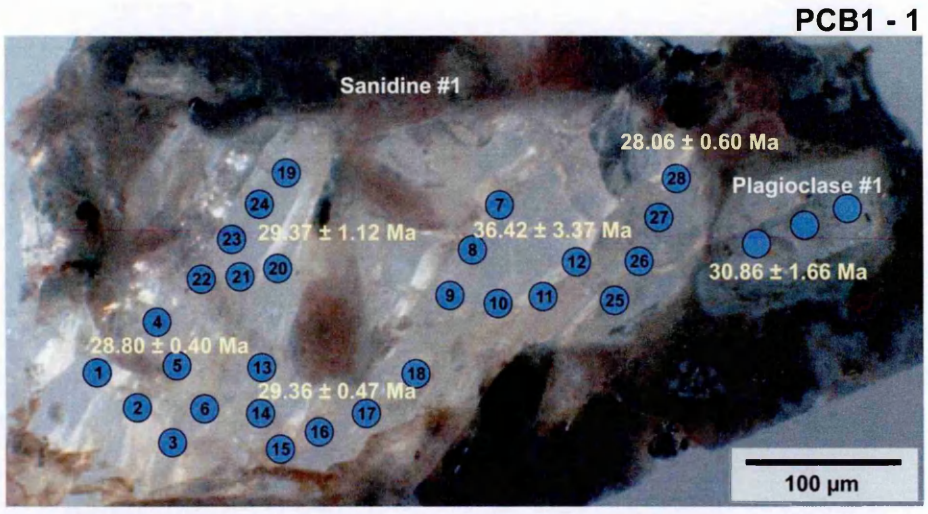

Figure 2.13. Photomicrograph of sample PCB 1 (PCB1 – 1) showing location of IR spots and corresponding Ar-Ar age (± 2σ). Where more than one age has been obtained from a single grain, IR spots are numbered so that they are easily linked to summary data in Table 2.6. Scale as indicated.

Table 2.6. Summary table of Ar-Ar IR *in situ* age data obtained for Pagosa Peak Dacite minerals. Sample name and *J*-value are given for each sample batch. ^{40}Ar presented as cc x 10^{-10}. Full data set, including instrument blanks and raw data can be found in Appendix section A3.1.1.

Sample #	Phase	Analysis #	^{40}Ar	± 2σ	$^{37}Ar/^{39}Ar$	± 2σ	Age (Ma)	± 2σ (Ma)	% $^{40}Ar^*$
PPD	Dacite								
Irradiation = McM# 60									
J-value = 0.006188361 ± 0.00003057									
BFC83 - 4	Biotite # 3		0.342	0.001	0.10	0.02	**27.57**	**1.18**	91
BFC83 - 4	Plagioclase #12		0.346	0.002	1.31	0.02	**30.11**	**1.50**	99
BFC83 - 4	Plagioclase #13		0.299	0.002	1.69	0.01	**27.11**	**1.27**	92
BFC83 - 4	Sanidine #3		1.484	0.001	0.27	0.00	**28.17**	**0.39**	99
BFC83 - 4	Sanidine #4		0.734	0.003	0.12	0.01	**27.84**	**0.59**	98
BFC83 - 4	Sanidine #5		0.405	0.001	1.26	0.01	**29.08**	**1.00**	96
BFC83 - 4	Sanidine #6		1.415	0.003	0.12	0.00	**27.65**	**0.39**	98
J-value = 0.006089515 ± 0.00003008									
PCB1 - 1	Sanidine #1	Spots 1 - 6	2.008	0.003	0.12	0.00	**28.80**	**0.40**	91
PCB1 - 1	Sanidine #1	Spots 7 - 12	0.421	0.001	0.08	0.03	**36.42**	**3.37**	40
PCB1 - 1	Sanidine #1	Spots 13 - 18	1.694	0.002	0.04	0.00	**29.36**	**0.47**	85
PCB1 - 1	Sanidine #1	Spots 19 - 24	0.287	0.001	0.07	0.02	**29.37**	**1.82**	89
PCB1 - 1	Sanidine #1	Spots 25 - 28	0.770	0.002	0.10	0.01	**28.06**	**0.60**	92
PCB1 - 1	Plagioclase #1		0.682	0.002	1.42	0.02	**30.86**	**1.66**	34

2.6.2.5 Fish Canyon Tuff: IR data

Sample BFC191

Biotite (Fig. 2.14) ages range from 27.90 ± 0.77 to 29.48 ± 0.58 Ma. $^{37}Ar/^{39}Ar$ values for all IR biotite ages are consistent and range 0.02 to 0.09. Biotite #1 – using the two ages determined for this grain (each made up of five individual IR spots) a weighted mean of 28.51 ± 0.49 (MSWD = 0.28). For one large plagioclase feldspar (Plagioclase #1, Fig. 2.14), IR ages range from 26.75 ± 2.14 to 28.61 ± 3.29 Ma with variable $^{37}Ar/^{39}Ar$ ratios (range 1.45 to 2.27). Plagioclase #2 (Fig. 2.14) gave an age of 27.24 ± 0.75 Ma. A single sanidine gave an age of 28.62 ± 0.39 Ma ($^{37}Ar/^{39}Ar$ value of 0.04).

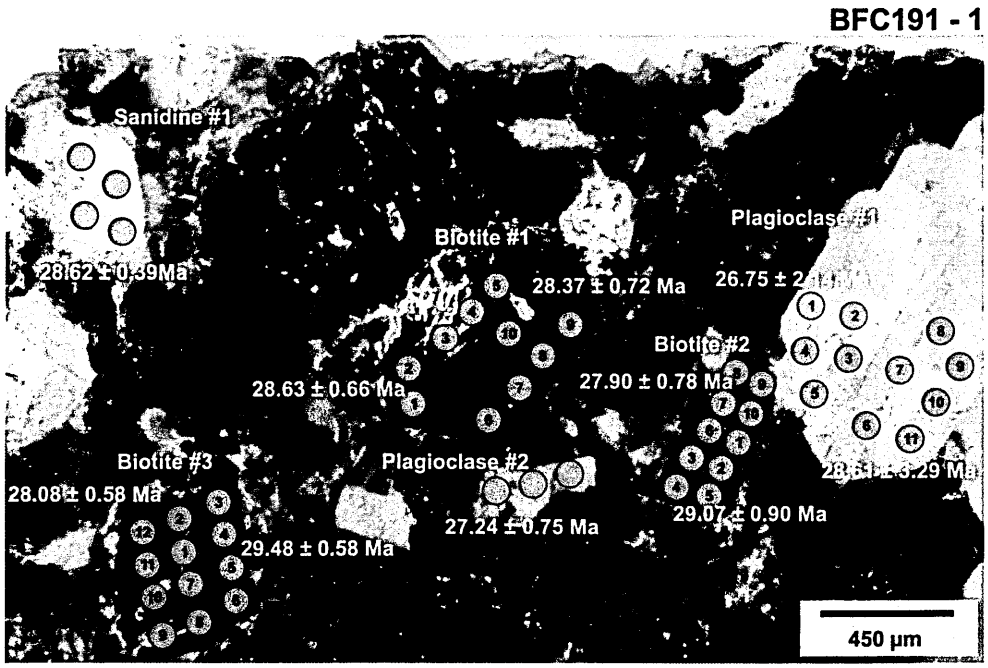

Figure 2.14. Photomicrograph of sample BFC191 (BFC191 – 1) showing location of IR spots and corresponding Ar-Ar age (± 2σ). Where more than one age has been obtained from a single grain, IR spots are numbered so that they are easily linked to summary data in Table 2.7. Scale as indicated.

Table 2.7. Summary table of Ar-Ar IR *in situ* age data obtained for Fish Canyon Tuff minerals. Sample name and *J*-value are given for each sample batch. ^{40}Ar presented as cc x 10^{-10}. Full data set, including instrument blanks and raw data can be found in Appendix section A3.1.1.

Sample #	Phase	Analysis #	^{40}Ar	± 2σ	$^{37}Ar/^{39}Ar$	± 2σ	Age (Ma)	± 2σ (Ma)	% $^{40}Ar^*$
FCT	Tuff								
Irradiation = McM# 60									
J-value = 0.006151294 ± 0.00003038									
BFC191 - 1	Biotite #1	Spots 1 - 5	0.783	0.001	0.08	0.01	**28.63**	**0.67**	89
BFC191 - 1	Biotite #1	Spots 6 - 10	0.702	0.002	0.08	0.01	**28.37**	**0.72**	88
BFC191 - 1	Biotite #2	Spots 1 - 5	0.543	0.001	0.03	0.01	**29.07**	**0.90**	89
BFC191 - 1	Biotite #2	Spots 6 - 10	0.616	0.002	0.03	0.01	**27.90**	**0.77**	93
BFC191 - 1	Biotite #3	Spots 1 - 6	1.110	0.003	0.03	0.01	**29.48**	**0.58**	81
BFC191 - 1	Biotite #3	Spots 7 - 12	1.057	0.002	0.10	0.00	**28.08**	**0.58**	84
BFC191 - 1	Plagioclase #1	Spots 1 - 4	0.219	0.001	1.58	0.02	**26.75**	**2.14**	90
BFC191 - 1	Plagioclase #1	Spots 5 - 11	0.141	0.001	2.27	0.03	**28.61**	**3.28**	96
BFC191 - 1	Plagioclase #2		0.528	0.001	0.45	0.01	**27.24**	**0.75**	94
BFC191 - 1	Sanidine #1		1.572	0.003	0.04	0.00	**28.62**	**0.39**	99

2.6.2.6 Nutras Creek Dacite: IR data

Sample BFC115

Two ages (29.01 ± 1.23 Ma and 29.46 ± 2.54 Ma) from a single sanidine (Fig. 2.15) give a weighted mean age of 29.1 ± 1.1 Ma (MSWD = 0.1). Plagioclase #1 (Fig. 2.15), yielded ages that ranged from 28.45 ± 5.61 to 33.05 ± 3.19 Ma, which also had variable $^{37}Ar/^{39}Ar$ ratios (ranging 0.714 ± 0.003 to 3.211 ± 0.036), suggesting variable Ca content between crystals. Two ages obtained from Plagioclase #2 (Fig. 2.15), were 28.18 ± 1.17 Ma and 31.17 ± 1.29 Ma and Plagioclase #3 and #4 were 29.98 ± 0.62 and 25.07 ± 1.8 Ma respectively.

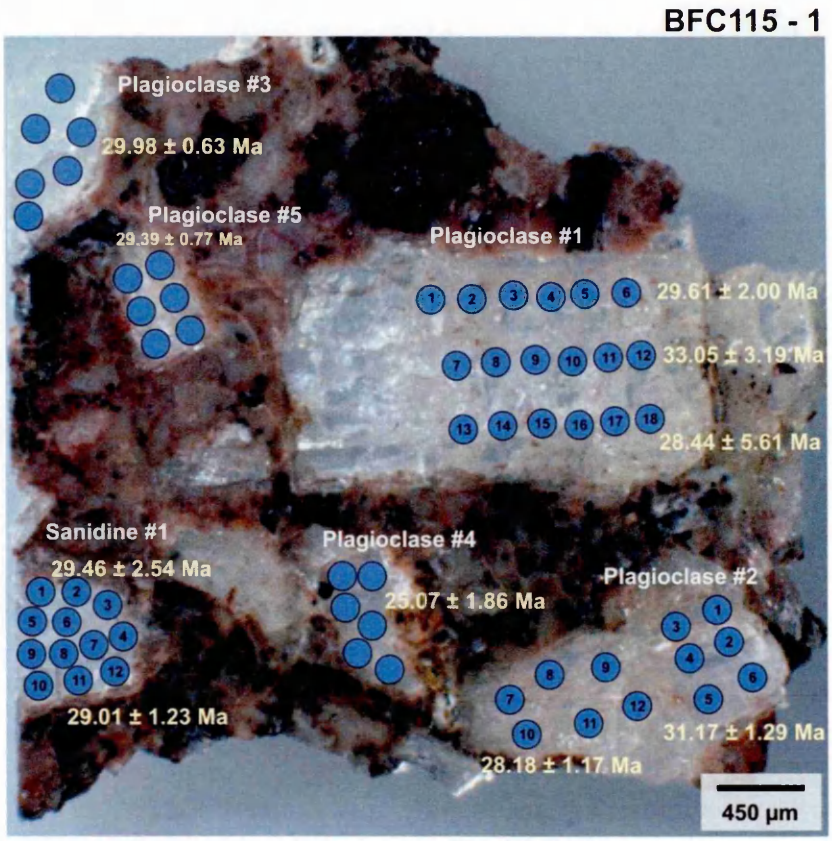

Figure 2.15. Photomicrograph of sample BFC115 (BFC115 – 1) showing location of IR spots and corresponding Ar-Ar age (± 2σ). Where more than one age has been obtained from a single grain, IR spots are numbered so that they are easily linked to summary data in Table 2.8. Scale as indicated.

Table 2.8. Summary table of Ar-Ar IR *in situ* age data obtained for Nutras Creek Dacite minerals. Sample name and *J*-value are given for each sample batch. ^{40}Ar presented as cc x 10^{-10}. Full data set, including instrument blanks and raw data can be found in Appendix section A3.1.1.

Sample #	Phase	Analysis #	^{40}Ar	± 2σ	$^{37}Ar/^{39}Ar$	± 2σ	Age (Ma)	± 2σ (Ma)	% $^{40}Ar^*$
NCD	Dacite								
Irradiation = McM# 60									
J-value = 0.006015668 ± 0.00002971									
BFC115 - 1	Sanidine #1	Spots 1 - 6	0.270	0.001	0.11	0.03	**29.46**	**2.54**	69
BFC115 - 1	Sanidine #1	Spots 7 - 12	0.528	0.002	0.17	0.01	**29.01**	**1.23**	93
BFC115 - 1	Plagioclase #1	Spots 1 - 6	0.338	0.001	1.41	0.02	**29.61**	**2.00**	59
BFC115 - 1	Plagioclase #1	Spots 7 - 12	0.187	0.002	1.64	0.04	**33.05**	**3.19**	86
BFC115 - 1	Plagioclase #1	Spots 13 - 18	0.144	0.003	3.21	0.07	**28.44**	**5.61**	85
BFC115 - 1	Plagioclase #2	Spots 1 - 6	0.491	0.002	1.61	0.02	**31.17**	**1.29**	78
BFC115 - 1	Plagioclase #2	Spots 7 - 12	0.494	0.002	2.08	0.02	**28.18**	**1.17**	56
BFC115 - 1	Plagioclase #3		1.209	0.003	0.71	0.01	**29.98**	**0.63**	93
BFC115 - 1	Plagioclase #4		0.411	0.003	1.51	0.02	**25.07**	**1.86**	72
BFC115 - 1	Plagioclase #5		0.762	0.003	1.19	0.01	**29.39**	**0.77**	78

2.7 Discussion

The results of the *in situ* Ar-Ar ages determined from single crystals of multiple phases from the Fish Canyon magma are in accordance with previously determined Ar-Ar ages (e.g., Bachmann *et al.*, 2007b), and those obtained using other geochronological techniques (e.g., U-Pb; Schmitz and Bowring 2001; Lanphere and Baadsgaard, 2001; Bachmann *et al.*, 2007). The advantage of applying this particular approach to samples which have previously been worked on (e.g., Bachmann *et al.*, 2002; 2007b) is the ability to make a direct comparison between multiple *in situ* Ar-Ar analysis, where ca. 5 mg of K-rich material (e.g., feldspar) is liberated for each *in situ* analysis in this study compared with melting single (or aliquots of) grains. The following sections discuss the application of the different laserprobe techniques to minerals of the FCT, and draws comparison between new data (this study) and previously published ages. Finally, various geological processes at work during the formation of the Fish Canyon magmatic system will be discussed in such a way as to offer a possible explanation for the range of ages achieved (25. 07 ± 1.86 Ma to 61.46 ± 10.11 Ma; Fig. 2.16).

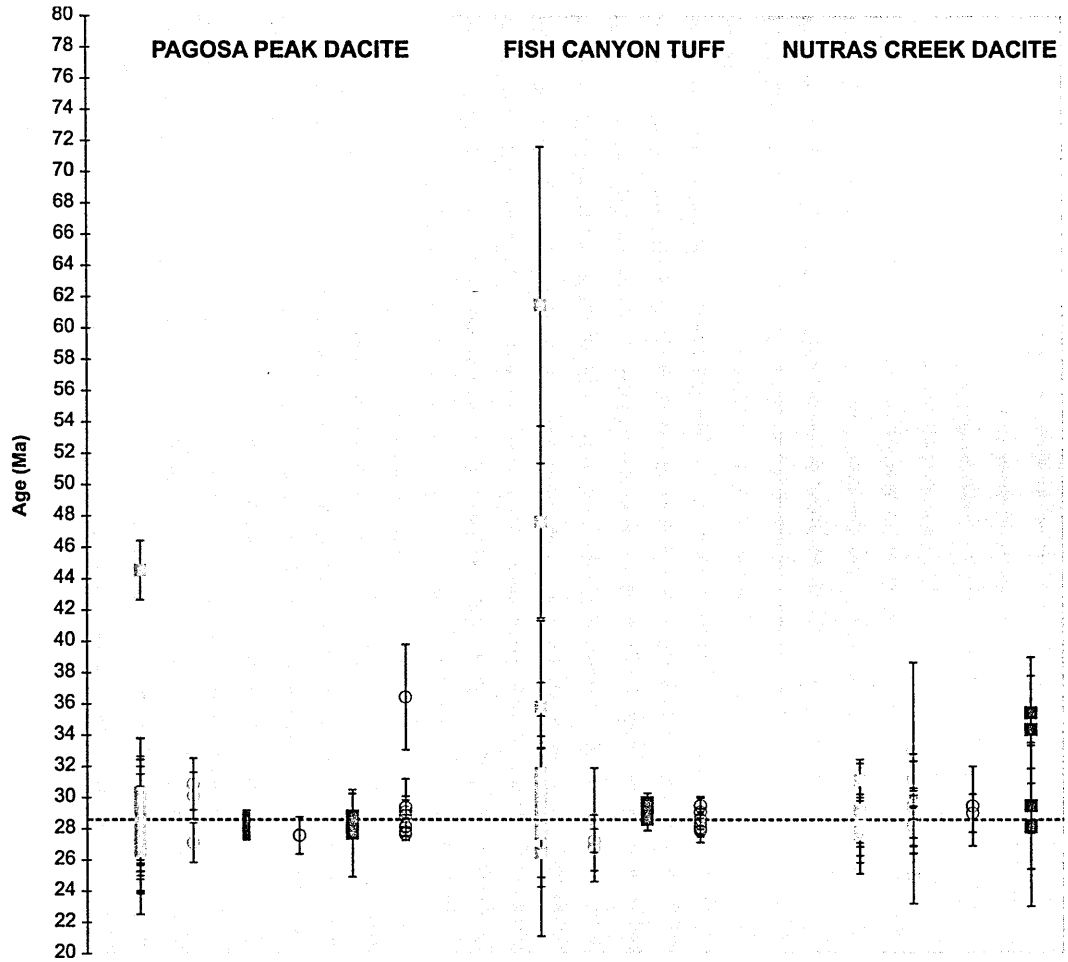

Figure 2.16. Diagram showing the range of ages (Ma ± 2σ) achieved for each Fish Canyon unit (Pagosa Peak Dacite, Fish Canyon Tuff and Nutras Creek Dacite). Blue symbols represent Ar-Ar ages determined on plagioclase, purple symbols represent Ar-Ar ages determined on sanidine and green symbols represent Ar-Ar ages determined on biotite. Closed squares = UV data and open circles = IR data. Dashed red line represents FCT eruption age at ~ 28.3 Ma (based on FCs age; Renne *et al.*, 2010).

2.7.1 Comparison of Ar-Ar ages derived from different laser probe extraction techniques

In situ ages have been obtained by both the UV (Nu Instruments Noblesse) and IR (MAP-215-50) laser probe method, allowing a comparison to be made between the two techniques as well as a direct comparison to total fusion ages determined on multiple mineral phases (biotite, sanidine, plagioclase) separated from the same sample suite (Bachmann *et al.*, 2007b).

2.7.1.1 UV vs. IR

Overall the Ar-Ar ages obtained by UV *in situ* laser ablation are in agreement (within 2σ uncertainty) of ages obtained by IR *in situ* spot analysis (Fig. 2.17). The data has revealed that both the UV and IR laser probe techniques are capable of identifying ages that are older than expected between single grains, as well as highlighting age heterogeneity within single grains.

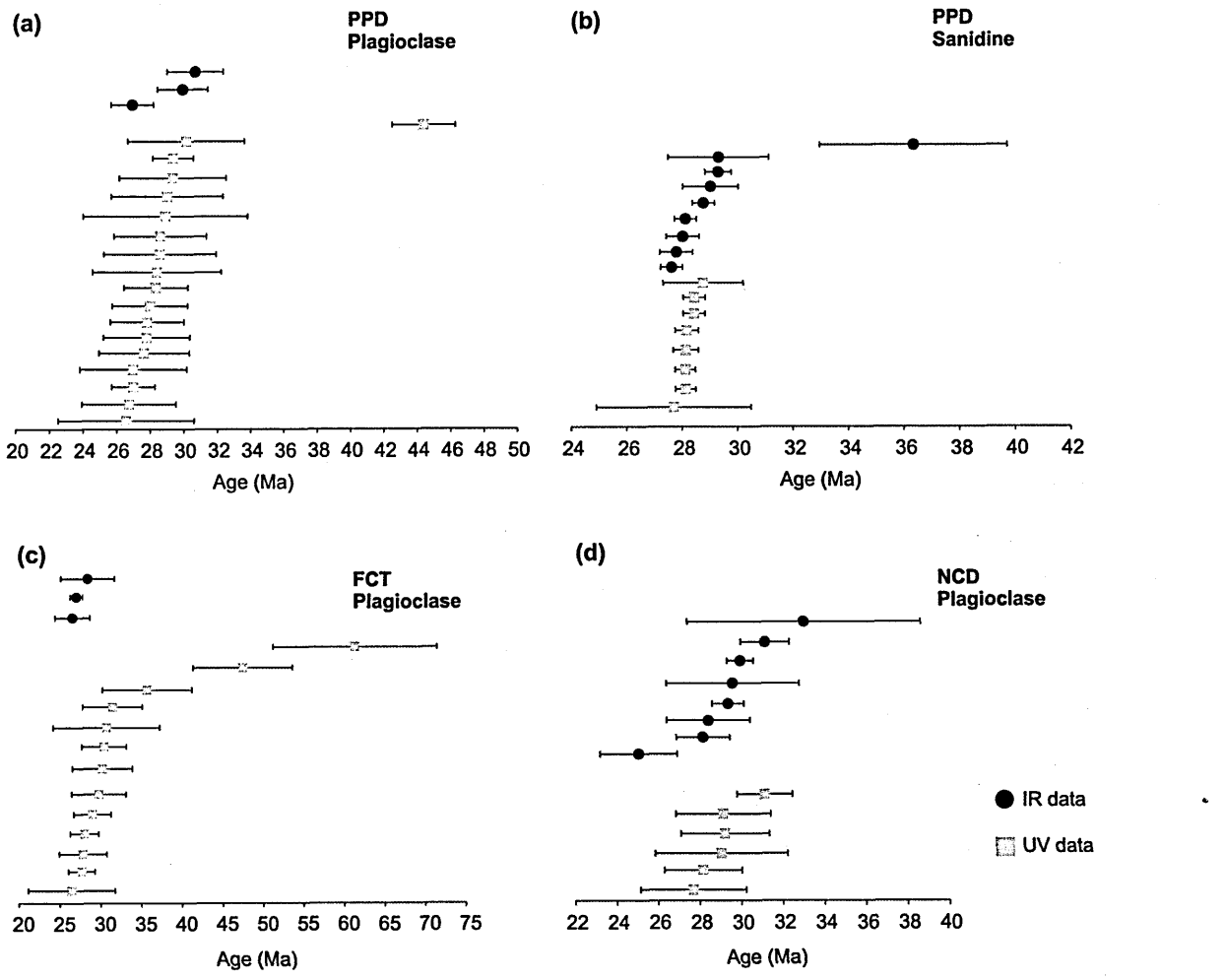

Figure 2.17. Selected data comparing apparent ages determined on Fish Canyon feldspar using the IR and UV laser probe technique. (a) and (b) Pagosa Peak Dacite plagioclase and sanidine; (c) Fish Canyon Tuff plagioclase; (d) Nutras Creek Dacite plagioclase. Note the use of different X-axis scale.

One of the key differences between laser/solid interaction for UV lasers and visible/near IR lasers is that the high power density of the UV laser pulses is absorbed by the top few microns of the sample resulting in ablation and release of gas from a restricted area. Kelley *et al.*, (1994) carried out UV spot and trench experiments on plagioclase and showed that minor melting (with no obvious melt halo) could occur in the area directly surrounding the laser pit, however the power emitted from an IR laser during spot analysis can heat the surrounding area resulting in a laser pit and a significant melt halo (Fig. A1.2; Appendix section A1). Therefore it may be expected that the IR laser could be analysing material from a larger area than intended by the user, which may lead to erroneous ages combined with no knowledge of what was actually analysed. Encouragingly, two Ar-Ar ages obtained from the same area within a single crystal (Sanidine #1; sample PCB 1), determined using the UV and IR techniques were indistinguishable at the 2σ level (UV age of 28.80 ± 1.44 and IR age of 28.80 ± 0.40 Ma).

For optically transparent minerals, such as sanidine, the near infrared range of wavelengths ($\lambda = 700$ to 1200 nm) have limited absorbance (< 40 %) compared to the strong absorbance (100 %) of the UV wavelength ($\lambda = 400$ to 200 nm) (Fig. 2.18; Kelley *et al.*, 1994; McDougall and Harrison, 1999). The ability of these clear minerals to transmit a high proportion of the power rather than absorbing it means internal refraction and reflection can cause the power to be lost to the surrounding sample holder and an inadequate volume of Ar gas to be released during analysis, resulting in ages with poor precision. This problem is further exacerbated when analysing young and/or K-poor (e.g., plagioclase) minerals where lower levels of radiogenic Ar are present.

There are several examples in the data where targeting clear, K-poor plagioclase feldspar with the IR laser, and measurement of Ar isotopes using the less sensitive MAP-215-50 mass spectrometer (i.e., compared to Nu Instruments Noblesse), has resulted in large age

uncertainties. This was particularly evident for NCD sample BFC115 where IR age uncertainties for plagioclase ranged ± 0.63 Ma to ± 5.61 Ma. Plagioclase #1 (sample BFC115 – 1; Fig. 2.15) yielded an IR age of 28.44 Ma, which was accompanied by a large uncertainty (± 5.61 Ma at 2σ level) and a ^{40}Ar and ^{39}Ar gas yield of 0.0987 and 0.0221 respectively. In comparison, a sanidine from the same sample (Sanidine #1; Fig. 2.15) yielded a ^{40}Ar and ^{39}Ar gas yield an order of magnitude higher (0.3615 and 0.1042 respectively) and consequently an age with better precision (uncertainty of ± 0.61 Ma).

Targeting K-rich minerals such as sanidine (contain ~ 12 wt. % K_2O compared to > 3 wt. % K_2O for plagioclase) with the IR laser can yield ages which have uncertainties similar to those determined using the UV laser. For example Sanidine #1 (sample PCB 1; Fig. 2.13) IR *in situ* age uncertainties ranged ± 0.47 Ma to ± 1.82 Ma, which is similar to those obtained using the UV laser (± 0.39 Ma to ± 1.44 Ma). Table 2.9 compares the laser pit size (cm^3) achievable for both techniques with the ^{40}Ar gas yield and % error on the age. It shows that despite limited coupling with the IR laser, the high potassium content of K - Feldspar, means that an age with suitable precision is still possible to achieve (0.69 % error compared to 8.97 % error for plagioclase). Therefore it appears that when circumstances are favourable, the IR laser probe technique could be successfully applied to K-rich feldspars.

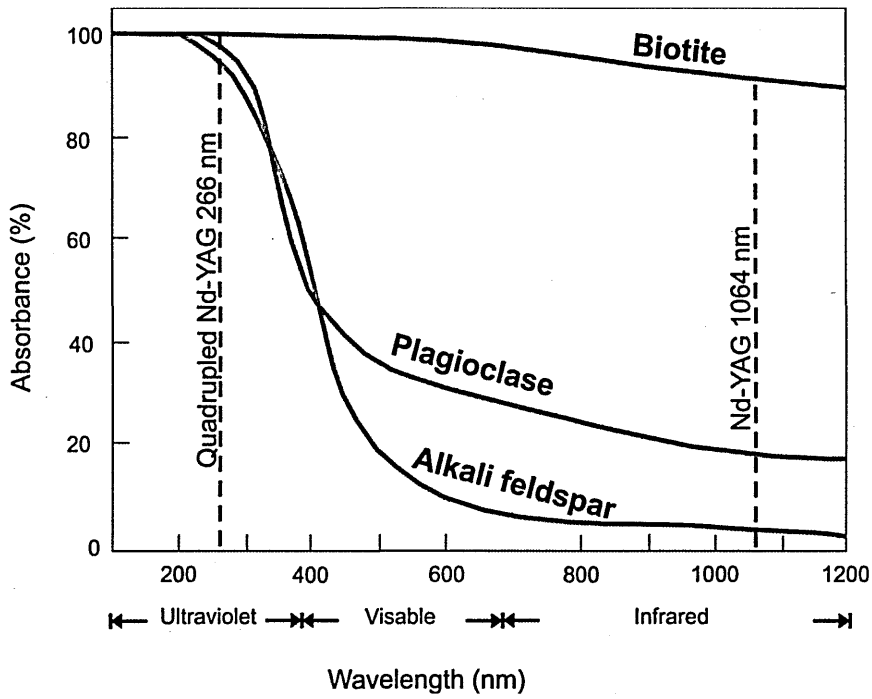

Figure 2.18. Generalised absorption spectra for mineral phases dated in this study (Alkali feldspar, plagioclase feldspar and biotite). Also shown are the characteristic wavelengths of lasers used in this study (Nd-YAG 266 nm = UV laser coupled with the Nu Instruments Noblesse and Nd-YAG 1064 nm = IR laser coupled with the MAP-215-50). For biotite almost 100 % of both the UV and IR wavelength is absorbed by the mineral whereas both Alkali feldspar and plagioclase absorb < 50 % of the IR wavelength in comparison to ~ 100 % of the UV wavelength (redrawn and modified after McDougal and Harrison, 1999).

Table 2.9. Comparison table outlining ^{40}Ar gas yield achievable based on K content of feldspar vs. technique (IR or UV) and % error on determined apparent age. Gas yield (^{40}Ar) is presented in cc x 10^{-10}.

Mineral:		Sanidine		Plagioclase	
Average K_2O content (%):		12		1.5	
Laser extraction technique	**Laser pit size (cm^3)**	**Gas yield (^{40}Ar)**	**% Error**	**Gas yield (^{40}Ar)**	**% Error**
UV	2.025×10^{-6} ^	1.019	0.648	0.116	3.857
IR	8.836×10^{-4} *	14.80	0.694	1.44	8.972

^ Volume of UV raster based on 450 μm^2 and an approximate depth of 10 µm

*** Approximate volume of IR analysis based on ~ 6 IR spots, each with a diameter of 100 µm**

The data also shows that even when using a UV laser, which couples intensely with clear silicate minerals, the low K content of the mineral stipulates that a large area be ablated. Therefore it may be possible to improve the precision of UV *in situ* ages obtained from low K minerals by increasing the size of the ablation pit or analysis area, although this increases the chance of targeting inclusions, areas of alteration or crossing grain boundaries and therefore is dependent on grain size, which can be affected by crystal shattering and dispersal upon eruption (Bachmann *et al.*, 2002). Another way that could increase the amount of material ablated for analysis is repeated rastering of the laser over the same area (e.g., Kelley *et al.*, 1994). The study by Kelley *et al.*, (1994) showed that ablation pits were blanketed internally by ejecta, which would make visual identification of material being analysed difficult. Experiments conducted in this study also saw evidence of this as well as considerable ejecta covering the glass sample cover slip, following analysis of biotite in particular.

2.7.1.2 *In situ* vs total fusion experiments

Total fusion analyses (single grains of biotite and sanidine (125 to 315 μm) and aliquots of 10 – 15 plagioclase grains) were performed using a CO_2 laser by Bachmann *et al.*, (2007b). Ages were calculated relative to Taylor Creek sanidine (TCs) standard age of 28.34 Ma (Renne *et al.*, 1998), and the ^{40}K decay constant of Steiger and Jäger (1977). In order to compare total fusion ages with the *in situ* UV and IR ages obtained in this study, the previous age determinations were recalculated relative to the ^{40}K decay constant and Taylor Creek sanidine (TCs) age (28.619 ± 0.034 Ma) or Renne *et al.*, (2010), and presented in summary Table 2.10.

Table 2.10. Summary table of total fusion age determinations of Bachmann *et al.*, (2007) recalculated using new ^{40}K decay constant.

Unit	Mineral Phase	Age* range (Ma)	n	Mean Age (Ma)	Stdv
PPD	sanidine	26.03 ± 0.14 to 28.42 ± 0.12	23	28.11	0.46
PPD	biotite	28.42 ± 0.2 to 28.62 ± 0.2	4	28.53	0.06
FCT	sanidine	28.28 ± 0.14 to 28.37 ± 0.1	12	28.31	0.03
FCT	plagioclase^	28.42 ± 0.24 to 28.65 ± 0.22	3	28.59	0.10
FCT	biotite	28.44 ± 0.22 to 28.61 ± 0.14	4	28.52	0.08
NCD	sanidine	28.29 ± 0.14 to 28.45 ± 0.14	27	28.34	0.04

*** Ar-Ar ages recalculated relative to ^{40}K decay constant of Renne *et al.*, (2010)**

^ Aliquots of 10 - 15 single grains melted for each analysis

UV and IR *in situ* age determinations from this study are generally in good agreement with the total fusion ages of Bachmann *et al.*, (2007b) (Fig. 2.19). This observation is encouraging and supports the application of the *in situ* laser probe method to material younger than ~ 50 Ma. In general PPD sanidine UV ages are in accordance with the range of PPD sanidine total fusion ages (Table 2.10). Reported total fusion sanidine results were shown to be extremely reproducible and all incremental heating experiments produced well-defined plateaus (Bachmann *et al.*, 2007b). The IR laser probe technique has identified ages (~ 29.3 Ma and an anomalously old age ~ 36.4 Ma) which fall above the upper age range and suggests grains are not completely homogeneous.

Bachmann *et al.*, (2007b) noted in general total fusion and incremental heating experiments for both biotite and plagioclase demonstrated good reproducibility, although the highest temperature step of a plagioclase step heating experiment yielded an age of > 30 Ma. FCT Plagioclase ages obtained by both UV and IR extraction techniques, despite large uncertainties, are generally in agreement with total fusion ages; however ages older than ~ 35 Ma have been identified using the UV laser (e.g., samples BFC129 – 1 and BFC129 – 2; Fig. 2.9). A number of FCT biotite UV ages (multiple analyses from two biotite grains) are slightly older than those obtained by single grain fusion and will be

discussed in more detail in section 2.7.2. In addition, Bachmann *et al.*, (2007b) analysed sanidine only from NCD sample (BFC115) and achieved a range in ages from 28.29 to 28.45 Ma. Both IR spot ages obtained from sanidine from this sample fall within this range.

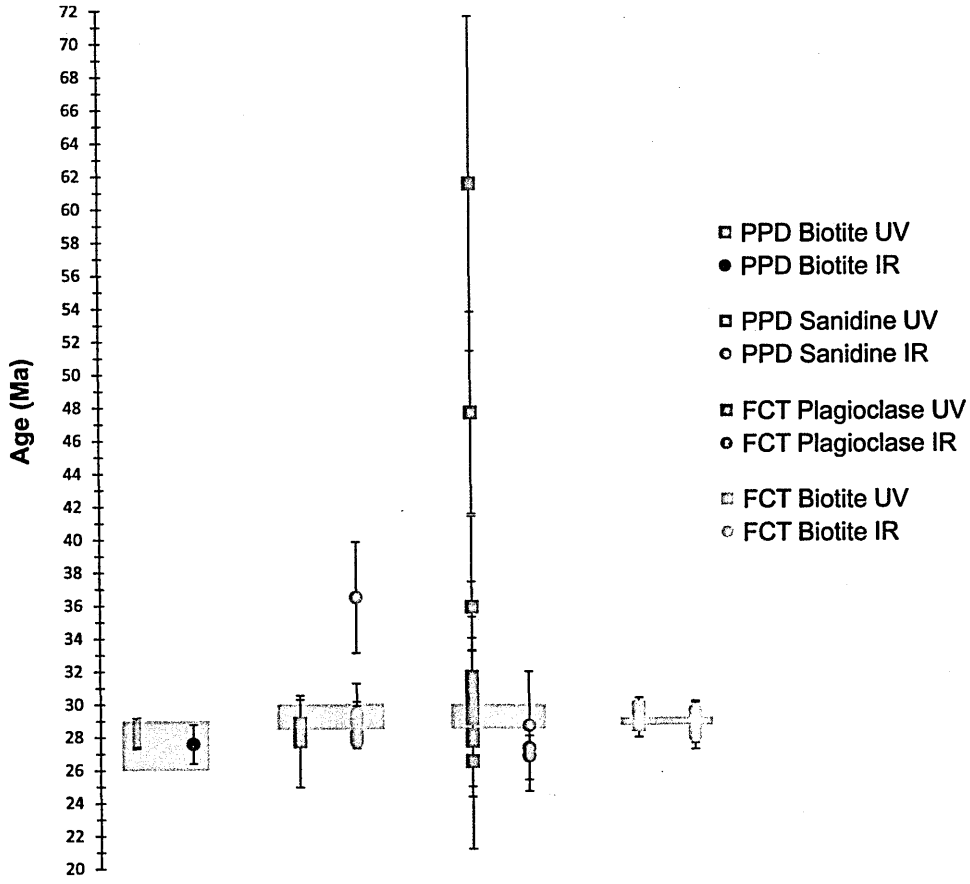

Figure 2.19. UV (squares) and IR (circles) *in situ* ages (this study; Ma ± 2σ) compared with the Ar-Ar total fusion age range (grey shaded box) of Bachmann *et al.*, (2007b) for selected minerals and Fish Canyon units. (PPD = Pagosa Peak Dacite, FCT = Fish Canyon Tuff).

2.7.2 Comparison of Ar-Ar *in situ* ages with previously published geochronological studies

Taking all minerals analysed in this study the age range seen is 25. 07 ± 1.86 Ma to 61.46 ± 10.11 Ma. In general ages obtained in this study range from the eruption age (within 2σ

uncertainty of FCs eruption age of 28.305 ± 0.036 Ma; Renne *et al.*, 2010) to ages slightly older (~ 29 to ~ 35 Ma) and significantly older (e.g., > 45 Ma) than the eruption age. Only one plagioclase (#4; BFC115 – 1, with an age of 25.07 ± 1.86 Ma) yielded an IR age significantly younger than the FCs eruption age. Minor alteration (sericitisation) of feldspar was noted during thin section analysis; therefore it is possible that this age is a result of laser coupling with altered feldspar not visible during Ar-Ar analysis.

2.7.2.1 Ar-Ar vs. U-Pb

For silicic volcanic rocks Ar-Ar and U-Pb dating techniques have potential to provide different views on the evolution of the unit of interest, for example pre-eruption residence times have previously been inferred (comparison of the Ar-Ar 'eruption' and U-Pb zircon ages) for silicic systems (e.g., Charlier and Zellmer, 2000; Reid *et al.*, 1997; Bachmann *et al.*, 2007; 2007b), and the identification of xenocrystic (e.g., Lanphere and Baadsgaard, 2001; Schmitt *et al.*, 2003; Simon and Reid, 2005; Bindeman *et al.*, 2006; 2008; Bachmann *et al.*, 2007b) and antecrystic zircons (e.g., Charlier *et al.*, 2005). U and Pb are retained by zircon at magmatic temperatures (> 700 °C) and therefore provide a record of mineral crystallisation (or remobilisation of crystal mush), which can occur over a range of timescales prior to eruption (e.g., Reid *et al.*, 1997; Bachmann *et al.*, 2007). It is acceptable for U-Pb ages to be older than Ar-Ar ages based on the difference in closure temperature (T_c), for the relative daughter products (Pb in zircon = > 800 °C; Cherniak and Watson, 2001, and Ar = < 500 °C; McDougall and Harrison, 1999).

The age discrepancy (≥ 0.4 Ma) identified between Ar-Ar single-grain fusion and step heating analyses, and U-Pb zircon ages by Bachmann *et al.*, (2007b) is inferred to represent a protracted crystallisation history in a large magma chamber, rather than due to bias in the decay parameters of ^{40}K (Simon *et al.*, 2008). Ar-Ar data in this study has been

corrected using newly optimised ^{40}K decay constant of Renne *et al.*, (2010). The FCs age, determined as part of the same study, is in agreement (2σ level) with astronomically tuned FCs age of Kuiper *et al.*, 2008 and Rivera *et al.*, (2011) calculated relative to Min *et al.*, (2000) ^{40}K decay constant. Therefore any age discrepancy resulting to calibration issues should be minimal, and ages obtained in this study can be compared to previously determined U-Pb ages.

Bachmann *et al.*, (2007b) $^{206}Pb/^{238}U$ single-crystal zircon ages (n = 29) and three multi-grain analyses yielded a range ~ 28.67 to 28.3 Ma for the bulk of the main-group zircons, covering a time span of ~ 300 ka (if taking FCT eruption age as ~ 28.3 Ma), and therefore recording a substantial time gap between magma crystallisation and extrusion. Similar observations were made by Schmitz and Bowring (2001) who achieved a zircon age range comparable to Bachmann *et al.*, (2007), whereas Lanphere and Baadsgaard (2001) found evidence of persistent inheritance and a zircon population with an age range of 1442 ± 19 Ma to 2350 ± 13 Ma. Inferred magma residence has also been noted in less voluminous magmatic systems, which can also yield zircon crystallisation histories in excess of 200 ka (e.g., Vazquez and Reid, 2004; Charlier *et al.*, 2005).

The uncertainties of the *in situ* ages obtained in this study preclude any attempt to conduct a meaningful reconciliation between the ages obtained in this study with the U-Pb zircon ages measured on the same sample set by Bachmann *et al.*, (2007b), however this study has identified a small number of *in situ* Ar-Ar ages which are older than the upper age limit (~ 28.67 Ma) set by the U-Pb zircon measurements (ID-TIMS) carried out by Bachmann *et al.*, (2007b). Although these ages are significantly older than the upper U-Pb age limit (e.g., PPD sanidine with an age of 36.42 ± 3.37 Ma; Fig. 2.20a; FCT biotite with an age of 29.67 ± 0.60 Ma; Fig. 2.20b; FCT plagioclase with an age of 61.46 ± 10.11 Ma; Fig. 2.20c and NCD plagioclase with an age of 31.12 ± 1.33 Ma; Fig. 2.20d), or slightly older (e.g.,

plagioclase ages ranging 30.11 ± 1.50 to 31.17 ± 1.17 Ma), all are younger in age than Precambrian zircon xenocrysts (1442 ± 19 Ma to 2350 ± 13 Ma) identified by Lanphere and Baadsgaard, (2001).

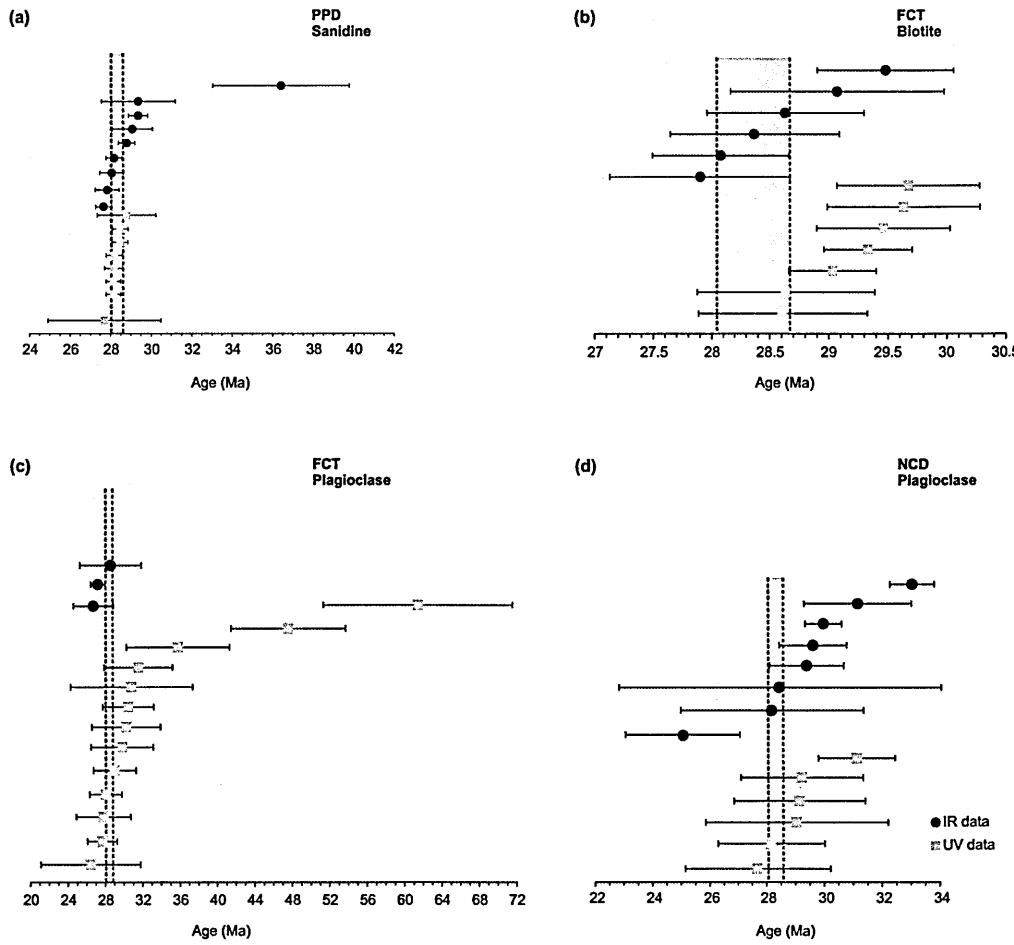

Figure 2.20. Selected Ar-Ar *in situ* ages (UV and IR) compared to range of U-Pb zircon ages (Bachmann *et al.*, 2007b), indicated by the red shaded area (uncertainty of Ar-Ar ages 2σ). (a) Pagosa Peak Dacite (PPD) sanidine; (b) Fish Canyon Tuff (FCT) biotite; (c) Fish Canyon Tuff (FCT) plagioclase; (d) Nutras Creek Dacite (NCD) plagioclase. Note the use of different scale.

2.7.2.2 Current age of the Fish Canyon sanidine (FCs)

Over the past 25 years the published ages of the FCs (see Rivera *et al.*, 2011 and references therein), has increased systematically from ~ 27.79 Ma (Cebula *et al.*, 1986) to ~ 28.3 Ma (Renne *et al.*, 2010) with a decrease in the age uncertainty from ± 0.19 Ma to ± 0.03 Ma. In recent years however changes to the age have centred on improvements to the ^{40}K decay

constant and measuring the standard on instruments capable of achieving increasingly higher resolution. Kuiper *et al.*, (2008) published an astronomically tuned age, relative to tephra of the Messadit section (Melilla Basin, Morocco) of 28.201 ± 0.023 Ma using the ^{40}K decay constant of Min *et al.*, (2000), which was later independently verified by Rivera *et al.*, (2011) with a published age of 28.172 ± 0.028 Ma. An age of 28.305 ± 0.036 Ma was published with the optimised ^{40}K decay constant of Renne *et al.*, (2010; 2011). In addition, Channell *et al.*, (2010) preferred an age of 27.93 Ma (~ 1.3 % younger than the other recently proposed FCs ages), for the FCs. This age for the FCs standard was selected by Channell *et al.*, (2010) over other recent age determinations (e.g., Kuiper *et al.*, 2008 and Renne *et al.*, 2010), in order to align Ar-Ar ages of Maui lavas that preserve the Matuyama-Brunhes (M-B) geomagnetic polarity reversal with the astronomical age of the M-B reversal.

In general, Ar-Ar *in situ* ages determined in this study are consistent with the recent Ar-Ar age determinations of the FCs with a small number of analyses falling above the upper eruption age limit set by Renne *et al.*, (2010) of ~ 28.3 Ma. The PPD sanidine ages in particular show to have good agreement. Although the uncertainties on measured *in situ* ages obtained in this study result in overlap with all recently determined FCs ages (Fig. 2.21), the data in this study once again show that the *in situ* method can be successfully applied to young (< 30 Ma) volcanic minerals, and that it is capable of highlighting older than expected apparent ages from discrete parts of single crystals (e.g., Ar-Ar age of ~ 36 Ma).

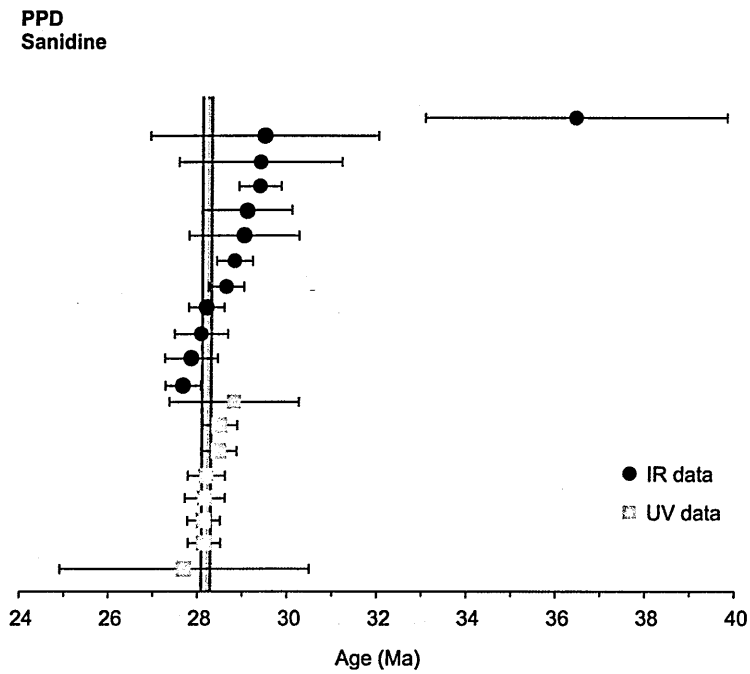

Figure 2.21. UV (squares) and IR (circles) $^{40}Ar/^{39}Ar$ *in situ* ages of PPD sanidine. Ar-Ar *in situ* ages are compared to recent FCs age determinations: purple line = 28.172 ± 0.0028 Ma (Rivera *et al.*, 2011); green line = 28.201 ± 0.023 Ma (Kuiper *et al.*, 2008), and red line = 28.305 ± 0.036 Ma (Renne *et al.*, 2010).

2.7.3 Older ages: extraneous Ar in the Fish Canyon magmatic system

Previous work on the Fish Canyon magmatic system has alluded to the occurrences of both excess and inherited Ar within different minerals (e.g., biotite and plagioclase). Dazé *et al.*, (2003) reported higher levels of variability, when comparing it to the relative reliability of the FCs, in both total fusion and step-heating analyses of Ar-Ar biotite standard FCT-3, due to $^{40}Ar_E$ hosted in contaminating phases too small to remove (e.g., ranging 26.93 ± 1.11 Ma to 29.14 ± 1.03 Ma). Other studies also demonstrated biotite heterogeneities at a single grain level using SEM imaging to identify inclusions of apatite, zircon, feldspar and iron oxide (Lanphere and Baadsgaard, 2001). Bachmann *et al.*, (2007b) found little evidence to support $^{40}Ar_E$ contamination of feldspar, biotite and hornblende, instead suggesting these minerals were capable of preserving small fractions of inherited Ar in retentive sites (structural traps) over much longer time periods (e.g., > 10^4 years), than had previously been suggested by diffusion modelling studies (e.g., Gardner *et al.*, 2002;

Gansecki *et al.*, 1996; Singer *et al.*, 1998). The data presented as part of this study also suggests the possible presence of small but significant amounts of heterogeneously distributed inherited Ar and/or $^{40}Ar_E$.

2.7.3.1 Inherited Ar

A protracted crystallisation history is favoured for the Fish Canyon magmatic system based on textural evidence (e.g., complex zoning patterns exhibited by minerals; Bachmann, 2001; Bachmann and Dungan, 2002; Bachmann *et al.*, 2002; Bachmann *et al.*, 2007b), thermal modelling (e.g., Bachmann and Bergantz, 2003) Sr isotopic heterogeneity (e.g., Charlier *et al.*, 2007), and Ar-Ar and U-Pb (ID-TIMS) zircon data (Bachmann *et al.*, 2007b). Therefore Ar-Ar ages which are significantly older than the eruption age could represent inherited Ar from a variety of different sources. The detailed petrographic study carried out by Bachmann (2001) identified co-magmatic holocrystalline granodiorite xenoliths in late erupted intra-caldera Fish Canyon Tuff with the same mineral assemblage as Fish Canyon magma but a higher proportion of quartz, sanidine, plagioclase and absence of glass as well as granitic xenoliths containing zoned plagioclase with calcic spikes up to An_{40} (Bachmann, 2001; Bachmann *et al.*, 2007b). A holocrystalline texture suggests it is likely to have cooled to temperatures lower than then main FC magma body (Charlier *et al.*, 2007), thus creating an environment where less diffusive re-equilibration could take place.

In addition to the main-group zircons, Bachmann *et al.*, (2007b) also obtained ID-TIMS U-Pb zircon ages from the sample of porphyritic granitic xenolith and granodioritic xenolith, which yielded mean ages indistinguishable from the main Fish Canyon Tuff zircons (mean age of 28.37 ± 44 and 28.40 ± 15 respectively, but with an age range of 28.18 ± 9 Ma to 30.29 ± 11 Ma). These samples were inferred to represent previously crystallised margins

of the Fish Canyon magma chamber. Charlier *et al.*, (2007) measured high whole rock $^{87}Sr/^{86}Sr_i$ ratios, and identified extremely radiogenic biotite, which they inferred to imply this sample was part of a fully crystallised rind of the Fish Canyon magma chamber. The high nature of the contamination is thought to have resulted from their close proximity to Precambrian wall rocks. This study has found several examples of older plagioclase ages which are similar to those obtained from the various xenolith samples, and therefore could be recording an earlier stage in the growth of the Fish Canyon magma chamber. PPD Plagioclase #12 (Fig 2.12; BFC83 - 4) yielded an IR age of 30.11 ± 1.50 Ma and PPD plagioclase #1 an IR age of 30.86 ± 1.66 Ma (Fig. 2.13; PCB 1) which are older than FCs eruption age of Renne *et al.*, (2010). Four further plagioclase analyses from BFC115 (Nutras Creek Dacite) also yielded ages ~ 30 Ma. Plagioclase #6 (raster #2; Fig. 2.11) yielded a UV age of 31.13 ± 1.33 Ma, plagioclase #2 yielded an IR age of 31.17 ± 1.17 Ma, plagioclase #3 yielded an IR age of 29.98 ± 0.63 Ma and plagioclase #5 yielded an IR age of 29.39 ± 0.77 Ma.

The plagioclase incremental heating experiments of Bachmann *et al.*, (2007b), yielded consistent plateaus and inverse isochron ages in agreement and with an atmospheric intercept, except one high-temperature step, which yielded an age of > 30 Ma. This age was inferred to represent a 'relic' core, recycled from an earlier stage of magma chamber evolution. Previous work (Whitney and Stormer, 1985; Bachmann *et al.*, 2002; 2007b) has demonstrated many of the plagioclases are oscillatory zoned with compositions ranging from An_{25} to An_{35} with abrupt calcic spikes (An_{40}) often < 100 μm apart as well as identifying plagioclase feldspar cores with a much higher anorthite content (up to An_{80}). The EMP study carried out as part of this work revealed just one plagioclase with a core value > An_{40}, possibly as a result of sampling bias. Unfortunately the size of ablation pits (> 400 μm wide) required for this study has made it impossible to investigate any relationship between measured Ar isotopes and reported these calcic spikes. In addition it

was not possible to test for the presence of $^{40}Ar_E$ using the inverse isochron method because more than three data points are required to construct an isochron (see Appendix section A1.5.3), and therefore $^{40}Ar_E$ contamination hosted in fluid or melt inclusions (e.g., Boven *et al.*, 2001), cannot be entirely ruled out.

The U-Pb zircon study of Bachmann *et al.*, (2007b), also presented evidence to support incorporation of the 35 to 31 Ma magmatic cycle of intermediate composition lavas and breccia, present around the perimeter of the San Juan volcanic field. U-Pb zircon ages distinctly older than the main group represented by ages > 28.7 Ma were again obtained from a xenolith sample from within the FCT. Biotite #2 (Nutras Creek Dacite; sample BFC115 – 2; Fig. 2.11), yielded two ages older than ~ 30 Ma (35.43 ± 3.56 Ma and 34.36 ± 3.44 Ma), and therefore may have been sourced from rocks of the 35 to 31 Ma magmatic cycle. However it should be noted that two other UV ages from the same biotite yielded ages in agreement with the FCs eruption age of Renne *et al.*, (2010). There is no evidence to suggest minerals (in particular biotite) have suffered significant K loss, which can result in older ages and an initial $^{40}Ar/^{36}Ar$ ratio higher than atmospheric (e.g., Smith *et al.*, 2008). EMP analysis of biotite from all samples revealed that K_2O (wt. %) content remained constant (ranging ~8 to ~10 %). Therefore $^{40}Ar_E$ contamination may be a likely explanation.

Xenocrystic minerals incorporated into magma at temperatures > 700 °C would be expected to be open and remain open to Ar loss by equilibration with the melt. Gardner *et al.*, (2002), modelled diffusive loss of Ar from biotite in the Toba Tuff magma (720 to 780 °C), and concluded that unlike hornblende and plagioclase, a biotite xenocryst (~ 1.5 Ma), would equilibrate and be completely reset in < 100 years (diffusion parameters of McDougal and Harrison, 1999), and would therefore not retain memory of an older source.

Thomas *et al.*, (2003) documented Toba Tuff biotite (and plagioclase) Ar-Ar ages that were significantly older than the eruption age, possibly due to inherited Ar from xenocrysts incorporated via crustal assimilation and/or remobilisation of previously erupted material. This would be a valid explanation if xenocrysts were considerably older and residence time in the magma was short, or xenocrysts were entrained during the eruption rendering complete diffusive re-equilibration impossible. Therefore it is also likely that $^{40}Ar_E$ contamination of both mineral phases could be responsible for the elevated ages.

The model of Charlier *et al.*, (2007), includes the assimilation of Precambrian country-rock blocks as well as crystallising Fish Canyon magma at magma chamber edges, and U-Pb zircon data of Lanphere and Baadsgaard showed evidence of contamination by grains of Precambrian zircons ($^{207}Pb/^{206}Pb$ age ranged 1442 ± 19 to 2350 ± 13), as well as zircons from earlier San Juan volcanic field eruptions. No Precambrian ages were found as part of this study; however several ages older than ~ 40 Ma were identified. PPD plagioclase #1 (Fig. 2.22a; BFC83 - 1) yielded an anomalously old UV *in situ* age of 44.54 ± 1.89 Ma, and FCT plagioclase #1 (Fig. 2.8; BFC129 - 1) yielded two older ages (47.61 ± 6.1 Ma and 61.46 ± 10.12 Ma; Fig. 2.22b). Both ages are associated with extremely high $^{37}Ar/^{39}Ar$ isotope ratios (11.99 ± 0.14 and 9.02 ± 0.16 respectively). Compared to other plagioclase analyses from the same sample where $^{37}Ar/^{39}Ar$ ratio range 2.45 to 3.77, this suggests a higher than average Ca content for this plagioclase, and therefore anorthite-rich. It is possible that these ages represent inherited Ar from a previous stage in the evolution of the magma chamber, however the ages are significantly older than the start of magmatism in that area (at ~ 35 Ma).

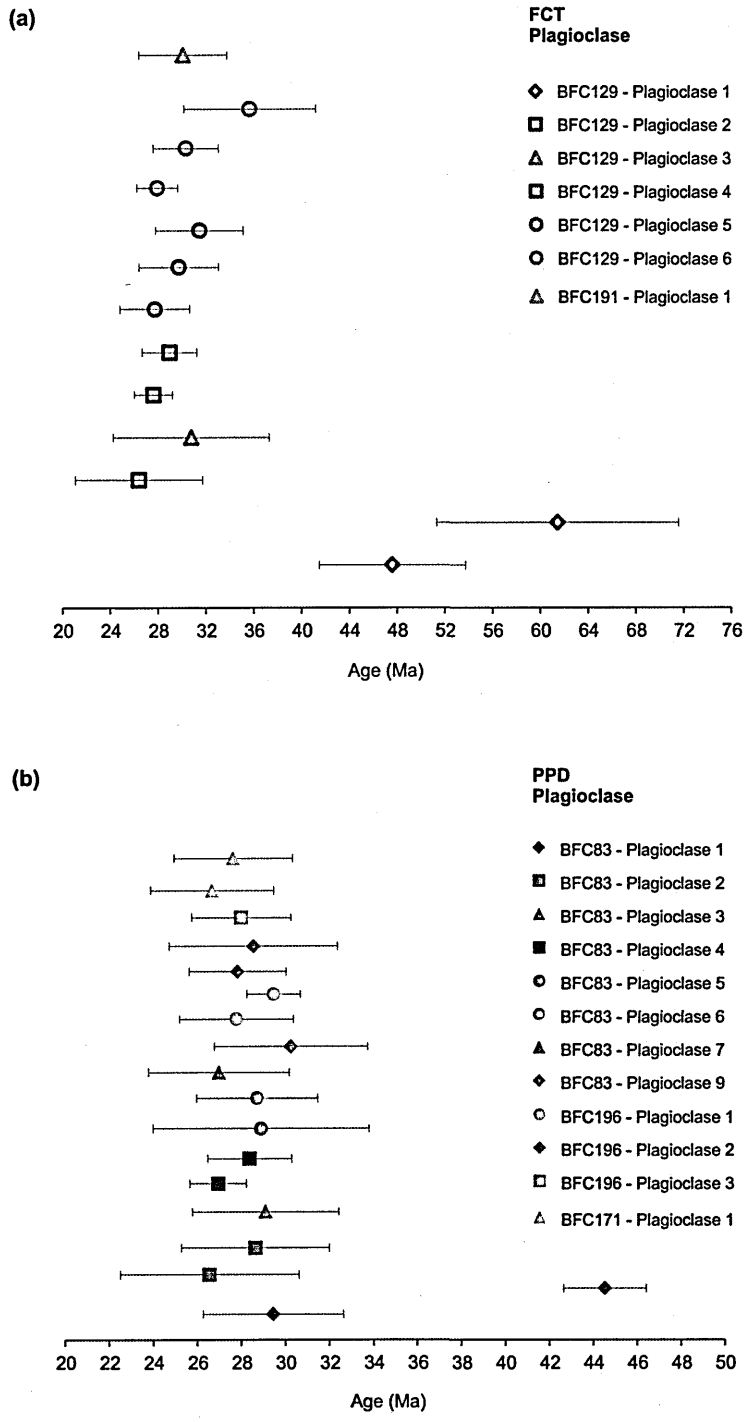

Figure 2.22. Individual UV *in situ* plagioclase Ar-Ar ages for (a) Pagosa Peak Dacite samples, and (b) Fish Canyon Tuff samples. Note the use of different scale.

The older UV *in situ* and IR plagioclase and biotite ages could represent partially re-set xenocrysts sourced from country-rocks assimilated during the evolution of the Fish Canyon magma chamber. Evidence for old (inherited) Ar in plagioclase has also been reported for the Young Toba Tuff (YTT), ignimbrite, which similar to the FCT, is thought

to have had a complex crystallisation history (Chesner *et al.*, 1998; Gardner *et al.*, 2002). The assimilation of crystallised Fish Canyon Magma (e.g., outer rind of the magma chamber; Charlier *et al.*, 2007; Bachmann *et al.*, 2007b), cooled to a temperature whereby the retention of radiogenic daughter product has occurred may be possible. The lack of strong and consistent coincidence between U-Pb zircon and Ar-Ar ages (i.e., this study has revealed Ar-Ar ages that are significantly older than the mean zircon age of Bachmann *et al.*, 2007b), required to prove the inheritance hypothesis means that $^{40}Ar_E$ contamination (e.g., incorporated during growth and/or hosted within fluid/melt inclusions), may be a more likely explanation for the older plagioclase and biotite ages.

2.7.3.2 The case for excess Ar ($^{40}Ar_E$)

The Fish Canyon magma chamber is considered to be an archetypal mushy magma chamber, which evolved in a shallow crustal reservoir (2.2 to 2.5 kbar) at near solidus temperatures (~ 700 °C), and that progressive re-heating of magma body from ~ 710 to 760 °C was responsible for re-mobilising ~ 5000 km^3 (dense rock equivalent) of material (Bachmann et al., 2007b). Bachmann and Bergantz (2003) proposed the upward percolation of a hot gas phase, released from mafic magmas positioned beneath the Fish Canyon magma body as a mechanism for thermally rejuvenating the crystal mush. Based on numerical modelling the study suggested 'gas sparging' could reheat > 5000 km^3 of Fish Canyon Mush from 720 to 760 ± 10 °C in ~ 150 to 200 kyr. An alternative model, proposed by Burgisser and Bergantz (2011), could remobilise the Fish Canyon mushy magma chamber in < 200 years. Burgisser and Bergantz (2011), also suggest that would take only a small number of successive overturns (remobilisation caused by mobile layer buoyantly rising into the crystal mush), to efficiently homogenise the magma body.

Textural evidence to support the process of thermal rejuvenation can be seen in the partial dissolution of feldspar and quartz phases (Bachmann, 2001; Bachmann *et al.*, 2007b). Evidence for the resorption of both phases are seen in the majority of samples analysed in this study, in particularly sample BFC83 (e.g., Fig. 2.23a), and sample BFC191. Feldspar and quartz exhibit a corroded, sieve texture with some containing melt embayments at their grain edges, which suggests melting has taken place.

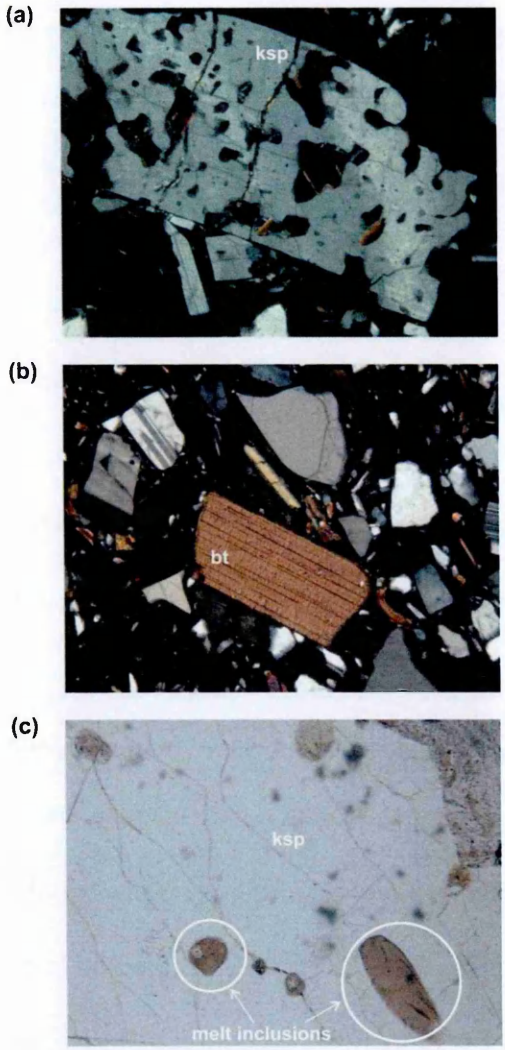

Figure 2.23. Thin section photomicrographs showing various textures of the Fish Canyon mineral phases. (a) Sample BFC83; Resorbed sanidine exhibiting a sieve texture and containing numerous inclusions. (b) Sample BFC191; Euhedral biotite exhibiting no signs of resorption. (c) Sample PCB 1; Large sanidine containing glassy brown melt inclusions. Some inclusions are rounded whilst others display an elongated shape. (Scale = Image width; 2.5 mm).

ICP-MS analysis of trace element concentrations in feldspars, hornblende, biotite, titanite, zircon, magnetite and interstitial glass carried out by Bachmann *et al.*, (2005), showed that this late stage dissolution of feldspar and quartz increased the proportion of melt in the final stages prior to eruption and interstitial glass yielded elevated Ba and Sr contents (e.g., 100 ppm Sr and 500 ppm Ba) and other feldspar compatible elements (e.g., Eu). In addition euhedral hydrous minerals (hornblende and biotite) were crystallising simultaneous to the dissolution of feldspar prior to eruption. Evidence to support this is seen in a rimward Sr and Ba increase in concentrically zones, euhedral, hornblende (Bachmann *et al.*, 2005; 2007b). Euhedral biotite is common in sample BFC191 (e.g., Fig. 2.23b), and show little to no resorption textures. Therefore it might be expected that the feldspars yield anomalous ages, because of the processes acting on them prior to eruption, as well as potentially originating from multiple sources (e.g., xenoliths, magma chamber wall rock material), and biotite should be the one phase to yield an eruption age due to its late stage growth in the magma chamber. $^{40}Ar_E$ (parentless radiogenic $^{40}Ar^*$) dissolved in the magma, can be liberated from any K-bearing rock (host rock), mineral (e.g., phenocrysts and xenocrysts), or part of a mineral (fluid/melt inclusions). Mechanisms by which excess radiogenic Ar can become decoupled from its parent isotope, include active assimilation and fractional crystallisation, whereby already crystallised material containing *in situ* produced Ar (from the decay of K) is assimilated into the melt, and therefore so is any associated radiogenic Ar (Kelley, 2002).

Assimilation of crystallised Fish Canyon magma (Bachmann, 2001) and wall-rock material (e.g., Charlier *et al.*, 2007) was thought to be an active process in the Fish Canyon magmatic system. A detailed Rb-Sr study carried out by Charlier *et al.*, (2007) showed that eruptive products of the Fish Canyon magmatic system, in some cases exhibited extreme Sr isotopic heterogeneity within individual crystals and between mineral phases (e.g., biotite and feldspar). Contamination by Precambrian wall-rocks of around (~ 1 %), via

assimilation events during residence in, and transport upwards through the crust probably occurred within < 10 000 years of the eruption. Their model describes the assembly in the upper crust of a dacitic magma chamber, built up by additions of silicic and mafic melt causing the temperature and crystallinity to oscillate. Partial digestion and disaggregation (e.g., liberation of radiogenic grain boundary melts and zircons) of roof and side wall country rocks via reactive bulk assimilation (and aided by thermal rejuvenation; Bachmann *et al.*, 2005) is thought to explain the presence of inherited radiogenic Sr from basement rocks in biotite, not present in the feldspars, which grew prior to assimilation event and were being resorbed prior to eruption (Charlier *et al.*, 2007).

The process of wall-rock assimilation and thermal rejuvenation of a crystal mush, in particular the late stage dissolution of K-bearing minerals (e.g., feldspars) could be an affective mechanism whereby radiogenic $^{40}Ar^*$ could be liberated and dissolved into the melt, increasing the concentration of Ar in the melt. Rejuvenation by 'gas sparging', stipulates the injection of gas must be balanced with the expulsion of a fraction of interstitial liquid (~ 9 to 10 km^3, after 150 to 200 kyr; numerical modelling carried out by Bachmann *et al.*, 2005). Therefore the mass movement of molten silicate melt through the mush body may create pockets of crystal poor/Ar-rich melt. Crystal poor fallout in the FC deposits, inferred to represent such melt pockets has previously been inferred by Bachmann *et al.*, (2005). The interstitial rhyolite of the Fish Canyon deposits has SiO_2 contents of ~ 76 wt. % (Bachmann, 2001). Solubility studies (e.g., Carroll and Stolper, 1993) have shown that Ar solubility increases with increasing SiO_2 content, and in rhyolite can be as high as 0.8 ppm bar^{-1} (Kelley, 2002). Excess $^{40}Ar^*$ could potentially be highly compatible with the interstitial melt in the magma chamber and could become concentrated in pockets of melt transported through the crystal mush. Equally, the assimilation of country rock/magma chamber rind, and the resorption of feldspar and quartz, could be efficiently achieved by 'stable front remobilisation' (Burgisser and Bergantz; 2011), and

the method of unzipping described by the authors, could aid the movement of $^{40}Ar_E$-rich pockets of melt throughout the remobilised mush.

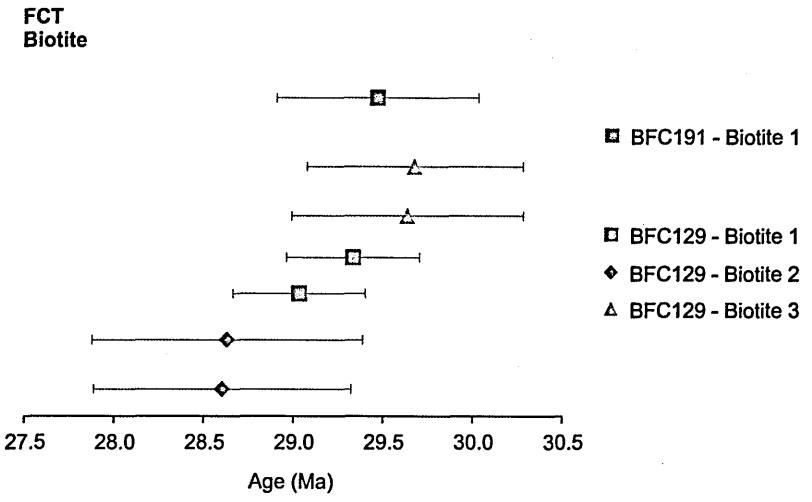

Figure 2.24. Individual UV *in situ* biotite Ar-Ar ages (± 2σ) for all Fish Canyon Tuff samples.

This study has identified the presence of minor $^{40}Ar_E$ in biotite and feldspar, previously undetected by single grain fusion and step heating experiments (e.g., Bachmann 2001; Bachman *et al.*, 2007b). Three biotite grains from FCT sample BFC129 (Fig. 2.24) yield UV *in situ* ages older than those achieved by previous total fusion and step heating experiments (e.g., Dazé *et al.*, 2003; Bachmann *et al.*, 2007). An inverse isochron diagram (Fig. 2.25), plotted for all UV *in situ* biotite ages for sample BFC129 yields an inverse isochron age of 28.82 ± 0.42 Ma (MSWD = 2.1), which is slightly older than FCs age (28.305 ± 0.04 Ma; Renne *et al.*, 2010). An atmospheric intercept of 309 ± 8.9 for the trapped Ar component is slightly higher than the atmospheric $^{40}Ar/^{36}Ar$ ratio value 298.56 (Lee *et al.*, 2006), suggesting $^{40}Ar_E$ contamination is responsible. In comparison, single grain fusion and step heating (aliquot of 10 to 15 grains) ages published by Bachmann *et al.*, (2007b) were reported as being reproducible with a weighted mean plateau age of 28.22 ± 0.11 Ma (MSWD 0.7) for PPD and 28.19 ± 0.09 Ma (MSWD = 1.4) for the FCT.

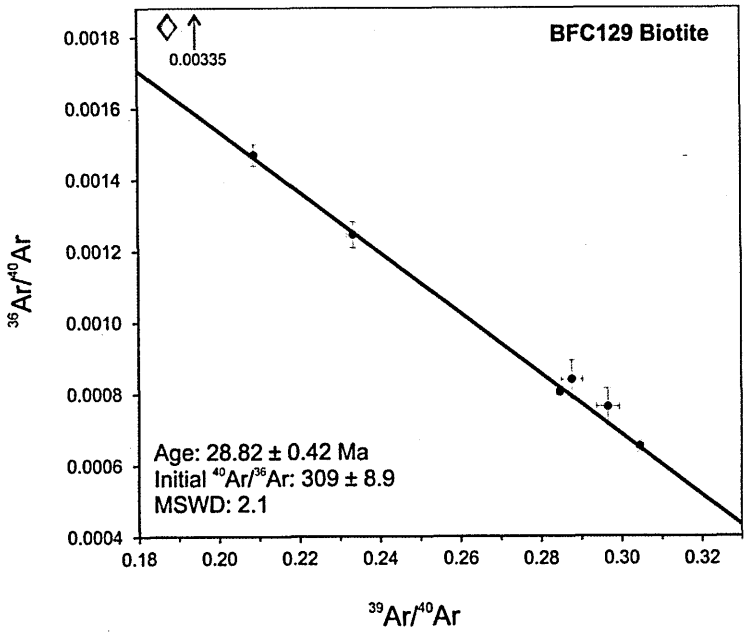

Figure 2.25. Inverse isochron plot for all UV *in situ* biotite analysis for FCT sample BFC129 (determined using Isoplot; Ludwig, 2011). The value of modern air ($^{36}Ar/^{40}Ar = 0.00335$) is indicated by a red diamond.

The highly incompatible nature of Ar in solid/melt (and solid/fluid) systems means that Ar strongly partitions from crystals into melts and from melts into bubbles in magmatic systems (Kelley, 2002). It is assumed that the transit of Ar through a magmatic system is unidirectional, and Ar lost to fluids and melts are therefore effectively lost to an 'infinite reservoir' whereby $^{40}Ar^*$ does not partition back into the minerals. However if $^{40}Ar^*$ in the melt reaches a significantly high concentration then excess $^{40}Ar^*$ can partition back or equilibrate into minerals (Kelley, 2002), and melts can act as Ar transfer media between mineral sources and recipient sink, whether this be diffusion into another mineral or degassing to the atmosphere. Increase in Ar concentration elevates partial pressure of Ar (P_{Ar}) and Ar equilibration between different phases depends on the relative solubilities (e.g., vapour phase >> melt >> biotite > sanidine). Biotite incorporates excess Ar due to relatively high Ar mineral/fluid partition coefficient and so therefore can yield

anomalously old ages compared to other K-bearing minerals, such as sanidine (Hora *et al.*, 2010).

The late stage growth of biotite in the Fish Canyon magma just prior to eruption should make it a reliable chronometer. However, occurrences of extraneous Ar in biotite, separated from volcanic rocks is not unusual, and has been routinely presented in the literature (e.g., Thomas *et al.*, 2003; Gardner *et al.*, 2002; Bachmann *et al.*, 2010; Hora *et al.*, 2010). A comparison study using Ar-Ar and U-Pb ages (Kos-Nisyros volcanic complex, Greece; Bachmann *et al.*, 2010), presented biotite data which highlighted the Ar-Ar biotite age spectra was disturbed, older than the U-Pb zircon ages in the same unit, and too old to represent the eruption age. Although U-Pb zircon ages revealed xenocrystic contamination, inverse isochron $^{40}Ar/^{36}Ar$ intercepts (either higher than the atmospheric value 298.56, or overlapped with 298.56 but within very large errors), support excess ^{40}Ar (^{40}Ar-rich reservoir not equilibrated with atmosphere), in the mineral structure or within inclusions. Hora *et al.*, (2010), presented a large database of Ar-Ar analyses on coeval volcanic biotite and sanidine from the Andean Central Volcanic zone (5.6 Ma to 40 ka), to show a ~ 600 kyr age difference between the two mineral phases. Biotite Ar-Ar age distribution was skewed towards older apparent ages as a result of partitioning and/or degassing behaviour for Ar among sanidine and biotite prior to eruption. The study also postulated that if the eruption temperature is lower than biotite T_c then $^{40}Ar_E$ already partitioned into biotite will remain. The mineral is effectively already locked to volume diffusion at the point of eruption, and therefore not able to fully equilibrate with the atmosphere.

The older ages yielded by biotite in sample BFC129 are interpreted as resulting from minor $^{40}Ar_E$ contamination. The processes of assimilation of country rocks (Pre-Cambrian), and

magma chamber roof and wall-rock (e.g., model to account for Rb-Sr heterogeneities; Charlier *et al.*, 2007), as well as the dissolution of K-bearing minerals (e.g., feldspars), during episodes of thermal rejuvenation of the crystal mush (e.g., Bachmann and Bergantz, 2003; Bachmann *et al.*, 2005; Burgisser and Bergantz; 2011), is a process by which excess $^{40}Ar^*$ could be dissolved into the melt. Concentration of $^{40}Ar^*$ in pockets of melt heterogeneously distributed and transported through the crystal mush could reach a significant level as to cause partitioning back into already crystallised biotite, or be incorporated into the mineral (lattice or inclusions) during late stage growth, simultaneous with the dissolution of feldspars prior to eruption.

$^{40}Ar_E$ rich inclusions can artificially elevate Ar-Ar apparent ages (e.g., Rama and Hart, 1965; Kelley *et al.*, 1986; Harrison *et al.*, 1994; Esser *et al.*, 1997; Boven *et al.*, 2001; Kelley, 2002 and references therein; Jones *et al.*, 2008). Fluid inclusions, owing to the relatively higher solubility of Ar in hydrous fluids compared to melt inclusions ($^{40}Ar_E$ contents of fluid inclusion can range ~ 0.08 to 22 ppm; Kelley, 2002), can be a significant source of $^{40}Ar_E$ but are often harder to detect with the naked eye and/or under a petrological microscope. Fish Canyon minerals contain numerous melt inclusions and melt pools (e.g., sample PCB 1; Fig. 2.23c), in particular in sanidine crystals, so inclusion derived $^{40}Ar_E$ might be expected to cause sanidine to yield older than expected ages. IR *in situ* analysis of a sanidine crystal (Fig. 2.8 and Fig. 2.13), has identified a heterogeneous age distribution with an age of ~ 36 Ma being obtained from one part of the crystal as well as significant Ca and Cl content variability. Although two UV *in situ* apparent ages are in good agreement with each other, $^{37}Ar/^{39}Ar$ and $^{38}Ar/^{39}Ar$ vs. age data scatter plots (Fig. 2.26) show these two data points alone highlight Ca, and possibly Cl distribution are heterogeneous at the single grain level. Prior to Ar-Ar analysis, a microscopic investigation did not reveal this crystal to be several crystals inter-grown (i.e., sample BFC129; Fig. 2.9) and inclusions, although not specifically located, may be present. The crystal was clear

(almost transparent), and areas analysed were located away from the grain edge, therefore neither the UV or IR laser is thought to have analysed the surrounding matrix.

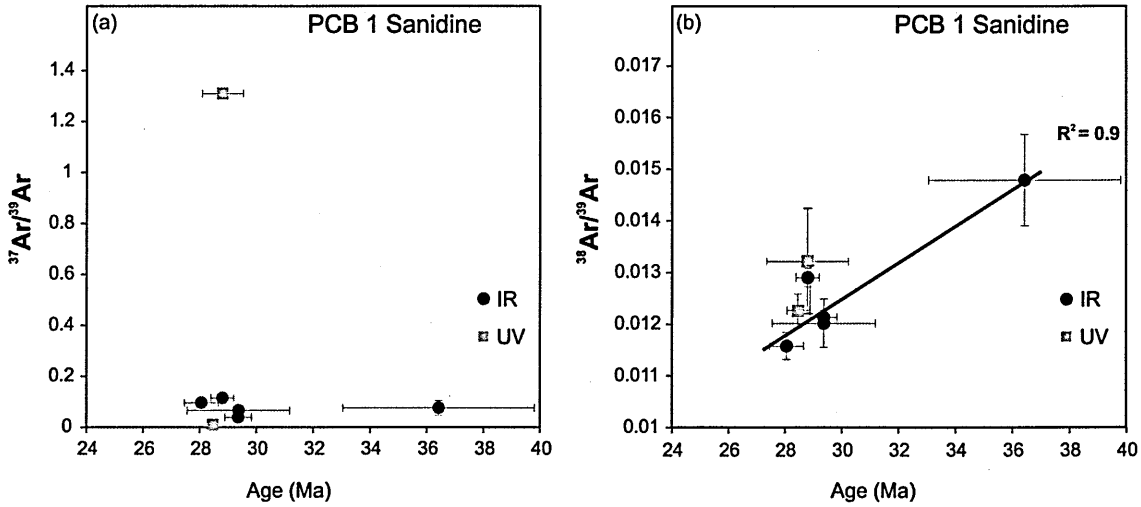

Figure 2.26. $^{37}Ar/^{39}Ar$ vs. age (Ma) and $^{38}Ar/^{39}Ar$ vs. age (Ma) plots for PPD sample PCB 1 (sanidine #1) showing both IR (circles) and UV (squares) data. (a) illustrates the differing Ca content between two UV analyses and (b) illustrates the positive correlation ($R^2 = 0.9$) between the Cl content and IR age. All errors shown are 2σ.

Previous work (e.g., Bachmann *et al.*, 2002) has demonstrated the poikilitic nature of resorbed sanidine, which can contain isolated swarms of plagioclase feldspar (An_{28} to An_{33} and range few microns to ~1 mm), possibly formed as plagioclase were engulfed by regrowth of sanidine, or nucleation of plagioclase from melting sanidine during multiple episodes of sanidine growth. EMP analysis from this study has highlighted a variation in An content (range from < 1 to > 30) within single grains, and some were found to have An rich rims, whilst others exhibited An rich cores. It is therefore possible that increases in $^{37}Ar/^{39}Ar$ could represent Ca-rich plagioclase feldspar inclusions, however the oldest age (Sanidine #1; PCB 1) corresponds to a low $^{37}Ar/^{39}Ar$ ratio (> 0.1) compared with a plagioclase crystal (plagioclase #1; sample PCB 1), which yielded a $^{37}Ar/^{39}Ar$ ratio of > 1.4 and suggests this older apparent age is not a result of a plagioclase inclusion being analysed. Further to this there does appear to be a correlation between IR age and $^{38}Ar/^{39}Ar$

ratio (Fig. 2.35; $R^2 = 0.9$), and the older apparent age is associated with a higher $^{38}Ar/^{39}Ar$ ratio (~ 0.015).

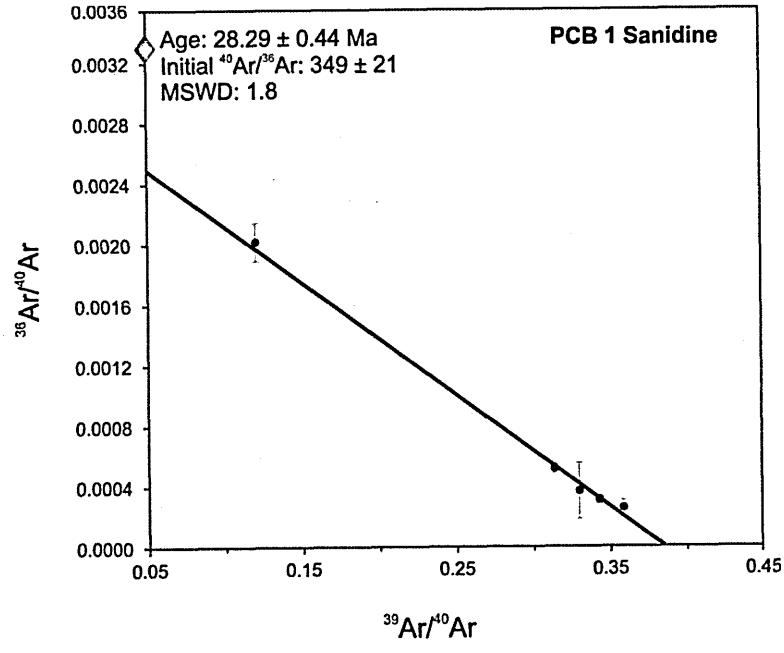

Figure 2.27. Inverse isochron for IR *in situ* sanidine ages (sample PCB 1) (determined using Isoplot; Ludwig, 2011). The value of modern air ($^{36}Ar/^{40}Ar = 0.00335$) is indicated by a red diamond.

An inverse isochron (Fig. 2.27) yielded an age of 28.29 ± 0.44 Ma but an initial $^{40}Ar/^{36}Ar$ ratio of 349 ± 21 (> 298.56) suggesting $^{40}Ar_E$ contamination of this sanidine. Both *in vacuo* crushing (quartz, e.g., Rama and Hart, 1965; Kelley *et al.*, 1986), and incremental heating experiments (K-feldspar, e.g., Harrison *et al.*, 1994; Esser *et al.*, 1997) have highlighted apparent age (and the release of $^{40}Ar_E$ from fluid inclusions) correlated with measured Cl/K ratio, which is based on the measurement of ^{38}Ar isotope from the rapid decay of ^{38}Cl. Therefore $^{38}Ar_{Cl}$ can be used as a proxy for the chlorine content of the sample. Therefore, an elevated $^{40}Ar/^{36}Ar$ ratio coupled with an elevated $^{38}Ar/^{39}Ar$ signal suggests the IR laser heated the analysis area and 'popped' a fluid inclusion, releasing $^{40}Ar_E$ as well as a true radiogenic Ar component ($^{40}Ar^*$), resulting in an age older than expected. This highlights the advantage of applying the *in situ* method and its ability to identify intra-grain age variation.

Despite continued use of FCs as an inter-laboratory standard and previous studies supporting its homogeneity (e.g., Baksi *et al.*, 1996; Renne *et al.*, 1998; Jourdan and Renne, 2007; Bachmann *et al.*, 2007b; Renne *et al.*, 2010; Rivera *et al.*, 2011), sample PCB 1 (sourced from the same magma chamber as the FCs), has shown that fluid inclusion hosted $^{40}Ar_E$ can reside within these crystals. The occurrences of $^{40}Ar_E$ may be low in sanidine due to a lower Ar partition coefficient compared to other minerals (e.g., biotite) (Kelley, 2002), and/or rapid diffusive equilibration with the atmosphere (e.g., Renne *et al.*, 1998; Hora *et al.*, 2007; 2010). If $^{40}Ar_E$ is present then it may go undetected due to sanidine having a relatively high K_2O content, and so therefore a higher radiogenic component that is capable of masking the $^{40}Ar_E$ signal (e.g., Hora *et al.*, 2007). Previous studies have analysed single FCs grains (e.g., Dazé *et al.*, 2003; Bachmann *et al.*, 2007; Renne *et al.*, 2010; Rivera *et al.*, 2011) as well as aliquots of multiple grains (e.g., step heating experiments of Bachmann *et al.*, 2007), which may homogenise the $^{40}Ar_E$ signal with *in situ* produced $^{40}Ar^*$ from within a single grain or from multiple grains, therefore concealing its presence but resulting in generally older ages.

The random occurrences of significantly older ages suggests strongly that small pockets of $^{40}Ar_E$ are responsible rather than due to inheritance, where you might expect a greater emphasis on older ages. It appears that not all crystals are affected, for example sample BFC83 contained a large (~ 2500 μm in length) sanidine crystal (Fig. 2.5; Sanidine #1; BFC83 – 3), which yielded UV *in situ* ages in agreement with each other at the 2σ level (range 28.13 ± 0.36 to 28.48 ± 0.38 Ma) and yielded a weighted mean age of 28.22 ± 0.18 at (MSWD = 0.57; probability = 0.69), which is in good agreement with recent age determinations of the FCs (e.g., Renne *et al.*, 2010; Kuiper *et al.*, 2008; Rivera *et al.*, 2011). When UV *in situ* ages are compared to total fusion Ar-Ar ages from the same

sample (Fig. 2.28) the range of ages achieved from analysing multiple single grains can also be obtained from within a single grain.

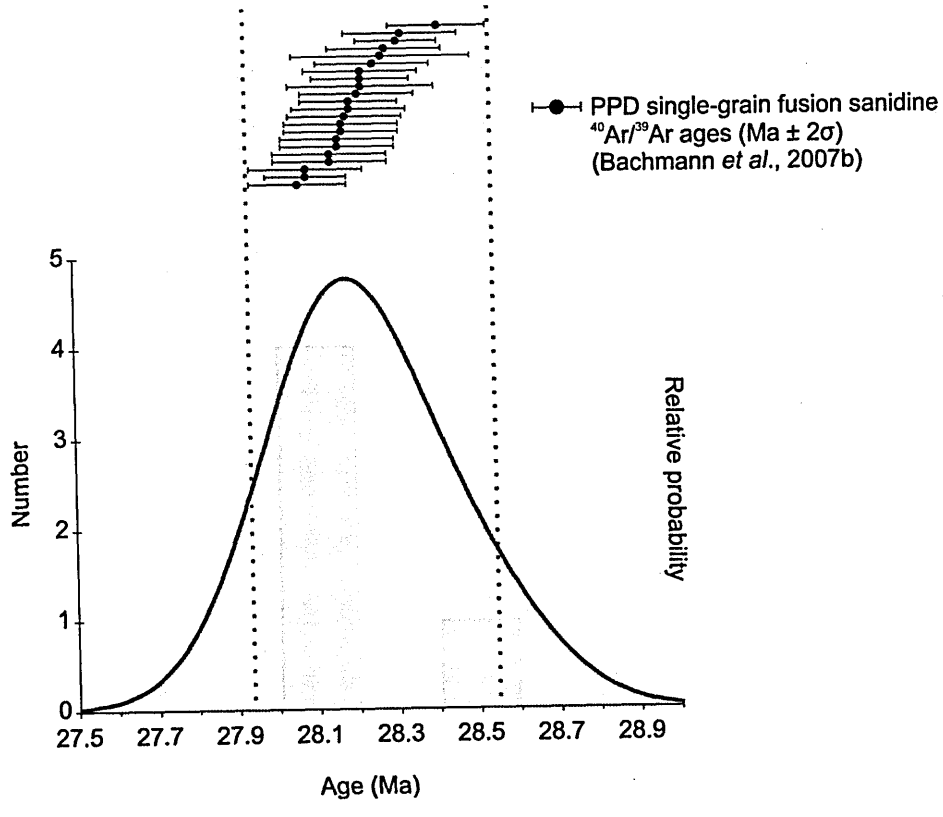

Figure 2.28. Probability curve of UV *in situ* Ar-Ar ages from a sanidine grain (Sanidine #2; sample BFC83 where n = 5). Compared to single grain fusion sanidine ages (n = 22) (Bachmann *et al.*, 2007b). The range of single grain fusion ages is marked by dashed red line.

2.7.3.3 Volatiles and degassing of the Fish Canyon magma

Heterogeneous degassing of volatiles and therefore Ar immediately prior to and during the eruption may be the reason why occurrences of $^{40}Ar_E$ are low but still exhibit occasional spikes. The explosive eruptive style of the Fish Canyon magmatic system is thought to be a result of shallow storage (2.2 to 2.5 kbar) of a volatile rich magma, saturated with a vapour phase (Bachmann, 2001; Bachmann and Bergantz, 2003). Depressurisation (e.g., Sparks, 1997) and late stage crystallisation (e.g., Tait *et al.*, 1989) results in the build-up of

volatiles in the interstitial melt, which may go on to trigger an eruption. Clay *et al.*, (2011) demonstrated that concentrations of $^{40}Ar_E$ in volcanic glass decreased with increasing sample vesicularity. This supports the current understanding that during the eruption Ar will naturally partition into the volatile rich interstitial melt/fluid/vapour phase over remaining in a solid phase, due to its incompatible nature (Kelley, 2002).

Bachmann (2001) noted a lack of textural evidence (e.g., reaction rims on hornblende or microlite nucleation in groundmass), constrains timing of degassing to shortly before or during eruption. Depressurisation during eruption of the less explosive PPD due to degassing in the eruption conduit and via multiple vents lead to instability of magma chamber roof, which triggered the eruption of FCT. Therefore varying degrees of degassing in different parts of the magma chamber prior to and during the eruption may have resulted in considerable equilibration with the atmosphere and the re-setting of most minerals. However, incomplete degassing of minerals which contain significant amounts of $^{40}Ar_E$ due to growing in a $^{40}Ar_E$ rich environment (e.g., biotite), and/or $^{40}Ar_E$ trapped in inclusions hosted in sanidine and plagioclase, although more noticeable in plagioclase owing to its relatively low K content compared to sanidine, has resulted in these older ages being recorded.

2.8 Conclusions

This study has produced a new data set of Ar-Ar ages corrected relative to the recently defined ^{40}K decay constant of Renne *et al.*, (2010) for multiple minerals phases (plagioclase, sanidine and biotite) of the Fish Canyon magmatic system, using both the UV and IR *in situ* method.

- This study has demonstrated that the UV *in situ* method, and in some cases the IR *in situ* method, can be successfully applied to young (< 40 Ma) volcanic minerals, thus providing a way to investigate both inter- and intra-grain Ar-Ar apparent age variation. Although this study has confirmed the limited use of the IR laser on K-poor, optically transparent minerals (e.g., plagioclase feldspar) due to the poor absorption of the IR wavelength, it can be applied with moderate success to K-rich feldspars such as sanidine and dark minerals such as biotite, and can be used to highlight Ar isotope (e.g., $^{38}Ar/^{39}Ar$ and $^{37}Ar/^{39}Ar$) ratio and apparent age variation within single grains.

- The UV laser has proved to be most useful in obtaining ages from all mineral phases analysed, although for young samples a large area (> 400 μm^2) needs to be ablated in order to release enough Ar gas, to allow a measurement with suitable precision to be made. Where crystals are large enough to permit multiple analysis, the UV *in situ* technique can be applied to minerals < 40 Ma. This work is significant because it has been able to spatially resolve apparent age variability within single crystals, whereas the previous Ar-Ar single grain fusion study of Bachmann *et al.*, (2007b) was able to highlight variability between single grains (n = < 30) and identify older incremental heating steps. This work has shown that the spread of ages within a single grain (e.g., Sanidine #2; sample BFC83), can span the range of single crystal ages determined by total fusion or step heating experiments. This 'homogenisation effect' whereby total fusion ages are a combination of ages yielded from different parts of a crystal may be a serious problem if parts of a crystal contain $^{40}Ar_E$ (e.g., Sanidine #1; PCB 1), therefore resulting in older apparent ages.

- The identification of fluid inclusion hosted $^{40}Ar_E$ in a sanidine (sample PCB 1), does suggest the presence of decoupled $^{40}Ar^*$ within pockets of interstitial melt/fluid in the Fish Canyon mush, which can be incorporated into minerals during growth. Minor contamination may previously have gone unnoticed owing to the high K content of K-feldspar (e.g., sanidine) and the homogenising effect (mixing of $^{40}Ar^*$ signal with minor $^{40}Ar_E$) of previous total fusion or multi-crystal step heating experiments.

- Fish Canyon biotite has reproducibly shown to yield older ages and $^{40}Ar_E$ contamination identified in this study may be a consequence of late stage crystallisation in an Ar rich environment due to the dissolution of K-bearing phases (e.g., Fish Canyon feldspar or assimilated wall-rock) prior to eruption. Owing to a higher partition coefficient, Ar* in the pockets of melt/fluid/vapour present in the crystal mush during thermal rejuvenation may have in parts of the magma chamber reached a significant concentration as to cause partitioning back into biotite, which was subsequently not lost (via degassing) from some crystals.

- The identification of slightly older plagioclase ages (~ 30 Ma) may represent inherited Ar from relic material recording a stage in Fish Canyon magma chamber assembly prior to eruption or partially re-set xenocrysts incorporated into the magma via the assimilation of wall-rock. U-Pb zircon ages has alluded to varying degrees of inheritance (e.g., Schmitz and Bowring, 2001; Lanphere and Baadsgaard, 2001; Bachmann *et al.*, 2007b). However, the occurrences of significantly older Ar-Ar ages (> 45 Ma), older than zircons analysed by Bachmann *et al.*, (2007b) are more likely to represent $^{40}Ar_E$ trapped in fluid and/or melt inclusions, which are common in plagioclase (e.g., Boven *et al.*, 2001). This

coupled with the lower K content of these minerals, means that even retaining small amounts of excess Ar can result in older ages.

- Finally, it has been shown that Ar-Ar ages obtained in this study are generally in good agreement with both single grain fusion ages previously determined by Bachmann *et al.*, (2007b) and current Ar-Ar age data for the FCs (e.g., Renne *et al.*, 2010; Rivera *et al.*, 2011). However inhomogeneity at the single grain level has been identified, and there is evidence to support the presence of $^{40}Ar_E$ in minerals of the FCT, PPD and NCD, which are all sourced from the same magma chamber. This work has shown $^{40}Ar_E$ contamination of the Fish Canyon magmatic system warrants further examination and particular attention should be paid to the FCs because of the invested interest the Ar-Ar community has in this extensively used Ar-Ar standard.

Chapter 3. Yellowstone: New insights into caldera and post-caldera activity.

3.1 Introduction

The Ar-Ar technique has been successfully applied to potassium-bearing minerals separated from volcanic rocks (e.g., Renne *et al.*, 1997), which are thought to effectively exclude initial Ar at magmatic temperatures. The assumption is that volcanic crystals remain 'open' to Ar diffusion until quenching on eruption, thereby making them ideal material for determining the timing of eruption. However several complicating factors exist (e.g., inherited Ar from xenocrystic contamination, $^{40}Ar_E$, recycling of previously crystallised material in the magma chamber termed 'self-cannibalisation'), which can reduce the accuracy of calculated ages. Increasing instrumental precision (e.g., dating events to the nearest 5000 years; Storey *et al.*, 2012), means that even small amounts of contamination can now significantly affect the conclusions of a dating study.

Contamination by older material is a major problem and evident in both effusive and explosive volcanic rocks (e.g., Gansecki *et al.*, 1998). $^{40}Ar_E$ trapped within inclusions (e.g., Esser *et al.*, 1997) or derived from mantle or shallow hydrothermal sources and trapped in defects in the crystal lattice (e.g., sanidine; Villa, 1991), can artificially elevate Ar-Ar apparent ages. Although present in older samples, it is often masked by sufficient radiogenic ingrowth. However, in the case of young and/or low-K samples, the effect can be significant, where only low concentrations of radiogenic Ar ($^{40}Ar^*$) are produced and measured. Therefore it is critical to understand the impact of such contamination and develop ways of mitigating the complications presented by it.

Feldspars are frequently used for Ar-Ar dating of volcanic samples, due to their abundance in the majority of silicic rocks. K-rich feldspars have a relatively high potassium content (up to 12 wt. %) compared to plagioclase feldspars (> 1 wt. %), which is critical for particularly young samples, where time for ingrowth of radiogenic Ar has been short, and the precision of ages determined using K-poor, and hydrous mineral phases is greatly reduced. It may prove useful to analyse a variety of mineral phases within the same sample, as well as the glass phase. Glass can be a significant host of potassium and its use is becoming increasingly more common where suitable phenocryst phases are unavailable (e.g., Garcia *et al.*, 2010). However the abundance of glass in some samples does not ensure its usefulness as a geochronometer due to its inherent instability. Compared with alkali feldspar, glass is susceptible alteration through hydration and devitrification processes, which can all lead to erroneous Ar-Ar ages either through radiogenic Ar loss, or $^{40}Ar_E$ gain (e.g., Kaneoka, 1972, Dalyrymple and Lanphere, 1969, Foland *et al.*, 1993). It has also been demonstrated that the concentration of atmospherically derived or $^{40}Ar_E$ can be orders of magnitude higher than radiogenic Ar (e.g., Walker and McDougall, 1982). However, in some cases it has been possible to obtain meaningful ages (e.g., Bigazzi *et al.*, 2008; Morgan *et al.*, 2009), due to samples showing a lack of microlites (which can be a source of contamination), and no systematic elemental spatial variation of the most mobile oxides (e.g., K_2O and Na_2O).

In this study, the Ar-Ar single grain fusion technique has been applied to feldspar, and where possible, glass separates from samples of both explosive (Huckleberry Ridge Tuff; HRT, and Mesa Falls Tuff; MFT), and effusive, dome building volcanic activity to occur in the Yellowstone Plateau Volcanic Field. Rocks of the Yellowstone Plateau Volcanic Field are ideal for investigating Ar systematics in a classic periodically reactivated large-volume silicic, mushy state magma body (Vazquez *et al.*, 2009). The aim of this study is to identify the presence of extraneous Ar within crystals. Extraneous Ar can be problematic

for young volcanic minerals where it can dominate the overall $^{40}Ar^*$ budget, especially in cases where minerals fail to be fully re-set upon eruption. It is not possible to determine the degree of partial degassing from single-fusion ages alone; however it is possible to model diffusive loss from contaminating crystals using a program for simulating Ar diffusion in minerals (e.g., DIFFARG; Wheeler, 1996).

The first major eruption to occur at Yellowstone (HRT) has been extensively investigated, and recent work (e.g., Ellis *et al.*, 2012) suggests that a significant time gap exists between HRT member B and C. This study has applied the Ar-Ar single grain fusion technique to the three members of the HRT and the MFT to identify erroneous ages and investigate possible reasons for them. In addition, prior to undertaking this work, no published Ar-Ar ages existed for Green Canyon Flow, Sheridan Reservoir or Snake River Butte domes (Table 3.1), which will also be presented here. Previously determined K-Ar for Sheridan Reservoir dome does not agree with other geochronometers (e.g., U-Pb zircon ages of Bindeman *et al.*, 2007; C. Wilson, *pers. com.*, 2012), or field relations (C. Wilson, *pers. com.*, 2011; 2012). Snake River Butte is a pre-HRT rhyolite dome and should thus yield older ages than HRT, however a previous K-Ar age determination of 1.99 ± 0.02 Ma (cited in Christiansen, 2001), which places it just after the HRT is therefore too young. Finally, Green Canyon Flow overlies the HRT and is overlain by MFT and therefore should record an eruption age between the two. A previously determined K-Ar of 1.17 ± 0.01 Ma (cited in Christiansen, 2001), is again too young.

Table 3.1. Summary table of previously published ages for the effusive, dome-building eruptions investigated in this study.

Unit Name	Age (Ma) K-Ar	Age (Ma) U-Pb	Age (Ma) Ar-Ar
Green Canyon Flow	1.17 ± 0.01*	1.35 (PDF peak age)[#]	Investigated in this study
Sheridan Reservoir	4.0 ± 0.4[¥]	2.07 ± 0.19^ 2.04 ± 0.02[##]	Investigated in this study
Snake River Butte Flow	1.99 ± 0.02*	Weighted average is 2.18 Ma 2.17 Ma and 2.23 Ma (PDF peak ages) [#]	Investigated in this study

[¥] Cited in Morgan *et al.*, (1984); * Obradovich (1992), cited in Christiansen, (2001); ^ Bindeman *et al.*, (2007); [#] C. Wilson (*pers. com.*, 2011); [##] C. Wilson (*pers. com.*, 2011) (n = 93, MSWD = 2.6).

3.2 Geological setting

3.2.1 Snake River Plain

Episodes of basaltic and silicic volcanism, which follow the 2 cm/yr SE migration of the Northern American plate over the concentrated high heat flow termed the Yellowstone hotspot, is responsible for numerous nested caldera clusters (Fig. 3.1a) for over ~ 16 Ma (Bindeman *et al.*, 2007; Perkins and Nash, 2002). Partial melting of the crust is responsible for the formation of large silicic magma bodies, which have erupted with both explosive and effusive styles, erupting through progressively thicker; more evolved silicic crust (Bindeman *et al.*, 2007). The track is defined by the eruption of metaluminous ($Al_2O_3 < CaO + Na_2O + K_2O$) ash-flow tuffs and rhyolites which young in a north eastward direction, and show systematic variations in magma composition, temperature, eruption frequency and erupted volume (e.g., 250 to 600 km^3). Unaltered silicic ash fall tuffs are abundant in Neogene sedimentary basins of the western USA, providing an important distal record of explosive volcanism along the hotspot track (e.g., Perkins and Nash, 2002).

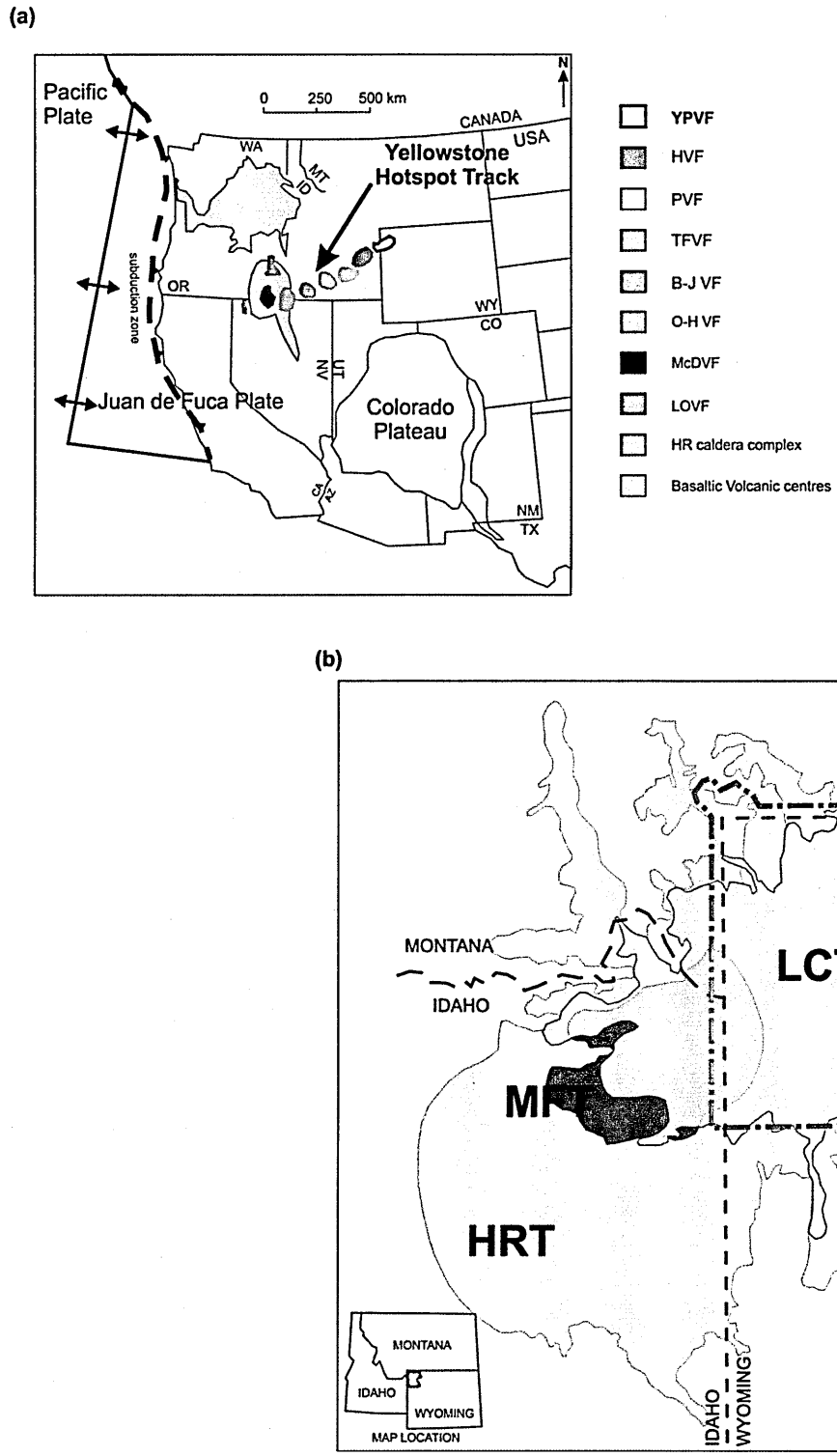

Figure 3.1. (a) Location and tectonic setting of the Yellowstone hotspot track marked by numerous caldera clusters. HR caldera complex = High Rock caldera complex; LOVF = Lake Owyhee Volcanic Field; McDVF = McDermitt Volcanic Field; O-H VF = Owyhee-Humboldt Volcanic Field; B-J VF = Bruneau-Jarbidge Volcanic Field; TFVF = Twin Falls Volcanic Field; PVF = Picabo Volcanic Field; HVF = Heise Volcanic Field and YPVF = Yellowstone Plateau Volcanic Field (redrawn and modified after Perkins and Nash, 2002); (b) Map of the VPVF, Wyoming, Idaho and Montana, showing the three major ash-flow sheets; Huckleberry Ridge Tuff, Mesa Falls Tuff and Lava Creek Tuff and generally accepted ages (redrawn and modified after Gansecki *et al.*, 1998).

3.2.2 The Yellowstone Plateau Volcanic Field (YPVF)

Yellowstone Caldera in the YPVF (within the states of Wyoming, Idaho and Montana) is the youngest of a series of large calderas formed along the Yellowstone hotspot track (Christiansen, 2001; Lanphere *et al.*, 2002; Perkins and Nash, 2002; Saunders *et al.*, 2007). The largest Yellowstone eruptions occurred within a period of > 2 Myr (late Pliocene to middle Pleistocene) and produced three major ash-flow sheets (Huckleberry Ridge Tuff, Mesa Falls Tuff and Lava Creek Tuff; Fig. 3.1b), collectively termed the Yellowstone Group, which are separated by distinct hiatuses in volcanic activity (Lanphere *et al*, 2002). Rhyolitic volcanism within the Yellowstone Plateau is not only confined to large explosive caldera forming events, it is also responsible for various inter- and intra-caldera dome-building events (e.g., Bindeman *et al.*, 2007, Vazquez *et al.*, 2009). Pre- and post-caldera rhyolites have been identified for each ash-flow tuff of the Yellowstone Group (e.g., Sheridan Reservoir dome and Green Canyon Flow dome) (Christiansen, 2001).

3.3 YPVF: Major explosive eruptions and effusive dome-building eruptions

Explosive volcanism in the YPVF is separated into three cycles, which are responsible for the three major ash-flow sheets mentioned above. During each of the caldera forming volcanic cycles (HRT, MFT and LCT); rhyolitic and basaltic lavas were erupted before and after the major ash-flow eruptions. Most of the rhyolitic lavas are restricted to the source areas of the major ash-flow sheets, where collapse of magma-chamber roofs form calderas. The geological setting of the first and second volcanic cycles and of each rhyolite dome assessed as part of this study are summarised below, and accompanied by previous geochronological work.

3.3.1 First cycle eruption: The Huckleberry Ridge Tuff (HRT)

The HRT (Fig. 3.2) is an extensive ash-flow sheet with an erupted volume of ~ 2450 km^3, which may have covered an initial area of > 15 000 km^2. The HRT can be divided into three distinct units, designated members A, B and C, each intercalated with fall deposits and a different source area (Christiansen, 2001; Lanphere *et al.*, 2002).

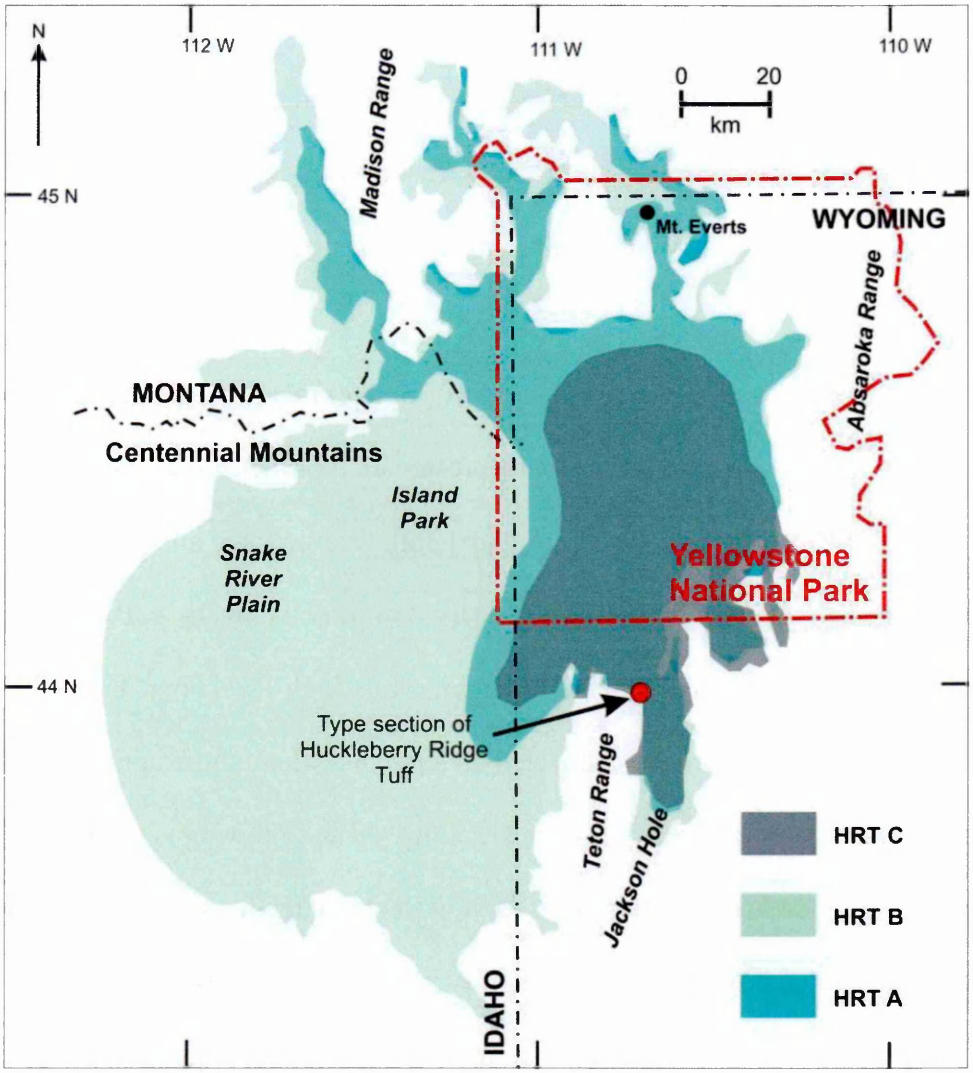

Figure 3.2. Map showing the approximate distribution of the Huckleberry Ridge Tuff members A, B and C. Also shown is the locality of the type section and Mt. Everts. State boundaries and Yellowstone National Park boundaries are shown for reference (redrawn and modified after Christiansen, 2001).

Field evidence suggests the HRT eruption was intermittent, prolonged and involved multiple magma types. New work has demonstrated the presence of time breaks between members. Based on cooling breaks and degassing histories inferred from field relationships (C. Wilson, *pers. com.*, 2010; 2011), members A and B are separated by weeks or more, and members B and C separated by years or more, possibly even decades. In addition, Christiansen (2001) notes a well-sorted, parallel-bedded fallout deposit between members B and C. However there is no evidence to support the existence of a significant erosional break between them (Christiansen 2001; Lanphere *et al.* 2002). A recent study (Ellis *et al.*, 2012) presented high-precision single crystal Ar-Ar ages and concluded that member C significantly post-dates members A and B by at least 6 kyr, suggesting it is a separate eruption and that explosive activity occurred more frequently.

Much of the main HRT eruptive area is buried by younger rocks and faults, some brecciated by erosion, which has affected the preservation of the first volcanic cycle compared with the third cycle (Lava Creek Tuff) unit. Stratigraphic and petrologic relations determined where possible have been used to infer members A, B and C may have represented the eruption of batches of magma from high-level crustal magma chamber or chambers, which were connected at depth and where the eruption of one triggered the eruption of the next (Christiansen, 2001). The following is a summary of the main features assigned to, and inferred for each of the three members (for a detailed explanation see Christiansen, 2001). It is only ever possible to see these features in part at any one locality, and it should be noted that intense welding of the ignimbrite, faulting and erosion makes locating fresh, juvenile material to work on difficult. All members of the HRT are present at the type section (see Fig. 3.2), 2 km northeast of Flagg Ranch in Wyoming, just south of the boundary of Yellowstone National Park. Interestingly, the Ellis *et al.*, (2012) study claimed to have collected samples of all three members from the type locality, although field locality photographs presented in the supplementary information

suggests that it may not have been the exact location of the type locality (C. Wilson, *pers. com.*, 2011).

HRT member A covers an estimated area of 6,280 km^2 with an erupted volume of > 820 km^3 and is mainly distributed around the edges of the Yellowstone Plateau. The percentage of phenocrysts present in member A changes with progression upwards from a phenocryst-rich welded tuff at the base to phenocryst-poor at the top caused by extreme sorting during eruption and emplacement rather than reflecting primary crystal abundance zonation in the magma chamber. Crystals tend to be concentrated near the source, whereas glass (which is less dense and can travel further), is more prevalent in distal deposits. The small number of welded pumice lapilli present (mostly at the base) suggests that the magma erupted with a violent release of contained gases causing the pumice to be disaggregated into phenocrysts and glass shards and sorting to occur. A basal fallout ash is present beneath Member A (best exposed on the cliffs of Mount Everts; Fig. 3.2), which is dominated by a fine grained ash deposited in continuous planar bedding (Christiansen, 2001). Evidence for regional re-working by wind or water, and multiple transport directions suggests a weak eruptive style rather than a violent surge (C. Wilson, *pers. com.* 2010; 2011). A similar fall deposit is also seen between B and C, suggesting the stop start nature of the eruption allowed the plume to dissipate prior to ignimbrite generation.

Member B is present over much of the area of the HRT (15,400 km^2 and a volume of 1,340 km^3). The base of member B is phenocryst-poor and similar to the upper part of member A. But in contrast to member A, the phenocryst-poor basal unit progresses up into more phenocryst-rich rocks and welded pumice inclusions contain phenocrysts in proportion to those of whole rocks suggesting that this variation resulted from compositional zonation in the erupted magma. The uppermost part of member B contains dark-grey and white crystallised pumice hosted in devitrified rocks. This two-pumice zone is only identified

from this member of the HRT, which makes it a useful lithological marker. Member B lies on member A in almost all exposures to the north except in the Southern Madison Range where it forms a vitrophyric welded tuff containing dark pumice inclusions.

Member C is the smallest distinct ash-flow subsheet (covered an estimated area of 3,690 km^2 with a volume of ~ 290 km^3) and is only present south of the Yellowstone Plateau (from northern Teton Ridge to Flat Mountain and from Red Mountains to Jackson Hole). The base of member C (where exposed), overlies member B and the unit is characterised by stretched pumices. The thicker sections of member C are in the vicinity of the type section where it is ~100 m thick. In comparison to members A and B, member C contains smaller phenocrysts and a higher ratio of quartz to feldspar phenocrysts. The contact between members B and C is mostly sharp with no glassy chilled zone; however Christiansen, (2001) noted a glassy bedded tuff seen at the base of member C in more distal sections, and field evidence highlights the bedded nature of the deposits, which again suggests there was a pause in the eruption long enough to allow normal grading of plume material to occur (C. Wilson, *pers. com.* 2010; 2011).

3.3.1.1 Previous work

The primary age of the HRT (Fig. 3.3), has been determined using K-Ar (e.g., Obradovich, 1992), Ar-Ar (e.g., Gansecki *et al.*, 1998), and U-Pb geochronological methods (e.g., Bindeman *et al.*, 2001), as well as fission track ages determined on zircons and glass shards from distal ashes (e.g., Naeser *et al.*, 1973; Ward *et al.*, 1993 cited in Christiansen, 2001). The latter have been used to correlate the Yellowstone ash layers, rather than to precisely date the eruptions. Obradovich (1992) reported a minimum K-Ar sanidine age of 2.018 ± 0.008 Ma due to incomplete extraction of Ar (Gansecki *et al.*, 1998), and Ar-Ar sanidine (total fusion and step heating) ages range from 2.003 ± 0.014 to 2.103 ± 0.019 Ma (ages cited in Lanphere *et al.*, 2002). Gansecki *et al.*, (1998) suggested Ar-Ar apparent

ages may record pre-eruptive ages whereby periods of gradual cooling and crystallisation of the magma chamber were interrupted by injections of hotter, less evolved material which would cause re-melting/remobilising of partially crystallised material. However, the U-Pb zircon age of 2.134 ± 0.248 Ma published by Bindeman *et al.*, (2001), thought to represent the best estimate for time of zircon crystallisation, is similar within error or younger than the eruption age of sanidine (determined by K-Ar and Ar-Ar). Bindeman *et al.*, (2001) on the basis of a very small sample set (n = 10), suggested there is no evidence to support long residence times and the HRT magmas contain only eruptive-age zircons, however it should be noted that other U-Pb zircon data (B. Charlier, *pers. com.,* 2010), has demonstrated the presence of older (> 100 ka older than eruption age) zircon grains. More recently Ellis *et al.*, 2012 conducted a study where high precision Ar-Ar ages (calculated relative to the ^{40}K decay constant of Renne *et al.*, 2010), including full uncertainty propagation, appear to discriminate between the eruption of members B (2.135 ± 0.006 Ma) and C (2.113 ± 0.004 Ma), resulting in a 12 % reduction in the total HRT volume.

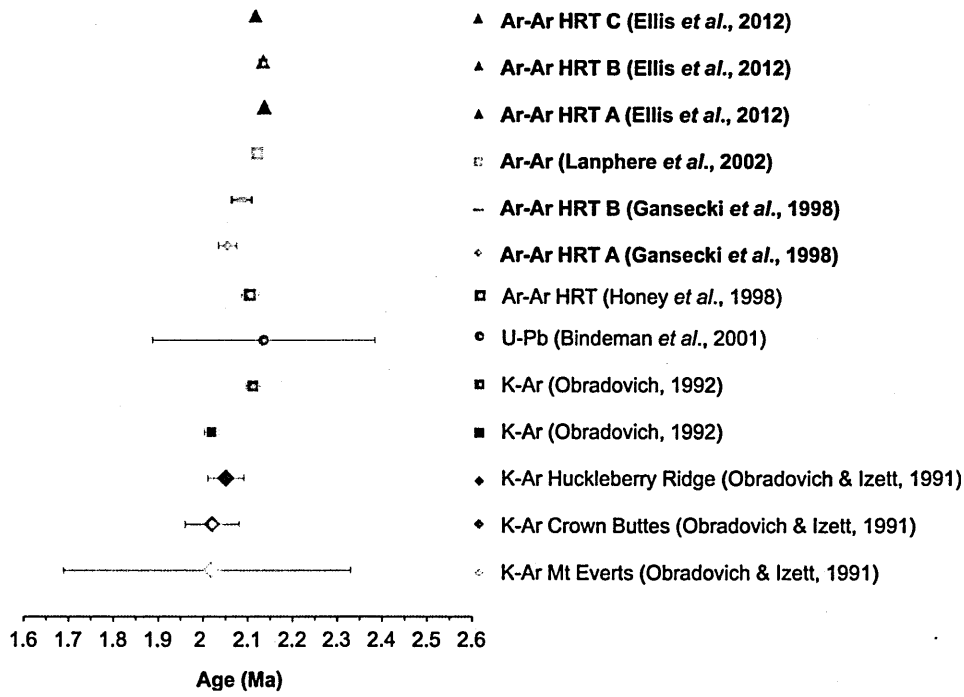

Figure 3.3. Summary of previously published K-Ar, U-Pb and Ar-Ar ages (± 2σ) for the Huckleberry Ridge Tuff. Where known the details of the specific unit dated have been given. For full details see

(*Fig. 3.3 cont.*) Table A5.2 in Appendix section A5. (**Bold text** in legend denotes those ages which have been calculated relative to the ^{40}K decay constant of Renne *et al.*, 2010).

3.3.1.2 Remnant magnetisation

Paleomagnetic studies, investigating the complex remnant magnetisation recorded by minerals, have previously distinguished between the three major tuffs of the Yellowstone Group. The application of this method proved to be significant in field correlation and mapping of the HRT members as well as establish any time intervals between the cooling units of the HRT, by comparing the mean direction of magnetisation of the separate cooling units within a section. The HRT is the most thoroughly studied unit of the Yellowstone Group and Reynolds (1977) analysed ~ 400 samples of drilled rock cylinders and hand specimens, from 57 sites representing 23 separate localities covering members A, B and C. Using magnetite and titanomagnetite (crystal size < 2 μm), which record the past direction and intensity of the earth's magnetic field, Reynolds (1977) showed that they carry stable remanence and have been unaffected by high-temperature oxidation. Based on multiple analyses, the remnant magnetic polarity of the HRT was determined to be subhorizontal. The study revealed the remnant magnetic polarity of the basal vitrophyre of member A is mostly stable and that the direction of the ash bed and ignimbrite flow of member A are similar. In addition, re-deposited ash beds in south-western Kansas, USA, also share the same remnant magnetic direction as the ash bed and ignimbrite flow, implying magnetisation and geomagnetic field direction was recorded at the time of HRT eruptions.

However, although the glassy rocks at the base of member A, and the rocks at the densely welded margins give consistent results and appear to be stable, there is a lack in consistency. Some samples indicated a normal polarity rather than subhorizontal, which

had been caused by the HRT cooling in a weak transitional geomagnetic field and natural remnant magnetization directions have been overprinted by remagnetisation in a field of normal polarity within last 700, 000 years (Reynolds, 1977). In addition, parts have been remagnetised during recrystallization of magnetic phases, ground-water interaction and formation of hematite. Chemical magnetisation has over printed the weak thermoremanent magnetisation (orientation of magnetic field preserved by mineral as rock cools through Curie temperature of that mineral – magnetisation locking in temperature), in particular the devitrified tuff, and caused dispersion of magnetic direction between sites within the HRT.

Despite this difficulty Reynolds (1977) showed that a similar subhorizontal south-westerly direction of remnant magnetisation is preserved in all three members of the HRT. Comparison of HRT samples with dissimilar rock types associated with or affected by the HRT eruption that have different magnetic mineralogy (e.g., sandstone beneath, and xenoliths within tuff), also share similar directions of magnetization, providing supporting evidence that the paleomagnetic mean signal preserved in HRT reflects the paleomagnetic field at the time of eruption. The mean remanence directions determined from the basal vitrophyre of Member A, the lower and upper chilled margins of Member B and the upper member of within the thick section of tuff of member C, sampled from the type section are essentially identical. Variability was observed in Member B, but was considered to be due to tectonic tilting or slumping because other parts of tuff at other locations yielded results indistinguishable from the mean. Member C also shows mean measurements which are similar to both A and B, and that deformation (highlighted by stretched and compacted pumice fragments and aligned phenocrysts), had no effect on the primary direction of magnetisation. Therefore this study could find no evidence to support the existence of significant time intervals separating the eruption of individual members of the HRT.

Within the Matuyama Reversed Chron (2.59 to 0.78 Ma) there was a short time span where the magnetic field had a normal direction termed the Reunion Normal-Polarity Subchron (C2r.1n) (named after lava flows on island of Reunion in the Indian Ocean which record normal polarity with reversed-polarity above and below). A second geomagnetic excursion (Reunion II; C2r.1r), not globally observed, has also been identified and is younger than the C2r.1n event. Lanphere *et al.*, (2002) concluded the HRT demonstrated a transitional magnetic direction, and the study compared their Ar-Ar age of HRT eruption (2.059 ± 0.004 Ma relative to ^{40}K decay constant of Steiger and Jäger (1977), and Taylor Creek sanidine age of 27.92 Ma), to the upper and lower boundary ages for the C2r.1n (2.15 ± 0.03 to 2.12 ± 0.03 Ma; determined by Baksi *et al.*, 1993). They concluded an HRT eruption age of 2.059 ± 0.004 Ma was younger than the C2r.1n event, but also younger than their recalculated age for C2r.1r event (2.09 ± 0.04 to 2.13 ± 0.04 Ma), and that a transitional magnetic direction represented a separate event not related to short Reunion II excursion (the 'Huckleberry Ridge event' of Lanphere *et al.*, 2002). Although if recalculated relative to Renne *et al.*, (2010) ^{40}K decay constant, their HRT eruption age can be placed within C2r.1n, which does not support the hypothesis of a separate 'Huckleberry Ridge event'.

Ellis *et al.*, (2012) used high-resolution Ar-Ar dating to obtain an age for each HRT member. Their ages for member A and B are in agreement with lower boundary of the Reunion Normal-Polarity Subchron (C2r.1n; 2.128 to 2.148 Ma; defined by ATNTS2004 timescale). Ellis *et al.*, (2012) report an age for HRT C, which is younger than members A and B and assign it to the Reunion II subchron C2r.1r. The Ellis *et al.*, (2012) study also claims that insufficient data reporting by Reynolds (1977) prevents detailed interrogation of the magnetic direction of C. The fact that Reynolds (1977) shows agreement between all three members of the HRT with respects to mean remnant magnetic direction (i.e., no strong evidence to support a significant time break), has clearly been overlooked by Ellis *et*

al., (2012), and one of their key lines of evidence is incorrect. The data presented in this thesis will support this claim.

3.3.2 Pre-HRT Snake River Butte dome

The Snake River Butte dome is one of the oldest recognised products of the plateau volcanism to occur along a ring-fracture zone adjacent to the first cycle source area (Fig. 3.4), prior to the eruption of the first-cycle ash-flow sheet (HRT). The rhyolite of Snake River Butte underlies the HRT, north of Ashton, Idaho, USA, and previous determinations place its age between 2.2 and 2.1 Ma (Christiansen, 2001).

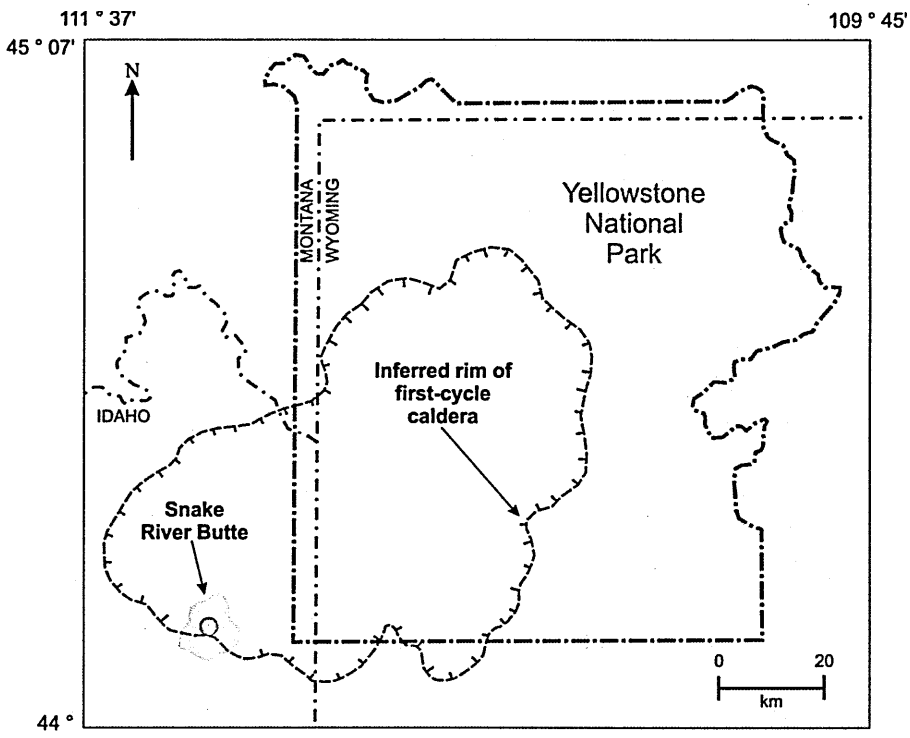

Figure 3.4. Summary map showing the inferred rim of the first-cycle (HRT) caldera and location of the precaldera rhyolitic lava flow Snake River Butte dome. State boundaries and Yellowstone National Park boundaries are shown for reference (redrawn and modified after Christiansen, 2001).

The age of the Snake River Butte rhyolitic lava flow has previously been determined by the K-Ar method, yielding an age of 1.99 ± 0.02 Ma (Obradovich, 1992 cited in Christiansen, 2001), which places it just after the eruption of the HRT. In contrast, unpublished U-Pb zircon ages (C. Wilson, *pers. com.*, 2012) have yielded two populations, one with a PDF peak of 2.17 Ma and a second PDF peak of 2.23 Ma. In addition, Bindeman and Valley (2001) analysed the oxygen isotope composition of quartz ($\delta^{18}O$ range 7 to 8 ‰) and sanidine ($\delta^{18}O$ range 6 to 7 ‰), which fell within their range for the HRT.

3.3.3 Post-HRT Sheridan Reservoir dome

The Heise caldera complex (6.6 to 4.0 Ma) precedes Yellowstone, and is made up of four successive eruptions, which produced four large-volume ignimbrite units, Blacktail Creek Tuff; Walcott tuff; Conant Creek Tuff and Kilgore Tuff. Heise magmas have been characterised as being high silica rhyolites (~ 75 wt. % SiO_2) with a similar phenocryst assemblage (to the Yellowstone eruptives) of sanidine, plagioclase, quartz, pyroxene, opaques, zircon ± biotite (Bindeman *et al.*, 2007). The location of Sheridan Reservoir dome (SRD), places it outside of the Heise caldera complex (Fig. 3.5a) but within the extent of the area covered by the Kilgore ignimbrite (last large-volume ignimbrite to erupt from Heise volcanic field at ~ 4.5 Ma (Morgan and McIntosh, 2005) and HRT member B (erupted at ~ 2.1 Ma; Fig. 3.5b).

(a)

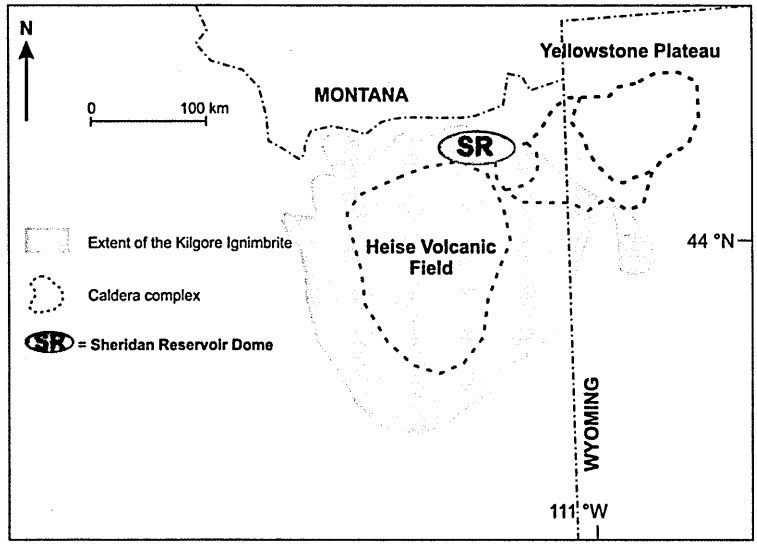

(b)

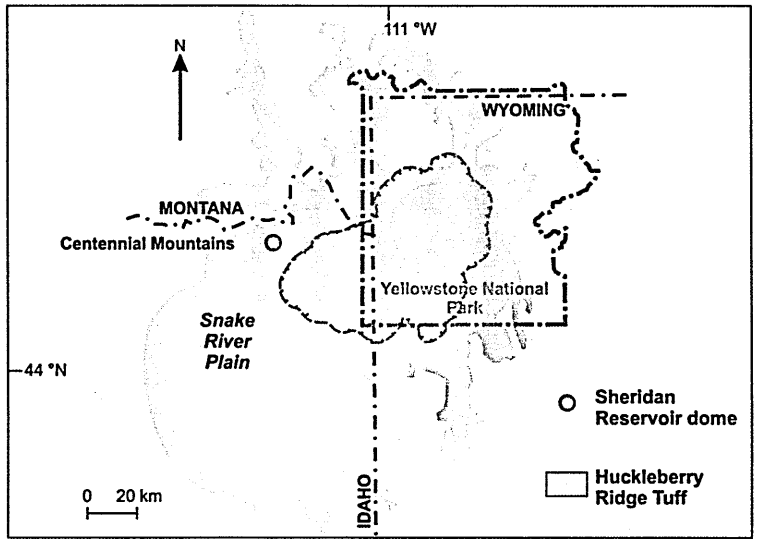

Figure 3.5. Maps showing the locality of Sheridan Reservoir dome (a) Map of Snake River Plain (SRP) showing the position of Sheridan Reservoir dome (SR) relative to Heise and Yellowstone Plateau caldera complexes (redrawn and modified after Bindeman *et al.*, 2007); (b) Map showing the position of Sheridan Reservoir relative to the distribution of the first-cycle eruption (HRT) at YPVF (redrawn and modified after Christiansen, 2001).

To date very few published ages exist for the Sheridan Reservoir dome; however, field relations show that it post-dates the HRT (C. Wilson, *pers. com.*, 2011). The dome has been dated using both the K-Ar (reported in Morgan *et al.*, 1984; anomalously old K-Ar age of 4.0 ± 0.4 Ma), and U-Pb (Bindeman *et al.*, 2007; 2.07 ± 0.19 Ma) techniques. The

latter overlaps with the generally accepted age of the HRT (~ 2.05 Ma; Christiansen, 2001) and is within error of HRT age determination presented in this study.

Earlier work has focused on the origin of the Snake River rhyolites (variation in $\delta^{18}O$ measurements made on quartz, zircon and sanidine) and why low-$\delta^{18}O$ rhyolites are followed by major-caldera forming eruptions (e.g., Bindeman *et al.*, 2001; Bindeman *et al.*, 2007). Based on the agreement of their U-Pb age with that of the generally accepted age of HRT, Bindeman *et al.*, (2007) concluded that relatively low $\delta^{18}O$ volcanism (Sheridan Reservoir; 2.25 to 4.55 ‰) at Heise was occurring at the same time as normal $\delta^{18}O$ volcanism at the developing Yellowstone centre (HRT; 6.5 to 7.5 ‰), and therefore volcanism begins with partial melting of pre-existing crust (normal $\delta^{18}O$ magmas), and ends by bulk melting, digestion or reactive assimilation of hydrothermally altered rocks (low $\delta^{18}O$ magmas). The Sheridan Reservoir rhyolite is thought to represent a small-volume portion of low $\delta^{18}O$ magma motivated by the input of fresh basalt, producing re-melting of the Kilgore batholith (Bindeman *et al.*, 2007). Pre- and post-caldera units of Yellowstone have been previously mapped, but few reliable age data exist for many of them. The Sheridan Reservoir dome is a rhyolitic dome where the lack of agreement between previous age determinations (e.g., the older than expected K-Ar age), which places it pre-HRT and field relations which place it post-HRT (C. Wilson, *pers. com.*, 2011), make it an interesting case study for the Ar-Ar single-grain dating technique.

3.3.4 Second cycle eruption: The Mesa Falls Tuff (MFT)

The MFT (eruptive volume of ~ 280 to 300 km^3; Gansecki *et al.*, 1998; Christiansen, 2001) is the smallest of the three ash-flow sheets and was erupted at ~ 1.3 Ma. The source area for this unit is confined to the Island Park area and its eruption created the Henry's Fork Caldera (Fig. 3.6). The MFT is distributed to the north of Island Park and is overlain by

basalts of the Snake River Plain to the west and unconformably overlies the HRT in many places. The tuff (which covered an area of approximately 3000 km^2; Christiansen, 2001) consists of a thick basal fall layer consisting of crystal-rich, bedded ash and pumice, which is overlain directly by partially to densely welded ignimbrite (Lanphere *et al.*, 2002). The MFT commonly forms boulder-like outcrops and has a distinctive pink colour (Fig. A2.3, Appendix section A2). The MFT contains abundant phenocrysts of sanidine, quartz, plagioclase (An_{15}), ferroaugite, magnetite, ilmenite, fayalite and accessory minerals (hornblende, zircon, chevkinite and allanite). Large welded pumice inclusions (10 to 30 cm in length) are abundant and minor welded tuff lithic inclusions derived from the underlying HRT (Christiansen, 2001) are rarely present. The thick-bedded basal ash and pumice deposit is best exposed in road cuts along the U.S. Highway 20, and has been correlated eastward within deposits of the southern Rocky Mountains and the Great Plains, as well as having been reworked into sediments in the Gulf of Mexico (Christiansen, 2001).

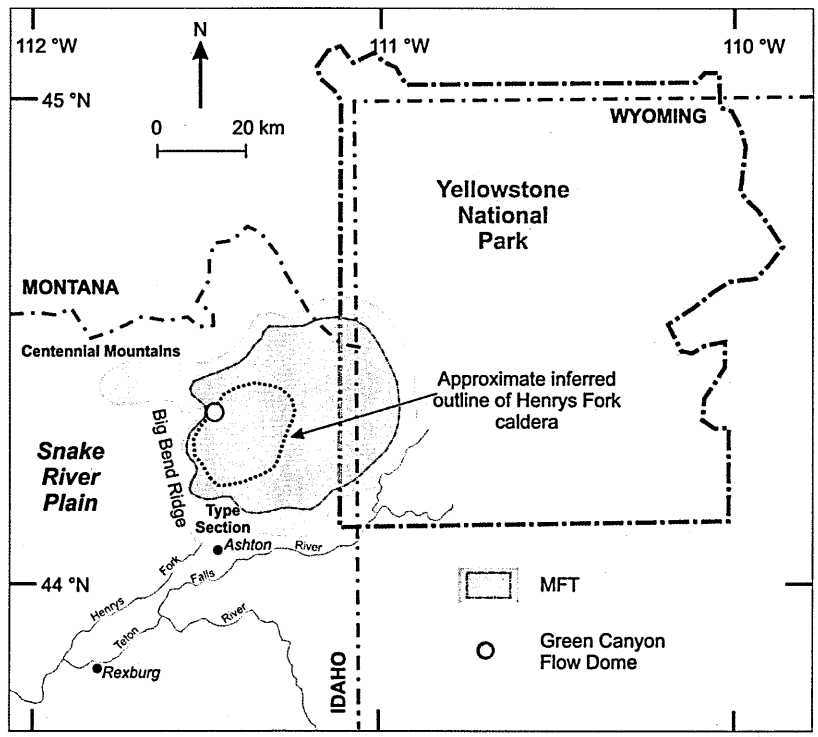

Figure 3.6. Map showing the extent of the Mesa Falls Tuff (MFT) ignimbrite eruption. Also shown is the locality of the type section (road cuts along U.S. Highway 20). State boundaries and Yellowstone National Park boundaries are shown for reference. Green Canyon Flow dome is also

(*Fig. 3.6 cont.*) marked on the map (red circle) and described in section 3.3.5 (redrawn and modified after Christiansen, 2001).

3.3.4.1 Previous work

The MFT has been the subject of less attention than its predecessor, although the issue of chemically indistinguishable xenocrysts has been reported (e.g., Obradovich, 1992; Gansecki *et al.*, 1996; 1998). Bulk-crystal K-Ar age of MFT yielded an unweighted mean of 1.27 ± 0.02 Ma and isochron age of 1.25 ± 0.01 Ma (Obradovich, 1992). Prior to this, a reconnaissance Ar-Ar dating study (Obradovich and Izett, 1991) yielded an age of 1.30 ± 0.02 Ma (two grains only). Previous Ar-Ar determined ages range 1.28 ± 0.01 Ma to 1.31 ± 0.01 Ma (2σ) (Fig. 3.7), and are younger than the previously determined U-Pb zircon age of 1.46 ± 0.05 Ma (Bindeman *et al.*, 2007) and the peak PDF age of 1.34 Ma (U-Pb zircon SIMS age, n = 35; C. Wilson, *pers. com.*, 2011).

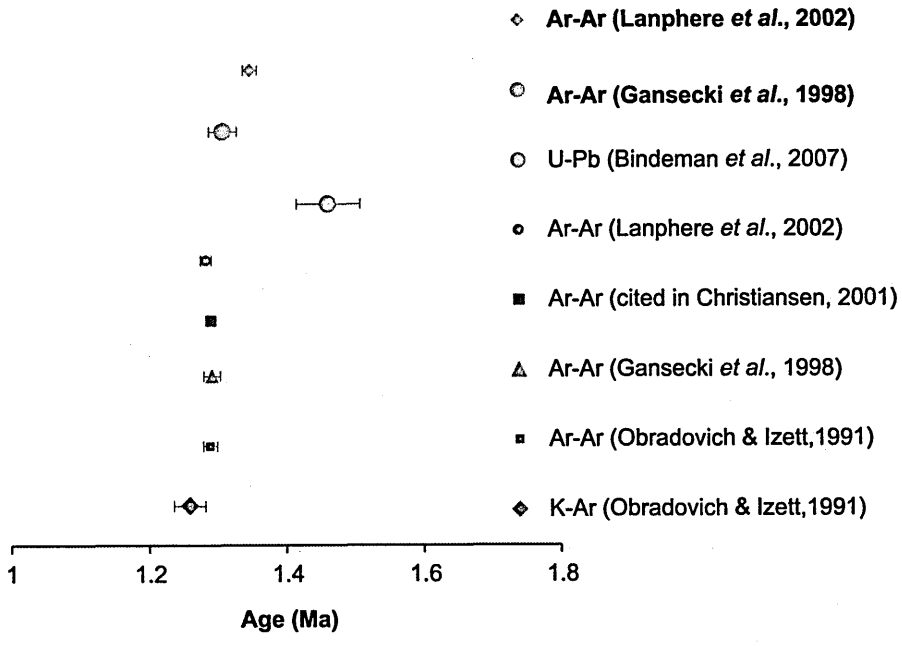

Figure 3.7. Summary of previously published K-Ar, U-Pb and Ar-Ar ages (± 2σ) for the Mesa Falls Tuff. Where known the details of the specific unit dated have been given. For full details see Table A5.2 in Appendix section A5. (**Bold text** in legend denotes those ages which have been re-calculated relative to decay constants of Renne *et al.*, 2010).

3.3.5 Pre-MFT Green Canyon Flow dome

The Green Canyon Flow dome is one of four rhyolitic lava flows to erupt post-HRT, at the north end of Big Bend Ridge previously identified as a single unit termed Big Bend Ridge Rhyolite. Green Canyon Flow was incorrectly mapped in the 1960s as younger than all the ash-flows on the rim of the Island Park Caldera, although subsequent geological mapping has shown that the flow overlies the HRT and underlies the MFT on the rim west of Island Park (Christiansen, 2001; Fig. 3.6). Previous work highlighted the challenge in assigning these lava flows to post-collapse first cycle lavas or pre-collapse second cycle lavas, and investigations have shown that some, based on measured low $\delta^{18}O$ values, are more closely related to the underlying HRT than overlying MFT (Christiansen, 2001).

The Green Canyon Flow contains abundant phenocrysts of quartz, sanidine and plagioclase. Mafic silicate minerals in the rocks are altered to iron-oxide minerals. In addition, small phenocrysts of biotite are also present and the Green Canyon Flow is one of only four chemically more evolved rhyolites of the YPVF known to carry this phase, which may represent magma erupted from a more evolved and partially isolated magma chamber at about the same time as the MFT (Christiansen, 2001). Therefore the Ar-Ar age of this dome may be comparable to that of the MFT. Previously this dome has been dated using the K-Ar method, which yielded an age of 1.17 ± 0.01 Ma (Obradovich, 1992 cited in Christiansen, 2001). In addition, separated zircons were dated using the U-Pb (SIMS) method and yielded a PDF peak age of 1.35 Ma (n = 39; C. Wilson, *pers. com.*, 2011), which is older than the previously published K-Ar age.

3.4 Materials and methods

3.4.1 Sample descriptions

3.4.1.1 Huckleberry Ridge Tuff (HRT)

Samples used in this study are from basal vitrophyre and juvenile rhyolitic pumice material from the HRT, Yellowstone, USA. The samples form part of the extensive collection of C. Wilson and B. Charlier collected during a 2009 field season. Sample YP127, which represents member A, was collected from the 'type section' at Huckleberry Ridge, 2 km northeast of Flagg Ranch (Fig. 3.3) and samples YP079 and YP081 representing members B and C respectively, were collected along the Teton River, north of Newdale. The details of each sample are outlined below in summary Table 3.2.

Table 3.2. HRT sample descriptions (taken with permission from sample catalogue of C. Wilson). For locality co-ordinates see sample description list in Appendix section A2.1.3.

Sample Number	Location	Unit	Description
YP127	Exposure in slump blocks below Huckleberry Ridge, Flagg Ranch	HRT(A)	>25 cm long glassy fiamme with medium crystal content in basal vitrophyric tuff in fallen block
YP079	Teton River, north of Newdale	HRT(B)	Dense, coarsely fibrous pumice. Very crystal-rich, many crystals are dark grey which could indicate presence of inclusions
YP081	Teton River, north of Newdale	HRT(C)	Low density pumice, outer rim brown suggesting oxidation. Inner parts pale grey suggesting non-oxidised. Texture is dominantly fibrous with a weak crimping. Moderate crystal content, intact, no exploded crystals

In thin section sample YP127 has a hypocrystalline texture containing a mixture of glass (vitrophyre groundmass; 40 %) and phenocrysts. Alkali feldspar (20 %) and plagioclase (20 %) exhibit zoning, twinning and micro-inclusions (minerals and melt). Feldspars exist

as both whole crystals as well as fragmented and shattered crystals. The crushed sample YP079 contained dark brown – rusty red fragments of low silica scoria as well as lithic fragments (possibly basaltic glass – black/iridescent in colour), which indicates contamination by previously erupted material, and could possibly represent fragments of pre-existing scoria cone or dome. The 500 μm – 1 mm sieve fraction contained mostly highly fragmented crystals (feldspar and quartz) and as a result intact crystals were difficult to locate. In thin section (sample CMW06 – see Appendix section A2.1.3) member B is similar to member A, although plagioclase feldspar (30 %) is the more dominant feldspar phase. In thin section HRT C (sample CMW08 - see Appendix section A2.1.3) contains phenocrysts of alkali feldspar (20 %), plagioclase (20 %), which contained minimal micro-inclusions, and quartz (20 %) hosted in a fine pumiceous groundmass showing moderate to high vesicularity.

3.4.1.2 Mesa Falls Tuff (MFT)

A sample of MFT pumice (CMW01) used in this study was collected June 2011 from the type locality; west side of a large road cut along U.S. Highway 20, approximately 6.8 km north of Ashton, Idaho, USA. The fresh crystal rich (> 60 %), coarsely vesicular white to light pink pumice was sampled from the glassy non-welded base of the ash-flow sheet, just above the fall out tuff. Previous studies (e.g., Obradovich and Izett, 1991; Gansecki *et al.*, 1998) have also analysed single crystals separated from material collected from this locality. In thin section the coarse vesicularity is clearly evident and phenocrysts of alkali feldspar (20 %), plagioclase (zoned) and quartz (rounded and fractured) sit in a fine glassy pumiceous groundmass.

3.4.1.3 Snake River Butte dome

A sample of light grey crystal-rich, glassy to perlitic pumiceous obsidian of Snake River Butte dome (YR185) Yellowstone, USA, collected by C. Wilson and B. Charlier in 2009, has been previously dated using the U-Pb method (Wilson and Charlier, *pers. com.*, 2009). The crushed sample contained feldspar crystals in both the 500 μm to 1 mm and 1 mm to 2 mm size sieve fractions. This presented the opportunity to pick larger intact feldspars (unavailable from the other samples) to allow comparison to be made between resulting Ar-Ar ages. In thin section (representative sample CMW02 - see Appendix section A2.1.3) plagioclase phenocrysts are compositionally zoned (some with inclusion rich cores) and alkali feldspar are large (> 1 mm). Based on the lack of spherulite growth in the groundmass, grains of glassy groundmass were also selected for Ar-Ar analysis.

3.4.1.4 Sheridan Reservoir dome

Samples (YR215 and YR217) of rhyolitic dome material (pumiceous dome lava) collected from Sheridan Reservoir dome (Yellowstone, USA), by C. Wilson and B. Charlier in 2009 have been used in this study. Two glass separates, and one feldspar separate from the two samples were analysed by Ar-Ar single grain fusion. Both samples were collected from an excavation pit in the grounds of privately owned Sheridan Reservoir Ranch. The details of each sample are outlined below in summary Table 3.3.

Table 3.3. Sheridan Reservoir dome sample (YR215 and YR217) descriptions (taken with permission from sample catalogue of C. Wilson). For locality co-ordinates see sample description list in Appendix section A2.1.3.

Sample Number	Location	Unit	Description
YR215	Sheridan Reservoir Ranch, Yellowstone Plateau Volcanic Field, Idaho, USA	Sheridan Reservoir Dome	Crystal rich pumiceous dome material. Sample consists of dark brown to black rhyolitic glass, pumice fragments and phenocrysts of feldspar and quartz.
YR217	Sheridan Reservoir Ranch, Yellowstone Plateau Volcanic Field, Idaho, USA	Sheridan Reservoir Dome	Crystal rich pumiceous dome material. Sample consists of pale brown rhyolitic glass, pumice fragments and phenocrysts of feldspar and quartz.

In thin section, representative sample CMW11 (see Appendix section A2.1.3) has groundmass that contains ovoid patches of dark black glassy vitrophyric material, interspersed with devitrified material (radial spherulite growth). The groundmass contains microphenocrysts of plagioclase feldspar as well as large (> 0.5 mm) crystals of alkali feldspar (30 %) and plagioclase (20 %), which contained numerous melt inclusions. There is also evidence of intergrowth between alkali feldspar and plagioclase, and feldspars show resorption textures.

3.4.1.5 Green Canyon Flow dome

A sample of crystal rich devitrified rhyolite of Green Canyon Flow dome (YR242) was collected in June 2011 (C. Wilson) for a combined Ar-Ar (this work) and U-Pb zircon age dating study. Previously collected sample (YR222) has already been dated and yielded a U-Pb zircon age of ~ 1.35 Ma (C. Wilson, *pers. com.* 2011). The crushed sample contained intact feldspars and small (< 250 μm) phenocrysts of biotite. Although the biotite was not separated for this study due to single grains being too small for single-grain fusion, as well as exhibiting variable preservation (oxidised based on visual inspection), this may provide a possible avenue for further work. In thin section, the devitrified groundmass comprised

of spherulites intergrown with feldspar and quartz microphenocrysts (fragmented laths). Plagioclase feldspars appear to contain numerous inclusions (melt), and exhibit resorbed grain edges, and cleavage highlighted by minor alteration. The majority of alkali feldspar however contain inclusions only, and appear to be void of significant alteration.

3.4.2 Sample preparation and methods of chemical analysis

For XRF whole rock analysis, crushed samples were powdered, and glass discs and powder pellets were prepared following methods outlined in Appendix section A1.8. Electron microprobe (Cameca SX100) analysis of individual feldspar crystals, and where appropriate grains of glassy groundmass, separated from each samples was carried out following methods outlined in Appendix section A1.9.

3.4.3 Sample preparation for Ar-Ar analysis

Samples were prepared following the methods outlined in Appendix section A1.7. Where possible intact feldspar crystals only and pieces of volcanic glass (samples YR215 and YR217; YR185 only) were hand-picked using a binocular microscope from the 500 μm to 1 mm sieve fraction, except sample YR185 where crystals from a larger sieve fraction (1 to 2 mm) were also picked. Foil wrapped samples were cadmium shielded (to minimise undesirable isotopic interference reactions), and irradiated in two batches for 1 hrs (3 MWH), and 1.05 hrs (3 MWH) respectively at McMaster reactor (Canada). Neutron flux monitored with biotite standard GA15-50 which has an age of 99.769 ± 0.108 Ma.

3.4.4 Analytical methods: Ar-Ar age determinations

In order to investigate age variations at a single grain level of erupted feldspars (and glassy groundmass) from each sample, crystals were fused along with a zero-age basaltic glass bead flux following methods outlined in Appendix section A1.3 and A1.7. Analysis are corrected for daily average system blank levels measured prior to every two analyses, ^{37}Ar decay (34.95 ± 0.08 d; Renne *et al.*, 2001), and neutron induced interference reactions. The following correction factors were used: $(^{39}Ar/^{37}Ar)_{Ca} = 0.00065 \pm 0.00003$, $(^{36}Ar/^{37}Ar)_{Ca} = 0.000265 \pm 0.000001$, $(^{40}Ar/^{39}Ar)_{K} = 0.0085 \pm 0.00004$, based on analysis of Ca and K salts. Ages are calculated relative to the newly defined ^{40}K decay constant, $5.549 \times 10^{-10} \pm 0.009 \times 10^{-10}$ a^{-1} (Renne *et al.*, 2010). Full Ar-Ar data tables, calculated *J*-values and average blank levels used for data processing are presented in Appendix section A3.1.2. All errors quoted in the text and tables are reported at the 2σ level unless otherwise stated.

3.5 Results

3.5.1 Sample chemistry: EMP and XRF whole rock

Mean electron microprobe analysis (EMP) results for individual feldspar crystals and glassy groundmass separated from samples YP127, YP079, YP081, CMW01, YR2185, YR215, YR217 and YR242 are given in summary Table 3.4 (full data tables are presented in Appendix section A4.1.2). XRF whole rock (major and trace element) analysis carried out on all samples are presented in Appendix section A4.1.1. Individual feldspar compositions are displayed in An-Or-Ab ternary diagrams (Fig. 3.8; YP127, YP079, YP081, CMW01, YR2185, YR215, YR217 and YR242).

Table 3.4. Mean electron microprobe (**bold, wt. %**) analysis of Yellowstone samples used in this study. The standard deviation of the mean is listed below the mean value and the number of analysis used to calculate the mean is given as, n.)

Sample	Phase	SiO_2	TiO_2	Al_2O_3	FeO	MnO	MgO	CaO	Na_2O	K_2O	BaO	SrO	F	Cl	Total
YP217	Sanidine	**65.48**	**0.02**	**18.96**	**0.11**	**0.00**	**0.00**	**0.44**	**4.51**	**9.45**	**0.96**	**0.05**	**0.03**	**0.00**	**99.68**
	n = 125	0.32	0.02	0.14	0.02	0.00	0.00	0.06	0.12	0.22	0.32	0.02	0.04	0.00	0.33
YP079	Sanidine	**65.66**	**0.02**	**18.86**	**0.10**	**0.00**	**0.00**	**0.44**	**4.55**	**9.50**	**0.79**	**0.05**	**0.02**	**0.00**	**99.59**
	n = 34	0.37	0.01	0.12	0.02	0.00	0.00	0.03	0.19	0.18	0.35	0.02	0.02	0.00	0.32
	Plagioclase	**63.76**	**0.02**	**22.05**	**0.20**	**0.00**	**0.00**	**3.95**	**8.11**	**1.72**	**0.11**	**0.04**	**0.01**	**0.00**	**99.79**
	n = 8	0.39	0.02	0.20	0.04	0.00	0.00	0.20	0.15	0.08	0.05	0.02	0.02	0.00	0.48
YP081	Sanidine	**66.14**	**0.01**	**18.78**	**0.10**	**0.00**	**0.00**	**0.32**	**4.56**	**9.84**	**0.13**	**0.03**	**0.03**	**0.00**	**100.51**
	n = 49	0.16	0.01	0.07	0.01	0.01	0.00	0.03	0.09	0.12	0.18	0.03	0.02	0.00	0.24
CMW01	Sanidine	**65.67**	**0.01**	**18.56**	**0.10**	**0.00**	**0.00**	**0.34**	**4.22**	**10.22**	**0.79**	**0.05**	**0.03**	**0.01**	**99.56**
	n = 20	0.28	0.01	0.19	0.01	0.00	0.00	0.03	0.11	0.09	0.42	0.03	0.05	0.00	0.42
	Plagioclase	**62.53**	**0.01**	**22.42**	**0.21**	**0.00**	**0.00**	**4.54**	**8.12**	**1.38**	**0.71**	**0.06**	**0.01**	**0.01**	**99.43**
	n = 3	0.31	0.02	0.37	0.02	0.00	0.00	0.39	0.18	0.21	0.26	0.01	0.01	0.00	0.46
YR215	Anorth#	**64.22**	**0.03**	**20.80**	**0.23**	**0.00**	**0.00**	**2.44**	**7.10**	**3.89**	**1.17**	**0.09**	**0.02**	**0.00**	**99.63**
	n = 131	0.67	0.02	0.69	0.09	0.00	0.01	0.68	0.42	0.92	0.33	0.03	0.03	0.00	0.38
	Sanidine	**64.96**	**0.03**	**19.49**	**0.16**	**0.01**	**0.00**	**0.95**	**5.94**	**6.64**	**1.75**	**0.07**	**0.01**	**0.00**	**99.40**
	n = 6	0.29	0.03	0.24	0.03	0.01	0.00	0.20	0.19	0.43	0.12	0.04	0.01	0.00	0.26
	Plagioclase	**62.40**	**0.03**	**22.84**	**0.27**	**0.00**	**0.01**	**4.81**	**7.74**	**1.43**	**0.36**	**0.08**	**0.02**	**0.00**	**99.75**
	n = 6	0.25	0.01	0.22	0.03	0.00	0.02	0.33	0.11	0.23	0.12	0.02	0.03	0.00	0.47
YR215	Glass	**76.87**	**0.05**	**11.39**	**2.11**	**0.04**	**0.03**	**0.63**	**3.63**	**4.89**	**0.16**	**0.04**	**0.12**	**0.05**	**100.03**
	n = 20	0.19	0.03	0.12	0.07	0.01	0.01	0.02	0.09	0.05	0.03	0.03	0.06	0.00	0.95
YR217	Glass	**76.55**	**0.01**	**11.81**	**2.09**	**0.04**	**0.04**	**0.64**	**3.57**	**4.89**	**0.17**	**0.04**	**0.10**	**0.05**	**100.74**
	n = 49	0.22	0.01	0.07	0.12	0.01	0.01	0.08	0.09	0.05	0.03	0.03	0.06	0.01	0.74
YR185	Sanidine	**65.50**	**0.03**	**18.79**	**0.10**	**0.00**	**0.00**	**0.46**	**4.52**	**9.67**	**1.01**	**0.06**	**0.02**	**0.00**	**99.73**
	n = 40	0.41	0.05	0.52	0.02	0.01	0.00	0.50	0.64	0.25	0.27	0.04	0.03	0.00	0.48
YR185*	Sanidine	**65.50**	**0.02**	**18.74**	**0.10**	**0.00**	**0.00**	**0.35**	**4.19**	**10.04**	**0.97**	**0.06**	**0.03**	**0.00**	**99.43**
	n = 50	0.10	0.02	0.07	0.02	0.00	0.00	0.02	0.10	0.07	0.03	0.02	0.04	0.01	0.26
YR185	Glass	**77.71**	**0.05**	**11.43**	**1.43**	**0.03**	**0.02**	**0.54**	**3.48**	**5.00**	**0.03**	**0.03**	**0.12**	**0.12**	**99.41**
	n = 14	0.26	0.03	0.12	0.26	0.01	0.01	0.02	0.12	0.10	0.02	0.03	0.06	0.01	0.32
YR242	Sanidine	**66.31**	**0.02**	**18.50**	**0.09**	**0.00**	**0.00**	**0.27**	**4.39**	**10.34**	**0.01**	**0.03**	**0.03**	**0.01**	**99.65**
	n = 77	0.09	0.02	0.07	0.02	0.00	0.00	0.03	0.10	0.09	0.01	0.02	0.04	0.01	0.35
	Plagioclase	**64.93**	**0.01**	**21.40**	**0.15**	**0.00**	**0.00**	**3.14**	**8.89**	**1.42**	**0.01**	**0.02**	**0.02**	**0.00**	**99.50**
	n = 22	0.15	0.01	0.12	0.02	0.00	0.00	0.09	0.15	0.04	0.01	0.02	0.03	0.00	0.25

n = number of analyses used to calculate the mean; * = 1 to 2 mm grain diameter; Anorth# = Anorthoclase feldspar.

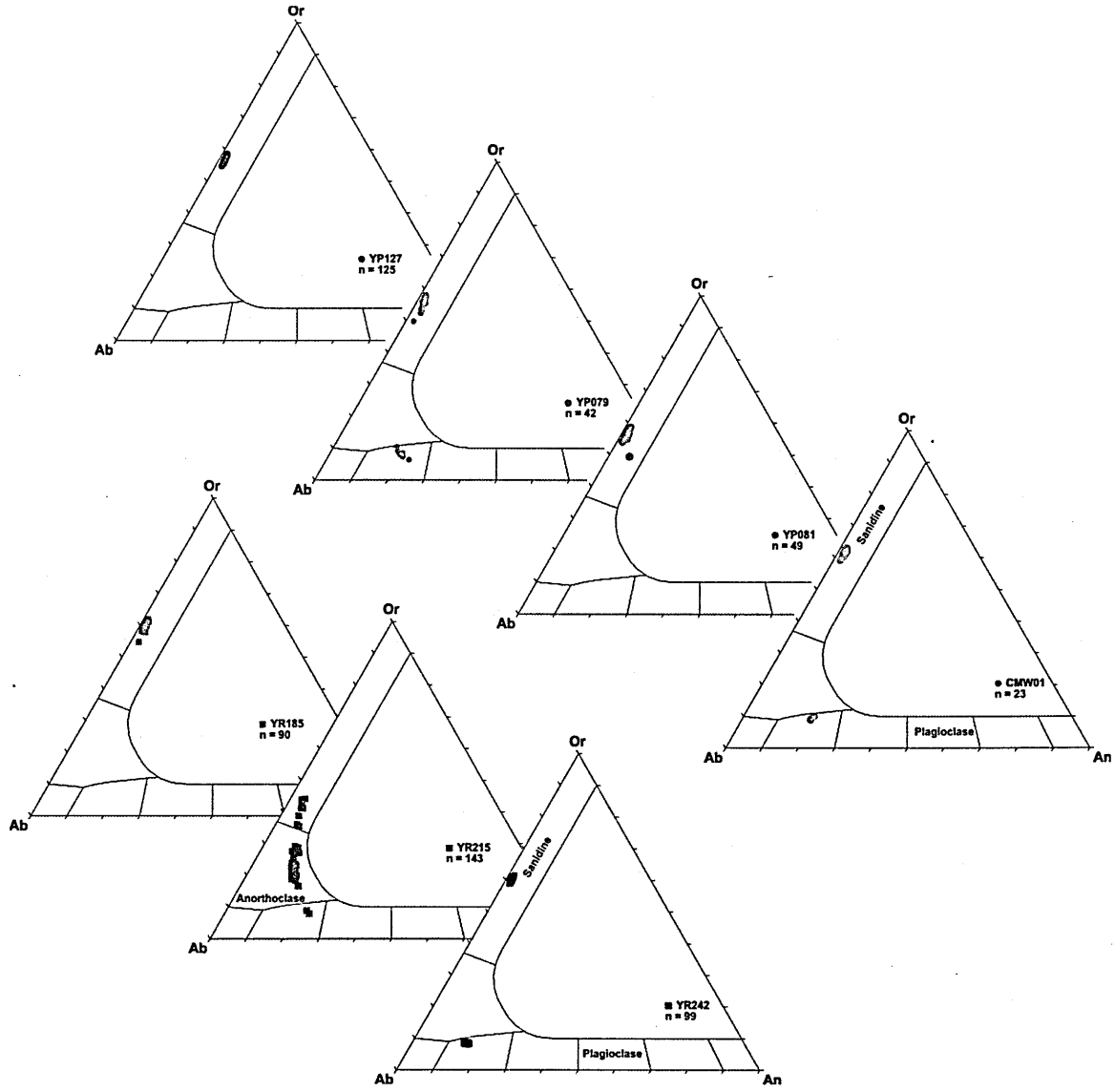

Figure 3.8. An-Or-Ab ternary diagrams showing individual feldspar compositions (determined by electron microprobe analysis) for each Yellowstone unit. Huckleberry Ridge Tuff (members A, B and C; samples YP127, YP079, YP081); Mesa Falls Tuff (sample CMW01); Snake River Butte dome (sample YR185); Sheridan Reservoir dome (sample YR215), and Green Canyon Flow dome (sample YR242).

3.5.1.1 Huckleberry Ridge Tuff (HRT)

Feldspar compositions for HRT A are tightly constrained to the sanidine field (Fig. 3.8; Or_{55} to Or_{60}), with mean K_2O, CaO and Na_2O contents of 9.45 %; 0.44 %, and 4.51 % respectively. Feldspar composition for HRT member B is bimodal, and both sanidine (Or_{50} to Or_{60}), and plagioclase (An_{17} to An_{26}) are present. Sanidine have mean K_2O, CaO and Na_2O values of 9.50 %, 0.44 %, and 4.55 % and plagioclase have mean K_2O, CaO and

Na_2O values of 1.72 %, 3.95 %, and 8.11 %. Like HRT member A, HRT member C feldspar composition also show to be tightly constrained to the sanidine field (Or_{48} to Or_{60}), with mean K_2O, CaO and Na_2O values of 9.84 %, 0.32 %, and 4.56 % respectively.

The results presented here are in agreement with those previously published (e.g., Gansecki *et al.*, 1998; Christiansen, 2001). Christiansen (2001) noted the similarity between members A and B stating member A has fewer quartz and more plagioclase phenocrysts than member B. My data suggests the opposite with regards to the plagioclase content; however this could simply be a result of sampling. Analysed crystals revealed no obvious xenocrystic compositions and limited core to rim variation with regards to K_2O. There also appears to be no Na or K loss, which is also in agreement with previous determinations (e.g., Christiansen, 2001). The count time was adjusted during EMP analysis to limit such loss.

Member C has slightly higher whole rock $Na_2O + K_2O$ (~ 9 wt. %) and SiO_2 (~ 76 wt. %) values than members B and C. Despite this, there appears to be minimal variation between samples with regards to major elements, although whole rock CaO abundance for member A is higher (1.17 %) compared with members B and C (0.66 % and 0.80 % respectively). Minor element variation was detected for Ba (all samples), and sample YP081 yields the lowest Ba value (207 ppm). This is not in accordance with analysis previously carried out on these samples where a Ba value of 1579 ppm was obtained (B. Charlier, *pers. com.*, 2010), or with data published in Bindeman and Valley (2001; Ba value of 1780 ppm), or Christiansen (2001; Ba value of 1500 ppm). Ba values for member A (vitrophyre), is in agreement with values reported by Bindeman and Valley (2001), and Christiansen (2001).

3.5.1.2 Mesa Falls Tuff (MFT)

The feldspar population is dominated by sanidine (Fig. 3.8), although minor plagioclase (~ An_{20}) was also detected. Sanidine compositions range from Or_{58} to Or_{62}, which is in agreement with previous determinations (e.g., Christiansen, 2001), where the average sanidine composition is ~ Or_{62} throughout the unit.

3.5.1.3 Snake River Butte dome

Feldspars are sanidine in composition (Or_{53} to Or_{61}; Fig. 3.8), with mean K_2O contents ranging 9.67 % to 10.04 %. In comparison, the mean K_2O value for separated glassy groundmass is 5.00 %. Major and trace element analysis on whole rock (sample YR185) was carried out by B. Charlier (2009). A L.O.I. value of 2.48 % indicates volatiles were released on ignition during XRF analysis.

3.5.1.4 Sheridan Reservoir dome

Feldspar compositions range from sanidine (Fig. 3.8; Or_{35} to Or_{45}), through anorthoclase (Or_{15} to Or_{30}), to plagioclase (An_{20} to An_{24}). Mean K_2O, CaO and Na_2O contents for feldspars therefore range 1.73 % to 6.64 %, 0.95 % to 5.18 %, and 5.94 % to 7.74 % respectively. Several feldspar crystals were selected for rim to core analysis (Fig. 3.9). Some demonstrated a subtle increase in CaO towards the centre of the grain and a slight decrease in K_2O. Data points along the transect that had low totals (deviation > 2 % either way from 100 %) due to uneven sample surface or accidental analysis of micro-inclusions were removed. Both samples of glassy groundmass appear to be in agreement, and contain ~ 5.00 wt. % K_2O, which is on average ~ 1 % higher than anorthoclase feldspar. Analyses have good totals (~ 100 %) suggesting pieces of groundmass separated for analysis are not hydrated or altered. One possible issue was the potential loss of alkalis during

volatilization of the glass under the beam current. In order to address this, element count time was minimized to limit loss and mobilization of Na and K. Major and trace element analysis on whole rock (sample YR215) was carried out by B. Charlier in 2009.

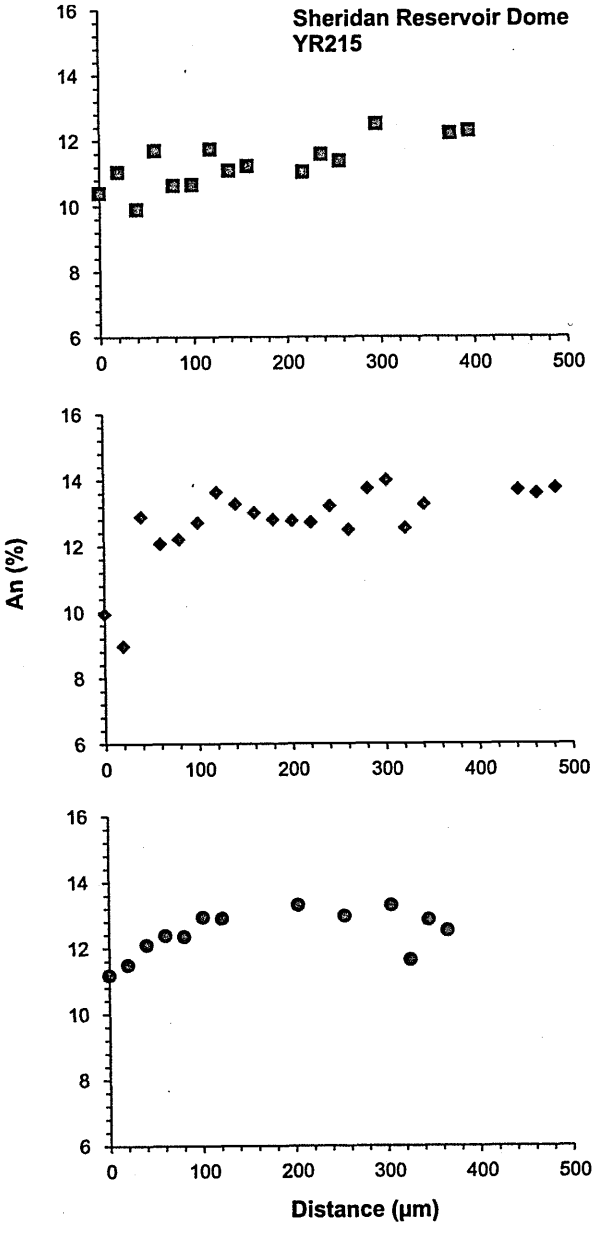

Figure 3.9. Example of An content (%) variation from crystal edge to core for selected feldspar phenocrysts (sample YR215). Plots represent transects across grains (0 = edge of the grain and distance increases towards the centre). See Appendix A4.1.2 for the full data set (Transect # 1, 2 and 3).

3.5.1.5 Green Canyon Flow dome

Feldspars are predominantly sanidine in composition, although minor plagioclase (An_{15} to An_{20}), was also detected (Fig. 3.8). Sanidine composition is tightly constrained (Or_{58} to Or_{62}), and do not show the same compositional diversity as Sheridan Reservoir dome.

3.5.2 Ar-Ar ages: Single grain fusion results

Ar-Ar data from laser-probe single grain fusion experiments of Yellowstone samples are presented in summary Table 3.5 and Table 3.6. For full Ar-Ar data tables refer to Appendix section A3.3. Weighted mean ages (± 2σ; MSWD value), inverse isochron analyses and probability density plots have been calculated using Isoplot (K. Ludwig, 2011), and details are discussed in Appendix section A1.6.2. Some samples require more than one inverse isochron to be plotted, representing the separate packets containing the sample during irradiation and therefore the unique *J*-value assigned to each packet. In addition, summary tables also include the arithmetic mean, which is given for reference only. The weighted mean age has been taken in all cases and discussed throughout the text.

3.5.2.1 Huckleberry Ridge Tuff (HRT)

Sample YP127 – unit A: Feldspar data

Ar-Ar total-fusion ages obtained from single feldspar grains range 2.01 ± 0.12 to 2.28 ± 0.14 Ma and yield a weighted mean age of 2.11 ± 0.02 Ma (n = 38; MSWD = 0.96). The age probability plot (Fig. 3.10) shows a symmetrical distribution with no evidence for the incorporation of xenocrystic material. The data were plotted on two separate inverse isochron diagrams (Fig. 3.11a and Fig. 3.11b), and yield ages of 2.05 ± 0.13 Ma (MSWD = 0.63) and 2.117 ± 0.05 Ma (MSWD = 1.2) respectively. Due to significant clustering of

data near the $^{39}Ar/^{40}Ar$ axis and limited dispersion along the mixing line, the resulting Ar-Ar ratio and uncertainty (trapped Ar composition) are extremely high (544 ± 280 and 348 ± 140 respectively), but given the large uncertainties, both lie within error of the atmospheric value 298.56. The majority of ages have been determined on sanidine (exhibit a $^{37}Ar/^{39}Ar$ ratio of ~ 0 to ~ 0.2).

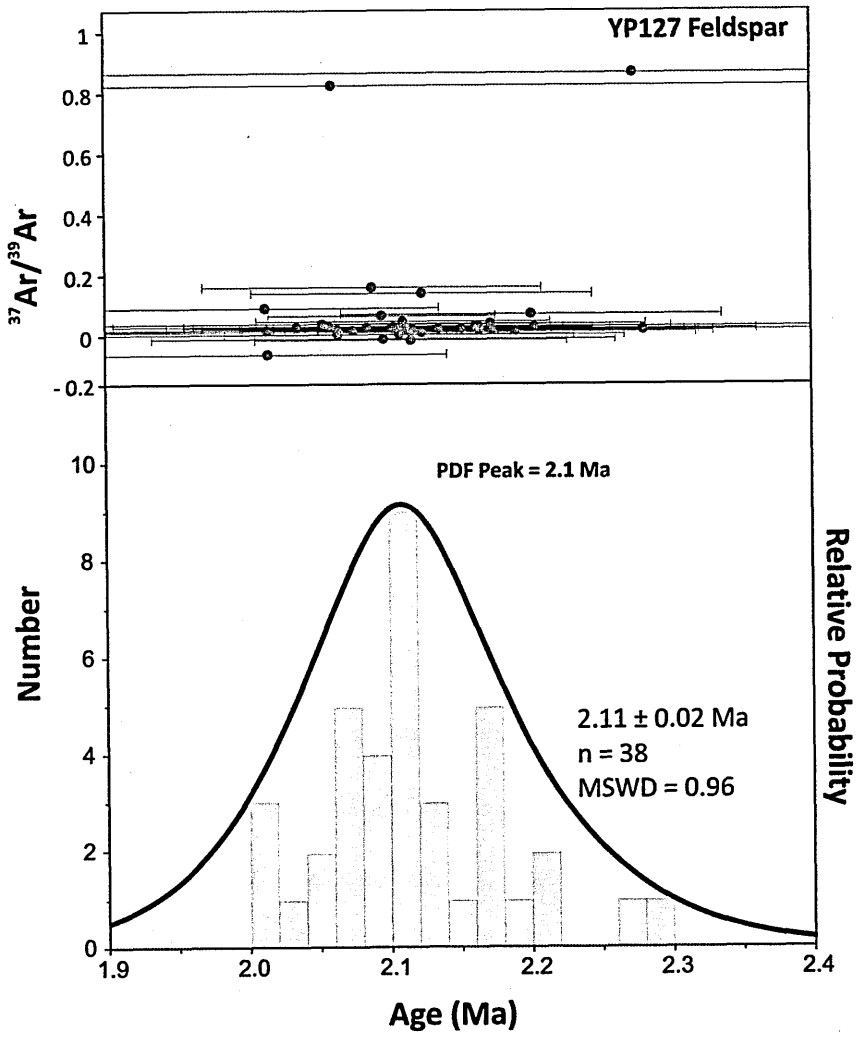

Figure 3.10. Age probability distribution diagram and age vs. $^{37}Ar/^{39}Ar$ correlation plot for HRT member A (sample YP127). PDF peak (value at x at which the probability density function has its maximum value) for data set are also given and the weighted mean age (determined separately using Isoplot; Ludwig, 2011), is also shown. All errors shown are 2σ.

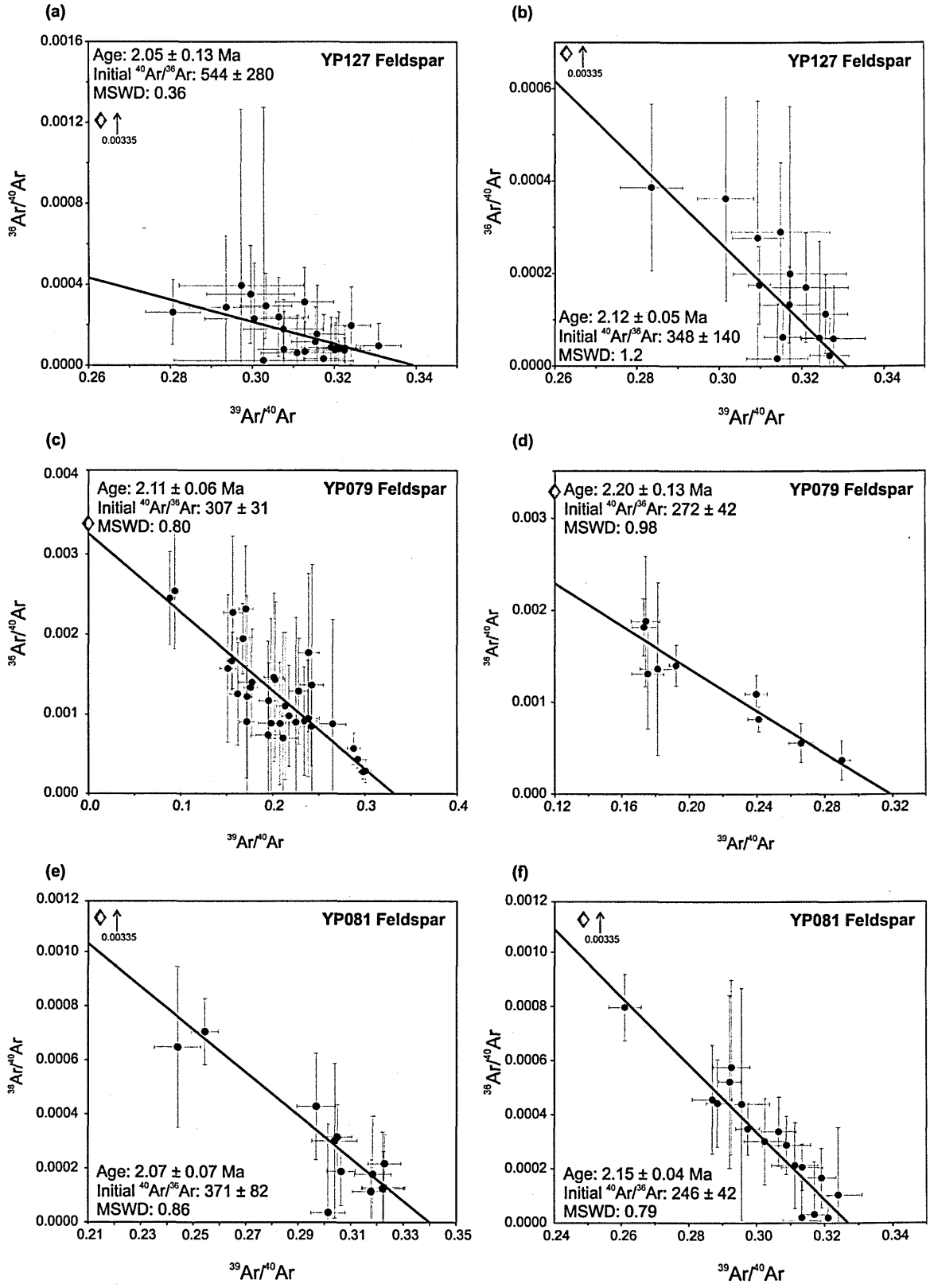
(a)
Age: 2.05 ± 0.13 Ma
Initial $^{40}Ar/^{36}Ar$: 544 ± 280
MSWD: 0.36
YP127 Feldspar
0.00335
$^{36}Ar/^{40}Ar$
$^{39}Ar/^{40}Ar$
(b)
YP127 Feldspar
0.00335
Age: 2.12 ± 0.05 Ma
Initial $^{40}Ar/^{36}Ar$: 348 ± 140
MSWD: 1.2
(c)
Age: 2.11 ± 0.06 Ma
Initial $^{40}Ar/^{36}Ar$: 307 ± 31
MSWD: 0.80
YP079 Feldspar
(d)
Age: 2.20 ± 0.13 Ma
Initial $^{40}Ar/^{36}Ar$: 272 ± 42
MSWD: 0.98
YP079 Feldspar
(e)
YP081 Feldspar
0.00335
Age: 2.07 ± 0.07 Ma
Initial $^{40}Ar/^{36}Ar$: 371 ± 82
MSWD: 0.86
(f)
YP081 Feldspar
0.00335
Age: 2.15 ± 0.04 Ma
Initial $^{40}Ar/^{36}Ar$: 246 ± 42
MSWD: 0.79

(Figure 3.11)

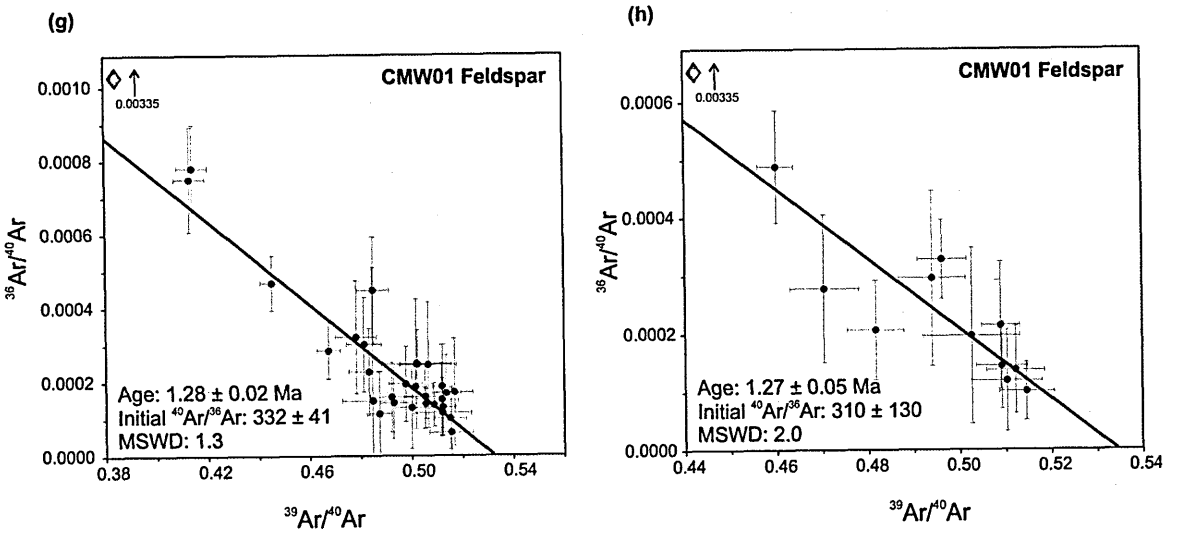

Figure 3.11. (including preceding page) Isotope correlation plots (inverse isochron) for feldspars separated from Yellowstone tuffs (determined using Isoplot; Ludwig, 2011). (a) and (b) HRT member A (sample YP127); (c) and (d) HRT member B (sample YP079); (e) and (f) HRT member C (sample YP081); (g) and (h) MFT (sample CMW01). Red diamond indicated intercept of modern air (0.00335).

Sample YP079 – unit B: Feldspar data

Ar-Ar total-fusion ages obtained from single feldspar grains range 1.29 ± 0.96 to 2.97 ± 0.86 Ma and yield a weighted mean age of 2.12 ± 0.04 Ma (n = 42; MSWD = 0.8). One anomalously older age of 5.09 ± 0.69 was also obtained from this sample but excluded from the calculation of the weighted mean. This sample contained a significant amount of plagioclase feldspar crystals, which formed 45 % of the crystals, analysed (estimated based on Ca/K ratios). The age uncertainties for the Ca-rich feldspars are significantly larger than those obtained from the K-rich feldspars, and as a result show much more variability (Fig. 3.12). The weighted mean age determined from plagioclase feldspar is 2.15 ± 0.19 Ma (n = 19; MSWD = 0.73). The data are plotted on two separate inverse isochron diagrams (Fig. 3.11c and Fig. 3.11d), and yield ages of 2.11 ± 0.06 Ma (MSWD = 0.8) and 2.20 ± 0.13 Ma (MSWD = 0.98) respectively. Both yield an initial $^{40}Ar/^{36}Ar$ ratio within error of 298.56 (307 ± 31 and 272 ± 42 respectively) although the plagioclase feldspars have limited dispersion along the line.

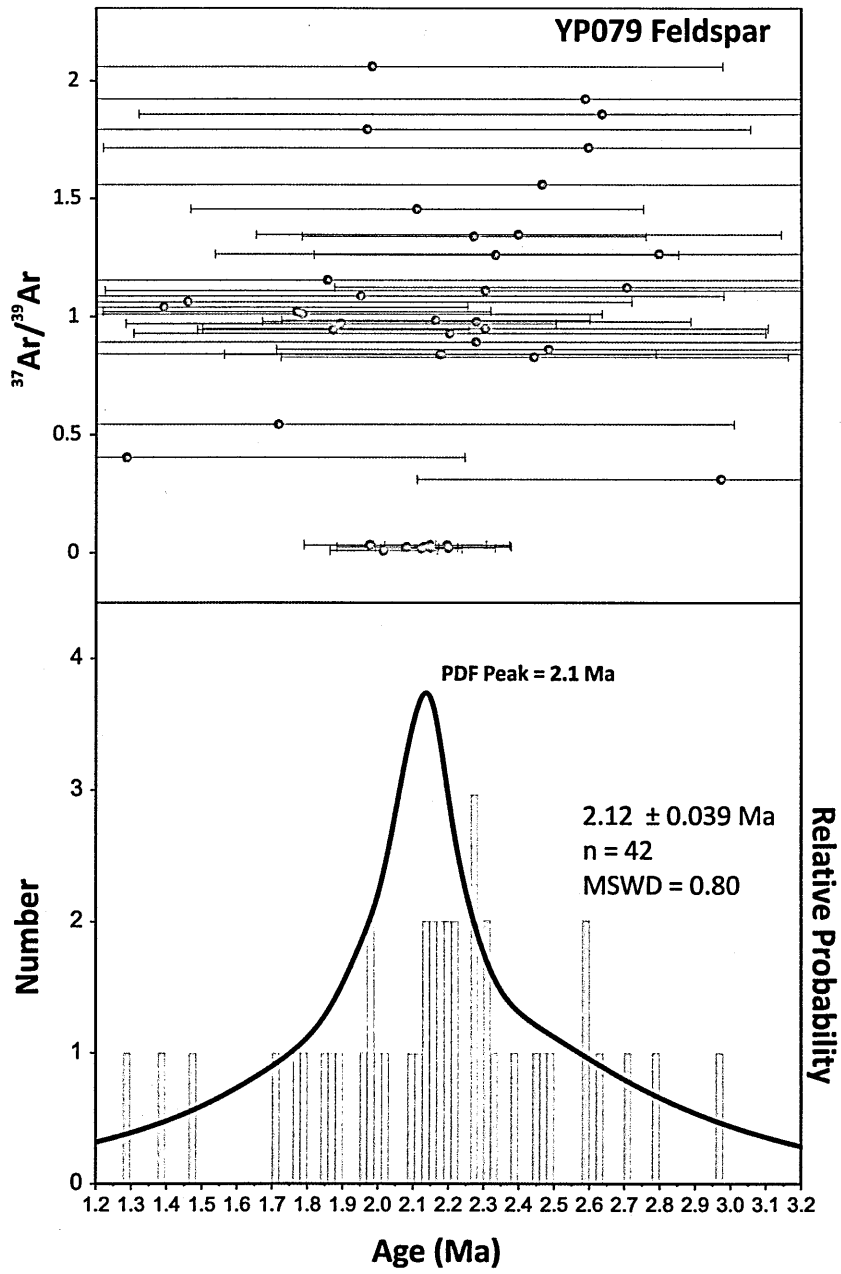

Figure 3.12. Age probability distribution diagram and age vs. $^{37}Ar/^{39}Ar$ correlation plot for HRT member B (sample YP079). PDF peak (value at x at which the probability density function has its maximum value) for data set is also given and the weighted mean age (determined separately using Isoplot; Ludwig, 2011), is also shown. All errors shown are 2σ.

Sample YP081 – unit C: Feldspar data

Ar-Ar total-fusion ages obtained from single feldspar grains range 1.99 ± 0.24 to 2.32 ± 0.26 Ma, and yield a weighted mean age of 2.11 ± 0.02 Ma (n = 29; MSWD = 0.99). The age probability plot (Fig. 3.13) shows a symmetrical distribution with no anomalously

older grains identified. The data are plotted on two separate inverse isochron diagrams (Fig. 3.11), and yield ages of 2.07 ± 0.07 Ma (MSWD = 0.86) and 2.15 ± 0.04 Ma (MSWD = 0.79) respectively. The first isochron (Fig. 3.11e) yields an initial $^{40}Ar/^{36}Ar$ ratio within error of 298.56 (371 ± 82), however the second (Fig. 3.11f) yields an initial $^{40}Ar/^{36}Ar$ ratio which is slightly less than the atmospheric value of 298.56 (246 ± 42).

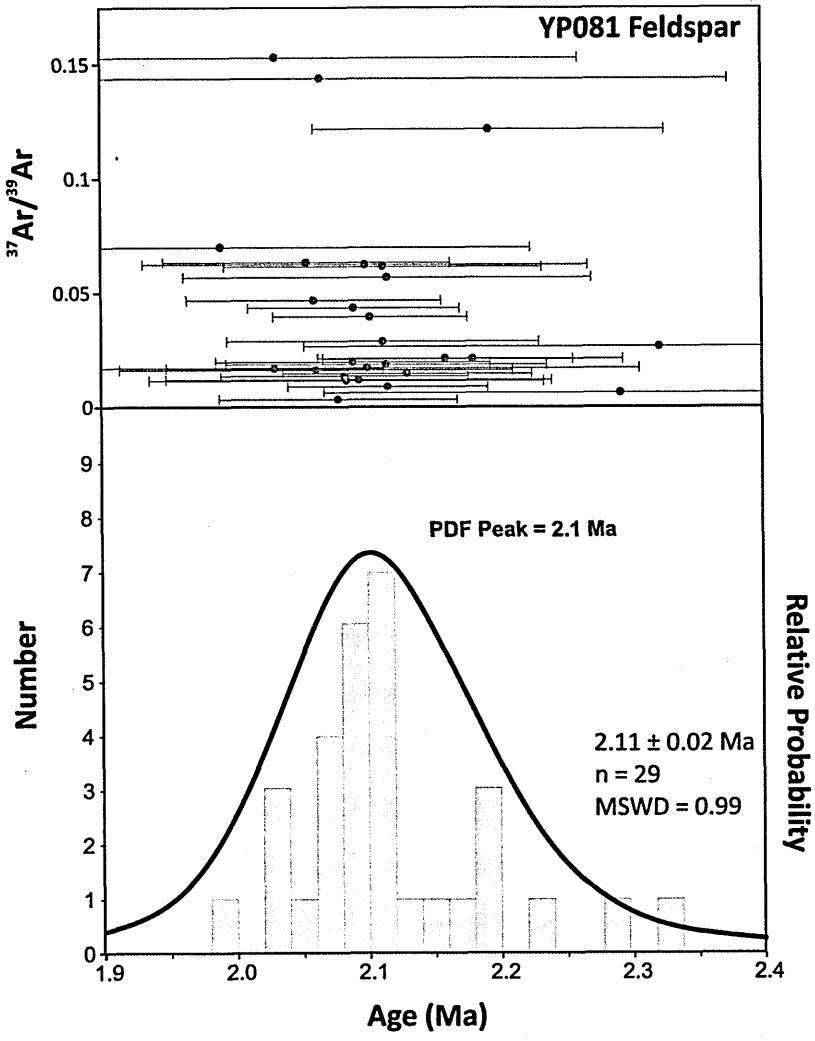

Figure 3.13. Age probability distribution diagram and age vs. $^{37}Ar/^{39}Ar$ correlation plot for HRT member C (sample YP081). PDF peak (value at x at which the probability density function has its maximum value) for data set are also given and the weighted mean age (determined separately using Isoplot; Ludwig, 2011), is also shown. All errors shown are 2σ.

3.5.2.2 Mesa Falls Tuff (MFT)

Sample CMW01: Feldspar data

Ar-Ar total-fusion ages obtained from single feldspar grains range 1.21 ± 0.06 to 1.34 ± 0.05 Ma and yield a weighted mean age of 1.28 ± 0.01 Ma (n = 40; MSWD = 1.4). The age probability plot (Fig. 3.14), shows a fairly symmetrical distribution with no evidence for the incorporation of xenocrystic material. The data are plotted on two separate inverse isochron diagrams (Fig. 3.11g and Fig. 3.11h), and yield ages of 1.28 ± 0.02 Ma (MSWD = 1.3) and 1.27 ± 0.05 Ma (MSWD = 2.0) respectively, both indistinguishable from the weighted mean age. Although clustering of data points and limited dispersion along the mixing line for the first set of feldspars, and scatter around the line for the second set of feldspars is quite clear, the initial $^{40}Ar/^{36}Ar$ ratio for both sets (332 ± 41and 310 ± 130 respectively), are within error of the atmospheric value of 298.56.

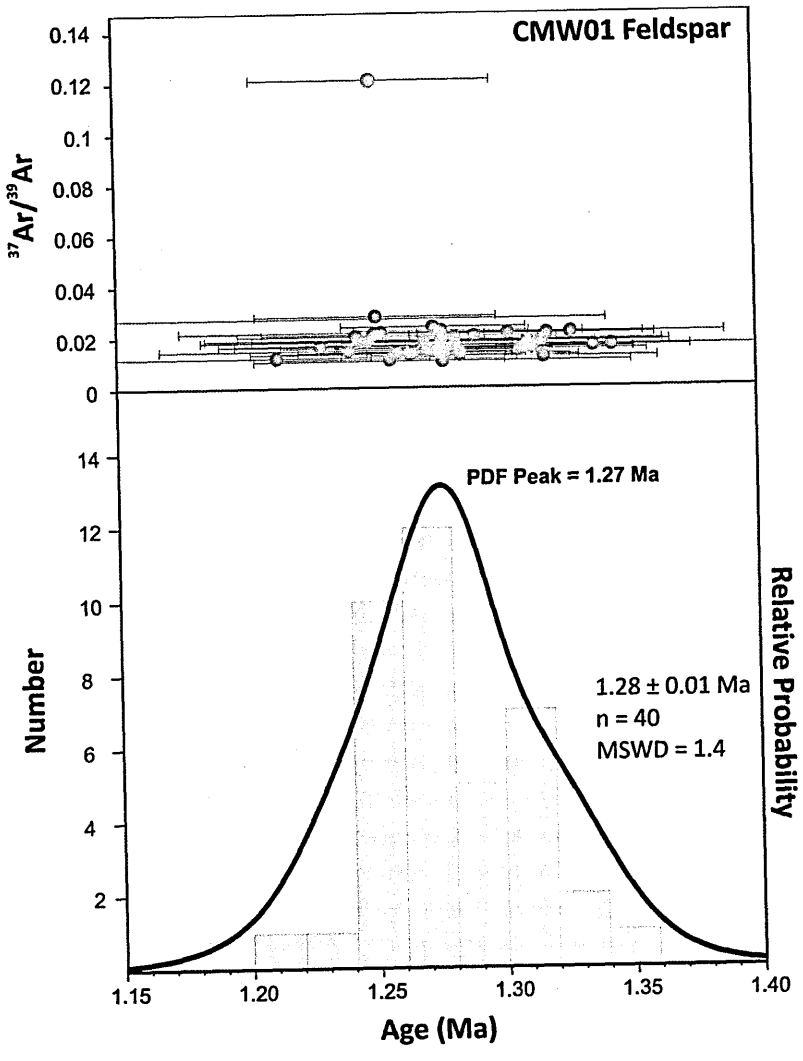

Figure 3.14. Age probability distribution diagram and age vs. $^{37}Ar/^{39}Ar$ correlation plot for MFT (sample CMW01). PDF peak (value at x at which the probability density function has its maximum value) for data set are also given and the weighted mean age (determined separately using Isoplot; Ludwig, 2011), is also shown. All errors shown are 2σ.

Table 3.5. Summary Ar-Ar age information for Huckleberry Ridge Tuff (member A, B and C) and Mesa Falls Tuff feldspars. The standard deviation (s.d.) of the arithmetic mean is given at the 95 % confidence level. Full data set, including average instrument blank measurements and calculated *J*-values used for data processing and raw data can be found in Appendix section A3.3.

Unit (sample)	Mineral phase	$^{37}Ar/^{39}Ar$	Max. Age (Ma)	± 2σ	Min. Age (Ma)	± 2σ	Arithmetic Mean Age (Ma)	s.d.	n	Weighted Mean Age (Ma)	± 2σ
Huckleberry Ridge Tuff											
A (YP127)	san	< 0.1	2.28	0.14	2.01	0.12	2.12	0.12	38	**2.11**	**0.02**
B (YP079)	fsp	-	2.97	0.86	1.29	0.96	2.14	0.70	42	**2.12**	**0.04**
	san	< 0.1	2.97	0.86	1.29	0.96	2.14	0.56	23	2.12	0.04
	plag	> 1	2.78	1.26	1.39	0.86	2.18	0.81	19	2.15	0.19
C (YP081)	san	< 0.1	2.32	0.26	1.99	0.24	2.12	0.14	29	**2.11**	**0.02**
Mesa Falls Tuff											
(CMW01)	san	< 0.1	1.34	0.05	1.21	0.06	1.28	0.06	40	**1.28**	**0.01**

fsp = plagioclase and sanidine; san = sanidine; plag = plagioclase

3.5.2.3 Snake River Butte dome

Sample YR185: Feldspar data

For 500 μm to 1 mm size fraction, a range of 1.61 ± 0.40 to 2.46 ± 0.25 Ma and a weighted mean age of 2.18 ± 0.01 Ma (n = 51; MSWD = 4.6) was determined (Fig. 3.15). MSWD > 4 suggests significant scatter exists in the data set. For feldspars (500 μm to 1 mm; n = 24) conventionally cleaned (in acetone), data plotted on two separate inverse isochron diagrams (Fig. 3.16a and 3.16b), yielding ages 2.17 ± 0.04 Ma and 2.10 ± 0.15 Ma, and $^{40}Ar/^{36}Ar$ ratios within error of the atmospheric value. To test the presence of $^{40}Ar_E$ in adhering glass, feldspars (n = 27; 500 μm to 1 mm), were washed in cold 10 % solution of HF. The range of ages was not significantly reduced (2.07 ± 0.20 to 2.32 ± 0.16 Ma). Despite clustering of data points at the radiogenic axis, the inverse isochron (Fig. 3.19c) gives an age of 2.19 ± 0.03 Ma and an initial $^{40}Ar/^{36}Ar$ ratio of 305 ± 21 (n = 27), which is within error of 298.56 and statistically valid (MSWD = 0.86).

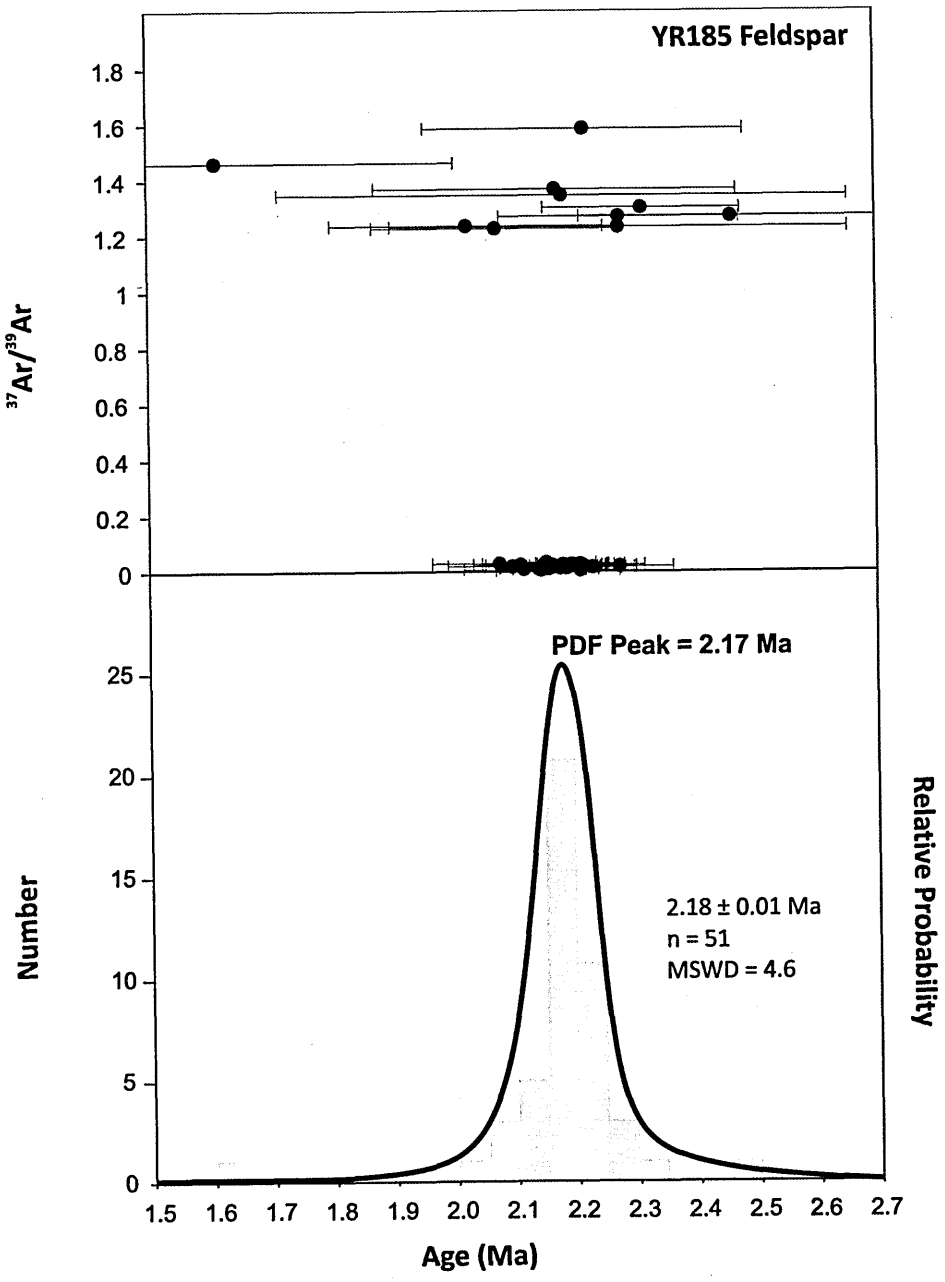

Figure 3.15. Age probability distribution diagram and age vs. $^{37}Ar/^{39}Ar$ correlation plot for Snake River Butte dome separated feldspars (HF and acetone washed; 500 μm to 1 mm; sample YR185). PDF peak (value at x at which the probability density function has its maximum value) for data set are also given and the weighted mean age (determined separately using Isoplot; Ludwig, 2011), is also shown. All errors shown are 2σ.

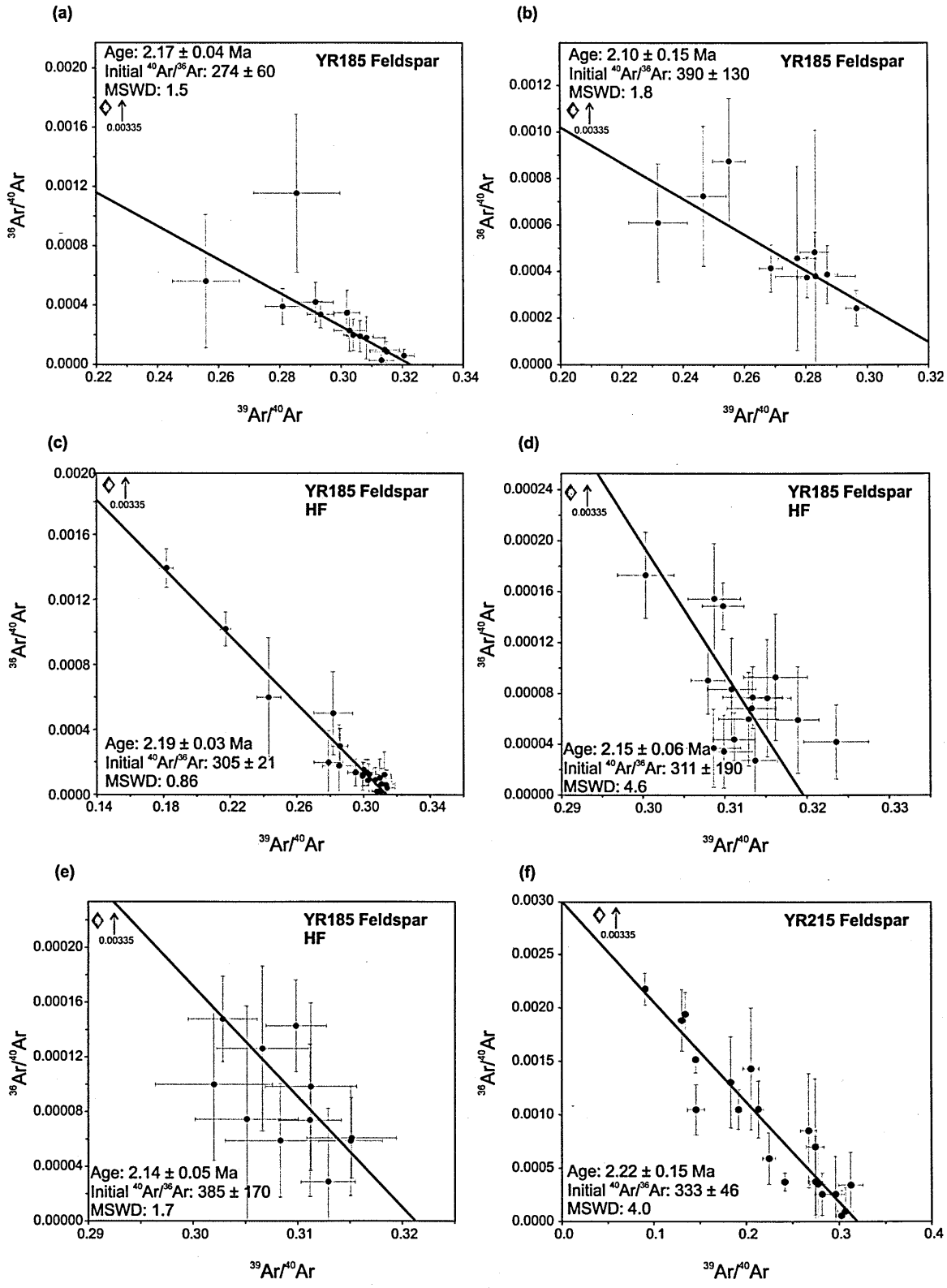
(a)
Age: 2.17 ± 0.04 Ma
Initial $^{40}Ar/^{36}Ar$: 274 ± 60
MSWD: 1.5
YR185 Feldspar
0.00335
$^{36}Ar/^{40}Ar$
$^{39}Ar/^{40}Ar$
(b)
Age: 2.10 ± 0.15 Ma
Initial $^{40}Ar/^{36}Ar$: 390 ± 130
MSWD: 1.8
YR185 Feldspar
0.00335
$^{36}Ar/^{40}Ar$
$^{39}Ar/^{40}Ar$
(c)
YR185 Feldspar
HF
0.00335
Age: 2.19 ± 0.03 Ma
Initial $^{40}Ar/^{36}Ar$: 305 ± 21
MSWD: 0.86
$^{36}Ar/^{40}Ar$
$^{39}Ar/^{40}Ar$
(d)
YR185 Feldspar
HF
0.00335
Age: 2.15 ± 0.06 Ma
Initial $^{40}Ar/^{36}Ar$: 311 ± 190
MSWD: 4.6
$^{36}Ar/^{40}Ar$
$^{39}Ar/^{40}Ar$
(e)
YR185 Feldspar
HF
0.00335
Age: 2.14 ± 0.05 Ma
Initial $^{40}Ar/^{36}Ar$: 385 ± 170
MSWD: 1.7
$^{36}Ar/^{40}Ar$
$^{39}Ar/^{40}Ar$
(f)
YR215 Feldspar
0.00335
Age: 2.22 ± 0.15 Ma
Initial $^{40}Ar/^{36}Ar$: 333 ± 46
MSWD: 4.0
$^{36}Ar/^{40}Ar$
$^{39}Ar/^{40}Ar$

(Figure 3.16)

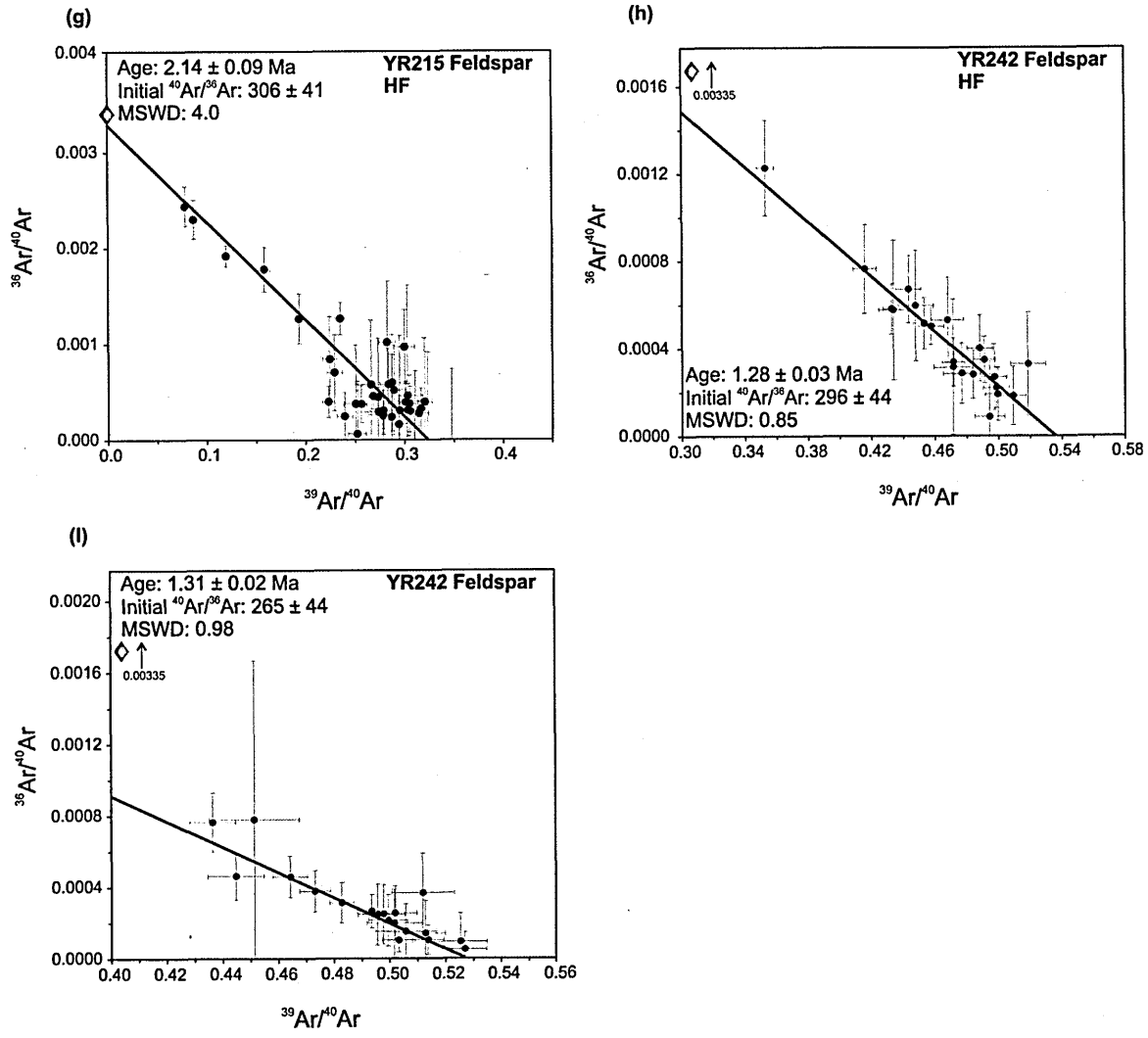

Figure 3.16. (including preceding page) Isotope correlation plots (inverse isochron) for feldspars separated from Yellowstone domes (determined using Isoplot; Ludwig, 2011). (a) and (b) Snake River Butte dome (sample YR185; 500 to 1 mm; acetone wash); (c) Snake River Butte dome (sample YR185; 500 – 1 mm; HF wash); (d) and (e) Snake River Butte dome (sample YR185; 1 to 2 mm; HF wash); (f) Sheridan Reservoir dome (sample YR215; acetone wash); (g) Sheridan Reservoir dome (sample YR215; HF wash); (h) Green Canyon Flow dome (Sample YR242; HF wash) and (i) Green Canyon Flow dome (Sample YR242; acetone wash). Red diamond indicated intercept of modern air (0.00335).

Ar-Ar total-fusion ages obtained from single feldspar grains (1 to 2 mm size fraction) range 2.09 ± 0.04 to 2.51 ± 0.42 Ma, and yield a weighted mean age of 2.15 ± 0.01 Ma (n = 59; MSWD = 1.3) (Fig. 3.17). Very limited dispersion along a mixing line for both determined inverse isochron plots (Fig. 3.16d and Fig. 3.16e) has resulted in large ratio values and uncertainties ($^{40}Ar/^{36}Ar$ ratio of 311 ± 190 and 385 ± 170) and large associated MSWDs (4.6 and a marginally better 1.7). Despite this both yield trapped component ratios

that are within error of 298.56, and inverse isochron ages which are in agreement with each other (2.15 ± 0.06 Ma and 2.14 ± 0.05 Ma respectively).

The above results do not include a set of data (n = 25; obtained from a single irradiation packet for sample YR185), because contamination by ^{36}Ar, possibly during sample loading is suspected. This contamination has resulted in high $^{36}Ar/^{40}Ar$ and $^{38}Ar/^{39}Ar$ isotope ratios and large errors (see full Ar-Ar data table in Appendix section A3.1.2.1), which was not seen in previous or subsequent batches of the same sample. Although the weighted mean age determined for this data is in agreement with all other weighted mean ages presented for this sample, the large ^{36}Ar values and associated errors mean the data do not contribute any useful information.

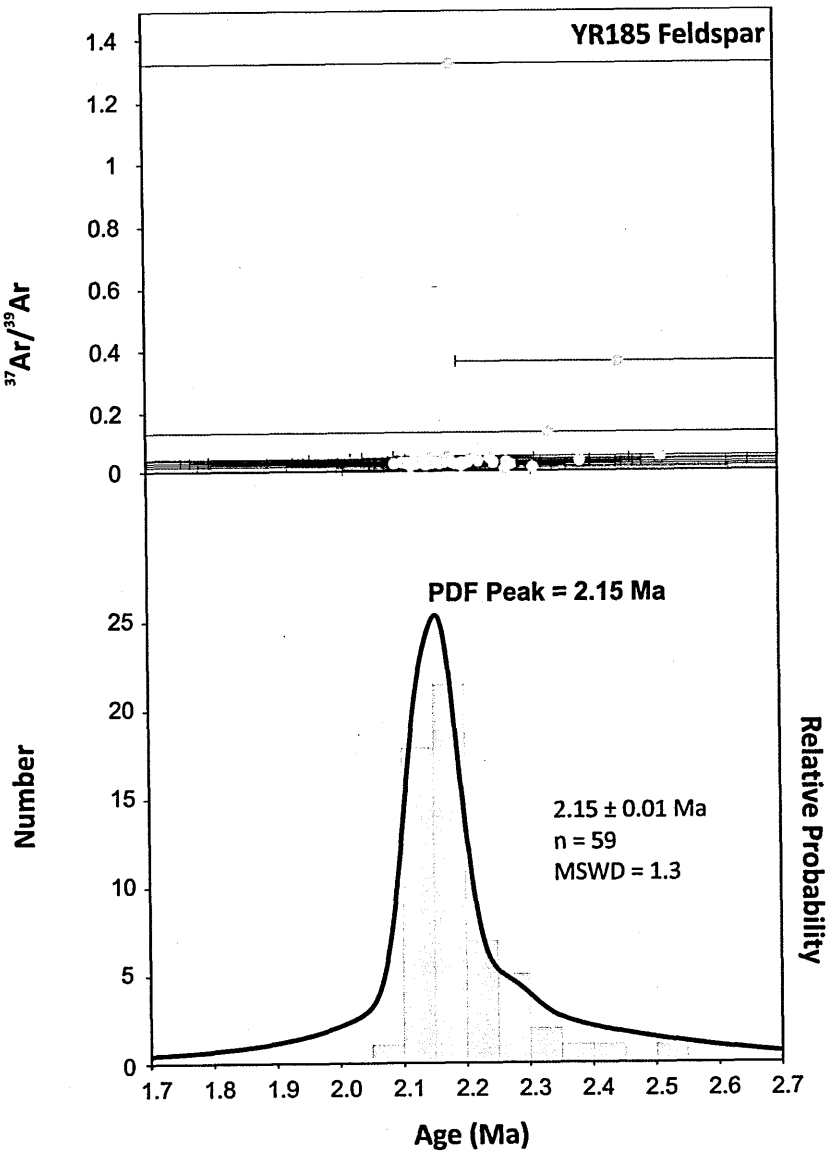

Figure 3.17. Age probability distribution diagram and age vs. $^{37}Ar/^{39}Ar$ correlation plot for Snake River Butte dome separated feldspars (HF and acetone washed; 1 to 2 mm; sample YR185). PDF peak (value at x at which the probability density function has its maximum value) for data set are also given and the weighted mean age (determined separately using Isoplot; Ludwig, 2011), is also shown. All errors shown are 2σ.

Samples YR185: Glassy groundmass

Ar-Ar total-fusion ages obtained from single grains of glassy groundmass range 1.81 ± 0.34 to 2.27 ± 0.20 Ma (Fig. 3.18). Weighted mean age for glassy groundmass analysis is 2.10 ± 0.08 Ma (n = 22, MSWD = 0.48). The range of ages is similar to that seen in the feldspars and the weighted mean age is in good agreement with weighted mean ages

determined for the feldspars. Data plotted on an inverse isochron (Fig. 3.19a) yield an age of 2.29 ± 0.28 Ma with an initial $^{40}Ar/^{36}Ar$ trapped component of 268 ± 36, which is in agreement with atmospheric Ar ratio (298.56).

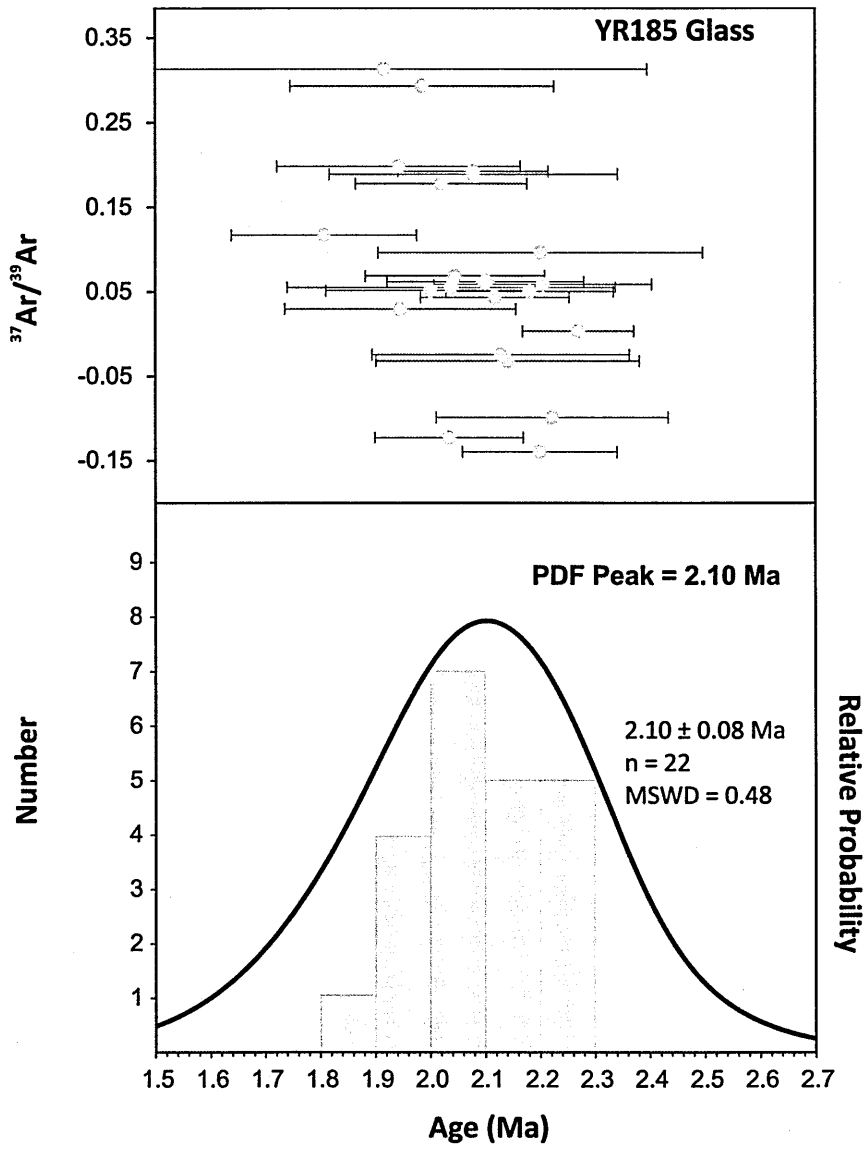

Figure 3.18. Age probability distribution diagram and age vs. $^{37}Ar/^{39}Ar$ correlation plot for Snake River Butte dome separated glass (sample YR185). PDF peak (value at x at which the probability density function has its maximum value) for data set are also given and the weighted mean age (determined separately using Isoplot; Ludwig, 2011), is also shown. All errors shown are 2σ.

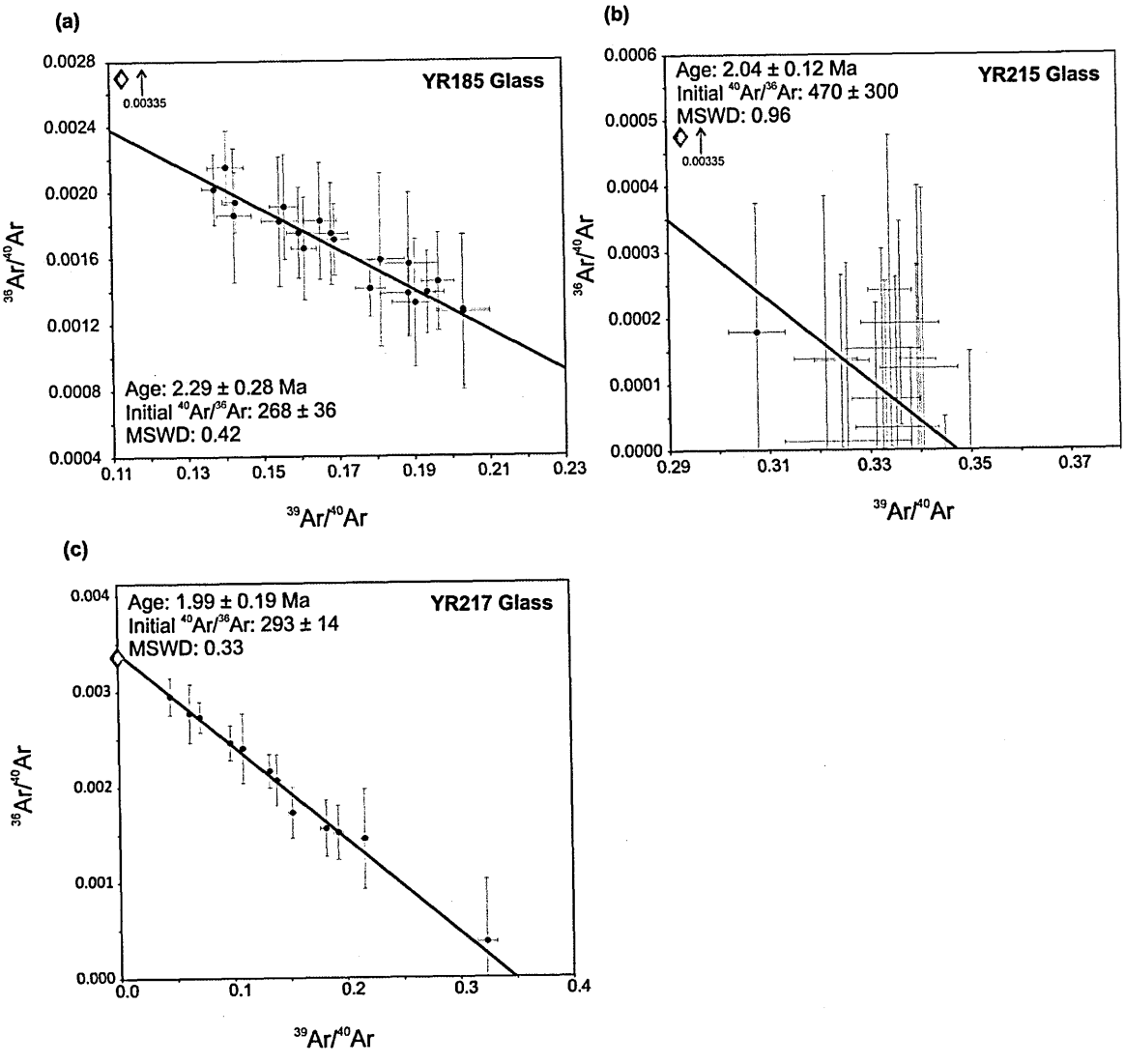

Figure 3.19. Isotope correlation plots (inverse isochron) for glass separated from Yellowstone rhyolite domes (determined using Isoplot; Ludwig, 2011). (a) Snake River Butte dome (sample YR185); (b) Sheridan Reservoir dome (sample YR215) and (c) Sheridan Reservoir dome (sample YR217). Red diamond indicated intercept of modern air (0.00335).

3.5.2.4 Sheridan Reservoir dome

Sample YR215: Feldspar data

Ar-Ar total-fusion ages (Fig. 3.20), obtained from single feldspar grains range 1.63 ± 0.3 to 3.34 ± 0.4 Ma and yield a weighted mean age of 2.25 ± 0.07 Ma (n = 60; MSWD = 5.8). The unacceptably large MSWD indicates significant scatter in total fusion ages. To test the presence of $^{40}Ar_E$ in adhering glass, feldspars (n = 40) were washed in cold 10 % solution

of HF. The HF wash slightly reduced the range in Ar-Ar ages achieved (in this case it was 1.63 ± 0.13 Ma to 2.71 ± 0.08 Ma), although not significantly (discussed further in section 3.6.2.1). The age probability plot is clearly skewed and reveals a tail toward older ages. Age vs. $^{37}Ar/^{39}Ar$ correlation plots (Fig. 3.21) for all feldspars shows only a weak correlation ($R^2 = 0.26$ for acetone washed grains and $R^2 = 0.20$ for HF washed grains) between age and Ca/K ratio. Not all grains analysed with a $^{37}Ar/^{39}Ar$ ratio > 0.2 yield an older than expected age, however it should be noted that no grains with a $^{37}Ar/^{39}Ar$ ratio < 0.15 yield older than expected ages.

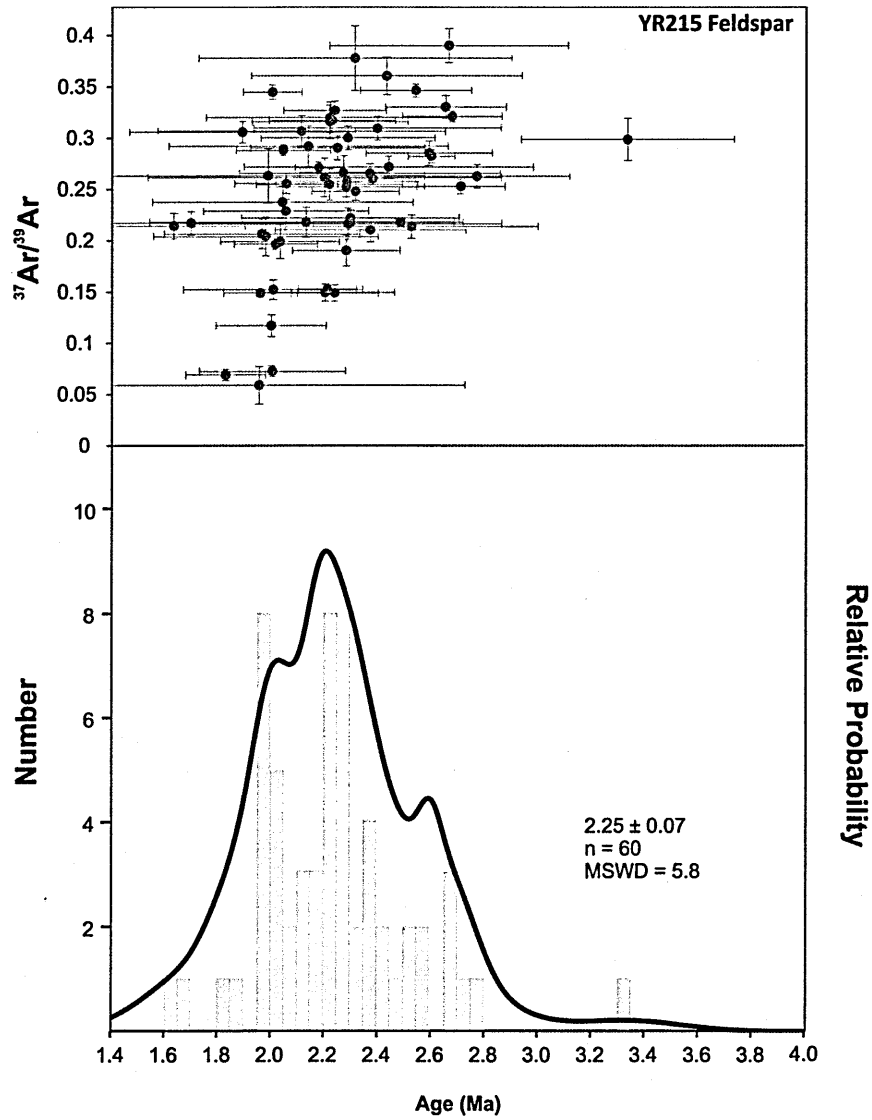

Figure 3.20. Age probability distribution diagram and age vs. $^{37}Ar/^{39}Ar$ correlation plot for Sheridan Reservoir dome (HF and acetone washed; sample YR215). The weighted mean age (determined separately using Isoplot; Ludwig, 2011), is also shown. All errors shown are 2σ.

Inverse isochron diagrams for both feldspar separates (Fig. 3.16f and Fig. 3.16g), yield inverse isochron ages that are within error of each other (2.22 ± 0.15 Ma and 2.14 ± 0.09 Ma respectively) and $^{40}Ar/^{36}Ar$ ratios within error of 298.56, however both have large associated MSWDs (MSWD = 4), and for the HF washed grains there is significant clustering of data near the $^{39}Ar/^{40}Ar$ axis. MSWDs greater than ~ 2.5 indicate greater dispersion from the mixing line and are indicative of the presence of geological errors, such as outliers or multiple populations of grains (Deino and Potts, 1992).

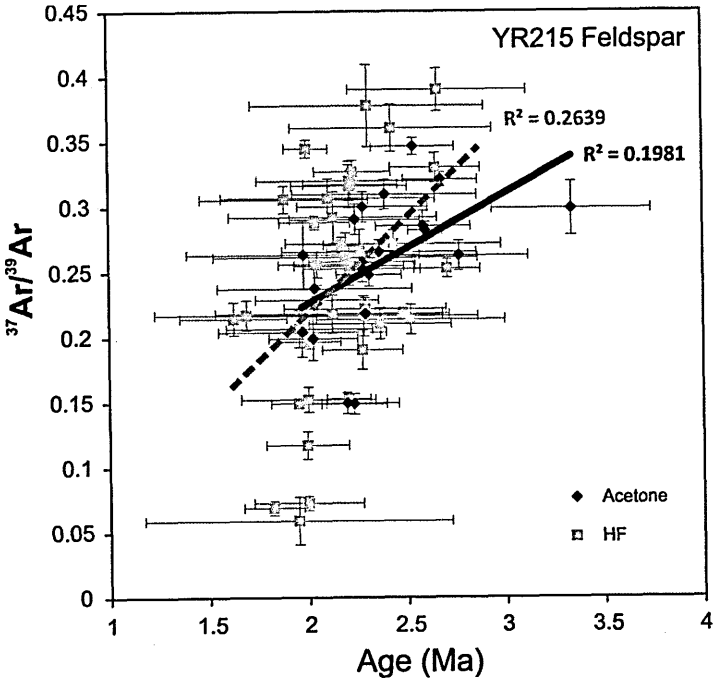

Figure 3.21. Age vs. $^{37}Ar/^{39}Ar$ correlation plot for HF and acetone washed Sheridan Reservoir feldspars (sample YR215), showing a weak correlation between age and Ca/K.

Samples YR215 and YR217: Glassy groundmass

Ar-Ar total-fusion ages obtained from single grains of glassy groundmass range 1.83 ± 0.6 to 2.34 ± 0.3 Ma. Weighted mean age for all glassy groundmass analysis (combined ages from sample YR215 and YR217) is 2.04 ± 0.03 Ma (n = 30, MSWD = 0.03). Compared with the age probability diagram of the feldspar separates, the distribution of ages for

combined groundmass data (Fig. 3.22) are more symmetrical and yields a PDF peak age of 2.03 Ma, which is indistinguishable from the weighted mean age.

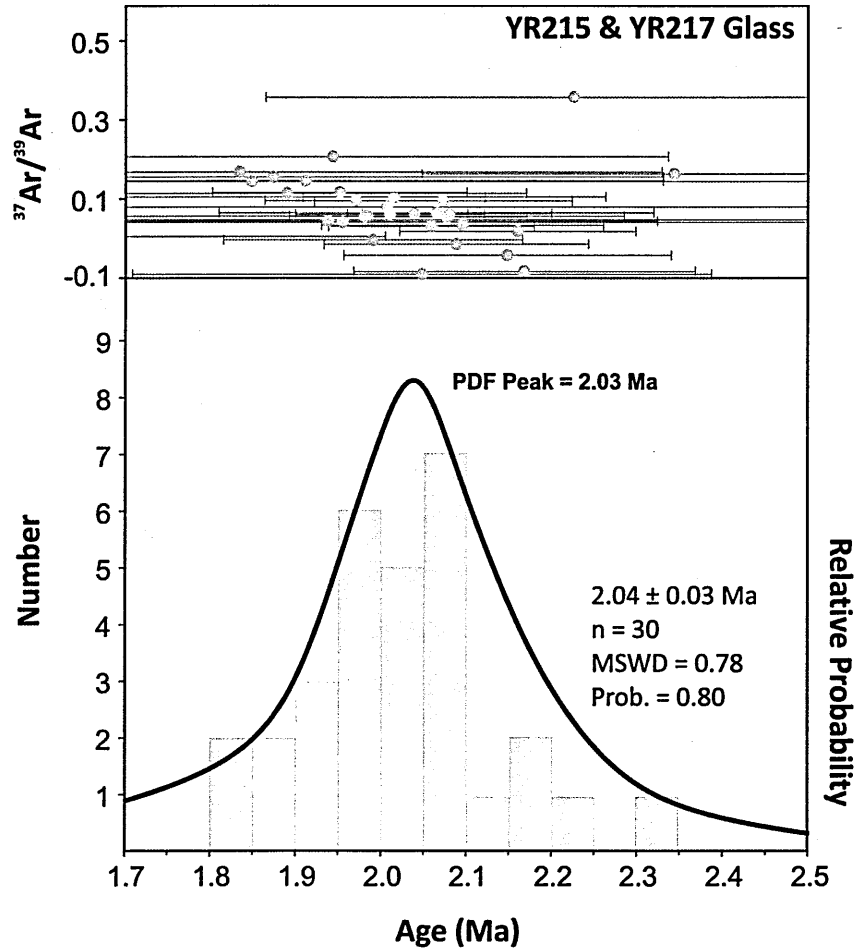

Figure 3.22. Age probability distribution diagram and age vs. $^{37}Ar/^{39}Ar$ correlation plot for Sheridan Reservoir dome separated glass (sample YR215 and YR217). PDF peak (value at x at which the probability density function has its maximum value) for data set are also given and the weighted mean age (determined separately using Isoplot; Ludwig, 2011), is also shown. All errors shown are 2σ.

Groundmass grains separated from sample YR217 have higher atmospheric content than grains separated from YR215 (Fig. 3.23). Being able to measure the ^{36}Ar in this sample has made it possible to construct a valid inverse isochron diagram (Fig. 3.19c), with an inverse isochron age of 1.99 ± 0.19 Ma (MSWD = 0.33). This age is in good agreement with the weighted mean age and an atmospheric intercept of 293 ± 14, which is in error of the

accepted value for the $^{40}Ar/^{36}Ar$ ratio of 298.56, and strongly suggests the trapped component is of atmospheric composition. It has not been possible however to calculate a useful inverse isochron diagram using the groundmass data from sample YR215 (shown in Fig. 3.19b for reference). There was significant clustering of data points near the $^{39}Ar/^{40}Ar$ axis and no spread along the line resulting in an initial $^{40}Ar/^{36}Ar$ value large with a large error 470 ± 300.

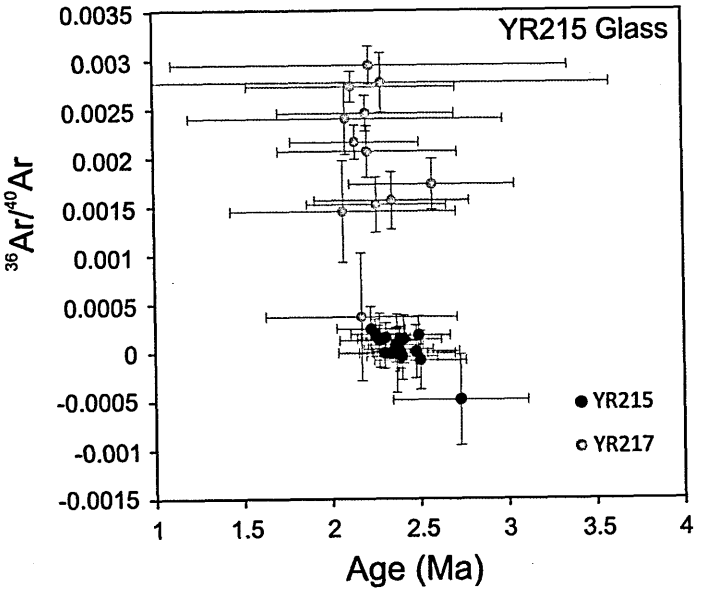

Figure 3.23. Age vs. $^{36}Ar/^{40}Ar$ correlation plot for glass separated from samples YR215 and YR217.

3.5.2.5 Green Canyon Flow dome

Sample YR242: Feldspar data

Ar-Ar total-fusion ages obtained from single feldspar grains range 1.20 ± 0.06 to 1.35 ± 0.10 Ma and gave a weighted mean age of 1.29 ± 0.01 Ma (n = 55) with an MSWD = 0.80 (Fig. 3.24). To test the presence of $^{40}Ar_E$ in adhering glass, feldspars (n = 21) were washed in cold 10 % solution of HF. The range of ages was not significantly reduced (1.29 ± 0.09 to 1.35 ± 0.1 Ma). For HF washed grains, an inverse isochron age of 1.28 ± 0.03 Ma

(MSWD = 0.85) is indistinguishable from the weighted mean age at the 2σ level and the trapped component is within error of 298.56 (Fig. 3.16h). Acetone washed grains yielded an inverse isochron (Fig. 3.16i) age of 1.31 ± 0.02 Ma which is in good agreement with the weighted mean age. Both have statistically valid MSWD values (< 1) and initial $^{40}Ar/^{36}Ar$ ratios within error of the atmospheric value of 298.56 (296 ± 44 and 265 ± 44 respectively).

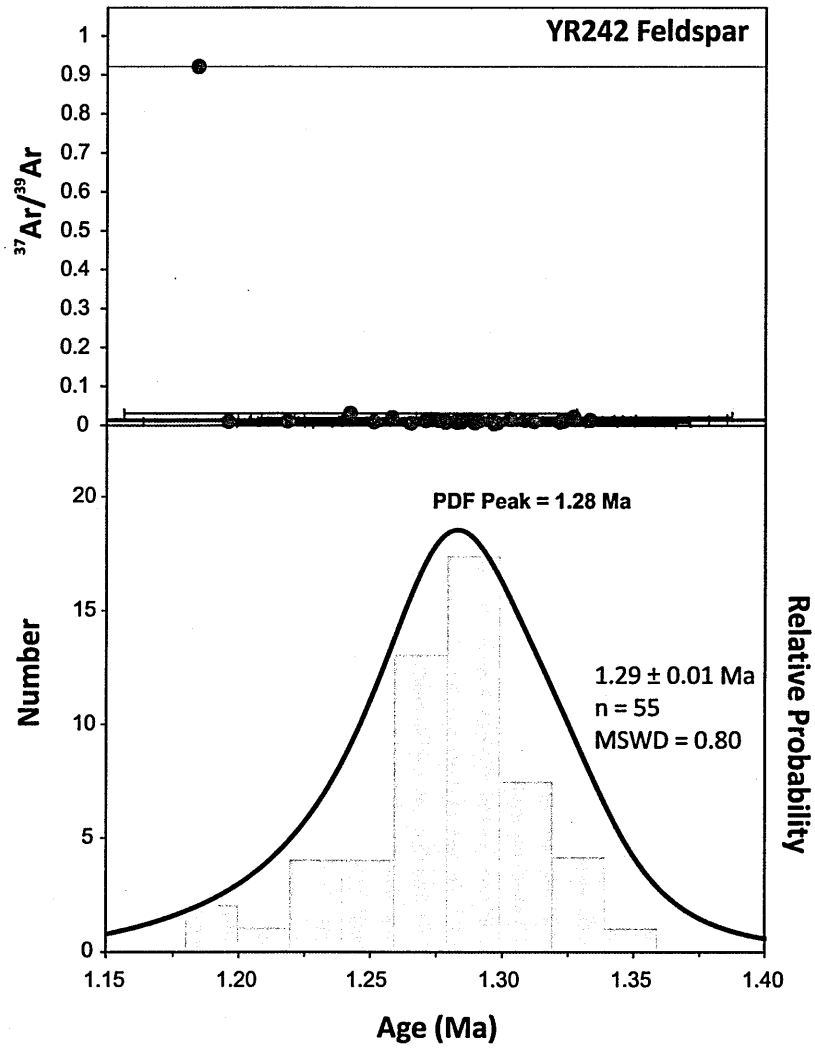

Figure 3.24. Age probability distribution diagram and age vs. $^{37}Ar/^{39}Ar$ correlation plot for Green Canyon Flow dome feldspars (HF and acetone washed; sample YR242). PDF peak (value at x at which the probability density function has its maximum value) for data set are also given and the weighted mean age (determined separately using Isoplot; Ludwig, 2011), is also shown. All errors shown are 2σ.

Table 3.6. Summary Ar-Ar age information for Sheridan Reservoir dome, Snake River Butte dome and Green Canyon Flow dome. The standard deviation (s.d.) of the arithmetic mean is given at the 95 % confidence level. Full data set, including average instrument blank measurements and calculated *J*-values used for data processing and raw data can be found in Appendix section A3.3.

Unit (sample)	Mineral phase*	$^{37}Ar/^{39}Ar$	Max. Age (Ma)	± 2σ	Min. Age (Ma)	± 2σ	Arithmetic Mean Age (Ma)	s.d.	n	Weighted Mean Age (Ma)	± 2σ
Sheridan Reservoir dome											
(YR215)	fsp#	< 1	3.34	0.40	1.63	0.26	2.24	0.57	60	**2.25**	**0.07**
(YR215 and YR217)	Glass	< 1	2.34	0.30	1.83	0.50	2.03	0.23	30	**2.04**	**0.03**
Snake River Butte											
(YR185)	fsp		2.46	0.25	1.61	0.40	2.17	0.11	51	**2.18**	**0.01**
	fsp ^		2.51	0.42	1.98	0.76	2.19	0.08	59	**2.15**	**0.01**
	fsp and fsp ^		-	-	-	-	2.18	0.19	110	**2.16**	**0.01**
	Glass	< 1	2.27	0.20	1.81	0.34	2.08	0.23	22	**2.10**	**0.08**
Green Canyon Flow											
(YR242)	fsp	< 1	1.35	0.11	1.17	0.40	1.28	0.06	55	**1.29**	**0.01**

^ = 1 to 2 mm sized grains; * fsp# = anorthoclase and sanidine, HF and acetone washed; fsp = plagioclase and sanidine, HF and acetone washed.

3.6 Discussion

The Ar-Ar data from Yellowstone presented here has highlighted varying degrees of contamination, which might be explained by (1) $^{40}Ar_E$, or (2) inherited Ar (xenocrystic contamination or radiogenic Ar produced *in situ* recording an event prior to eruption). Previous work, investigating the eruptive units of Yellowstone (e.g., Gansecki *et al.*, 1996; 1998), has highlighted the fact that both ash-fall and ignimbrite deposits can show the most severe contamination by xenocrysts, sourced from nearby volcanics, incorporated just prior to and during explosive fragmentation. Post-caldera rhyolites are not completely immune and lesser contamination has also been noted for some of the effusive Yellowstone eruptives (e.g., Christiansen, 2001). The following discussion considers the range of ages seen in explosive (e.g., HRT and MFT) and effusive (e.g., Sheridan Reservoir) eruptions

and draws comparison between the severity and type of contamination identified. Section 3.6.5 presents a summary of all new Ar-Ar ages determined in this study, and an updated stratigraphy of the Yellowstone Plateau volcanic field, specifically focussing on the units studied here.

An important attribute of this study has been to compare, where possible, new Ar-Ar data sets (using ^{40}K decay constants that remove comparison issues alluded to in older studies, e.g., Bachmann *et al.*, 2007b) with U-Pb zircon ages obtained from the same individual pumice (e.g., Sheridan Reservoir sample YR215 and HRT sample YP127). The U-Pb radioisotopic dating method applied to the mineral zircon, is a widely used geochronological tool, applied to volcanic systems (e.g., Bachmann *et al.*, 2007b; Bindeman *et al.*, 2001; Reid *et al.*, 2011). Zircon is a common accessory mineral in silicic volcanic products (e.g., tephra layers, juvenile pumices) and can be dated alongside other co-existing minerals such as feldspar (e.g., Bachmann *et al.*, 2007b; Simon and Reid, 2005). Zircon can crystallise and remain in the melt for long periods of time (> 100 ka) prior to eruption. The slow diffusion of Pb in zircon, even at magmatic temperatures (> 700 °C; Cherniak and Watson, 2001), increases the chances of crystals retaining a memory of pre-eruptive processes (such as magma mixing) whilst resident in the magma chamber (e.g., Bachmann *et al.*, 2007b; Simon *et al.*, 2008 and references therein), and provide evidence of contamination of older material by yielding xenocrystic populations (e.g., Bindeman *et al.*, 2001; Beard *et al.*, 2005).

The close comparison of single-grain fusion Ar-Ar ages and U-Pb data have allowed subtle extraneous Ar contamination to be identified and lead to a better understanding of the potential effects of magma chamber residence and crystal composition upon obtaining accurate eruption ages. This is of particular importance when the magma chamber history has not been established, especially where it is not possible to distinguish xenocrysts

and/or antecrysts (chemically or optically), from true phenocrysts causing the resulting 'eruption age' to be incorrect. $^{40}Ar_E$ incorporated into a mineral during crystallisation, introduced into the mineral lattice by subsequent diffusion or hosted within fluid and/or melt inclusions within young minerals can artificially elevate Ar-Ar apparent ages resulting in reduced accuracy (e.g., Vila, 1991; Renne *et al.*, 1997; Esser *et al.*, 1997; Layer and Gardner, 2001). Rather than extraneous Ar in the form of $^{40}Ar_E$, the range of ages might also be interpreted to represent grain to grain differences in the incorporation of an inherited Ar component. Single crystal Ar-Ar dating commonly reveals xenocrystic contamination (e.g., Deino and Potts, 1992; Spell and Harrison, 1993; Chen *et al.*, 1996; Gardner *et al.*, 2002), representing material incorporated into the magma, that did not have time to equilibrate isotopically, or material entrained and redistributed during the eruption. In addition several studies (e.g., Gansecki *et al.*, 1996; 1998), have highlighted a more subtle pattern of contamination where age distributions are defined by a tail off to older ages. This may represent the partially equilibrated age of crystallised portions of the magma chamber (e.g., magma chamber margins), which have been incorporated shortly prior to eruption.

U-Pb zircon ages from silicic eruptives range from the eruption age to ages significantly older than the eruption and have commonly been variously interpreted.

For example zircon ages have been inferred to represent magma residence time (e.g., Reid *et al.*, 1997; Reid and Coath, 2000, Vazquez and Reid, 2002), or have been interpreted as the eruption age (youngest U-Pb zircon population). Bindeman *et al.*, (2001) based on a limited number of samples, reported agreement between Ar-Ar sanidine and U-Pb zircon ages of the three ignimbrite-forming eruptions at Yellowstone (HRT, MFT and LCT), suggesting zircon crystallisation did not significantly predate the eruption. A similar observation was made in a later study (Bindeman *et al.*, 2007) where zircons yielded crystallisation ages that were comparable to Ar-Ar eruption ages. Simon *et al.*, (2008)

suggest bias correcting U-Pb zircon ages if they are to be interpreted as an eruption age, to take into account for residence time in the magma chamber, however the bias correction method does not account for the recycling of antecrystic material (not representing storage in a single long standing magma chamber), which is clearly a probable process that must be considered (e.g., Charlier *et al.*, 2005).

3.6.1 Huckleberry Ridge Tuff (HRT)

Single grain fusion data obtained in this study supports the conclusions of previous geochronological (e.g., Gansecki *et al.*, 1998; Lanphere *et al.*, 2002), and fieldwork (e.g., Christiansen, 2001; C. Wilson, *pers. com.*, 2010; 2011) studies, which have demonstrated that the three members of the HRT erupted in quick succession, with only minor intervening time breaks. Weighted mean ages of each individual member are in agreement with each other at the 2σ level. Member A yielded a weighted mean age of 2.11 ± 0.02 Ma (n = 38; MSWD = 0.96), which is indistinguishable from the weighted mean ages of both member B (2.12 ± 0.04 Ma; n = 42; MSWD = 0.8), and member C (2.11 ± 0.02 Ma; n = 29; MSWD = 0.99). Taking into consideration the Ar-Ar data only, a preferred sanidine eruption age for the HRT (members A, B and C) is 2.11 ± 0.01 Ma, with no evidence to support the significant time break between the eruption of members B and C inferred by Ellis *et al.*, (2012).

3.6.1.1 Determining an eruption age

Previous work has shown that contamination of tephra horizons and whole rock ignimbrite deposits (e.g., Gansecki *et al.*, 1996; 1998; Semaw *et al.*, 1997), and of juvenile material (e.g., pumice; van den Bogaard *et al.*, 1989; 1995; Wilson and Hildreth, 1997; 1998), can be significant due to the explosive nature of the eruption incorporating random lithic

material from earlier eruptions. Determination of the trapped Ar component (inverse isochron method), for each HRT member has not provided evidence to support excess Ar contamination, although the Ar-Ar ratio and uncertainty for YP127 (member A) were both higher than the atmospheric value (544 ± 280 and 348 ± 140 respectively). Sample YP079 (member B) yielded initial $^{40}Ar/^{36}Ar$ ratios within error of 298.56 (307 ± 31 and 272 ± 42 respectively). Sample YP081 yielded one isochron with an initial $^{40}Ar/^{36}Ar$ ratio within error of 298.56 (371 ± 82). The lack of $^{40}Ar_E$ is in accordance with the results of recent studies (e.g., Ellis *et al.*, 2012).

The weighted mean ages for members A and C are identical (at the 2σ level), and single grain fusion ages, when plotted on a probability plot have a Gaussian distribution. It appears the unusual shape of the probability distribution plot ('wide skirt', Fig. 3.12), for sample YP079 is a result of plagioclase feldspar analyses. Analysed crystals of member A and C lack significantly calcic feldspars ($^{37}Ar/^{39}Ar$ ratio < 1), therefore this pattern is unique to the analysed sample of member B. The narrow peak corresponds mostly to sanidine in this sample (analyses with $^{37}Ar/^{39}Ar < 1$); however the wide skirt includes a spread in ages ranging from ~ 1.3 to ~ 3 Ma, which mostly correspond to poorer precision plagioclase feldspar data (analyses with $^{37}Ar/^{39}Ar > 1$).

Is this range of ages recorded by the plagioclase feldspars significant? It is possible that the older ages represent grains which have been contaminated by $^{40}Ar_E$ and/or contain variable amounts of inherited Ar. The presence of significantly younger ages could represent a picked aliquot containing a mixture of disturbed grains (e.g., experienced Ar loss) that have undergone alteration, and undisturbed phenocrysts. Unfortunately, reduced precision (large uncertainties) associated with the K poor nature of plagioclase feldspar (~ 1.5 wt. % K_2O), and therefore containing less measureable radiogenic Ar compared to sanidine (~ 10

wt. % K_2O), renders all ages within 2σ uncertainty of each other. It is therefore not possible to assess the true significance of the spread in ages.

The sample of HRT member B (YP079) contained one anomalously older grain, which yielded an age of 5.09 ± 1.39 Ma. This probably represents a plagioclase xenocryst of a slightly different composition, as it also yielded the highest $^{37}Ar/^{39}Ar$ ratio (2.29 ± 0.11) compared with other plagioclase in this sample which record ages closer to that of the eruption (e.g., $^{37}Ar/^{39}Ar$ ratio of < 1.5). Outliers were identified in each sample analysed by Ellis *et al.*, (2012) and subsequently rejected as xenocrysts. Gansecki *et al.*, (1996; 1998) also noted the severe contamination of pumice and vitrophyre samples separated from Yellowstone Group tuffs by xenocrysts incorporated into the magma during fracturing and conduit propagation, as well as explosive fragmentation upon eruption. EMP analysis of sample YP079 has revealed no obvious xenocrystic compositions, nor do plagioclase phenocryst compositions exhibit a particularly wide range (An_{20} to An_{30}). However an age of ~ 5 Ma is significantly older than the eruption age and so analysis of a single rogue xenocryst is the most likely explanation in this case.

3.6.1.2 Evidence for a significant time break?

U-Pb SIMS age determinations on zircons, carried out in a parallel study (Wilson and Charlier., on-going), but including samples YP127, YP079 and YP081, as well as additional juvenile material (e.g., rhyodacite and granophyre blebs in HRT A), support a single unitary population with a weighted mean age of ~ 2.12 Ma (n = 248; MSWD = 2.7). The weighted mean age of over 200 individual SIMS spot analyses is identical to the weighted mean Ar-Ar age for each of the HRT members obtained in this study, suggesting the zircons grew in the magma chamber over a short period of time up to the point of eruption. The combined Ar-Ar results of this study and extensive U-Pb zircon study of

Wilson and Charlier, strongly suggest the HRT units are the same age and therefore the new data presented here do not support the recent '2-eruption' model of Ellis *et al.*, (2012).

Our preferred weighted mean Ar-Ar ages of HRT A, B and C are in agreement with one another at the 2σ level and are also in agreement with the weighted mean U-Pb zircon age (2.12 Ma), which also supports the classic single eruption model. Field evidence (C. Wilson; *pers. com.*, 2010; 2011) suggests time breaks did exist between HRT members, and it is likely that member A and B were separated by weeks to months and members B and C separated by years to decades. However, to date there has been no conclusive field evidence to support the existence of a significant erosional break (Christiansen, 2001; Lanphere *et al.*, 2002; C. Wilson, *pers. com.*, 2010; 2011). Therefore, the new age data (Ar-Ar and U-Pb) presented here supports observations made in the field, which suggests an eruption that was intermittent and prolonged, and likely to present units separated by minor time breaks, for example long enough to allow normal grading of plume material to occur (C. Wilson, *pers. com.* 2010; 2011), but which are all within error of a single age. In addition, the paleomagnetic data of Reynolds (1977) showed that a similar subhorizontal southwesterly direction of remnant magnetisation had been preserved by all three members of the HRT, and member C was shown to have mean measurements similar to both A and B. Therefore, the mean remnence direction for each unit is identical. This critical point, seemingly over looked by Ellis *et al.*, (2012), again supports the classic single eruption model.

3.6.2 Snake River Butte dome and Sheridan Reservoir dome

New single-grain Ar-Ar age data presented here for both Sheridan Reservoir and Snake River Butte domes tend to show a range of ages and a distribution characterised by a tail of slightly older ages. The previously determined K-Ar age (~ 1.99 Ma; Obradovich, 1992

cited in Christiansen, 2001), for Snake River Butte dome is younger than expected and could have resulted from incomplete extraction of Ar from sanidine during K-Ar analysis, or analysis of whole rock samples which had undergone alteration of K-bearing phases (known to be a problem for this technique; McDougall and Harrison, 1999). Sheridan Reservoir dome data shows the most significant spread in Ar-Ar ages, and a previously determined K-Ar age (~ 4 Ma; cited in Morgan *et al.*, 1984) is significantly older than expected. Reasons for older K-Ar include the analysis of xenocrystic/antecrystic and/or $^{40}Ar_E$ contaminated material during multi-aliquot measurements and/or analysis of material which has experienced significant K loss (McDougall and Harrison, 1999).

3.6.2.1 Excess Ar ($^{40}Ar_E$)

Inclusion hosted $^{40}Ar_E$

Feldspar crystals separated from each dome contained variable amounts of black-brown glassy inclusions. This observation was most significant in the case of Sheridan Reservoir dome (sample YR215), which also yielded the largest spread in Ar-Ar single-grain fusion ages, and is therefore discussed in more detail below. Melt inclusions, resulting from melt entrapment due to rapid growth of crystals, become isolated following entrapment and can therefore represent non-degassed, or partially degassed magma (Esser *et al.*, 1997). van den Bogaard and Schirnick (1995) showed that diffusional loss of Ar from Bishop Tuff quartz-hosted melt inclusions was negligible and believed that melt inclusions contained Ar trapped over a million years prior to the Bishop Tuff eruption.

Macro-inclusions (visible under a binocular microscope), and micro-inclusions (Fig. 3.25) of trapped melt exhibiting a glassy appearance (pale brown to almost black) are prevalent in the feldspar crystals separated from sample YR215. The majority of inclusions appear to be euhedral, ranging from vermicular and elongated to well-rounded in shape. Some

crystals show multiple stages of entrapment and display inclusions within inclusions, whilst others show a concentration of inclusions at their rim. Single crystals contain varying amounts of inclusions, ranging from < 10 % to ~ 40 %. The spread in single crystal Ar-Ar ages obtained for sample YR215 may represent contamination by $^{40}Ar_E$ hosted within melt inclusions. Melt inclusions in equilibrium with a magma which contains $^{40}Ar_E$ may host 100 to 1000 times more Ar than the mineral lattice (Kelley *et al.*, 2002). For young and/or low-K feldspars, such as anorthoclase, the dominant feldspar phase in sample YR215, this could be significant because there is insufficient radiogenic product to mask the effect of contamination.

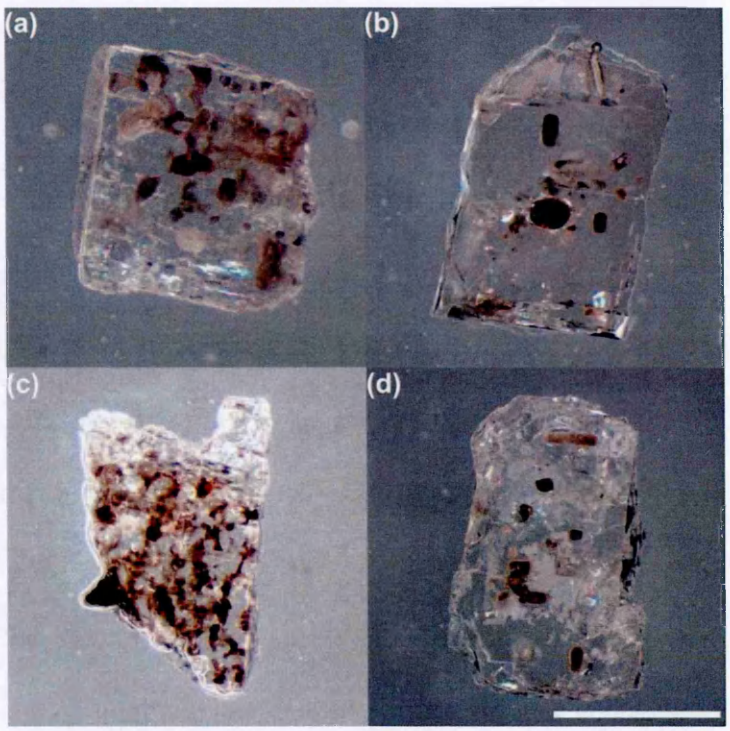

Figure 3.25. Representative photomicrographs showing examples of melt inclusions in Sheridan Reservoir dome feldspars (single crystals mounted in resin blocks). Melt inclusion shapes range from vermicular and elongated (a) to rounded (b). Some feldspar crystals contain an interconnected network, some connected to the grain edge (c), whilst some contain gas bubbles and inclusions within inclusions (d). (Scale bar length, bottom right picture = 500 µm).

The impact of $^{40}Ar_E$ hosted melt inclusions in volcanic systems, in particular anorthoclase feldspar, is well documented. Esser *et al.*, (1997) demonstrated that during sample heating, mixing of $^{40}Ar_E$ (melt inclusions) and lattice hosted $^{40}Ar^*$ resulted in the multiple sources becoming homogenised and elevating apparent ages. In order to assess a possible link between inclusion-rich feldspars and older Sheridan Reservoir dome Ar-Ar ages, a second set of single feldspar grains were photographed prior to analysis to allow assessment of any relationship between inclusion density and Ar-Ar age. Figure 3.26 shows each feldspar crystal prior to analysis and the resulting Ar-Ar apparent age. Based on 10 to 40 % melt inclusion contamination versus age variation, there appears to be no correlation between increasing apparent age and inclusion content.

Figure 3.26. Photograph of each Sheridan Reservoir dome feldspar crystal analysed by Ar-Ar single-grain fusion. Analysis number given in the bottom left corner and Ar-Ar apparent age (Ma ± 2σ) is given in the top right corner. Crystal size varies 500 µm to 1 mm in size.

Fluid inclusions are harder to detect (with the naked eye/under a petrological microscope) than melt inclusions and the relatively higher solubility of Ar in hydrous fluids means they can be a significant source of $^{40}Ar_E$ (Kelley, 2002). *In vacuo* crushing (quartz; e.g., Rama and Hart, 1965; Kelley *et al.*, 1986), and incremental heating experiments (K-feldspar; e.g., Harrison *et al.*, 1994) highlighted apparent age (and the release of $^{40}Ar_E$ from fluid inclusions) correlated with measured Cl/K ratio. During sample irradiation, reactions on chlorine isotopes (^{35}Cl and ^{37}Cl yield ^{36}Cl and ^{38}Cl respectively), with subsequent β^- decay, produce ^{36}Ar and ^{38}Ar isotopes respectively. The rapid decay of ^{38}Cl to ^{38}Ar ($t_{1/2}$ = 37.3 minutes) by the time of sample analysis, means the measurement of ^{38}Ar from chlorine ($^{38}Ar_{Cl}$) can therefore be used to determine the presence of chlorine in the sample.

The release of $^{40}Ar_E$ from fluid inclusions has previously been correlated with measured Cl/K ratio, and Esser *et al.*, (1997) noted similarities in high- and low- temperature degassing behaviour of $^{38}Ar_{Cl}$ and $^{40}Ar_E$, the source most likely being the melt inclusions rather than the anorthoclase crystal lattice, which contains no measurable chlorine. Based on the Sheridan Reservoir dome data set (Fig. 3.27), no correlation could be identified between apparent age and $^{38}Ar/^{39}Ar$ (a proxy for Cl/K) ratio, suggesting $^{40}Ar_E$ hosted in fluid or melt inclusions is not responsible for the range of ages seen. During sample fusion, crystals are heated to over 1000 °C, so it is unlikely that chlorine hosted within fluid/melt inclusions would not have been liberated, especially as the decrepitation of fluid inclusions is achievable at temperatures (< 800 °C; Harrison *et al.*, 1994) lower than those needed to decrepitate melt inclusions.

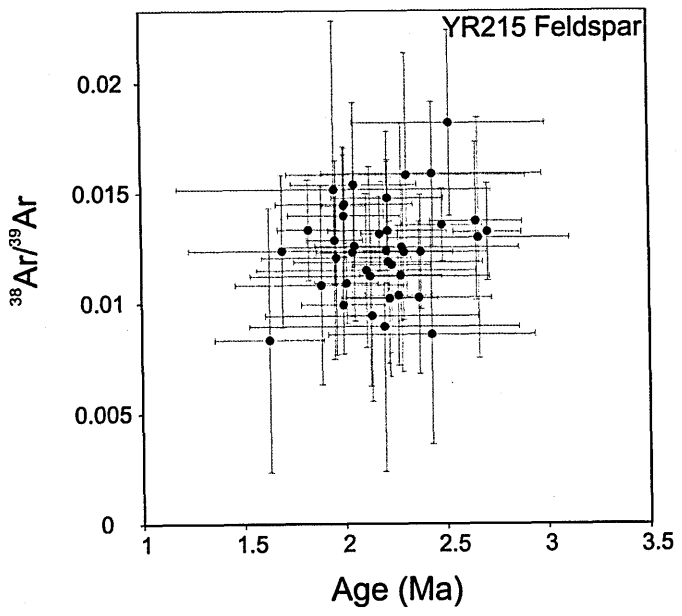

Figure 3.27. Age vs. $^{38}Ar/^{39}Ar$ correlation plot for Sheridan Reservoir dome feldspars (samples YR215), showing no correlation between $^{38}Ar/^{39}Ar$ and Ar-Ar apparent age.

$^{40}Ar_E$ in adhering glass

Previous work (e.g., Morgan and McIntosh, 2005) suggests anomalous Ar-Ar ages may be due to incompletely outgassed adhering matrix groundmass or glass and/or minor surface alteration and its removal is common practice (e.g., Spell and Harrison, 1993; Gansecki *et al.*, 1996; Esser *et al.*, 1997; Bachmann *et al.*, 2007; Cassata *et al.*, 2009; McDougall *et al.*, 2012). Trapped Ar of an atmospheric composition is noted for separated feldspars (500 μm to 1 mm) from Snake River Butte dome (statistically valid inverse isochron (MSWD = < 2), with initial $^{40}Ar/^{36}Ar$ ratio within 2σ error of atmospheric value 298.56). Feldspars separated from Sheridan Reservoir dome produced an inverse isochron, with a large initial $^{40}Ar/^{36}Ar$ value, associated uncertainty and MSWD (= 4). Although the inverse isochron suggests no $^{40}Ar_E$ contamination (initial $^{40}Ar/^{36}Ar$ ratio within error of atmospheric value), it may represent a mixture of crystals containing ^{40}Ar of atmospheric composition (tie the mixing line to Y-axis), and some containing $^{40}Ar_E$ hosted within the feldspar structure or in adhering glass.

To test the possible significance of $^{40}Ar_E$ trapped in adhering glass (in particular samples YR215 and YR185), and the potential impact acid etching may have on the Ar-Ar single-grain fusion ages, a second aliquot of feldspar crystals were cleaned in a weak (10 %) cold solution of HF prior to irradiation. One potential problem for Ar-Ar dating of acid etched grains is that in addition to removing adhering glass, acid etching may also cause an atmospheric component to become absorbed to crystal surfaces during the procedure. However, age verses $^{36}Ar/^{40}Ar$ isotope ratio plots (Fig. 3.28), show that there is no difference between feldspar batches (HF and acetone washed) and therefore no evidence to suggest atmospheric Ar (^{36}Ar) has been absorbed to the crystal surface during the procedure.

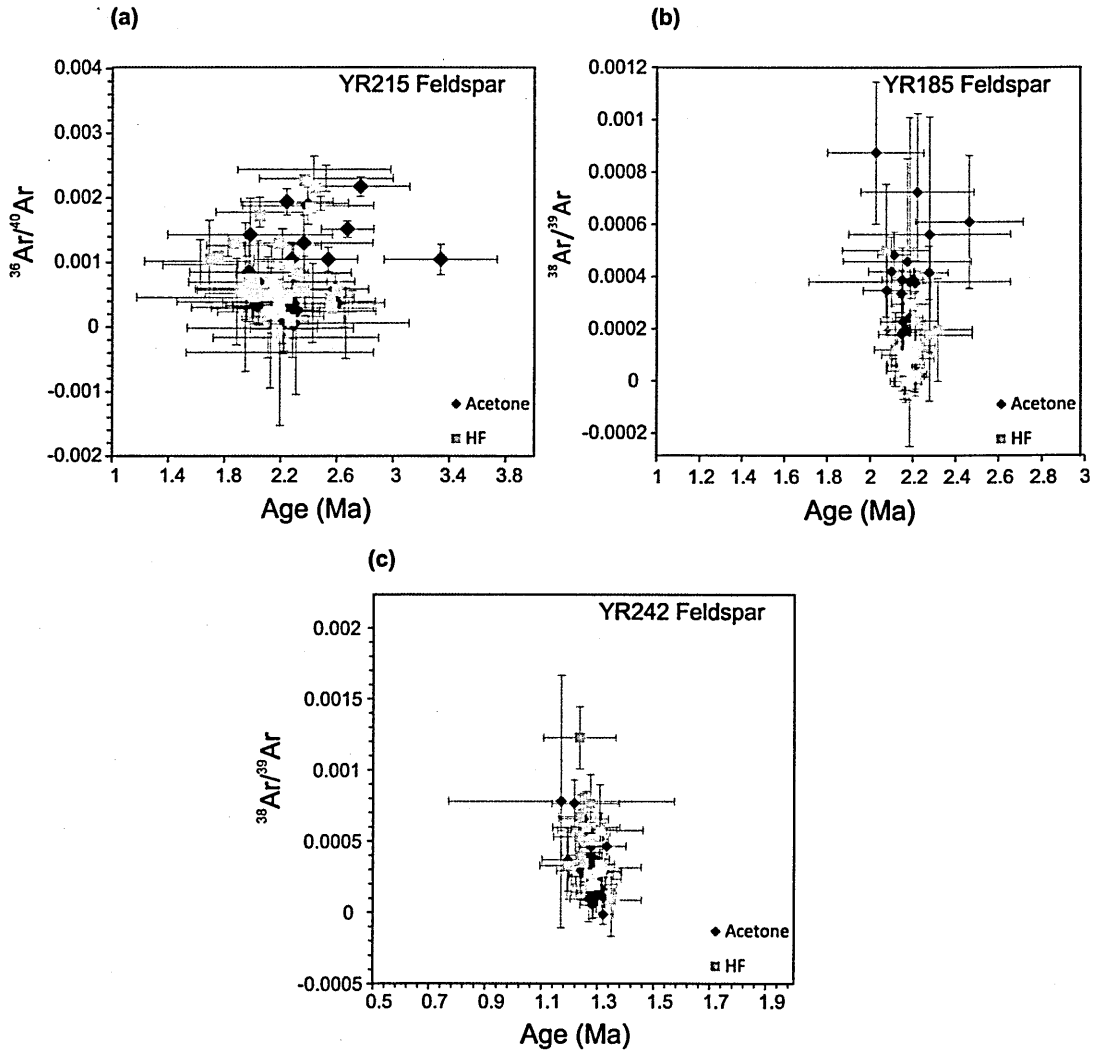

Figure 3.28. Age vs. $^{36}Ar/^{40}Ar$ correlation plots for rhyolite dome eruptions Sheridan Reservoir dome (samples YR215), Snake River Butte dome (sample YR185), and Green Canyon Flow dome (sample YR242), showing HF wash had very little to no effect on measured $^{36}Ar/^{40}Ar$ ratios.

The results of the Ar-Ar single-grain fusion experiments on acid etched feldspars of sample YR215 (Sheridan Reservoir dome), did yield a slight improvement in the overall scatter of ages (e.g., 1.63 to 2.71 Ma compared to 1.97 to 3.33 Ma). The cleaning procedure had little to no effect on sample YR185 (Snake River Butte dome), and there was no significant change to the range of ages achieved. Despite this slightly reduced scatter for sample YR215, a range of ages still exists; suggesting adhering glass is not a source of $^{40}Ar_E$ contamination in this case.

3.6.2.2 Inherited Ar

The spread in single crystal Ar-Ar ages (in particular sample YR215), and the tail off to older than expected ages may represent grain to grain differences in the incorporation of an inherited Ar component due to xenocrystic contamination (e.g., Deino and Potts, 1992; Gansecki *et al.*, 1996; Chen *et al.*, 1996; Renne *et al.*, 2012) and may explain why a previous age determination for Sheridan Reservoir dome (cited in Morgan *et al.*, 1984) yielded an older K-Ar age. Dating individual crystals by total laser fusion is useful in identifying xenocrysts and therefore allowing the accurate determination of an eruption age as defined by a juvenile population (e.g., Spell *et al.*, 2001). However, there is no obvious clustering of ages which could implicate a direct source of contamination, and Ar-Ar apparent ages (and U-Pb zircon age data) obtained for Sheridan Reservoir dome do not represent a simple bi-modal age distribution (e.g., Semaw *et al.*, 1997).

U-Pb zircon ages: evidence to support inheritance

The spread in U-Pb zircon ages for Snake River Butte dome (~ 1.92 to ~ 2.4 Ma; n = 41; Fig. 3.29a), and Sheridan Reservoir dome (~ 1.81 to ~ 2.83 Ma; n = 89; Fig. 3.29b), potentially suggests a signal of inheritance is being detected. The subtle spread in ages may

represent an extended period of zircon crystallisation (e.g., Reid *et al.*, 1997; Simon *et al.*, 2008), or incorporation of slightly older cogenetic material, rather than true xenocrystic contamination due to the absence of a bimodal age distribution. The similarity seen in the spread of individual U-Pb and Ar-Ar ages is most pronounced for Sheridan Reservoir dome (YR215). Four older U-Pb zircon ages (range 2.4 to ~3 Ma) could suggest an upper limit for this contamination and both the Ar-Ar age determinations and the U-Pb ages appear to reflect a trail of inheritance that goes back ~ 3 Ma (Fig. 3.29b). Previous work (e.g., Bindeman *et al.*, 2007) carried out on volcanic centres along the Snake River Plain suggests that a cyclic occurrence of high $\delta^{18}O$ magmas followed by low $\delta^{18}O$ magmas is due to progressive re-melting of hydrothermally altered intracaldera rocks of previous eruptions. Bindeman *et al.* (2007) also reported a U-Pb zircon age of 2.07 ± 0.19 Ma for Sheridan Reservoir dome, with individual zircon ages ranging ~ 1.63 to ~ 3.09 Ma. Despite their limited sample set (n = 14), their data also appears to support a signal of inheritance (extending back to ~ 3 Ma).

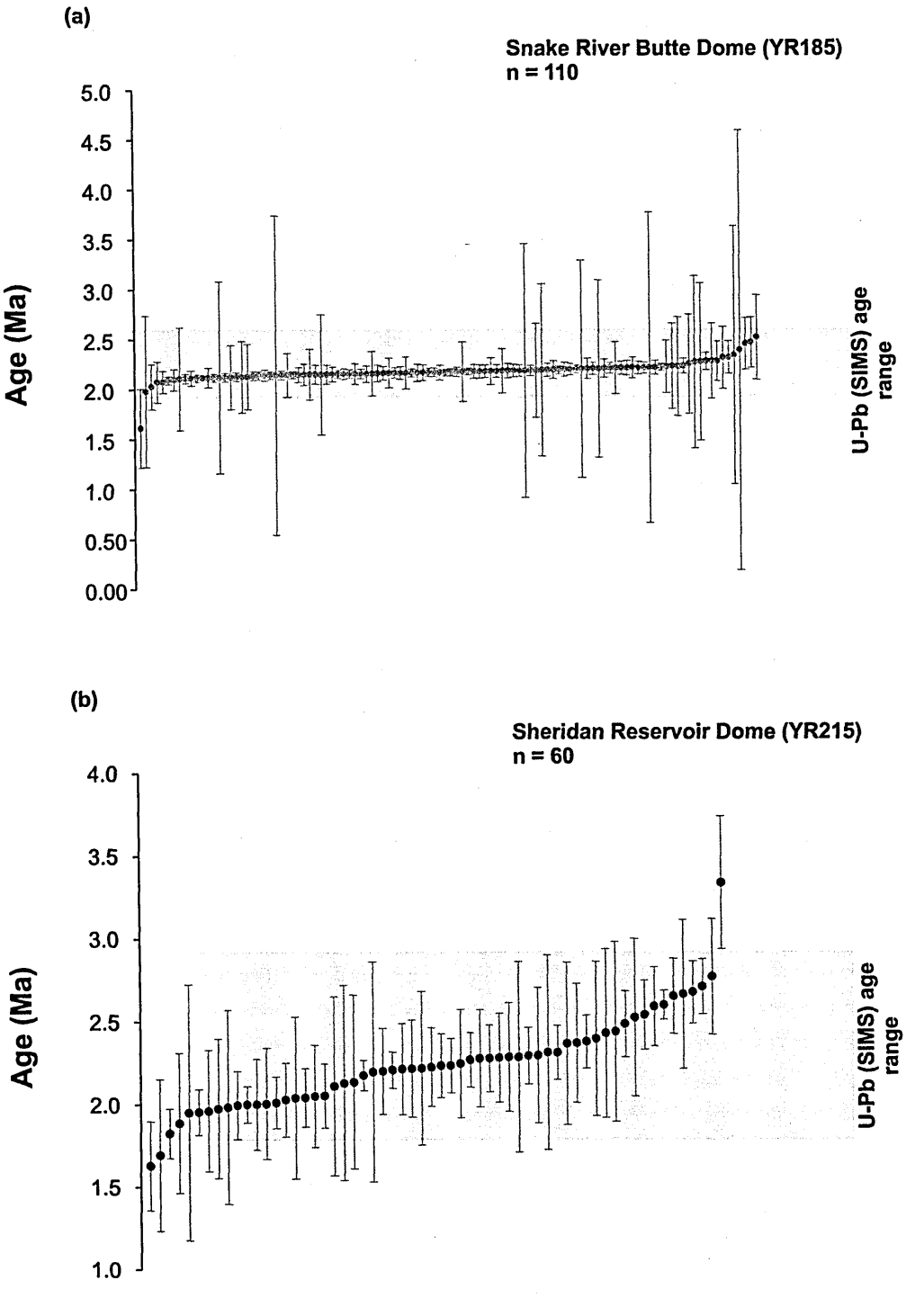

Figure 3.29. Summary diagram showing the spread in single Ar-Ar feldspar ages (± 2σ), compared with the range of *in situ* U-Pb ages obtained from zircon separated from the same sample for (a) Snake River Butte dome (sample YR185), and (b) Sheridan Reservoir dome (sample YR215).

The assimilation of hydrothermally altered and subvolcanic rocks by bulk melting (e.g., Bindeman and Valley, 2001) or reactive assimilation (Beard *et al.*, 2005) could explain the contamination and the range of apparent Sheridan Reservoir dome feldspar ages. van den

Bogaard *et al.*, (1987) identified contaminating material in tephra deposits of the Eifel volcanic field, which may have been sourced from previous volcanic units in the area during magma ascent and eruption. However the U-Pb and Ar-Ar data in this study, and indeed the U-Pb ages of Bindeman *et al.*, (2007) do not yield Heise ages (> 4 Ma), which one might expect if recycling of material from previous eruptions is not only a key process, but one that is repeated several times.

Self-contamination: source of inherited Ar

Another explanation for the spread in both U-Pb and Ar-Ar data of Sheridan Reservoir dome, revealing ages significantly older than the eruption, could be the cannibalisation of previously crystallised material (i.e., antecrysts) prior to eruption (e.g., Deino and Potts, 1992; Gansecki *et al.*, 1998; Chen *et al.*, 1996), rather than partially resorbed xenocrysts (e.g., Renne *et al.*, 2012). Gansecki *et al.*, (1998) defined a small range in sanidine compositions and noted the absence of obvious xenocrystic material (which could have derived from underlying Tertiary mafic volcanic rocks or Precambrian basement). Voluminous silicic magma chambers (such as Yellowstone; the Fish Canyon magmatic system and the Long Valley magmatic system) may be more susceptible to the process of 'self-cannibalisation' and contamination by antecrysts, because they undergo periods of gradual cooling and crystallisation, interspersed with periods of rejuvenation by influx of hotter, more mafic material (e.g., Bachmann *et al.*, 2002) and volatiles (hot gas percolation or 'gas sparging'; e.g., Bachmann and Bergantz, 2003), which may even trigger an eruption (e.g., Bachmann *et al.*, 2007b).

It is possible that previously crystallised dome magma chamber roof or side wall material, entrained prior to the eruption, could result in the range of Ar-Ar ages yielded by crystals which are indistinguishable visually or chemically from phenocrysts. Resorption of large

feldspar crystals is evident from analysis of thin sections (Fig. 3.30). Some grains exhibit a sieve texture, while others show resorbed margins. Similar observations have been made for feldspar and quartz of the Fish Canyon magma body (e.g., Bachmann *et al.*, 2002; 2007; Charlier *et al.*, 2007), whereby crystals underwent an extended crystallisation period spanning an age interval of at least ~ 0.3 Ma. Sheridan Reservoir dome data in particular showed that older single-grain Ar-Ar ages correlate with analyses that yielded a larger $^{37}Ar/^{39}Ar$ ratio (> 0.2) and therefore a lower K content. However, the correlation is not as marked as seen in previous studies (e.g., Gansecki *et al*, 1996) where the majority of xenocrystic grains were plagioclase (> An_{30}) in composition.

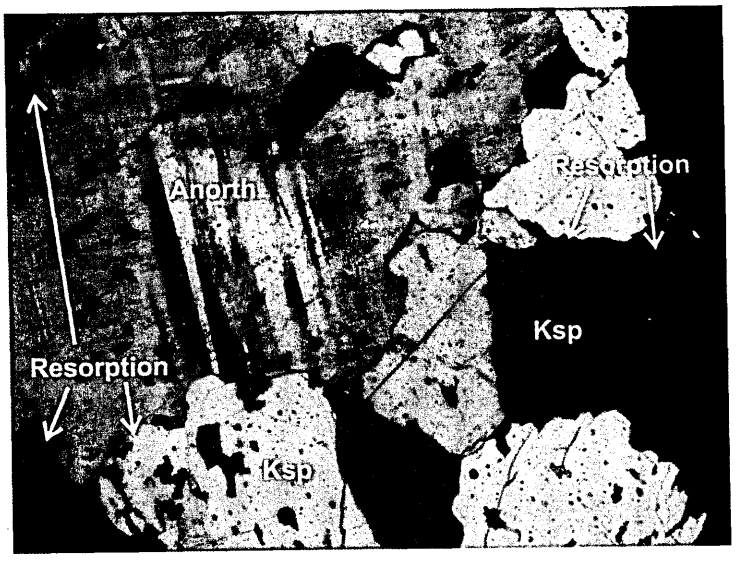

Figure 3.30. Thin section photomicrograph of Sheridan Reservoir sample YR215 showing evidence of resorption at grain edges (Anorth = anorthoclase; Ksp = sanidine). Scale = image width; 2.5 mm).

3.6.2.3 Partial re-setting of feldspars: modelling Ar loss

When xenocrysts, antecrysts (specifically in the case of Sheridan Reservoir dome), and $^{40}Ar_E$ contaminated grains, are incorporated into a magma at magmatic temperatures (i.e., above a minerals closure temperature) they should diffusively lose radiogenic Ar.

Diffusive loss of Ar occurs at high temperatures, where Ar is mobile and is free to equilibrate between melt, mineral and vapour phases present. Therefore, if the temperature is high there is likely to be total Ar loss and little Ar accumulation (assuming Ar is removed and lost to an 'infinite reservoir'). As the temperature decreases, diffusion slows until there is little ^{40}Ar loss and essentially all ^{40}Ar is retained (Dodson, 1973).

The most significant range of ages is seen in the Ar-Ar single-grain fusion measurements made on separated Sheridan Reservoir feldspars (sample YR215). I will use known parameters to model the diffusive loss of Ar from crystals to investigate the extent to which contaminating grains might have degassed in the magma prior to eruption. Diffusive loss of Ar has been modelled for both sanidine and plagioclase to provide an upper and lower limit on magma residence time of Sheridan Reservoir feldspars. In order to model diffusive loss it is necessary to define the parameters that DIFFARG will use (see Appendix section A1.10 for instructions on running the DIFFARG programme). For simplicity, DIFFARG has been run assuming:

1. Bulk diffusion
2. Spherical geometry of grain (grain radius 0.5 mm)
3. Ar concentration in the grain boundary (surrounding melt) is zero, so that Ar diffusing from the grain into grain boundary is lost to the 'infinite reservoir'
4. Diffusion radius is equal to the grain radius
5. Diffusion coefficient (D_0) – experimentally derived
6. Activation energy (Ea) – experimentally derived

For this study, experimentally derived parameters for K-feldspar have been taken from the study carried out by Foland (1974) where $D_0 = 0.982$ mm^2/sec; $E_a = 43.8 \pm 1.0$ kcal/mol). Previous studies (e.g., Gansecki *et al.*, 1996; Singer *et al.*, 1998; Layer and Gardner, 2001;

Gardner *et al.*, 2002) have modelled diffusive loss from K-feldspar also using these parameters. Diffusion parameters for plagioclase used in this study are D_0 = 112000 mm^2/sec and E_a = 26.72 kcal/mol (Wartho *et al.*, 2012). These parameters differ from those published by Cassata *et al.*, (2009), where both experimentally derived D_0 and E_a changed with grain size. To date there are currently no experimentally derived diffusion parameters for anorthoclase ((Na, K) $AlSi_3O_8$; dominant phase of the Sheridan Reservoir feldspars). Using plagioclase parameters to simulate the diffusive behaviour of anorthoclase is justified in this case as both anorthoclase and plagioclase have the same crystal structure (triclinic).

It is assumed that the diffusion radius is equal to the grain radius. Feldspar crystals used in this study were separated by hand from a 500 μm to 1 mm sieve fraction, and therefore models have been run assuming a diffusion radius of 0.5 mm to represent the size of crystals analysed. The models are run assuming Ar concentration at the grain boundaries is zero, which means when Ar reaches the edge of the grain is lost to an 'infinite reservoir', and there is no partitioning of Ar back into the grain. Models have been run at 700 °C, 750 °C and 800 °C in order to reflect the likely range of magmatic temperatures (not exceeding zircon dissolution temperature of > 800 °C; e.g., Beard *et al.*, 2005). Previous studies have used a range of different temperatures to model diffusive loss of Ar from minerals at silicic magmatic temperatures. Spell and Harrison (1993), assumed a temperature of 750 °C for rhyolitic magma prior to and during the eruption as well as 500 °C for pyroclastic flows following emplacement. Gardner *et al.*, (2002) modelled diffusive loss from feldspar, biotite and hornblende at Toba Tuff magma temperatures ranging 720 to 780 °C. Gansecki *et al.*, (1996) assumed a temperature of 900°C (based in Fe-Ti oxide temperatures), and Singer *et al.*, (1998) used 1000°C (minimum for andesite).

The following results (Table 3.7 and Table 3.8), represent the modelled ages which may occur if feldspar crystals containing an inherited Ar signal (i.e., antecrysts contributed from already crystallised magma chamber material) are reincorporated into the magma, and held at different temperatures for varying amounts of time before being erupted at 2 Ma (estimate of eruption age of Sheridan Reservoir dome, based on weighted mean age and inverse isochron age for glassy groundmass). Additional ages have been calculated using an expression that calculates the fractional loss of Ar from a sphere (see Appendix section A1.10.4 for explanation and equation).

Table 3.7. Summary model Ar-Ar apparent ages using DIFFARG parameters outlined in the text. Ar-Ar age (Ma) represents (a) 1 Ma plagioclase and (b) 1.5 Ma plagioclase, entrained into magma of varying temperatures (700 °C, 750 °C and 800 °C) for varying times prior to eruption (1 to 10,000 years).

(a)

Temperature of magma (°C):	700	750	800
Time in magma (years)		**Age (Ma)**	
1*	2.998	2.997	2.995
5*	2.997	2.995	2.991
10*	2.988	2.977	2.959
100	2.892	2.799	2.661
150	2.843	2.714	2.537
250	2.752	2.571	2.355
500	2.566	2.326	2.126
1000*	2.320	2.106	2.016
5000*	2.003	2.000	2.000
10000*	2.000	2.000	2.000

(b)

Temperature of magma (°C):	700	750	800
Time in magma (years)		**Age (Ma)**	
1*	3.498	3.496	3.493
5*	3.496	3.493	3.469
10*	3.483	3.466	3.439
100	3.338	3.199	2.992
150	3.264	3.072	2.806
250	3.128	2.857	2.533
500	2.849	2.489	2.189
1000*	2.480	2.159	2.024
5000*	2.005	2.000	2.000
10000*	2.000	2.000	2.000

Table 3.8. Summary model Ar-Ar apparent ages using DIFFARG parameters outlined in the text. Ar-Ar age (Ma) represents (a) 1 Ma sanidine and (b) 1.5 Ma sanidine, entrained into magma of varying temperatures (700 °C, 750 °C and 800 °C) for varying times prior to eruption (0.001 to 1000 years).

(a)

Temperature of magma (°C)	700	750	800
Time in magma (years)		**Age (Ma)**	
0.001*	2.999	2.999	2.998
0.1*	2.984	2.953	2.878
1	2.855	2.622	2.272
5	2.457	2.093	2.001
10	2.209	2.008	2.000
50	2.000	2.000	2.000
100*	2.000	2.000	2.000
1000*	2.000	2.000	2.000

(b)

Temperature of magma (°C)	700	750	800
Time in magma (years)		**Age (Ma)**	
0.001*	3.499	3.499	3.498
0.1*	3.476	3.430	3.317
1	3.283	2.933	2.408
5	2.686	2.139	2.002
10	2.314	2.013	2.000
50	2.000	2.000	2.000
100*	2.000	2.000	2.000
1000*	2.000	2.000	2.000

*** = Apparent ages calculated using fractional loss equation (see Appendix section A1.10.4)**

Diffusion calculations indicate that it would take 10 to 50 years; at temperatures of 750 to 800 °C, 1 to 1.5 Ma sanidine antecrysts to be fully reset and yield an eruption age (Table 3.8). Therefore antecrystic sanidine entrained into the magma would be indistinguishable from phenocrysts after ~ 50 years (Fig. 3.31). In contrast, calculations for plagioclase antecrysts (1 to 1.5 Ma) suggest it would take > 1000 years to completely reset and yield an eruption age (Fig. 3.32). Incorporation of antecrysts up to ~ 1.5 Ma (of varying compositions) will yield the range of ages seen (~ 2 Ma up to ~ 3 Ma) simply by retaining varying amounts of inherited Ar. Thus, on the basis of the modelling, we must conclude that there may be a significant compositional control on measured Ar-Ar ages. The age data obtained from sample YR215 suggests low Ca, high K-feldspars (sanidine) yield ages

in agreement with the best estimate for the eruption age (glass Ar-Ar age; ~ 2 Ma) and that the relatively lower K feldspars (i.e., anorthoclase and plagioclase) can yield ages older than the eruption age.

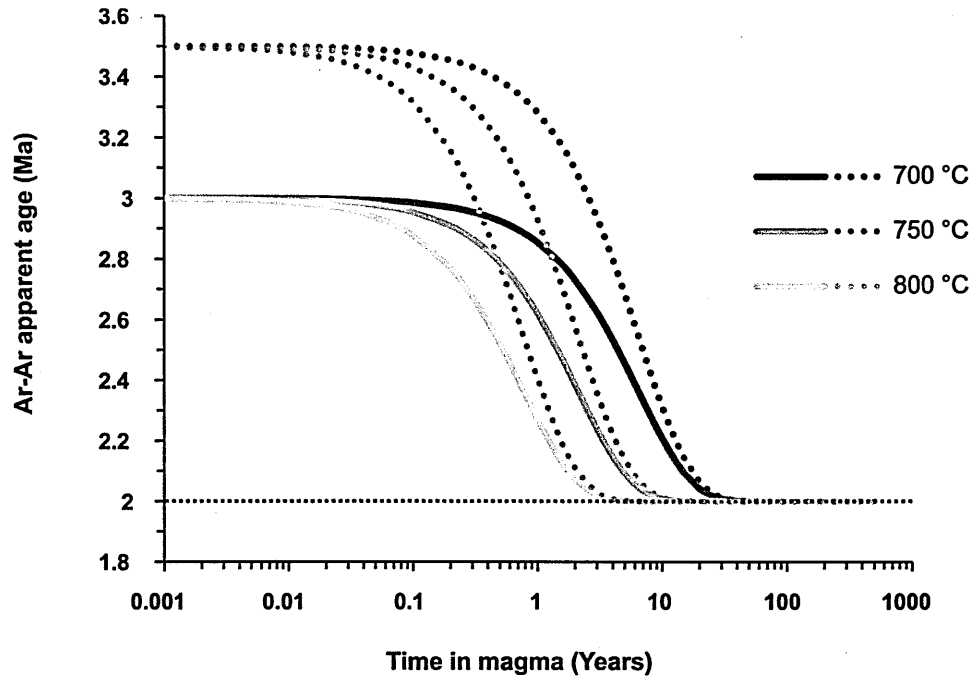

Figure 3.31. Diffusion model shows diffusive loss from 1 Ma sanidine (solid lines) and 1.5 Ma sanidine (dashed lines), for time in magma (in years; log scale to base 10) versus resultant apparent age. Curves were calculated for assumed magma temperature of 700 °C, 750 °C and 800 °C. Red dashed line represents approximate eruption age for Sheridan Reservoir dome at ~ 2 Ma (* based on analysed glass separated from samples YR215 and YR217). DIFFARG parameters: 0.5 mm radius, spherical geometry, Ar concentration at grain boundary = zero. Additional apparent ages calculated using fractional loss equation (see Appendix section A1.10.4).

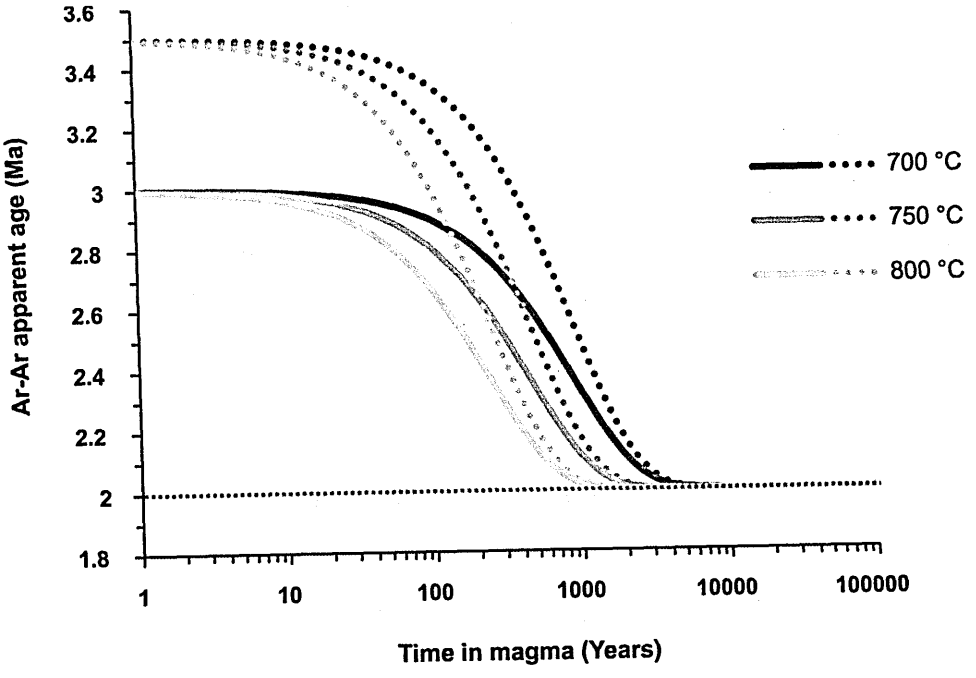

Figure 3.32. Diffusion model shows diffusive loss from 1 Ma plagioclase (solid lines) and 1.5 Ma plagioclase (dashed lines), for time in magma (in years; log scale to base 10) versus resultant apparent age. Curves were calculated for assumed magma temperature of 700 °C, 750 °C and 800 °C. Red dashed line represents approximate eruption age for Sheridan Reservoir dome at ~ 2 Ma (* based on analysed glass separated from samples YR215 and YR217). DIFFARG parameters: 0.5 mm radius, spherical geometry, Ar concentration at grain boundary = zero. Additional apparent ages calculated using fractional loss equation (see Appendix section A1.10.4).

In the case of Sheridan Reservoir dome it is inferred that a mixture of feldspar antecrysts (sanidine, anorthoclase and plagioclase), incorporated into the magma prior to eruption (with a modelled residence time of between > 50 years and less than < 1000 years) and phenocrysts are responsible for the range of Ar-Ar ages (1.97 ± 0.21 Ma to 3.34 ± 0.2 Ma) achieved. Residence time of less than 50 years we would expect the K-feldspars to record older ages and more than 1000 years we would expect the plagioclase to be reset. $^{40}Ar_E$ is not responsible in this case, because Ar-Ar ages significantly older that U-Pb zircon ages have not been identified.

It is clear that determining a true eruption age for rhyolite domes using the Ar-Ar technique can potentially be problematic when the dome magma has incorporated older

crystals, specifically through the stoping and partial assimilation of earlier-crystallised magma chamber side wall or roof material. This self-contamination has been recorded by both zircons and K-bearing minerals. Although the recording of pre-eruption crystallisation is expected in the U-Pb isotopic system, this study shows that K-bearing minerals (specifically anorthoclase and plagioclase), have the ability to record this information when crystals (i.e., antecrysts) have not been resident in the magma for long enough to allow effective resetting. The inability to identify a true xenocrystic population with a clear provenance results in generally older ages, which are not representative of the eruption age. The dome eruptions appear to be degassed with respects to Ar and glassy groundmass separated from both Sheridan Reservoir dome and Snake River Butte dome show no signs of $^{40}Ar_E$ contamination and have yielded statistically valid ages, which can be taken to represent an eruption age. Therefore the range of ages achieved for Sheridan Reservoir dome represents a mixture of antecrysts (containing an inherited radiogenic Ar) and phenocrysts and not due to $^{40}Ar_E$ contamination.

3.6.2.4 Volcanic glass: determining an eruption age

Volcanic glass in rhyolitic and phonolitic systems commonly contain a significant proportion of K, and therefore has the potential to be a useful geochronological tool (e.g., Singer *et al.*, 1998; Clay *et al.*, 2011). For samples YR215 and YR185, where previous experiments have shown that the glass may be clear of $^{40}Ar_E$ contamination, it may prove to be useful for determining an eruption age as diffusion experiments suggest it should rapidly equilibrate (e.g., Caroll and Stolper, 1991). However the loss of $^{40}Ar^*$ (e.g., Walker and McDougall, 1982) and/or K (e.g., Cerling *et al.*, 1985) from glass due to hydration and devitrification can mobilise K and Ar and lead to disturbed K-Ar and Ar-Ar ages. Cases of $^{40}Ar_E$ have been described for submarine glasses (e.g., Dalrymple and Lanphere, 1969); in melt inclusions contained within phenocrysts (e.g., Esser *et al.*, 1997), and Ar trapped and

retained in glass due to incomplete outgassing (e.g., Clay *et al.*, 2011). However useful information has been extracted and glass has provided K-Ar ages which are concordant with co-existing feldspars (e.g., Drake *et al.*, 1980), or undisturbed Ar-Ar ages for phenocryst poor obsidian samples (e.g., Bigazzi *et al.*, 2005; Vogel *et al.*, 2006).

Glassy groundmass was separated from Sheridan Reservoir dome (samples YR215 and YR217) and Snake River Butte dome (YR185). The inverse isochron method has revealed no evidence for $^{40}Ar_E$ and all samples yield initial trapped Ar compositions that are within error of the atmospheric value 298.56 (e.g., $^{40}Ar/^{36}Ar$ intercept = 268 ± 36; sample YR185). For sample YR215 and YR217 average K content (single-grain EMP analysis) for glassy groundmass is ~ 5 wt. % which is ~ 1 wt. % higher than the average K content of the feldspars. Combined Ar-Ar single-grain fusion ages for samples YR215 and YR217 yield a weighted mean age of 2.04 ± 0.03 Ma (n = 30, MSWD = 0.03). In contrast, the average K content of the glassy groundmass separated from sample YR185 is ~ 5 wt. % compared with ~ 10 wt. % for co-existing feldspars. Glassy groundmass from sample YR185 yielded a weighted mean age of 2.10 ± 0.08 Ma (n = 21, MSWD = 0.48), which is in agreement with the weighted mean age obtained from YR185 feldspars (e.g., 2.15 ± 0.01 Ma and 2.19 ± 0.01 Ma). Therefore, in this case both the feldspars and the glass appear to be representative of the eruption age (Fig. 3.33).

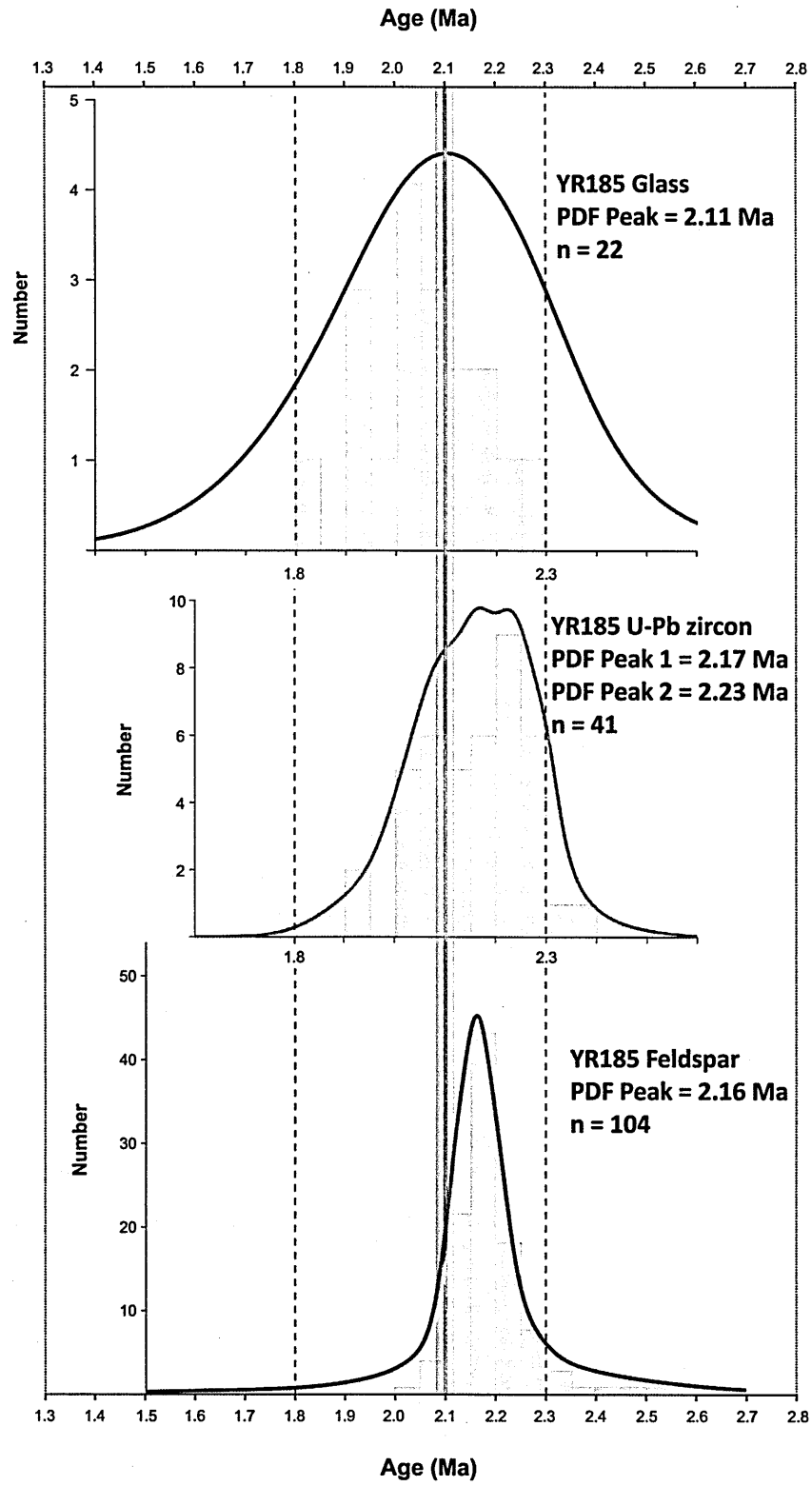

Figure 3.33. Snake River Butte dome Ar-Ar single-grain fusion age determinations for separated feldspars and glassy groundmass (sample YR185), and *in situ* U-Pb zircon age determinations (YR185). PDF peak (value at x at which the probability density function has its maximum value) for all data sets is also shown. Solid red line indicates HRT Ar-Ar eruption age (± 2σ; shaded box) determined in this study.

Alteration of K-bearing glassy groundmass can result in variable ages, and higher H_2O contents (>1 %) has been shown to correlate with loss of radiogenic Ar, resulting in younger than expected ages (e.g., Kaneoka, 1972). Ignition of samples prior to XRF analysis causes volatiles (e.g., water) to be lost from micro-inclusions (Clay *et al.*, 2011). XRF data obtained for sample YR215 correspond to a loss on ignition (L.O.I.) value of 0.80 and a resulting total of 99.97 %, suggesting the glass contains minimal volatiles. Sample YR185 yielded a L.O.I. value of 2.48 %, which may represent a higher degree of trapped volatiles. It may also mean that Snake River Butte dome material has undergone some post emplacement hydration.

There is no evidence to suggest the glass of Sheridan Reservoir or Snake River Butte domes contains an excess Ar component, which may have remained had degassing of Ar present in the melt been restricted. Sample YR215 does not appear to be hydrated, and therefore is unlikely to have undergone significant Ar loss or K mobility during post-emplacement. The slightly higher L.O.I. value for sample YR185 may indicate minor hydration, although measured Ar isotope ratios (e.g., $^{36}Ar/^{40}Ar$ and $^{39}Ar/^{40}Ar$) did not suggest atmospheric Ar contamination or K loss due to weathering. Ar-Ar age information obtained from glassy groundmass separated from Sheridan Reservoir dome in particular appears to be less disturbed than co-existing feldspars (Fig. 3.34), and is thus a preferred eruption age for Sheridan Reservoir dome (2.04 ± 0.03 Ma). This age is younger than the weighted mean age yielded for the feldspars (2.25 ± 0.07 Ma).

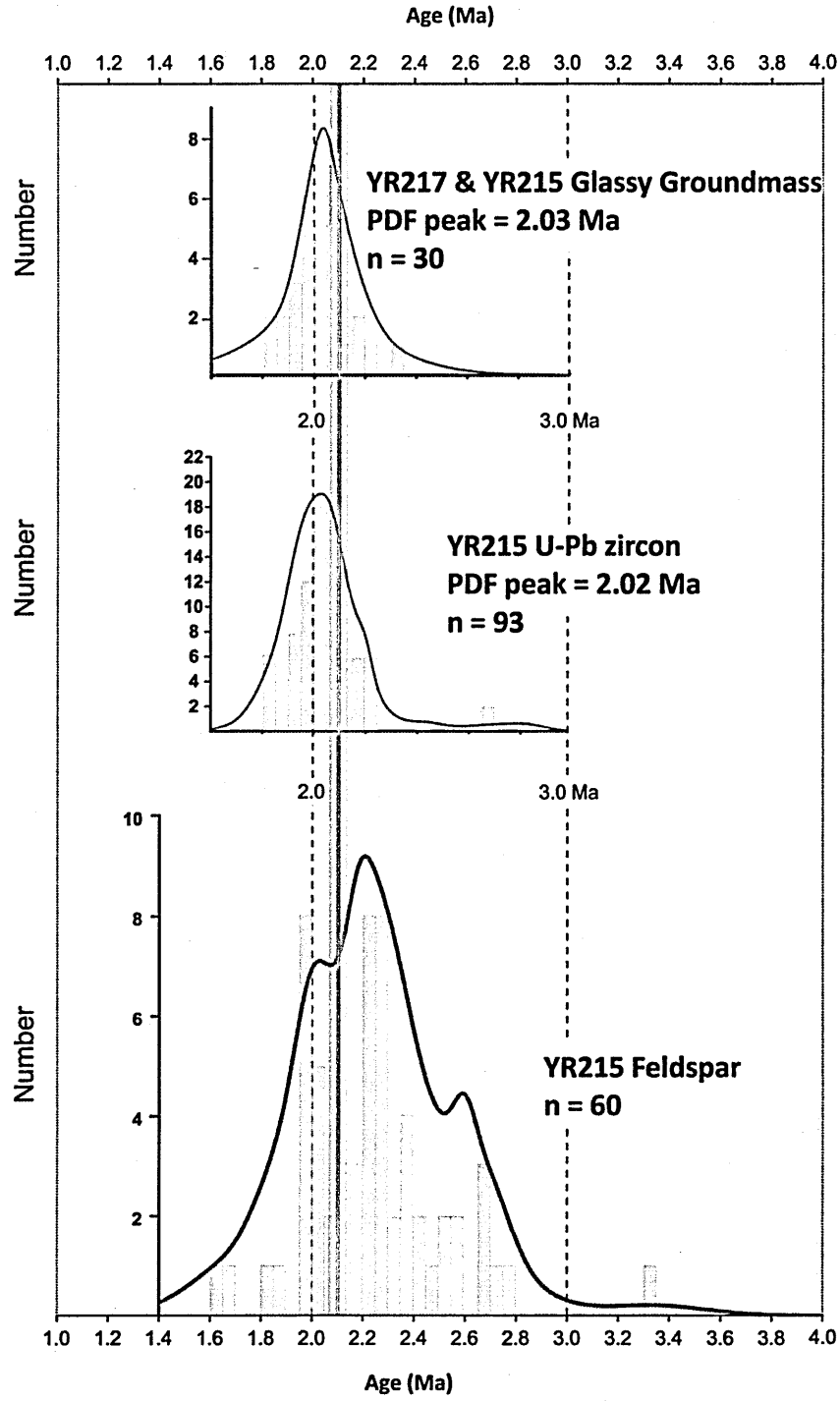

Figure 3.34. Sheridan Reservoir dome Ar-Ar single-grain fusion age determinations for separated feldspar (YR215) and glassy groundmass (YR215 and YR217) and *in situ* U-Pb zircon age determinations (YR215). PDF peak (value at x at which the probability density function has its maximum value) has been given for glassy groundmass and single grain U-Pb zircon age determinations. Solid red line indicates HRT Ar-Ar eruption age (± 2σ; shaded box) determined in this study.

3.6.3 Mesa Falls Tuff (MFT)

Weighted mean age (n = 40; MSWD = 1.4) of the MFT eruption determined in this study using the decay constants of Renne *et al.*,(2010) is 1.28 ± 0.01 Ma. This new Ar-Ar single grain fusion age is slightly younger than the generally accepted age of the Mesa Falls Tuff ~ 1.3 Ma (e.g., Lanphere, 2000 cited in Christiansen, 2000; Gansecki *et al.*, 1998; Lanphere *et al.*, 2002). Sample CMW01 (juvenile pumice from taken from the base of MFT) showed no signs of disturbance (e.g., Ar loss) and radiogenic Ar ($^{40}Ar^*$) released during each single grain fusion analysis ranged 77 to 98 %. Only one sanidine yielded a high $^{36}Ar/^{40}Ar$, $^{38}Ar/^{39}Ar$ and low $^{39}Ar/^{40}Ar$ ratio corresponding to a low age (1.14 ± 0.2 Ma), indicating a possible alteration product, but this analysis was dismissed and not used in further age calculations or inverse isochron analysis.

A sample of devitrified, densely welded MFT ignimbrite, previously dated by Gansecki *et al.*, (1998), produced a wide range of Ar-Ar single-grain fusion ages with two definite clusters, one at ~ 1.19 Ma and another at ~ 1.28 Ma (~ 1.22 Ma and ~ 1.31 Ma relative to ^{40}K decay constant of Renne *et al.*, 2010). The sample was considered to have suffered Ar loss possibly due to microscopic exsolution during devitrification thereby producing the younger age cluster. A second sample (basal pumice) yielded an age of 1.29 ± 0.01 Ma (2σ). Calculated relative to the new ^{40}K decay constant this preferred age increases to ~ 1.32 Ma, which is only slightly older than the weighted mean age obtained from this study. Lanphere *et al.*, (2002) analysed aliquots of sanidine and determined small amounts of excess Ar, released during low temperature Ar-Ar incremental heating steps. The effect was consistent with their slightly older total fusion age (1.312 ± 0.005 Ma; recalculated to 1.345 ± 0.01 Ma).

Therefore, previous studies which may have been plagued by minor $^{40}Ar_E$ contamination or disturbance due to possible sampling bias, may have presented an age slightly older than

the eruption age. Lanphere *et al.*, (2002) provides no supplementary data and therefore no information of $^{37}Ar/^{39}Ar$ ratio for each single-grain fusion analysis, however Gansecki *et al.*, 1998 supplementary information states K/Ca ratio of Mesa Falls Tuff feldspars range 15 to 97, suggesting some grains were more calcic in composition. A few older Ar-Ar ages do correspond to a low K/Ca value; however there is no strong correlation between the older Ar-Ar ages and calcic plagioclase. It could still be possible that the incorporation of excess Ar, perhaps hosted in rogue plagioclase crystals as well as sanidine may have been responsible for the older ages presented in previous studies. Separated feldspars used for Ar-Ar age determinations in this study were sanidine ($^{37}Ar/^{39}Ar$ ratio < 0.04) with only one analysis showing to have a ratio greater than 0.1 and therefore more calcic in composition. EMP analysis of single grains revealed feldspars of both high K content (Or_{58} to Or_{62}), and plagioclase (An_{22} to An_{28}), although only sanidine was analysed by Ar-Ar dating.

Our preferred eruption age of 1.28 ± 0.01 Ma is younger than the U-Pb zircon age (1.46 ± 0.05 Ma) presented by Bindeman *et al.*, (2007) and the U-Pb zircon SIMS age of ~ 1.34 Ma (C. Wilson, *pers. com.*, 2011). Although Bindeman *et al.*, (2001; 2007) reported zircon ages of the three ignimbrite forming eruptions at Yellowstone (HRT, MFT and LCT), as being comparable to Ar-Ar eruption ages, perhaps determined ages are recording a period of zircon growth which has occurred sometime prior to the eruption, which is identifiable at the current level of precision. Therefore, the data presented here infers Ar-Ar ages are recording an eruption age that is ~ 50 kyr younger than the mean zircon age.

3.6.4 Green Canyon Flow dome

In contrast to both Sheridan Reservoir dome and Snake River Butte dome of the first cycle there appears to be little evidence of contamination in the second cycle eruptions. The narrow range of Ar-Ar and U-Pb ages for both MFT and Green Canyon Flow compared to

domes of the first cycle has revealed clearly defined eruption ages (feldspars) and zircon crystallisation ages.

The preferred eruption age for Green Canyon Flow dome is 1.29 ± 0.01 Ma (n = 54; MSWD = 0.80). This age is older than the previously determined K-Ar eruption age of 1.17 ± 0.01 Ma (Christiansen, 2001), which incorrectly placed it following the MFT. The new Ar-Ar age is better constrained than the K-Ar age, and places the eruption between the new HRT and MFT ages determined in this study (2.11 ± 0.01 Ma and 1.28 ± 0.01 Ma). Inverse isochron analysis has determined no excess Ar contamination of the analysed feldspars. The weighted mean age for Green Canyon Flow feldspars is younger than the U-Pb zircon PDF peak age (~ 1.34 Ma) determined on material collected from the same locality (although a different sample; YR222). The age difference observed between the Ar-Ar eruption age and U-Pb zircon ages is ~ 50 kyr, which is similar to the age difference inferred for the MFT (Fig. 3.35). Green Canyon Flow dome is erupted from the rim of Henry's Fork caldera, west of Island Park, and is thought to represent magma erupted just prior to the MFT (Christiansen, 2001). Therefore it could be possible that the difference between Ar-Ar eruption age and a period of zircon growth recorded for both Green Canyon Flow and MFT be comparable.

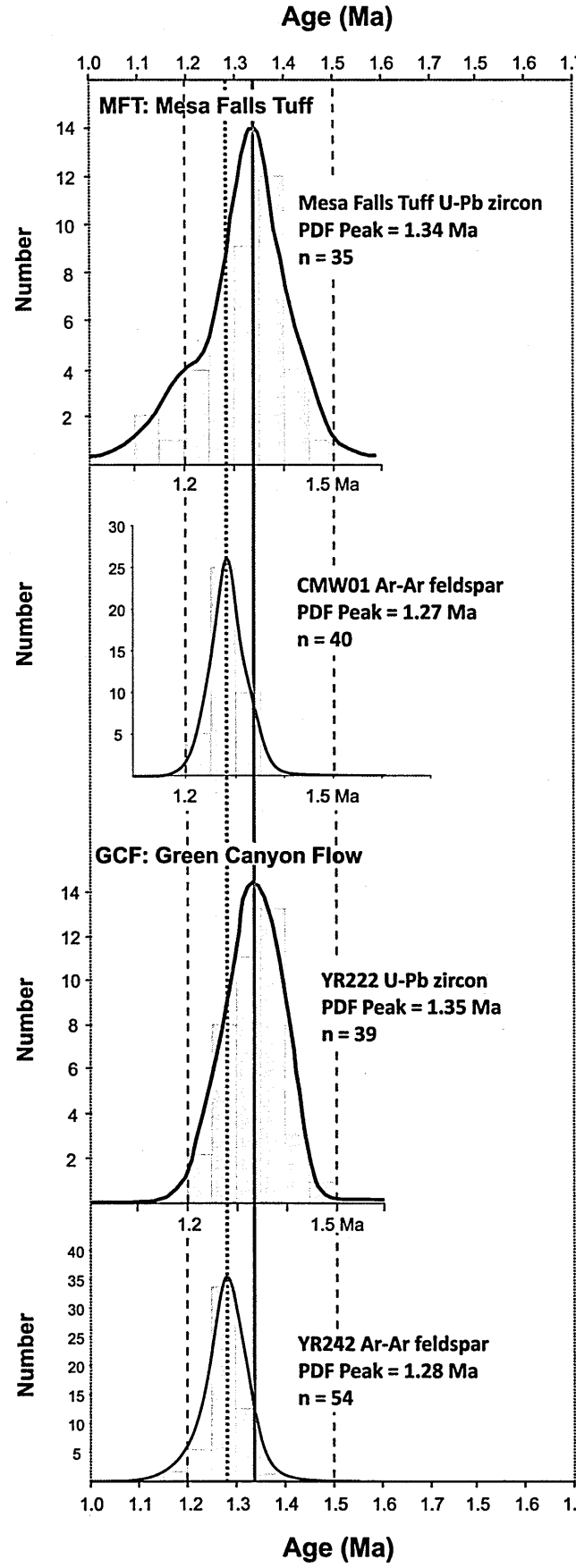

Figure 3.35. Mesa Falls Tuff and Green Canyon Flow dome Ar-Ar single-grain fusion age determinations for separated feldspars (samples CMW01 and YR242) and single grain U-Pb zircon age determinations. PDF peak (value at x at which the probability density function has its maximum value) for all data sets has also been given. Solid red line connects PDF peak age for

(*Fig. 3.35 cont.*) both ignimbrite and dome U-Pb zircon ages, which represent crystallisation age of zircons. Dashed red line connects PDF peak age for both ignimbrite and dome Ar-Ar feldspar ages, which represents the eruption age.

3.6.5 New Ar-Ar ages for Yellowstone dome eruptions

Prior to this study being undertaken no published Ar-Ar ages existed for Green Canyon Flow, Sheridan Reservoir or Snake River Butte domes, and previous ages determined by the K-Ar technique appeared to be at odds with field evidence. Incomplete extraction of Ar from sanidine during K-Ar single-grain analysis or analysis of alteration products during K-Ar whole rock analysis are common problems which can result in K-Ar ages younger than expected (McDougall and Harrison, 1999). Figure 3.36 compares the relative stratigraphy based on previous K-Ar age determinations, and new Ar-Ar age determinations presented in this study.

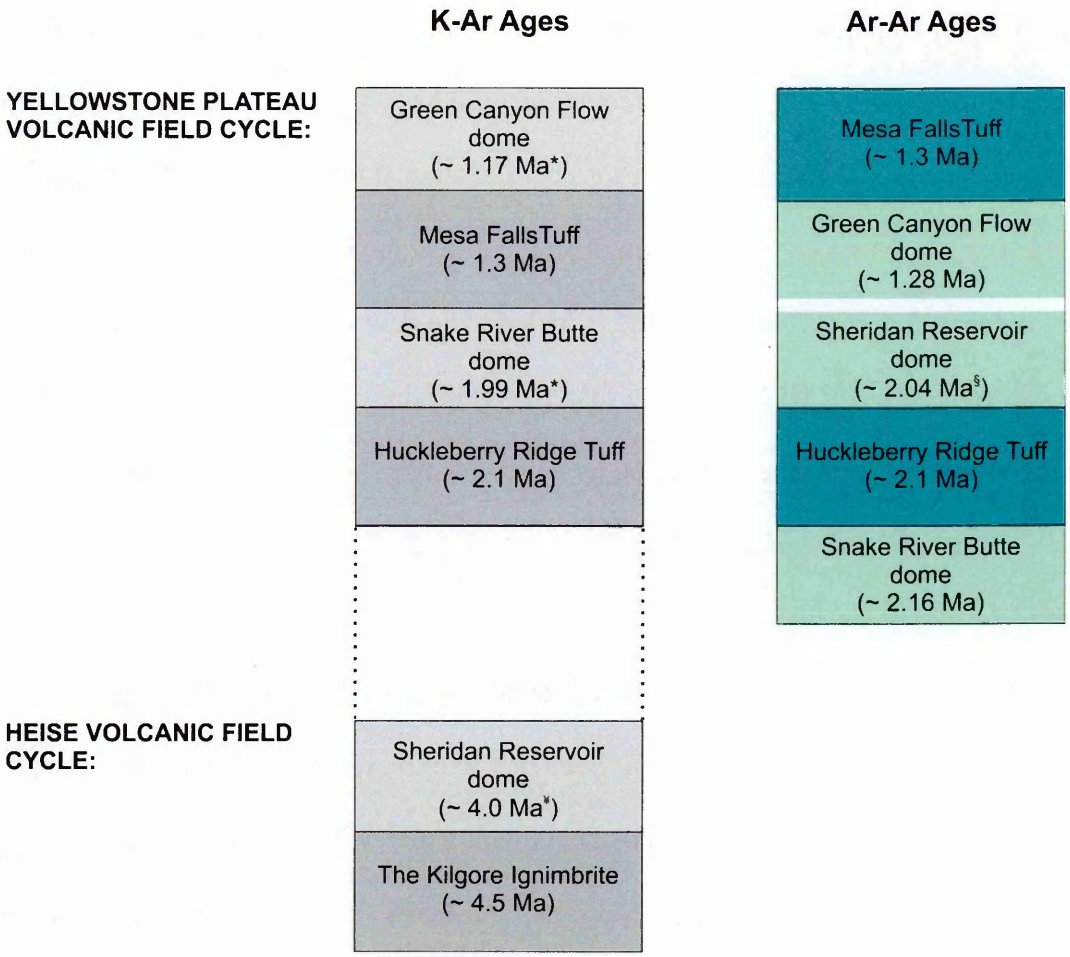

Figure 3.36. Summary diagram comparing the old stratigraphy (based on K-Ar ages; * = cited in Christiansen, 2001; ¥ = cited in Morgan *et al.*, 1984), with an updated version (based on Ar-Ar feldspar ages obtained in this study; except § = glass eruption age), for rhyolite dome eruptions of the Yellowstone Plateau Volcanic field.

Snake River Butte is a pre-HRT rhyolite dome; however its K-Ar age (cited in Christiansen, 2001), places it just after the HRT. Similarly, Green Canyon Flow dome (thought to be closely related to the MFT eruption), based on field evidence (C. Wilson, *pers. com.*, 2012), is pre-MFT in age, however its K-Ar age (cited in Christiansen, 2001), places it after the MFT. In contrast, the K-Ar age (cited in Morgan *et al.*, 1984) for Sheridan Reservoir dome is older than the field evidence suggests (C. Wilson, *pers. com.*, 2012), and has instead assigned it to a previous volcanic cycle (Heise). The elevated K-Ar age is perhaps not out of the ordinary in view of the contamination identified in this study,

and analysis of contaminated material during multi-aliquot K-Ar measurements is a likely cause. Identification of extraneous Ar contamination has prevented an inaccurate eruption age (based on a mixed feldspar population) being assigned to the dome. An age of 2.25 ± 0.07 Ma (n = 60; MSWD = 5.8), although younger than the K-Ar age, is older than the HRT, and therefore disagrees with field evidence. The new Ar-Ar eruption age (based on analysis of glass) of ~ 2.04 Ma for Sheridan Reservoir dome, which is ~ 2 Ma younger than the Heise unit, is further supported by a previously published U-Pb zircon age of 2.07 ± 0.19 Ma (e.g., Watts *et al.*, 2011).

The new Ar-Ar eruption ages for all domes dated as part of this study are in agreement with field evidence, and therefore it has been possible to present an updated stratigraphy for part of the Yellowstone Plateau Volcanic Field, which will aid our general understanding of the evolution of Yellowstone. Furthermore, this work may prompt other Yellowstone domes (e.g., Headquarters flow), assigned a single K-Ar age to be reviewed.

3.7 Conclusions

This study has produced a new data set of Ar-Ar ages (feldspar and glass), corrected relative to the newly defined ^{40}K decay constants of Renne *et al.*, (2010), for both explosive and effusive eruptions of the Yellowstone Plateau Volcanic Field, and including new Ar-Ar ages for rhyolitic dome eruptions previously only dated using the K-Ar technique. Direct comparison with U-Pb zircon ages determined on the same units has allowed occurrences of subtle contamination to be investigated.

- Ar-Ar single-grain fusion dating of three effusive rhyolite domes has revealed variable levels of contamination. Green Canyon Flow dome yielded a narrow range

of ages and no evidence to support extraneous Ar contamination. Snake River Butte dome feldspars revealed a range in ages and a slight tail off to older ages, which was definitely more pronounced in the U-Pb zircon data. Despite this tail off to older ages the weighted mean Ar-Ar age in in agreement with the younger PDF peak defined by the U-Pb zircon ages. Sheridan Reservoir dome feldspars yield the most significant range of ages and a signal of inheritance recorded by both feldspars and zircons. The spread in ages achieved for Sheridan Reservoir dome has made it difficult to determine an eruption age by applying the Ar-Ar technique to separated anorthoclase feldspar crystals.

- Extraneous Ar contamination, most severe in the case of Sheridan Reservoir dome, is most likely due to subtle self-contamination and retention of inherited Ar in antecrysts rather than due to $^{40}Ar_E$, despite the presence of potentially obvious $^{40}Ar_E$ sources, namely melt inclusions and adhering matrix glass. Therefore thorough testing of potential sources is necessary to determine the actual cause of disturbed Ar-Ar age data.

- Feldspars contaminated with varying amounts of inherited Ar are most likely to be sourced from remobilised magma chamber side wall and/or roof material rather than material relating to an unconnected eruption. EMP and Ar isotope (e.g., $^{37}Ar/^{39}Ar$) data could not distinguish between true xenocrysts and phenocrysts and neither Ar-Ar nor U-Pb ages yielded a bi-modal age distribution. The close correlation between zircon and feldspar ages has enabled this subtle inheritance to be detected, which could potentially go undetected in older rocks or in bulk analysis.

- Diffusion modelling has shown that a strong compositional control exists, and that plagioclase feldspar (and anorthoclase) is able to retain Ar at magmatic temperatures for longer (up to 1000 years), compared to sanidine, which will be re-set after 10 to 50 years. This differential outgassing means that sanidine is more likely to yield an eruption age (e.g., Green Canyon Flow dome), but care should be taken if dating plagioclase (and anorthoclase), especially if xenocrysts and/or antecrysts cannot be successfully distinguished from phenocrysts.

- This study has emphasised the importance of dating multiple co-existing phases using the Ar-Ar technique (e.g., feldspar and glass). Successful dating of glass separated from two rhyolitic domes (Sheridan Reservoir and Snake River Butte domes) has proved to be a useful geochronological tool and has provided a good estimate of the eruption age. For example, the preferred eruption age of 2.04 ± 0.03 Ma is taken for Sheridan Reservoir dome where the feldspar ages exhibit a wide range and significant contamination. For Snake River Butte dome, where contamination of feldspar phase (based on sample analysed) appears to be relatively less disturbed, the glass age of 2.10 ± 0.08 Ma is in agreement with the mean feldspar age and the youngest zircon population. Both domes appear to be well outgassed with regards to Ar and if a $^{40}Ar_E$ component had been present in the melt it has now been lost and/or was not significant at the time of melt inclusion entrapment.

- This subtle type of contamination is not evident in all Yellowstone rhyolite domes investigated and therefore self-contamination does not appear to be a process that is always recorded. The potential impact on Ar-Ar ages depends heavily on mineralogy and equilibration time of older material prior to eruption. For example, Green Canyon Flow dome Ar-Ar age data revealed a narrow range of ages in

comparison with Sheridan reservoir dome. If older material had been incorporated, it perhaps was held in the magma long enough to allow complete re-equilibration.

- MFT age determined as part of this study is younger than previous age determinations, but they may have been plagued by $^{40}Ar_E$ contamination which has not been detected here. The analysis of K-rich sanidine has resulted in a narrow range of ages, which clearly define a period of time between stage of zircon growth recorded and ignimbrite eruption. Based on Ar-Ar data presented here and U-Pb zircon data previously collected (Wilson and Charlier, *pers. com.*, 2009), a time gap of ~ 50 kyr can be inferred. This has also been possible for Green Canyon Flow dome, where separated sanidine has yielded an eruption age ~ 50 kyr younger than mean U-Pb zircon age.

- Despite the explosive nature of the eruptions that formed the MFT and HRT, previously inferred to show the most severe contamination by xenocrysts, sourced from nearby volcanics, incorporated just prior to and during explosive fragmentation, this study has not revealed contamination at this extreme level. The HRT in particular shows no signs of significant xenocryst contamination or disturbance. The data presented here confirms that the three members of HRT, which although separated by minor time breaks identifiable in the field, are essentially the same age within uncertainty, and therefore no evidence can be found to support the recent study by Ellis *et al.*, (2012) which appeals to a model of much longer hiatuses between the eruptive units. Ar-Ar feldspar ages determined as part of this study are in agreement with U-Pb zircon ages, and the extensive paleomagnetic study by Reynolds (1977), which also confirms HRT members A, B and C to be the same age.

Chapter 4. The Bishop Tuff: New Ar-Ar ages for ash fall and ignimbrite flow units.

4.1 Introduction

The Bishop Tuff (~ 0.76 Ma) was produced during an episode lasting approximately 6 days (Hildreth and Wilson, 2007), and saw more than 600 km^3 of material erupted from the Long Valley magma chamber, eastern California, USA. The growth and development of the Bishop Tuff magma chamber inferred to include, the incorporation of previously active Glass Mountain magma reservoir (e.g., Metz and Mahood, 1985; Hildreth and Wilson, 2007), assimilation of magma chamber wall- and roof-rock material (e.g., Hildreth and Wilson, 2007), the mixing of crystals grown and contained in adjacent domains within the reservoir (e.g., Anderson *et al*, 2000; Hildreth and Wilson, 2007), possibly subjected to varying timescales of magma residence (e.g., van den Bogaard, 1995; Reid and Coath, 2000). In addition, contamination of the Bishop Tuff magma (immediately prior to and throughout the eruption e.g., during caldera collapse), by xenocrystic material has also been noted (e.g., Christensen and DePaolo, 1993; Wilson and Hildreth, 2003).

The well constrained eruptive sequence (e.g., Hildreth, 1979; Wilson and Hildreth, 1997; 1998; Hildreth and Wilson, 2007), consists of ash-fall units and ash-flow packages and represents the inverse zonation of the Bishop Tuff magma chamber (Hildreth, 1985; Halliday *et al.*, 1984; Wallace *et al.*, 1999; Anderson *et al.*, 2000; Hildreth and Wilson, 2007 and references therein; Reid *et al.*, 2011). The early erupted units represent withdrawal from a melt dominant zone located at the top of the magma chamber, rich in volatiles but relatively crystal-poor. Later units represent magma sourced from deeper

levels within the chamber, possibly tapping in to a crystal-rich (feldspar + quartz) mush zone, which is maintained by injections of a more mafic magma at the base of the chamber (Hildreth and Wilson, 2007).

Although volcanic material such as pumice represents fresh juvenile, phenocryst-rich material, they have the potential to also contain a mixture of crystals that contain $^{40}Ar_E$, perhaps record an extended magma chamber residence time (i.e., antecrysts), or are xenocrystic in origin. The impact of $^{40}Ar_E$ in minerals such as feldspar and biotite has previously been shown to significantly affect the accuracy of Ar-Ar ages (e.g., Renne *et al.*, 1997; Esser *et al.*, 1997; Hora *et al.*, 2010; Bachmann *et al.*, 2010), in particular in a 'mush' setting (e.g., Chapter 2). Winick *et al.*, (2001) noted the incorporation of $^{40}Ar_E$ within in the melt inclusions of Bishop Tuff quartz, and hypothesised $^{40}Ar_E$ contamination of coexisting sanidine may be a significant problem. Elevated Ar-Ar ages may also result from incomplete resetting of xenocrysts and/or antecrysts (in particular anorthoclase and plagioclase), which have shown to retain an inherited Ar component (e.g., Chapter 3).

The aim of this study is to track the presence of extraneous Ar through the course of a single eruption, using samples of plinian ash fall units and ignimbrite flow packages which represent the compositionally zoned Bishop Tuff magma chamber. This study applies the Ar-Ar single-grain fusion technique to individual crystals separated from pumices sampled from five stratigraphically known sub-units of the Bishop Tuff in order to investigate any differences in Ar-Ar apparent age between feldspar phases (i.e., plagioclase and sanidine), between mineral phases (e.g., feldspar and biotite), and between units of the Bishop Tuff (e.g., early erupted plinian and ignimbrite, and late erupted ignimbrite deposits). This study has highlighted the challenges associated with analysing young (< 1 Ma), often K-poor minerals, as well as mineral phases which are less abundant (< 1 %) in sampled pumices, and potentially more susceptible to alteration (e.g., biotite).

4.2 Background

4.2.1 Geological setting

4.2.1.1 The Long Valley Volcanic Field (LVVF)

The Long Valley Volcanic Field (LVVF; Fig. 4.1a) is located on the western margin of the extensional basin and range province and north of the town of Bishop, California, USA (Mahood *et al.*, 2010). During the Pliocene to Holocene it was the focal point of intense activity, giving rise to initial volcanism that was both extensive and mafic to intermediate in composition between 4.5 to 2.5 Ma (Hildreth and Wilson, 2007). The progression from accumulation at deep crustal levels to evolved and shallow magma systems hosted in granites of the Sierra Nevada occurred from 3.6 Ma to 2.1 Ma. Between ~ 2.1 to 0.79 Ma this shallow magma system became the source of Glass Mountain (GM) high-silica-rhyolitic volcanism, which erupted intermittently for > 1 Myr prior to the climactic eruption of the Bishop Tuff at ~ 0.76 Ma and the collapse of the Long Valley caldera (Hildreth and Wilson, 2007).

The Glass Mountain complex is the product of two main eruptive episodes (Metz and Mahood, 1985), from more than 60 precaldera vents (Hildreth and Wilson, 2007), giving rise to ~ 100 km^3 of intercalated rhyolitic lava domes and pyroclastic deposits (Metz and Mahood, 1985). The collapse of the Long Valley caldera, following the evacuation of > 600 km^3 Bishop Tuff magma (Hildreth and Wilson, 2007), has been the site of early postcaldera phenocryst poor rhyolites (0.76 to 0.65 Ma), and later intermediate and mafic volcanism from 0.52 Ma to the present day (e.g., Hildreth, 2004).

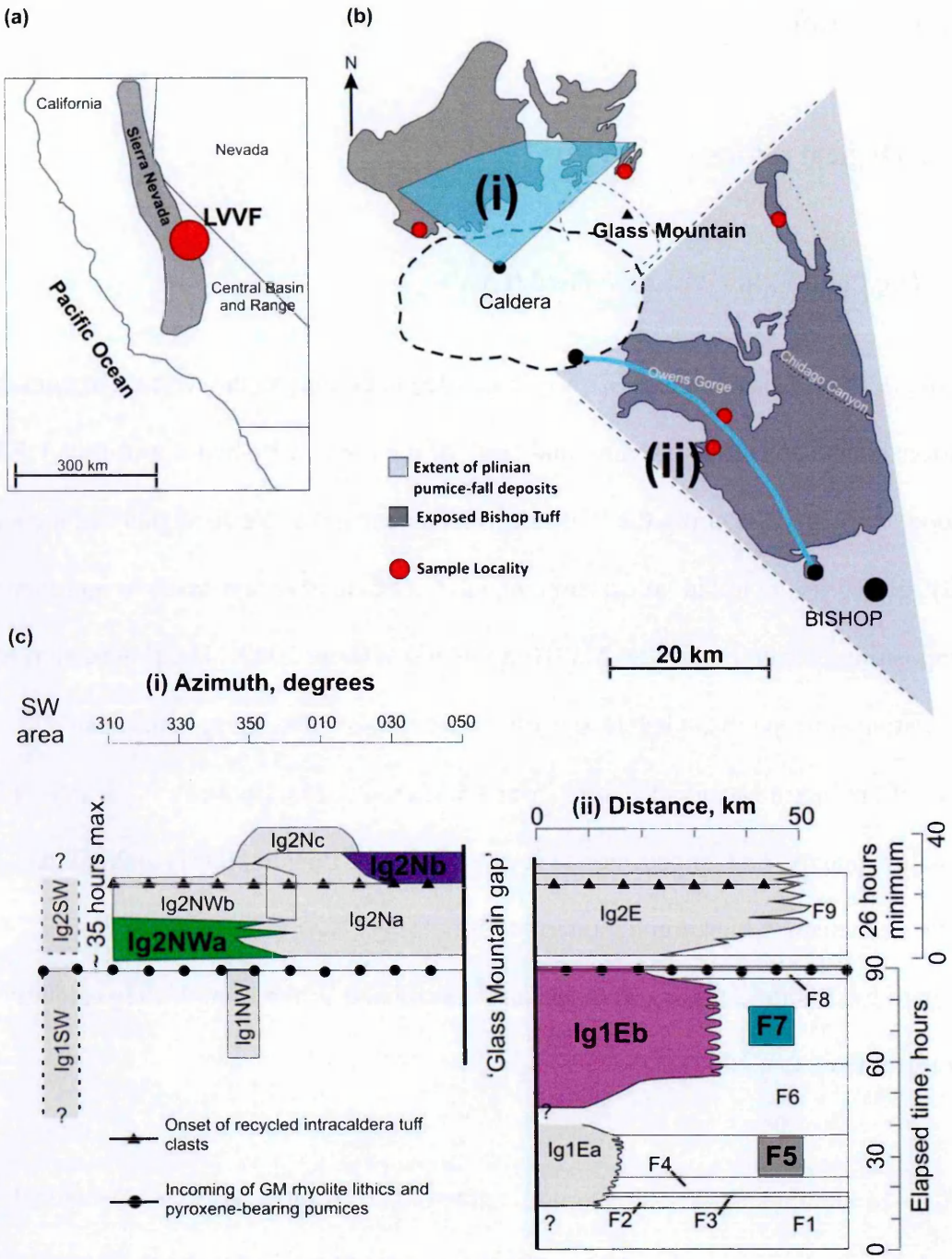

Figure 4.1. Geological setting of the Long Valley Volcanic Field (LVVF), and the Bishop Tuff. (a) Map of the western United States highlighting the location of the LVVF (red dashed line) between the westernmost margin of the Basin and Range Province and the Sierra Nevada (modified and redrawn after Winick, 2000); (b) Map of the Long Valley caldera (caldera margin marked by thick dashed line), and the exposed deposits of the Bishop Tuff (dark grey). Glass Mountain, which represents the oldest rhyolites of the Long Valley magma system, the extent of the plinian pumice-fall deposits, which are preserved within the easterly sector and intercalated with ignimbrite packages that flowed east on exiting the caldera, and sample locations are also shown (see Appendix section A2 for sample information); (c) Summary diagram showing the eruptive stratigraphy (see Wilson and Hildreth, 1997 for detailed explanation), and estimated emplacement durations (hours). The Bishop Tuff is divided into ignimbrite packages (prefix Ig) and fall units (prefix F) and units worked on in this study have been highlighted in colour, all other units have been greyed out. (i) hypothetical west to east section along arc 310 to 050 ° (relative to grid north - see blue shaded area (i) Fig. 4.1b), and (ii) proximal to distal area

(*Fig. 4.1 cont.*) (along blue line (ii) Fig. 4.1b). 'Glass Mountain gap' represents an erosional gap and therefore the absence of Bishop Tuff deposits directly to the east of Glass Mountain. Ig1 and Ig2 ignimbrite packages are subdivided based on the appearance of Glass Mountain (GM) lithics and pyroxene-bearing pumices. The appearance of recycled intracaldera tuff clasts in Ig2 is also shown (parts (b) and (c) modified and redrawn after Hildreth and Wilson, 2007).

4.2.1.2 The Bishop Tuff

The Bishop Tuff, produced during one of the largest Quaternary eruptions, was deposited ~ 0.76 Ma as multiple plinian fall deposits interbedded within ash-flow packages (Fig. 4.1b; Wilson and Hildreth, 1998; Hildreth and Wilson, 2007; Mahood *et al.*, 2010). The eruption, one of > 200 eruptions to occur in the LVVF over a 4.5 Myr time period, lasted approximately 6 days with no significant time breaks. Ash fallout has been preserved from the Pacific Ocean to Nebraska, covering an area in excess of 2.5×10^6 km^2, and ash-flows have been mapped > 70 km SE along Owens Valley, *ca.* 50 km east towards the White Mountains, north into Mono Basin and Adobe Valley and SW down the San Joaquin River canyon (Hildreth and Wilson, 2007).

The Bishop Tuff comprises primarily of ash and pumice clasts of biotite ± plagioclase-quartz-sanidine high-silica rhyolite (74 to 77.7 % SiO_2), as well as rare pumice types which are more dacitic in composition (Hildreth and Wilson, 2007). Partly welded ignimbrite sheets (up to 170 km thick), are variable preserved ranging from unconsolidated or variably welded vitric zones to zones which are fully devitrified and zones which have undergone intense vapour-phase crystallisation (Wilson and Hildreth, 2003; Hildreth and Wilson, 2007). The plinian deposits (pumice-fall) are preserved and collated with ash-flow deposits within the easterly zone, due to prevailing wind direction at the time of the eruption. Proximal to medial fall deposits are relatively coarse and consist of pumice lapilli and crystal-rich ash. Distal deposits (> 200 km from source vent) the ash is predominantly

glassy (vitric) and include both plinian and ignimbrite material (Wilson and Hildreth, 1997; Hildreth and Wilson, 2007).

4.2.2 Eruptive stratigraphy: fall and flow

The eruptive sequence of Bishop Tuff deposits has been previously divided into ash fall units and ignimbrite flow packages and sub-packages (Fig. 4.1c), and the following description uses the names assigned to ash fall and ignimbrite flow units after Wilson and Hildreth (1997) rather than the 'lobes' of Hildreth (1979). The Bishop Tuff fall (F) deposit is divided into nine units (F1 to F9), which are correlated between deposits based on bedding, grain size and the composition of included lithic fragments (Wilson and Hildreth, 1998). Bishop Tuff ignimbrite (Ig) packages (~ 13 distinctive bodies of tuff), are syn-plinian and were emplaced in a sequence of rapid pulses and are divided into those that are void of pyroxene phenocrysts (Ig1) and those that are pyroxene bearing (Ig2) (Hildreth and Wilson, 2007).

Earlier ignimbrite packages were deposited predominantly eastward, and as a result are interbedded with ash fall deposits. Ignimbrite 1 (Ig1Ea and Ig1Eb), deposited synchronously with fall units F2 to F8, are dominated by pumices that lack pyroxene and tend to be crystal poor and yield Fe-Ti oxide temperatures ~ 725 to 737 °C. Later crystal-rich pumice bearing Ig2E (a, b and c), flowed eastward across Glass Mountain, synchronously with fall units F8 and F9, and are characterised by the inclusion of Glass Mountain rhyolite lithics (e.g., Wilson and Hildreth, 1997). Ignimbrite packages deposited to the north and northwest of the caldera are not interbedded with fall units. Early ignimbrite packages are pyroxene free and lack Glass Mountain lithics, whereas later packages, Ig2N (a, b and c) and Ig2NW (a, and b), are dominated by pyroxene-bearing

pumice and varying amounts (sparse to abundant) of Glass Mountain lithics (Wilson and Hildreth, 2003; Hildreth and Wilson, 2007).

4.2.3 The Bishop Tuff magma chamber

Based on physical and chemical evidence (e.g., Halliday *et al.*, 1984; Christensen and DePaolo, 1993; Wilson and Hildreth, 1997; Wallace *et al.*, 1999; Anderson *et al.*, 2000; Wilson and Hildreth, 2003; Hildreth and Wilson, 2007), the current model of the Bishop Tuff magma chamber describes a unitary magma chamber that was compositionally and thermally zoned (see Hildreth and Wilson (2007), and references therein for a detailed review). The stratigraphically constrained Bishop Tuff ash fall and ignimbrite flow packages are an inverted expression of this zoned magma chamber and represent progressive tapping of adjacent zones in a single magma body (e.g., Wilson and Hildreth, 1997; 1998; Hildreth and Wilson, 2007).

The conceptual model of Hildreth and Wilson (2007), shown in Figure 4.2, illustrates how the Bishop Tuff reservoir grew incrementally by incorporating mafic magmas reaching the upper crust and penetrating the expanding crystal mush reservoir. The expansion of the Bishop Tuff magma reservoir and integration of the Glass Mountain reservoir to create the Bishop Tuff magma chamber took place in the last few hundred thousand years before the Long Valley caldera forming eruption at ~ 0.76 Ma. During this process the resorption of Glass Mountain crystals, including zircons that are older than ~ 0.9 Ma, is inferred to have taken place (Hildreth and Wilson, 2007). Zircon ages have previously been reported to be no older than 0.926 ± 0.036 Ma, averaging ~ 0.850 Ma (Reid and Coath, 2000). A current study investigating the age of the Bishop Tuff zircons reports a mean age of 0.778 ± 0.002 Ma and no evidence for zircons older than ~0.9 Ma (C. Wilson, *pers. com.*, 2012).

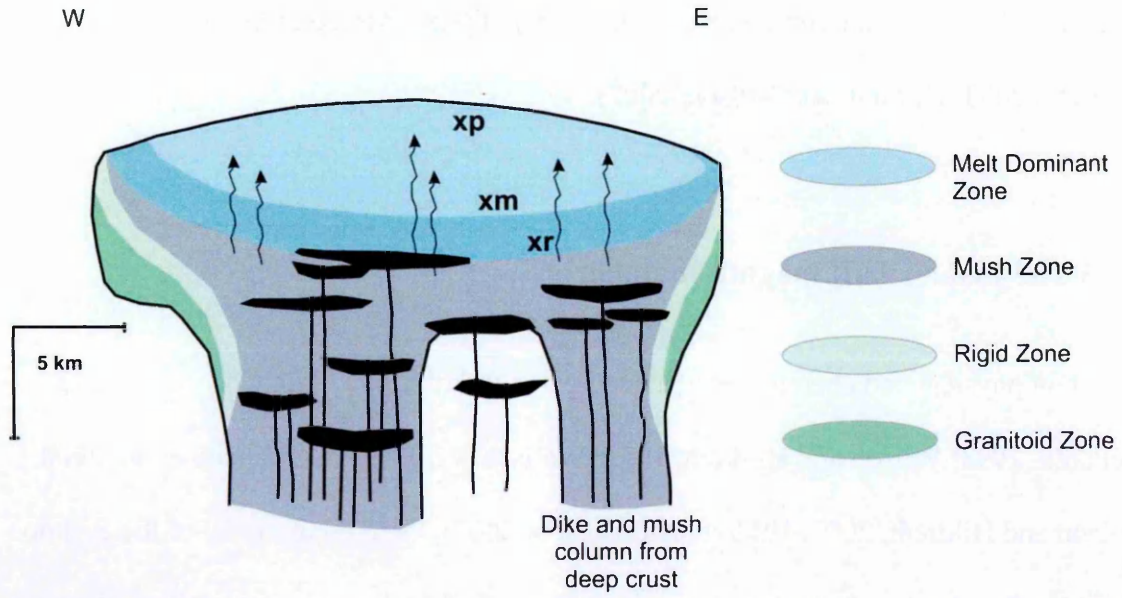

Figure 4.2. Schematic illustration detailing the model of Hildreth and Wilson (2007). The Bishop Tuff magma reservoir, which grew incrementally and shown here in a mature stage just prior to eruption, is fed by root zones comprising quartz-feldspar rich mush (relatively melt poor) and mafic, hybrid, or silicic dikes. The mush zone, dikes and melt lenses (black) extend upwards into the middle part of the reservoir. The upper part of the magma chamber is divided into layers based on crystal content and gets progressively crystal-poor and therefore relatively melt-rich towards the top of the magma chamber. Arrows denote the upward movement of melt sourced from the mush dominant zone. Rigid zones at chamber margins are both capable of contributing melt through assimilation (rigid zone) and solidifying completely (granitoid zone) (modified and redrawn after Hildreth and Wilson, 2007).

Evidence to support a chemically and thermally zoned magma chamber includes, the eruption of predominantly crystal-poor pumices in the early part of the eruption (e.g., Ig1 and F1 to F8), followed by crystal-rich pumices (pyroxene-bearing) included in later eruptives (Wilson and Hildreth, 1997; 1998; 2003; Pamukcu *et al.*, 2012). Gas-saturation pressures estimated for melt inclusions in quartz crystals show some overlap between Ig1 and Ig2, but Ig2 extends to pressures > 0.7 kbar suggesting that Ig2 magma was withdrawn from the chamber at similar depths to Ig1 but also 2 km deeper (Hildreth and Wilson, 2007). Therefore high-silica rhyolite magma that was most differentiated, lowest in temperature, richest in an exsolved gas phase (e.g., Wallace *et al.*, 1999), and poorest in phenocrysts, resided at the top of the magma chamber and was tapped first. This was followed by the eruption of material sourced from deeper levels. In summary, the Bishop

Tuff magma reservoir underwent incremental assembly and repeated rejuvenation, which is now considered central to processes occurring in long lived upper crustal magma systems (e.g., Fish Canyon and Yellowstone magmatic systems).

4.3 Previous work

The stratigraphic relationship between ash fall and ignimbrite flow units, and the petrology of the different units identified has previously been studied in detail by Hildreth (1977, 1979); Wilson and Hildreth (1997, 1998) and Hildreth and Wilson (2007). The growth and assembly of the Bishop Tuff reservoir and the origin of the compositional zoning of the Bishop Tuff magma chamber has long been investigated (e.g., Hildreth, 1977; 1985; Halliday *et al.*, 1984; Wallace *et al.*, 1999; Anderson *et al.*, 2000; Hildreth and Wilson, 2007 and references therein; Reid *et al.*, 2011). Pre-eruptive magma residence time has been considered by Christensen and DePaolo (1993); van den Bogaard and Schirnick (1995); Reid and Coath (2000); Winick (2000); Winick *et al.*, (2001); Simon and Reid, (2005) and Simon *et al.*, (2008).

4.3.1 Geochronology

The Bishop Tuff has long been the focus of numerous geochronological studies due to its classification as an 'archetypical' silicic system, and because it lies at the Matuyama-Brunhes geomagnetic reversal. The eruption age (see summary Table A5.3) of the tuff has been determined by K-Ar (e.g., Dalrymple *et al.*, 1965; Hurford and Hammerschmidt, 1985; Izett *et al.*, 1988 and references therein), and Ar-Ar (e.g., Hurford and Hammerschmidt, 1985; Pringle *et al.*, 1992; Izett and Obradovich, 1994; van den Bogaard and Schirnick, 1995; Sarna-Wojcicki *et al.*, 2000; Winick *et al.*, 2001; Kuiper *et al.*, 2008; Rivera *et al.*, 2011; Mark *et al.*, 2012).

Incomplete degassing of radiogenic Ar and measurement of rogue xenocrysts are both reasons suggested for the variability seen in previous feldspar, biotite, and glass K-Ar age determinations (e.g., 0.639 ± 0.07 to 0.754 ± 0.08; Dalrymple *et al.*, 1965; 0.741 ± 0.014 Ma; Hurford and Hammerschmidt, 1985; 0.66 ± 0.08 Ma to 0.83 ± 0.20 Ma; Izett *et al.*, 1988). Izett *et al.*, (1988), found no analytically detectable amounts of $^{40}Ar_E$ in sanidine, plagioclase, biotite or glass. The interchange of material between ignimbrite flows en route from vents to depositional position is expected, and the work of Hildreth and Wilson (2007), estimated the contribution of lithic fragments entrained during the eruption and outflow is minor (up to 4 wt. % of fall units and > 10 wt. % of ignimbrite).

Sampling of intact pumices, rather than whole rock ignimbrite has been carried out for this work, which should limit the occurrences of xenocrystic contamination. However, the presence of xenoliths inside Bishop Tuff pumice clasts (e.g., metasediments), although rare, has previously been noted (e.g., Hildreth and Mahood, 1986; Hildreth and Wilson, 2007; Christensen and DePaolo, 1993). Contamination by xenocrysts may therefore prove to be a particular problem in the context of this study, for example northern Ig1Eb material contains sparse rhyolite lithics and other recognisably locally derived lithologies, inferred to have been picked up as early flows covered areas of the Glass Mountain volcaniclastic fan. Distinctive ignimbrite lithic fragments have also been found at the top of sub-package Ig2Na. Sub- to well-rounded, poorly welded, glassy fragments and moderate proportions of Glass Mountain-rhyolite lithics are inferred to be recycled Bishop ignimbrite, torn away as vent enlargement (or migration), disrupted ignimbrite that had accumulated within the caldera (e.g., Wilson and Hildreth, 1997).

Although, Hurford and Hammerschmidt (1985) carried out Ar-Ar step heating experiments on sanidine, and suggested samples had not undergone any significant post-depositional Ar loss, Bishop Tuff deposits have undergone variable devitrification (loss of Si) and vapour-

phase crystallisation resulting in oxidation and alteration of many phenocryst phases, for example biotite. Therefore careful sampling of pumice from fresh glassy parts of emplacement packages is critical. Hydration of volcanic glass can lead to significant Na loss and the relative enrichment of K, as well as real enrichment of K during interaction with ground or surface waters (Smith and Bailey, 1966). This can also be a problem for susceptible minerals, such as biotite. Previous work (e.g., Hildreth and Wilson, 2007) demonstrated that samples may have been variably hydrated (measured L.O.I. values at 900 °C for both vitraphyre and pumice clasts ranged 1 to 3 wt. % and 2 to 5 wt. % respectively), the wide scatter in Na_2O and K_2O values for analysed pumice clasts suggests alkali mobility had taken place across the deposits due to groundwat er leaching and ion exchange. It was also noted in the same study that the data most likely reflected magmatic zoning and real differences among Bishop Tuff pumice types that were co-erupted.

Vapour phase crystallisation, occurring in pore spaces (interstices between glass shards) and in vesicles of pyroclastic deposits during circulation and release of an exsolved gas phase combined with ground and/or surface waters, can cause secondary minerals to crystallise. In the study by Smith and Bailey (1966), christobalite and tridymite (high-temperature polymorphs of quartz), iron oxides and alkali feldspar, were all noted as products of direct crystallisation of Bandelier Tuff pumice and glass shards bought about by vapour-phase interaction. Accidental analysis of such phases, especially alkali feldspar, is likely to result in anomalous Ar-Ar ages due to crystallisation in an exsolved gas (including Ar) rich environment and/or significant alkali mobility.

The widespread dispersion of the BT and its temporal proximity to the Matuyama-Brunhes (M-B) geometric polarity reversal (BT post-dates the M-B by ~ 15.3 ± 2.2 ka; Sarna-Wojcicki *et al.*, 2000), makes it an important stratigraphic marker, and the 'eruption age' of the Bishop Tuff has been determined on numerous occasions. Previously published

single-grain fusion Ar-Ar data (where possible re-calculated relative to Renne *et al.*, 2010 ^{40}K decay constant in order to allow comparison with the current data set), determined on sanidine (single crystals and multi-crystal aliquots), range ~ 0.76 to ~ 0.77 Ma. Pringle *et al.*, (1992; cited in Sarna-Wojcicki *et al.*, 2000) analysed sanidine separates and obtained an age of ~ 0.778 Ma (re-calculated relative to ^{40}K decay constant of Renne *et al.*, 2010; published age originally 0.759 ± 0.003 Ma relative to 27.92 Ma Taylor Creek sanidine standard and Steiger and Jäger ^{40}K decay constant, 1977). Izett and Obradovich (1994) used samples from upper ignimbrite and lower ash fall deposits, reporting ages of 0.776 ± 0.018 Ma and 0.783 ± 0.010 Ma respectively (re-calculated relative to the ^{40}K decay constant of Renne *et al.*, 2010; published ages originally 0.757 ± 0.009 Ma (1 σ), and 0.764 ± 0.005 Ma (1 σ) relative to Taylor Creek sanidine standard (27.92 Ma), and the ^{40}K decay constant of Steiger and Jäger, 1977).

Sarna-Wojcicki *et al.*, (2000) reported a weighted mean age of 0.766 ± 0.006 Ma (2σ) for basal ash fall, and 0.770 ± 0.010 Ma (2σ) for the upper ignimbrite package (re-calculated relative to the ^{40}K decay constant of Renne *et al.*, 2010; published ages originally 0.758 ± 0.002 Ma (1σ) and 0.762 ± 0.005 Ma (1σ) relative to Taylor Creek sanidine standard (28.34 Ma), and the ^{40}K decay constant of Steiger and Jäger, 1977). Their study revealed little variation between single ages, and excluded only one age determination due to an elevated age and associated uncertainty (> 1 Ma), reasoning the sample aliquot probably contained a mixture of plagioclase and sanidine. Rivera *et al.*, (2011) carried out multi-crystal (20 to 25 sanidine grains) Ar-Ar total fusion experiments, and reported various Ar-Ar ages relative to different standard ages and the ^{40}K decay constant value of Min *et al.*, (2000), including an age of 0.7689 ± 0.0030 Ma (2σ) calculated relative to FCs age of 28.201 Ma (Kuiper *et al.*, 2008), and 0.7667 ± 0.0030 Ma (2σ) calculated relative to A1Ts (A1 tephra sanidine astronomical age of 6.943 ± 0.005 Ma, 2σ). An age of 0.7719 ± 0.0036 Ma (2σ) also presented in the same study has been calculated relative to FCs age of 28.305

Ma and the Renne *et al.*, (2010) ^{40}K decay constant, and therefore can be directly compared to the ages determined in the current study. Recently, Mark *et al.*, (2012), presented an age of 0.7764 ± 0.0018 (2σ; relative to ^{40}K decay constant of Renne *et al.*, 2011; which reduces the age by ~ 0.04 % compared to using the parameters presented in Renne *et al.*, 2010). Despite this relative change, their age is still within uncertainty (2σ) of the Rivera *et al.*, (2011) age of 0.7719 ± 0.0036 Ma (relative to Renne *et al.*, 2010), or 0.7715 ± 0.0036 Ma (relative to Renne *et al.*, 2011), and not ~ 6 ka older as reported.

Pre-eruptive residence times for the Long Valley Volcanic Field have previously been modelled using various isotopic studies (e.g., Rb-Sr and Ar-Ar), and haven inferred lengthy residence times. Haliday *et al.*, (1989) used Rb/Sr and ε_{Nd} data to allude to magma residence times in the order of 10^5 to 10^6 years, suggesting the nature of the Sr-depleted rhyolites of the Glass Mountain and Bishop Tuff imply extensive crystallisation during a long residence time. Similar Rb-Sr model ages for various feldspar crystals and melt inclusion bearing quartz (MIBQ), were interpreted as representing a possible 0.3 to 1.7 Myr residence time (e.g., Christiansen and DePaolo, 1993; Davies and Halliday, 1998), however the Rb-Sr isotopic study by Christiansen and DePaolo (1993) inferred a small fraction of biotite analysed was xenocrystic and sourced from roof-rock material, incorporated during the eruption.

van den Bogaard and Schirnick (1995) suggested Ar-Ar ages determined on quartz hosted melt inclusions were representative of Bishop Tuff magma residence timescales and not $^{40}Ar_E$ contamination. The study hypothesised quartz phenocrysts grew, trapped glass inclusions which contained Ar with initial atmospheric ratio, and remained a closed system with respect to Ar at 2.3 to 2 Ma. This was later challenged by the work of Winick *et al.*, (2001) who presented evidence to support $^{40}Ar_E$ contamination of quartz, placing doubt on the ability of melt inclusions to accurately record a residence time. To date, the

occurrences of $^{40}Ar_E$ in Bishop Tuff feldspar phases has been negligible. Both Izett and Obradovich (1994) and Rivera *et al.*, (2011), reported inverse isochron $^{40}Ar/^{36}Ar$ intercepts within uncertainty of atmospheric value. Winick *et al.*, (2001) predicted possible $^{40}Ar_E$ contamination of sanidine, but suggest K content of sanidine may be capable of masking the effects. It may be possible $^{40}Ar_E$ contamination will be more easily identifiable in K poor phases (e.g., plagioclase), and it may be possible to test that in this study.

The range of Bishop Tuff zircon crystallisation ages has also been determined by the fission-track (e.g., Izett and Naeser, 1976); U-Pb (ID-TIMS; e.g., Crowley *et al.*, 2007), and U-Pb methods (SIMS; e.g., Reid and Coath, 2000; Simon and Reid, 2005). Izett *et al.*, 1988 remarked that their average K-Ar age of the lower air-fall unit was nearly identical to the average zircon fission-track age (0.74 ±0.05 Ma) from the same unit reported by Izett and Naeser, (1976); however older K-Ar age determinations were plagued by xenocryst contamination. Reid and Coath (2000), reported zircon crystallisation ages determined on plinian ash fall and early ignimbrite units. Zircon interiors recorded an average U-Pb age of 0.823 ± 0.011 Ma, suggesting the Bishop Tuff magma chamber erupted shortly after it began to crystallise (~ 100 kyr). One zircon from the fallout deposit yielded ages in excess of 200 Ma and was inferred to be a zircon xenocryst sourced from the nearby Triassic Wheeler Crest Quartz Monzonite. A study carried out by Simon and Reid (2005), also reported identical mean zircon crystallisation ages (~ 90 kyr older than the caldera forming eruption) for samples of early and late erupted Bishop Tuff.

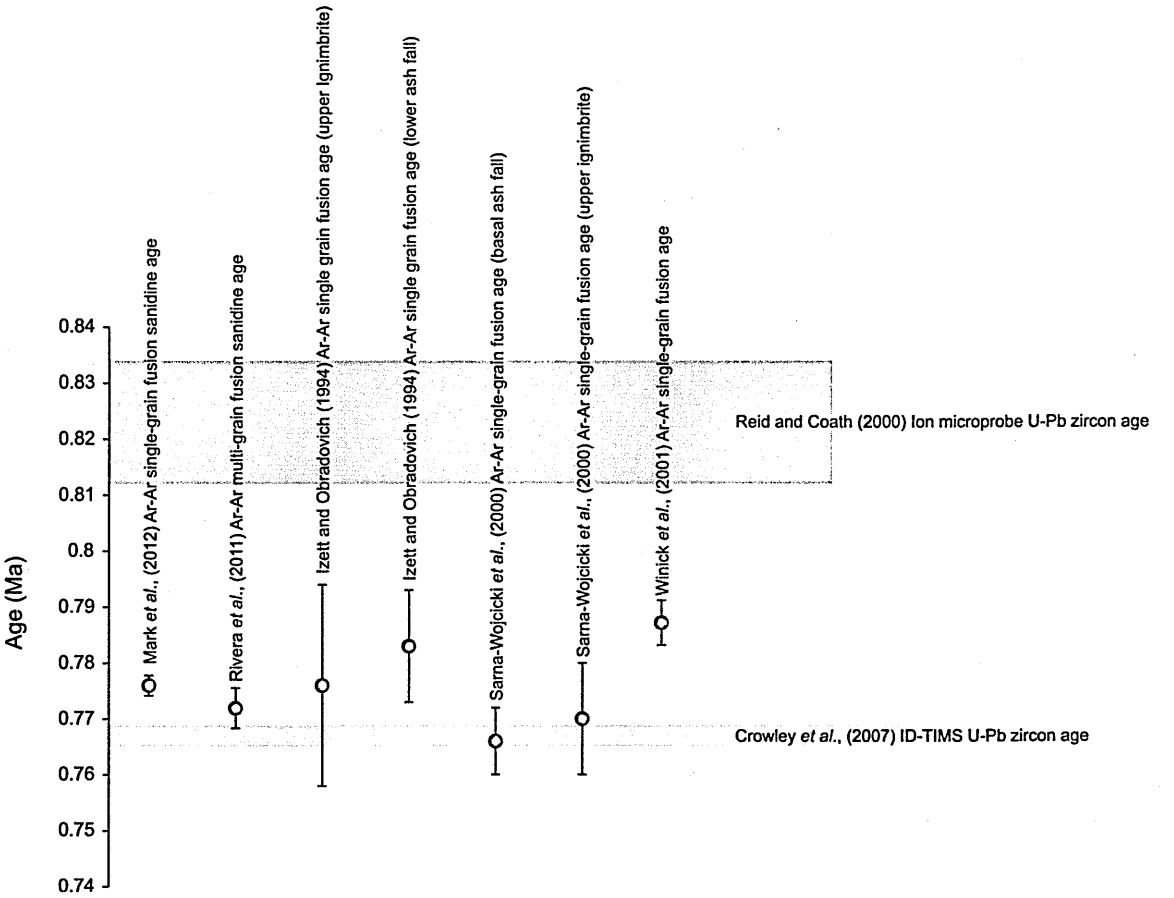

Figure 4.3. Summary of previously published Ar-Ar ages (red circles) and U-Pb zircon ages (grey boxes) for the Bishop Tuff. Uncertainties are reported as ± 2σ and Ar-Ar ages shown have been calculated relative to the ^{40}K decay constant of Renne *et al.*, (2010).

Crowley *et al.*, (2007) reported a mean U-Pb zircon age of 0.7671 ± 0.0019 Ma (2σ), determined on zircons extracted from densely welded vitrophyre concluding a magma residence time of < 10 kyr prior to eruption. The study questioned the validity of the U-Pb ages presented by Simon and Reid (2005), which inferred a longer residence time. Several Bishop Tuff eruption ages reported by Rivera *et al.*, (2011), relative to different ^{40}K decay constants and standard ages, overlap (at the 2σ level) with the U-Pb zircon age of Crowley *et al.*, (2007). Figure 4.3 illustrates that the recalculated ages of Sarna-Wojcicki *et al.*, (2000), as well as the Rivera *et al.*, (2011) age (relative to ^{40}K decay constant of Renne *et al.*, 2010), overlap at the 2σ level, and although Mark *et al.*, (2012) claim their age (0.7764 ± 0.0018 Ma; 2σ) is 'indistinguishable' from the age presented by Crowley *et al.*, (2007;

age of 0.7671 ± 0.0018 Ma; 2σ), the age reported by Mark *et al.*, (2012) is older than the U-Pb zircon age.

Investigations into the geochronological information recorded by Bishop Tuff zircons is continuing to be considered and a U-Pb zircon study is being carried out concurrently with this work (K. Chamberlain and C. Wilson, *pers. com.*, 2011; 2012). Preliminary work has so far revealed ages that tail-back to ~ 0.840 Ma, but the majority of zircon rims reveal ages around 0.778 to 0.780 Ma, again reaffirming the idea that zircons began crystallising in an integrated magma reservoir ~ 100 kyr prior, and up to the point of eruption (C. Wilson, *pers. com.*, 2012). Despite previous isotopic studies providing evidence to support a long (> 500 kyr) magma residence time (e.g., Christiansen and DePaolo, 1993; van den Bogaard and Schirnick, 1995), ion-probe (U-Pb) dating of zircons, one of the earliest crystallising phases in the Bishop Tuff magma, have revealed crystallisation ages of no more than ~ 160 kyr older than eruption with grain to grain ages ranging from near to eruption age and back to ~ 0.9 Ma (e.g., Reid and Coath, 2000; Simon and Reid, 2005; Hildreth and Wilson, 2007).

4.4 Materials and methods

4.4.1 Sample descriptions

Pumices in Bishop Tuff fall units and flow packages exhibit a variety of textures and have been divided into a dominant normal spectrum, based on crystal content (< 1 % to 25 wt. %), and textures, plus rare variant types, divided into sub-groups (glistening, swirly, dark, Dacite; see Hildreth and Wilson, 2007). Pumices separated from various fall and flow units, which fall within the 'normal spectrum' have been used for Ar-Ar age

determinations, and rare pumices have not been dealt with in this study. For representative thin section images and locality information see Appendix section A2.

Table 4.1. Summary table detailing sample lithology, main groundmass and phenocryst descriptions for Bishop Tuff samples analysed in this study (AF = ash fall deposit; IgF = ignimbrite flow).

			Assemblage	
Sample	**Unit**	**Lithology**	**Groundmass**	**Main Phenocryst**
BP029	F5	Pumice (AF)	High silica rhyolite	Sanidine-plagioclase-quartz-
CMW12	F7	Multiple pumice (AF)	High silica rhyolite	Sanidine-plagioclase-quartz-biotite
BP097	Ig1Eb	Pumice (IgF)	High silica rhyolite	Sanidine-plagioclase-quartz-biotite
BP113	Ig2NWa	Pumice (IgF)	High silica rhyolite	Sanidine-plagioclase-quartz-
BP168	Ig2Nb	Pumice (IgF)	High silica rhyolite	Sanidine-plagioclase-quartz-pyroxene-biotite

BP029

Sample BP029 is representative of the normal pumice range erupted early in the Bishop Tuff sequence and deposited as fall unit F5. Individual pumices range 2 to 5 cm in length. Pumice clasts are noticeably low density, crystal poor (previously estimated < 6 wt. % crystals; Hildreth and Wilson 2007) and highly porous. Some exhibit a smooth, appearance and microvesicular texture, whilst others appear frothy with large vesicles, often stretched to define a fine lineation. The majority are white in colour suggesting they have not been oxidised. Inclusion-rich phenocrysts of feldspar and quartz, which vary in size (< 500 μm to > 1 mm) are set in a glassy groundmass.

CMW12

Sample CMW12 is similar to BP097 (low density and crystal poor), and is representative of the coarser fall unit F7. Individual pumice clasts are white in colour, range in size from

fist to block sized, and contain both intact and highly fractured feldspar phenocrysts, as well as minor biotite.

BP097

Sample BP097 (three individual pumices), collected from the non-welded basal flow unit of ignimbrite package Ig1Eb, is representative of the most voluminous package of ignimbrite on the eastern side. Pumices are crystal poor, low density and highly vesicular. A weak fibrous texture is defined by slightly elongated vesicles. The glassy groundmass wraps around sparse phenocrysts of quartz and feldspar, which are often fragmented. Plagioclase feldspar is the dominant phase and minor biotite is also present.

BP113

Sample BP113 is representative of the earliest eruptives from vents on the north side of the caldera and was taken from the proximal, non-welded base of ignimbrite package Ig2NWa. Sampling locality is the same as previously documented by Anderson *et al.*, (2000). Pumice is predominantly crystal rich containing isolated phenocrysts and clusters of crystals, some cloudy in appearance. Groundmass fabric is coarsely fibrous and has a crimped wavy texture. Although not found during this study, Anderson *et al.*, (2000) noted the inclusion of fragments of dark basaltic and intermediate volcanic and granitoid rocks within samples collected from this locality.

BP168

Sample BP168 is part of a single pumice block which was trimmed (removing pink-orange rind) to reveal a silver grey, dense, crystal rich and even textured interior. This sample is representative of the main ignimbrite (Ig2Nb) in that sector, north of the caldera. Glassy groundmass has a coarsely fibrous, crimped wavy texture and a silky appearance. Some pore spaces show evidence of discolouration (orange coating), possibly caused by

interaction with a vapour phase. The characteristic lineation is defined by extended vesicles and stringers of feldspar and quartz phenocrysts, many broken. Biotite and pyroxene are present in minor quantities, and some biotite appears to be fresh (in hand specimen and thin section).

4.4.2 Sample preparation and methods of chemical analysis

For XRF whole rock analysis, pieces of single pumice (or multiple whole pumice clasts; e.g., sample BP029; F5, and sample CMW12; F7), were crushed and powdered, and used to prepare XRF glass discs and powder pellets as outlined in Appendix section A1.8. XRF major and minor element results are given in Appendix section A4.1.1. Electron microprobe (Cameca SX100) analysis of feldspar crystals and biotite (sample BP168 only), carried out following methods outlined in Appendix section A1.9. Average mean probe analyses for each sample are listed in Table 4.2, and full data tables are presented in Appendix section A4.1.2.

4.4.3 Sample preparation for Ar-Ar analysis

Samples were prepared following the methods outlined in Appendix section A1.7. Where possible, intact feldspar crystals only were hand-picked using a binocular microscope from the 500 μm – 1mm sieve fraction. Biotite (samples CMW12, BP097 and BP168), was also hand-picked, but from the 250 to 500 μm sieve fraction as to avoid those that looked golden and flaky. Biotite grains that failed to survive this standard cleaning process (biotite separated from samples CMW12 and BP097), were reduced to minute fragments and were washed away. Samples were irradiated in two batches each for 1 hr (3 MWH).

4.4.4 Analytical methods: Ar-Ar age determinations

In order to investigate age variations at a single grain level of erupted feldspars (and biotite) from each sample, crystals were fused along with a zero-age basaltic glass bead flux (except biotite), following methods outlined in Appendix section A1.3, and corrected following the methods outlined in Chapter 3 (section 3.4.4). Full Ar-Ar data tables, calculated *J*-values and average blank levels used for data processing are presented in Appendix section A3.1.2. All errors quoted in the text and tables are reported at the 2σ level unless otherwise stated.

4.5 Results

4.5.1 Sample chemistry: EMP and XRF whole rock

Mean electron microprobe analysis (EMP) results for individual feldspar crystals separated from samples BP029, CMW12, BP097, BP113 and BP168 and biotite (separated from sample BP168 only) are given in summary Table 4.2. Individual feldspar compositions are displayed in An-Or-Ab ternary diagrams (Fig. 4.4). Full data tables are presented in Appendix section A4.

Table 4.2. Mean electron microprobe (bold, wt. %) analysis of all Bishop Tuff samples by phase. The standard deviation of mean is listed below the mean value, and the number of analysis used to calculate the mean is given as, n.). Full data tables are presented in Appendix section A4.1.2.

Sample	Phase	SiO_2	TiO_2	Al_2O_3	FeO	MnO	MgO	CaO	Na_2O	K_2O	BaO	SrO	F	Cl	Total
BP029	Sanidine	**66.50**	**0.01**	**18.20**	**0.07**	**0.00**	**0.00**	**0.16**	**3.94**	**11.02**	**0.02**	**0.04**	**0.03**	**0.00**	**99.64**
	n = 33	0.14	0.01	0.15	0.01	0.01	0.00	0.01	0.10	0.07	0.03	0.03	0.03	0.00	0.47
	Plagioclase	**65.07**	**0.01**	**21.22**	**0.12**	**0.00**	**0.00**	**3.12**	**9.21**	**1.18**	**0.01**	**0.04**	**0.01**	**0.00**	**99.69**
	n =6	0.21	0.01	0.17	0.01	0.00	0.00	0.19	0.11	0.07	0.01	0.04	0.02	0.00	0.44
CMW12	Sanidine	**66.42**	**0.01**	**18.14**	**0.08**	**0.00**	**0.00**	**0.17**	**3.90**	**11.19**	**0.02**	**0.04**	**0.02**	**0.01**	**97.69**
	n = 40	0.15	0.01	0.16	0.01	0.01	0.00	0.02	0.10	0.08	0.03	0.03	0.04	0.00	0.73
	Plagioclase	**65.08**	**0.02**	**21.05**	**0.13**	**0.01**	**0.00**	**3.11**	**9.24**	**1.29**	**0.02**	**0.04**	**0.02**	**0.01**	**98.01**
	n = 9	0.19	0.02	0.18	0.01	0.01	0.00	0.17	0.23	0.08	0.02	0.04	0.04	0.01	0.37
BP097 #1	Sanidine	**66.28**	**0.02**	**18.17**	**0.07**	**0.00**	**0.00**	**0.16**	**4.03**	**11.18**	**0.02**	**0.03**	**0.03**	**0.00**	**97.12**
	n = 22	0.15	0.02	0.20	0.01	0.01	0.00	0.01	0.14	0.14	0.02	0.03	0.04	0.00	1.29
	Plagioclase	**64.98**	**0.01**	**21.05**	**0.13**	**0.00**	**0.00**	**3.07**	**9.50**	**1.19**	**0.01**	**0.03**	**0.01**	**0.00**	**97.14**
	n = 10	0.30	0.02	0.22	0.02	0.01	0.00	0.18	0.09	0.05	0.01	0.02	0.02	0.00	0.96
BP097 #2	Sanidine	**66.48**	**0.02**	**18.23**	**0.07**	**0.00**	**0.00**	**0.16**	**3.91**	**11.05**	**0.02**	**0.03**	**0.03**	**0.00**	**99.65**
	n = 29	0.17	0.02	0.14	0.01	0.00	0.00	0.01	0.09	0.08	0.02	0.03	0.03	0.00	0.38
	Plagioclase	**65.24**	**0.01**	**21.17**	**0.12**	**0.01**	**0.00**	**3.04**	**9.18**	**1.17**	**0.01**	**0.03**	**0.02**	**0.00**	**99.71**
	n = 18	0.32	0.02	0.24	0.01	0.01	0.00	0.19	0.15	0.06	0.01	0.03	0.03	0.00	0.43
BP113	Sanidine	**66.02**	**0.03**	**18.58**	**0.09**	**0.00**	**0.00**	**0.24**	**3.72**	**11.04**	**0.21**	**0.05**	**0.03**	**0.00**	**100.38**
	n = 22	0.26	0.04	0.12	0.01	0.01	0.00	0.02	0.09	0.13	0.24	0.03	0.04	0.00	0.34
BP168	Sanidine	**65.75**	**0.02**	**18.64**	**0.10**	**0.00**	**0.00**	**0.27**	**3.66**	**11.06**	**0.40**	**0.07**	**0.03**	**0.00**	**100.30**
	n = 31	0.42	0.02	0.13	0.02	0.01	0.00	0.04	0.08	0.20	0.40	0.03	0.04	0.00	0.28
BP168	Biotite	**39.39**	**4.71**	**13.49**	**18.67**	**0.12**	**13.09**	**0.03**	**0.58**	**9.28**	**0.20**	**0.02**	**0.32**	**0.09**	**95.45**
	n = 19	0.75	0.12	0.24	0.61	0.02	0.44	0.05	0.10	0.14	0.25	0.02	0.24	0.01	0.94

n = number of analyses used to calculate the mean.

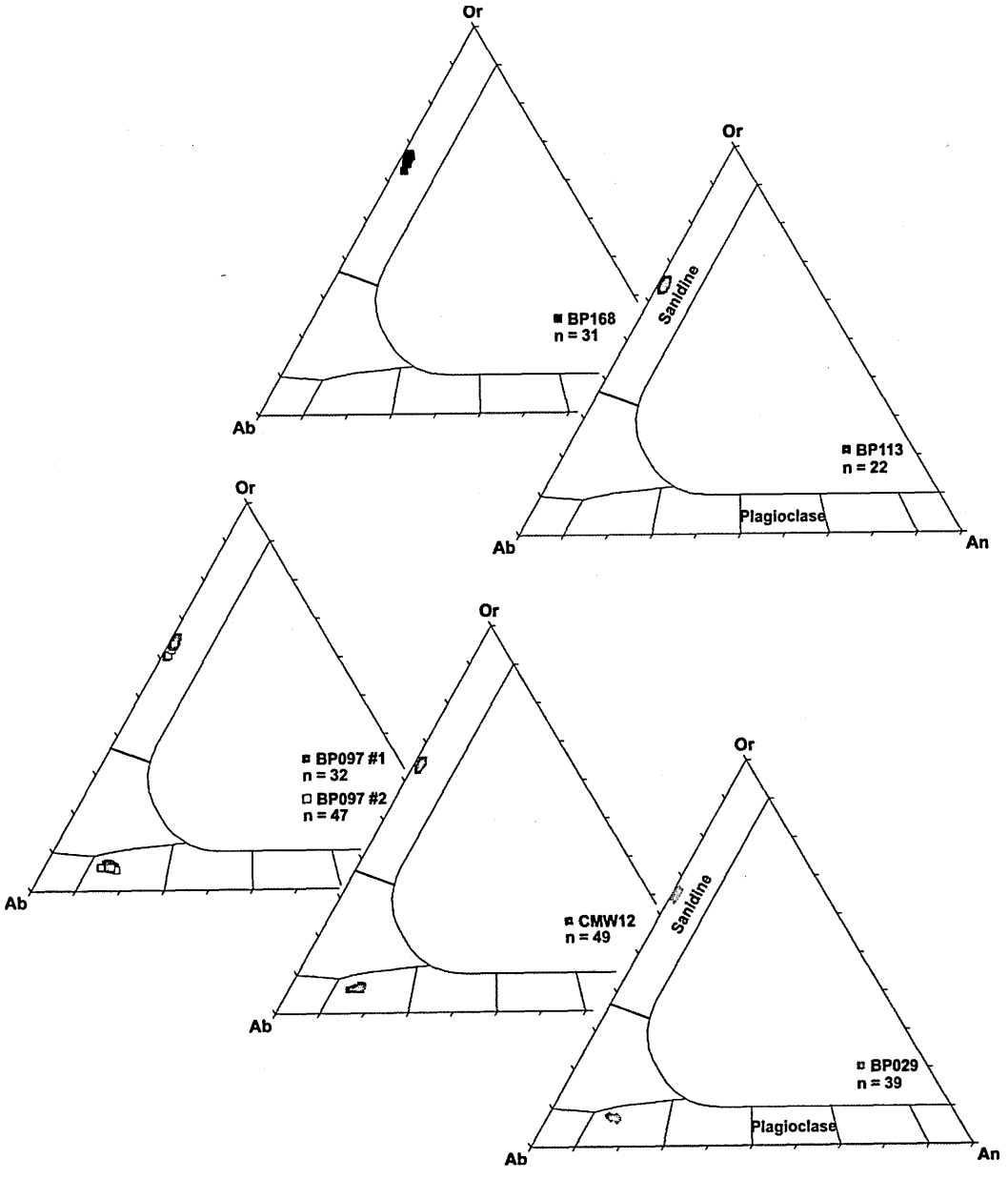

Figure 4.4. An-Or-Ab ternary diagrams showing individual feldspar compositions (determined by electron microprobe analysis) for each Bishop Tuff unit (samples BP029, CMW12, BP097, BP113, and BP168).

Feldspars from sample BP029 (unit F5), are sanidine (Or_{63} to Or_{66}) and plagioclase (An_{14} to An_{16}). Feldspar compositions for F7 are similar to unit F5, and sample CMW12 contained both sanidine (Or_{63} to Or_{67}), and plagioclase (An_{13} to An_{16}). Separated feldspars for ignimbrite unit Ig1Eb (sample BP079) are both sanidine (Or_{63} to Or_{67}), and plagioclase (An_{11} to An_{16}) in composition. Feldspars separated from two individual pumices (BP079 #1 and #2) showed no significant differences. In general the above samples (representing

the early erupted Bishop Tuff units); contain sanidine with ~ 11.00 % K_2O, and plagioclase with ~ 1.20 % K_2O.

Based on this EMP study, sanidine (~ 11.00 % K_2O) appears to be the dominant feldspar composition for the later erupted ignimbrite units Ig2NWa (sample BP113), and Ig2Nb (sample BP168). Sanidine composition range Or_{64} to Or_{67} for both samples. Sanidine compositions are in agreement with those determined in previous studies (e.g., sanidine = Or_{62-66}; Hildreth 1977, Anderson *et al.*, 2000). In addition, this EMP study found no obvious xenocrystic compositions (e.g., plagioclase cores = An_{32-48}; Hildreth, 1977). Mean K_2O and CaO values for biotite (separated from sample BP168 only) are 9.28 % and 0.03 % respectively.

XRF whole rock analysis

Hildreth and Wilson (2007) have identified various different pumice types in samples spanning the entire eruption of the Bishop Tuff. Pumice clasts in the Bishop Tuff are assigned to one of several types based on their primary textures and crystal content. The dominant 'normal' spectrum generally makes up 93 to 99 % of the juvenile clasts in all deposits, and ranges widely in crystal content (crystal-poor = xp, medium = xm, or crystal-rich = xr). In addition to the normal pumice spectrum, a number of variant types have also been identified and described, including rare glistening, swirly, and dark pumices (see Hildreth and Wilson (2007) for descriptions). Based on visual inspection in the field all pumice samples analysed fall into the dominant normal spectrum, and do not exhibit the textures of the rare pumice types.

Major oxide (wt. %), and trace element (ppm) analysis on whole rock samples (BP029, CMW12, BP097, BP113, BP168) are presented in Appendix section A4.1. The whole rock

value plots in the rhyolite field of the total-alkali-silica diagram (not shown). Selected major oxide and trace element contents have been compared with data of Hildreth and Wilson (2007) and are shown in Table 4.3. Data from this study are in good agreement with the normal pumice spectrum data of Hildreth and Wilson (2007), and therefore fall within this normal pumice range.

Table 4.3. Summary of the range of pumice compositions used in this study determined by XRF whole rock analysis compared with the data of Hildreth and Wilson (2007), which represents their range of normal pumice compositions.

Clast type		SiO_2	Al_2O_3	FeO*	MgO	CaO	Na_2O	K_2O	TiO_2	MnO
normal pumice suite*	xr	73.4 - 77.6	12.2 - 15.1	0.71 - 1.73	0.01 - 0.48	0.46 - 1.61	2.5 - 3.9	4.8 - 6.0	0.08 - 0.25	0.02 - 0.05
	xm	74.5 - 77.7	12.2 - 15.1	0.56 - 1.26	0.01 - 0.35	0.42 - 1.15	2.5 - 3.9	4.6 - 5.8	0.08 - 0.21	0.02 - 0.06
	xp	75.6 - 77.9	12.2 - 13.9	0.40 - 1.00	0.01 - 0.23	0.45 - 1.02	2.6 - 3.9	4.5 - 5.8	0.08 - 0.12	0.03 - 0.05
THIS STUDY^		**74.8 - 77.2**	**12.4 - 13.9**	**0.73 - 1.10**	**0.05 - 0.22**	**0.46 - 0.90**	**2.88 - 3.74**	**4.6 - 5.9**	**0.07 - 0.20**	**0.02 - 0.04**

Clast type		Rb	Sr	Ba	Y	Zr	Nb
normal pumice suite*	xr	75 - 183	10 - 185	5 - 614	8 - 27	71 - 154	7 - 25
	xm	85 - 195	9 - 116	2 - 474	9 - 33	75 - 138	9 - 31
	xp	125 - 198	9 - 49	2 - 140	20 - 31	75 - 102	14 - 26
THIS STUDY^		**87 - 180**	**4 - 112**	**10 - 498**	**11 - 25**	**84 - 126**	**10 - 22**

*** = reproduced from Hildreth and Wilson (2007); ^ = Range includes all samples analysed as part of this study (BP029; CMW12; BP079 #1 and #2; BP113, and BP168), normalised to 99.6 wt. % (leaving 0.4 wt. % for trace oxides and halogens); FeO* is total iron calculated as FeO.**

In order to carry out further comparison, XRF data determined as part of this study has been plotted along with the normal pumice spectrum data of Hildreth and Wilson (2007). In general the data obtained in this study fall within the normal pumice composition field defined by Hildreth and Wilson (2007). Figure 4.5 shows variation vs SiO_2 of key major oxide and trace element contents. Hildreth and Wilson (2007) reported data for the normal crystal-poor pumices cluster at the high-silica, low-Ca-Fe-Ti ends of the main arrays. This is also the case for the crystal-poor pumices used in this study (early erupted units F5, F7 and Ig1Eb). Pumices representing the later erupted units Ig2Nb and Ig2NWa are crystal-

rich, and have lower SiO_2 contents than crystal-poor pumice samples. These samples also have higher CaO, FeO*, and TiO_2 contents compared with the early erupted pumices.

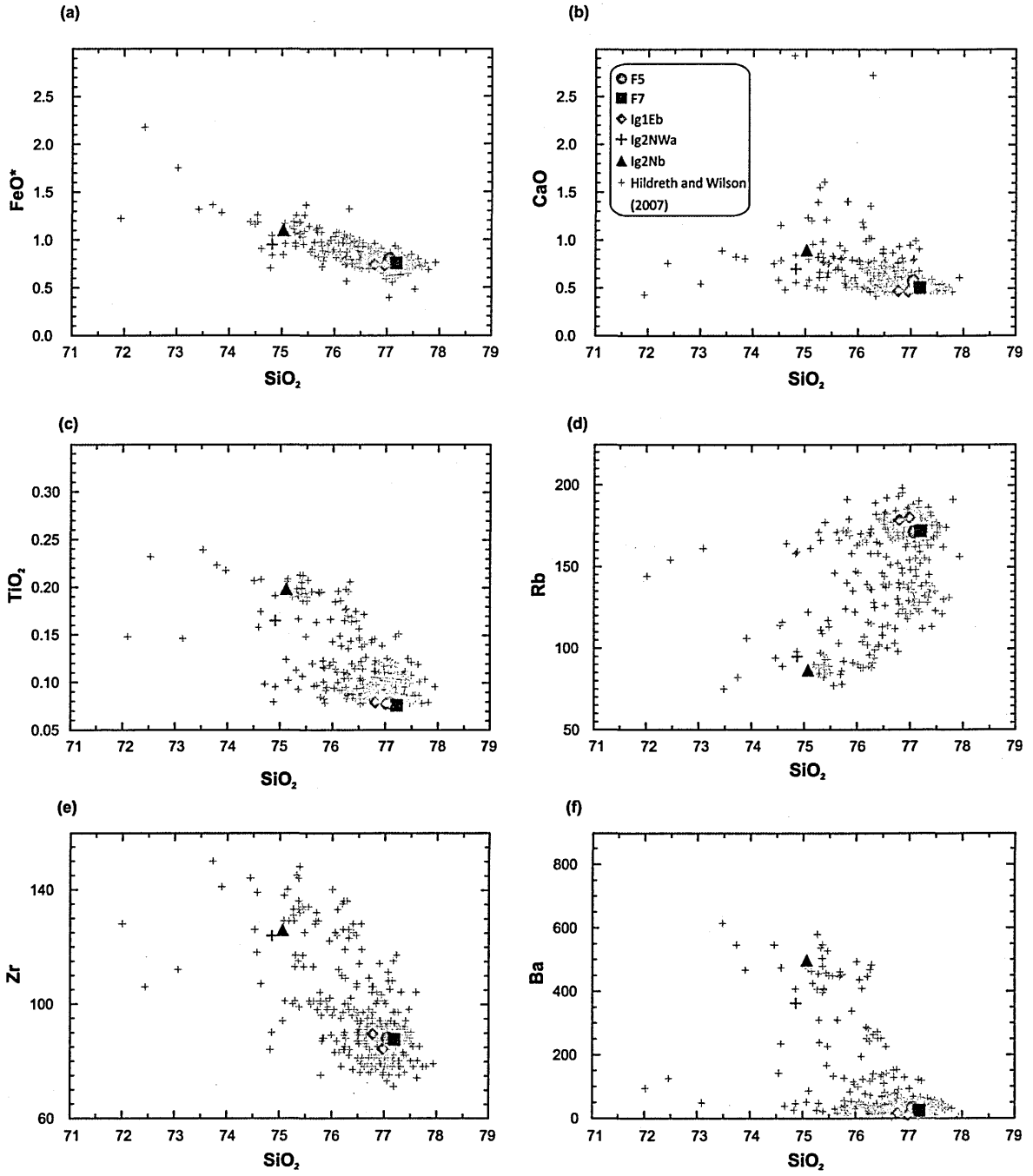

Figure 4.5. FeO*, CaO, and TiO_2 contents vs. SiO_2, and Rb, Zr, and Ba contents vs. SiO_2 (oxides in wt. %; elements in ppm), for pumice samples used in this study (coloured symbols). Also plotted for comparison are data from Hildreth and Wilson (2007), which represents the main xp-xm-xr suite of pumice clasts in the Bishop Tuff to show how the samples used in this study fit into the normal pumice range of Hildreth and Wilson (2007). Major element data has been normalised to 99.6 wt. % anhydrous (leaving 0.4 wt. % for trace oxides and halogens; after the method of Hildreth and Wilson (2007). FeO* is total iron calculated as FeO).

Hildreth and Wilson (2007), report high-silica crystal-poor normal pumice samples tend to be concentrated at the high-Rb, low-Zr, low Ba ends of the main arrays. Crystal-poor pumices used in this study also show this pattern, whereas crystal-rich pumices once again plot away from the crystal-poor pumices, and have comparatively low-Rb, high-Zr and high-Ba contents. Pumices of the plinian deposit (e.g., F5 and F7), and Ig1Eb represent the more evolved half of the compositional spectrum erupted. Figure 4.6 illustrates variations of Nb, TiO_2, Zr, and Ba/Sr ratio vs wt. % FeO*. Later erupted Ig2 pumices once again plot away from the early erupted plinian and Ig1 pumices, and have comparatively low-Nb, high-TiO_2, high-Zr and high-Ba/Sr ratio. In addition, Ig2 pumices also exhibit low-Rb, high-Zr, high-Ba, and high-Sr contents compared to the early erupted units. This was also noted by Hildreth and Wilson (2007), inferred to be characteristic of the crystal poor (feldspar deficient) nature of the earlier erupted units.

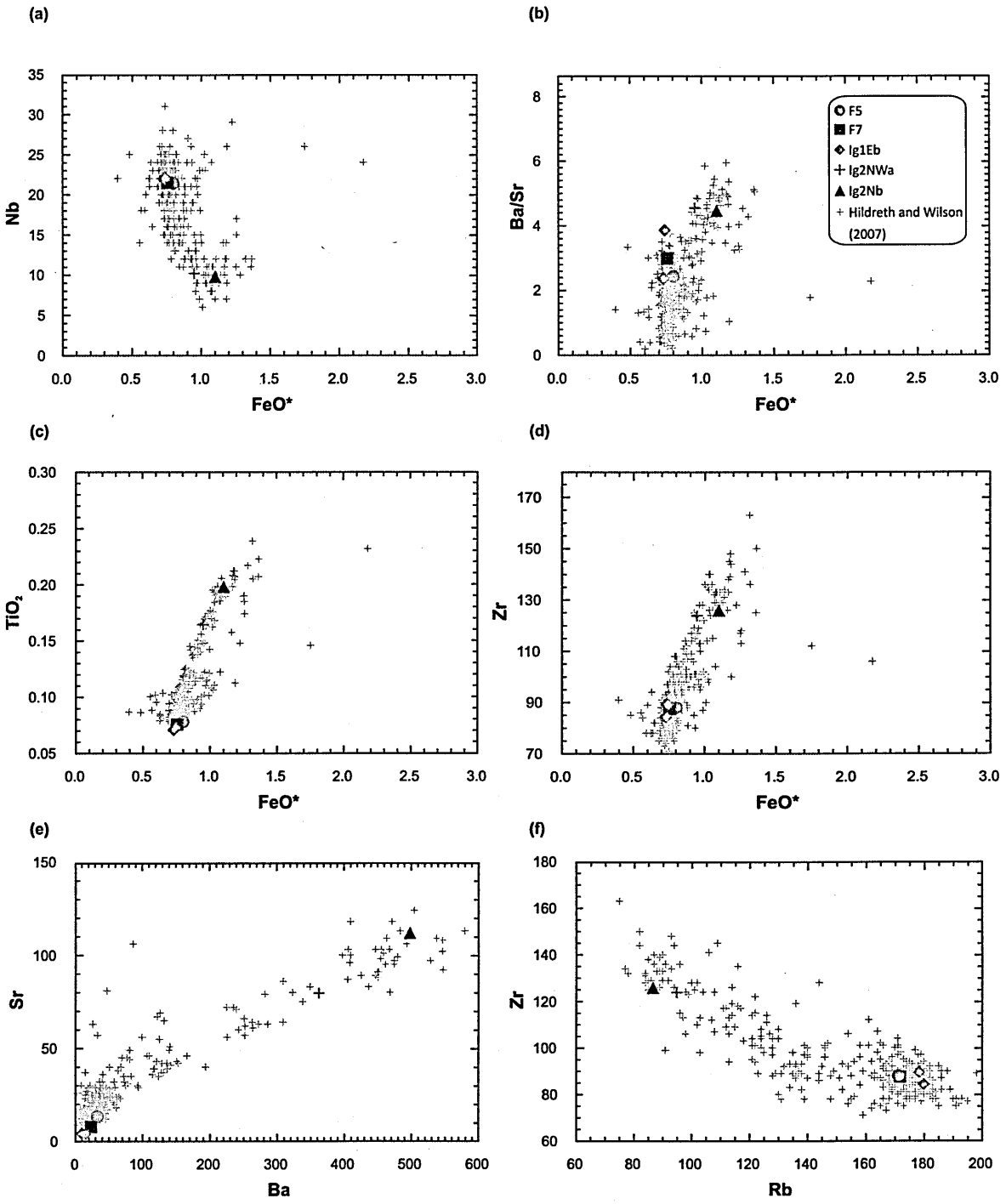

Figure 4.6. Variations of Nb, TiO_2, and Zr vs. FeO* and Ba/Sr ratio vs. wt. % FeO*, and variations of Sr vs. Ba, and Zr vs. Rb (oxides in wt. %; elements in ppm), for pumice samples used in this study (coloured symbols). Also plotted for comparison are data from Hildreth and Wilson (2007), which represents the main xp-xm-xr suite of pumice clasts in the Bishop Tuff to show how the samples used in this study fit into the normal pumice range of Hildreth and Wilson (2007). Major element data has been normalised to 99.6 wt. % anhydrous (leaving 0.4 wt. % for trace oxides and halogens; after the method of Hildreth and Wilson, 2007. FeO* is total iron calculated as FeO).

4.5.1.1 Alteration indices

Samples containing high proportions of glass and mineral phases, such as feldspars, are particularly susceptible to weathering, resulting in the production of secondary clay minerals (e.g., kaolinite, illite and smectite) (Harnois, 1988). The samples used in this study are glassy pumices which exhibit a range of crystal content. Thin section analysis has highlighted possible minor alteration of glass (e.g., sample CMW12) and feldspar phases (e.g., sample BP168), although this was rare. Fresh biotite has been extremely difficult to locate and the majority of biotite present was golden brown and flaky. The weathering rate of biotite has been reported to be slightly more rapid, but similar to that of plagioclase (e.g., Nesbitt and Young, 1984), therefore it is important to fully characterise the samples used in this study and attempt to determine the level of alteration potentially experienced by mineral phases used for Ar-Ar dating.

One possible method is to calculate weathering index values for selected samples and make comparison between the samples, which may have experienced different post-eruptive histories. Weathering and alteration indices combine molecular proportions of oxides (calculated from the percentage of each oxide based on weight), to produce a single value for each sample, which is then compared to the indices optimum fresh and optimum weathered values (Price and Velbel, 2003). Different weathering indices can be used to assess the degree of alteration of a particular sample and indices suitable for volcanic rocks, previously used to assess glass-rich samples (e.g., Clay *et al.*, 2012), include the Chemical Index of Alteration (CIA; Nesbitt and Young, 1982); the Chemical Index of Weathering (CIW; Harnois, 1988) and the Weathering Index of Parker (WIP; Parker, 1970). These indices are most suitable because they exclude iron from their calculations. An increase in iron can compensate for the loss of alkalis, therefore resulting in an index value reflecting a less advanced stage of weathering (Price and Velbel, 2003).

Calculations

The CIA of Nesbitt and Young (1982) considers K_2O as a mobile component (Eq. 4.1), and suggests the degree of weathering is proportional to the conversion of feldspar to clay. The CIW (e.g., Harnois, 1988), is similar to the CIA, however it eliminates K_2O from the equation (Eg. 4.2), and considers CaO and Na_2O as mobile components. Values for K-feldspar rich rocks, irrespective of how chemically weathered the feldspars might be, may be higher because the CIW does not consider the mobility of K_2O (Price and Velbel, 2003). The WIP (Parker, 1970) is an index of weathering for silicate rocks, based on proportions of Na, K, Mg and Ca present and their relative mobility based on bond strength with oxygen (Eq. 4.3).

$$\text{CIA} = (100) * \left(\frac{Al_2O_3}{Al_2O_3 + CaO + Na_2O + K_2O}\right) \quad (4.1)$$

$$\text{CIW} = (100) * \left(\frac{Al_2O_3}{Al_2O_3 + CaO + Na_2O}\right) \quad (4.2)$$

$$\text{WIP} = (100) * \left(\frac{2Na_2O}{0.35} + \frac{MgO}{0.90} + \frac{2K_2O}{0.25} + \frac{CaO}{0.7}\right) \quad (4.3)$$

The Plagioclase Index of Alteration (PIA; Eq. 4.4), proposed by Fedo *et al.*, (1995) can be used as an alternative to the CIW, because it considers plagioclase, which is abundant in silicate rocks, and can dissolve relatively rapidly. This index can be applied if plagioclase weathering needs to be monitored. For example pumice samples used in this study (especially those erupted early in the sequence) contain a high proportion of plagioclase, and therefore significant alteration will have implications for Ar-Ar ages obtained using this phase.

$$\text{PIA} = (100) * \left(\frac{Al_2O_3 - K_2O}{Al_2O_3 + CaO + Na_2O - K_2O}\right) \quad (4.4)$$

Table 4.4. Summary table of alteration and weathering indices for whole rock samples of the Bishop Tuff fall units and flow packages.

Index	Optimum fresh value	Optimum weathered value	BP029	CMW12	BP079 #1	BP079 #2	BP113	BP168
CIA*	<50	100	51	51	51	51	53	51
CIW$^+$	<50	100	64	67	66	66	70	65
WIP$^¥$	>100	0	73	73	76	76	78	79
PIA^	<50	100	51	52	52	52	56	51

(CIA* = Chemical Index of Alteration, CIW$^+$ = Chemical Index of Weathering, WIP$^¥$ = Weathering Index of Parker, PIA^ = Plagioclase Index of Alteration). CaO calculated as following to remove minor calcium contribution from apatite: $CaO = CaO_{total} - (10/3) * P_2O_5$ (after Fedo *et al.*, 1995; Price and Velbel, 2003).

Comparing weathering index values to optimum fresh and weathered values (listed in Table 4.4), the CIA and PIA index gives values of 51 to 53 and 51 to 56 respectively, which are close to the optimum fresh value (< 50), and suggest pumice samples are fresh and lack significant alteration. The CIW index gives values that range 64 to 70 and are notably higher than the optimum fresh value of < 50, which may indicate minor chemical weathering has taken place. However, CIW values are expected to be slightly higher than CIA values, owing to the fact that the CIW index does not consider the mobility of K_2O (Price and Velbel, 2003). The WIP index gives yields values that range 73 to 80, which although fall below 100 (optimum fresh value), they are significantly greater than 0 (the optimum weathered value). In summary the values obtained using the different indices do not vary significantly between samples and in general results suggest samples are not significantly disturbed.

4.5.1.2 Alkali mobility

Applying the above weathering indices to samples used in this study has not been particularly useful. Hildreth and Wilson (2007) used alkali mobility (K and Na), as a method of assessing the degree of weathering. Interaction with fluids during weathering can result in major element mobility (e.g., Na, K, Mg and Ca), which has serious implications for K- and Ar-loss and therefore Ar-Ar dating of such samples. Therefore it may be more informative to compare samples used in this study with the alkali mobility plots of Hildreth and Wilson (2007).

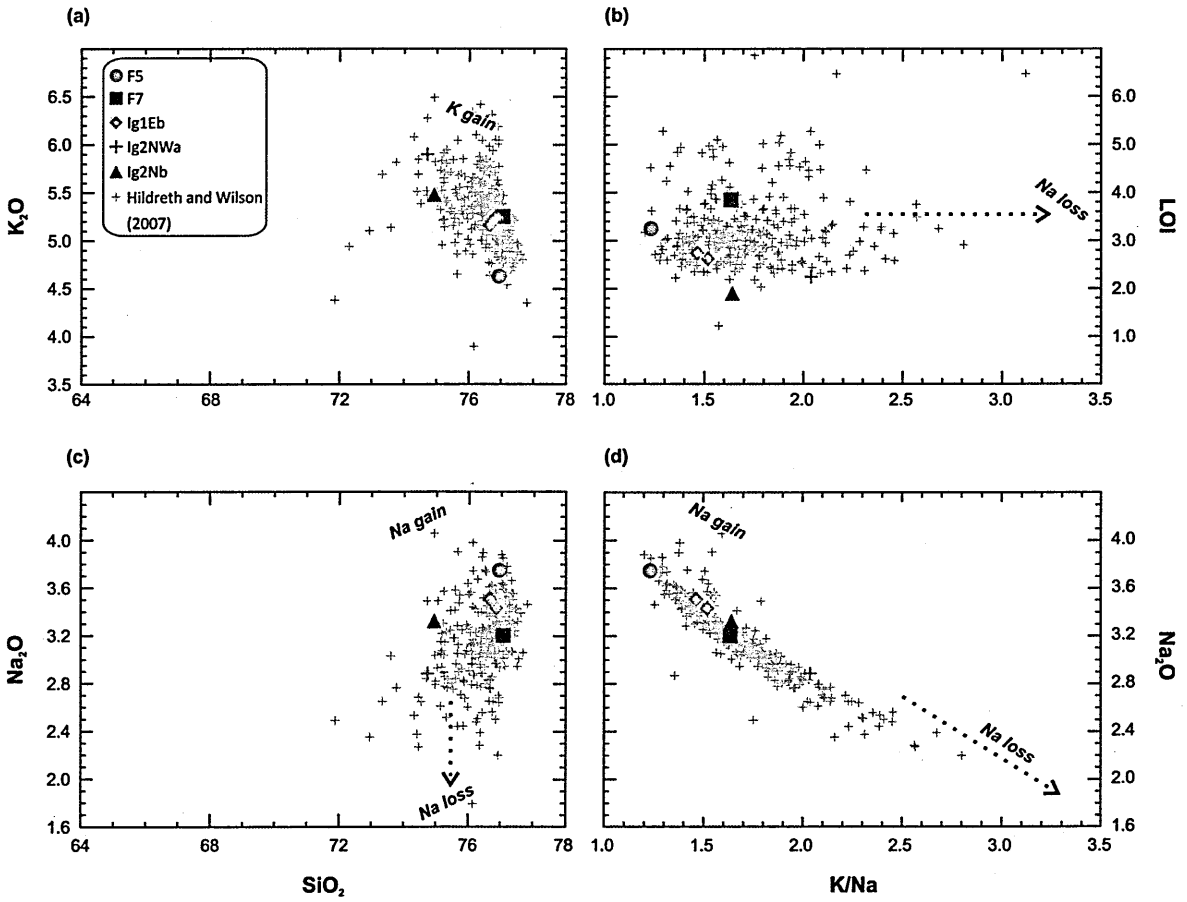

Figure 4.7. Alkali variation and mobilisation for pumice samples used in this study (coloured symbols). (a) K_2O vs. SiO_2 (K gain marked on to highlight variation of K in samples); (b) L.O.I. (wt. %) vs. K/Na wt. ratio (Na loss trend marked on to highlight mobilisation of Na in samples); (c) Na_2O vs. SiO_2 (Na loss trend and Na gain marked on to highlight variation and mobilisation of Na in samples); (d) Na_2O vs. K/Na wt. ratio (Na loss trend and Na gain marked on to highlight variation and mobilisation of Na in samples). Also plotted for comparison are data from Hildreth and Wilson (2007), which represents the main xp-xm-xr suite of pumice clasts in the Bishop Tuff to show if samples used in this study have undergone significant hydration or alkali mobility (oxides

(*Fig. 4.7 cont.*) in wt. %; normalised to 99.6 wt. % anhydrous (leaving 0.4 wt. % for trace oxides and halogens; after the method of Hildreth and Wilson, 2007).

Figure 4.7 confirms samples analysed in this study fall comfortably within the range previously published by Hildreth and Wilson, 2007, and although there is variation between individual pumices, there is no evidence to support significant alkali mobility in the samples used in this study. Excess K_2O (> 6 wt. %), has not been identified in samples used in this study, which have K_2O values that range 4.5 to 5.8 wt. % (Fig. 4.7a). K/Na wt. ratio vs. loss on ignition (L.O.I.; determined at 900 to 1000 °C), is a rough measure of the degree of hydration. The L.O.I. values range 1.89 to 3.84 wt. %, and samples fall within the field defined by Hildreth and Wilson (2007). In particular, values do not extend to higher K/Na ratios, which would indicate Na loss has occurred (Fig. 4.7b). Hildreth and Wilson (2007) suggested Na_2O values < 2.8 wt. % may indicate samples have lost Na, while a value of > 3.8 wt. % may indicates Na gain. Samples in this study have Na_2O values that fall within this range (Fig. 4.7c), and therefore do not appear to have undergone Na loss or gain. The final panel (Fig. 4.7d), shows Na_2O vs. K/Na wt. ratio, and again the samples used in this study fall within the field previously defined, and show no substantial Na loss or gain.

4.5.2 Ar-Ar ages: single-grain fusion results

Ar-Ar data from laser-probe single-grain fusion experiments of Bishop Tuff feldspar (all samples), and biotite (sample BP168 only) are summarised in Table 4.5. Complete data tables can be found in Appendix section A3.1.2. Weighted mean ages (± 2σ; MSWD value), inverse isochron analyses and probability density plots have been calculated using Isoplot (K. Ludwig, 2011), and details are discussed in Appendix section A1.6.2. Some samples require more than one inverse isochron to be plotted, representing the separate

packets containing the sample during irradiation and therefore the unique *J*-value assigned to each packet. In addition, summary tables also include the arithmetic mean, which is given for reference only. The weighted mean age has been taken in all cases and discussed throughout the text.

4.5.2.1 Sample BP029 (F5)

$^{40}Ar/^{39}Ar$ total-fusion ages obtained from single feldspar grains range 0.435 ± 0.612 to 1.190 ± 0.436 Ma and yield a weighted mean age of 0.763 ± 0.010 Ma (n = 43; MSWD = 0.75). This sample split contained 12 plagioclase grains ($^{37}Ar/^{39}Ar$ ratio ~ 0.8 to ~ 1.3), which are responsible for the lower and upper limits of the range of ages seen. The PDF peak, defined by the age probability plot for all analyses (Fig. 4.8a) has a mode at ~ 0.766 Ma, and a smaller peak at about 0.73, although the variation is within analytical errors. The probability plot for sanidine only (Fig. 4.8b), has a more symmetrical shape. The age range achieved determined on sanidine fall between the plagioclase and yield a weighted mean age of 0.763 ± 0.011 Ma (n = 31; MSWD = 0.77). Plagioclase on its own yielded a weighted mean age of 0.76 ± 0.13 Ma (n = 12; MSWD = 0.76). All weighted mean ages are in agreement.

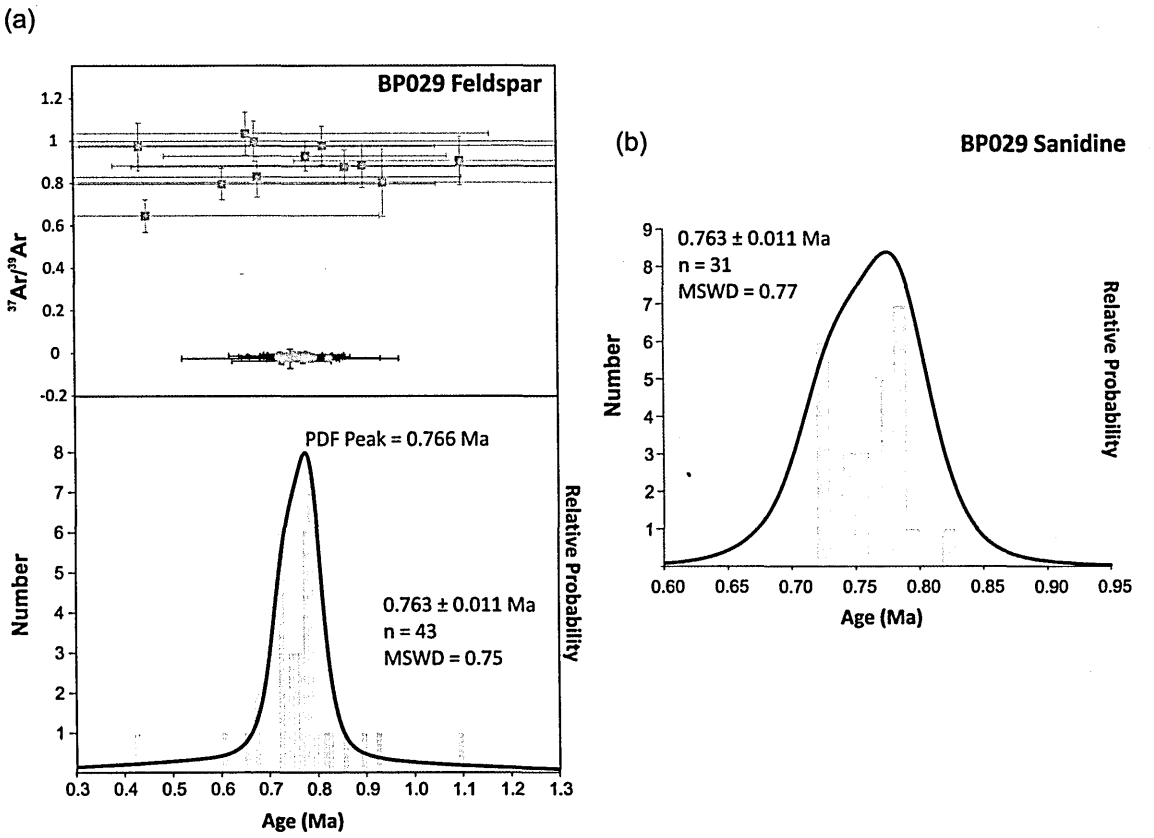

Figure 4.8. (a) Age probability distribution diagram and age vs. $^{37}Ar/^{39}Ar$ correlation plot for all feldspar analyses (plagioclase and sanidine) for Fall unit F5 (sample BP029); (b) Age probability distribution diagram for sanidine only. PDF peak (value at x at which the probability density function has its maximum value) for data set is given for both (a) and (b), and the weighted mean ages (determined separately using Isoplot; Ludwig, 2011), are also shown. All errors shown are 2σ.

An inverse isochron age of 0.770 ± 0.014 Ma (MSWD = 0.73) including both sanidine and plagioclase (Fig. 4.9a) is indistinguishable from inverse isochron ages obtained from sanidine (0.770 ± 0.015 Ma; MSWD = 0.78) and plagioclase (0.85 ± 0.18 Ma; MSWD = 0.67) individually. Despite large uncertainties for plagioclase analyses, due to small amounts of measurable K (McDougall and Harrison, 1999), and the sanidine isochron showing clustering of data near the $^{39}Ar/^{40}Ar$ axis and limited dispersion along the mixing line, all initial $^{40}Ar/^{36}Ar$ rations are within error of atmospheric value 298.56, suggesting the trapped component is of atmospheric composition.

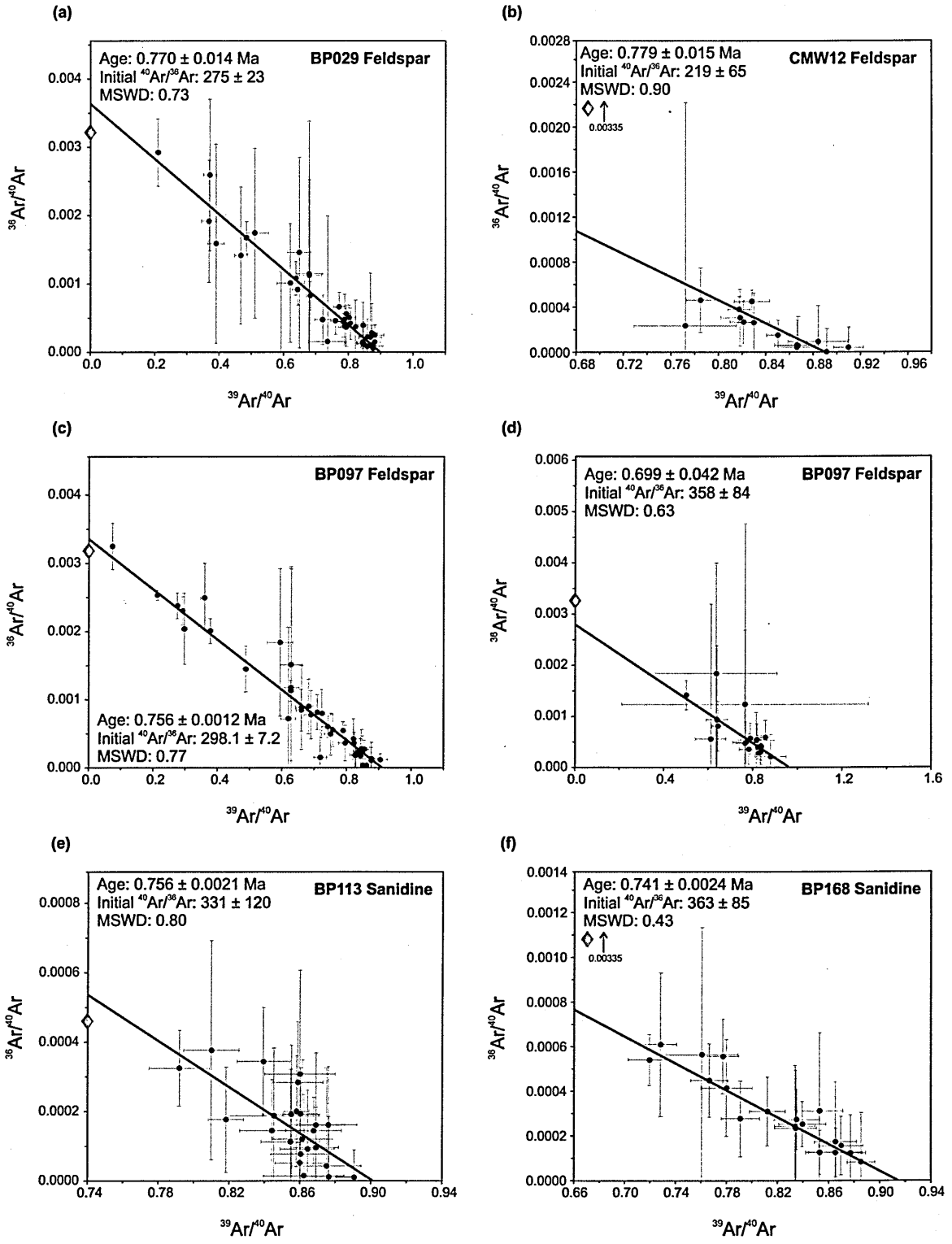
(a)
Age: 0.770 ± 0.014 Ma
Initial $^{40}Ar/^{36}Ar$: 275 ± 23
MSWD: 0.73
BP029 Feldspar
$^{36}Ar/^{40}Ar$
$^{39}Ar/^{40}Ar$
(b)
Age: 0.779 ± 0.015 Ma
Initial $^{40}Ar/^{36}Ar$: 219 ± 65
MSWD: 0.90
CMW12 Feldspar
0.00335
$^{36}Ar/^{40}Ar$
$^{39}Ar/^{40}Ar$
(c)
BP097 Feldspar
Age: 0.756 ± 0.0012 Ma
Initial $^{40}Ar/^{36}Ar$: 298.1 ± 7.2
MSWD: 0.77
$^{36}Ar/^{40}Ar$
$^{39}Ar/^{40}Ar$
(d)
Age: 0.699 ± 0.042 Ma
Initial $^{40}Ar/^{36}Ar$: 358 ± 84
MSWD: 0.63
BP097 Feldspar
$^{36}Ar/^{40}Ar$
$^{39}Ar/^{40}Ar$
(e)
Age: 0.756 ± 0.0021 Ma
Initial $^{40}Ar/^{36}Ar$: 331 ± 120
MSWD: 0.80
BP113 Sanidine
$^{36}Ar/^{40}Ar$
$^{39}Ar/^{40}Ar$
(f)
Age: 0.741 ± 0.0024 Ma
Initial $^{40}Ar/^{36}Ar$: 363 ± 85
MSWD: 0.43
BP168 Sanidine
0.00335
$^{36}Ar/^{40}Ar$
$^{39}Ar/^{40}Ar$

(Figure 4.9)

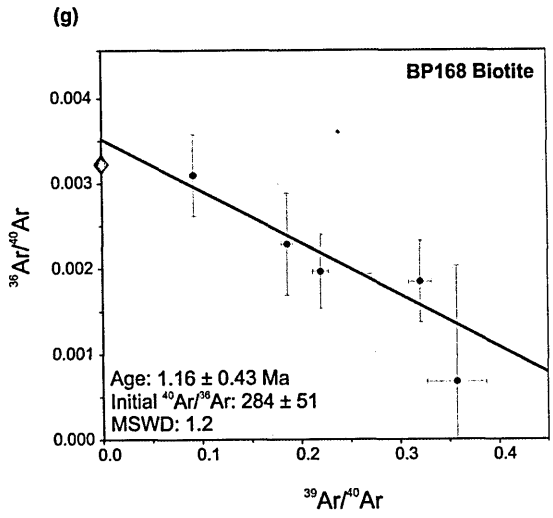

Figure 4.9. (including preceding page) Isotope correlation plots (inverse isochron) for all Bishop Tuff samples (determined using Isoplot; Ludwig, 2011). (a) BP029 Feldspar (sanidine and plagioclase); (b) CMW12 Feldspar (sanidine and plagioclase); (c) and (d) BP097 Feldspar (sanidine and plagioclase); (e) BP113 sanidine; (f) BP168 sanidine and (g) BP168 biotite. Red diamond indicates intercept of modern air (0.00335).

4.5.2.2 Sample CMW12 (F7)

$^{40}Ar/^{39}Ar$ total-fusion ages obtained from single feldspar grains range 0.723 ± 0.029 to 0.966 ± 0.300 Ma and yield a weighted mean age of 0.766 ± 0.012 Ma (n = 17; MSWD = 1.3). The age probability plot (Fig. 4.10) overall shows a symmetrical distribution and a PDF modal value of ~ 0.772 Ma. Only two plagioclase grains were analysed from this sample and both fall within 2σ error of sanidine ages. An inverse isochron age of 0.779 ± 0.015 Ma (MSWD = 0.90) is in agreement with the weighted mean age, however an initial $^{40}Ar/^{36}Ar$ ratio of 219 ± 65 is slightly less than the generally accepted value of 298.56 (Fig. 4.9b).

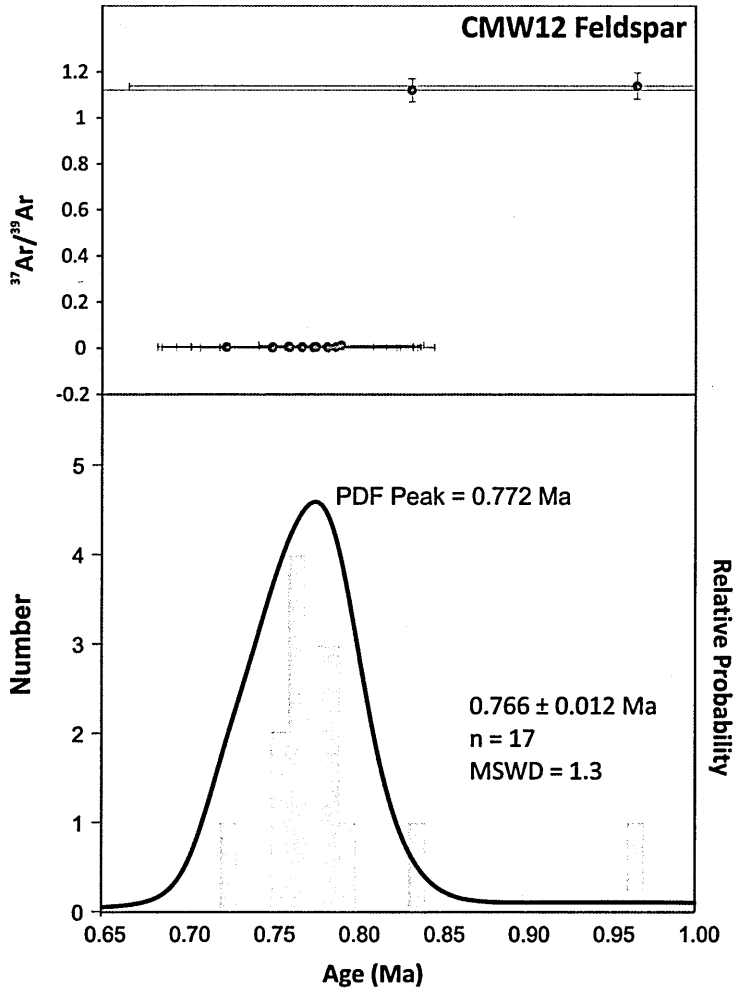

Figure 4.10. Age probability distribution diagram and age vs. $^{37}Ar/^{39}Ar$ correlation plot for fall unit F7 (sample CMW12). PDF peak (value at x at which the probability density function has its maximum value) for data set are also given and the weighted mean age (determined separately using Isoplot; Ludwig, 2011), is also shown. All errors shown are 2σ.

4.5.2.3 Sample BP097 (Ig1Eb)

$^{40}Ar/^{39}Ar$ total-fusion ages have been obtained from two individual pumices (BP097 #1 and BP097 #2) and ages range 0.371 ± 0.927 to 1.107 ± 0.371 Ma and yield a weighted mean age of 0.749 ± 0.008 Ma (n = 60; MSWD = 0.88). The PDF peak, defined by the age probability plot (Fig. 4.11a) is ~ 0.75 Ma and again plagioclase feldspar analysed in this sample is responsible for the lower and upper limits of the range of ages seen (0.7 Ma > ages > 0.9 Ma). Plagioclase on its own yielded a weighted mean age of 0.785 ± 0.079 Ma (n = 15; MSWD = 1.01). Probability plot of sanidine ages alone produced a symmetrical,

Gaussian shaped curve (Fig. 4.11b). The age range achieved from sanidine falls between the plagioclase and yields a weighted mean age of 0.748 ± 0.008 Ma (n = 46; MSWD = 0.84). All weighted mean ages are in agreement at the 2σ level.

The data was plotted on two separate inverse isochron diagrams (Fig. 4.9c and Fig. 4.9d). Sample BP097 #1 (both sanidine and plagioclase) yields an inverse isochron age of 0.756 ± 0.012 Ma, which is indistinguishable from the inverse isochron ages obtained from sanidine and plagioclase separately. Sample BP097 #2 (both sanidine and plagioclase) yields an inverse isochron age of 0.699 ± 0.042 Ma, which is indistinguishable from inverse isochron age obtained from sanidine only (plagioclase data produced an invalid isochron). Both samples have initial $^{40}Ar/^{36}Ar$ ratios within error of the atmospheric value 298.56 (#1 = 298.1 ± 7.2; #2 = 358 ± 84), although BP097 #2 shows significant clustering of data near the $^{39}Ar/^{40}Ar$ axis and limited dispersion along the mixing line.

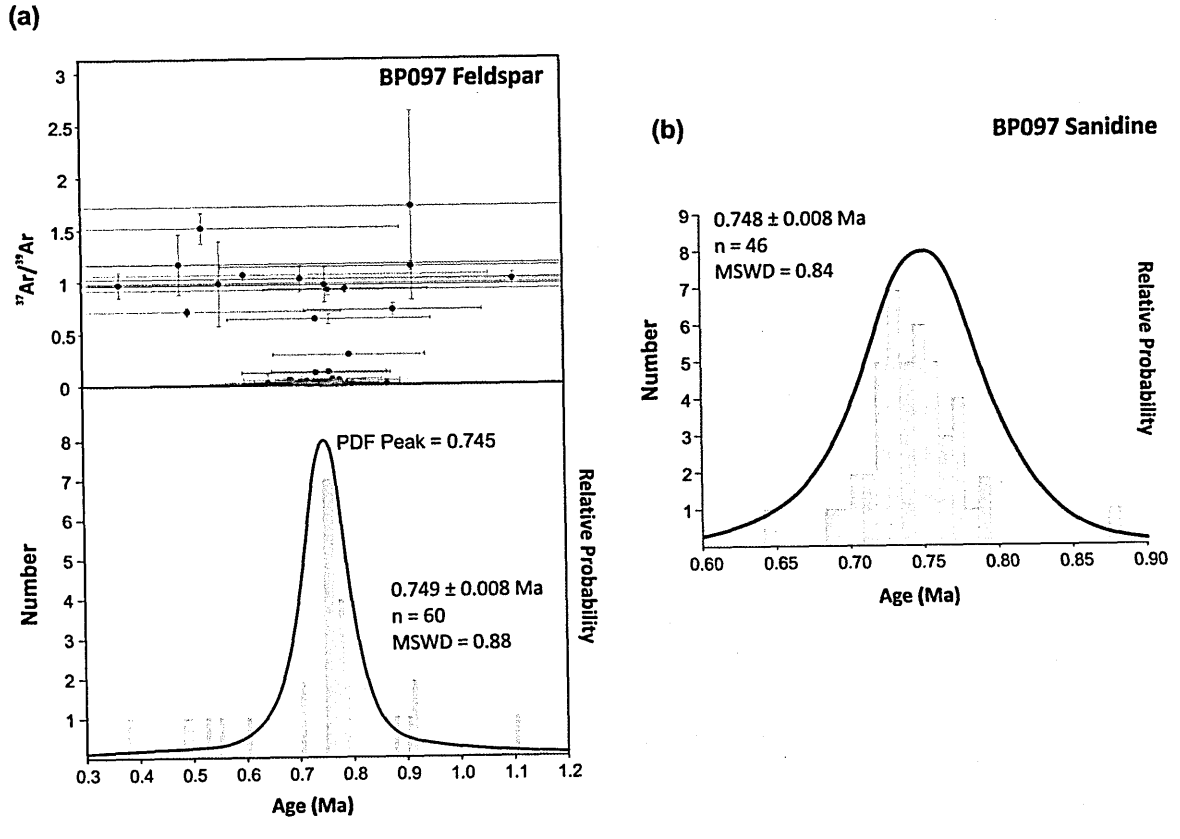

Figure 4.11. (a) Age probability distribution diagram and age vs. $^{37}Ar/^{39}Ar$ correlation plot for all feldspar analyses (plagioclase and sanidine) for Ignimbrite package Ig1Eb (sample BP097); (b) Age

(*Fig. 4.11 cont.*) probability distribution diagram for sanidine only. PDF peak (value at x at which the probability density function has its maximum value) for data set is given for both (a) and (b), and the weighted mean ages (determined separately using Isoplot; Ludwig, 2011), are also shown. All errors shown are 2σ.

4.5.2.4 Sample BP113 (Ig2NWa)

$^{40}Ar/^{39}Ar$ total-fusion ages obtained from single feldspar grains (sanidine only), range 0.719 ± 0.072 to 0.788 ± 0.039 Ma. Two crystals yielded significantly older than expected ages (6.411 ± 0.225 Ma and 1.057 ± 0.069 Ma) and have not been used in weighted mean age calculations, although their significance is discussed later in section 4.6.2. The weighted mean age of 0.759 ± 0.008 Ma (n = 25; MSWD = 0.71) is in agreement with the PDF peak value of ~ 0.76 Ma, and data produced an age probability plot with a symmetrical distribution (Fig. 4.12). An inverse isochron (Fig. 4.9e) age of 0.756 ± 0.021 Ma (MSWD = 0.80) is again in agreement with the weighted mean age. Due to significant clustering of data near the $^{39}Ar/^{40}Ar$ axis and limited dispersion along the mixing line, the resulting $^{40}Ar/^{39}Ar$ ratio and uncertainty (trapped Ar composition) is high (334 ± 120), although within error of atmospheric value 298.56.

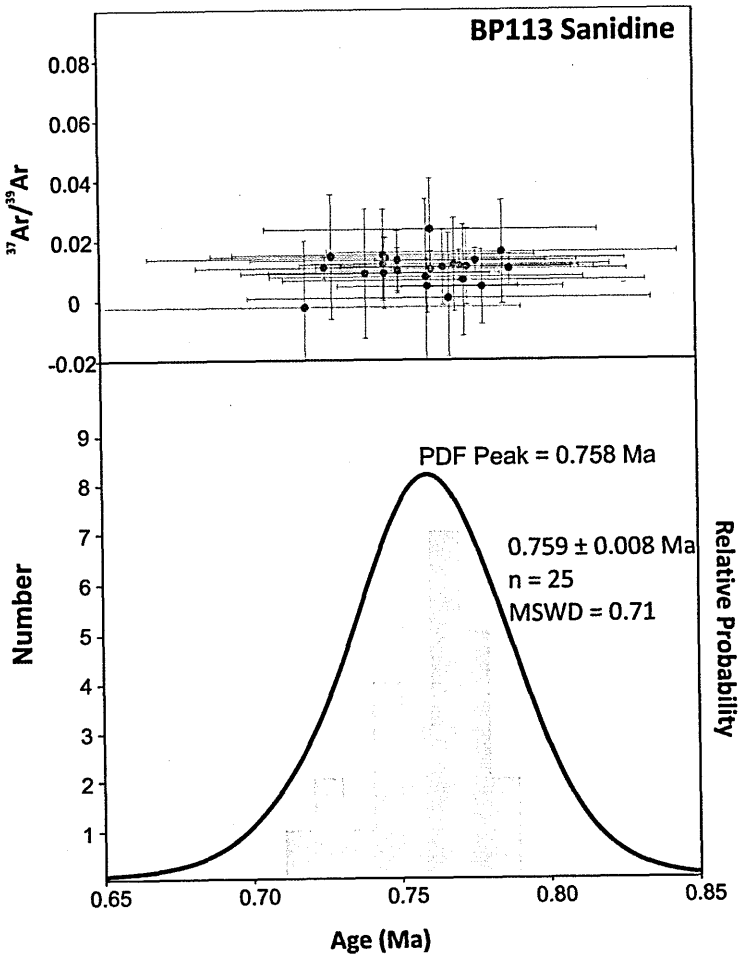

Figure 4.12. Age probability distribution diagram and age vs. $^{37}Ar/^{39}Ar$ correlation plot for Ignimbrite package Ig2NWa (sample BP113). PDF peak (value at x at which the probability density function has its maximum value) for data set are also given and the weighted mean age (determined separately using Isoplot; Ludwig, 2011), is also shown. All errors shown are 2σ.

4.5.2.5 Sample BP168 (Ig2Nb)

$^{40}Ar/^{39}Ar$ total-fusion ages obtained from single feldspar grains range 0.720 ± 0.084 to 0.789 ± 0.038 Ma. A number of grains showed signs of alteration (> 2σ lower $^{39}Ar/^{40}Ar$ and higher $^{36}Ar/^{40}Ar$ ratios than other data) and analyses have not been used in further calculations. The age probability plot (Fig. 4.13) shows a symmetrical distribution with a PDF peak of ~ 0.75 Ma. The inverse isochron age of 0.741 ± 0.024 Ma (MSWD = 0.43) is indistinguishable from the weighted mean (0.754 ± 0.010 Ma; n = 19; MSWD = 0.54) at the 2σ level, and has an initial trapped component within error of atmospheric value 298.56 (363 ± 85; Fig. 4.9f).

This sample provided the best opportunity to date biotite and only a limited number of grains survived the sample cleaning process. $^{40}Ar/^{39}Ar$ total-fusion ages range 0.619 ± 1.029 Ma to 1.502 ± 0.763 Ma (n = 5), and yielded a weighted mean age of 1.10 ± 0.21 Ma (MSWD = 0.96). Despite the low number of analyses the biotite weighted mean is slightly older than the weighted mean determined on feldspar (sanidine) separated from the same pumice. However, the data yield an inverse isochron (Fig. 4.9g) with an initial trapped component within error of atmospheric value (284 ± 51).

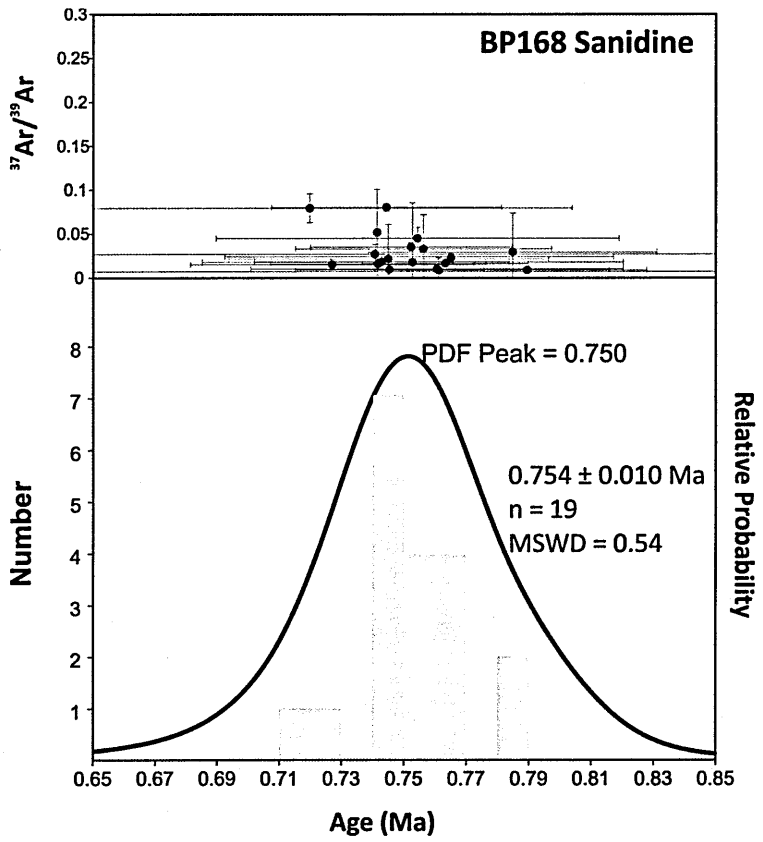

Figure 4.13. Age probability distribution diagram and age vs. $^{37}Ar/^{39}Ar$ correlation plot for Ignimbrite package Ig2Nb (sample BP168). PDF peak (value at x at which the probability density function has its maximum value) for data set are also given and the weighted mean age (determined separately using Isoplot; Ludwig, 2011), is also shown. All errors shown are 2σ.

Table 4.5. Summary Ar-Ar age information for all Bishop Tuff feldspars and biotite* (*sample BP168 only).The standard deviation (s.d.) of the arithmetic mean is given at the 95 % confidence level. Full data set, including average instrument blank measurements and calculated *J*-values used for data processing and raw data can be found in Appendix section A3.3.

Unit (sample)	Mineral phase[§]	$^{37}Ar/^{39}Ar$	Max. Age (Ma)	± 2σ	Min. Age (Ma)	± 2σ	Arithmetic Mean Age (Ma)	s.d.	n	Weighted Mean Age (Ma)	± 2σ
F5	fsp		1.190	0.436	0.435	0.612	0.757	0.222	43	**0.763**	**0.010**
	san	< 1	-	-	-	-	0.761	0.052	31	**0.763**	**0.011**
	plag	< 1	-	-	-	-	0.748	0.426	12	**0.760**	**0.130**
F7	fsp	< 1 to ~ 1	0.966	0.300	0.723	0.015	0.768	0.036	17	**0.764**	**0.012**
Ig1Eb	fsp		1.107	0.371	0.499	0.288	0.740	0.208	60	**0.749**	**0.008**
	san	< 1	-	-	-	-	0.749	0.072	46	**0.748**	**0.008**
	plag	> 1	-	-	-	-	0.712	0.406	14	**0.785**	**0.079**
Ig2NWa	san	< 1	0.788	0.039	0.719	0.072	0.758	0.037	25	**0.759**	**0.008**
Ig2Nb	san	< 1	0.789	0.038	0.720	0.084	0.752	0.034	19	**0.754**	**0.010**
	bio	< 1	1.502	0.763	0.619	1.029	1.105	0.673	5	**1.100**	**0.210**

[§] **(fsp = sanidine and plagioclase; san = sanidine; plag = plagioclase; bio = biotite).**

4.6 Discussion

4.6.1 New Ar-Ar dataset

Samples of Bishop Tuff pumice were collected from five localities and have been dated using the Ar-Ar single-grain fusion technique. Two of these pumice samples represent the plinian ash fall units F5 and F7, and three represent ignimbrite flow packages; Ig1Eb erupted early in the sequence and Ig2NWa and Ig2Nb represent later units, erupted north of the caldera. Weighted mean ages for analysed units range 0.749 ± 0.008 Ma to 0.765 ± 0.012 Ma, which overlap at the 2σ level. It should be noted that the sample collected from Ig1Eb yielded the youngest weighted mean age. All pumices sampled in this study were collected from basal, non-welded sections and therefore the pumice from Ig1Eb is similar to the other samples analysed with respect to its thermal history. Interaction with a volatile-rich gas or fluid phase can result in alteration of feldspars to form secondary clay minerals, accompanied by the introduction of ^{36}Ar (Barry *et al.*, 2010; Baksi *et al.*, 2012). However,

there was no trace of oxidation or any vapour-phase alteration at that sample locality (C. Wilson, *pers. com.*, 2012) and the youngest individual ages do not strongly correlate with high $^{36}Ar/^{40}Ar$ values, suggesting accidental analysis of alteration products has not occurred.

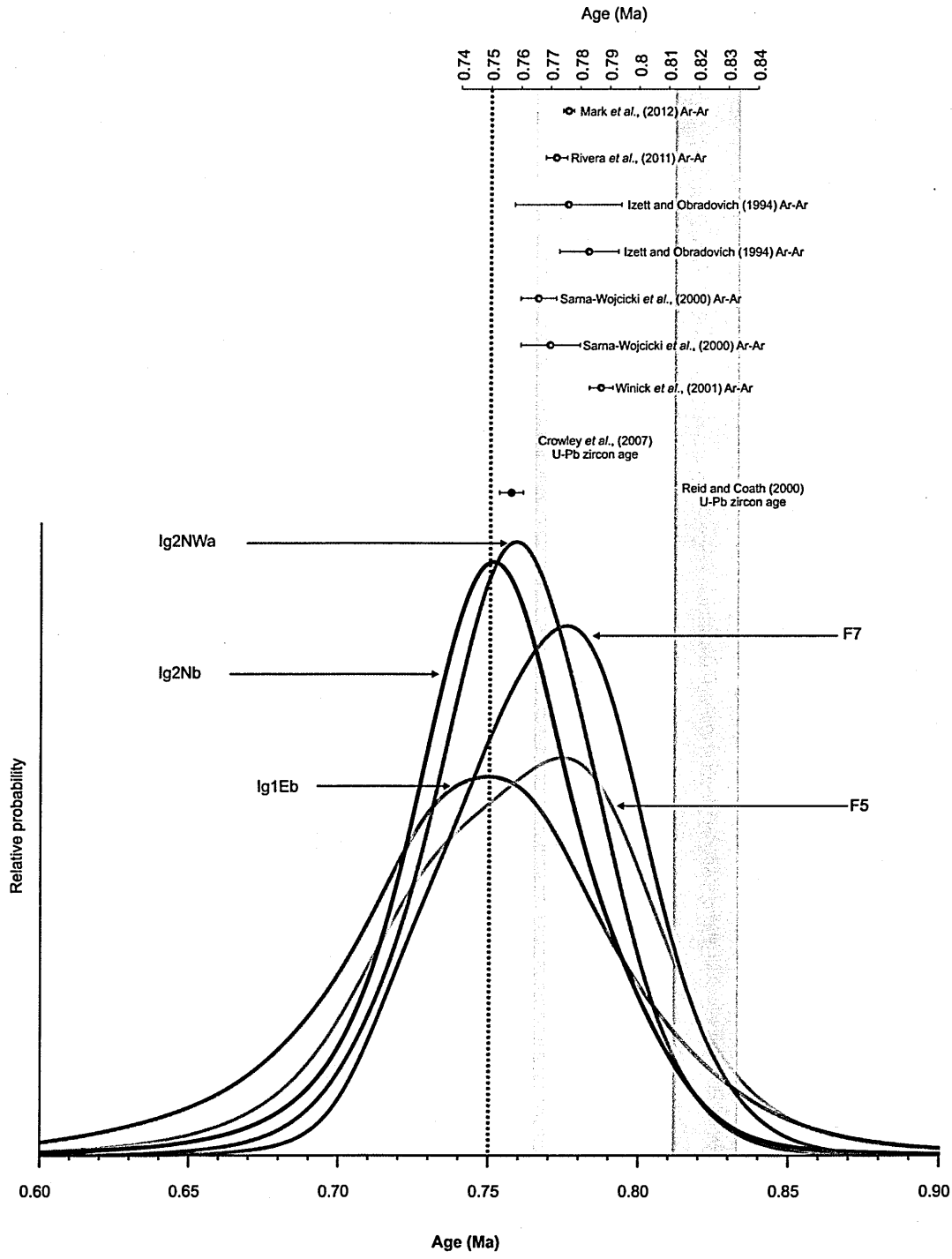

Figure 4.14. Comparison of the relative probability plots for sanidine Ar-Ar apparent ages showing that pumice samples from two fall units (F5, F7), and three ignimbrite packages (Ig1Eb, Ig2NWa and Ig2Nb) of the Bishop Tuff yield essentially the same age. Weighted mean Ar-Ar

(*Fig. 4.11 cont.*) age (n = 135 single sanidine analyses) of 0.757 ± 0.004 Ma is shown (black circle). Also shown for reference are previously published Ar-Ar (red circles), and U-Pb (grey boxes) ages for the Bishop Tuff (uncertainties shown at the 2σ level).

Combing Ar-Ar ages obtained from both fall units and flow packages, our best estimate for the eruption age is 0.757 ± 0.004 Ma (weighted mean age; MSWD = 0.83), determined on 135 single sanidine analyses. There is no significant difference in mean eruption ages determined for fall units and flow packages of the Bishop Tuff (Fig. 4.14), which supports the conclusions previously determined by Izett *et al.*, (1988), stating there is no significant difference between the lowermost and uppermost units of the tuff. This age is younger than recently published Ar-Ar ages (e.g., Rivera *et al.*, 2011 and Mark *et al.*, 2012), and recalculated ages (e.g., Sarna-Wojcicki *et al.*, 2000; Winick *et al.*, 2001), corrected relative to the ^{40}K decay constant of Renne *et al.*, (2010). The new Ar-Ar eruption is also younger than previously determined U-Pb zircon crystallisation ages (e.g., Reid and Coath, 2000; Simon and Reid, 2005; Crowley *et al.*, 2007; C. Wilson, *pers. com.*, 2012), and still records a time gap (≤ 90 kyr) between zircon crystallisation and eruption age recorded by sanidine crystals.

Although the BT eruption age can differ depending on which ^{40}K decay constant is used, it is clear that this issue is two-fold, and a lack of consistency still exists even when applying the same ^{40}K decay constant to data from various sources. For example, the BT eruption age presented in this study and by Mark *et al.*, (2012), Rivera *et al.*, (2011), Sarna-Wojcicki *et al.*, (2000), and Winick *et al.*, (2001) are generally inconsistent. As a result the age for the M-B geometric polarity reversal, which pre-dates the Bishop Tuff eruption by ~ 15.3 ± 2.2 ka (Sarna-Wojcicki *et al.*, 2000), occurred at either ~ 0.791 Ma (relative to Mark *et al.*, (2012) BT eruption age); ~ 0.787 Ma (relative to Rivera *et al.*, 2011); ~ 0.781 Ma (relative to recalculated Sarna-Wojcicki *et al.*, (2000) BT eruption age); ~ 0.796 Ma

(relative to recalculated Winick *et al.*, (2001) BT eruption age), or even ~ 0.772 Ma relative to BT eruption age presented in this study.

The use of different Ar-Ar techniques and crystal sizes may explain why the BT eruption age presented in this study is younger than previous age determinations. For example, Rivera *et al.*, (2011), analysed large crystal populations (due to small grain size) rather than single grains and may have inadvertently included grains that recorded an age older than eruption, resulting in an elevated age. It may also be possible that previous studies (e.g., Mark *et al.*, 2012; Sarna-Wojcicki *et al.*, 2000 and Winick *et al.*, 2001), which have undertaken single-grain fusion experiments, may have analysed feldspars containing an inherited component. For example, Mark *et al.*, (2012) report their new robust Ar-Ar eruption age is based on measurements made on 'coarse-grained' pumice samples. A large grain size could mean analysis of cores containing an inherited Ar component (e.g., sourced from Triassic material identified through U-Pb zircon analysis; Reid and Coath, 2000), however this is only hypothesised as a lack of specific details of their study (i.e., raw data, methods and techniques), prevents further comment at this time. Another explanation for the older ages could be the incorporation of $^{40}Ar_E$. Winick *et al.*, (2001) did predict possible $^{40}Ar_E$ contamination of sanidine, however evidence to support $^{40}Ar_E$ contamination has not been reported in previous studies, nor has any evidence been found for $^{40}Ar_E$ contamination of feldspar (specifically sanidine) during the course of this work.

4.6.2 Bishop Tuff biotite: disturbed Ar-Ar ages

Bishop Tuff pumice clasts contain variable proportions of biotite-plagioclase-quartz-sanidine (Hildreth and Wilson, 2007). This study has highlighted the difficulty in finding and separating fresh biotite for Ar-Ar analysis, which is probably why very few studies have previously attempted to analyse the phase. Izett *et al.*, (1988) reported weighted mean

K-Ar age of combined sanidine, plagioclase and biotite for both the upper (pyroxene-bearing; 0.736 ± 0.010 Ma), and lower (pyroxene-free; 0.738 ± 0.006 Ma) Bishop Tuff units. Biotite K-Ar ages included 1.10 ± 0.52 Ma and 1.14 ± 0.60 Ma, and both were plagued by low $^{40}Ar^*$ yield (~ 2 %), resulting in large uncertainties. However, isochron analysis showed no analytically detectable amounts of $^{40}Ar_E$ (Izett *et al.*, 1988).

Mahood *et al.*, (2010) investigated young mafic and trachydacite lavas (erupted < 190,000 years) at Mammoth Mountain, Long Valley caldera, and reported Ar-Ar ages determined on biotite to be consistently older than coexisting sanidine. The Ar-Ar (step heating) experiments on biotite were highly variable, and several determinations yielded distinctive saddle shaped gas release spectra. The Ar-Ar step heating method releases Ar gas in a series of increments with increasing temperature and the apparent age of each gas fraction is presented against the cumulative ^{39}Ar released. Saddle shaped release spectra are consistent with the incorporation of $^{40}Ar_E$ (McDougall and Harrison, 1999). Mahood *et al.*, (2010) hypothesised resorbed plagioclase containing biotite inclusions within some samples, possibly representing xenocrystic or older cognate material with a pre-existing $^{40}Ar^*$ signal, had become incorporated during preparation of sample splits (~ 5 grains), resulting in anomalously old ages. They found no evidence to support incorporation of $^{40}Ar_E$ as inverse isochron analysis yielded a $^{40}Ar/^{36}Ar$ intercept within uncertainty of atmospheric composition.

Biotite Ar-Ar apparent ages determined for this study (sample BP168), range 0.619 ± 1.029 Ma to 1.502 ± 0.763 Ma (n = 6) and yield a weighted mean age of 1.10 ± 0.21 Ma, which is slightly older than the ~ 0.76 Ma eruption. Although the inverse isochron plot yields a $^{40}Ar/^{36}Ar$ intercept of atmospheric composition (284 ± 51; within uncertainty of 298.56), suggesting $^{40}Ar_E$ is not responsible for the older ages, it is difficult to ignore the examples that show biotite to be highly susceptible to $^{40}Ar_E$ contamination (e.g., Hora *et*

al., 2010; Bachmann *et al.*, 2010). Conversely the slightly older biotite ages could represent either partially re-set xenocrysts (e.g., Glass Mountain pyroclastic debris; Hildreth and Wilson, 2007 or metamorphosed country rock; Christensen and DePaolo, 1993), or antecrysts sourced from the crystal-rich magma chamber rind and/or mush zone (e.g., Charlier *et al.*, 2007; Kay *et al.*, 2011).

It may also be likely that the slightly older biotite ages are the result of post-eruption alteration (e.g., interaction with a pre- or syn-eruptive gas phase, surface and/or groundwater), causing alkali mobility. For example if significant K is lost, then Ar concentration will be relatively too high, resulting in an older apparent age. Hildreth and Wilson (2007) identified biotite that were strongly enriched in Cs and Rb, reflecting pre- or post-eruptive vapour-phase transport meaning interaction with a fluid phase, during or after eruption is possible. Due to the difficulty in separating out fresh (black and not flaky) biotite, any that failed to survive the cleaning process (acetone and agitation in a sonic bath) were not used for analysis.

The weathering indices values for BP168 are not significantly different to the other samples worked on, and no alkali mobility is suspected for this sample, although several feldspar analyses showed signs of disturbance (high $^{36}Ar/^{40}Ar$ value of ~ 0.002 compared with ~ 0.0003, low $^{39}Ar/^{40}Ar$ ratios 0.2 compared with ~ 0.9). Ar-Ar data revealed $^{40}Ar^*$ (%) to be highly variable, ranging 80 % to 32 %, as well as variable ^{36}Ar contents (0.0007 to 0.0058 volts), however EMP totals are in the range expected for biotite (e.g., ~ 96 %) and K_2O and CaO contents range 8 to 10 % and < 1 % respectively. Whether the older Ar-Ar ages determined on biotite are a result of $^{40}Ar_E$ or post-deposition alteration, this work has highlighted that Bishop Tuff biotite is not a suitable phase for Ar-Ar dating.

4.6.3 Contamination of the Bishop Tuff magma chamber

The current Bishop Tuff magma chamber model, which envisages a large-scale mush zone of predominantly quartz and feldspar, is similar to the model proposed for the Fish Canyon magmatic system, and therefore could be a focus of $^{40}Ar_E$ contamination. Remelting of K-bearing minerals (as well as K-bearing wall rock), hosted in magma chamber mush zones during periods of rejuvenation (e.g., Charlier *et al.*, 2007; Bachmann, 2001; Bachmann *et al.*, 2007b) may be a source of significant dissolved $^{40}Ar_E$ in interstitial melt. Bishop Tuff feldspars in samples sourced from later erupted units show evidence of over-growths (e.g., Hildreth and Wilson, 2007), strongly suggesting the mush zone experienced cyclic crystallisation and remelting episodes.

The high-silica rhyolite of the Bishop Tuff has measured SiO_2 contents of 74 to ~ 78 wt. % (Hildreth and Wilson, 2007) and Ar solubility in rhyolite magma can be as high as 0.8 ppm bar^{-1} (Kelley, 2002). The highly compatible nature of Ar with rhyolite magma means that high-silica interstitial melt could become concentrated in $^{40}Ar_E$. $^{40}Ar_E$ dissolved in interstitial melt, sourced from the crystal mush zone, could be incorporated into growing crystals (e.g., in fluid and/or melt inclusions), as well as partitioning back into crystals if $^{40}Ar_E$ concentration of the melt reaches such a level as to overcome the generally incompatible nature of Ar in solid/melt (and solid/fluid) systems (Kelley, 2002).

$^{40}Ar_E$ dissolved in melt (and fluids) in which crystal growth is taking place can contaminate crystals commonly used for Ar-Ar dating (e.g., feldspars), as well as phases not routinely used for determining an apparent age (e.g., quartz), which can instead be used to indicate the presence of $^{40}Ar_E$ in the melt, because inclusions represent non-degassed, or partially degassed magma. Izett *et al.*, (1988), reported K-Ar age determined using plagioclase and quartz of 1.36 ± 0.26 Ma, and a further study by Winick *et al.*, (2001)

provided evidence to support $^{40}Ar_E$ contamination of quartz (hosted in melt inclusions), and also suggested $^{40}Ar_E$ contamination could be a significant problem for co-existing feldspar.

The current model of the Bishop Tuff magma chamber prior to eruption (Hildreth and Wilson, 2007), suggests quartz and feldspar crystallised coevally and erupted simultaneously and both contain numerous rhyolite glass inclusions containing ~ 5 wt. % K_2O (Winick 2000; Winick *et al.*, 2001), either trapped, or exposed and connected to the exterior of the crystal (Winick 2000; van den Bogaard and Schirnick, 1995). Winick *et al.*, (2001) found significant $^{40}Ar_E$ in melt inclusions, particularly those fully trapped within quartz, resulting in an age range of ~ 1.88 to ~ 3.76 Ma, and hypothesised $^{40}Ar_E$ within trapped melt inclusions might be capable of increasing sanidine apparent ages by several thousand years relative to the actual eruption age. The data presented here displays little evidence to suggest sanidine phenocrysts are contaminated by $^{40}Ar_E$. In general, inverse isochron plots for separated sanidine yield $^{40}Ar/^{39}Ar$ intercepts in agreement with the atmospheric value 298.56 (e.g., sample BP029 = 275 ± 29; BP097 = 299.8 ± 8.0; BP113 = 334 ± 120 and BP168 = 363 ± 85), although $^{40}Ar/^{36}Ar$ value for sample BP097 was dictated by one data point anchoring the isochron to the Y-axis.

Previous chapters have investigated the occurrences of extraneous Ar in other large volume, silica-rich magmatic systems, for example Fish Canyon and Yellowstone, undergoing multiple crystallisation and rejuvenation episodes. In particular plagioclase feldspar (and anorthoclase) has been shown in some cases to preferentially diffuse Ar slower and therefore record older ages (e.g., discussed in Chapter 3), and contain variable amounts of $^{40}Ar_E$ (e.g., inclusion hosted $^{40}Ar_E$; discussed in Chapter 2), therefore resulting in older Ar-Ar apparent ages. Pumices used in this study contained both sanidine and plagioclase and therefore presented the opportunity to identify any age variability between

the two phases. Owing to the low K content, incorporation of $^{40}Ar_E$ can have a significant effect on the measured age (Kelley, 2002). Layer and Gardner, (2001), reported $^{40}Ar_E$ in young (< 4000 ybp) plagioclase crystals, increasing apparent ages by 10^5 to 10^6 years. Therefore $^{40}Ar_E$ contamination recorded by MIBQ may also be recorded by co-existing plagioclase.

Plagioclase is a commonly used mineral for Ar-Ar dating where other K-bearing phases are unavailable, for example in basaltic and andesitic lavas. Because the Ar-Ar dating method is based upon the accumulation of $^{40}Ar^*$, its application to young and K-poor minerals can therefore be problematic (McDougall and Harrison, 1999). Analytical limitations include large associated age uncertainties due to relatively low $^{40}Ar^*$ (%) yield. For example, Sarna-Wojcicki *et al.*, (2000) excluded one determination from the calculation of their average age due to the accompanying error being 8 times greater than other age determinations, concluding the sample split contained plagioclase grains as well as sanidine. This overall decrease in precision has resulted in errors on plagioclase age determinations ranging 6 % to 66 %, and emphasises the reduced applicability of K-poor minerals as the younger limit is approached. Based on the level of precision achievable in this study the weighted mean ages determined using plagioclase only (samples BP029 and BP097), were not significantly different (at the 2σ level) to weighted mean ages determined using sanidine, nor did they present evidence to suggest $^{40}Ar_E$ contamination.

Only two significantly older ages have been found, both separated from pumice erupted late in the sequence (Ig2NWa). A single feldspar yielded an age of 6.412 ± 0.225 Ma, and corresponded to a high $^{37}Ar/^{39}Ar$ ratio (0.512 ± 0.009), indicating it is a calcic plagioclase. The other yielded an age of 1.057 ± 0.069 Ma, which has a $^{37}Ar/^{39}Ar$ ratio < 0.001. Ig2NWa represents the earliest ignimbrite erupted during the latter half of the eruption, along the northern caldera margin. It has previously been characterised by a lithic-rich (160

to 630 clasts/m^2; Wilson and Hildreth, 1997) clast supported matrix, with a notable lithic contribution from metamorphic and mafic lavas, which both crop out nearby on the caldera rim and underlie intracaldera tuff. Hildreth (1977) noted plagioclase crystals with inherited cores (e.g., antecrysts), and Hildreth and Wilson (2007) have hypothesised that the Bishop Tuff magma could have been contaminated by Glass Mountain pyroclastic debris, concentrating xenocrysts (quartz, biotite, feldspar), that are difficult to distinguish from juvenile phenocryst populations, during the Ig2 stage of the eruption. However, the anomalously older plagioclase crystal is older than mafic and intermediate activity (4.5 to 2.5 Ma), and older than the Glass Mountain rhyolitic activity which followed (2.2 to 0.79 Ma), which could be a probable source for the older, less calcic feldspar.

Previous U-Pb studies have noted the lack of zircons older than ~ 0.9 Ma, except for a few ~ 200 Ma zircons found in pumices thought to be sourced from a Triassic pluton cut by part of caldera (e.g., Reid and Coath, 2000; Simon and Reid, 2005; C. Wilson, *pers com.*, 2012). If we assume the older plagioclase has been sourced from same Triassic pluton then it can be estimated to take ~ 1500 years in the Bishop Tuff magma (at 700 to 750 °C) to yield an age of ~ 6 Ma. Measured $^{36}Ar/^{40}Ar$ and $^{38}Ar/^{39}Ar$ ratios are similar to phenocrysts analysed in the same sample and the high Ca content (based on $^{37}Ar/^{39}Ar$ ratio), which is not similar to other phenocrysts suggests a xenocrystic origin. van den Bogaard *et al.*, (1989; 1995) investigated samples of the East Eifel Volcanic Field (EEVF), and identified older feldspar Ar-Ar ages. These older grains were interpreted as xenocrysts, derived from nearby Tertiary and Pleistocene Eifel volcanics, incorporated into magma prior to eruption and therefore retaining some of their original $^{40}Ar^*$. Therefore the plagioclase could either be a partially reset xenocryst containing an inherited and juvenile component, or a single crystal containing inclusion hosted $^{40}Ar_E$, resulting in a geologically meaningless age.

4.7 Conclusions

Ar-Ar single-grain fusion experiments were carried out on a number of samples representing early and late erupted material of the Bishop Tuff deposit, California, USA. Feldspar (sanidine and plagioclase) and biotite were analysed in order to investigate the nature of extraneous Ar from this silicic magma system.

- This work has demonstrated that there is no significant Ar-Ar age difference between ash fall and ignimbrite flow deposits of the Bishop Tuff. Weighted mean ages determined on crystals separated from whole pumices overlap at the 2σ level, and our best estimate for the eruption age (combing Ar-Ar sanidine ages obtained from both fall units and flow packages) is 0.757 ± 0.004 Ma (n = 135; MSWD = 0.83).

- The Ar-Ar eruption age of 0.757 ± 0.004 Ma (n = 135; MSWD = 0.83), is significantly younger than the most recent Bishop Tuff eruption age determinations (i.e., Mark *et al.*, 2012, and Rivera *et al.*, 2011). Potential reasons for this difference may lie in the technique used (e.g., analysis of single coarse grained crystals or multi-crystal aliquots) resulting in the accidental incorporation of partially degassed feldspars (e.g., crystal cores containing an inherited Ar component). The lack of solid evidence to support $^{40}Ar_E$ contamination of sanidine means this is a less likely explanation.

- One key attribute of this study has been able to sample crystal poor pumice inferred to represent the top of the magma chamber, and crystal rich pumice inferred to represent deeper (mush) layers within the chamber. It was hypothesised that the crystal rich samples might contain measurable $^{40}Ar_E$ contamination.

Despite the wide range of samples, this study has not detected significant levels of extraneous Ar contamination (inverse isochron analyses of all samples have shown the trapped Ar component to be atmospheric in composition), and consequently no difference between crystal poor and crystal rich samples. Inclusion hosted $^{40}Ar_E$ contamination of sanidine, as hypothesised by Winick *et al.*, (2001), has not been detected despite analysed crystals containing abundant inclusions. Neither did plagioclase grains yield significantly older ages despite the higher closure temperature and potential for xenocrystic/antecrystic contamination.

- Contamination of the Bishop Tuff magma by xenocrystic material prior to and during the eruption, although noted by others (e.g., Hildreth and Mahood, 1986; Hildreth and Wilson, 2007; Christensen and DePaolo, 1993), was not a significant factor during this study. In the course of dating > 260 single feldspar crystals separated from five sampling localities, only two crystals yielded older (at the 2σ level) than expected ages. These crystals are inferred to represent contaminating xenocrystic material, because there is no isotopic evidence (e.g., no correlation with $^{38}Ar/^{39}Ar$ ratio and therefore fluid inclusions), to suggest the older ages are due to $^{40}Ar_E$ contamination.

- This study has demonstrated biotite to be inadequate for Ar-Ar dating. Biotite was separated from a number of pumice samples but only one sample survived the cleaning procedure and Ar-Ar ages were generally older than feldspars from the same sample. It is not clear if the older ages are due to $^{40}Ar_E$ contamination (inverse isochron analysis suggests not), vapour-phase alteration/post depositional weathering or inherited Ar, however this does reaffirm the importance of sampling

fresh material for Ar-Ar dating, which can be a challenge even for relatively young (> 1 Ma) eruptions.

- There appears to be a significant contrast between the ages obtained from the Bishop Tuff and those obtained from other samples studied here, including the Huckleberry Ridge Tuff and associated domes, where individual crystals exhibited significant age variations (e.g., Sheridan Reservoir dome). It is noteworthy in this respect that the associated zircon ages also show the same pattern, with very little variation in the Bishop Tuff, and a spread to older ages, indicating extended periods of zircon crystallisation in the Sheridan Reservoir dome magma chamber. It might be possible to evoke a mechanism relating the two observations – for example, the contamination of feldspars is related directly to the longevity of the volcanic system or the age of the country rocks hosting the magma chamber - but further testing on other volcanic systems is prudent before drawing such a conclusion.

Chapter 5. Synthesis and Conclusions.

5.1 Introduction

This chapter provides a synthesis of the data discussed in Chapters 2, 3 and 4, and summarises the key outcomes of this work in the wider context of extraneous Ar in long-lived silicic magma systems with respects to the original project aims outlined in Chapter 1. The final conclusions (including a summary of new Ar-Ar ages for the various geological units generated) of this study (section 5.4) are presented as summarised bullet points, and organised in chapter order. This section also outlines some recommendations and important considerations concerning the application of Ar-Ar techniques to products of silicic volcanism. The final section (5.5) provides a list of suggestions for further work and how this data set may be improved.

5.2 Develop techniques and methods in identifying extraneous Ar

One aspect of this work has been to investigate how the application of a variety of different Ar-Ar techniques can be used to identify extraneous Ar in silicic volcanic systems and assess the distribution of Ar ($^{40}Ar_E$, inherited and $^{40}Ar^*$) between different mineral phases commonly used for Ar-Ar dating. This study has used IR and UV laser systems to achieve *in situ* (IR and UV), and single-grain fusion (plus basalt flux to improve IR laser coupling with clear minerals) Ar-Ar datasets.

5.2.1 Applicability of Ar extraction techniques

5.2.1.1 *In situ* Ar-Ar analysis

Application of *in situ* Ar extraction techniques to samples of the Fish Canyon magmatic system (with an age of ~ 28.3 Ma), has demonstrated that the UV *in situ* method, and in some cases the IR *in situ* method, can be successfully applied to young (< 40 Ma) volcanic minerals. While it doesn't produce the highest precision measurements, laser ablation and laser melting allows the identification of fluid inclusion hosted $^{40}Ar_E$ in sanidine, inclusion hosted $^{40}Ar_E$ in plagioclase, and reproducibly older biotite Ar-Ar ages due to $^{40}Ar_E$ and extraneous Ar contamination of a mushy state magma chamber to be investigated (discussed further in section 5.3.1). $^{40}Ar_E$ contamination of sanidine is of particular importance because sanidine is a mineral commonly used for dating young eruptions and as standards in Ar-Ar dating, especially the Fish Canyon sanidine because of its continued use as a secondary standard by the Ar-Ar community.

5.2.1.2 Ar-Ar single-grain fusion analysis

For all other samples (< 3 Ma) the total fusion technique has been used to obtain multiple single-grain ages from a variety of mineral phases and glass. This has allowed in some cases xenocrysts and antecrysts to be identified from optically and chemically similar phenocrysts (e.g., the Bishop Tuff and Sheridan Reservoir dome), as well as producing age ranges that are strikingly similar to U-Pb ages determined on zircon (e.g., Snake River Butte and Sheridan Reservoir domes). Well characterised decay rates (i.e., ^{40}K) and Ar-Ar standards have made it possible to compare U-Pb zircon and Ar-Ar single-grain ages at a high precision (e.g., Sheridan Reservoir dome Ar-Ar age range 1.63 ± 0.3 to 3.34 ± 0.4 Ma can be compared to a U-Pb zircon age range of 1.81 ± 0.11 to 2.83 ± 0.14 Ma). This has

allowed subtle contamination (e.g., recycling of crystallised magma chamber side walls/roof; discussed further in section 5.3.2), and the incorporation of antecrysts into the eruptible 'holding chamber' of large silicic magma reservoirs (e.g., Charlier *et al.*, 2005) to be identified.

5.2.2 Suitability of mineral phase: implications for Ar-Ar dating

Geochronological information was obtained from similar multiple mineral phases (e.g., sanidine, plagioclase, biotite), and glass separated from the eruptive products of three silicic magma systems. In general feldspar (sanidine, anorthoclase and plagioclase) was the most abundant mineral phase and K_2O contents ranged < 1 % to ~ 14 %. Biotite and rhyolite glass, where possible, were also analysed, although variable preservation state (e.g., Bishop Tuff biotite) negated its usefulness in all samples.

5.2.2.1 Sanidine

This work appears to be in agreement with other studies (e.g., Renne *et al.*, 1997), which have also found sanidine to be reproducible and free from significant contamination. The phase has been particularly useful in dating multiple units of the Bishop Tuff (e.g., ages range 0.749 ± 0.008 Ma to 0.765 ± 0.012 Ma), and the HRT (e.g., 2.11 ± 0.02 Ma, 2.12 ± 0.04 Ma and 2.11 ± 0.01 Ma for members A, B and C respectively), and showing in both cases there is no identifiable difference (in Ar-Ar age) between the units of a single eruption. In addition sanidine yielded an Ar-Ar age for the eruption of Green Canyon Flow dome that is in agreement with field evidence (better constrained than previously presented K-Ar age; Obradovich, 1992 cited in Christiansen, 2001), and shows no evidence to support $^{40}Ar_E$ contamination.

$^{40}Ar_E$ contamination of Fish Canyon sanidine has however been identified and resulted in at least one area of sanidine with an age *ca.* ~ 8 Ma older than the generally accepted eruption age (at ~ 28.3 Ma). IR *in situ* analysis identified a heterogeneous age distribution (single age of ~ 36 Ma) and a significant Ca and Cl content variability. Using $^{38}Ar_{Cl}$ as a proxy for the chlorine content (previously been shown to correlate with fluid inclusion hosted $^{40}Ar_E$; e.g., Rama and Hart, 1965; Kelley *et al.*, 1986), an elevated $^{40}Ar/^{36}Ar$ ratio (349 ± 21, which is > 298.56), coupled with an elevated $^{38}Ar/^{39}Ar$ signal strongly suggests the IR laser heated the analysis area and 'popped' a fluid inclusion incorporated by the mineral during growth in an environment hosting pockets of $^{40}Ar_E$ rich fluid (e.g., circulating hydrothermal fluids) and melt.

5.2.2.2 Plagioclase

Plagioclase can often be the only K-bearing phase available for Ar-Ar dating (Renne *et al.*, 1992), and has previously been shown to incorporate significant amounts of $^{40}Ar_E$ (e.g., inclusion hosted; Layer and Gardner, 2001; Boven *et al.*, 2001; Jones *et al.*, 2008). Plagioclase ages from the Fish Canyon samples range from slightly older than the eruption (e.g., ~ 30 Ma) to ages > 45 Ma, which are also older than reported U-Pb zircon ages (e.g., Bachmann *et al.*, 2007b). The elevated ages represent $^{40}Ar_E$ trapped in fluid and/or melt inclusions, which were commonly observed in the plagioclase grains. The rise in age is more easily identified in the case of plagioclase because the lower K content means even retaining small amounts of $^{40}Ar_E$ can result in noticeably older ages.

In contrast to Fish Canyon, Bishop Tuff and Yellowstone plagioclase (with the exception of Sheridan Reservoir dome, discussed in section 5.3.2), did not yield ages many millions of years older than the eruption, and therefore did not contain measurable amounts of $^{40}Ar_E$. Bishop Tuff units F5 (sample BP029), and Ig1Eb (sample BP097), contained

abundant plagioclase (up to An_{16}). Despite the low K content (generally < 4 %), which resulted in poor analytical precision and large associated uncertainties, plagioclase weighted mean ages were within errors of sanidine weighted mean ages and were therefore not significantly different (e.g., sanidine age of 0.76 ± 0.01 Ma compared to plagioclase age of 0.76 ± 0.13 Ma; sample BP029). The same was also noted for Huckleberry Ridge Tuff member B, where 45 % of crystals analysed were plagioclase and a plagioclase weighted mean age of 2.15 ± 0.19 Ma is within uncertainty of the weighted mean age determined using sanidine (2.12 ± 0.04 Ma).

5.2.2.3 Biotite

It has proved extremely difficult to separate fresh biotite from samples of the Bishop Tuff and Green Canyon Flow dome. The hydrous phase is rare, and contributes < 1 % of phenocrysts present in both units. The majority of biotite located appeared to have undergone alteration (e.g., vapour phase alteration prior to or during eruption) or post-depositional weathering (e.g., interaction with ground and/or surface waters). Based on a small number of viable analyses made on biotite separated from the Bishop Tuff (sample BP168), ages ranged 0.619 ± 1.029 Ma to 1.502 ± 0.763 Ma (n = 6) and yielded a weighted mean age of 1.10 ± 0.21 Ma.

The highly variable Bishop Tuff biotite ages could be a result of partially re-set xenocrysts (e.g., Glass Mountain pyroclastic debris; Hildreth and Wilson (2007), or metamorphosed country rock; Christensen and DePaolo, 1993), or antecrysts sourced from the crystal-rich magma chamber rind and/or mush zone (e.g., Charlier *et al.*, 2007; Kay *et al.*, 2011). An alternative explanation for the older ages is that they are the result of post-eruption alteration (e.g., interaction with a pre- or syn-eruptive gas phase, surface and/or groundwater), causing ^{36}Ar contamination and/or significant K loss, although this is not

suggested by EMP results where biotite from sample BP168 contained 8 to 9 % K_2O and yielded totals of ~ 96 %. Finally, an inverse isochron plot yielded a $^{40}Ar/^{36}Ar$ intercept of atmospheric composition (284 ± 51; within uncertainty of 298.56), which may be a result of modern air contamination, makes confirming $^{40}Ar_E$ contamination difficult.

Fish Canyon biotite yielded older ages as a consequence of late stage crystallisation in an Ar rich environment ($^{40}Ar^*$ liberated from the dissolution of K-bearing phases prior to eruption). An inverse isochron diagram plotted for all UV *in situ* biotite ages (sample BFC129) yielded an inverse isochron age of 28.82 ± 0.42 Ma (MSWD = 2.1), which is slightly older than FCs age (28.305 ± 0.04 Ma; Renne *et al.*, 2010), and yielded an atmospheric intercept of 309 ± 8.9 for the trapped Ar component, which is also slightly higher than the atmospheric $^{40}Ar/^{36}Ar$ ratio value 298.56. Interestingly, single grain fusion and step heating (aliquots of 10 to 15 grains) ages published by Bachmann *et al.*, (2007b), were reported as reproducibly yielding an 'eruption' age; however it seems likely that this minor $^{40}Ar_E$ contamination was homogenised with true radiogenic Ar during sample analysis and therefore previously went unnoticed.

5.2.2.4 Glass

Glass can be a significant host of K, and in the case of Sheridan Reservoir dome, separated glass contained ~ 1 % more K than separated feldspars (predominantly anorthoclase). Glass can contain measurable concentrations of atmospherically derived Ar or $^{40}Ar_E$ several orders of magnitude higher than radiogenic Ar (e.g., Walker and McDougall, 1982), however there is no evidence to suggest the glass of Sheridan Reservoir or Snake River Butte dome contain an excess Ar component (samples yielded initial trapped Ar compositions that are within error of the atmospheric value 298.56, e.g., $^{40}Ar/^{36}Ar$ intercept = 268 ± 36; Snake River Butte dome; sample YR185). In addition, previous work has

highlighted the susceptibility of glass to alteration, through hydration and devitrification processes (e.g., Kaneoka, 1972; Dalyrymple and Lanphere, 1969; Foland *et al.*, 1993; Clay *et al.*, 2011), however measured Ar isotope ratios (e.g., $^{36}Ar/^{40}Ar$ and $^{39}Ar/^{40}Ar$) indicate significant atmospheric Ar contamination or K loss due to weathering has not been detected in these samples.

5.2.3 The importance of variation in Ar solubility

Partitioning of Ar, and equilibration between different phases depends on the relative solubilities. The solubility of Ar in melts is similar to that of CO_2, which is readily exsolved, suggesting that in well-degassed volcanic systems, Ar will partition into the vapour phase and it will be lost (Carroll and Stolper, 1993; Kelley, 2002; Clay *et al.*, 2011). In general, partition coefficients for mineral/fluid and mineral/melt range 0.01 to 7 $\times 10^{-6}$ for Ar, implying that Ar exhibits an incompatible behaviour in minerals compared with melt or hydrous fluids. Ar solubility in silicate liquids (basalts to rhyolites) can range from 0.05 to 0.1 ppm bar^{-1} and up to 1.8 ppm bar^{-1} in pure silica melts (Carroll and Stolper, 1993), indicating a higher Ar solubility in rhyolite compared to basalt. This also indicates that when Ar is free to equilibrate between mineral phases and rhyolite melt it will preferentially partition into the melt phase (Kelley, 2002). Therefore, melts can act as an Ar transfer medium between minerals (which act as both sources and sinks for Ar), whether this results in late stage diffusion into another mineral or degassing to the atmosphere. Therefore, other than melt or fluid inclusion hosted $^{40}Ar_E$ trapped in the crystal lattice ,$^{40}Ar_E$ will only cause significant problems when Ar concentrations in the melt reaches a significant level and causes partitioning of Ar back into the mineral phase (Kelley, 2002).

5.2.3.1 Ar solubility in fluids and melts

The release of $^{40}Ar_E$ from fluid (e.g., Rama and Hart, 1965; Kelley *et al.*, 1986; Harrison *et al.*, 1994), and melt (e.g., Layer and Gardner, 2001) inclusions has been correlated with measured Cl/K ratio during sample analysis. It is likely that specific targeting of an IR laser during *in situ* analysis of Fish Canyon sanidine, showed strong correlation with Cl/K ratio tapped into an inclusion. Therefore the incorporation of inclusions during growth has resulted in part of a single crystal yielding an age that is older than expected (~ 36 Ma). Fish Canyon plagioclase (some melt inclusion rich), also yielded UV and IR *in situ* ages older than expected (> 45 Ma). This suggests that melt and fluids in the Fish Canyon magma system were aiding the transport of $^{40}Ar_E$, which could be incorporated into growing crystals.

This study has highlighted the significant impact that inclusion hosted $^{40}Ar_E$ can have on Ar-Ar apparent ages. In the case of the Fish Canyon minerals, discrete parts of crystals yield age increases of ~ 2 to ~ 17 Ma. This could have a detrimental effect on single-grain fusion ages where $^{40}Ar_E$ would be homogenised with *in situ* produced $^{40}Ar^*$. This study has also highlighted the importance of testing an inclusion hosted $^{40}Ar_E$ theory, which has previously shown to cause a serious problem when using anorthoclase to determine an eruption age (e.g., Esser *et al.*, 1997). For example anorthoclase (also sanidine and plagioclase), separated from Sheridan Reservoir dome pumice, contained numerous melt inclusions (range from < 10 % to ~ 40 %), and yielded a wide range of ages (e.g., 1.6 to ~ 3 Ma). It might be expected that rhyolite melt inclusions (SiO_2 > 76 %) contain significant amounts of dissolved $^{40}Ar_E$ because Ar solubility has been shown to increase with silica content (Carroll and Stolper, 1993; Kelley, 2002). A detailed visual of variable melt inclusion density detected no correlation between $^{38}Ar/^{39}Ar$ (a proxy for Cl/K) ratio and/or

inclusion content (10 to 40 %) and apparent age, leading to the conclusion that inclusions are not universally a cause for $^{40}Ar_E$ contamination.

The incompatible nature of Ar in solid/melt (and solid/fluid) systems means that Ar strongly partitions from crystals into melts and from melts into bubbles in magmatic systems (Kelley, 2002). Useful geochronological information (i.e., no evidence to support $^{40}Ar_E$ contamination) obtained from rhyolitic glass from both Snake River Butte and Sheridan Reservoir domes, suggests Ar successfully transferred between the melt and the atmosphere (during exsolution of gas phase and vesiculation), which is expected in well-degassed volcanic systems (e.g., Carroll and Stolper, 1993; Clay *et al.*, 2011).

5.2.3.2 Ar solubility in minerals

If $^{40}Ar^*$ in the melt reaches a high concentration then measurable $^{40}Ar_E$ can partition back or equilibrate into minerals (Kelley, 2002). Some minerals contain locations in their crystal structure that can accommodate Ar, such as mica (e.g., biotite), which in turn has a greater tendency to incorporate $^{40}Ar_E$, since such minerals have a relatively high Ar mineral/fluid partition coefficient. $^{40}Ar_E$ contamination of Fish Canyon biotite has occurred due to pockets of melt within range of biotite becoming significantly enriched in Ar, which has preferentially partitioned into biotite over other co-existing phases. Occurrences of $^{40}Ar_E$ in biotite are not uncommon in both igneous and metamorphic rocks (e.g., Thomas *et al.*, 2003; Gardner *et al.*, 2002; Bachmann *et al.*, 2010; Hora *et al.*, 2010), and the phase often yields ages too old to represent an eruption age. Fish Canyon biotite (and possibly Bishop Tuff biotite) can yield anomalously old ages compared to other K-bearing minerals, such as sanidine, which has a relatively high K_2O content, and so therefore a higher radiogenic component that is capable of masking the $^{40}Ar_E$ signal (e.g., Hora *et al.*, 2007 Hora *et al.*,

2010). In contrast Ar tends to display the lowest solubility in minerals, such as plagioclase (Kelley, 2002), and the numerous cases of $^{40}Ar_E$ contaminated plagioclase identified in this study (e.g., Fish Canyon plagioclase) are a result of inclusion hosted $^{40}Ar_E$ coupled with less radiogenic Ar to mask the $^{40}Ar_E$ signal.

5.2.4 Diffusion of extraneous Ar: implications for Ar-Ar dating

When older grains (either xenocrysts, or in the case of Sheridan Reservoir dome, antecrysts) are incorporated into a magma at magmatic temperatures (i.e., above a minerals closure temperature) they should diffusively lose radiogenic Ar, however the time required for complete re-setting may not be achieved and the result is partially re-set crystals which impart an inherited Ar component. Diffusion calculations (using experimentally derived parameters for K-feldspar where $D_0 = 0.982$ mm^2/sec; Ea = 43.8 ± 1.0 kcal/mol; Foland (1974), and plagioclase where $D_0 = 112000$ mm^2/sec and $E_a = 26.72$ kcal/mol; Wartho *et al.*, 2012), indicate that it would take 10 to 50 years, at temperatures of 700 to 800 °C for a 1 mm (grain diameter) sanidine antecryst (up to 1.5 Ma in age) to be fully reset and yield an eruption age, and therefore antecrystic sanidine entrained into the magma would be indistinguishable from phenocrysts after ~ 50 years. This reaffirms the understanding that sanidine experiences rapid diffusive equilibration with a 'sink', whether this be the surrounding melt or the atmosphere (e.g., Renne *et al.*, 1998; Hora *et al.*, 2007; 2010).

In contrast Ar loss from plagioclase (or anorthoclase) antecrysts (up to 1.5 Ma in age), at the same temperature would take > 1000 years to completely reset and yield an eruption age. This will have a significant impact on the accuracy of Ar-Ar eruption age determinations made on samples containing a mixture of crystals (with different compositions), indistinguishable from each other, which may contain an inherited Ar (or

indeed a $^{40}Ar_E$) component resulting in generally older ages. Specifically in the case of Sheridan Reservoir dome, it is inferred that a mixture of feldspar phenocrysts and antecrysts (incorporated between > 50 years and less than < 1000 years) are responsible for the range of Ar-Ar ages (1.97 ± 0.21 Ma to 3.34 ± 0.2 Ma) achieved. It is also inferred that residence time of more than 1000 years would see the anorthoclase and plagioclase reset, and therefore yield an eruption age.

5.3 Extraneous Ar in silicic magma systems

The main impetus for conducting this work has been to investigate occurrences of extraneous Ar in silicic volcanic systems, and in particular further our understanding of how magma chamber processes (e.g., 'self-cannibalisation'), and Ar distribution in a 'mush' magma chamber setting can impact on Ar-Ar determined ages.

5.3.1 Ar in a mush magma body

The magma reservoirs which produced the Fish Canyon Tuff (and associated dacitic eruptions), Huckleberry Ridge Tuff, Mesa Falls Tuff and associated rhyolitic domes, and the Bishop Tuff, all illustrate the concept of a mushy state magma body. $^{40}Ar_E$ contamination has not been detected in all case studies and reviewing the current magma reservoir models available for each system has proved extremely useful in understanding why this may be. The homogenous magma body of the Fish Canyon magmatic system (~ 45 % crystals), represents the reactivated (rejuvenated) stage of the mush model (e.g., Lipman *et al.*, 1997; Bachmann *et al.*, 2002; 2005; Bachmann and Bergantz 2003; 2008; Charlier *et al.*, 2005; Burgisser and Bergantz, 2011), and therefore provided the best opportunity to investigate $^{40}Ar_E$ contamination in a mush-dominant zone.

The identification of fluid inclusion hosted $^{40}Ar_E$ in a sanidine (~ 36 Ma; sample PCB 1), and significantly older plagioclase Ar-Ar ages (> 45 Ma) indicate that minerals grew in an environment containing $^{40}Ar^*$ decoupled from its parent K. Bachmann *et al.*, (2002) inferred at least 50 % of a mushy state magma reservoir volume is interstitial rhyolitic liquid, which can be retained for long periods of time (up to several thousand years). If this is the case then interstitial melt may act as an effective transport medium for $^{40}Ar_E$. Processes such as wall-rock assimilation, and thermal rejuvenation (e.g., 'gas sparging'; Bachmann *et al.*, 2002; Bachmann and Bergantz, 2003, or 'stable front remobilisation'; Burgisser and Bergantz, 2011) of the crystal mush, causing the dissolution of K-bearing minerals (e.g., feldspars) could be an affective mechanism whereby radiogenic $^{40}Ar^*$ is liberated and dissolved into pockets of interstitial melt.

In particular, the late stage growth of biotite in the Fish Canyon magma just prior to eruption should make it a reliable chronometer. However, Fish Canyon biotite generally yielded older ages, which suggests $^{40}Ar_E$ contamination occurred during late stage crystallisation in an Ar-rich environment due to the dissolution of K-bearing phases prior to eruption. Previous work (e.g., Bachmann *et al.*, 2002; 2005) has shown that Fish Canyon biotite was crystallising during feldspar and quartz resorption, and owing to its higher partition coefficient, Ar* in the pockets of gas-rich melt and fluid moving through, or locked within a crystal mush during thermal rejuvenation, may have reached a concentration that caused measurable concentrations in biotite via partitioning and diffusion processes.

The magma reservoirs that generated the HRT (and MFT), and the Bishop Tuff are thought to have been compositionally zoned (consisting of a melt dominant eruptible 'holding chamber' fed by a mush dominant root zone), and at a more mature stage at the point of eruption compared with the Fish Canyon magma body (Bachmann and Bergantz, 2008).

Early Bishop Tuff units (e.g., samples F5, F7, and Ig1Eb), contain predominantly crystal-poor pumices sourced from the high-silica rhyolite magma that was most differentiated, lowest in temperature, richest in an exsolved gas phase (e.g., Wallace *et al.*, 1999), and which resided at the top of the magma chamber (Hildreth and Wilson, 2007). The HRT, members A, B and C were the products of melt rising from depth to form three semi-independent magma bodies (Christiansen, 2001). The lack of $^{40}Ar_E$ contamination of HRT and Bishop Tuff samples could be attributed to the fact that significant proportions of the crystal-mush or crystallised side wall/roof material (e.g., absence of such material noted specially for Bishop Tuff ejecta, e.g., Wilson and Hildreth, 2007), was not tapped during eruption. An alternative explanation may be that the country rocks, which host these large silicic systems, which were presumably digested during magma chamber assembly and growth, were not a considerable source of K (and therefore $^{40}Ar_E$). For example Pre-Cambrian country rocks (e.g., in the case of Fish Canyon), could be a considerable source of $^{40}Ar_E$ dissolved in the melt.

Ar (similar to CO_2) tends to preferentially partition into an exsolved gas/vapour phase (Carroll and Stolper, 1993; Kelley, 2002), and may explain why $^{40}Ar_E$ has not been identified in crystals growing, or held in suspension, in the melt-dominant part of the magma chamber(s). Later units of the Bishop Tuff (e.g., Ig2Nb and Ig2NWa) contain relatively crystal-rich pumices which represent material sourced from deeper levels. Gas-saturation pressures (estimated for melt inclusions in quartz crystals; Hildreth and Wilson, 2007) suggests that Ig2 magma was withdrawn from the chamber at similar depths to Ig1 but also ~ 2 km deeper. Although the crystal rich nature of the Ig2 eruptive products (+ high temperature minerals such as pyroxene), suggests the more crystal rich, mush-dominant zone (predominantly feldspar + quartz) was excavated, perhaps significant amounts of mush remained. Cases of $^{40}Ar_E$ contamination in the Bishop Tuff appear to be associated with quartz (e.g., Winick *et al.*, 2001), although contamination of feldspar was

hypothesised. $^{40}Ar_E$ contamination of feldspar has not been detected in this study; therefore the K content of feldspar is possibly masking the effects of minor $^{40}Ar_E$ contamination (if present) in this case.

5.3.2 Inherited Ar contamination: antecrysts and xenocrysts

Effusive, less explosive eruptions, which are emplaced prior to and after explosive eruptions have been identified for several large, long-lived silicic magma systems (e.g., post-FCT Nutras Creek Dacite and pre-Bishop Tuff mafic to intermediate eruptions). This study has shown the task of determining an accurate eruption age for rhyolite domes using the Ar-Ar technique may be a difficult process and that systems recording a larger range of U-Pb ages due to recycling of xenocrysts and/or antecrysts, may be more likely to yield disturbed Ar-Ar ages. For example, the spread in U-Pb zircon ages for Snake River Butte dome (~ 1.92 up to ~ 2.4 Ma) and Sheridan Reservoir dome (~ 1.81 to ~ 2.83 Ma) record a 0.4 to ~ 1 Ma range in ages. Ar-Ar ages determined on the same samples also yielded a significant age range (although not identical), for example 1.61 to 2.46 Ma and 1.63 to 3.34 Ma for Snake River Butte dome and Sheridan Reservoir dome respectively. In contrast U-Pb ages for the Bishop Tuff and other Yellowstone magma systems (e.g., HRT, MFT and Green Canyon Flow dome), record a 0.1 to < 0.3 Ma range in ages, and significant disturbance (inherited or $^{40}Ar_E$) to Ar-Ar ages has not been detected.

The range of ages obtained for Sheridan Reservoir dome (and to a lesser extent, Snake River Butte dome) suggests prior to eruption, both magma chambers were actively contaminating through 'self-cannibalisation' (e.g., Gansecki *et al.*, 1996; 1998). Self-cannibalisation (process of recycling crystallised magma chamber material via stoping and partial assimilation of magma chamber wall/roof rock), is an effective way of incorporating a mixture of crystals (i.e., antecrysts and xenocrysts) from a variety of

sources and distribute them amongst a phenocryst population. The bulk assimilation model (e.g., Beard *et al.*, 2005), has provided a useful analogue and describes the incorporation and disintegration of small fragments of country rock. An effective tracer of reactive bulk assimilation is the presence of xenocrysts, in particular inherited zircon as a consequence of xenolith disintegration at magmatic temperatures < 800 °C (zircon dissolution temperature). Voluminous silicic magma chambers (such as Yellowstone; the Fish Canyon magmatic system and the Long Valley magmatic system) may be more susceptible to this process of 'self-cannibalisation' and contamination by antecrysts due to periods of gradual cooling and crystallisation, interrupted by periods of rejuvenation and recycling of crystallised material.

5.4 Conclusions

5.4.1 Application of *in situ* Ar-Ar extraction technique to minerals of the Fish Canyon magmatic system

- The UV *in situ* method (and in some cases the IR *in situ* method) can be successfully applied to young (< 40 Ma) volcanic minerals to investigate both inter- and intra-grain age variations.
- The success of an Ar-Ar extraction method can depend on mineral phase analysed (e.g., low K content of the mineral stipulates that a large area be ablated, but also varying partition between mineral phases and Ar diffusion rates), and crystal size (e.g., large enough to avoid inclusions, areas of alteration or crossing grain boundaries).
- The Nd-YAG laser has limited use on K-poor, optically transparent minerals (e.g., plagioclase feldspar) due to the poor absorption of the IR wavelength but it can be applied with moderate to high success to K-rich feldspars such as sanidine (possible

to achieve 0.69 % error compared to 8.97 % error for plagioclase), and dark minerals such as biotite.

- The *in situ* laser extraction techniques can be used to highlight Ar isotope ratio (e.g., $^{37}Ar/^{39}Ar$ and $^{38}Ar/^{39}Ar$) variation within single grains. This has been particularly important in identifying Ca-rich and K-poor zones within single crystals as well as allowing correlation of Cl/K ratio with apparent age.
- *In situ* Ar-Ar ages are in accordance with previously determined Ar-Ar ages (e.g., Ar-Ar total fusion ages of Bachmann *et al.*, 2007b), however this study has revealed an age range for various Fish Canyon minerals of > 30 Ma (25. 07 ± 1.86 Ma to 61.46 ± 10.11 Ma) with some minerals (e.g., plagioclase) yielding ages older than those determined by other geochronological techniques (e.g., U-Pb; Schmitz and Bowring 2001; Lanphere and Baadsgaard, 2001; Bachmann *et al.*, 2007b).
- This work has identified age variability within single crystals (e.g., age range of 28.06 ± 0.60 Ma to 36.42 ± 3.37 Ma in a single sanidine crystal), and between mineral phases (e.g., biotite has yielded ages > 1 Ma older than expected ages in some cases). Minor contamination has previously gone unnoticed owing to the high K content of K-feldspar (e.g., sanidine) and the 'homogenising effect' (mixing of $^{40}Ar^*$ signal with minor $^{40}Ar_E$) of previous total fusion or multi-crystal step heating experiments.
- Identification of slightly older ages (> 29 Ma), and significantly older Ar-Ar ages (> 45 Ma) are likely to represent $^{40}Ar_E$ released from fluid and/or melt inclusions (e.g., feldspars) and/or $^{40}Ar_E$ partitioned into minerals during growth (e.g., biotite).

Ar-Ar *in situ* analysis of multiple Fish Canyon mineral phases provided valuable insight into Ar distribution in a 'mushy' magma body prior to eruption.

- Interstitial rhyolitic liquid (which can form at least 50 % of magma reservoir volume; Bachmann *et al.*, 2002) can act as an effective transport medium for $^{40}Ar_E$

due to a high Ar solubility in rhyolite melts (e.g., > 0.1 ppm bar^{-1}; Carroll and Stolper, 1993).

- The presence of inclusion hosted $^{40}Ar_E$ in sanidine and plagioclase indicate minerals trapped $^{40}Ar_E$ sourced from pockets of interstitial melt during growth. This process would be repeated during cycles of crystal mush reheating and remelting events.
- Ar equilibration between different phases depends on the relative solubilities. Biotite incorporates excess Ar due to relatively high Ar mineral/fluid partition coefficient, which has therefore resulted in older than expected ages. Therefore, despite crystallising just prior to eruption, $^{40}Ar_E$ contamination (retained by the mineral following eruption) has rendered this phase an unreliable chronometer without separate corroboration of the ages.

5.4.2 Yellowstone: new insights into caldera and post-caldera activity

This work has provided the opportunity to determine new Ar-Ar eruption ages for rhyolite domes of the Yellowstone Plateau Volcanic Field previously only dated using the K-Ar technique.

- Green Canyon Flow dome: 1.29 ± 0.01 Ma (n = 55; MSWD = 0.80)
- Sheridan Reservoir dome: 2.04 ± 0.03 Ma (n = 30; MSWD = 0.03)
- Snake River Butte dome: 2.15 ± 0.01 Ma (1 – 2 mm feldspar ; n = 59; MSWD = 1.3)

The new ages determined on separated sanidine (Green Canyon Flow dome), and glass (Snake River Butte dome and Sheridan Reservoir dome) are now in agreement with field evidence and new Ar-Ar eruption ages determined for Huckleberry Ridge Tuff (HRT) and Mesa Falls Tuff (MFT) in this study.

New Ar-Ar eruption ages for Huckleberry Ridge Tuff (HRT members A, B and C) and Mesa Falls Tuff (MFT) of the Yellowstone Plateau Volcanic Field are as follows:

- HRT Member A: 2.11 ± 0.02 Ma (n = 38; MSWD = 0.96)
- HRT Member B: 2.12 ± 0.04 Ma (n = 42; MSWD = 0.8)
- HRT Member C: 2.11 ± 0.02 Ma (n = 29; MSWD = 0.99)

The Ar-Ar ages for individual members of the HRT eruption are indistinguishable from each other and are in agreement with U-Pb zircon ages (Wilson and Charlier, on-going study), and the paleomagnetic study by Reynolds (1977), which favour the single eruption model. The data presented here do not reproduce those found in the study of Ellis *et al.*, (2012), which resulted in a model of at least one much longer hiatus between the eruptive units (~ 6 kyr between eruption of member B and C). A single eruption age (combining sanidine ages from each member) is 2.11 ± 0.01 Ma (including external errors and those associated with the decay factor).

- Mesa Falls Tuff: 1.28 ± 0.01 Ma (n = 40; MSWD = 1.4)

The new Ar-Ar age is slightly younger than the previously reported age of ~ 1.3 Ma (e.g., Lanphere, 2000 cited in Christiansen, 2000; Gansecki *et al.*, 1998; Lanphere *et al.*, 2002).

Single-grain fusion ages determined for a variety of eruptive units of the Yellowstone Plateau volcanic field has provided insight into magma chamber processes and the potential implications for Ar-Ar dating.

- Ar-Ar single-grain fusion dating of three effusive rhyolite domes has revealed variable levels of contamination. Green Canyon Flow dome yielded a narrow range of feldspar ages (1.20 ± 0.06 to 1.35 ± 0.10 Ma), and no evidence of extraneous Ar contamination. In contrast, Snake River Butte dome feldspars revealed a range in

ages with a tail to older ages (1.61 ± 0.40 to 2.46 ± 0.25 Ma), and Sheridan Reservoir dome feldspars yielded the most significant range of ages (1.63 ± 0.3 to 3.34 ± 0.4 Ma), a range which is also recorded by coexisting zircons from Sheridan Reservoir dome.

- The spread to older ages is a result of a mixture of crystals (antecrysts imparting an inherited Ar component and phenocrysts) present within a single pumice, which are chemically similar to each other and therefore cannot be separated prior to analysis.
- During thin section analysis resorption of large feldspar crystals (e.g., Sheridan Reservoir dome) was noted. Some grains exhibit a sieve texture, while others show resorbed margins suggesting recycling and remelting of crystallised material occurred.

Diffusion modelling has shown sanidine reintroduced into the magma chamber is able to diffusively re-equilibrate over a shorter timescale compared with plagioclase feldspar (and anorthoclase).

- Sanidine is more likely to yield an eruption age (e.g., Green Canyon Flow dome), whereas magma systems dominated by antecrystic anorthoclase and/or plagioclase (e.g., Sheridan Reservoir dome feldspar composition predominantly anorthoclase Or_{15} to Or_{50}) may yield a range of ages.
- Analysis of multiple co-existing phases using the Ar-Ar technique (e.g., feldspar and glass), is key to assessing the degree of contamination. For example accepting an age of 2.25 ± 0.07 Ma (n = 60; MSWD = 5.8) determined using Sheridan Reservoir dome feldspar is not in accordance with field information.
- Successful dating of glass separated from two rhyolitic domes (Sheridan Reservoir and Snake River Butte domes) has proved to be a useful geochronological tool and has provided a good estimate of the eruption age. Glass from both domes contained ~ 5 wt. % K_2O and did not appear to have undergone hydration or alteration.

5.4.3 Bishop Tuff: new Ar-Ar ages for ash fall and ignimbrite flow units

New Ar-Ar ages determined on samples of Bishop Tuff pumice collected from five basal, non-welded sections (F5 and F7 represent the plinian ash fall units, and Ig1Eb Ig2NWa and Ig2Nb represent ignimbrite flow packages) yield ages as follows:

- Fall Unit 5: 0.763 ± 0.010 Ma (n = 43; MSWD = 0.75)
- Fall Unit 7: 0.766 ± 0.012 Ma (n = 17; MSWD = 1.3)
- Ignimbrite Unit Ig1Eb: 0.749 ± 0.008 Ma (n = 60; MSWD = 0.88)
- Ignimbrite Unit Ig2NWa: 0.759 ± 0.008 Ma (n = 25; MSWD = 0.71)
- Ignimbrite Unit Ig2Nb: 0.754 ± 0.010 Ma (n = 19; MSWD = 0.54)

- This work has not detected a significant Ar-Ar age difference between ash fall and ignimbrite flow deposits of the Bishop Tuff and weighted mean ages determined on crystals separated from whole pumices overlap at the 2σ level which is close to 10,000 years.
- The preferred eruption age of the Bishop Tuff (combining Ar-Ar sanidine ages obtained from both fall units and flow packages) is 0.757 ± 0.004 Ma (n = 135; MSWD = 0.83). This age is younger than recently reported Ar-Ar ages for the Bishop Tuff, in particular compared to the Rivera *et al.*, (2011) age of 0.772 Ma and the Winick *et al.*, (2001) age of 0.781 Ma (calculated relative to ^{40}K decay constant of Renne *et al.*, 2010). The Ar-Ar age determined in this study is younger than previously reported U-Pb ages (e.g., 0.811 to 0.823 Ma; Simon and Reid, (2005), and 0.767 Ma; Crowley *et al.*, (2007)).
- The various weathering indices (CIA, PIA, CIW and WIP) do not vary between samples, and in general results suggest samples are not significantly disturbed. Further testing using the alkali mobility plots of Hildreth and Wilson (2007), also suggests samples have not been significantly hydrated.

- This study has not identified measurable amounts of extraneous Ar contamination (inverse isochron analyses of all samples have shown the trapped Ar component to be atmospheric in composition) of separated feldspar crystals.
- No significant difference in Ar-Ar age could be identified between crystal poor pumice (inferred to represent the top of the magma chamber), and crystal rich pumice (inferred to represent deeper 'mush' layers within the chamber).
- Inclusion hosted $^{40}Ar_E$ contamination of sanidine, as hypothesised by Winick *et al.*, (2001), has not been detected despite analysed crystals containing abundant inclusions.
- Bishop Tuff units F5 (sample BP029), and Ig1Eb (sample BP097), contained abundant plagioclase (up to An_{16}). Ar-Ar ages determined on plagioclase are within error of sanidine weighted mean ages (e.g., sample BP029; sanidine age of 0.76 ± 0.01 Ma compared to plagioclase age of 0.76 ± 0.13 Ma).
- The low K content (generally < 4 %) and therefore relatively smaller $^{40}Ar^*$ yield has resulted in lower analytical precision for plagioclase and large associated uncertainties. An overall decrease in precision has resulted in errors on plagioclase age determinations ranging 6 % to 66 %, which emphasises the reduced applicability of K-poor minerals separated from < 1 Ma units.
- Only two single feldspar crystals (out of > 260) yielded older (at the 2σ level) ages. The elevated ages may represent $^{40}Ar_E$ contamination or xenocrysts (in particular for Ca-rich grain where a measured $^{37}Ar/^{39}Ar$ ratio of 0.512 ± 0.009 was significantly higher compared to other analyses). Therefore crystals contaminated by extraneous Ar appear to be rare to absent.
- Biotite Ar-Ar apparent ages (sample BP168), range 0.619 ± 1.029 Ma to 1.502 ± 0.763 Ma (n = 6) and yield a weighted mean age of 1.10 ± 0.21 Ma, which is slightly older than the ~ 0.76 Ma eruption taking into account the analytical errors.

The inverse isochron plot yields a $^{40}Ar/^{36}Ar$ intercept of atmospheric composition (284 ± 51; within uncertainty of 298.56), providing no evidence to support $^{40}Ar_E$ contamination. An alternative explanation is that the slightly older biotite ages represent either partially re-set xenocrysts (e.g., pyroclastic debris or country rock), or antecrysts sourced from the crystal-rich magma chamber rind and/or mush zone.

5.4.4 Important considerations and recommendations

Despite extraneous Ar contamination, Ar-Ar dating can be successfully applied to the products of silicic volcanism. The following section outlines some recommendations based on the results and conclusions of this study, which if followed may aid successful Ar-Ar dating of products of silicic volcanic systems.

- **Sample selection**

Contamination of tephra horizons and whole rock ignimbrite deposits by older foreign material (i.e., xenocrysts), can be significant (e.g., Gansecki *et al.*, 1996; 1998; Semaw *et al.*, 1997). Therefore, it is recommended that phases suitable for Ar-Ar dating are separated from juvenile clasts (e.g., whole pumices). The results of this study tend to show a significant lack of persistent contamination by significantly older material sourced from surrounding country rocks or previously erupted deposits. This is particularly true for Yellowstone and Bishop Tuff samples, and may in part be due to fact that minerals and phases of interest have been carefully separated from intact pumice clasts, which have therefore not incorporated older random material during explosive eruption. It should be noted that although previous work has shown that contamination of juvenile material (e.g., pumice; van den Bogaard *et al.*, 1989; 1995; Wilson and Hildreth, 1997; 1998) can occur,

this work suggests the impact on Ar-Ar dating can be minimal and significantly older ages are easily identifiable and therefore can be justifiably rejected.

It is essential that samples are characterised and assessed for potential alteration prior to Ar-Ar analysis. For this study extreme care had been taken over sampling, and only fresh pumices from glassy non-welded areas of ignimbrite, rhyolite dome, and air fall deposits were collected. Processes such as groundwater, surface water and vapour-phase interaction (during welding) can lead to significant chemical alteration, recrystallization of the glass phase or crystallisation of secondary alteration minerals (Wilson and Hildreth, 1997; Hildreth and Wilson, 2007). Pumice freshness can be tested in the field (pumice will 'squeak' when rubbed together), and oxidised rinds (orange or pink in colour), can be easily removed. This is extremely important for deposits which exhibit a variable preservation state (e.g., the Bishop Tuff). Application of weathering indices to samples that are barely altered is not advised, and assessing the degree of alkali mobility (K and Na), may prove to be more useful. This is of particular importance to Ar-Ar dating, where interaction with fluids and/or a vapour-phase during weathering, can result in redistribution of K and/or Ar.

- **Material to analyse**

This study has highlighted the difficulty in obtaining precise and accurate geochronological information from various phases which are commonly and routinely used for Ar-Ar dating. For example, analysis of biotite has provided further evidence in support of previous work, which has reported that biotite can alter readily (e.g., Hildreth and Wilson, 2007) and incorporate $^{40}Ar_E$ (e.g., Thomas *et al.*, 2003; Dazé *et al.*, 2003; Hora *et al.*, 2010; Bachmann *et al.*, 2010). Plagioclase is commonly separated from low-K samples (e.g., basalts), and used to determine eruption ages. This study has found several examples

of older plagioclase ages, most notably from samples of the Fish Canyon magmatic system, due to inclusion hosted $^{40}Ar_E$. Diffusion modelling has shown plagioclase feldspar (and anorthoclase), reintroduced into the magma chamber will diffusively re-equilibrate over a longer timescale compared with other feldspar phases (e.g., sanidine). This may explain why sanidine is more likely to yield an eruption age (e.g., Green Canyon Flow dome), and why magma systems dominated by antecrystic anorthoclase and plagioclase (e.g., Sheridan Reservoir dome) will yield a range of ages.

It is recommended that the application of the Ar-Ar technique to biotite is avoided and its application to plagioclase and anorthoclase be limited. If possible sanidine should be separated and analysed. *In situ* and single-grain fusion experiments have shown that sanidine, although not completely void of contamination, often yields the best results, and perhaps in young samples the K content of sanidine (~ 12 %) is capable of masking the effects of minor $^{40}Ar_E$ contamination. In addition to sanidine, separating where possible fresh glass from samples may also yield useful geochronological information. Successful dating of glass (rhyolitic glassy groundmass) separated from Yellowstone rhyolite domes, Sheridan Reservoir and Snake River Butte domes has proved to be extremely useful in determining an eruption age. In both cases, although most notable in the case of Sheridan Reservoir dome, separated feldspars (minor sanidine, anorthoclase, and minor plagioclase), were identified as being compromised due to recycling of previously crystallised material. Previous work has highlighted the susceptibility of glass to alteration, through hydration and devitrification processes (e.g., Kaneoka, 1972; Dalyrymple and Lanphere, 1969; Foland *et al.*, 1993; Clay *et al.*, 2011), therefore it is recommended that appropriate characterisation of glassy samples be carried out. This should involve conducting thorough thin section analyses to check for spherulite growth and crystallisation of secondary alteration minerals. XRF analysis of samples should be carried out, and L.O.I. values should be monitored, as a high L.O.I. value may indicate samples are hydrated. If possible

a single-grain EMP study should be undertaken to assess the K content of the glass as well as identifying low SiO_2 contents (< 97 %), which may indicate the presence of water (± other volatiles), and therefore hydrated samples.

- **Analytical method**

The application of various Ar-Ar extraction techniques (e.g., UV and IR *in situ* and IR single-grain fusion) throughout the course of this study has been extremely useful in identifying cases of extraneous Ar in silicic volcanic systems. The UV and IR *in situ* technique has provided a method of identifying $^{40}Ar_E$ hosted in fluid and melt inclusions in a variety of minerals, and its ability to identify minerals, which reproducibly yield older ages (e.g., biotite and plagioclase). Although the application to young samples and K-poor minerals is limited (due to sample size required), the UV *in situ* technique in particular is recommended to investigate heterogeneities at a single-grain level, and can provide a method to avoid pockets of $^{40}Ar_E$ within single crystals (owing to the precision and control of the UV laser compared with the IR *in situ* or single-grain fusion techniques). The strong coupling of the UV laser with clear minerals, such as feldspar, means it is possible to spatially resolve otherwise undetected apparent age variability within single crystals (e.g., Bachmann *et al.*, 2007b).

Analysing single crystals by single-grain fusion will highlight those grains which yield older than expected ages and therefore identify obvious contamination (e.g., Deino and Potts, 1992). The technique is better suited for locating contaminating crystals amongst a juvenile phenocryst population compared with bulk total-fusion experiments where by any inherited Ar component is diluted by $^{40}Ar^*$ released from phenocryst phases. Therefore it not recommended to carry out bulk total-fusion on samples where determining an eruption age is the ultimate goal (e.g., Rivera *et al.*, 2011). Instead, dating single grains of multiple

phases (e.g., sanidine and glass), can provide a statistically robust eruption age, and identify the presence of subtle contamination (e.g., recycling of crystallised magma chamber side walls/roof) by antecrysts (e.g., Sheridan Reservoir dome).

- **Data reduction**

One of the keys to obtaining high precision $^{40}Ar/^{39}Ar$ ages is precise and accurate measurement of ^{36}Ar contamination. For minerals of the Fish Canyon magmatic system, containing low (at or just above instrument blank level) amounts of ^{36}Ar, data can be corrected without applying the ^{36}Ar corrections ($^{40}Ar_A$ component and reactor induced ^{36}Ar due to ^{40}Ca). Applying this correction in cases where a negative ^{36}Ar value is obtained, which is then propagated through the age equation, can result in slightly older ages than if the ^{36}Ar corrections were not applied. In the case where the ^{36}Ar measurement is at blank level, then applying the corrections can result in errors being propagated through the age equation. It is recommended that data is corrected with and without applying the ^{36}Ar corrections in order to assess the difference between the two methods, and if ages are within error of each other, then either age can be taken. Where the 'no ^{36}Ar correction' age is taken then the error should be doubled to account for this (following method after Sherlock *et al.*, 2008).

- **Data interpretation**

The use of the error-weighted mean is justified in most cases (e.g., determining the eruption age of Green Canyon Flow dome and HRT members A, B and C), it should be used alongside the full range of data. It is recommended the spread in Ar-Ar single-grain fusion ages, obtained from a single sample be assessed in order to interpret the final age. For example, taking the weighted mean age of 2.25 ± 0.07 Ma (2σ; n = 60) for the eruption of Sheridan Reservoir dome, would not be advised as this age is too old (relative to HRT

based on field evidence). Therefore considering the full range of ages for this sample in this study resulted in the identification of inherited Ar contamination. Where possible it is recommended that Ar-Ar ages be compared to U-Pb zircon ages obtained from the same sample. The distribution of zircon ages may be used as a tracer for self-contamination processes, and may allude to varying degrees of inheritance.

Diffusion modelling has revealed plagioclase and anorthoclase feldspar will diffusively lose radiogenic Ar at a slower rate compared to sanidine at magmatic temperatures. This can be a particular problem where recycling of already crystallised material results in self-contamination and mixing of antecrysts (containing an inherited Ar component), with a phenocryst population and indicated by the subtle spread of Ar-Ar ages (although not identified for all effusive rhyolite eruptions investigated). Therefore the relative Ar retention properties of different feldspar phases should also be considered when interpreting Ar-Ar single-grain fusion ages.

The use of the inverse isochron method is recommended but should be used with caution. A common feature of this data set is inverse isochron plots characterised by clustering of data points at the X-axis, and limited dispersion along the mixing line. The most likely reason for a poor fit to a straight line is that the data array is actually nonlinear and there is no simple mixing between $^{40}Ar^*$ and a trapped Ar component atmospheric in composition. Samples unsurprisingly do contain a mixture of crystals which are of slightly different ages due to containing either inherited (in situ produced and $^{40}Ar_E$) or variable amounts of $^{40}Ar_E$, and therefore using this method to distinguish between crystals from multiple sources is not possible.

5.5 Future work

It has not been possible to pursue all additional research ideas which formulated over the course of this study. The following list provides some possible avenues for future work including suggestions which may improve and expand the current data set

- Application of the Ar-Ar laserprobe technique to the products of other silicic 'mushy' magma chambers, which may have different magma storage histories (e.g., Toba Caldera Complex), in particular those volcanic systems which may be suitable for the *in situ* approach (e.g., oldest ignimbrites erupted 11 to 10 Ma from the Altiplano-Puna volcanic complex of the central Andes, South America), would be useful to test the findings of this study.

- The precision of single-grain fusion ages determined on low K minerals (e.g., plagioclase) could be improved if extracted Ar isotopes (in particular ^{36}Ar and ^{37}Ar used in corrections and relatively small amounts of $^{40}Ar^*$) are measured in a high-resolution mass spectrometer (e.g., Nu Instruments Noblesse). In order to prevent contamination of the mass spectrometer by unwanted volatiles released from the sample during degassing, a cold trap would need to be used.

- Further investigation into age differences recorded by minerals (in particular anorthoclase and plagioclase), and glass would be extremely useful. Identifying several different case studies and analysing specifically crystal and glass mixes would assess how reproducible the differences in age recorded by two phases are.

- This study has demonstrated some Yellowstone rhyolite domes are 'self-contaminating' and previous K-Ar determinations are inconsistent with field

observations. Applying the Ar-Ar technique to products of other dome-building eruptions (e.g., Big Bend Ridge Rhyolites; Headquarters Flow dome and Blue Creek Flow dome), will further our understanding of the Yellowstone magmatic system, as well as provide ages which are better constrained.

- A comparative study concentrating on extraneous Ar in large-scale intermediate volcanic systems (e.g., the eruptive products of the Trans-Mexican Volcanic Belt), which generally have a lower K content and a mineral abundance dominated by plagioclase feldspar would be interesting. How prevalent is the contamination of plagioclase? How useful could glass be as a geochronological tool in such systems?

References

Anderson, A. T., Davis, A. M. & Lu, F. (2000). Evolution of Bishop Tuff Rhyolitic Magma Based on Melt and Magnetite Inclusions and Zoned Phenocrysts. *Journal of Petrology* **41**, 449 - 473.

Arnaud, N. O. & Kelley, S. P. (1997). Argon behaviour in gem-quality orthoclase from Madagascar: Experiments and some consequences for 40Ar/39Ar geochronology. *Geochimica et Cosmochimica Acta* **61**, 3227 - 3255.

Bachmann, O. (2001). The Volcanology, Petrology, and Geochronology of the Fish Canyon Magmatic System, San Juan Volcanic Field, USA. PhD Thesis.

Bachmann, O. & Bergantz, G. W. (2003). Rejuvenation of the Fish Canyon magma body: A window into the evolution of large-volume silicic magma systems. *Geology* **31**, 789 - 792.

Bachmann, O. & Bergantz, G. W. (2004). On the origin of crystal-poor rhyolites: extracted from batholithic crystal mushes. *Journal of Petrology* **45**, 1565 - 1582.

Bachmann, O. & Bergantz, G. W. (2006). Gas percolation in upper-crustal silicic crystal mushes as a mechanism for upward heat advection and rejuvenation of near-solidus magma bodies. *Journal of Volcanology and Geothermal Research* **149**, 85 - 102.

Bachmann, O. & Bergantz, G. W. (2008). The Magma Reservoirs That Feed Supereruptions. *Elements* **4**, 17 - 21.

Bachmann, O., Charlier, B. L. A. & Lowenstern, J. B. (2007). Zircon crystallization and recycling in the magma chamber of the rhyolitic Kos Plateau Tuff (Aegean arc). *Geology* **35**, 73 - 76.

Bachmann, O., Dungan, M. A. & Lipman, P. W. (2002). The Fish Canyon Magma Body, San Juan Volcanic Field, Colorado: Rejuvenation and Eruption of an Upper-Crustal Batholith. *Journal of Petrology* **43**, 1469 - 1503.

Bachmann, O., Oberli, F., Dungan, M. A., Meier, M., Mundil, R. & Fischer, H. (2007b). $^{40}Ar/^{39}Ar$ and U-Pb dating of the Fish Canyon magmatic system, San Juan Volcanic field, Colorado: Evidence for an extended crystallization history. *Chemical Geology* **236**, 134 - 166.

Bachmann, O., Dungan, M. A. & Bussy, F. (2005). Insights into shallow magmatic processes in large silicic magma bodies: The trace element record in the Fish Canyon magma body, Colorado. *Contributions to Mineralogy and Petrology* **149**, 338 - 349.

Bachmann, O., Schoene, B., Schnyder, C. & Spikings, R. (2010). The $^{40}Ar/^{39}Ar$ and U/Pb dating of young rhyolites in the Kos-Nisyros volcanic complex, Eastern Aegean Arc, Greece: Age discordance due to excess ^{40}Ar in biotite. *Geochemistry Geophysics Geosystems* **11**, 1 - 14.

Bacon, C. R. & Lowenstern, J. B. (2005). Late Pleistocene granodiorite source for recycled zircon and phenocrysts in rhyodacite lava at Crater Lake, Oregon. *Earth and Planetary Science Letters* **233**, 277 - 293.

Baksi, A. K., Archibald, D. A. & Farrar, E. (1996). Intercalibration of $^{40}Ar/^{39}Ar$ dating standards. *Chemical Geology* **129**, 307 - 324.

Baksi, A. K., Hoffman, K. A. & McWilliams, M. (1993). Testing the accuracy of the geomagnetic polarity time-scale (GPTS) at 2-5 Ma, utilizing $^{40}Ar/^{39}Ar$ incremental heating data on whole-rock basalts. *Earth and Planetary Science Letters* **118**, 135 - 144.

Baksi, A. K. (2012). "New $^{40}Ar/^{39}Ar$ dating of the Grande Ronde lavas, Columbia River Basalts, USA: Implications for duration of flood basalt eruption episodes" by Barry *et al.*, (2010) – Discussion. *Lithos* **146 – 147**, 293 - 299.

Barry, T. L., Self, S., Kelley, S. P., Reidel, S., Hooper, P. & Widdowson, M. (2010). New $^{40}Ar/^{39}Ar$ dating of the Grande Ronde lavas, Columbia River Basalts, USA: Implications for duration of flood basalt eruption episodes. *Lithos* **118**, 213 - 222.

Beard, J. S., Ragland, P. C. & Crawford, M. L. (2005). Reactive bulk assimilation: A model for crust-mantle mixing in silicic magmas. *Geology* **33**, 681 - 684.

Bindeman, I. N., Fu, B., Kita, N. T. & Valley, J. W. (2008). Origin and Evolution of Silicic Magmatism at Yellowstone Based on Ion Microprobe Analysis of Isotopically Zoned Zircons. *Journal of Petrology* **49**, 163 - 193.

Bigazzi, G., Laurenzi, M. A., Soligo, M. & Tuccimei, P. (2005). Multi-method approach to dating glass: The case of Basiluzzo Islet (Aeolian archipelago, Italy). *Journal of Volcanology and Geothermal Research* **177**, 244 - 250.

Bindeman, I. N., Schmitt, A. K. & Valley, J. W. (2006). U-Pb zircon geochronology of silicic tuffs from the Timber Mountain/Oasis Valley caldera complex, Nevada: Rapid generation of large volume magmas by shallow-level remelting. *Contributions to Mineralogy and Petrology* **152**, 649 - 665.

Bindeman, I. N. & Valley, J. W. (2001). Low-$\delta^{18}O$ Rhyolites from Yellowstone: Magmatic Evolution Based on Analysis of Zircons and Individual Phencrysts. *Journal of Petrology* **42**, 1491 - 1517.

Bindeman, I. N., Valley, J. W., Wooden, J. L. & Persing, H. M. (2001). Post-caldera volcanism: *in-situ* measurement of U-Pb age and oxygen isotope ratio in Pleistocene zircons from Yellowstone caldera. *Earth and Planetary Science Letters* **189**, 197 - 206.

Bindeman, I. N., Watts, K. E., Schmitt, A. K., Morgan, L. A. & Shanks, P. W. C. (2007). Voluminous low $\delta^{18}O$ magmas in the late Miocene Heise volcanic field, Idaho: Implications for the fate of Yellowstone hotspot calderas. *Geology* **35**, 1019 - 1022.

Boven, A., Pasteels, P., Kelley, S. P., Punzalan, L., Bingen, B. & Demaiffe, D. (2001). $^{40}Ar/^{39}Ar$ study of plagioclases from the Rogaland anorthosite complex (SW Norway); An attempt to understand argon ages in plutonic plagioclase. *Chemical Geology* **176**, 105 - 135.

Burgisser, A. & Bergantz, G. W. (2011). A rapid mechanism to remobilize and homogenize highly crystalline magma bodies. *Nature* **471**, 212 – 216.

Carroll, M. R. (1991). Diffusion of Ar in rhyolite, orthoclase and albite composition glasses. *Earth and Planetary Science Letters* **103**, 156 - 168.

Carroll, M. R. & Stolper, E. M. (1991). Argon solubility and diffusion in silica glass: Implications for the solution behaviour of molecular gases. *Geochimica et Cosmochimica Acta* **55**, 211 - 225.

Carroll, M. R. & Stolper, E. M. (1993). Noble gas solubilities in silicate melts and glasses: New experimental results for argon and the relationship between solubility and ionic porosity. *Geochimica et Cosmochimica Acta* **57**, 5039 - 5051.

Cassata, W. S. Renne, P. R. & Shuster, D. L. 2009. Argon diffusion in plagioclase and implications for thermochronometry: A case study from the Bushveld Complex, South Africa. *Geochimica et Cosmochimica Acta*, **73**, 6600 - 6612.

Cerling, T. E., Brown, F. H. & Bowman, J. R. (1985) Low-temperature alteration of volcanic glass: Hydration, Na, K, ^{18}O and Ar mobility. *Chemical Geology* **52**, 281 - 293.

Chamorro, E. M., Brooker, R. A., Wartho, J.-A., Wood, B. J., Kelley, S. P. & Blundy, J. D. (2002). Ar and K partitioning between clinopyroxene and silicate melt to 8 GPa. *Geochimica et Cosmochimica Acta* **66**, 507 - 519.

Channel, J. E. T., Hodell, D. A., Singer, B. S. & Xuan, C. (2010). Reconciling astrochronological and $^{40}Ar/^{39}Ar$ ages for the Matuyama-Brunhes boundary and late Matuyama Chron. *Geochemistry Geophysics Geosystems* **11**, 1 - 21.

Charlier, B. L. A., Bachmann, O., Davidson, J. P., Dungan, M. A. & Morgan, D. J. (2007). The Upper Crustal Evolution of a Large Silicic Magma Body: Evidence from Crystal-scale Rb-Sr Isotopic Heterogeneities in the Fish Canyon Magmatic System, Colorado. *Journal of Petrology* **48**, 1875 - 1894.

Charlier, B. L. A., Wilson, C. J. N., Lowenstern, J. B., Blake, S., Van Calsteren, P. W. & Davidson, J. P. (2005). Magma Generation at a Large, Hyperactive Silicic Volcano (Taupo, New Zealand) Revealed by U-Th and U-Pb Systematics in Zircons. *Journal of Petrology* **46**, 3 - 32.

Charlier, B. & Zellmer, G. (2000). Some remarks on U-Th mineral ages from igneous rocks with prolonged crystallisation histories. *Earth and Planetary Science Letters* **183**, 457 - 469.

Chen, Y., Smith, P. E., Evensen, N. M., York, D. & Lajoie, K. R. (1996) The Edge of Time: Dating Young Volcanic Ash Layers with $^{40}Ar/^{39}Ar$ laser probe. *Science* **274**, 1176 - 1178.

Chesner, C. A. (1998). Petrogenesis of the Toba Tuffs, Sumatra, Indonesia. *Journal of Petrology* **39**, 397 - 438.

Cherniak, D. J. & Watson, E. B. (2001) Pb diffusion in zircon. *Chemical Geology* **172**, 5 – 24.

Christensen, J. N. & DePaolo, D. J. (1993). Time scales of large volume silicic magma systems: Sr isotopic systematics of phenocrysts and glass from the Bishop Tuff, Long Valley, California. *Contributions to Mineralogy and Petrology* **113**, 100 - 114.

Christensen, J. N. & Halliday, A. N. (1996). Rb-Sr ages and Nd isotopic compositions of melt inclusions from the Bishop Tuff and the generation of silicic magma. *Earth and Planetary Science Letters* **144**, 547 - 561.

Christiansen, R. L. (2001). The Quaternary and Pliocene Yellowstone Plateau Volcanic Field of Wyoming, Idaho, and Montana. *U.S. Geological Survey Professional Paper* **729-G**.

Clay, P. L., Kelley, S. P., Sherlock, S. C. & Barry, T. L. (2011). Partitioning of excess argon between alkali feldspars and glass in a young volcanic system. *Chemical Geology* **289**, 12 - 30.

Crowley, J. L., Schoene, B. & Bowring, S. A. (2007). U-Pb dating of zircon in the Bishop Tuff at the millennial scale. *Geology* **35**, 1123 - 1126.

Dalrymple, G. B., Cox, A. & Doell, R. R. (1965). Potassium-Argon Age and Paleomagnetism of the Bishop Tuff, California. *Geological Society of America Bulletin* **76**, 665 - 674.

Dalrymple, G. B. & Lanphere, M. A. (1969) Potassium-Argon Dating – Principles, techniques and Applications to Geochronology. W. H. Freeman and Company, San Francisco.

Dalrymple, B. & Moore, J. G. (1968). Argon-40: Excess in Submarine Pillow Basalts from Kilauea Volcano, Hawaii. *Science* **161**, 1132 - 1135.

Dáze, A., Lee, J. K. W. & Villeneuve, M. (2003). An intercalibration study of the Fish Canyon sanidine and biotite $^{40}Ar/^{39}Ar$ standards and some comments on the age of the Fish Canyon Tuff. *Chemical Geology* **199**, 111 - 127.

Deino, A. L., Orsi, G., De Vita, S. & Piochi, M. (2004). The age of the Neapolitan Yellow Tuff caldera-forming eruption (Campi Flegrei caldera - Italy) assessed by $^{40}Ar/^{39}Ar$ dating method. *Journal of Volcanology and Geothermal Research* **133**, 157 - 170.

Deino, A. & Potts, R. (1990). Single-Crystal $^{40}Ar/^{39}Ar$ Dating of the Olorgesailie Formation, Southern Kenya Rift. *Journal of Geophysical Research* **95**, 8453 - 8470.

Deino, A. & Potts, R. (1992). Age-Probability Spectra For Examination Of Single-Crystal $^{40}Ar/^{39}Ar$ Dating Results: Examples From Olorgesailie, Southern Kenya Rift. *Quaternary International* **13/14**, 47 - 53.

Deino, A. L., Tauxe, L., Monaghan, M. & Hill, A. (2002). $^{40}Ar/^{39}Ar$ geochronology and paleomagnetic stratigraphy of the Lukeino and lower Chemeron Formations at Tabarin and Kapcheberek, Tugen Hills, Kenya. *Journal of Human Evolution* **42**, 117 - 140.

Dodson, M. H. (1973). Closure Temperature in Cooling Geochronological and Petrological Systems. *Contributions to Mineralogy and Petrology* **40**, 259 - 27.

Drake, R. E., Curtis, G. H., Cerling, T. E., Cerling, B. W. & Hampel, J. (1980). KBS dating and geochronology of tuffaceous sediments in the Koobi Fora and Shungura Formations, East Africa. *Nature* **283**, 368 – 372.

Ellis, B. S., Mark, D. F., Pritchard, C. J. & Wolff, J. A. (2012). Temporal dissection of the Huckleberry Ridge Tuff using the $^{40}Ar/^{39}Ar$ dating technique. *Quaternary Geochronology* **9**, 34 – 41.

Esser, R. P., McIntosh, W. C., Heizler, M. T. & Kyle, P. R. (1997). Excess argon in melt inclusions in zero-age anorthoclase feldspar from Mt. Erebus, Antarctica, as revealed by the $^{40}Ar/^{39}Ar$ method. *Geochimica et Cosmochimica Acta* **61**, 3789 - 3801.

Fedo, C. M., Nesbitt, H. W. & Young, G. M. (1995). Unravelling the effects of potassium metasomatism in sedimentary rocks and paleosols, with implications for paleoweathering conditions and provenance. *Geology* **23**, 921 – 924.

Flude, S., Burgess, R. & McGarvie, D. W. (2008). Silicic volcanism at Ljósufjöll, Iceland: Insights into evolution and eruptive history from Ar-Ar dating. *Journal of Volcanology and Geothermal Research* **169**, 154 - 175.

Foland, K. A. (1974). ^{40}Ar diffusion in homogeneous orthoclase and an interpretation of Ar diffusion in K-feldspars. *Geochimica et Cosmochimica Acta* **38**, 151 - 166.

Foland, K. A., Fleming, T. H., Heimann, A. & Elliot, D. H. (1993). Potassium-argon dating of fine-grained basalts with massive Ar loss: Application of the $^{40}Ar/^{39}Ar$ technique to plagioclase and glass from the Kirkpatrick Basalt, Antarctica. *Chemical Geology* **107**, 173 - 190.

Gansecki, C. A., Mahood, G. A. & McWilliams, M. O. (1996). $^{40}Ar/^{39}Ar$ geochronology of rhyolites erupted following collapse of the Yellowstone caldera, Yellowstone Plateau volcanic field: implications for crustal contamination. *Earth and Planetary Science Letters* **142**, 91 - 107.

Gansecki, C. A., Mahood, G. A. & McWilliams, M. (1998). New ages for the climactic eruptions at Yellowstone: Single-crystal $^{40}Ar/^{39}Ar$ dating identifies contamination. *Geology* **26**, 343 – 346.

Garcia, T., Feraud, G., Falgueres, C., de Lumley, H., Perrenoud, C. & Lordkipanidze, D. (2010). Earliest human remains in Eurasia: New $^{40}Ar/^{39}Ar$ dating of the Dmanisi hominid-bearing levels, Georgia. *Quarternary Geochronology* **5**, 443 – 451.

Gardner, J. E., Layer, P. W. & Rutherford, M. J. (2002). Phenocrysts versus xenocrysts in the youngest Toba Tuff: Implications for the petrogenesis of 2800 km^3 of magma. *Geological Society of America* **30**, 347 - 350.

Girard, G. & Stix, J. (2009). Magma Recharge and Crystal Mush Rejuvenation Associated with Early Post-collapse Upper Basin Member Rhyolites, Yellowstone Caldera, Wyoming. *Journal of Petrology* **50**, 2095 - 2125.

Girard, G. & Stix, J. (2010). Rapid extraction of discrete magma batches from a large differentiating magma chamber: The Central Plateau Member rhyolites, Yellowstone Caldera, Wyoming. Contributions to Mineralogy and Petrology **160**, 441 – 465.

Halliday, A. N., Fallick, A. E., Hutchinson, J. & Hildreth, W. (1984). A Nd, Sr and O isotope investigation into the causes of chemical and isotopic zonation in the Bishop Tuff, California. *Earth and Planetary Science Letters* **68**, 379 - 391.

Halliday, A. N., Mahood, G. A., Holden, P., Metz, J. M., Dempster, T. J. & Davidson, J. P. (1989). Evidence for long residence times of rhyolitic magma in the Long Valley

magmatic system: the isotopic record in precaldera lavas of Glass Mountain. *Earth and Planetary Science Letters* **94**, 274 – 290.

Harnois, L. (1988). The CIW index: a new chemical index weathering. *Sedimentary Geology* **55**, 319 – 322.

Harrison, T. M., Heizler, M. T., Lovera, O. M., Wenji, C. & Grove, M. (1994). A chlorine disinfectant for excess argon released from K-feldspar during step heating. *Earth and Planetary Science Letters* **123**, 95 – 104.

Heizler, M. T. & Harrison, T. M. (1988). Multiple trapped argon isotope components revealed by $^{40}Ar/^{39}Ar$ isochron analysis. *Geochimica et Cosmochimica Acta* **52**, 1295 - 1303.

Hess, J. C. & Lippolt, H. J. (1986). $^{40}Ar/^{39}Ar$ ages of tonstein and tuff sanidines: New calibration points for the improvement of the upper Carboniferous time scale. *Chemical Geology* **59**, 143 - 154.

Hildreth, W. (1979). The Bishop Tuff: Evidence for the origin of compositional zonation in silicic magma chambers. *Geological Society of America Special Paper* **180**, 43 - 75.

Hildreth, W. (2004) Volcanological perspectives on Long Valley, Mammoth Mountain, and Mono Craters: several contiguous but discrete systems. *Journal of Volcanology and Geothermal Research* **136**, 168 – 198.

Hildreth, W. & Mahood, G. (1985). Correlation of ash-flow tuffs. *Geological Society of America Bulletin* **96**, 968 - 974.

Hildreth, W. & Mahood, G. (1986). Ring-fracture eruption of the Bishop Tuff. *Geological Society of America Bulletin* **97**, 396 - 403.

Hildreth, W. & Wilson, C. J. N. (2007). Compositional Zoning of the Bishop Tuff. *Journal of Petrology* **48**, 951 - 999.

Honey, J. G., Hudson, M. R. & Obradovich, J. D. (1998). The occurrence of the Reunion II Subchron in lacustrine beds in the Beaver Basin, Utah, *in* Tomida, Y., Flynn, L.J., and Jacobs, L.L., eds., *Advances in vertebrate palaeontology and geochronology*: Tokyo, National Science Museum Monograph **14**, 17 - 38.

Hora, J. M., Singer, B. S., Jicha, B. R., Beard, B. L., Johnson, C. M., de Silva, S. & Salisbury, M. (2010). Volcanic biotite-sanidine $^{40}Ar/^{39}Ar$ age discordances reflect Ar partitioning and pre-eruption closure in biotite. *Geology* **38**, 923 - 926.

Hora, J. M., Singer, B. S. & Wörner, G. (2007). Volcano evolution and eruptive flux on the thick crust of the Andean Central Volcanic Zone: $^{40}Ar/^{39}Ar$ constraints from Volcán Parinacota, Chile. *Geological Society of America Bulletin* **119**, 343 - 362.

Hurford, M. T. & Hammerschmidt, K. (1985). $^{40}Ar/^{39}Ar$ and K-Ar dating of the Bishop and Fish Canyon Tuffs: Calibration ages for fission-track dating standards. *Chemical Geology* (Isotope Geoscience Section) **58**, 23 - 32.

Izett, G. A. & Obradovich, J. D. (1994). $^{40}Ar/^{39}Ar$ age constraints for the Jaramillo Normal Subchron and the Matuyama-Brunhes geomagnetic boundary. *Journal of Geophysical Research* **99**, 2925 - 2934.

Izett, G. A., Obradovich, J. D. & Mehnery, H. H. (1988). The Bishop Ash Bed (Middle Pleistocene) and Some Older (Pliocene and Pleistocene) Chemically and Mineralogically Similar Ash Beds in California, Nevada, and Utah. *U. S. Geological Survey Bulletin* **1675**.

Jones, D. A., Layer, P. W. & Newberry, R. J. (2008). A 3100-year history of argon isotopic and compositional variation at El Chichón volcano. *Journal of Volcanology and Geothermal Research* **175**, 427 – 443.

Jourdan, F., Matzel, J. P. & Renne, P. R. (2007). ^{39}Ar and ^{37}Ar recoil loss during neutron irradiation of sanidine and plagioclase. *Geochimica et Cosmochimica Acta* **71**, 2791 - 2808.

Jourdan, F. & Renne, P. R. (2007). Age calibration of the Fish Canyon sanidine $^{40}Ar/^{39}Ar$ dating standard using primary K-Ar standards. *Geochimica et Cosmochimica Acta* **71**, 387 - 402.

Kaneoka, I. (1972). The effect of hydration on the K/Ar ages of volcanic rocks. *Earth and Planetary Science Letters* **14**, 216 – 220.

Kay, S. M., Coira, B., Wörner, G., Kay, R. W. & Singer, B. S. (2011). Geochemical, isotopic and single crystal $^{40}Ar/^{39}Ar$ age constraints on the evolution of the Cerro Galán ignimbrites. *Bulletin of Volcanology* **73**, 1487 - 1511.

Kelley, S. (2002). Excess argon in K-Ar and Ar-Ar geochronology. *Chemical Geology* **188**, 1 - 22.

Kelley, S. P., Arnaud, N. O. & Turner, S. P. (1994). High spatial resolution $^{40}Ar/^{39}Ar$ investigations using a ultra-violet laser probe extraction technique. *Geochimica et Cosmochimica Acta* **58**, 3519 - 3525.

Kelley, S., Turner, G., Butterfield, A. W. & Shepherd, T. J. (1986). The source and significance of argon isotopes in fluid inclusions from areas of mineralization. *Earth and Planetary Science Letters* **79**, 303 - 318.

Kuiper, K. F., Deino, A., Hilgen, F. J., Krijgsman, W., Renne, P. R. & Wijbrans, J. R. (2008). Synchronizing Rock Clocks of Earth History. *Science* **320**, 500 - 504.

Kuiper, K. F., Hilgen, F. J., Steenbrink, J. & Wijbrans, J. R. (2004). $^{40}Ar/^{39}Ar$ ages of tephras intercalated in astronomically tuned Neogene sedimentary sequences in the eastern Mediterranean. *Earth and Planetary Science Letters* **222**, 583 - 597.

Landoll, J. D., Foland, K. A. & Henderson, C. M. B. (1989). Excess argon in amphiboles from fluid interaction and short intrusion interval at the epizonal Marangudzi complex, Zimbabwe. *Journal of Geophysical Research* **94**, 4053 - 4069.

Lanphere, M. A. & Baadsgaard, H. (2001). Precise K-Ar, $^{40}Ar/^{39}Ar$, Rb-Sr and U/Pb mineral ages from the 27.5 Ma Fish Canyon Tuff reference standard. *Chemical Geology* **175**, 653 - 671.

Lanphere, M. A., Champion, D. E., Christiansen, R. L., Izett, G. A., & Obradovich, J. D. (2002). Revised ages for tuffs of the Yellowstone Plateau volcanic field: Assignment of the Huckleberry Ridge Tuff to a new geomagnetic polarity event. *Geological Society of America Bulletin* **114**, 559 – 568.

Lanphere, M. A. & Dalrymple, G. B. (2000). First-Principles Calibration of ^{38}Ar Tracers: Implications for the Ages of $^{40}Ar/^{39}Ar$ Fluence Monitors. *U.S. Geological Survey Professional Paper* **1621,** 1 - 10.

Layer, P. W. & Gardner, J. E. (2001). Excess argon in Mount St. Helens plagioclase as a recorder of magmatic processes. *Geophysical Research Letters* **28**, 4279 - 4282.

Lee, J. K. W. (1995). Multipath diffusion in geochronology. *Contributions to Mineralogy and Petrology* **120**, 60 - 82.

Lee, J.-Y., Marti, K., Severinghaus, J, P., Kawamura, K., Yoo, H-S., Lee, J. B. & Kim, J. S. (2006). A redetermination of the isotopic abundances of atmospheric Ar. *Geochimica et Cosmochimica Acta* **70**, 4507 - 4512.

Le Maître, R. W., Bateman, P., Dudek, A., Keller, J., Lameyre Le Bas, M. J., Sabine, P.A., Schmid, R., Sorensen, H., Streckeisen, A., Woolley, A. R. & Zanettin, B. (1989). *A classification of igneous rocks and glossary of terms*. Blackwell, Oxford.

Lipman, P. W, Dungan, M. & Bachmann, O. (1997). Comagmatic granophyric granite in the Fish Canyon Tuff, Colorado: Implications for magma-chamber processes during a large ash-flow eruption. *Geology* **25**, 915 - 918.

Lipman, P. W. & McIntosh, W. C. (2008) Eruptive and noneruptive calderas, northeastern San Juan Mountains, Colorado: Where did the ignimbrites come from? *Geological Society of America Bulletin* **120**, 771 - 795.

Lo Bello, Ph., Féraud, G., Hall, C. M., York, D., Lavina, P. & Bernat, M. (1987). $^{40}Ar/^{39}Ar$ Step-heating and Laser Fusion Dating of a Quaternary Pumice from Neschers, Massif Central, France: The Defeat of Xenocrystic Contamination. *Chemical Geology* **66**, 61 - 71.

Lovera, O. M., Richter, f. M. & Harrison, T. M. (1989). The $^{40}Ar/^{39}Ar$ Thermochronology for Slowly Cooled Samples Having a Distribution of Diffusion Domain Sizes. *Journal of Geophysical Research* **94**, 17917 - 17935.

Lowenstern, J. B., Persing, H. M., Wooden, J. L., Lanphere, M., Donnelly-Nolan, J. & Grove, T. L. (2000). U-Th dating of single zircons from young granitoid xenoliths: new tools for understaning volcanic processes. *Earth and Planetary Science Letters* **183**, 291 – 302.

Ludwig, K. R. (2011). *Isoplot/Ex version 4.15: A Geochronological Toolkit for Microsoft™ Excel™*. Berkeley, CA: Berkeley Chronology Centre.

Mahood, G. A., Ring, J. H., Manganelli, S. & McWilliams, M. O. (2010). New $^{40}Ar/^{39}Ar$ ages reveal contemporaneous mafic and silicic eruptions during the past 160,000 years at Mammoth Mountain and Long Valley caldera, California. *Geological Society of America Bulletin* **12**, 396 - 407.

Mahood, G. A. (1990). Evidence for long residence times of rhyolite magma in the Long Valley magmatic system: The isotopic record in precaldera lavas of Glass Mountain: Reply: *Earth and Planetary Science Letters* **99**, 395 – 399.

Mark, D. F., Renne, P. R., Morgan, L. E., Deino, A., Smith, V. C., Ellis, B. S., and Pearce, N. J. (2012). $^{40}Ar/^{39}Ar$ dating of Pleistocene tuffs: an accurate age for the Matuyama-Brunhes geomagnetic reversal (MBGR). AGU Fall Meeting Abstract, San Francisco, USA.

Metz, J. M. & Mahood, G. A. (1985). Precursors to the Bishop Tuff Eruption: Glass Mountain, Long Valley, California. *Journal of Geophysical Research* **90**, 11121 - 11126.

McDougall, I. (1985). K-Ar and $^{40}Ar/^{39}Ar$ dating of the hominid-bearing Pliocene-Pleistocene sequence at Koobi Fora, Lake Turkana, northern Kenya. *Geological Society of America Bulletin* **96**, 159 – 175.

McDougall, I. & Harrison, T. M. (1999). *Geochronology and Thermochronology by the $^{40}Ar/^{39}Ar$ Method*, 2nd ed. New York: Oxford Univ. Press.

McDougall, I., Brown, F. H., Vasconcelos, P. M., Cohen, E. B., Thiede, D. S. & Buchanan, M. J. (2012). New single crystal 40Ar/39Ar ages improve time scale for deposition of the Omo Group, Omo-Turkana Basin, East Africa. *Journal of the Geological Society* **169**, 212 – 226.

Min, K., Mundil, R., Renne, P. R. & Ludwig, K. R. (2000). A test for systematic errors in $^{40}Ar/^{39}Ar$ geochronology through comparison with U/Pb analysis of a 1.1-Ga rhyolite. *Geochimica et Cosmochimica Acta* **64**, 73 - 98.

Morgan, L. A., Doherty, D. J. & Leeman, W. P. (1984). Ignimbrites of the eastern Snake River Plain: Evidence for major caldera-forming eruptions. *Journal of Geological Research* **89**, 8665 - 8678.

Morgan, L. A. & McIntosh, W. C. (2005). Timing and development of the Heise volcanic field, Snake River Plain, Idaho, western USA. *Geological Society of America Bulletin* **117**, 288 - 306.

Morgan, L. E., Renne, P. R., Taylor, R. E. & WoldeGabriel, G. (2009). Archaeological age constraints from extrusion ages of obsidian: Examples from the Middle Awash, Ethiopia. *Quaternary Geochronology* **4**, 193 - 203.

Naeser, C. W., Izett, G. A. & Wilcox, R. E. (1973). Zircon Fission-Track Ages of Pearlette Family Ash Beds in Meade County, Kansas. *Geology* **1**, 187 - 189.

Nesbitt, H. W. & Young, G. M. (1984). Prediction of some weathering trends of plutonic and volcanic rocks based on thermodynamic and kinetic considerations. *Geochimica Cosmochimica Acta* **48**, 1523 - 1534.

Nielson, J. E., Lux, D. R., Dalrymple, G. B. & Glazner, A. F. (1990). Age of the Peach Springs Tuff, Southeastern California and Western Arizona. *Journal of Geophysical Research* **95**, 571 - 580.

Nier, A. O. (1947). A mass spectrometer for isotope and gas analysis. *Rev. Sci. Inst.* **18**, 398 – 411.

Obradovich, J. D. (1992). Geochronology of the late Cenozoic volcanism of Yellowstone National Park and adjoining areas, Wyoming and Idaho: *U.S. Geological Survey Open-File Report.*

Obradovich, J. D. & Izett, G. A. (1991). $^{40}Ar/^{39}Ar$ ages of upper Cenozoic Yellowstone Group tuffs: *Geological Society of America Abstracts with Programs* **23** (2), p. A84.

Odin, G. S., Takahashi, M. & Cosca, M. (1995). $^{40}Ar/^{39}Ar$ geochronology of biostratigraphically controlled Miocene tuffs from central Japan: Comparison with Italy and age of the Serravallian-Tortonian boundary. *Chemical Geology* **125**, 105 - 121.

Pamukcu, A. S., Guilherme, A. R. & Anderson, A. T. (2012). Crystallization Stages of the Bishop Tuff Magma Body Recorded in Crystal Textures in Pumice Clasts. *Journal of Petrology* **53**, 589 - 609.

Parker, A. (1970). An Index of weathering for silicate rocks. *Geological Magazine* **107**, 501 - 504.

Perkins, M. E. & Nash, B. P. (2002). Explosive silicic volcanism of the Yellowstone hotspot: The ash fall tuff record. *Geological Society of America Bulletin* **114**, 367 - 381.

Price, J. R. & Velbel, M. A. (2003). Chemical weathering indices applied to weathering profiles developed on heterogeneous felsic metamorphic parent rocks. *Chemical Geology* **202**, 397 - 416.

Pringle, M. S., McWilliams, M., Houghton, B. f., Lanphere, M. A. & Wilson, C. J. N. (1992). $^{40}Ar/^{39}Ar$ dating of Quaternary feldspar: Examples from the Taupo Volcanic Zone, New Zealand. *Geology* **20**, 531 - 534.

Putlitz, B., Cosco, M. A. & Schumacher, J. C. (2005). Prograde mica $^{40}Ar/^{39}Ar$ growth ages recorded in high pressure rocks (Syros, Cyclades, Greece). *Chemical Geology* **214**, 79 – 98.

Rama, S. N. I. & Hart, S. R. (1965). Excess Radiogenic Argon in Fluid Inclusions. *Journal of Geophysical Research* **70**, 509 - 511.

Reddy, S. M., Potts, G. J. & Kelley, S. P. (2001). $^{40}Ar/^{39}Ar$ ages in deformed potassium feldspar: Evidence of microstructural control on Ar isotope systematics. *Contributions to Mineralogy and Petrology* **141**, 186 - 200.

Reddy, S. M., Potts, G. J., Kelley, S. P. & Arnaud, N. O. (1999). The effects of deformation-induced microstructures on intragrain $^{40}Ar/^{39}Ar$ ages in potassium feldspar. *Geology* **27**, 363 - 366.

Reid, M. R. & Coath, C. D. (2000). *In situ* U-Pb ages of zircons from the Bishop Tuff: No evidence for long crystal residence times. *Geology* **28**, 443 - 446.

Reid, M. A. & Coath, C. D., Harrison, T. M. & McKeegan, K. D. (1997) Prolonged residence times for the youngest rhyolites associated with Long Valley Caldera: ^{230}Th-238U ion microprobe dating of young zircon. *Earth Planetary Science Letters* **150**, 27 - 39.

Reid, M. R., Vazquez, J. A. & Schmitt, A. K. (2011). Zircon-scale insights into the history of a Supervolcano, Bishop Tuff, Long Valley, California, with implications for the Ti-in-zircon geothermometer. *Contributions to Mineralogy and Petrology* **161**, 293 – 311.

Renne, P. R., Balco, G., Ludwig, K. R., Mundil, R. & Min, K. (2011). Response to the comment by W. H. Schwarz *et al.* on "Joint determination of ^{40}K decay constants and ^{40}Ar*/^{40}K for the Fish Canyon sanidine standard, and improved accuracy for ^{40}Ar/^{39}Ar geochronology" by P.R. Renne *et al.*, 2010. *Geochimica et Cosmochimica Acta* **75**, 5097 - 5100.

Renne, P. R., Deino, A. L., Hames, W. E., Heizler, M. T., Hemming, S. R., Hodges, K. V., Koppers, A. A. P., Mark, D. F., Morgan, L. E., Phillips, D., Singer, B. S., Turrin, B. D., Villa, I. M., Villeneuve, M. & Wijbrans, J. R. (2009). Data reporting norms for ^{40}Ar/^{39}Ar geochronology. *Quaternary Geochronology* **4**, 346 - 352.

Renne, P.R., Deino, A.L., Walter, R.C., Turrin, B.D., Swisher, C.C., Becker, T.A., Curtis, G.H., Sharp, W.D. & Jaouni, A.-R. (1994). Intercalibration of astronomical and radioisotopic time. *Geology* **22**, 783-786.

Renne, P. R., Mundil, R., Balco, G., Min, K. & Ludwig, K. R. (2010). Joint determination of ^{40}K decay constants and ^{40}Ar*/^{40}K for the Fish Canyon sanidine standard, and improved accuracy for ^{40}Ar/^{39}Ar geochronology. *Geochimica et Cosmochimica Acta* **74**, 5349 - 5367.

Renne, P. R., Mulcahy, S. R., Cassata, W. S., Morgan, L. E., Kelley, S. P., Hlusko, L. J. & Njau, J. K. (2012). Retention of inherited Ar by alkali feldspar xenocrysts in a magma: Kinetic constraints from Ba zoning profiles. *Geochimica et Cosmochimica Acta* **93**, 129 - 142.

Renne, P. R. & Norman, E. B. (2001). Determination of the half-life of ^{37}Ar by mass spectrometry. *Physical Review C*, **63**.

Renne, P. R., Sharp, W. D., Deino, A. L., Orsi, G. & Civetta, L. (1997). $^{40}Ar/^{39}Ar$ Dating into the Historical Realm: Calibration Against Pliny the Younger. *Science* **277**, 1279 - 1280.

Renne P. R., Sharp Z. D. & Heizler M. T. (2008). Cl-derived argon isotope production in the CLICIT facility of OSTR reactor and the effects of the Cl-correction in $^{40}Ar/^{39}Ar$ geochronology. *Chemical Geology* **255**, 463 - 466.

Renne, P. R., Swisher, C. C., Deino, A. L., Karner, D. B., Owens, T. L. & DePaolo, D. J. (1998). Intercalibration of standards, absolute ages and uncertainties in $^{40}Ar/^{39}Ar$ dating. *Chemical Geology* **145**, 117 - 152.

Renne, P. R., Ernesto, M., Pacca, I. G., Coe, R. S., Glen, J. M., Prévot, M. & Perrin, M. (1992). The age of Paraná Flood Volcanism, Rifting of Gondwanaland, and the Jurassic-Cretaceous Boundary. *Science* **258**, 975 – 979.

Reynolds, R. L. (1977). Paleomagnetism of Welded Tuffs of the Yellowstone Group. Journal of Geophysical Research **82**, 3677 – 3693.

Rivera, T. A., Storey, M., Zeeden, C., Hilgen, F. J. & Kuiper, K. (2011). A refined astronomically calibrated $^{40}Ar/^{39}Ar$ age for Fish Canyon sanidine. *Earth and Planetary Science Letters* **311**, 420 - 426.

Rutherford, E. & Soddy, F. (1902). The cause and nature of radioactivity. *Philosophical Magazine*. Series 6 (**4**).

Sarna-Wojcicki, A. M., Pringle, M. S. & Wijbrans, J. (2000). New $^{40}Ar/^{39}Ar$ age of the Bishop Tuff from multiple sites and sediment rate calibration for the Matuyama-Brunhes boundary. *Journal of Geophysical Research* **105**, 21431 - 21443.

Saunders, A. D., Jones, S. M., Morgan, L. A., Pierce, K. L., Widdowson, M. & Xu, Y. G. (2007). Regional uplift associated with continental large igneous provinces: The role of mantle plumes and the lithosphere. *Chemical Geology* **241**, 282 - 318.

Semaw, S., Renne, P., Harris, J. W. K., Feibel, C. S., Bernor, R. L., Fesseha, N. & Mowbray, K. (1997). 2.5-million-year-old stone tools from Gona, Ethiopia. *Nature* **385**, 333 - 336.

Schmitz, M. D. & Bowring, S. A. (2001). U-Pb zircon and titanite systematics of the Fish Canyon Tuff: an assessment of high-precision U-Pb geochronology and its application to young volcanic rocks. *Geochimica et Cosmochimica Acta* **65**, 2571 - 2587.

Schmitz, M. D., Bowring, S. A., Ludwig, K. R. & Renne, P. R. (2003). Comment on "Precise K-Ar, $^{40}Ar/^{39}Ar$, Rb-Sr and U-Pb mineral ages from the 27.5 Ma Fish Canyon Tuff reference standard" by M. A. Lanphere and H. Baadsgaard. *Chemical Geology* **199**, 277 - 280.

Schwanethal, J. (2008) ArMaDiLo Instruction Manual, 11p.

Sherlock, S. C. & Arnaud, N. O. (1999). Flat plateau and impossible isochrons: Apparent $^{40}Ar/^{39}Ar$ geochronology in a high-pressure terrain. *Geochimica et Cosmochimica Acta* **63**, 2835 - 2838.

Sherlock, S. C. & Kelley, S. P., (2002). Excess argon evolution in HP-LT rocks: a UVLAMP study of phengite and K-free minerals, NW Turkey. *Chemical Geology* **182**, 619 - 636.

Sherlock, S., Kelley, S., Inger, S., Harris, N. & Okay, A. (1999). $^{40}Ar/^{39}Ar$ and Rb-Sr geochronology of high-pressure metamorphism and exhumation history of the Tavsanli Zone, NW Turkey. *Contributions to Mineralogy and Petrology* **137**, 46 - 58.

Sherlock, S. C., Lucks, T., Kelley, S. P. & Barnicoat, A. (2005). A high resolution record of multiple diagenetic events: Ultraviolet laser microprobe $^{40}Ar/^{39}Ar$ analysis of zoned K-feldspar overgrowths. *Earth and Planetary Science Letters* **238**, 329 - 341.

Sherlock, S. C., Zalasiewicz, J., Kelley, S. P. & Evans, J. (2008). Excess argon ($^{40}Ar_E$) uptake during slate formation; A $^{40}Ar/^{39}Ar$ UV laserprobe study of muscovite strain-fringes from the Palaeozoic Welsh Basin, UK. *Chemical Geology* **257**, 203 - 217.

Simon, J. I. & Reid, M. R. (2005). The pace of rhyolite differentiation and storage in an 'archetypical' silicic magma system, Long Valley, California. *Earth and Planetary Science Letters* **235**, 123 - 140.

Simon, J. I., Renne, P. R. & Mundil, R. (2008). Implications of pre-eruptive magmatic histories of zircons for U-Pb geochronology of silicic extrusions. *Earth and Planetary Science Letters* **266**, 182 - 194.

Singer, B. S., Wijbrans, J. R., Nelson, S. T., Pringle, M. S., Feeley, T. C. & Dungan, M. A. (1998). Inherited argon in Pleistocene andesite lava: $^{40}Ar/^{39}Ar$ incremental-heating and laser-fusion analyses of plagioclase. *Geology* **26**, 427 - 430.

Smith, R. L. & Bailey, R. A. (1966). The Bandelier Tuff: A Study of Ash-flow Eruption Cycles from Zoned Magma Chambers. *Bulletin of Volcanology* **29**, 83 – 103.

Smith, M. E., Singer, B. S., Carroll, A. R. & Fournelle, J. H. (2008). Precise dating of biotite in distal volcanic ash: Isolating subtle alteration using $^{40}Ar/^{39}Ar$ laser incremental heating and electron microprobe techniques. *American Mineralogist* **93**, 784 - 795.

Sparks, R. S. J. (1997). Causes and consequences of pressurisation in lava dome eruptions. *Earth and Planetary Science Letters* **150**, 177 – 189.

Spell, T. L. & Harrison, T. M. (1993). $^{40}Ar/^{39}Ar$ Geochronology of Post-Valles Caldera Rhyolites, Jemez Volcanic Field, New Mexico. *Journal of Geophysical Research* **98**, 8031 - 8051.

Spell, T. L., Harrison, T. M. & Wolff, J. A. (1990). $^{40}Ar/^{39}Ar$ dating of the Bandelier Tuff and San Diego Canyon ignimbrites, Jemez Mountains, New Mexico: Temporal constraints on magmatic evolution. *Journal of Volcanology and Geothermal Research* **43**, 175 - 193.

Spell, T. L. & McDougall, I. (2003). Characterization and calibration of $^{40}Ar/^{39}Ar$ dating standards. *Chemical Geology* **198**, 189 – 211.

Spell, T. L., Smith, E. I., Sanford, A. & Zanetti, K. A. (2001). Systematics of xenocrystic contamination: Preservation of discrete feldspar populations at McCullough Pass Caldera revealed by $^{40}Ar/^{39}Ar$ dating. *Earth and Planetary Science Letters* **190**, 153 - 165.

Steiger, R. H. & Jäger, E. (1977). Subcommission on geochronology: Convention on the use of the decay constants in geo- and cosmochemisrty. *Earth and Planetary Science Letters* **36**, 359 – 362.

Storey, M., Roberts, R. G. & Saidin, M. (2012). Astronomically calibrated $^{40}Ar/^{39}Ar$ age of the Toba supereruption and global synchronization of late Quaternary records. Proceedings of the National Academy of Sciences of the United States of America **109**, 18684 - 18688.

Tait, S., Jaupart, C. & Vergniolle, S. (1989). Pressure, gas content and eruption periodicity of a shallow, crystallising magma chamber. *Earth and Planetary Science Letters* **92**, 107 – 123.

Thomas, L., Blake, S., Kelley, S. & Van Calsteren, P. (2003). Evolution of the Youngest Toba Tuff: Evidence for Magma Generation by Remobilisation of an Igneous Complex. SOTA, Mt Hood, OR.

Thomas, J. B., Cherniak, D. J. & Watson, E. B. (2008). Lattice diffusion and solubility of argon in forsterite enstatite, quartz and corundum. *Chemical Geology* **253**, 1 - 22.

Ton-That, T., Singer, B.S. & Paterne, M. (2001). $^{40}Ar/^{39}Ar$ of latest Pleistocene (41 ka) marine tephra in the Mediterranean Sea: implications for global climate records. *Earth and Planetary Science Letters* **184**, 645 - 658.

Turbeville, B. N. & Self, S. (1988). San Diego Canyon Ignimbrite: Pre-Bandelier Tuff Explosive Rhyolitic Volcanism in the Jemez Mountains, New Mexico. *Journal of Geophysical Research* **93**, 6148 - 6156.

van den Bogaard, P. (1995). $^{40}Ar/^{39}Ar$ ages of sanidine phenocrysts from Laacher See Tephra (12,900 yr BP): Chronostratigraphic and petrological significance. *Earth and Planetary Science Letters* **133**, 163 - 174.

van den Bogaard, P., Hall, C. M., Schmincke, H.-U. & York., D. (1987) $^{40}Ar/^{39}Ar$ laser dating of single grains: Ages of Quaternary tephra from East Eifel volcanic field. *Geophysical Research Letters* **14**, 1211 - 1214.

van den Bogaard, P., Hall, C. M., Schmincke, H.-U. & York, D. (1989). Precise single-grain $^{40}Ar/^{39}Ar$ dating of a cold to warm climate transition in Central Europe. *Nature* **342**, 523 – 525.

van Den Bogaard, P. & Schirnick, C. (1995). $^{40}Ar/^{39}Ar$ laser probe ages of Bishop Tuff quartz phenocrysts substantiate long-lived silicic magma chamber at Long Valley, United States. *Geology* **23**, 759 - 762.

Vazquez, J. A., Kyriazis, S. F., Reid, M. R., Sehler, R. C. & Ramos, F. R. (2009). Thermochemical evolution of young rhyolites at Yellowstone: Evidence for a cooling but periodically replenished post-caldera magma reservoir. *Journal of Volcanology and Geothermal Research* **188**, 186 – 196.

Vazquez, J. A. & Reid, M. A. (2002). Time scales of magma storage and differentiation of voluminous high-silica rhyolites at Yellowstone caldera, Wyoming. *Contributions to Mineralogy and Petrology* **144**, 274 - 285.

Vazquez, J. A. & Reid, M. A. (2004). Probing the Accumulation History of the Voluminous Toba Magma. *Science* **305**, 991 - 994.

Villa, I. M. (1991). Excess Ar geochemistry in potassic volcanites. *Schweizerische Mineralogische und Petrographische Mitteilungen* **71**, 205 - 219.

Villeneuve, M., Sandeman, H. A. & Davis, W. J. (2000). A method for intercalibration of U-Th-Pb and $^{40}Ar/^{39}Ar$ ages in the Phanerozoic. *Geochimica et Cosmochimica Acta* **64**, 4017 - 4030.

Vogel, N., Nomade, S., Negash, A. & Renne, P. (2006) Forensic $^{40}Ar/^{39}Ar$ dating: a provenance study of Middle Stone Age obsidian artifacts from Ethiopia. *Journal of Archaeological Science* **33**, 1749 - 1765.

Walker, D. A. & McDougall, I. (1982). $^{40}Ar/^{39}Ar$ and K-Ar dating of altered glassy volcanic rocks: the Dabi Volcanics, P.N.G. *Geochimica et Cosmochimica Acta* **46**, 2181 - 2190.

Wallace, P. J., Anderson Jr, A. T. & Davis, M. (1999). Gradients in H_2O, CO_2, and exsolved gas in a large-volume silicic magma system: Interpreting the record preserved in melt inclusions from the Bishop Tuff. *Journal of Geophysical Research* **104**, 20097 - 20122.

Warren, C. J., Hanke, F. & Kelley, S. P. (2011). When can muscovite $^{40}Ar/^{39}Ar$ dating constrain the timing of metamorphic exhumation. *Chemical Geology* **291**, 79 - 86.

Warren, C. J., Smye, A. J., Kelley, S. P. & Sherlock, S. C. (2012). Using white mica $^{40}Ar/^{39}Ar$ data as a tracer for fluid flow and permeability under high-*P* conditions: Tauern Window, Eastern Alps. *Journal of Metamorphic Geology* **30**, 63 - 80.

Wartho, J.-A., Kelley, S. P., Brooker, R. A., Carroll, M. R., Villa, I. M. & Lee, M. R. (1999). Direct measurement of Ar diffusion profiles in a gem-quality Madagascar K-feldspar using the ultra-violet laser ablation microprobe (UVLAMP). *Earth and Planetary Science Letters* **170**, 141 - 153.

Wartho, J-A., Kelley, S. P. & Elphick, S. C. (2012). Ar Diffusion and Solubility Measurements in Plagioclases using the Ultra-Violet Laser Depth Profiling Technique. *Journal of the Geological Society* (***In Press***).

Watson, E. B. & Cherniak, D. J. (2003). Lattice diffusion of Ar in quartz, with constraints on Ar solubility and evidence of nanopores. *Geochimica et Cosmochimica Acta* **67** (11), 2043 – 2062.

Watts, K. E., Bindeman, I. N. & Schmitt, A. K. (2011). Large-volume Rhyolite Genesis in Caldera Complexes of the Snake River Plain; Insights from the Kilgore Tuff of the Heise Volcanic Field, Idaho, with Comparison to Yellowstone and Bruneau-Jarbidge Rhyolites. *Journal of Petrology* **52**, 857 - 890.

Whitney, J. A. & Stormer J. C. (1985). Mineralogy, Petrology, and Magmatic Conditions from the Fish Canyon Tuff, Central San Juan Volcanic Field, Colorado. *Journal of Petrology* **26**, 726 - 762.

Wheeler, J. (1996). Diffarg: A Program for Simulating Argon Diffusion Profiles in Minerals. *Computers and Geosciences* **22**, 919 - 929.

Wilson, C. J. N. & Hildreth, W. (1997). The Bishop Tuff: New Insights from Eruptive Stratigraphy. *The Journal of Geology* **105**, 407 - 439.

Wilson, C. J. N. & Hildreth, W. (1998). Hybrid fall deposits in the Bishop Tuff, California: A novel pyroclastic depositional mechanism. *Geology* **26**, 7 - 10.

Wilson, C. J. N. & Hildreth, W. (2003). Assembling an Ignimbrite: Mechanical and Thermal Building Blocks in the Bishop Tuff, California. *The Journal of Geology* **111**, 653 - 670.

Winick, J. A. (2000). Excess Argon ($^{40}Ar_E$) In Melt Inclusion Bearing Quartz and Sanidine from The Bishop and Bandelier Tuffs. MSc Thesis. Department of Earth and Environmental Science, New Mexico Institute of Mining and Technology, Socorro, New Mexico, USA.

Winick, J. A., McIntosh, W. C. & Dunbar, N. W. (2001). Melt-inclusion-hosted excess ^{40}Ar in quartz crystals of the Bishop and Bandelier magma systems. *Geology* **29**, 275 – 278

Appendix

Introduction

This appendix is divided into the following five sub-sections:

A1. Methods

Part A1 contains details of all methods used, including sample preparation, Ar extraction systems, data correction, and parameters used with DIFFARG (Ar diffusion modelling programme).

A2. Sample Descriptions

Part A2 details all field locality information (summary maps), and sample descriptions. In addition this section also contains a summary petrographic study accompanied by representative thin section and EMP images.

A3. Ar-Ar Data

Part A3 contains all Ar-Ar data collected (from September 2010 to February 2012) on Nu Instruments Noblesse and MAP-215-50 mass spectrometers at the Ar-Ar and Noble Gas Research Laboratory at the Open University. Tables are ordered by irradiation and then by sample. Additional information pertaining to particular preparation details are presented in footnotes.

A4. Chemical Data

Part A4 details all XRF and EMP data collected (from January 2010 to March 2012). Data are presented in tables and are ordered by sample and then mineral phase.

A5. Summary Tables

Part A5 contains summary tables listing previously published ages (e.g., U-Pb, Rb-Sr, K-Ar), for geological units that have a large existing geochronological database, for example units of the Fish Canyon Magmatic System, USA, and the explosive eruptions at Yellowstone and the Bishop Tuff, California, USA.

A1. Methods

A1.1 Background to the Ar-Ar method

A1.1.1 The age equation

The following is a summary of the key equations, for all equations and a full explanation see McDougall and Harrison (1999). Radioactive substances decay following an exponential law, and production of a daughter species is proportional to the number of radioactive atoms present, (Eq. A.1), where $\frac{-dN}{dt}$ is disintegrations of parent atom with time, and N is the number of atoms present. Therefore where N is the number of atoms present at time t and λ is the decay constant of proportionality (Eq. A.2), which is characteristic of the nuclide in question (Rutherford and Soddy, 1902). The term $\frac{dN}{dt}$ is the rate of change of number of parent atoms and is negative because it decreases with time.

$$\frac{-dN}{dt} \propto N \tag{A.1}$$

$$\frac{dN}{dt} = -\lambda N \tag{A.2}$$

The half-life ($t_{1/2}$) is the time required for half the number of radioactive parent atoms to decay, and can be shown to be related to the decay constant by equation (A.3):

$$t_{1/2} = \frac{ln2}{\lambda} = \frac{0.693}{\lambda} \tag{A.3}$$

Therefore N represents the number of radioactive atoms present at time t, and N_0 is the number of radioactive atoms present at time t = 0, which is some time in the past (Eq. A.4):

$$N = N_0\, e^{-\lambda t} \tag{A.4}$$

Equation (A.5) represents the radioactive decay of parent N to daughter product D. Therefore $(N + D)$ is the number of parent and daughter atoms present at a given time. Rearranging for t, we get (Eq. A.6), the basic equation used in geochronology:

$$N = (N + D)e^{-\lambda t} \tag{A.5}$$

$$t = \frac{1}{\lambda} ln\left(1 + \frac{D}{N}\right) \tag{A.6}$$

A1.1.2 Application to the Ar-Ar system

^{40}K has dual decay to both ^{40}Ar and ^{40}Ca (10.5 % and 89.5 % respectively). The branch of interest (dominated by electron capture), for both K-Ar and ^{40}Ar/^{39}Ar dating is the fraction of ^{40}K to ^{40}Ar (f_{Ar}), which in equation (A.7) is shown to be the ratio of relevant partial decay constants ($\lambda_e + \lambda_{e'}$; decay via electron capture) to the decay of ^{40}K (λ). Combining with the basic geochronology equation, where the decay constant is known and $\left(\frac{^{40}Ar*}{^{40}K}\right)$ is the ratio of radiogenic Ar (^{40}Ar*) to ^{40}K present in the sample now – the age of the sample can be calculated (Eq. A.8) and rearranged in terms of ^{40}Ar* (Eq. A.9).

$$f_{Ar} = \frac{\lambda_e + \lambda_{e'}}{\lambda_e + \lambda_{e'} + \lambda\beta} = \frac{\lambda_e + \lambda_{e'}}{\lambda} \tag{A.7}$$

$$t = \frac{1}{\lambda} ln\left(1 + \frac{\lambda}{\left(\lambda_e + \lambda_{e'}\right)} \frac{^{40}Ar*}{^{40}K}\right) \quad \text{(A.8)}$$

$$^{40}\text{Ar}* = \frac{^{40}K\left(\lambda_e + \lambda_{e'}\right)}{\lambda} [(exp\lambda t) - 1] \quad \text{(A.9)}$$

A1.1.3 Standard/fluence monitor analysis and determination of *J*-value

Ar-Ar age determinations of unknowns rely upon a sample of precisely known age (e.g., primary standard whose age has been determined by K-Ar) for an indirect determination of the neutron flux received by the unknown sample during irradiation. Alternatively the age of an unknown can be based on secondary (or higher order) standards whose ages must be based on $^{40}Ar/^{39}Ar$ intercalibration with a primary standard (Renne *et al.*, 1998; McDougall and Harrison, 1999). A sample needs to meet certain criteria before it can be considered a suitable standard for $^{40}Ar/^{39}Ar$ dating. Grain to grain homogeneity based on a uniform $^{40}Ar*$ to ^{40}K ratio is important, as is the homogeneous distribution of both isotopes so that precise $^{40}K/^{40}Ar$ ages, which relies on determining absolute concentrations of $^{40}Ar*$ and ^{40}K can be measured (Renne *et al.*, 1994). Minerals commonly used as primary standards include; biotite (e.g., GA15-50; used in this study), hornblende and muscovite (McDougall and Harrison, 1999). With the development of the $^{40}Ar/^{39}Ar$ technique K-feldspar (e.g., sanidine), has become a commonly used standard because precise and reproducible Ar isotopic data can be obtained from this mineral (e.g., Renne *et al.*, 1998).

The amount of ^{39}Ar produced from ^{39}K (during sample irradiation) is proportional to ^{40}K present in the sample because the $^{40}K/^{39}K$ ratio is effectively constant in samples at the present day. Equation (A.10) describes how the number of ^{39}Ar atoms produced ($^{39}Ar_K$) from ^{39}K present in the sample depends on the irradiation duration (Δ), the amount of neutron flux (ϕ(E)) at energy E, and the neutron capture cross section ($\sigma(E)$) at energy E.

$$^{39}Ar_K = {}^{39}K\Delta\int \phi(E)\sigma(E)dE \quad \text{(A.10)}$$

Therefore combining equation (A.9) with irradiation parameter information (A.10), the age ($^{40}Ar^*/^{39}Ar_K$) of an irradiated sample can be calculated (Eq. A.11):

$$\frac{^{40}Ar*}{^{39}Ar_K} = \frac{^{40}K}{^{39}K}\frac{\lambda_e + \lambda_{e'}}{\lambda}\frac{1}{\Delta\int \phi(E)\sigma(E)dE}\frac{[(exp\lambda t)-1]}{} \quad \text{(A.11)}$$

The irradiation parameter (*J*-value) relative to each sample position within the reactor can be calculated (Eq. A.12):

$$J = \frac{^{40}K}{^{39}K}\frac{\lambda_e + \lambda_{e'}}{\lambda}\Delta\int \phi(E)\sigma(E)dE \quad \text{(A.12)}$$

In order to determine the irradiation parameters, for example the neutron energy received by the sample in the reactor, a standard mineral of precisely known age is required to be irradiated along with the unknown sample in order to monitor the dose received. Therefore, because the age of the standard is known $\left(\frac{^{40}Ar*}{^{39}Ar_K}\right)$, the parameter *J* for each sample can be determined (Eq. A.13):

$$J = \frac{(exp\lambda t)-1}{\frac{^{40}Ar*}{^{39}Ar_K}} \quad \text{(A.13)}$$

The *J*-value is used along with the measured $\left(\frac{^{40}Ar*}{^{39}ArK}\right)$ ratio of the unknown sample irradiated at the same time so that the sample age can be calculated. Combining equation (A.8) with the *J*-value assigned to each sample (Eq. A.13), allows calculation of the age at time *t* (Ma) of the sample (Eq. A.14):

$$t = \frac{1}{\lambda}ln\left(1 + J\frac{^{40}Ar*}{^{39}ArK}\right) \quad \text{(A.14)}$$

A1.1.4 Corrections

Correcting for atmospheric Ar

Correction is applied in conjunction with mass discrimination corrections of the mass spectrometer, and corrections for other known sources of ^{36}Ar (e.g., neutron induced ^{36}Ar). For terrestrial samples a value of 295.5 (recommended by Steiger and Jäger, 1977) for $(^{40}Ar/^{36}Ar)_A$ is commonly used, although this value has been re-determined in recent years to ~ 298.56 (Lee *et al.*, 2006) and supported evidence in Renne *et al.*, (2008; 2009). $^{40}Ar_T$ is the total Ar of mass 40, which is the sum of atmospheric $(^{40}Ar)_A$ plus radiogenic ^{40}Ar ($^{40}Ar^*$) (Eq. A.15):

$$^{40}Ar_T = (^{40}Ar)_A + {}^{40}Ar^* \qquad \text{(A.15)}$$

Therefore that portion of the total ^{40}Ar which is radiogenic can be calculated using equation (A.16):

$$^{40}Ar^* = {}^{40}Ar_T - (298.56 \times {}^{36}Ar_A) \qquad \text{(A.16)}$$

Corrections for interfering reactions

^{37}Ar produced almost entirely from ^{40}Ca, is used as a proxy for the calcium content of a sample and can be used to correct for both reactor induced ^{36}Ar and ^{37}Ar. Determination of $(^{36}Ar/^{37}Ar)_{Ca}$ and $(^{39}Ar/^{37}Ar)_{Ca}$ ratios are carried out by analysing calcium and potassium salts. Interfering reactions need to be corrected for to avoid incorrect $^{40}Ar/^{39}Ar$ age determinations. Corrections were made to the data presented in this thesis using an in house programme, ArMaDiLo (section A1.4).

A1.2 Mass spectrometry

The following is a summary outlining the key details of mass spectrometry and specific procedures associated with the measurements made throughout the course of this work. For a more detailed explanation of mass spectrometry see McDougall and Harrison (1999). Details of laser extraction (laserprobe) are outlined in section A1.3.

A1.2.1 Nu Instruments Noblesse

UV *in situ* measurements were made using a New Wave Instruments UV 213 nm, pulsed quintupled Nd-YAG laser coupled with a Nu Instruments Noblesse noble gas mass spectrometer. The Noblesse is a multi-ion counter, single focusing, 75° magnetic sector design used for the measurement of noble gases under static vacuum conditions. The ion source is based on the standard Nier-type (Nier, 1947) design with a getter located behind the source for minimising impurity peaks during analysis. The Nu Instruments Noblesse measures ^{36}Ar precisely because it can distinguish it from interfering hydrocarbon (HC) peaks, which have a similar mass. The sensitivity of the mass spectrometer (1.13×10^{-15} cc per count) for the largest ion beam (^{40}Ar) allows for small amounts of gas to be measured. ^{40}Ar was usually in the range of 4.0×10^{3} to 1.7×10^{5} counts for the unknowns with $^{40}Ar^{*}/^{39}Ar$ ratios of 2.01 to 5.66, depending upon age.

A1.2.2 Mass Analyser Products (MAP) 215-50

IR *in situ* and IR total fusion measurements were made using either a SPI CW/pulsed 1090 nm diode infrared fibre laser or a SPI CW 1062 nm infrared fibre laser coupled with a MAP-215-50 noble gas mass spectrometer. The MAP-215-50 has a Nier-type source and a multiplier to enable the detection of small signals and a mass resolution of 300. The sensitivity of the mass spectrometer for the largest ion beam (^{40}Ar) is 1.46×10^{-9} cc per

volt). ^{40}Ar was usually in the range of 0.02 to 11.18 volts for the unknowns with $^{40}Ar^*/^{39}Ar$ ratios of 0.19 to 9.43, depending upon age.

A1.2.3 Mass discrimination

In order to correct data for modern atmospheric Ar contamination, a value for $^{40}Ar/^{36}Ar$ of 295.5 recommended by Steiger and Jäger (1977) has been routinely used. However, the relative abundance of natural isotopes in atmospheric Ar was re-determined by Lee *et al.*, (2006) by measuring mixtures of highly enriched ^{36}Ar and ^{40}Ar. Lee *et al.*, (2006) presented a new ratio for $^{40}Ar/^{36}Ar = 298.56 \pm 0.3$ (0.1 %). This value has been used throughout this study to compare inverse isochron determined $^{40}Ar/^{36}Ar$ values to in order to ascertain if an excess of radiogenic ^{40}Ar is present.

During data collection a higher measured ratio value would indicate the mass spectrometer discriminates in favour of mass ^{40}Ar; therefore a correction factor needs to be applied in order to obtain a standard value. It is therefore important that corrections to data are made relative to actual measured ratios as opposed to the standard recommended value, because mass spectrometers in general do not yield absolute ratios of isotopes being analysed due to isotope fractionation (McDougall and Harrison, 1999) that occurs during the measurement process. Calibration of the mass spectrometer for isotopic analysis of Ar is carried out by using the measured value for atmospheric Ar. For example, the Nu Instruments Noblesse data is corrected with a value for $^{40}Ar/^{36}Ar$ of 295. This value is based on measurements made on a sample of glass, where the Ar gas in the glass is of atmospheric composition. The measured $^{40}Ar/^{36}Ar$ value of 295 demonstrates that there is a slight mass discrimination in favour of ^{36}Ar. This is also the case with the MAP-215-50, where there is mass discrimination in favour of ^{36}Ar. Data is corrected with a value for

$^{40}Ar/^{36}Ar$ of 283, based on routinely carried out air calibration experiments using a fully calibrated custom built air cylinder permanently attached to the extraction line.

A1.2.4 Air calibration

MAP-215-50 mass spectrometer is equipped with a permanent air calibration cylinder, which contains known ratios of $^{40}Ar/^{36}Ar$ (297.25 ± 0.63) and $^{38}Ar/^{36}Ar$ (0.1875 ± 0.0013). Air calibration is carried out by measuring Ar isotopes (40, 38, and 36) in shots of air released from the cylinder. Values are blank corrected and the measured $^{40}Ar/^{36}Ar$ and $^{38}Ar/^{36}Ar$ normalised to the known ratio values in the gas cylinder (because the cylinder does not contain $^{40}Ar/^{36}Ar$ ratio equal to modern air). If the final value (average taken of normalised $^{40}Ar/^{36}Ar$ values) is within error of 283 then no significant drift in the system has occurred (Fig. A1.1).

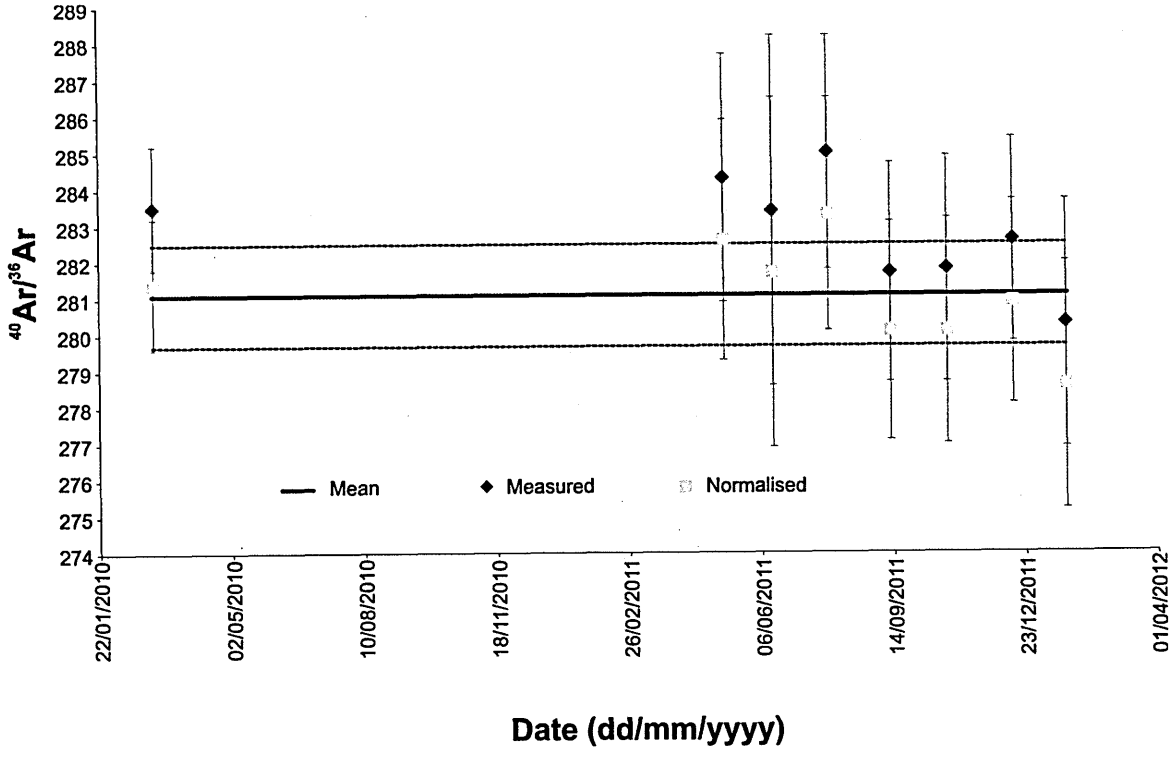

Figure A1.1. Measured and normalised air calibration measurements made on MAP-215-50 mass spectrometer covering the time period of data collection for this study. Solid blue line indicates the mean and the dashed blue lines represent the standard deviation on the mean. All measurements $^{40}Ar/^{36}Ar$ are within error of 283.

A1.3 Ar Extraction and gas clean-up

A1.3.1 Laser microprobes

The $^{40}Ar/^{39}Ar$ ages presented in this study have been determined by the laser extraction techniques, UV *in situ* and IR total fusion. In summary, a laser emits light by the amplification of light photons generated by high-intensity lamps in several different modes; pulsed laser output (e.g., quintupled Nd-YAG) and continuous wave (CW) output (e.g., 1090 nm diode infrared) (McDougall and Harrison, 1999). The use of laserprobe technology in $^{40}Ar/^{39}Ar$ geochronology, combined with improved mass spectrometry (i.e., reduced background levels, measurement sensitivity), permits the release of Ar from small multigrain samples, single crystals or parts of crystals (e.g., Kelley 1994; 1995; Sherlock *et al.*, 2008) to produce precise Ar-Ar ages. The use of lasers is better suited for this particular study instead of, for example, bulk extraction techniques, where large samples (> 1 mg) of mineral-separate are heated incrementally in a vacuum furnace (e.g., Flude *et al.*, 2008). The distribution of Ar in mineral grains can be investigated without the vacuum breakdown of samples during bulk heating methods and age variations between mineral phases and single minerals of the same phase can be investigated.

A1.3.1.1 Ar-Ar *in situ* analysis

In order to investigate age variations within individual minerals of the Fish Canyon magmatic system, data were collected using an ultraviolet laser ablation microprobe (UVLAMP) and an infrared laser ablation microprobe (IRLAMP). Kelley *et al.*, (1994) demonstrated that the ultraviolet (UV) wavelength could be readily absorbed by clear minerals, such as feldspar (e.g., sanidine and plagioclase), so in order to effectively analyse these minerals a New Wave Instruments UV 213 nm, pulsed quintupled Nd-YAG laser was applied to all samples of the Fish canyon magmatic system. *In situ* laser spot

extraction is a spatially-resolving technique with the main advantage being that Ar can be released from discrete parts of the crystal at high spatial resolution through accurate targeting of the laser. However with decreasing age of sample the amount of material that is required to be ablated increases due to the short accumulation time of the radiogenic daughter product. This is also true for low potassium minerals (e.g., plagioclase feldspar). $^{40}Ar/^{39}Ar$ apparent ages were obtained by ablating areas (measuring ~ 450 μm^2) within single crystals (Fig. A1.2a). Laser power was set to 65 % at 20 Hz with a 50 µm spot, 50 µm spacing and 10 µm depth pass of the raster. Scan speed was calculated and input as 11 $\mu m/sec^{-1}$ with a 600 second sequence file before automatic inlet, which equates to 420 seconds laser ablating.

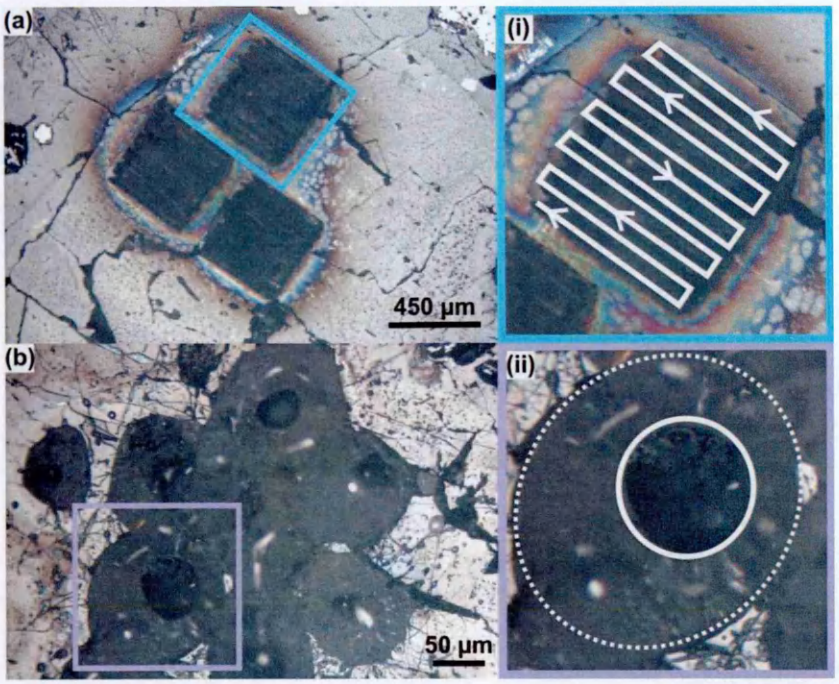

Figure A1.2. (a) Photograph of the UV laser ablation pit. The area within the blue box has been enlarged (i) and the white line represents the user defined path of the laser. (b) Photograph of the IR laser melt pits. The area within the purple box has been enlarged (ii) to show a central pit (within the solid white line) and a surrounding melt zone (within the dashed white line).

In addition to this, selected samples (BFC83, PCB 1, BFC191 and BFC115), were also analysed using a SPI CW/pulsed 1090 nm diode infrared fibre laser. $^{40}Ar/^{39}Ar$ apparent

ages were obtained by releasing gas from multiple spots (Fig. A1.2b). The laser was manually operated to fire single shots onto the sample surface with a fixed spot size of 50 μm, maximum power of 25 W and a 50 % beam splitter. The IR wavelength did not always couple well with the clear feldspars and therefore the number of spots required to release measurable gas needed to be increased. One disadvantage with this technique is possible heating and Ar loss of surrounding areas or the melting of more susceptible minerals outside the analysis area. Experimental work has suggested that dark inclusions or adjacent minerals at distances of up to 500 μm may degas and contribute to the analysis (McDougall and Harrison, 1999).

A1.3.1.2 Ar-Ar total fusion analysis

$^{40}Ar/^{39}Ar$ total fusion analysis of single crystals can produce reproducible ages for young volcanic samples as well as identifying xenocrystic material (e.g., Deino and Potts, 1990; Semaw *et al.*, 1997; Hora *et al.*, 2010). The technique involves heating single crystals/grains, usually in one heating step (although some workers degas with a defocused beam prior to total fusion e.g., Rivera *et al.*, 2011), until totally fused. Samples were degassed using either a SPI CW/pulsed 1090 nm diode infrared fibre laser (fixed spot size of 50 μm, 50 % beam splitter, maximum power 25 W) or a SPI CW 1062 nm infrared fibre laser (fixed spot size of 50 μm, maximum power 20W). Fusion was achieved by applying laser power for ~ 100 seconds or until sample had completely fused. Feldspar separates were fused along with a flux (degassed unirradiated basalt) in order to facilitate heating (see section A1.7.5).

A1.3.2 Extraction system blanks

The blank of the extraction system encompasses the signal detected above background at each of the supposed masses for the Ar isotopes. The blank measurement follows the normal extraction procedures but in the absence of the sample. The Nu Instruments Noblesse mass spectrometer was particularly sensitive to changes in room temperature. Blank measurements would tend to increase throughout the day (Fig. A1.3) due to a gradual increase in temperature (~ 0.5 to 2 °C), causing the mobilisation of gas adhered to the interior of the extraction line. It was also discovered that turning off the microscope light between analyses meant that the sample chamber and sample surface were not continuously heated, which could also cause an increase in blank levels throughout the day. Data collected using the Nu Instruments Noblesse are corrected for split am/pm average system blank levels, which were measured prior to each analysis.

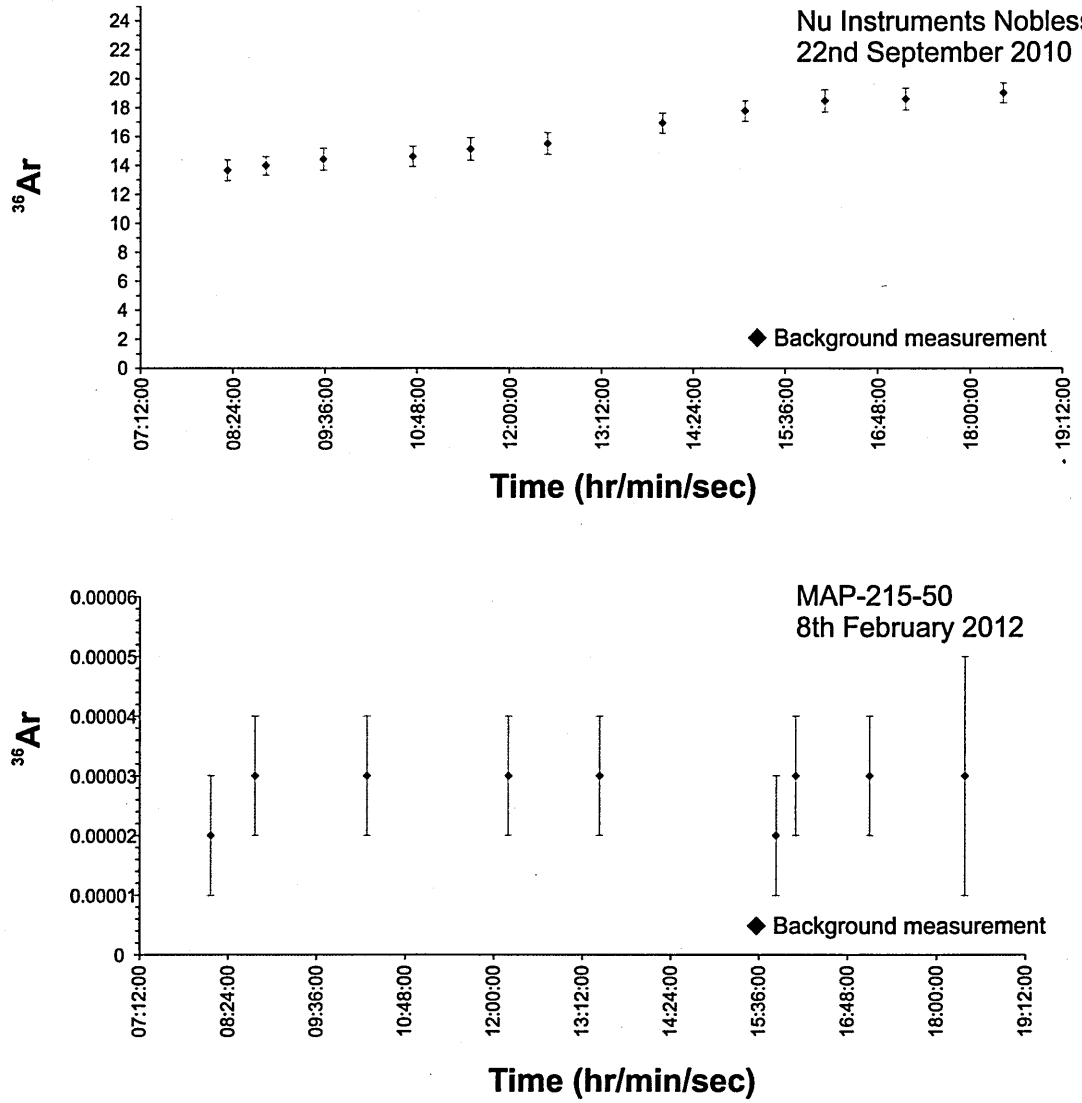

Figure A1.3. Example of background measurements. (a) Measurements made on the Nu Instruments Noblesse, which highlights the subtle increase in blanks during the day. (b) Measurements made on the MAP-215-50, which shows the relative stability of the MAP-215-50 blank measurements throughout the course of a day.

For samples analysed with the MAP-215-50 mass spectrometer data are corrected for system blanks measured prior to every two analyses. Ideal system blanks were low (e.g., < 0.01 volts on the ^{40}Ar), and stable throughout the day. Blanks tended to decrease with time as samples in the sample chamber were outgassed.

A1.3.3 Gas clean-up

Following sample extraction, all gasses other than Ar must be removed prior to isotopic analysis through the use of getters in the extraction system. A cold getter (at room temperature) is required to remove hydrogen, and a hot getter (operated at ~ 450 °C) is used to remove oxygen, nitrogen and other gases, which if not removed, may lead to oxidisation of the ion source. For samples analysed with the Nu Instruments Noblesse, extracted gases were subjected to 10 minute gettering and cleaned by two SAES AP10-N getters (one at 450 °C and one at room temperature) prior to automatic inlet into the mass spectrometer. For samples analysed with the MAP-215-50 mass, 5 minute gettering and cleaning by three SAES AP10 getters (one at 450 °C and two at room temperature) was carried out prior to inlet. In addition to the getters, the MAP-215-50 mass spectrometer is also fitted with a U-shaped cold finger filled with ball bearings, which is immersed in liquid nitrogen (external temperature cooled to -197 °C). All released gases were forced through the cold trap, trapping unwanted volatiles released from the sample during degassing.

A1.4 Data Reduction: ArMaDiLo

Data collection was carried out using Nu Noble software (Nu Instruments Noblesse) and a custom designed software created in Labview 6 (MAP-215-50). Data reduction was achieved using an in-house programme – ArMaDiLo (Argon Macro Direct Loader). The following is a brief summary of the steps followed and corrections used. A complete discussion of all ArMaDiLo functions can be found in the unpublished ArMaDiLo instruction manual (Schwanethal, 2008).

A1.4.1 Loading data

The data file (text file taken directly from the mass spectrometer software) is first converted into a 'filename.dat' format, which allows it to be loaded into the ArMaDiLo programme. The programme requires the 'Argon' correction option to be selected, which separates the blanks from the data.

A1.4.2 Blank correction and mass discrimination

Blank correction is calculated as follows for each individual blank equal to (b_i), and the error on the blank measurement ($\pm \Delta b_i$). Multiple blank measurements are selected and a mean blank value ($\bar{b}$) is calculated for a set of (N) blank data collected in a single day. The error on multiple blanks is the standard deviation of the blank data ($\sigma = \Delta B$) and is calculated using equation (A.17):

$$\sigma = \sqrt{\frac{1}{N}\sum_{i=1}^{N}(b_i)^2 - \left(\bar{b}\right)^2} \quad \text{(A.17)}$$

The mean daily blank value $B \pm \Delta B$ is subtracted from the data ($D \pm \Delta D$) to give the corrected value ($A \pm \Delta A$) as shown in equation (A.18). This approach allows specific sets of blanks to be selected and used to correct the data (i.e., morning/afternoon split).

$$A \pm \Delta A = (D - B) \pm \sqrt{\Delta D^2 + \Delta B^2} \quad \text{(A.18)}$$

The mass discrimination value needs to be specified: 295 is used to correct Nu Instruments Noblesse data and 283 for MAP-215-50 data (previously discussed in section A1.2.3). The discrimination correction is applied to ^{40}Ar, ^{39}Ar, ^{38}Ar and ^{37}Ar. The discrimination per

atomic mass unit (d/amu) is calculated (Eq. A.19), where r_{disc} is the measured $^{40}Ar/^{36}Ar$ ratio (either 283 or 295):

$$d/amu = \left(\frac{\frac{298.56}{r_{disc}} - 1}{4}\right) \quad (A.19)$$

The correction factor (C) is calculated for each isotope (Eq. A.20), where n = 4 for ^{40}Ar, n = 3 for ^{39}Ar, n = 2 for ^{38}Ar and n = 1 for ^{37}Ar (n = number of units heavier than ^{36}Ar). Applied to the data, each isotope is then corrected by equation (A.21):

$$C = [(d/amu - 1) \times n] + 1 \quad (A.20)$$

$$A \pm \Delta A = (C \times A) \pm (C \times \Delta A) \quad (A.21)$$

A1.4.3 Decay correction: ^{37}Ar and ^{39}Ar

Radioactive substances decay. Starting with N_0 radioactive atoms, then after a time (t) there will be $N = N_0 e^{-\lambda t}$ remaining, where λ = decay constant (in units of reciprocal time). Two isotopes require correction: ^{37}Ar and ^{39}Ar to account for decay of the isotopes between the time of the irradiation (t') and the experiment (t). ^{37}Ar has a half-life of 34.95 ± 0.08 days (Renne *et al.*, 2001) and ^{39}Ar has a half-life of 269 ± 3 years. Therefore from the time of irradiation, $\lambda_{37} = 0.01974778292$ day $^{-1}$, and $\lambda_{39} = 7.055 \times 10^{-6}$ day^{-1}. Although the general equation for this correction (Eq. A.22) takes into account both the duration of the irradiation (t) and how much the isotope of interest has decayed since irradiation (t'), in the case where irradiations have taken place in stages then equation (A.23) is used, where P_i is the reactor power at each stage:

$$N_0 = \left(\frac{N\,\lambda t e^{\lambda t'}}{1-e^{-\lambda t}}\right) \quad \text{(A.22)}$$

$$\frac{N_0}{N} = \frac{\sum_{i=1}^{n} P_i t_i}{\sum_{i}^{n} P_i\left(\frac{1-e^{-\lambda t}}{\lambda e^{\lambda t'}}\right)} \quad \text{(A.23)}$$

Therefore once again if $C = \left(\frac{N_0}{N}\right)$ for ^{37}Ar and ^{39}Ar, it can be used to correct the data using equation (A.24).

$$A \pm \Delta A = (C \times A) \pm (C \times \Delta A) \quad \text{(A.24)}$$

A1.4.4 Interactions with calcium

During the irradiation process isotopes of Ar are produced by interactions of neutrons with isotopes of Ca, K and Ar. The following correction factors were used to correct the data in this study: $(^{39}Ar/^{37}Ar)_{Ca} = 0.00065 \pm 0.00003$, $(^{36}Ar/^{37}Ar)_{Ca} = 0.000265 \pm 0.000001$, $(^{40}Ar/^{39}Ar)_{K} = 0.0085 \pm 0.00004$, based on ^{40}Ar, ^{39}Ar, ^{37}Ar and ^{36}Ar measurements made on irradiated Ca and K salts (CaF_2 and K_2SO_4 respectively). To make the correction of reactor induced ^{36}Ar due to ^{40}Ca the value of the $^{37}Ar \pm \Delta^{37}Ar$ is multiplied by the '^{36}Ar due to Ca' correction factor ($C \pm \Delta C$) to give $^{37}Ar_{Ca} \pm \Delta^{37}Ar_{Ca}$. $^{37}Ar_{Ca}$ is then used to correct the value of ^{36}Ar (Eq. A.25).

$$^{36}Ar \pm \Delta^{36}Ar = (^{36}Ar - {}^{37}Ar_{Ca}) \pm \sqrt{(\Delta^{36}Ar)^2 + (\Delta^{37}Ar_{Ca})^2} \quad \text{(A.25)}$$

The same is carried out to correct for reactor induced ^{39}Ar from ^{42}Ca. In this case the '^{39}Ar due to Ca' correction factor is used (Eq. A.26):

$$^{39}\mathrm{Ar} \pm \Delta^{39}\mathrm{Ar} = (^{39}\mathrm{Ar} - {}^{37}\mathrm{Ar_{Ca}}) \pm \sqrt{(\Delta^{39}Ar)^2 + (\Delta^{37}Ar_{Ca})^2} \quad \text{(A.26)}$$

A1.4.5 Production of ^{40}Ar due to ^{40}K

To make the correction of reactor induced ^{40}Ar due to ^{40}K the value of the $^{39}\mathrm{Ar} \pm \Delta^{39}\mathrm{Ar}$ is multiplied by the 'potassium' correction factor ($C \pm \Delta C$) to give $^{39}\mathrm{Ar_K} \pm \Delta^{39}\mathrm{Ar_K}$. $^{39}\mathrm{Ar_K}$ is then used to correct the value of ^{40}Ar (Eq. A.27).

$$^{40}\mathrm{Ar} \pm \Delta^{40}\mathrm{Ar} = (^{40}\mathrm{Ar} - {}^{39}\mathrm{Ar_K}) \pm \sqrt{(\Delta^{40}Ar)^2 + (\Delta^{39}Ar_K)^2} \quad \text{(A.27)}$$

A1.4.6 Calculation of ^{40}Ar*/^{39}Ar

The ^{40}Ar*/^{39}Ar ratio *(R)* is calculated using equation (A.28), where $\left(\frac{^{40}Ar}{^{36}Ar}\right)_A$ is the ratio of atmospheric Ar (298.56). The error on the ratio (ΔR) is calculated using equation (A.29):

$$R = \left(\frac{^{40}Ar - \left(\left(\frac{^{40}Ar}{^{36}Ar}\right)_A \times {}^{36}Ar\right)}{^{39}Ar} \right) \quad \text{(A.28)}$$

$$\Delta R = R \times \sqrt{\left(\frac{\sqrt{(\Delta^{40}Ar)^2 + \left(\left(\frac{^{40}Ar}{^{36}Ar}\right)_A \times {}^{36}Ar\right)^2}}{^{40}Ar - \left(\left(\frac{^{40}Ar}{^{36}Ar}\right)_A \times {}^{36}Ar\right)} \right)^2 + \left(\frac{\Delta^{39}Ar}{^{39}Ar}\right)^2} \quad \text{(A.29)}$$

A1.4.7 Age calculation

The age (t) of the sample (once the J-value associated with that sample is applied) is calculated (Eq. A.30). Where R = $^{40}Ar^*/^{39}Ar = \left(\frac{^{40}Ar^*}{^{39}Ar_K}\right)$ and (λ) is the decay constant for $^{40}Ar_K$ ($5.543 \pm 0.010 \times 10^{-10}$ a^{-1}; Steiger and Jäger, 1977):

$$t = \frac{1}{\lambda} \ln (1 + JR) \tag{A.30}$$

The associated uncertainty on the age (Δt) is calculated including the uncertainties in the J-value and R using equation (A.31):

$$\Delta t = \frac{J^2 \Delta R^2 + R^2 \Delta J^2}{\left(\frac{1}{\lambda}\right)^2 (1+RJ)^2} \tag{A.31}$$

A1.4.8 J-value determination and calculation

The irradiation factor (J-value) for each foil packet containing the unknown sample was determined by laser total fusion (MAP-215-50) analysis of between 10 to 12 biotite grains of fluence monitor GA15-50 from each standard foil packet, which were intercalated with the sample packets and irradiated along with the unknowns. The J-value is critical in the age equation because it allows the neutron flux received by the unknowns to be calculated. Rearranging equation (A.30) with $\frac{1}{\lambda}$ = 1804.077 (millions of years), yields equation (A.32):

$$J = \frac{exp\left[\frac{t}{1804.077}\right] - 1}{R} \tag{A.32}$$

The uncertainty on the *J*-value is based on the uncertainty of both the standard analysed (ΔR) and the decay constant (Eq. A.33). The error (± 3.255) is the uncertainty on the decay constant:

$$J = \frac{exp\left[\frac{t \pm \Delta t}{1804.077 \pm 3.255}\right] - 1}{R \pm \Delta R} \quad \text{(A.33)}$$

The uncertainty will lead to $\left(J^{+\Delta J_1}_{-\Delta J_2}\right)$. Each *J*-value is assigned a weighting based on its uncertainty (the more uncertain a *J*-value the less weighting it is given). The weighting factor (W) is calculated using equation (A.34), and the weighted mean (J_w) for the entire set of *J*-values using equation (A.35). Where ($w_i J_i$) is the weighting factor (w_i), multiplied by its *J*-value.

$$W = \frac{J}{\left(\frac{\Delta J_1 + \Delta J_2}{2}\right)} \quad \text{(A.34)}$$

$$J_w = \frac{\sum_{i=1}^{n} w_i J_i}{\sum_{i=1}^{n} w_i} \quad \text{(A.35)}$$

The variance (spread of data) of the data set is calculated using equation (A.36) and the standard error of the mean (σ_m) calculated using equation (A.37):

$$\sigma^2 = \frac{\sum_{i=1}^{n} w_i (x_i - J_w)^2}{\sum_{i=1}^{n} w_i} \quad \text{(A.36)}$$

$$\sigma_m = \frac{\sigma}{\sqrt{N}} \quad \text{(A.37)}$$

By increasing the number of measurements (N), the standard error of the mean of a dataset is decreased.

A1.4.9 Finalisation of calculations

Data is exported to comma separated variable (CSV) files, which include R, ΔR, Age, ΔAge, isotope values, isotope ratios, blank data and correction factors in the accompanying log file.

A1.5 Recalculation of age using redefined ^{40}K decay constant

Currently there are several ^{40}K decay constants in use (e.g., Steiger and Jäger, 1977; Min *et al.*, 2000; Renne *et al.*, 2010; 2011), with recent redeterminations designed to reconcile U-Pb and Ar-Ar ages, and improve precision and accuracy on existing measurements (Renne *et al.*, 2010; 2011). Due to the rapidly improving precision and accuracy of the methods, Ar-Ar ages in the recent literature may be corrected to one of three decay constants; the Steiger and Jäger (1977) decay constant of 5.543×10^{-10} a^{-1}, which does not consider uncertainties associated with this value (e.g., McDougall *et al.*, 2012); the Min *et al.*, (2000) decay constant of 5.463×10^{-10} a^{-1} (e.g., Kuiper *et al.*, 2008; Rivera *et al.*, 2011), or the Renne *et al.*, (2010) decay constant of 5.549×10^{-10} a^{-1} (e.g., Ellis *et al.*, 2012), which includes full uncertainty propagation (both λ_ε and λ_β branches of the ^{40}K decay constant and the $^{40}Ar^*/^{40}K$ standard ratio).

Data collected during this study and presented in this thesis have been corrected using the decay constant for $^{40}Ar_K$ ($5.543 \pm 0.010 \times 10^{-10}$ a^{-1}; Steiger and Jäger, 1977), in the first instance, and then re-corrected using a value of $5.549 \pm 0.009 \times 10^{-10}$ a^{-1} (Renne *et al.*,

2010) and a conversion spread sheet 'ArArReCalc' (nmclean@mit.edu). In order to recalculate the ages, a value of $5.549 \pm 0.009 \times 10^{-10}$ a^{-1} for the ^{40}K decay constant and an age of 99.769 ± 0.108 Ma (1σ) for fluence monitor GA15-50 (Renne *et al.*, 2010) was used. In addition to this the previously calculated age, internal uncertainty (error on the *J*-value and $^{40}Ar/^{39}Ar$ ratio of the sample), and *J*-value was also required. The output from this spread sheet included the new age (1.01 % increase on the previous age which used GA15-50 standard age of 98.79 ± 0.96 Ma; Renne *et al.*, 1998), the error on the age (including the internal, standard age, and decay constant uncertainties), and a new *J*-value, which is used in all further data handing (i.e., plotting inverse isochrons). *J*-values are listed along with Ar-Ar data in Appendix tables (section A3).

There has been a great deal of discussion in the literature concerning the decay constant and standards in Ar-Ar dating. Here I have chosen to standardise on the values in Renne *et al.*, (2010), since these were extant for much of this study. A more recent update (Renne *et al.*, 2011) in a comment reply has provided a minor change which reduces the ages by around 0.04 % (GA15-50 standard age reduced to 99.738 ± 0.104 Ma (1σ) compared with the value of 99.769 ± 0.108 Ma (1σ) used in this study), but this is significantly below the precision of the ages I have produced and does not affect the conclusions of the thesis. Therefore all age values have been calculated on this basis.

A1.6 Data handling

A1.6.1 Data filtering and outlier rejection

Various studies have carried out data 'cleansing' to statistically counteract the bias towards older ages, in order to obtain an eruption age (e.g., van den Bogaard, 1987; Gansecki *et al.*,

1996; Ellis *et al.*, 2012). Data are ordered with increasing apparent age and a running weighted mean and MSWD calculated. Data that fall above a 'critical value' cut off point (normally but not always, defined by a clear jump of the running weighted average to larger values) are rejected from the final weighted mean age. This method is recommended if the objective is to discard obvious older ages obtained from xenocrysts. However this method is not recommended for data sets which show subtle contamination and a spread to older ages, because the 'critical value' may be arbitrarily selected, and the true geological spread in the age data overlooked. This method has not been carried out here because the range of ages present, which can often be subtle, is of interest.

Unless Ar-Ar isotope measurements made on individual mineral grains or glass showed signs of significant disturbance, for example high $^{36}Ar/^{40}Ar$ accompanied by low $^{39}Ar/^{40}Ar$ ratios suggesting alteration product, or samples were unfused (specifically prior to using flux), or gas had been released from a rogue quartz crystal (identifiable by no measurable ^{39}Ar), and rejection could therefore be justified, all analyses were included in the final dataset. Data filtering methods commonly used, such as eliminating data with a Ca/K ratio > 1 (e.g., Kuiper *et al.*, 2008; Rivera *et al.*, 2011), or calculating a running weighted mean where data points falling above a 'critical value' are dismissed as outliers (e.g., Ton-That *et al.*, 2001; Gansecki *et al.*, 1996; Spell and Harrison, 1993), have not been used in this study. For data collected using the Nu Instruments Noblesse, analyses yielding a ^{40}Ar isotope measurement less than blank level were rejected.

A1.6.2 Age probability spectra and statistical analysis

Single grain fusion data has been displayed using age-probability plots (after Deino and Potts, 1990; Spell *et al.*, 1990; Simon *et al.*, 2008), where the curve of the line is the sum of the Guassian probability distribution on individual age determinations, based on their

uncertainties (Deino and Potts, 1992). This particular method has been applied to all data because it highlights age variation within sample sets where the vertical scale is a relative probability measure that states the likelihood of a given age occurring in a sample. Probability distribution plots in this study have been displayed with a corresponding probability density function (PDF) peak value. The PDF peak value is determined using the probability distribution plot, and is the value at x (i.e., Ar-Ar age; Ma), at which its probability density function has its maximum value. For most samples data display a single peak, however for a number of data sets (e.g., Snake River Butte dome zircon U-Pb ages; sample YR185; Fig. 3.33, and Sheridan Reservoir dome feldspar Ar-Ar ages; sample YR215; Fig. 3.34), multiple peaks are displayed.

Weighted mean ages presented in this study have been calculated using Isoplot/Ex (v. 4.15) add-in for Microsoft Excel; K. Ludwig, 2011), and are accompanied by a mean squares of weighted deviates (MSWD) value, which provides a measure of the scatter of the data from the weighted mean value. MSWD values < 2.5 are generally acceptable for data-set sizes used in this study (Deino and Potts, 1992; McDougall and Harrison, 1999). The error-weighted (or more precisely the inverse-variance weighted) mean value of a data set is weighted based on the age uncertainty; those data points with smaller analytical uncertainties will be given weighting preference over data points with large analytical uncertainties. If all the weights are equal then the weighted mean will be the same as the arithmetic mean. One issue with this particular method is that it assumes that those data points, which have greater precision, are more likely to represent the 'true value'. Error-weighted mean ages ($\pm 2\sigma$; MSWD value) have been reported in summary tables, displayed on probability distribution plots, as well as discussed throughout the text. It should be noted that the weighted mean value cannot be determined using the probability distribution plot and is displayed on the diagram for reference only.

Summary tables, in addition to including the range of Ar-Ar ages achieved for a particular sample (i.e., minimum and maximum Ar-Ar age), and the weighted mean age, also include the arithmetic mean with standard deviation (2σ) quoted as a measure of the spread of the data. For the purpose of this study the arithmetic mean and accompanying standard deviation have been calculated using the same measurements used to determine the weighted mean value. This is not necessarily an appropriate method for averaging data, as it assumes that a sample population is normally distributed, and the inclusion of outliers present will cause distortion to the arithmetic mean. Therefore the weighted mean age (± 2σ) has been taken in all cases and discussed throughout the text; however the arithmetic mean, which in some cases is equal to the weighted mean value, has been included in summary tables for reference only.

A1.6.3 Identifying $^{40}Ar_E$: use of the inverse isochron

Inverse isochron analysis of data is used for determining the composition of the trapped Ar component (the non $^{40}Ar^*$ part of total ^{40}Ar measured) and results in a closed array of data with a negative slope (Fig. A1.4). The inverse isochron age is given by the X-axis (the inverse Ar-Ar ratio comprising the K-derived $^{40}Ar^*$ and neutron induced ^{39}Ar), and a trapped composition (should be equal to atmospheric Ar, 298.56), corresponds to the Y-intercept (the inverse $^{40}Ar/^{36}Ar$ ratio). The two intercepts correspond to the composition of pure trapped and pure radiogenic components in the sample, and data should lie on the mixing line between them (McDougall and Harrison, 1999).

Blank corrected isotope values (^{40}Ar, ^{39}Ar and ^{36}Ar), are required only, and data is plotted without preconception of the trapped Ar component (i.e., no atmospheric correction is made to data prior to inverse isochron analysis). The line (best-fit) is calculated using a linear least-squares regression, which weights the data points based on measurement

uncertainty. Therefore, the slope of the line is proportional to the age of the sample, the X-intercept corresponds to the age of the sample (reciprocal of the $^{40}Ar/^{39}Ar^*$ ratio). The uncertainty on the isochron age has been determined by propagation of the analytical errors associated with each point, the standard error of the line slope and intercept, and error in the *J*-value. The isochron age ($\pm 2\sigma$) in all cases has been calculated using Isoplot (Ludwig, 2011), however a complete explanation and equations can be found in McDougall and Harrison (1999).

The inverse isochron method can be used to determine varying amounts of a $^{40}Ar_E$ component of non-atmospheric composition ($^{40}Ar/^{36}Ar$ ratio > 298.56) incorporated in a sample. Renne *et al.*, (1997) identified a trapped Ar component, not atmospheric in composition (306.9 ± 1.3) whilst dating sanidine separated from the pumice deposited by the Plinian eruption of Vesuvius in 79 A.D, and were able to correct for the excess ^{40}Ar present in the sanidine to produce an Ar-Ar isochron age in agreement with the Gregorian calendar-based age. However, multiple $^{40}Ar_E$ and atmospheric ^{40}Ar components can prevent data plotting along a single mixing line (e.g., Heizler and Harrison, 1988; Simon *et al.*, 2008). It may be possible to distinguish xenocrystic contributions (where a trapped value of 298.56 would suggest crystallisation from a magma free of $^{40}Ar_E$) as dispersion along multiple arrays; one representing the juvenile phenocrysts in the samples population and another for xenocrystic material caught up in the eruption. However this method has limited application when there is clustering of data points and low dispersion along the mixing line (e.g., Deino and Potts, 1992) resulting in large errors (isochron age and $^{40}Ar/^{36}Ar$ ratio).

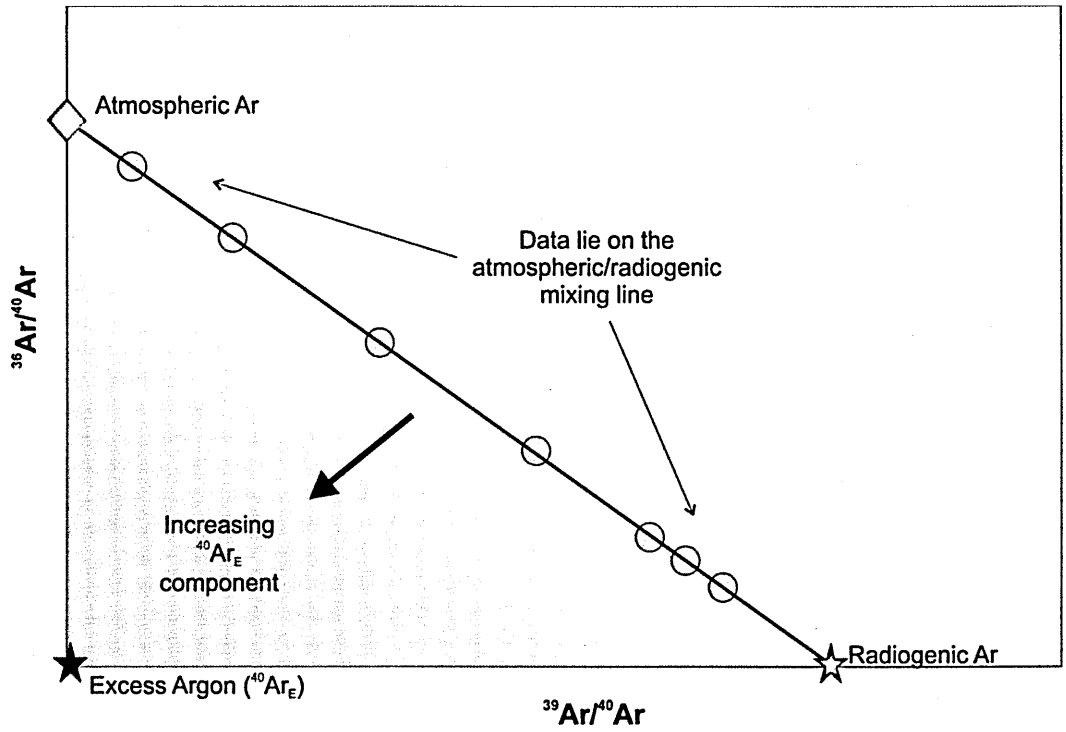

Figure A1.4. Diagram illustrating an inverse isochron plot used for determining the presence of a $^{40}Ar_E$ component showing the 'mixing line' between radiogenic Ar (red star) and atmospheric Ar (red diamond). The X-axis intercept corresponds to the pure radiogenic component in the sample and corresponds to the age of the sample. The Y-axis intercept corresponds to the pure trapped component. A trapped component with a $^{40}Ar/^{36}Ar > 298.56$ (increasing $^{40}Ar_E$ component, moving down towards the purple star), suggests $^{40}Ar_E$ contamination of the sample.

Where is has been possible, data from this study has been plotted on an inverse isochron (created in Isoplot/Ex (v. 4.15) add-in for Microsoft Excel; K. Ludwig, 2011) and the isochron age has been discussed throughout the text. Where this has not been possible an explanation has been given. All inverse isochron diagrams are displayed with an inverse isochron age and MSWD (mean squares of weighted deviates) value. This provides a measure of the uncertainty in the age and initial ratios. The MSWD is a measure of the fit of the line to the data within the limits of analytical error. In general, data in this study used for inverse isochron analysis yielded MSWD values of 2.0 to < 1.0, with a few exceptions where MSWD values exceeded 4.0 (e.g., Fig. 3.16d and Fig. 3.16f). It should be noted that in some cases, where an 'acceptable' MSWD value was determined (e.g., Fig.4.9e), the uncertainties associated with the individual data points were large, and therefore data

would always be within analytical uncertainty of the line. This is a problem for data with low precision (i.e., young or K-poor samples), as actual spread in the data may be masked.

A1.7 Sample preparation

A1.7.1 UV/IR *in situ* laserprobe analysis

Polished thick sections (~ 350 μm thickness) were soaked in beakers of acetone for 48 hours to remove them from the glass slides (Fig. A1.5). Visual inspection of the slides under a binocular microscope was carried out to ensure they were clear of adhering glue and subjected to further soaking if required. Sections were carefully broken into selected pieces (based on crystal phase and size) measuring 0.5 to 1 cm^2 using scalpel and tweezers. Those pieces finally selected for irradiation were again cleaned ultrasonically for 20 minutes in acetone and deionized water after handling. This is carried out to ensure contamination by grease/oil (which can contribute hydrocarbons) and perspiration (which contribute K and Na) during sample crushing and handling is removed prior to analysis and interfering peaks (e.g., hydrocarbons) which may have a similar mass to Ar isotopes of interest are kept to a minimum.

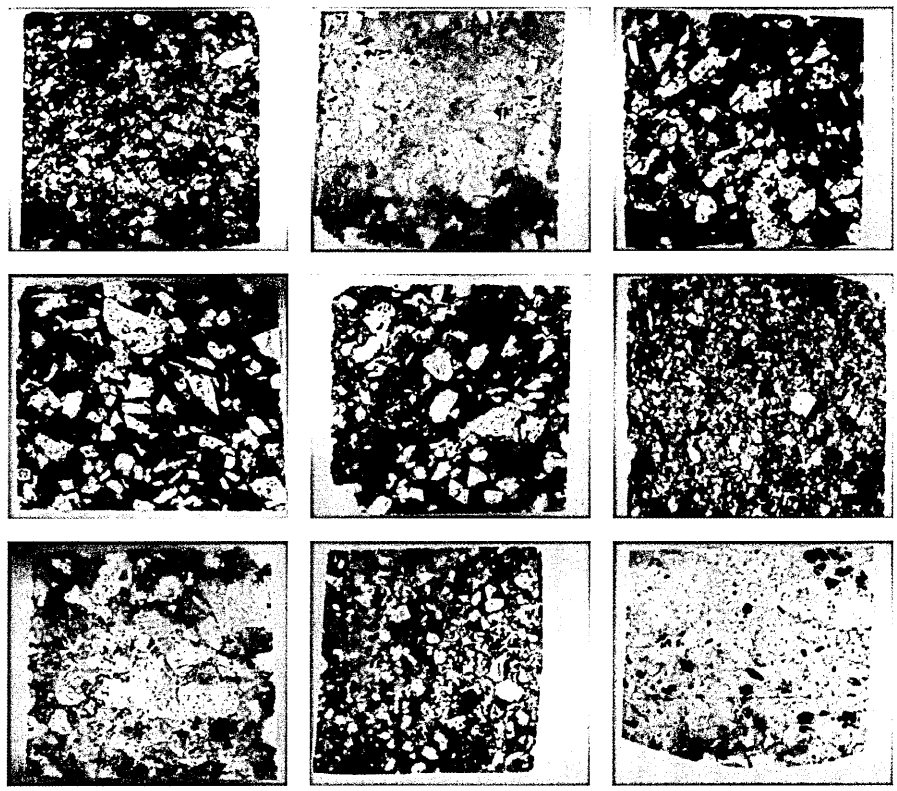

Figure A1.5. Photographs of Fish Canyon samples (polished thick sections) in transmitted light. Sample numbers from top left to bottom right, BFC83b; PCB 1; BFC196; BFC83a; BFC191; BFC113; BFC115; BFC171a; BFC129. Images taken using a Leica Wild M28 binocular microscope with a Leica DFC 480 camera attached (each section is 2 cm wide).

A1.7.2 Infrared (IR) single-grain fusion analysis

Whole rock samples were roughly crushed (using a rock splitter and jaw-crusher) and the resulting crushate was wet sieved into 3 fractions (250 to 500 μm; 500 μm to 1 mm and 1 to 2 mm), before being dried overnight in an oven set to 50 °C. Where possible whole mineral grains, and rounded glassy groundmass were hand-picked using a binocular microscope from the 500 μm to 1mm and 1 mm to 2 mm sieve fraction. Hand picking of the grains ensured a variety of different crystals could be analysed (i.e., inclusion free and inclusion rich). All samples were cleaned ultrasonically for 20 minutes each in acetone and deionised water prior to packaging for irradiation. The only exception to the normal cleaning regime was a second hand-picked separate of feldspar from samples YR215, YR185 and YR242, which were first washed in a cold weak (10 %) solution of

hydrofluoric acid to remove adhering glass (method discussed below). Exact details pertaining to each sample (e.g., grain size) can be found as footnotes accompanying Ar-Ar data tables in Appendix section A3.

A1.7.3 Hydrofluoric acid (HF) wash

Washing grains in hydrofluoric acid (HF) to remove glass adhered on the exterior of feldspar grains (as well as melt inclusions from crushed crystals), is common practice and has successfully been used in previous studies (e.g., Esser *et al.*, 1997; Bachmann *et al.*, 2007b). However, Layer and Gardner (2001) elected not to treat separated plagioclase from Mount St. Helens tephra layers (< 4000 ybp) with acid, to avoid isotopic contamination and dissolution of plagioclase and melt inclusions. Samples YR185 (MY25); YR185 (MY26 and MY27); YR242 (MY28); YR215 (MY29) and YR215 (MY30) were cleaned with HF to remove glass adhering to grain surfaces. The following method was followed and the implications of this technique are discussed in Chapter 3.

1. 10 % Hydrofluoric Acid (HF) solution was prepared by adding 1 ml (29 to 30 molar) concentrated HF to 9 ml of deionised water.
2. Place sample in Teflon beaker
3. Pipette approximately 1 ml of HF solution into each Teflon beaker
4. Seal lid of Teflon beaker and sonicate for 60 seconds
5. Wash sample in deionised water, repeat twice.
6. Cover sample with methanol and sonicate for 5 minutes
7. Wash sample with deionised water
8. Carry out a visual inspection under a microscope and repeat process if necessary.

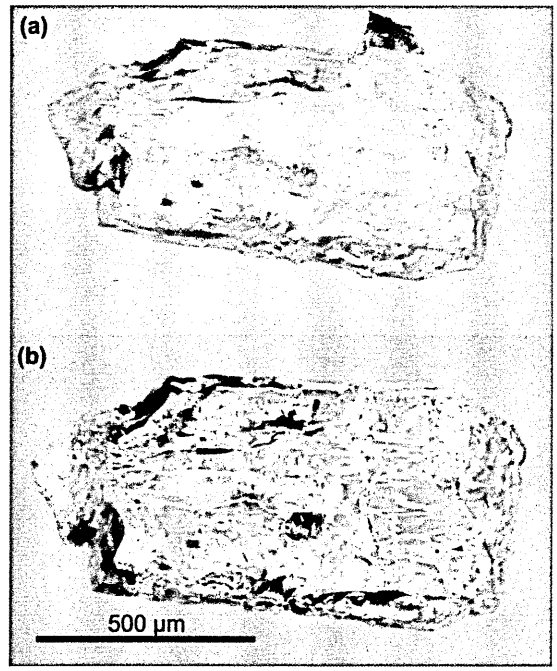

Figure A1.6. Photograph of feldspar crystal taken before (a) and after (b) being treated with hydrofluoric acid. (Photographs taken using a Leica Wild M28 binocular microscope with a Leica DFC 480 camera attached) in reflected light (additional light produced by a Microtec MFO-90 fibre optics lamp).

In order to ensure that washed crystals were not partially dissolved or developed a cloudy appearance following treatment in weak HF, all crystals were photographed before and after HF treatment (Fig. A1.6).

A1.7.4 Sample irradiation

Prior to analysis samples were irradiated in four separate batches at the McMaster University reactor (Canada). The $^{40}Ar/^{39}Ar$ technique relies on the transmutation of ^{39}K to ^{39}Ar by neutron bombardment during the irradiation process. Aliquots of mineral grains (n = 25 to 40) for single grain fusion experiments, and carefully selected pieces (0.5 to 1 cm^2) of polished thick sections (~ 350 µm) for *in situ* UV/IR experiments were loaded into numbered foil packets, which were intercalated with packets (positioned between every 10 packets of unknown) of the fluence monitor GA15-50. Samples were cadmium shielded

and irradiated in the standard 5C position. McM#60 has a longer irradiation time and higher irradiation power due to the samples being older than samples sent in subsequent irradiations (~28 Ma compared with ~2 Ma).

Table A1.1 Details of McMaster irradiations. Fish Canyon samples were irradiated in batch McM#60, all other samples were irradiated in batches McM#62, #65 and #70.

Irradiation #Number	Power (MWH)	Time in reactor (hrs)	Date sent	Date returned
McM#60	50	16.67	25/06/10	22/07/10
McM#62	3	1.00	18/10/10	17/11/10
McM#65	3	1.00	23/02/11	25/03/11
McM#70	3	1.05	17/10/11	24/11/11

A1.7.5 Flux

The advantages and disadvantages of various lasers and the final choice of lasers used in this study are discussed in more detail in section A1.3. This sub-section deals with the production of a 'flux' to facilitate the melting of clear crystals with longer wavelength lasers (i.e., IR). To completely fuse and achieve near total absorbance of the radiation by optically transparent minerals, such as feldspars and quartz, either an argon-ion or CO_2 continuous wave laser (λ = 10,600 nm), would be the most appropriate choice. $^{40}Ar/^{39}Ar$ single-grain fusion experiments for this study have been carried out using either an SPI CW/pulsed 1090 nm diode infrared fibre laser or a SPI CW 1062 nm infrared fibre laser coupled with a MAP-215-50 noble gas mass spectrometer. The CW fibre laser has a similar wavelength to an Nd-YAG laser (λ = 1064 nm), which has previously demonstrated poor coupling with clear minerals (McDougal and Harrison, 1999). The decision in this case, to use the CW fibre laser, rather than a CO_2 laser, which emits a wavelength readily absorbed by clear minerals, was based on the type of laser available for use.

Although the use of a flux is an established technique (e.g., Renne *et al.*, 1998; Lanphere *et al.*, 2002), recommended methods for producing the flux are either vague or absent. The majority of previous workers report that unirradiated basalt, fully melted to produce dark coloured glass beads, is fused along with the irradiated sample. The infrared (IR) wavelength is better absorbed by the dark glass bead and allows heating of the transparent minerals via conduction.

Specifically for this study, a roughly crushed sample of basalt lava flow (Ar-Ar basalt whole rock step heating age of 677 ± 86 ka; ~ 1.3 wt. % K_2O; Tenerife, Canary Islands, collected and dated by Dr. Alison Halton), was selected for use. Basalt whole rock must be unirradiated and clear of obvious alteration. Prior to flux production, chips of basalt (hand-picked from the 63 to 125 μm sieve fraction, and checked for alteration under a binocular microscope), were cleaned ultrasonically for 20 minutes each in acetone and deionised water, and left to dry on an electric hot plate. Once completely dry, 2 to 3 chips of basalt were loaded (using tweezers), into each hole of a 57-hole sample holder (Fig. A1.7a). Basalt chips were heated using an IR laser (5 % beam splitter, 25 W power), for approximately 30 seconds or until completely fused. Fusion is complete once the basalt chips pull together to form a spherical glass bead (Fig. A1.7b). This process was undertaken with the sample port shut off to the extraction line (and therefore the mass spectrometer), and pumping on the turbo pump. The basalt flux was stored in a glass vial until required. In order to fuse clear minerals using an IR laser, a basalt flux bead was loaded into each hole along with a single feldspar crystal (Fig. A1.7c). The laser was focussed onto the flux and the power steadily increased, until the feldspar started to glow cherry red (~ 800 °C). At this point the laser beam was refocused onto the feldspar where upon it fused.

It should be noted that early experiments, which involved fusing 4 to 6 chips of basalt, resulted in glass beads that were larger than required and would not sit next to the feldspar crystals. In order to assess if beads of this size were fully outgassed, the sample port was open to the extraction line and the beads were re-heated using the IR laser, and the liberated gas measured using the MAP-215-50 mass spectrometer. The ^{40}Ar measurement was above blank level, suggesting beads were not fully outgassed and were contributing a minor ^{40}Ar signal. Although the $^{40}Ar/^{36}Ar$ ratio from these experiments was determined to be atmospheric in composition (~298), and would therefore be corrected for during data reduction (i.e., using ArMaDiLo), significant contribution from the flux could cause the instrument to become saturated with gas during measurement, resulting in high and unstable instrument blanks. It is not advised to fuse a basalt bead more than once during flux production, as this causes the bead to stick to the base of the sample holder making it very difficult to extract for use. Therefore it is recommended that no more than 2 to 3 chips of unirradiated crushed basalt (63 to 125 μm) be used to make each flux bead.

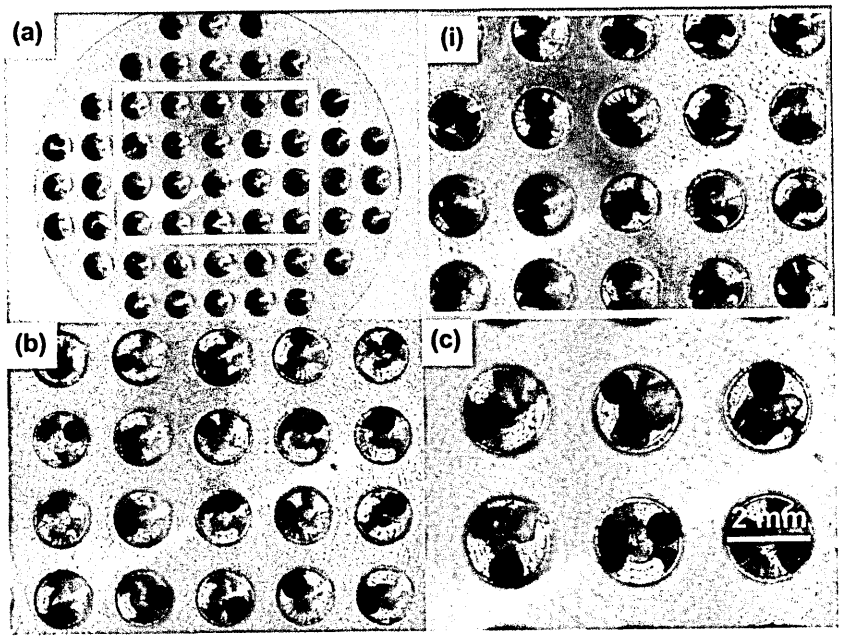

Figure A1.7. (a) Photograph showing pieces of unirradiated basalt (2 to 3), loaded into a 57 hole sample holder (area within the blue box has been enlarged (i)). (b) Photograph shows rounded glass beads formed after the basalt chips are heated using an IR laser (5 % beam splitter, 25 W

(*Fig. A1.7 cont.*) power, < 30 seconds). (c) Photograph showing basalt flux placed next to feldspar crystals prior to total fusion using an IR laser.

A1.7.6 Sample loading

For IR fusion analysis single feldspar crystals and rounded and transparent glassy groundmass grains plus flux, were loaded into an aluminium 57 hole holder (e.g., Fig. A1.7). For UV/IR *in situ* analysis, pieces of polished thick section (slabs) were loaded into flat sample holder. Samples were then loaded into an ultra-high vacuum (UHV) sample chamber. The pressure of the sample chamber was taken to $\times 10^{-9}$ mbars using a turbo and ion pump combination. The sample port, which is exposed to air during the loading procedure, was baked-out under vacuum at *c.* 120 °C for 10 hours. This is carried out to remove atmospheric Ar which has adhered to the surface of the grains or slabs as well as to the inside of the sample holder and laser port. Following the loading of one set of glassy groundmass (samples YR217 and YR185) many of the grains were found to have jumped out of the holes they were placed in, possibly as a result of 'explosive' degassing at low temperatures (e.g., Bigazzi *et al.*, 2008). Another explanation of this could be either static charging of these grains or a result of turbo pumping and achieving vacuum.

A1.8 X-ray fluorescence spectrometry (XRF)

Major and trace element determinations were undertaken at The Open University using an ARL® *8420* + dual goniometer wavelength dispersive XRF spectrometer, equipped with a Rh anode 3-kW end-window X-ray tub, and five diffraction crystals: LiF220, LiF200, AX06, PET and Ge111. Major-element analysis was performed on glass discs (mixture of dried rock powder and lithium tetraborate flux). Loss-on-ignition (L.O.I.) was also determined to account for those constituents (e.g., H_2O, CO_2) lost during glass formation.

Trace element analysis was performed on pressed powder pellets (mixture of dried rock powder and polyvinylpyrollidone-methyl cellulose binder). Standard samples WS-E (dolerite) and OU-3 (microgranite) were also included on the sample runs. Estimates of precision and accuracy for both major and trace element determination can be found in Ramsey (1995), including full details of sample preparation. XRF data tables are presented in Appendix section A4.

A1.9 Electron microprobe analysis

Electron microprobe analysis to determine major element concentrations (SiO_2, TiO_2, Al_2O_3, FeO, MnO, MgO, CaO, Na_2O, K_2O, BaO, SrO, F and Cl) of selected phenocryst phases and glass was performed using the wavelength-dispersive Cameca SX100 electron microprobe at The Open University. Operating parameters were: 20 kV accelerating voltage, a 20 nA current and a defocused 10-15 μm spot size was used for feldspar analyses to minimize loss of alkalis. Analyses were performed on carbon coated microprobe slides (slices of whole rock > 30 μm thick) and resin blocks (single grains mounted in epoxy). Resin blocks were also painted with liquid silver to prevent charging issues. Counting times were between 10 and 40 on peaks, and kept to a minimum where possible to reduce volatilisation effects in the glass.

Standards used for calibration were a combination of natural minerals for Na (jadeite), Mg (olivine), Al (corundum), Si and Ca (wollastonite), Ti (rutile); synthetic compounds for P ($ScPO_4$), K (KBr), and pure metals (for V, Mn, Fe, Co and Ni). V was corrected for the interference from Ti. Beam verification analyses were carried out on a secondary standard of Garnet 1 before each data collection run. The following crystal parameters were used: spectrometer 1 - TAP (Na, Al), spectrometer - 2 LTAP (F, Mg, Si), spectrometer 3 - LLIF

(Mn, Fe), spectrometer 4 - LPET (K, Ca, Cl) and spectrometer 5 - PET (Ti, Sr, Ba). Relative precision is limited to statistical error and is in general ± 2 % (2σ) for major elements, including uncertainties in the standard compositions and errors associated with corrections based on repeated analysis of standards.

Table A1.2. Crystal parameters and count times used for Electron microprobe analyses in this study.

Element/oxide	Crystal	Count time
Mn	LLIF	20
Fe	LLIF	15
Na	TAP	25
Al	TAP	20
K	LPET	20
Ca	LPET	10
F	LTAP	40
Mg	LTAP	10
Si	LTAP	20
Cl	LPET	20
Ti	PET	15

A1.10 DIFFARG

A1.10.1 Introduction

DIFFARG (Wheeler, 1996), is a computer programme (created in Matlab v.4.1) which simulates Ar diffusion profiles for a user defined history. It allows complex histories involving, for example reheating and $^{40}Ar_E$ events to be modelled to obtain theoretical profiles (e.g., Warren *et al.*, 2012). These profiles can be used with $^{40}Ar/^{39}Ar$ age data to

determine the thermal history of a mineral. The modelling in this study concentrates on the diffusive loss of Ar from xenocrysts and/or antecrysts entrained into a magma body prior to an eruption, similar to the study by Gansecki *et al.*, (1996).

To take into account production of ^{40}Ar from ^{40}K within the grain, a source term S is added to the diffusion equation (modified version of Fick's 2nd Law; Eq. A.38), and c is the concentration of ^{40}Ar, t is the time, and $D=D_0\exp(-E_a/RT)$, the temperature-dependent diffusion coefficient (determined by a pre-exponential factor D_0 and the activation energy E_a, based on release ^{39}Ar as a function of temperature during heating experiments).

$$\frac{\partial c}{\partial t} = D\nabla^2 c + S \qquad \text{(A.38)}$$

$$S = \lambda[^{40}K]_i \, e^{-\lambda t} \qquad \text{(A.39)}$$

The concentration of ^{40}Ar in the mineral represents the 'apparent age' and the source term 'S' relates to the production of ^{40}Ar within the grain (Eq. A.39), where λ is the decay constant for ^{40}K and $[^{40}K]i$ is the concentration of ^{40}K at $t = 0$.

DIFFARG models are run assuming:

(1) Concentration of Ar at the grain boundary is zero

(2) Bulk diffusion (lattice diffusion) is the dominant process.

(3) The apparent age (concentration of ^{40}Ar) is a function of K concentration, which is assumed constant and to have a homogeneous distribution within the crystal at all times.

(4) Spherical geometry of grain (0.5 mm grain radius)

(5) Diffusion radius is equal to the grain radius

(6) Diffusion coefficient (D_0) – experimentally derived

(7) Activation energy (E_a) – experimentally derived

A1.10.2 Instructions for running DIFFARG

Models are run in Octave, version 3.4.3 but can be run in MatLab. For a more detailed explanation of DIFFARG see Wheeler (1996). The following example is modelling diffusive loss of Ar from a plagioclase crystal with a radius of 0.5 mm entrained into a magma which is at a temperature of 800 °C. The plagioclase is held at 800 °C for 250 years before being cooled to 0 °C and therefore erupted at ~ 2 Ma. The total model run time is 3 Ma. The following is an example of a model run input (*input in italics*).

octave-3.4.3>diffargP_minerals
1: Linear temperature history
2: Flat-top pulse of temperature
3: Piecewise linear
4: User defined history
Input required temperature history *3*

Input T at time 0 Ma *0*
Input next time (-1 to finish) *0.999749*
Input T at time 0.999749 Ma *0*
Input next time (-1 to finish) *0.999750*
Input T at time 0.999500 Ma *800*
Input next time (-1 to finish) *1*
Input T at time 1 Ma *800*
Input next time (-1 to finish) *1.000001*
Input T at time 1.000001 Ma *0*
Input next time (-1 to finish) *3*
Input T at time 3 Ma *0*
Input next time (-1 to finish) *-1*

1: Linear pressure (default=1) history
2: Flat-top pulse of pressure (default=1)
3: Piecewise linear
4: User defined history
Input required pressure (default=1) history *1*
Input initial pressure (default=1) (GPa) *0*
Input rate of pressure (default=1) decrease (GPa/Ma) *0*

1: Linear edge age history
2: Flat-top pulse of edge age
3: Piecewise linear
4: User defined history
Input required edge age history *1*
Input initial edge age (Ma) *0*
Input rate of edge age decrease (Ma/Ma) *0*

4: K-feldspar
7: Plagioclase
Select mineral *7*

1: plate
2: cylinder
3: sphere
Select grain shape *3*

Enter grain radius (or slab half-width) in mm *0.5*
Enter the mesh length (an even integer) *20* ***(NOTE: each model is run 3 times using increasing mesh lengths e.g., 20, 40 and 60 in order to extrapolate to a precise bulk age)***
1: Fully explicit
2: Crank –Nicholson
Enter finite difference scheme *1*

1: No display
2: Summary figure with four graphs
3: Summary and individual figures
4: Summary and individual figures with data display toggle
Enter display required *2*
Enter time to next display in Ma (or 0 to quit, -1 to print) *3*

The output file is saved as a text file named *age1.txt*. This file is overwritten every run so

each file needs to be saved following a model run. The following is an example of the

output file:

======= New Run ==========
>>> parameter vector: ***This records the input parameters***
1.000000 3.000000 0.000000 0.999749 0.000000 0.999750 800.000000 1.000000
800.000000 1.000001 0.000000 3.000000 0.000000 -1.000000 2.000000 1.000000
0.000000 0.000000 3.000000 1.000000 0.000000 0.000000 4.000000 7.000000
3.000000 0.500000 20.000000 5.000000 1.000000 2.000000 6.000000 3.000000
0.000000 7.000000

>>> concentration as function of radius: ***This records the apparent age as a function of the radius distance (given as the mesh separation value, below)***
2.302435 2.301207 2.297536 2.291477 2.283113 2.272565 2.259981 2.245539
2.229443 2.211918 2.193211 2.173580 2.153298 2.132641 2.111888 2.091315
2.071191 2.051769 2.033289 2.015969 0.000000

>>> meshseparation: 0.025000 ***This is the mesh spacing in mm***

>>> runtimes: ***This records the run time intervals – in this case the run is for 3 Ma***

0.000000 3.000000 0.000000 0.000000 0.000000 0.000000 0.000000 0.000000
0.000000 0.000000 0.000000 0.000000 0.000000 0.000000 0.000000 0.000000
0.000000 0.000000 0.000000 0.000000 0.000000 0.000000 0.000000 0.000000
0.000000 0.000000 0.000000 0.000000 0.000000 0.000000 0.000000 0.000000
0.000000 0.000000 0.000000 0.000000 0.000000 0.000000 0.000000 0.000000
0.000000 0.000000 0.000000 0.000000 0.000000 0.000000 0.000000 0.000000
0.000000 0.000000 0.000000 0.000000 0.000000 0.000000 0.000000 0.000000
0.000000 0.000000 0.000000 0.000000 0.000000 0.000000 0.000000 0.000000
0.000000 0.000000 0.000000 0.000000 0.000000 0.000000 0.000000 0.000000
0.000000 0.000000 0.000000 0.000000 0.000000 0.000000 0.000000 0.000000
0.000000 0.000000 0.000000 0.000000 0.000000 0.000000 0.000000 0.000000
0.000000 0.000000 0.000000 0.000000

>>> runavgs: ***This records the bulk average age for each run time listed above.***

0.000000 1.992339 0.000000 0.000000 0.000000 0.000000 0.000000 0.000000
0.000000 0.000000 0.000000 0.000000 0.000000 0.000000 0.000000 0.000000
0.000000 0.000000 0.000000 0.000000 0.000000 0.000000 0.000000 0.000000
0.000000 0.000000 0.000000 0.000000 0.000000 0.000000 0.000000 0.000000
0.000000 0.000000 0.000000 0.000000 0.000000 0.000000 0.000000 0.000000
0.000000 0.000000 0.000000 0.000000 0.000000 0.000000 0.000000 0.000000
0.000000 0.000000 0.000000 0.000000 0.000000 0.000000 0.000000 0.000000
0.000000 0.000000 0.000000 0.000000 0.000000 0.000000 0.000000 0.000000
0.000000 0.000000 0.000000 0.000000 0.000000 0.000000 0.000000 0.000000
0.000000 0.000000 0.000000 0.000000 0.000000 0.000000 0.000000 0.000000
0.000000 0.000000 0.000000 0.000000 0.000000 0.000000 0.000000 0.000000
0.000000 0.000000 0.000000 0.000000

A1.10.3 DIFFARG age error calculation

The error on the DIFFARG age has been calculated by running 4 models, each one representing the uncertainty (+) and (-) for the experimentally derived diffusion parameters D_0 and E_a for both plagioclase and K-feldspar diffusion parameters. For plagioclase parameters used in this study, the error on $E_a = \pm 4.58$ kcal/mol, and the error on $D_0 = (+ 8.79 \times 10^{-8})$ and $(- 8.79 \times 10^{-9})$ $cm^2\ s^{-1}$ at the 95 % confidence level (Wartho *et al.*, 2012). For K-feldspar parameters used in this study, the error on $E_a = \pm 1.0$ kcal/mol, and the error on $D_0 = (+ 0.00660)$ and $(- 0.00371)$ $cm^2\ s^{-1}$. DIFFARG age uncertainties (1σ), calculated

relative to a reference model (0.5 mm grain radius, spherical geometry, held at 750 °C for 0.000001 Ma), are ± 0.09 Ma for K-feldspar and ± 0.01 Ma for plagioclase.

A1.10.4 Fractional loss of Ar

Using DIFFARG (Wheeler, 1996) to run multiple models can be time consuming, with some models taking up to 7 days to complete using a standard desktop PC. This was the case where diffusional loss of Ar was high over an extended period of time (e.g., sanidine at 750 °C for 100 years, or plagioclase at 800 °C for 5000 years). In order to produce adequate diffusional loss data for sanidine and plagioclase (also a proxy for anorthoclase), additional models where calculated using equation (A.40), where f is the fractional loss of Ar from a sphere, and Dt/r^2 is the diffusion coefficient (D), multiplied by the time (t) over which diffusion is taking place, divided by the sphere radius (i.e., grain radius) squared (McDougall and Harrison, 1999).

$$f = 1 - \left(\frac{6}{\pi^2}\right) \sum_1^\infty (1/n^2)\, exp(-n^2\pi^2 Dt/r^2) \qquad \text{(A.40)}$$

Using this equation produces an age identical to a DIFFARG modelled age, but only in the case where fractional loss of Ar, due to a single heating event, is being considered and the length of the heating event is negligible compared to the age of the sample. Therefore this expression can be used to support models run using DIFFARG.

A2. Sample Descriptions

A2.1 Field locations and sample descriptions

A2.1.1 Introduction

The following section outlines sample descriptions for all samples used in this study accompanied by field locality maps. UV and IR *in situ* analysis of mineral phases of the Fish Canyon magmatic system were carried out on nine polished thick sections, made at the Open University from material which formed part of a study by Dr B. Charlier (Charlier *et al.*, 2007) and were obtained from the thesis collection belonging to Dr O. Bachmann were also used. The locality map (Fig. A2.1) simply shows the sample localities and the reader is referred to Bachmann (2001), for full sample locality descriptions. Samples of the Yellowstone Plateau Volcanic field (YP127, YP079, YP081, YR215, YR217, and YR185) were collected by Prof. C. Wilson and Dr B. Charlier (2009) and existed as crushed separates only, with the exception of YP127 and sample localities are shown in Figure A2.2. Bishop Tuff samples (BP029, BP097, BP113 and BP168) were collected by Prof. C. Wilson (October 2010) for U-Pb zircon dating (Fig. A2.3). The use of these samples for this work offered a chance to carry out Ar-Ar dating of various mineral phases on the same samples, so that comparison between the two techniques could be made. In addition, field work to collect a sample of Mesa Falls Tuff (CMW01) and Bishop Tuff fall unit 7 (CMW12) was also carried out in June 2011.

A2.1.2 Fish Canyon magmatic system

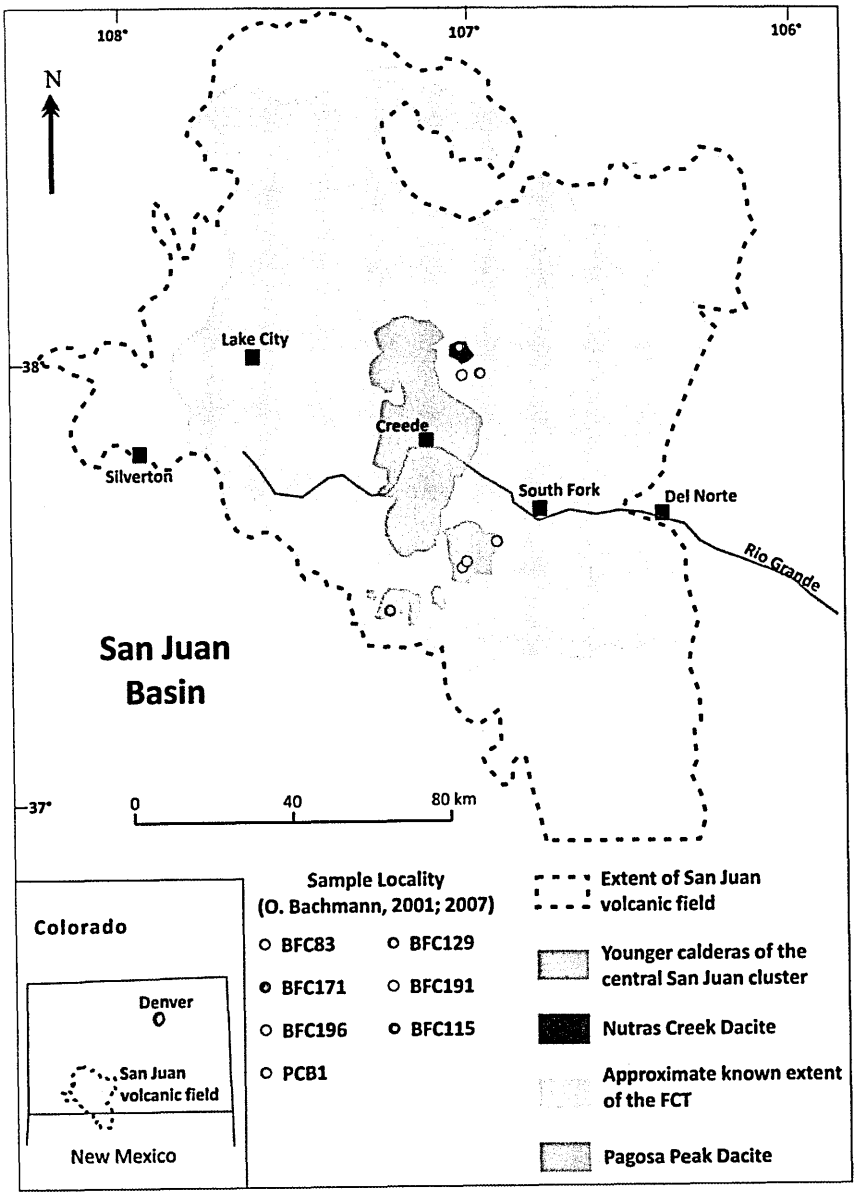

Figure A2.1. Summary map (modified after Bachmann *et al.*, 2007b), showing the sampling localities for Fish Canyon samples used in this study (BFC83; BFC196; BFC171; PCB 1; BFC129; BFC191 and BFC115).

Sample: BFC83

Location: San Juan Volcanic Field, USA

Formation/Unit: Pagosa Peak Dacite, Fish Canyon magmatic system

GPS: N 37 29' 17" W 106 52' 12" (Bachmann *et al.*, 2007b)

Rock type: Dacite

Field Description: N/A

Thin Section Description: Yes

Ar-Ar: UV an IR *in situ* analysis

EMP: Yes

XRF: No

Notes: Collected by Olivier Bachmann.

Sample: BFC196

Location: San Juan Volcanic Field, USA

Formation/Unit: Pagosa Peak Dacite, Fish Canyon magmatic system

GPS: N/A

Rock type: Dacite

Field Description: N/A

Thin Section Description: Yes

Ar-Ar: UV *in situ* analysis

EMP: Yes

XRF: No

Notes: Collected by Olivier Bachmann in 1997. Collected from the same location as BFC83 (O. Bachmann *pers. com.*, 2011).

Sample: BFC171

Location: San Juan Volcanic Field, USA

Formation/Unit: Pagosa Peak Dacite, Fish Canyon magmatic system

GPS: N/A

Rock type: Dacite

Field Description: N/A

Thin Section Description: Yes

Ar-Ar: UV *in situ* analysis

EMP: Yes

XRF: No

Notes: Collected by Olivier Bachmann. UTM coordinates 316-317, 4148-4149 (Bachmann, 2001).

Sample: PCB 1

Location: San Juan Volcanic Field, USA

Formation/Unit: Pagosa Peak Dacite, Fish Canyon magmatic system

GPS: N 37 34' W 106 46' (O. Bachmann, *pers. com.*, 2011)

Rock type: Dacite

Field Description: N/A

Thin Section Description: Yes

Ar-Ar: UV and IR *in situ* analysis

EMP: Yes

XRF: No

Notes: Collected by M. Dungan in 1994 (O. Bachmann, *pers. com.*, 2011).

Sample: BFC129

Location: San Juan Volcanic Field, USA

Formation/Unit: Fish Canyon Tuff, Fish Canyon magmatic system

GPS: N/A

Rock type: Tuff

Field Description: N/A

Thin Section Description: Yes

Ar-Ar: UV *in situ* analysis

EMP: Yes

XRF: No

Notes: Collected by Olivier Bachmann. UTM coordinates 339000, 4197-4198 (Bachmann, 2001).

Sample: BFC191

Location: San Juan Volcanic Field, USA

Formation/Unit: Fish Canyon Tuff, Fish Canyon magmatic system

GPS: N/A

Rock type: Tuff

Field Description: N/A

Thin Section Description: Yes

Ar-Ar: UV and IR *in situ* analysis

EMP: Yes

XRF: No

Notes: Collected by Olivier Bachmann. UTM coordinates 343-345, 4200-4205 (Bachmann, 2001).

Sample: BFC115

Location: San Juan Volcanic Field, USA

Formation/Unit: Nutras Creek Dacite, Fish Canyon magmatic system

GPS: N 38 01' 37" W 106 50' 03" (Bachmann *et al.*, 2007b)

Rock type: Dacite

Field Description: N/A

Thin Section Description: Yes

Ar-Ar: UV and IR *in situ* analysis

EMP: Yes

XRF: No

Notes: Collected by Olivier Bachmann.

A2.1.3 Yellowstone Plateau Volcanic Field

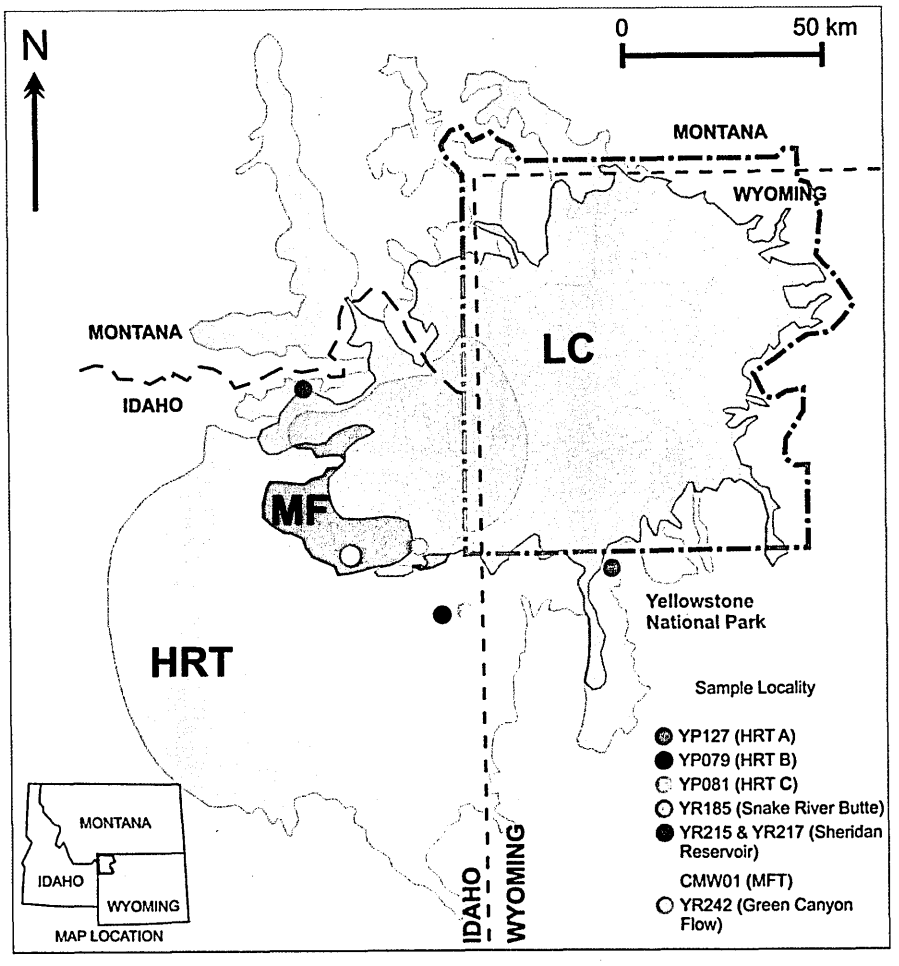

Figure A2.2. Summary map (modified after Christiansen, 2001), showing the sampling localities for units of the Yellowstone Volcanic Plateau Field used for Ar-Ar analysis in this study (YP127; YP079; YP081; YR185; YR215 and YR217; CMW01 and YR242). HRT = Huckleberry Ridge Tuff; MF = Mesa Falls Tuff; LCT = Lava Creek Tuff.

Sample: YP127

Location: Flagg Ranch, Yellowstone Plateau Volcanic Field, Wyoming, USA

Formation/Unit: Huckleberry Ridge Tuff, Member A

GPS: N/A

Rock type: Tuff - basal vitrophyre

Field Description: N/A

Thin Section Description: Yes

Ar-Ar: IR single grain fusion

EMP: Yes

XRF: Yes

Notes: Collected by C. Wilson and B. Charlier (2009).

Sample: YP079

Location: Teton River, north of Newdale, Yellowstone Plateau Volcanic Field, Idaho, USA

Formation/Unit: Huckleberry Ridge Tuff, Member B

GPS: N/A

Rock type: Pumice

Field Description: N/A

Thin Section Description: No

Ar-Ar: IR single grain fusion

EMP: Yes

XRF: Yes

Notes: Collected by C. Wilson and B. Charlier (2009).

Sample: CMW06

Location: Teton River, north of Newdale, Yellowstone Plateau Volcanic Field, Idaho, USA

Formation/Unit: Huckleberry Ridge Tuff, Member B

GPS: N 43 56' 109" W111 36' 284"

Rock type: Pumice

Field Description: Large pumice block from top of HRT B. Feldspars are large and augen (eye) shaped. Many appear shattered.

Thin Section Description: Yes

Ar-Ar: No

EMP: No

XRF: No

Notes: Collected in June 2011.

Sample: YP081

Location: Teton River, north of Newdale, Yellowstone Plateau Volcanic Field, Idaho, USA

Formation/Unit: Huckleberry Ridge Tuff, Member C

GPS: N/A

Rock type: C-type magma pumice

Field Description: N/A

Thin Section Description: No

Ar-Ar: IR single grain fusion

EMP: Yes

XRF: Yes

Notes: Collected by C. Wilson and B. Charlier (2009).

Sample: CMW08

Location: Teton River, north of Newdale, Yellowstone Plateau Volcanic Field, Idaho, USA

Formation/Unit: Huckleberry Ridge Tuff, Member C

GPS: N 43 55' 040" W 111 31' 670"

Rock type: Type-C pumice

Field Description: Sample taken from bottom of scree. The rim of this pumice block was oxidised and discarded on site. The dense and fibrous core (grey in colour), which was not oxidised was kept. Sample has moderate crystal content and crystals appear to be intact.

Thin Section Description: Yes

Ar-Ar: No

EMP: No

XRF: No

Notes: Collected in June 2011.

Sample: CMW01

Location: Road cutting on Route 20, Idaho, USA

Formation/Unit: Mesa Falls Tuff

GPS: N 44° 07.280' W 111° 26.517'

Rock type: Pumice

Field Description: Section of Mesa Fall Tuff basal section, road side cutting on Route 20, Idaho, USA. Exposed locality (Fig. A2.3a) at the base of the ignimbrite where flow and ash fall are intercalated (Fig. A2.3b). Fresh pumice was collected from the base of the ignimbrite containing pumice clasts (Fig. A2.3c).

Thin Section Description: Yes

Ar-Ar: IR single grain fusion

EMP: Yes

XRF: Yes

Notes: Collected in June 2011.

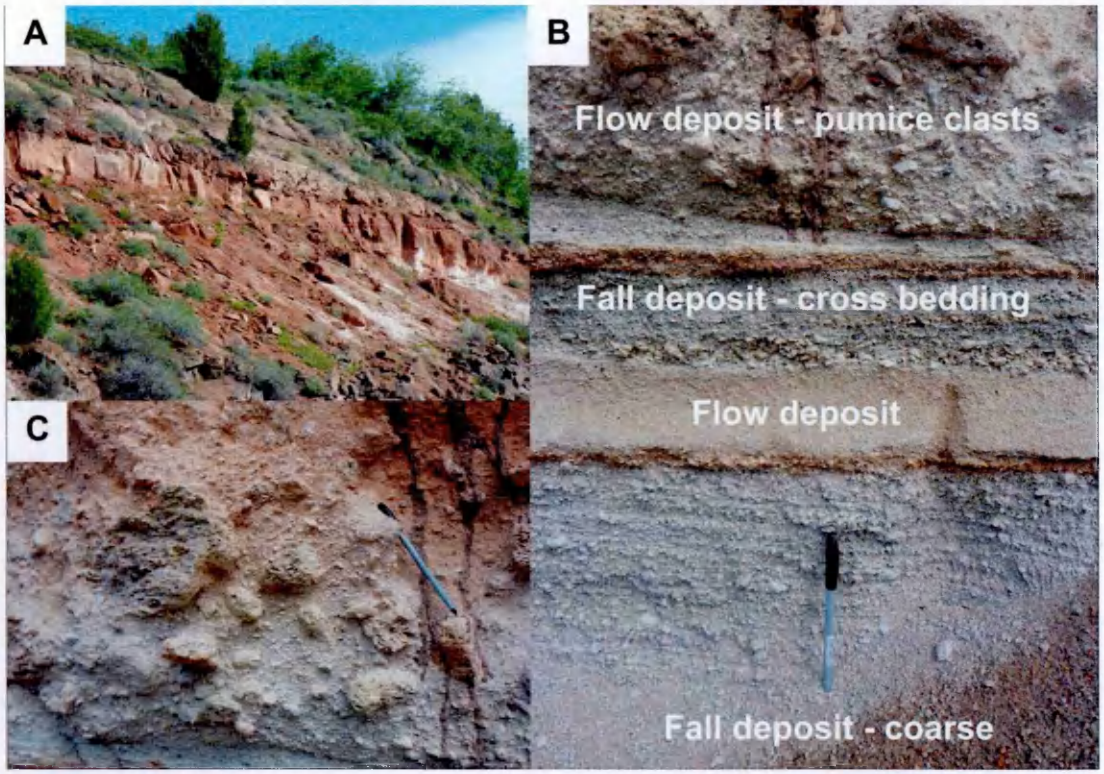

Figure A2.3. Photographs taken of the basal section of Mesa Falls Tuff. (a) Exposed basal section in a road cutting, Route 20, Idaho, USA; (b) detailed relationship between ignimbrite and ash fall, illustrating the range of textures present; (c) coarse, pumice rich flow deposit from which sample CMW01 was collected (scale = pen length 14 cm).

Sample: YR185

Location: Snake River Butte, Yellowstone Plateau Volcanic Field, Idaho, USA

Formation/Unit: Snake River Butte dome lava

GPS: N/A

Rock type: Grey, crystal-rich, glassy to perlitic pumiceous obsidian of Snake River Butte dome.

Field Description: N/A

Thin Section Description: No

Ar-Ar: IR single grain fusion

EMP: Yes

XRF: Provided by B. Charlier

Notes: Collected by C. Wilson and B. Charlier (2009).

Sample: CMW02

Location: Snake River Butte, Yellowstone Plateau Volcanic Field, Idaho, USA

Formation/Unit: Snake River Butte dome

GPS: N 44° 07' 541" W 111° 19' 945"

Rock type: Dome pumice

Field Description: Sample collected from a small excavation pit (Fig. A2.4a). Dome material is obsidian rich, although clearly weathered in places (hydrated pumiceous obsidian (Fig. A2.4b). Iron and magnesium bearing minerals appear to have been weathered out but feldspars look clear and flow banding structure were visible (Fig. A2.4c).

Thin Section Description: Yes

Ar-Ar: No

EMP: No

XRF: No

Notes: Collected in June 2011.

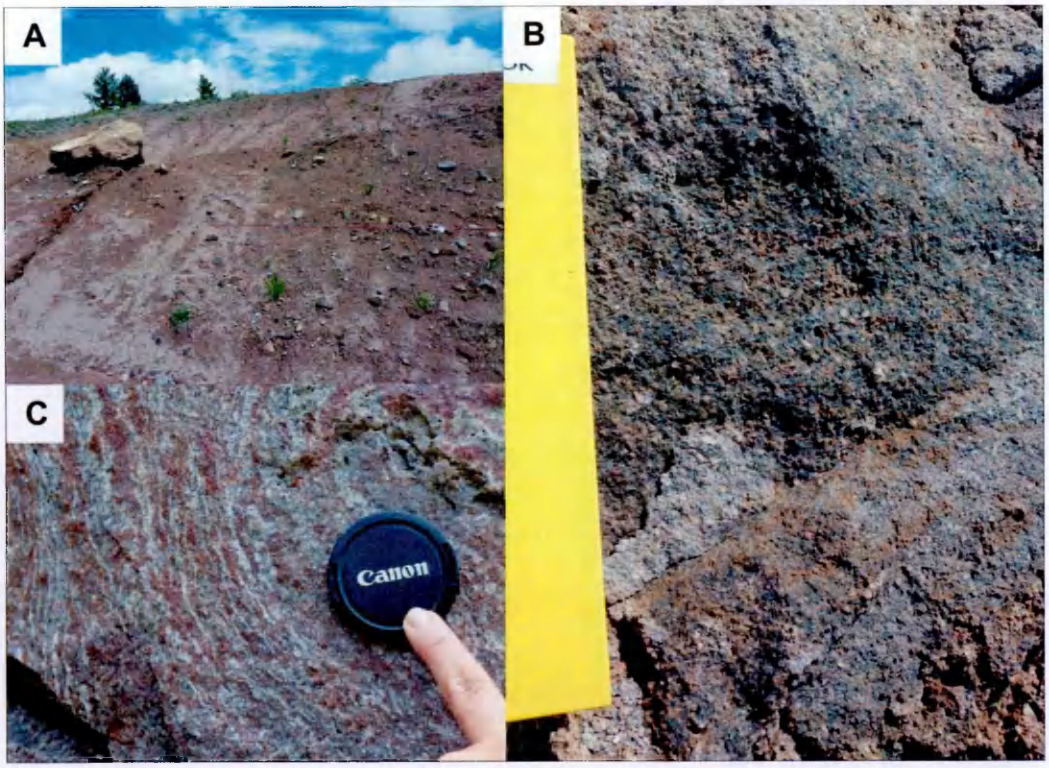

Figure A2.4. Photographs taken of the Snake River Butte dome (sample CMW02) sampling locality. (a) Excavation pit, previously dug out exposing dome material; (b) Obsidian rich dome material, some potentially hydrated owing to its crumbly nature; (c) Flow textures preserved in parts (scale = field notebook length 20 cm and camera lens cap ~ 5 cm diameter).

Sample: YR215

Location: Sheridan Reservoir Ranch, Yellowstone Plateau Volcanic Field, Idaho, USA

Formation/Unit: Sheridan Reservoir dome

GPS: N/A

Rock type: Crystal rich pumiceous dome material. Sample consists of dark brown to black rhyolitic glass, pumice fragments and phenocrysts of feldspar and quartz.

Field Description: N/A

Thin Section Description: No

Ar-Ar: IR single grain fusion

EMP: Yes

XRF: Provided by B. Charlier

Notes: Collected by C. Wilson and B. Charlier (2009).

Sample: YR217

Location: Sheridan Reservoir Ranch, Yellowstone Plateau Volcanic Field, Idaho, USA

Formation/Unit: Sheridan Reservoir dome

GPS: N/A

Rock type: Crystal rich pumiceous dome material. Sample consists of pale brown rhyolitic glass, pumice fragments and phenocrysts of feldspar and quartz.

Field Description: N/A

Thin Section Description: No

Ar-Ar: IR single grain fusion

EMP: Yes

XRF: Provided by B. Charlier

Notes: Collected by C. Wilson and B. Charlier (2009).

Sample: CMW11

Location: Sheridan Reservoir Ranch (privately owned land), Yellowstone Plateau Volcanic Field, Idaho, USA

Formation/Unit: Sheridan Reservoir dome

GPS: N 44° 27' 20.5" W 111° 41' 1.5"

Rock type: Dense welded de-vitrified dome rhyolite

Field Description: Sampling carried out in a small quarry pit (dug out by the owners for land development purposes (Fig. A2.5a). Pumice clasts (honey coloured) containing obsidian nodules (fused breccia) were also common (Fig. A2.5b). CMW11 is a piece of densely welded, de-vitrified rhyolite, light grey in colour and crystal rich (Fig. A2.5c).

Thin Section Description: Yes

Ar-Ar: No

EMP: No

XRF: No

Notes: Collected in June 2011.

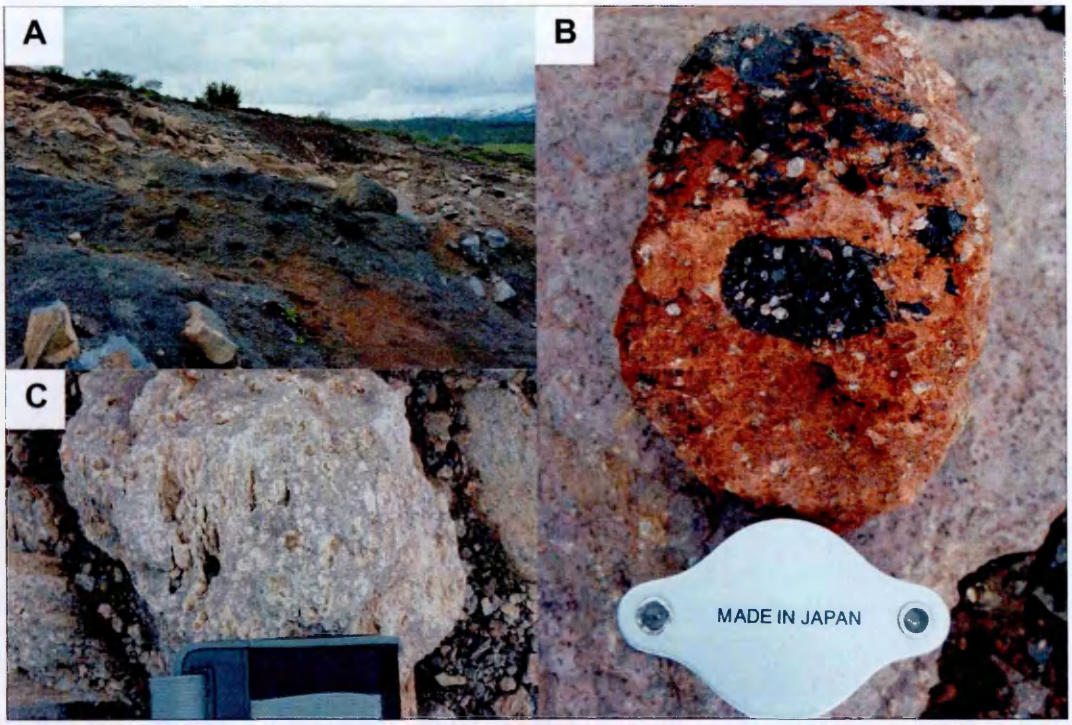

Figure A2.5. Photographs taken of the Sheridan Reservoir dome sampling locality. (a) Quarry pit, previously dug out by Ranch owner exposing dome material; (b) Honey coloured pumice clasts containing obsidian and large (> 2 mm) feldspar crystals; (c) Sample CMW11 (scale = camera case length ~ 9.5 cm and hand lens ~ 3 cm).

Sample: CMW242

Location: Green Canyon Flow, Yellowstone Plateau Volcanic Field, Idaho, USA

Formation/Unit: Green Canyon Flow

GPS: N/A

Rock type: Crystal-rich, devitrified dome rhyolite, containing phenocrysts of feldspar, quartz and biotite (oxidised based on visual inspection).

Field Description: N/A

Thin Section Description: Yes

Ar-Ar: Yes

EMP: Yes

XRF: Yes

Notes: Collected in June 2011 by C. Wilson. Grid reference (m) 0457410 E, 4910531 N (C. Wilson, *pers. com.*, 2012).

A2.1.4 The Bishop Tuff

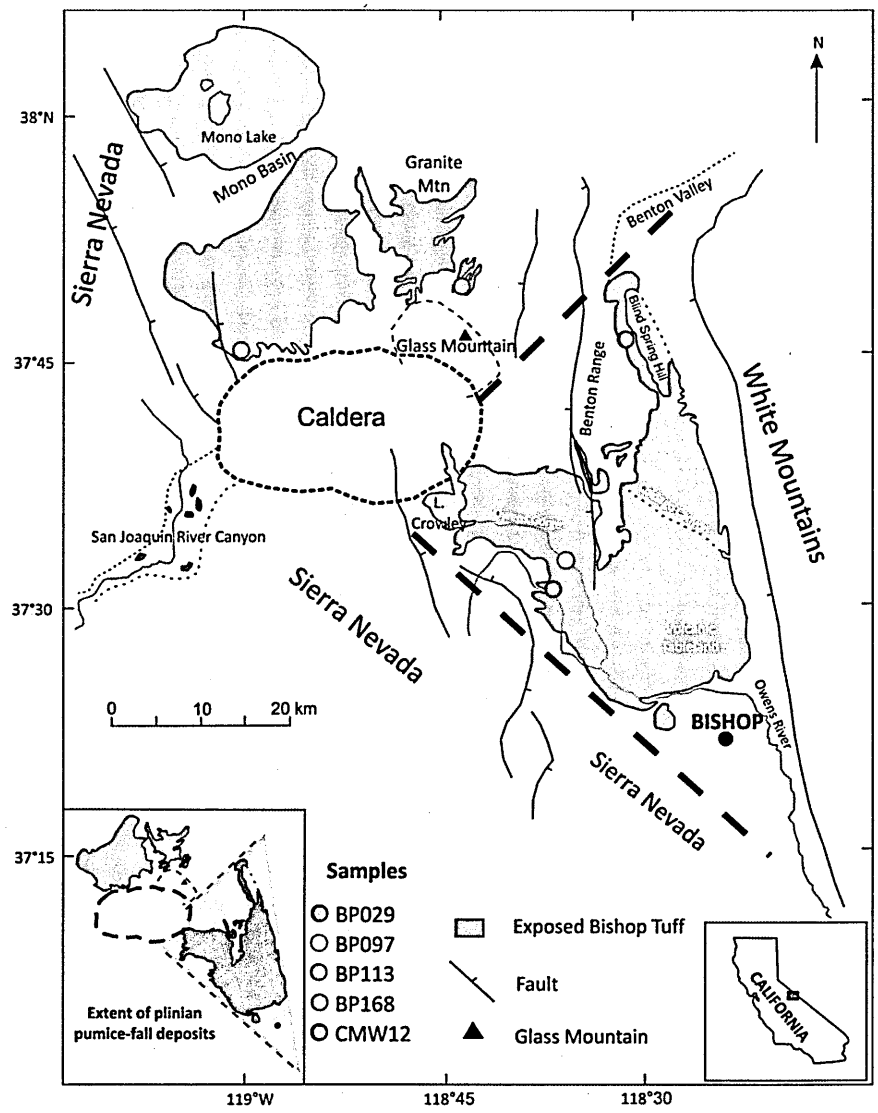

Figure A2.6. Summary map (modified after Hildreth and Wilson, 2007), showing the sampling localities for units of the Bishop Tuff, Long Valley Caldera, California, USA used in this study (BP029; CMW12; BP097; BP113 and BP168).

Sample: BP029

Location: Long Valley Caldera, California, USA

Formation/Unit: Bishop Tuff, Fall unit 5 (F5)

GPS: N/A

Rock type: Pumice

Field Description: N/A

Thin Section Description: Yes

Ar-Ar: IR single grain fusion

EMP: Yes

XRF: Yes

Notes: Collected by C. Wilson (October 2010). UTM 100 m grid reference 558 532.

Sample: BP097

Location: Long Valley Caldera, California, USA

Formation/Unit: Bishop Tuff, Ignimbrite package Ig1Eb

GPS: N/A

Rock type: 3 pumices from the basal flow unit

Field Description: N/A

Thin Section Description: Yes

Ar-Ar: IR single grain fusion

EMP: Yes

XRF: Yes

Notes: Collected by C. Wilson (October 2010). UTM 100 m grid reference 594 564.

Sample: BP113

Location: Long Valley Caldera, California, USA

Formation/Unit: Bishop Tuff, Ignimbrite package Ig2NWa

GPS: N/A

Rock type: Pumice from the base of ignimbrite package

Field Description: N/A

Thin Section Description: Yes

Ar-Ar: IR single grain fusion

EMP: Yes

XRF: Yes

Notes: Collected by C. Wilson (October 2010). UTM 100 m grid reference 241 812.

Sample: BP168

Location: Long Valley Caldera, California, USA

Formation/Unit: Bishop Tuff, Ignimbrite package Ig2Nb

GPS: N/A

Rock type: Single fibrous pumice

Field Description: N/A

Thin Section Description: Yes

Ar-Ar: IR single grain fusion

EMP: Yes

XRF: Yes

Notes: Collected by C. Wilson (October 2010). UTM 100 m grid reference 476 871.

Sample: CMW12

Location: Tungsten Mine Pits (Lower pit; Fig. A2.7a) Long Valley Caldera, California, USA

Formation/Unit: Bishop Tuff, Fall unit 7 (F7)

GPS: N 37 47' 23" W 118 32' 45"

Rock type: Pumice

Field Description: Collected various individual pumices (10 to 5cm in diameter), from non-welded fall deposit (Fig. A2.7b), which were white in colour and glassy with a moderate crystal content. Biotite identified in hand specimen but golden brown in colour

indicating phase is likely to be weathered. Thin layer of fall unit 8 (F8) and fall unit 9 (F9) overlies F7 at this locality and a thin layer of Ig2E caps the fall deposit (Fig. A2.7c).

Thin Section Description: Yes

Ar-Ar: IR single grain fusion

EMP: Yes

XRF: Yes

Notes: Collected in June 2011

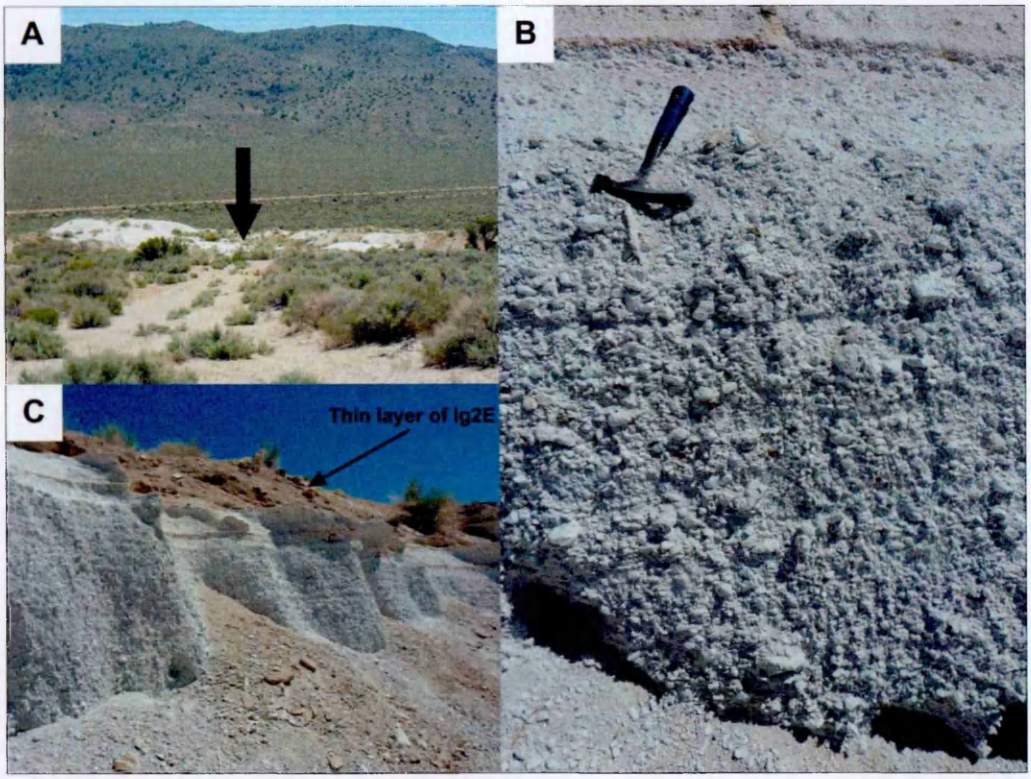

Figure A2.7. F7 sample locality. (a) Tungsten Mine Pits (arrow indicates lower pit); (b) non-welded fall deposit containing abundant white pumices; (c) Fall deposit (F7) is capped by a thin layer of Ig2E (scale = geological hammer length ~ 30 cm).

A2.2 Thin section descriptions

The fieldwork trip (June 2011) also presented an opportunity to collect additional samples on which petrographic and EMP analysis could be conducted. This section summarises the petrographic study undertaken to assess the suitability (i.e., abundant mineral type, inclusion content of phenocrysts, crystal size) of the various phases used for Ar-Ar dating. Thin section descriptions are accompanied by a selection of representative thin section and EMP images.

A2.2.1 Fish Canyon Magmatic system

Petrographic analysis of samples BFC83a, BFC83b, PCB 1, BFC171a, BFC196 (Pagosa Peak Dacite), BFC129, BFC191 (Fish Canyon Tuff) and BFC115 (Nutras Creek Dacite) is summarised in Table A2.1 and representative thin section and EMP images are presented in Figure A2.8.

Table A2.1. Thin section descriptions for Fish Canyon magmatic system samples used for Ar-Ar study including estimated proportions of main phenocryst phases and groundmass (**% in bold**).

Sample number	Rock type	Thin section description
BFC83	Dacite	Glassy pumice matrix. Some shattering of grains has occurred – most noticeable in quartz (> 1 mm). Feldspar exhibits oscillatory zoning. Twinned plagioclase (> 1 mm) contains various inclusions, internal melt pools and exhibits zoning. A number of small (< 1 mm) euhedral phenocrysts of amphibole are also seen. **Alkali Feldspar (20%) Plagioclase Feldspar (30%) Quartz (30%) Amphibole (10%) Biotite (10%)**
BFC171a	Dacite	Coarse groundmass contains euhedral amphibole (10%) and biotite (10%) phenocrysts. Some phenocrysts of feldspar (sanidine) and quartz show resorption textures and contain inclusions of mostly plagioclase. **Alkali Feldspar (20%) Plagioclase Feldspar (40%) Quartz (20%) Amphibole (10%) Biotite (10%)**
BFC115	Dacite	Glassy, devitrified groundmass showing radial and fibrous spherulite growth. Both sanidine and quartz appear to show resorption textures (long melt channels connected to matrix). Intergrowth of two feldspars is common and both show complex zoning and twinning. **Alkali Feldspar (30%) Plagioclase Feldspar (40%) Quartz (15%) Amphibole (< 5 %) Biotite (10%)**
BFC129	Pumice - intra-caldera	Very fine glassy groundmass. Majority of phenocrysts are small (<1mm), angular fragments of broken crystals, some intergrowth between plagioclase and alkali feldspar also visible. Many feldspars in this section appear to show dissolution textures and contain melt inclusions. Amphibole and biotite are also present. **Alkali Feldspar (20%) Plagioclase Feldspar (30%) Quartz (30%) Amphibole (10%) Biotite (10%)**
BFC191	Tuff - intra-caldera	Groundmass varies between fine glassy and coarse grained. Zoned alkali feldspar and quartz contain plagioclase inclusions. Plagioclase also appears as zoned phenocrysts with minor amphibole and biotite. **Alkali Feldspar (30%) Plagioclase Feldspar (30%) Quartz (25%) Amphibole (10%) Biotite (<5%)**
BFC196	Dacite	Fine glassy matrix containing phenocrysts of plagioclase, alkali feldspar and quartz, which all show resorption textures and intergrowth of various mineral phases (plag+hbl+bt). **Alkali Feldspar (30%) Plagioclase Feldspar (30%) Quartz (20%) Amphibole (10%) Biotite (10%)**
PCB 1	Dacite	Fine grained glassy matrix. Euhedral phenocrysts of amphibole contain numerous inclusions, and show resorption textures. Biotite phenocrysts are <1mm in size. Alkali feldspars contain inclusions of plagioclase and exhibit dissolution textures and intergrowth with plagioclase and quartz. **Alkali Feldspar (40%) Plagioclase Feldspar (15%) Quartz (20%) Amphibole (20%) Biotite (<5%)**

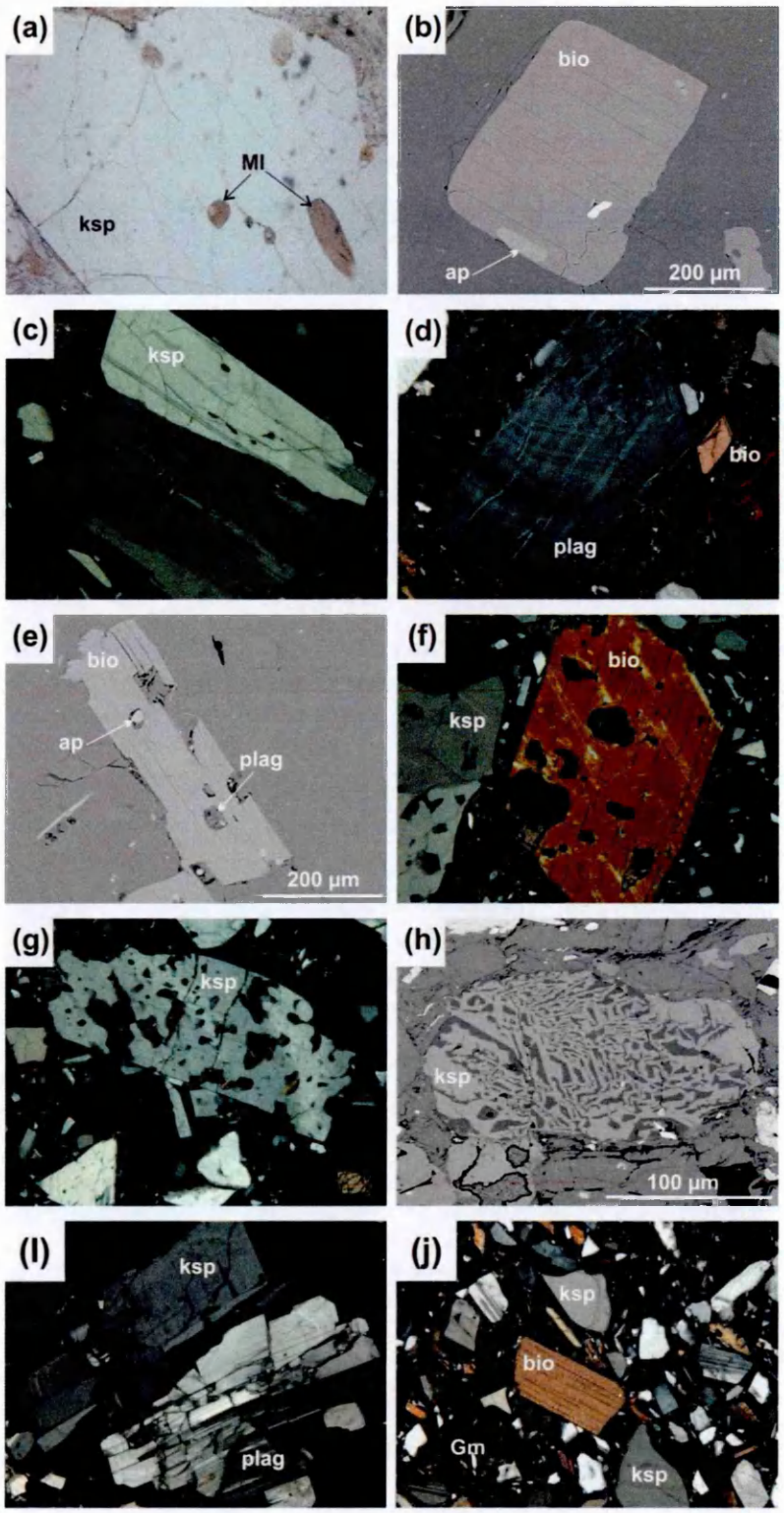

Panel (a) Sample PCB 1 showing a large sanidine containing glassy brown melt inclusions.

Panel (b) Sample BFC129 showing biotite containing apatite inclusion.

Panel (c) Sample BFC196 showing sanidine exhibiting simple twin.

Panel (d) Sample BFC191 showing plagioclase with fine oscillatory zonation pattern. Spherulite growth in groundmass is noticeable.

Panel (e) Sample BFC83 showing biotite containing both apatite and feldspar inclusions.

Panel (f) Sample BFC115 showing a biotite and sanidine, both which have undergone some resorption.

Panel (g) Sample BFC83 showing a resorbed sanidine exhibiting a sieve texture and containing numerous inclusions (e.g., biotite).

Panel (h) Sample BFC83 showing un-mixing of feldspar end members. Light grey represent high K_2O and dark grey represents high CaO.

Panel (I) Sample BFC115 showing sanidine and plagioclase intergrown.

Panel (j) Sample BFC129 showing small (<1mm), angular fragments of crystals set in a very fine glassy groundmass.

Figure A2.8. Selected thin section images and selected EMP images for Fish Canyon samples (PCB 1, BFC83, BFC196 = Pagosa Peak Dacite; BFC129, BFC191 = Fish Canyon Tuff; BFC115 = Nutras Creek Dacite). Ksp = sanidine, plag = plagioclase, ap = apatite, bio = biotite, MI = melt inclusions, Gm = groundmass. Image scale is 2.5 mm (picture width) unless otherwise indicated by a scale bar.

A2.2.2 Yellowstone Plateau Volcanic Field

Table A2.2 summarises the petrographic analysis of samples representing the first and second caldera forming eruptions and a number of post-caldera (rhyolite) dome eruptions of the Yellowstone Plateau Volcanic Field. Huckleberry Ridge Tuff (HRT) members A, B and C (YP127; CMW03 and CMW08 respectively); Mesa Falls Tuff (MFT; CMW01); Sheridan Reservoir dome (SRD; CMW11); Snake River Butte dome (SRB; CMW02) and Green Canyon Flow (GCF; YR242).

Table A2.2. Thin section descriptions for Yellowstone ignimbrite and rhyolite dome samples used for Ar-Ar age study (YP127, CMW01, YR242), and additional samples representative of the units dated, including estimated proportions of main phenocryst phases and groundmass (**% in bold**).

Sample number	Rock type	Thin section description
YP127 – HRT A	Tuff – basal vitrophyre	Hypocrystalline texture. Mixture of glassy groundmass and phenocrysts. Alkali feldspar and plagioclase exhibit zoning, twinning and inlusions (microphenocrysts, melt). Feldspars exist as both euhedral phenocrysts as well as fragmented and shattered crystals. **Alkali Feldspar (20%) Plagioclase Feldspar (20%) Quartz (20%) Vitrophyre groundmass (40%)**
CMW06 – HRT B	Pumice	Hypocrystalline texture. Mixture of glassy groundmass and phenocrysts. Alkali feldspar, plagioclase and quartz all contain inclusions (microphenocrysts of and melt inclusions). Sample also contains minor clinopyroxene. **Alkali Feldspar (10%) Plagioclase Feldspar (30%) Quartz (20%) Vitrophyre groundmass (40%) Clinopyroxene (<1%)**
CMW08 – HRT C	Pumice	Fine pumiceous groundmass showing moderate to high vesicularity. Phenocrysts of Alkali feldspar, plagioclase and quartz contain minor inclusions (microphenocrysts of and melt inclusions). **Alkali Feldspar (20%) Plagioclase Feldspar (20%) Quartz (20%) Groundmass (40%)**
CMW01 - MFT	Pumice	Fine pumiceous groundmass showing high vesicularity. Phenocrysts of Alkali feldspar, plagioclase (zoned) and quartz (rounded and fractured) contain minor inclusions (microphenocrysts of and melt inclusions). **Alkali Feldspar (20%) Plagioclase Feldspar (30%) Quartz (20%) Groundmass (30%)**
CMW11 - SRD	Rhyolite	Dense devitrified groundmass. 60% groundmass spherulite growth, fine needles of glass intergrown with quartz and feldspar. Groundmass contains microphenocrysts of plagioclase feldspar. Sample also contains ovoid patches of dark black glassy vitrophyric groundmass. Alkali feldspar and plagioclase contain numerous melt inclusions some containing magnetite+ilmenite. Intergrowth of alkali feldspar and plagioclase, some feldspars show resorption textures. Minor clinopyroxene also present. **Alkali Feldspar (30%) Plagioclase Feldspar (20%) Quartz (10%) De-vitrophyred groundmass (30%) Vitrophyre groundmass (10%) Clinopyroxene (< 1%)**

Table A2.2. *(continued)*

Sample number	Rock type	Thin section description
CMW02 - SRB	Pumiceous obsidian	Vitrophyric groundmass showing flow structures. Sample is crystal rich - plagioclase (zoned, some with inclusion rich cores), alkali feldspar (large phenocrysts (>1 mm), some highly fractured with numerous melt inclusions). Minor clinopyroxene showing resorption textures and opaques. **Alkali Feldspar (30%) Plagioclase Feldspar (20%) Quartz (20%) Vitrophyre groundmass (30%) Clinopyroxene (< 1%) Opaques (< 1%)**
YR242 - GCF	Rhyolite	De-vitrophyred groundmass of spherulites intergrown with feldspar and quartz contains microphenocrysts and fragmented feldspar laths. Some plagioclase and alkali feldspar are fragmented and contain inclusions (melt). Plagioclase feldspars exhibit exsolution textures, cross-hatch twinning, resorption and cleavage highlighted by minor alteration. Micro-laths of biotite present - appears to be accessory mineral only. **Alkali Feldspar (20%) Plagioclase Feldspar (20%) Quartz (20%) De-vitrophyred groundmass (40%) Biotite (< 1%)**

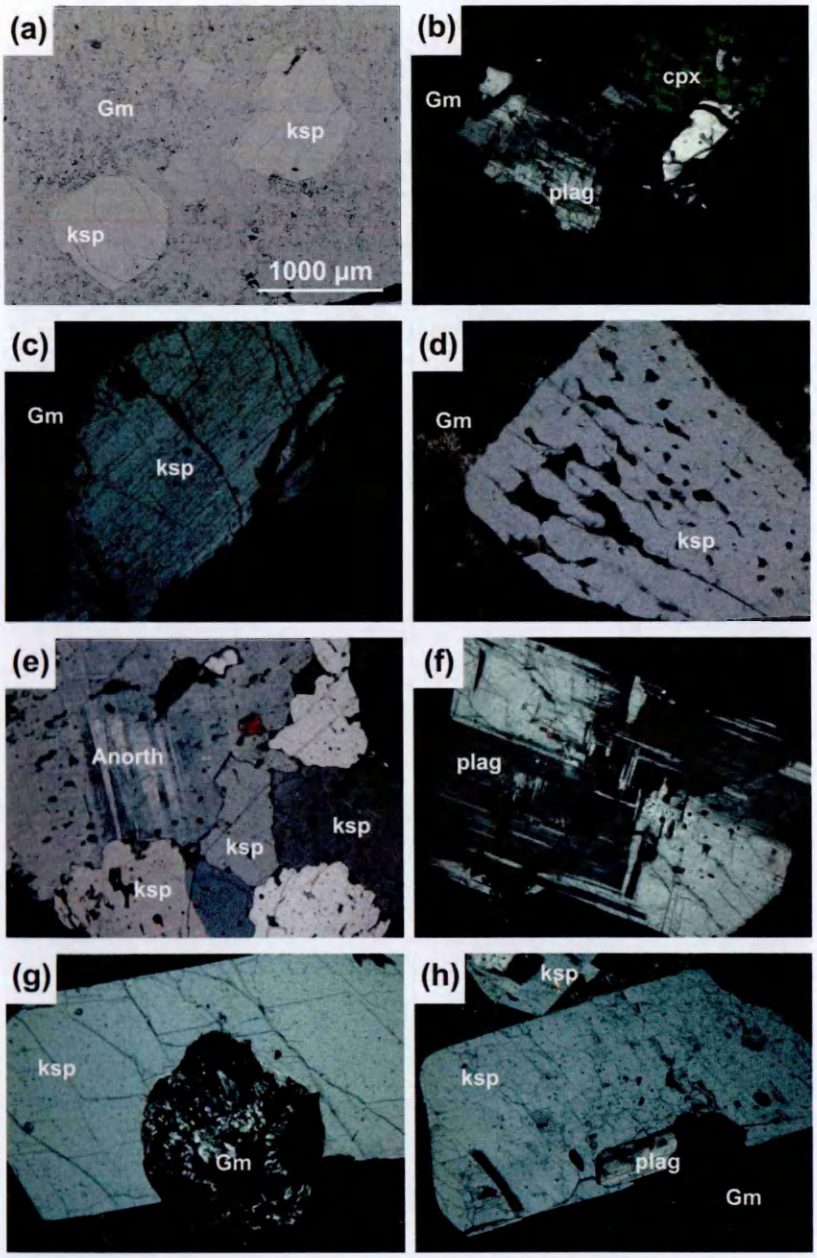

Panel (a) Sample CMW08 showing sanidine phenocrysts set in a glassy homogenous groundmass.

Panel (b) Sample CMW01 showing plagioclase and rare clinopyroxene set in a glassy pumiceous matrix.

Panel (c) Sample CMW01 showing large sanidine phenocryst set in a glassy pumiceous matrix.

Panel (d) Sample CMW11 showing large sanidine containing numerous melt inclusions.

Panel (e) Sample CMW11 showing evidence of resorption of anorthoclase and sanidine at grain edges.

Panel (f) Sample CMW02 showing sector zoned plagioclase and micro inclusions.

Panel (g) Sample YR242 showing sanidine phenocryst and devitrified groundmass of spherulites.

Panel (h) Sample YR242 showing sanidine contaning plagioclase inclusion.

Figure A2.9. Selected thin section images and selected EMP images for Yellowstone samples (CMW08 = HRT member C; CMW01 = MFT; CMW11 = Sheridan Reservoir dome; CMW02 = Snake River Butte dome; YR242 = Green Canyon Flow dome). Ksp = sanidine, plag = plagioclase, Anorth = anorthoclase, cpx = clinopyroxene, Gm = groundmass. Image scale is 2.5 mm (picture width) unless otherwise indicated by a scale bar.

A2.2.3 The Bishop Tuff

Table A2.3 summarises the petrographic analysis of samples representing both Bishop Tuff ash fall and ignimbrite flow deposits. Fall units F5 (BP029), F7 (CMW12) and ignimbrite packages Ig1Eb (BP097), Ig2NWa (BP113) and Ig2Nb (BP168).

Table A2.3. Thin section descriptions for samples representing both Bishop Tuff fall (BP029 and CMW12), and flow (Ignimbrite) deposits (BP097; BP113 and BP168), used for Ar-Ar age study, including estimated proportions of main phenocryst phases and groundmass (**% in bold**).

Sample number	Rock type	Thin section description
BP029 – F5	Pumice	Pumiceous glassy groundmass (high vesicularity) containing phenocrysts of feldspar and quartz. No biotite present. Alkali feldspar and plagioclase feldspar crystals are inclusion rich (melt, magnetite+ilmenite). Pumice clasts are crystal-poor, and crystal sizes vary substantially (<500 μm to >1mm). **Alkali Feldspar (30%) Plagioclase Feldspar (20%) Quartz (10%) Groundmass (40%)**
CMW12 – F7	Pumice	Pumiceous glassy groundmass (moderate to high vesicularity) containing phenocrysts of Alkali feldspar and plagioclase (often patchy zoning within crystals). Feldspars contain inclusions (melt) and show possible minor alteration. Minor biotite present, appears to be altered. crystal poor Pumice clasts are crystal poor compared with sample BP029 **Alkali Feldspar (20%) Plagioclase Feldspar (25%) Quartz (20%) Groundmass (30%) Biotite (< 5%)**
BP097 – Ig1Eb	Pumice	Pumiceous glassy groundmass (moderate to high vesicularity) containing phenocrysts of feldspar and minor biotite and melt-inclusion bearing quartz.. Euhedral plagioclase feldspar crystals are often fragmented. Pumice clasts are crystal poor compared with Ig2 samples BP113 and BP168. Minor alkali feldspar contains inclusions (melt, magnetite+ilmenite). **Alkali Feldspar (10 %) Plagioclase Feldspar (35 %) Quartz (10 %) Groundmass (40%) Biotite (< 5 %)**
BP113 – Ig2NWa	Pumice	Pumiceous glassy groundmass (moderate vesicularity) and crystal-rich, containing phenocrysts of plagioclase and alkali feldspar. Minor fragmentation of feldspars and moderate to low inclusion (melt, magnetite+ilmenite) content. Well rounded melt inclusion bearing quartz crystals common. **Alkali Feldspar (35 %) Plagioclase Feldspar (20 %) Quartz (20 %) Groundmass (25 %)**
BP168 – Ig2Nb	Pumice	Pumiceous glassy groundmass (moderate) and crystal-rich, containing phenocrysts of feldspar, quartz and minor biotite and pyroxene. Alkali feldspar fragmented, exhibits simple twinning and contains inclusions (melt, opaque minerals magnetite+ilmenite). Minor plagioclase feldspar (zoned) some showing microperthite textures. **Alkali Feldspar (30 %) Plagioclase Feldspar (10 %) Quartz (20 %) Groundmass (25 %) Biotite and Pyroxene (15 %)**

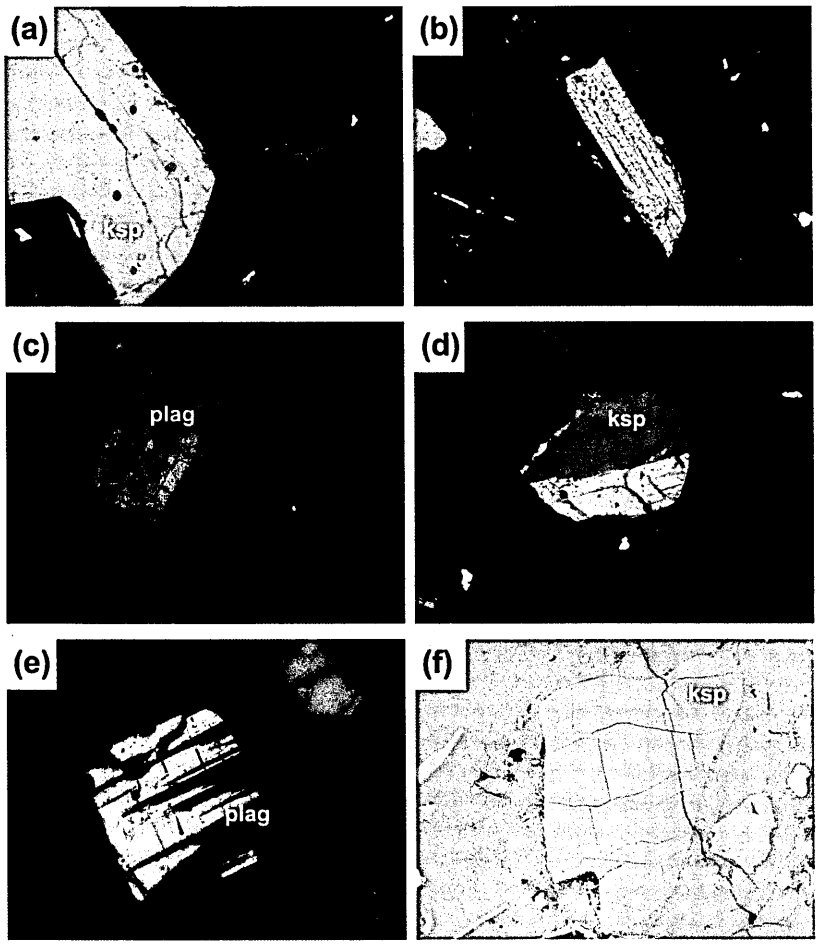

Panel (a) Sample BP029 showing a sanidine phenocryst set in a glassy pumiceous matrix.

Panel (b) Sample BP168 showing rare biotite.

Panel (c) Sample BP097 showing plagioclase, which was a common phase in this sample.

Panel (d) Sample BP113 showing sanidine phenocryst set in a glassy pumiceous matrix.

Panel (e) Sample CMW12 showing showing plagioclase set in a glassy homogenous groundmass.

Panel (f) Sample BP168 showing sanidine, which was a common phase in this sample.

Figure A2.10. Selected thin section images and selected EMP images for Bishop Tuff samples (BP029 = F5, BP168 = Ig2Nb, BP097 = Ig2Eb, BP113 = Ig2NWa, CMW12 = F7). Ksp = sanidine, plag = plagioclase, bio = biotite. Image scale is 2.5 mm (picture width) unless otherwise indicated by a scale bar.

A3. Ar-Ar Data

A3.1 Introduction

Data tables are divided into two parts, the first presents all *in situ* data collected using the Nu Instruments Noblesse (September 2010 to December 2010) and MAP-215-50 (December 2010), and the second presents all IR single-grain fusion data collected using the MAP-215-50 (January 2011 to February 2012).

Section A3.1.1: UV and IR *in situ* Ar-Ar data sets

Ar-data isotope values and ratios represent UV and IR *in-situ* experiments on all samples presented in Chapter 2. Data are presented in Ar isotope form (^{40}Ar, ^{39}Ar, ^{38}Ar, ^{37}Ar and ^{36}Ar), ratio form ($^{40}Ar^*/^{39}Ar$) and % radiogenic ^{40}Ar ($^{40}Ar^*$), along with average background blank measurements used to correct data. Ar-Ar apparent ages are presented in (Ma) and the *J*-value (± error) is presented for each sample. The irradiation identifier (e.g., McM#60) is also listed. The sample identification number (e.g., BFC115) and the geological name (e.g., Nutras Creek Dacite) are also given.

Section A3.1.2: IR single-grain fusion Ar-Ar data sets

Ar-data isotope values and ratios represent single-grain fusion experiments on all samples presented in Chapter 3 (section A3.1.2.1) and Chapter 4 (section A3.1.2.2). Data are presented in Ar isotope form (^{40}Ar, ^{39}Ar, ^{38}Ar, ^{37}Ar and ^{36}Ar), ratio form ($^{40}Ar^*/^{39}Ar$) and % radiogenic ^{40}Ar ($^{40}Ar^*$), along with average background blank measurements used to correct data. Ar-Ar apparent ages are presented in (Ma) and the *J*-value (± error) is presented for each sample. The irradiation identifier (e.g., McM#65), the sample identification number (e.g., YR215) and the geological name (e.g., Sheridan Reservoir) are given. 'HF' refers to a specific cleaning regime applied to some feldspar separates (cold 10 % hydrofluoric acid solution), all other mineral separates were cleaned in acetone.

A3.1.1 UV and IR *in situ* Ar-Ar data sets

Phase	Analysis #	^{40}Ar	± 1σ	^{39}Ar	± 1σ	^{38}Ar	± 1σ	^{37}Ar	± 1σ	^{36}Ar	± 1σ	$^{40}Ar^*/^{39}ArK$	± 1σ	Age (Ma)	± 1σ	% $^{40}Ar^*$	
McM#60	Pagosa Peak Dacite																
J-value = 0.00600480236244169 ± 0.000029658																	
						BFC83 - 1											
Plag #1	R #1	4220.31	105.48	1579.92	8.34	17.11	1.73	4909.01	17.20	-0.40	0.71	2.75	0.15	28.648	1.479	100	#
Plag #1	R #2	8658.18	71.29	2117.58	10.15	27.21	1.36	8589.71	16.97	11.51	0.53	2.20	0.08	44.537	0.947	60	#
Plag #2	R #1	3886.13	105.16	1382.74	7.94	19.79	1.54	4192.54	17.22	0.65	0.64	2.67	0.16	28.650	1.676	95	
Plag #2	R #2	3508.86	105.16	1223.58	7.94	14.39	0.85	3190.31	17.24	1.62	0.70	2.48	0.19	26.566	2.026	86	
	Background:	*2671.16*	*15.33*	*52.23*	*0.77*	*3.31*	*0.54*	*228.17*	*2.80*	*11.70*	*0.65*						
Plag #2	R #3	1122.58	70.67	451.95	4.82	5.47	0.96	1338.03	4.52	-0.38	0.75	2.73	0.52	29.297	5.481	100	*
Plag #3		4158.12	71.58	1576.74	9.32	19.27	1.09	4450.81	4.52	-0.42	0.79	2.71	0.16	28.286	1.059	100	#
Plag #4	R #1	7527.69	72.39	2895.10	11.03	41.60	3.21	7376.49	4.53	-0.46	0.82	2.65	0.09	27.892	0.636	100	#
	Background:	*3001.44*	*13.00*	*52.12*	*0.72*	*3.58*	*0.49*	*224.61*	*1.95*	*12.93*	*0.66*						
Plag #4	R #2	13550.85	92.81	5385.83	15.06	76.12	1.61	5541.09	6.50	0.04	1.02	2.51	0.06	26.972	0.643	100	
Bio #1	R #1	46898.71	110.44	17477.07	52.10	278.85	12.04	453.84	6.50	4.67	1.00	2.60	0.02	27.938	0.259	97	
Bio #1	R #2	38136.63	96.31	14288.58	22.06	209.11	2.43	1397.78	6.51	2.44	1.01	2.62	0.02	28.087	0.282	98	
Bio #2		97737.55	100.51	36871.40	40.11	562.39	7.43	461.19	16.96	5.41	0.84	2.61	0.01	28.818	0.179	98	
	Background:	*2858.94*	*12.71*	*51.22*	*0.81*	*2.68*	*0.65*	*227.43*	*1.89*	*12.33*	*0.64*						
J-value = 0.00603412481694059 ± 0.000029803																	
						BFC83 - 2											
Plag #5		3083.52	33.39	983.58	7.28	16.30	1.41	3588.35	6.55	0.45	1.07	3.00	0.32	32.300	3.471	96	*
Plag #5		5522.54	36.20	1583.58	9.72	22.61	1.11	5634.64	6.55	4.31	1.21	2.68	0.23	28.921	2.446	77	
	Background:	*4273.33*	*16.00*	*26.27*	*0.54*	*3.01*	*0.88*	*182.67*	*1.87*	*18.30*	*0.75*						
Plag #6		6101.15	37.27	2255.82	9.94	28.87	1.43	5922.63	9.85	0.28	0.96	2.67	0.13	28.752	1.373	99	
Plag #7		5602.35	36.12	2016.22	10.04	26.77	1.43	4493.11	9.87	1.86	1.00	2.51	0.15	27.022	1.595	90	
	Background:	*4390.00*	*16.00*	*25.33*	*0.54*	*3.55*	*0.71*	*184.00*	*1.78*	*18.15*	*0.77*						
Plag #3		3401.42	118.46	1099.44	9.03	16.75	1.96	334.36	112.14	4.02	3.92	2.01	1.06	21.736	11.360	65	*
San #1		23839.59	122.96	8927.01	20.39	111.33	4.81	228.99	112.05	3.05	3.89	2.57	0.13	27.700	1.395	96	
	Background:	*3925.00*	*16.00*	*22.80*	*2.90*	*1.66*	*2.87*	*177.75*	*3.88*	*14.19*	*3.02*						
J-value = 0.00601457651394132 ± 0.000029706																	
						BFC83 - 3											
Plag #9		8118.53	45.96	2023.71	10.10	29.62	1.83	5547.87	11.26	8.15	1.10	2.82	0.16	30.298	1.740	70	
Plag #10		4355.82	44.53	1593.78	8.11	19.91	1.33	3962.48	11.28	1.77	0.99	2.40	0.19	25.854	1.989	88	*
San #2	R #1	83898.00	72.03	31342.64	39.11	382.91	7.06	358.31	11.27	2.73	1.09	2.65	0.01	28.481	0.195	99	
San #2	R #2	90183.97	79.75	34249.24	34.10	428.95	7.86	222.99	11.27	1.56	1.02	2.62	0.01	28.146	0.183	99	
San #2	R #3	99670.25	87.68	37756.73	36.10	474.99	8.55	811.81	11.29	2.70	1.10	2.62	0.01	28.134	0.182	99	
	Background:	*4178.00*	*16.40*	*27.22*	*0.54*	*3.41*	*0.53*	*183.20*	*1.64*	*17.83*	*0.76*						
Plag #11		4301.48	31.68	1622.73	14.06	18.70	1.22	5523.18	26.02	0.46	0.92	2.57	0.17	27.591	1.813	97	*
San #2	R #4	57652.93	83.45	21520.64	54.13	265.00	6.05	305.04	25.98	4.24	0.98	2.62	0.02	28.157	0.225	98	
San #2	R #5	60844.73	53.18	23124.33	34.09	270.01	5.65	154.15	26.00	0.58	0.97	2.62	0.01	28.189	0.208	100	
	Background:	*4162.00*	*15.40*	*27.32*	*0.58*	*4.22*	*0.53*	*182.80*	*1.62*	*17.78*	*0.74*						
J-value = 0.00603412481694059 ± 0.000029803																	
						BFC83 - 2											
Plag #5		3083.52	33.39	983.58	7.28	16.30	1.41	3588.35	6.55	0.45	1.07	3.00	0.32	32.300	3.471	96	*
Plag #5		5522.54	36.20	1583.58	9.72	22.61	1.11	5634.64	6.55	4.31	1.21	2.68	0.23	28.921	2.446	77	
	Background:	*4273.33*	*16.00*	*26.27*	*0.54*	*3.01*	*0.88*	*182.67*	*1.87*	*18.30*	*0.75*						
Plag #6		6101.15	37.27	2255.82	9.94	28.87	1.43	5922.63	9.85	0.28	0.96	2.67	0.13	28.752	1.373	99	
Plag #7		5602.35	36.12	2016.22	10.04	26.77	1.43	4493.11	9.87	1.86	1.00	2.51	0.15	27.022	1.595	90	
	Background:	*4390.00*	*16.00*	*25.33*	*0.54*	*3.55*	*0.71*	*184.00*	*1.78*	*18.15*	*0.77*						

Phase	Analysis #	^{40}Ar	±1σ	^{39}Ar	±1σ	^{38}Ar	±1σ	^{37}Ar	±1σ	^{36}Ar	±1σ	$^{40}Ar^*/^{39}ArK$	±1σ	Age (Ma)	±1σ	% $^{40}Ar^*$	
McM#60	Pagosa Peak Dacite																
J-value = 0.00603412481694059 ± 0.000029803																	
					BFC83 - 2												
Plag #8		3401.42	118.45	1099.44	9.03	16.75	1.96	334.36	112.14	4.02	3.92	2.01	1.06	21.736	11.360	65	*
San #1		23839.59	122.96	8927.01	20.39	111.33	4.81	228.99	112.05	3.05	3.89	2.57	0.13	27.700	1.395	96	
	Background:	*3925.00*	*16.00*	*22.80*	*2.90*	*1.66*	*2.87*	*177.75*	*3.88*	*14.19*	*3.02*						
J-value = 0.00595593160494353 ± 0.000029417																	
					BFC196 - 1												
Plag #1	R #1	15264.17	40.30	5296.47	14.04	61.95	2.12	12454.32	26.20	1.93	0.97	2.77	0.06	29.506	0.605	96	
Plag #1	R #2	7964.97	87.66	2603.51	10.03	38.45	2.35	7944.72	8.35	3.91	1.02	2.62	0.12	27.832	1.289	85	
Plag #2	R #1	5442.39	27.34	1743.51	9.16	19.70	1.11	4740.32	26.04	2.66	1.05	2.67	0.18	28.590	1.913	85	
Plag #2	R #2	9775.80	38.51	2694.62	12.04	35.45	1.53	5306.33	26.25	9.20	0.92	2.62	0.10	27.862	1.099	72	
Plag #3		10229.09	30.79	3086.53	12.06	47.22	3.09	4713.54	26.06	7.27	1.09	2.62	0.10	28.037	1.125	79	
	Background:	*3903.04*	*14.80*	*45.10*	*0.67*	*3.49*	*0.58*	*225.61*	*2.32*	*15.97*	*0.70*						
J-value = 0.00604389896844022 ± 0.000029851																	
					BFC171 - 1												
Bio #1	R #1	106984.11	228.91	36480.76	41.08	579.90	8.44	4076.41	7.88	38.86	1.62	2.62	0.01	28.262	0.221	89	
	Background:	*3574.32*	*13.80*	*45.72*	*0.74*	*3.66*	*0.45*	*227.26*	*2.00*	*14.69*	*0.70*						
Bio #1	R #2	80900.01	83.25	28113.73	34.13	470.57	6.90	3326.17	6.87	29.65	1.14	2.57	0.01	27.706	0.203	89	
Bio #1	R #3	68006.29	90.67	24298.03	32.13	384.96	6.99	790.45	6.88	16.08	1.40	2.60	0.02	28.106	0.244	93	
Bio #2		71524.42	84.54	24996.07	39.13	390.81	7.98	537.32	6.89	20.00	1.57	2.62	0.02	28.338	0.258	92	
Bio #3		75413.61	84.54	26892.44	39.13	418.68	7.19	525.58	6.89	18.27	1.42	2.60	0.02	28.108	0.233	93	
Plag #1		2678.20	66.09	951.45	6.85	9.42	1.87	2947.63	6.90	0.15	1.24	2.77	0.39	29.878	4.191	98	*
	Background:	*4072.09*	*14.83*	*47.91*	*0.84*	*4.15*	*0.58*	*230.04*	*2.05*	*17.05*	*0.74*						
Plag #2	R #1	6374.15	98.28	2350.41	9.43	29.83	1.30	9812.21	12.40	1.18	0.93	2.56	0.12	27.681	1.345	94	
Plag #2	R #2	5393.29	98.05	2111.90	8.53	26.81	1.47	5834.57	12.41	0.57	0.87	2.47	0.13	26.727	1.403	97	
Plag #3		2434.24	96.72	744.03	6.43	11.00	1.10	2301.86	12.42	2.34	0.88	2.34	0.37	25.310	4.017	71	*
Plag #4		2884.97	97.42	931.53	6.33	8.31	1.90	2693.63	12.43	0.39	0.88	2.97	0.30	32.057	3.205	96	*
	Background:	*3510.92*	*13.83*	*44.39*	*0.69*	*2.70*	*0.75*	*226.15*	*1.93*	*14.73*	*0.68*						
J-value = 0.00608951504990821 ± 0.000030076																	
					PCB1 - 1												
San #1	R #1	23004.91	76.13	8286.54	18.12	109.57	4.23	10350.69	34.27	3.60	1.81	2.65	0.07	28.798	0.722	95	
San #1	R #2	131404.19	115.41	50121.92	51.13	614.43	7.92	509.58	34.30	0.77	1.81	2.62	0.01	28.466	0.197	100	
	Background:	*5692.84*	*17.75*	*39.27*	*0.68*	*4.68*	*0.68*	*221.90*	*2.55*	*23.24*	*0.70*						
	Fish Canyon Tuff																
J-value = 0.00613337269521309 ± 0.000030293																	
					BFC129 - 1												
Bio #1	Line	94363.32	73.91	28735.10	35.09	452.36	8.76	2673.83	8.75	61.59	0.74	2.65	0.01	29.032	0.184	81	
Bio #1	R #1	107959.33	86.06	30738.03	33.09	508.41	8.36	4868.55	8.76	86.81	0.80	2.68	0.01	29.331	0.186	76	
	Background:	*4952.50*	*15.00*	*25.43*	*0.54*	*3.02*	*0.75*	*187.00*	*1.78*	*19.90*	*0.72*						
Bio#2	Line	50252.54	224.22	14905.95	26.13	229.26	4.37	417.47	30.18	38.33	1.27	2.61	0.03	28.608	0.359	77	
Bio#2	R #1	51455.43	222.53	14805.59	24.13	230.26	5.96	644.30	30.20	43.17	1.38	2.61	0.03	28.633	0.377	75	
Bio #3	Line	80970.50	227.83	18912.48	28.12	324.34	6.25	3780.74	30.23	100.84	1.43	2.71	0.03	29.632	0.323	63	
Bio #3	R #1	104485.63	229.00	21820.45	33.13	362.37	8.94	1237.94	30.26	153.51	1.51	2.71	0.02	29.673	0.301	56	
	Background:	*4506.00*	*16.00*	*26.16*	*0.62*	*3.94*	*0.50*	*183.80*	*1.74*	*18.16*	*0.74*						
Plag #1	R #1	42838.19	85.20	1087.16	7.03	41.92	1.41	13035.21	17.85	128.90	1.00	4.37	0.28	47.605	3.059	10	
Plag #1	R #2	9485.38	75.63	664.80	6.13	11.60	0.96	5998.70	17.86	19.36	1.03	5.66	0.47	61.464	5.057	39	
Plag #2		6075.56	73.78	1143.72	6.53	14.10	1.08	3112.15	17.89	11.23	0.91	2.41	0.24	26.437	2.659	45	
	Background:	*4725.00*	*16.25*	*26.75*	*0.53*	*4.41*	*0.54*	*187.00*	*1.85*	*18.65*	*0.73*						
Plag #3		8316.22	182.44	1415.20	8.80	19.70	0.98	3579.54	22.66	16.35	1.30	2.82	0.30	30.823	3.267	45	
	Background:	*3986.67*	*15.00*	*25.60*	*0.57*	*4.02*	*0.54*	*181.00*	*1.80*	*16.70*	*0.69*						

Phase	Analysis #	^{40}Ar	±1σ	^{39}Ar	±1σ	^{38}Ar	±1σ	^{37}Ar	±1σ	^{36}Ar	±1σ	$^{40}Ar^*/^{39}ArK$	±1σ	Age (Ma)	±1σ	% $^{40}Ar^*$	
McM#60	Fish Canyon Tuff																
J-value = 0.00612008977011452 ± 0.000030227																	
					BFC129 - 2												
Plag #4	R #1	24942.48	103.60	5174.28	16.05	72.65	4.00	15121.48	8.59	40.11	1.21	2.53	0.07	27.663	0.801	52	
Plag #4	R #2	11195.97	104.78	3968.33	13.04	52.22	2.56	11936.73	8.59	2.23	1.35	2.66	0.10	29.022	1.143	94	
Plag #5	R #1	10292.80	115.66	2330.47	9.43	32.56	2.76	5712.22	5.38	12.04	1.27	2.89	0.17	31.564	1.832	65	
Plag #5	R #2	8593.87	104.53	2662.80	11.04	35.09	2.19	8111.86	8.61	4.49	1.33	2.73	0.15	29.817	1.662	84	
Plag #5	R #3	11235.87	104.53	3151.62	11.04	39.99	1.50	11891.92	8.60	10.89	1.38	2.54	0.13	27.810	1.458	71	
	Background:	*4725.00*	*16.25*	*26.75*	*0.53*	*4.41*	*0.54*	*187.00*	*1.85*	*18.65*	*0.73*						
Plag #6	R #1	8814.96	120.22	2850.94	14.04	35.01	1.24	10318.29	5.37	2.93	1.13	2.79	0.12	30.463	1.364	90	
Plag #6	R #2	12436.73	170.07	1618.48	8.10	23.81	1.40	4664.14	11.06	24.11	1.27	3.28	0.25	35.813	2.753	42	
Plag #6	R #3	23322.47	118.94	4302.92	14.04	63.74	3.65	13028.02	5.37	41.57	1.06	2.57	0.08	28.048	0.864	47	
	Background:	*4741.61*	*16.00*	*48.84*	*0.67*	*4.98*	*0.58*	*228.43*	*1.80*	*19.33*	*0.73*						
Plag #7		3540.38	84.77	560.33	5.06	7.28	1.34	1717.22	6.07	5.92	1.06	3.20	0.58	34.904	6.259	50	*
	Background:	*4187.79*	*16.43*	*46.84*	*0.72*	*3.50*	*0.66*	*227.74*	*1.87*	*17.32*	*0.76*						
J-value = 0.00615129416636773 ± 0.000030382																	
					BFC191 - 1												
Plag #1		11136.34	171.86	4015.67	13.12	50.89	1.46	9693.26	41.16	0.25	2.21	2.75	0.17	30.253	1.840	99	
Bio #1		168622.39	197.22	41794.47	41.11	672.87	11.03	444.92	41.21	191.28	2.91	2.68	0.02	29.461	0.282	66	
	Background:	*5706.28*	*17.33*	*37.01*	*0.64*	*4.54*	*0.59*	*221.26*	*2.87*	*23.16*	*0.65*						
	Nutras Creek Dacite																
J-value = 0.00601566781744382 ± 0.000029712																	
					BFC115 - 1												
Plag #1	R #1	11558.68	80.34	3903.75	12.05	46.18	1.69	12779.13	8.02	4.51	1.10	2.62	0.09	28.150	0.933	88	
Plag #1	R #2	8766.90	78.73	3216.52	13.05	37.80	1.53	10131.13	8.03	0.05	1.03	2.72	0.10	29.230	1.060	100	
Plag #1	R #3	7230.16	79.66	2564.64	9.85	30.30	1.69	5869.57	8.04	2.11	0.99	2.58	0.12	27.680	1.268	91	
Plag #1	R #4	9970.87	344.10	3126.71	11.02	41.79	2.23	9570.73	12.33	5.15	1.05	2.70	0.15	29.030	1.590	85	
Bio #1		70522.58	97.60	26334.06	37.08	411.02	7.67	1571.67	8.05	5.37	0.96	2.62	0.01	28.130	0.199	98	
	Background:	*6042.58*	*17.50*	*36.38*	*0.62*	*4.95*	*0.55*	*219.59*	*1.84*	*23.12*	*0.81*						
J-value = 0.00600864824556412 ± 0.000029677																	
					BFC115 - 2												
Bio #2	R #1	8261.54	129.96	1848.53	8.79	74.21	3.74	15720.68	18.23	10.77	1.10	2.75	0.19	29.484	2.024	61	
Bio #2	R #2	5358.58	129.21	1620.16	9.09	59.10	3.07	12450.13	18.25	3.13	0.95	2.74	0.19	35.428	1.779	83	
Bio #2	R #3	5358.16	129.39	1671.05	8.69	54.89	1.64	11243.72	18.26	2.15	1.04	2.83	0.20	34.356	1.722	88	#
	Background:	*5536.67*	*17.00*	*25.27*	*0.61*	*4.45*	*0.63*	*186.50*	*1.78*	*21.57*	*0.78*						
Bio #2	R #4	4215.07	34.41	1122.08	7.19	40.81	1.61	7590.15	8.73	4.29	0.91	2.63	0.24	28.197	2.575	70	
Plag #6	R #1	2783.58	41.53	1014.71	12.07	11.79	1.10	3174.78	8.74	0.76	0.88	2.52	0.26	29.138	1.140	92	#
Plag #6	R #2	4532.03	34.41	1545.51	8.88	20.10	1.34	3722.91	8.75	0.81	0.83	2.78	0.16	31.130	0.664	95	#
	Background:	*4952.50*	*15.00*	*25.43*	*0.54*	*3.02*	*0.75*	*187.00*	*1.78*	*19.90*	*0.72*						

Phase	Analysis #	^{40}Ar	± 1σ	^{39}Ar	± 1σ	^{38}Ar	± 1σ	^{37}Ar	± 1σ	^{36}Ar	± 1σ	$^{40}Ar^*/^{39}ArK$	± 1σ	Age (Ma)	± 1σ	% $^{40}Ar^*$
McM#60	**Pagosa Peak Dacite**															
***J*-value = 0.00618836102883889 ± 0.000030565**																
					BFC83 - 4											
Bio # 3		0.234215	0.000445	0.085884	0.000127	0.001382	0.000013	0.008562	0.000794	0.000068	0.000015	2.494057	0.052006	**27.574**	**0.590**	91
Plag #12		0.237109	0.000535	0.086443	0.000243	0.001208	0.000023	0.113032	0.000752	0.000005	0.000019	2.725716	0.066932	**30.114**	**0.751**	99
Plag #13		0.204455	0.000523	0.076773	0.000069	0.000942	0.000016	0.129629	0.000502	0.000055	0.000015	2.451468	0.056095	**27.107**	**0.633**	92
San #3		1.016721	0.000415	0.394182	0.000459	0.004887	0.000024	0.107974	0.000502	0.000041	0.000015	2.548791	0.011284	**28.175**	**0.197**	99
San #4		0.503057	0.001034	0.195852	0.000418	0.002485	0.000033	0.022762	0.000503	0.000033	0.000015	2.518316	0.023073	**27.841**	**0.295**	98
San #5		0.277337	0.000474	0.101424	0.000316	0.001320	0.000033	0.127739	0.000503	0.000036	0.000015	2.631046	0.043158	**29.077**	**0.499**	96
San #6		0.969408	0.000890	0.380832	0.000266	0.004581	0.000016	0.047042	0.000503	0.000057	0.000015	2.501374	0.011588	**27.655**	**0.197**	98
***J*-value = 0.00608951504990821 ± 0.000030076**																
					PCB1 - 1											
San #1	S (1 - 6)	1.375416	0.000983	0.471485	0.000290	0.006083	0.000042	0.054591	0.000498	0.000429	0.000018	2.648264	0.011630	**28.802**	**0.201**	91
San #1	S (7 - 12)	0.288640	0.000434	0.034688	0.000216	0.000513	0.000015	0.002644	0.000498	0.000583	0.000018	3.355813	0.155842	**36.420**	**1.686**	40
San #1	S (13 - 18)	1.160113	0.000597	0.364003	0.000871	0.004417	0.000023	0.014563	0.000499	0.000600	0.000018	2.700263	0.016113	**29.363**	**0.236**	85
San #1	S (19 - 24)	0.196382	0.000315	0.064785	0.000177	0.000779	0.000015	0.004325	0.000499	0.000072	0.000018	2.701011	0.082839	**29.371**	**0.908**	89
San #1	S (25 - 28)	0.527392	0.000798	0.189051	0.000418	0.002189	0.000024	0.018274	0.000504	0.000134	0.000014	2.579457	0.023680	**28.059**	**0.298**	92
Plag #1		0.467258	0.000584	0.057604	0.000206	0.000840	0.000016	0.081524	0.000504	0.001028	0.000014	2.839444	0.075520	**30.863**	**0.831**	34
	Fish Canyon Tuff															
***J*-value = 0.00615129416636773 ± 0.000030382**																
					BFC191 - 1											
Bio #1	S (1 - 5)	0.536024	0.000416	0.182317	0.000332	0.002772	0.000022	0.014637	0.000903	0.000206	0.000016	2.605976	0.026989	**28.631**	**0.333**	89
Bio #1	S (6 - 10)	0.480893	0.000757	0.164897	0.000208	0.002455	0.000014	0.013005	0.000903	0.000187	0.000016	2.582022	0.029804	**28.370**	**0.360**	83
Bio #2	S (1 - 5)	0.371585	0.000306	0.124879	0.000137	0.001903	0.000022	0.003345	0.000904	0.000139	0.000016	2.646377	0.038832	**29.071**	**0.452**	89
Bio #2	S (6 - 10)	0.421776	0.000591	0.154614	0.000476	0.002332	0.000042	0.004991	0.000905	0.000099	0.000016	2.539335	0.032405	**27.904**	**0.385**	93
Bio #3	S (1 - 6)	0.760349	0.000877	0.230669	0.000487	0.003620	0.000032	0.007733	0.000905	0.000478	0.000016	2.683996	0.022006	**29.481**	**0.289**	81
Bio #3	S (7 - 12)	0.724090	0.000643	0.238558	0.000308	0.003732	0.000023	0.023834	0.000496	0.000387	0.000018	2.555611	0.022784	**28.082**	**0.292**	84
Plag #1	S (1 - 4)	0.149714	0.000389	0.055394	0.000167	0.000727	0.000015	0.087398	0.000497	0.000050	0.000018	2.433859	0.096924	**26.754**	**1.068**	90
Plag #1	S (5 - 11)	0.096691	0.000298	0.035764	0.000163	0.000441	0.000023	0.081021	0.000497	0.000012	0.000018	2.603731	0.149999	**28.606**	**1.642**	95
Plag #2		0.361632	0.000357	0.137201	0.000296	0.002046	0.000033	0.061077	0.000504	0.000073	0.000014	2.478231	0.031693	**27.238**	**0.376**	94
San #1		1.076747	0.000859	0.410599	0.000500	0.005429	0.000033	0.017300	0.000504	0.000025	0.000014	2.604570	0.011074	**28.616**	**0.197**	99
	Nutras Creek Dacite															
***J*-value = 0.00601566781744382 ± 0.000029712**																
					BFC115 - 1											
Plag #1	S (1 - 6)	0.231679	0.000319	0.058117	0.000256	0.000717	0.000023	0.082165	0.000499	0.000242	0.000018	2.757060	0.092834	**29.615**	**1.002**	69
Plag #1	S (7 - 12)	0.128085	0.000613	0.038902	0.000233	0.000482	0.000023	0.063940	0.000747	0.000028	0.000019	3.079368	0.149091	**33.045**	**1.595**	93
Plag #1	S (13 - 18)	0.098740	0.000921	0.022096	0.000099	0.000298	0.000023	0.070952	0.000747	0.000136	0.000019	2.647266	0.252592	**28.445**	**2.804**	59
Plag #2	S (1 - 6)	0.336248	0.000585	0.099275	0.000223	0.001382	0.000033	0.159705	0.000750	0.000163	0.000019	2.902826	0.058316	**31.167**	**0.644**	86
Plag #2	S (7 - 12)	0.338418	0.000665	0.109353	0.000195	0.001464	0.000033	0.226958	0.000750	0.000175	0.000019	2.622213	0.052897	**28.178**	**0.585**	85
Plag #3		0.828298	0.001083	0.231136	0.000800	0.003170	0.000023	0.164981	0.000499	0.000620	0.000018	2.791157	0.025476	**29.978**	**0.317**	78
Plag #4		0.281229	0.000994	0.057663	0.000159	0.000963	0.000023	0.102044	0.000750	0.000418	0.000019	2.331000	0.086019	**25.070**	**0.929**	56
Plag #5		0.522026	0.000875	0.177946	0.000142	0.002302	0.000033	0.211710	0.000751	0.000119	0.000019	2.736188	0.032610	**29.392**	**0.383**	93
San #1	S (1 - 6)	0.184743	0.000490	0.048649	0.000159	0.000626	0.000023	0.005206	0.000748	0.000174	0.000019	2.742850	0.118401	**29.463**	**1.272**	72
San #1	S (7 - 12)	0.361517	0.000535	0.104289	0.000272	0.001382	0.000023	0.017520	0.000749	0.000270	0.000019	2.700455	0.055561	**29.012**	**0.613**	78
	Background:	***0.001616***	***0.000040***	***0.000070***	***0.000010***	***0.000020***	***0.000010***	***0.000573***	***0.000020***	***0.000030***	***0.000010***					

Notes:

Plag = Plagioclase

San = Sanidine

Bio = Biotite

R = Raster

S = IR spots

*** = Data rejected - ^{40}Ar gas yield less than blank**

 # = Age not corrected for ^{36}Ar because ^{36}Ar measurement was either at or less than ^{36}Ar blank level

A3.1.2 IR single-grain fusion Ar-Ar data sets

A3.1.2.1 Yellowstone single-grain fusion Ar-Ar data

Sample #	^{40}Ar	±1σ	^{39}Ar	±1σ	^{38}Ar	±1σ	^{37}Ar	±1σ	^{36}Ar	±1σ	$^{40}Ar^*/^{39}ArK$	±1σ	Age (Ma)	±1σ	% $^{40}Ar^*$
McM#65	Huckleberry Ridge Tuff - A														
J-value = 0.000385567 ± 0.0000019															
				Feldspar											
YP127	0.260298	0.001355	0.081396	0.000818	0.000882	0.000063	0.007350	0.003377	0.000081	0.000022	2.902451	0.087077	2.014	0.061	91
YP127	0.183283	0.001155	0.057707	0.001035	0.000657	0.000073	0.000962	0.003388	0.000053	0.000014	2.904311	0.089940	2.015	0.063	91
YP127	0.329166	0.001547	0.106692	0.000601	0.001199	0.000113	-0.006703	0.003373	0.000065	0.000031	2.904851	0.089836	2.015	0.063	94
YP127	0.241666	0.001153	0.079954	0.000540	0.000965	0.000083	0.002157	0.000409	0.000024	0.000013	2.934911	0.055529	2.036	0.040	97
YP127	0.200916	0.001047	0.060593	0.000611	0.000790	0.000053	0.002244	0.003387	0.000073	0.000022	2.961105	0.113304	2.054	0.079	89
YP127	0.050796	0.000716	0.015102	0.000322	0.000166	0.000043	0.012453	0.003374	0.000020	0.000022	2.971439	0.440148	2.061	0.305	88
YP127	0.182395	0.002284	0.054639	0.000695	0.000873	0.000035	0.000932	0.000408	0.000064	0.000022	2.991841	0.131464	2.076	0.092	90
YP127	0.342647	0.002145	0.103916	0.000859	0.001465	0.000064	0.016475	0.002429	0.000101	0.000028	3.011182	0.084748	2.089	0.060	91
YP127	0.044038	0.000578	0.014152	0.000188	0.000330	0.000034	-0.005446	0.003385	0.000005	0.000022	3.012067	0.465597	2.090	0.323	97
YP127	0.493571	0.001668	0.159230	0.000994	0.002037	0.000104	0.010328	0.002428	0.000042	0.000028	3.021304	0.055492	2.096	0.040	97
YP127	0.228830	0.001865	0.072258	0.000456	0.000872	0.000084	-0.000835	0.002420	0.000035	0.000028	3.022827	0.117134	2.097	0.082	95
YP127	0.439294	0.001868	0.141657	0.001262	0.001599	0.000083	0.003385	0.000409	0.000033	0.000013	3.031469	0.041171	2.103	0.031	98
YP127	0.225438	0.001071	0.069080	0.000736	0.000914	0.000093	0.001799	0.000409	0.000054	0.000022	3.033275	0.100493	2.104	0.071	93
YP127	0.302931	0.001534	0.097263	0.000642	0.001087	0.000094	0.000278	0.002420	0.000025	0.000028	3.038816	0.087496	2.108	0.062	98
YP127	0.284230	0.000972	0.091084	0.000601	0.001179	0.000084	0.004177	0.002423	0.000024	0.000021	3.043007	0.073116	2.111	0.052	97
YP127	0.285191	0.002176	0.091026	0.000756	0.001209	0.000104	-0.001392	0.002422	0.000025	0.000021	3.050729	0.077771	2.116	0.055	97
YP127	0.296747	0.001817	0.095010	0.000755	0.001116	0.000164	0.002059	0.000153	0.000023	0.000020	3.052853	0.068686	2.118	0.049	98
YP127	0.529931	0.001761	0.164111	0.000456	0.001945	0.000103	0.001604	0.003390	0.000093	0.000022	3.061810	0.042146	2.124	0.031	95
YP127	0.281491	0.001517	0.088771	0.000652	0.000767	0.000072	0.012375	0.001577	0.000033	0.000024	3.062038	0.085277	2.124	0.060	97
YP127	0.300858	0.003023	0.092545	0.001128	0.001149	0.000054	0.002005	0.000409	0.000054	0.000022	3.079288	0.085952	2.136	0.061	95
YP127	0.143393	0.001625	0.043078	0.000714	0.000503	0.000054	0.000952	0.000153	0.000033	0.000020	3.102679	0.149560	2.152	0.104	93
YP127	0.149224	0.001585	0.043812	0.000486	0.000626	0.000054	0.001292	0.000154	0.000043	0.000026	3.116961	0.183981	2.162	0.128	91
YP127	0.124218	0.000855	0.039423	0.000117	0.000556	0.000044	0.000728	0.000408	0.000004	0.000013	3.120236	0.103746	2.165	0.073	99
YP127	0.187473	0.000873	0.058647	0.000580	0.000708	0.000113	0.002236	0.003376	0.000013	0.000014	3.132411	0.077448	2.173	0.055	98
YP127	0.210854	0.001848	0.065561	0.000724	0.000769	0.000044	0.000955	0.000154	0.000013	0.000020	3.157783	0.099564	2.191	0.070	98
YP127	0.294602	0.001308	0.090548	0.000838	0.000934	0.000064	0.008416	0.002427	0.000023	0.000028	3.173998	0.095573	2.202	0.067	98
YP127	0.035400	0.000663	0.010718	0.000332	0.000187	0.000053	0.009287	0.003384	0.000001	0.000022	3.278966	0.621619	2.275	0.431	99
YP127	0.168289	0.001401	0.047217	0.000407	0.000546	0.000054	0.000881	0.000408	0.000044	0.000013	3.288461	0.093802	2.281	0.066	92
Background:	*0.007500*	*0.000349*	*0.000040*	*0.000020*	*0.000020*	*0.000010*	*0.000488*	*0.000050*	*0.000060*	*0.000010*					
J-value = 0.00038668 ± 0.00000019															
				Feldspar											
YP127	0.373404	0.002461	0.119855	0.001748	0.001538	0.000144	0.003547	0.000410	0.000063	0.000022	2.959280	0.072207	2.059	0.051	95
YP127	0.121188	0.002076	0.038431	0.000509	0.000495	0.000063	0.000476	0.000410	0.000024	0.000022	2.967646	0.181503	2.065	0.127	94
YP127	0.287315	0.001236	0.093583	0.000673	0.001196	0.000052	0.001795	0.000155	0.000032	0.000012	2.967922	0.046017	2.065	0.034	97
YP127	0.082380	0.000575	0.025481	0.000179	0.000276	0.000032	0.000074	0.000154	0.000023	0.000012	2.968111	0.144853	2.065	0.101	92
YP127	0.370705	0.001889	0.121492	0.001303	0.001656	0.000103	0.003090	0.000154	0.000022	0.000021	2.997657	0.062719	2.086	0.045	98
YP127	0.203452	0.001092	0.065992	0.000312	0.000818	0.000072	0.001633	0.000154	0.000012	0.000021	3.027327	0.097383	2.106	0.069	98
YP127	0.329492	0.002065	0.104423	0.000984	0.001384	0.000083	0.002320	0.000411	0.000044	0.000013	3.031790	0.051610	2.109	0.038	96
YP127	0.525890	0.002014	0.171856	0.001065	0.002116	0.000072	0.002785	0.000155	0.000012	0.000021	3.039216	0.042685	2.115	0.032	99
YP127	0.354113	0.000928	0.111682	0.000724	0.001359	0.000082	0.003035	0.000154	0.000022	0.000012	3.112366	0.039014	2.165	0.030	98
YP127	0.243607	0.002284	0.069080	0.000664	0.000853	0.000073	0.001345	0.000410	0.000094	0.000022	3.124645	0.103972	2.174	0.073	88
YP127	0.227309	0.001940	0.071395	0.000592	0.000832	0.000063	0.002009	0.000410	0.000004	0.000013	3.168273	0.057399	2.204	0.048	100
Background:	*0.001325*	*0.000158*	*0.000030*	*0.000020*	*0.000010*	*0.000010*	*0.000468*	*0.000050*	*0.000020*	*0.000010*					

Sample #	^{40}Ar	± 1σ	^{39}Ar	± 1σ	^{38}Ar	± 1σ	^{37}Ar	± 1σ	^{36}Ar	± 1σ	$^{40}Ar^*/^{39}ArK$	± 1σ	Age (Ma)	± 1σ	% $^{40}Ar^*$	
McM#65	Huckleberry Ridge Tuff - B															
J-value = 0.00038779 ± 0.0000019																
				Feldspar												
YP079	0.044384	0.000366	0.006963	0.000220	0.000133	0.000032	0.007395	0.000155	0.000101	0.000021	2.092390	0.903253	1.460	0.630	32	
YP079	0.059059	0.000573	0.009910	0.000179	0.000137	0.000045	0.010123	0.000226	0.000115	0.000013	2.535955	0.394327	1.770	0.275	42	
YP079	0.065146	0.001013	0.014889	0.000250	0.000157	0.000045	0.014445	0.000225	0.000084	0.000022	2.714729	0.437433	1.894	0.305	62	
YP079	0.398700	0.001796	0.116541	0.001086	0.001380	0.000062	0.002996	0.000155	0.000172	0.000021	2.984826	0.062459	2.083	0.045	87	
YP079	0.288157	0.002118	0.086657	0.000724	0.001135	0.000082	0.001641	0.000155	0.000082	0.000021	3.044204	0.080433	2.124	0.057	91	
YP079	0.263000	0.000979	0.078408	0.000518	0.001053	0.000042	0.001798	0.000155	0.000072	0.000012	3.081481	0.051868	2.150	0.038	92	
YP079	0.052436	0.000533	0.012699	0.000291	0.000178	0.000027	0.012505	0.000226	0.000044	0.000013	3.100920	0.313361	2.164	0.219	75	
YP079	0.045894	0.000526	0.009815	0.000179	0.000143	0.000032	0.009117	0.000155	0.000050	0.000021	3.157454	0.642811	2.203	0.448	67	
YP079	0.036661	0.000675	0.006519	0.000230	0.000143	0.000042	0.006181	0.000155	0.000051	0.000012	3.302005	0.574822	2.304	0.401	58	
YP079	0.054844	0.000613	0.010745	0.000250	0.000065	0.000045	0.013550	0.000225	0.000064	0.000013	3.346634	0.370101	2.335	0.258	65	
YP079	0.067278	0.000553	0.010921	0.000271	0.000147	0.000035	0.012264	0.000226	0.000084	0.000022	3.880726	0.595815	2.707	0.416	63	
Background:	*0.001325*	*0.000158*	*0.000030*	*0.000020*	*0.000010*	*0.000010*	*0.000468*	*0.000050*	*0.000020*	*0.000010*						
YP079	0.068525	0.000776	0.011715	0.000229	0.000217	0.000034	0.004731	0.002116	0.000159	0.000027	1.845042	0.687344	1.288	0.480	31	
YP079	0.054522	0.000694	0.013044	0.000280	0.000125	0.000034	0.013566	0.002116	0.000096	0.000027	1.995809	0.617384	1.393	0.431	47	
YP079	0.035816	0.000786	0.008694	0.000126	0.000125	0.000025	0.004727	0.002114	0.000049	0.000027	2.462678	0.925711	1.719	0.646	59	
YP079	0.142168	0.000754	0.013349	0.000239	0.000264	0.000052	0.015407	0.002231	0.000361	0.000052	2.660666	1.143793	1.857	0.798	24	
YP079	0.049646	0.000923	0.013171	0.000259	0.000182	0.000065	0.014313	0.003237	0.000043	0.000033	2.796626	0.737212	1.951	0.514	74	
YP079	0.051464	0.000928	0.010372	0.000198	0.000217	0.000053	0.018598	0.002115	0.000075	0.000027	2.823114	0.778737	1.970	0.543	56	
YP079	0.048661	0.000535	0.009880	0.000228	0.000172	0.000041	0.020359	0.002222	0.000070	0.000024	2.843488	0.712070	1.984	0.497	57	
YP079	0.241159	0.001588	0.069452	0.000725	0.000795	0.000074	0.000702	0.003245	0.000137	0.000024	2.889582	0.107910	2.016	0.076	83	
YP079	0.064975	0.000584	0.015504	0.000373	0.000202	0.000037	0.022558	0.003248	0.000061	0.000024	3.025007	0.459998	2.111	0.321	72	
YP079	0.069886	0.000952	0.016389	0.000404	0.000213	0.000037	0.013765	0.003236	0.000063	0.000024	3.119248	0.438904	2.176	0.306	73	
YP079	0.112230	0.001323	0.009916	0.000259	0.000151	0.000055	0.008342	0.003245	0.000275	0.000033	3.124830	0.984536	2.180	0.687	27	
YP079	0.130779	0.001028	0.020398	0.000290	0.000356	0.000041	0.027320	0.002228	0.000218	0.000024	3.256802	0.349207	2.272	0.244	50	
YP079	0.049715	0.000903	0.011198	0.000187	0.000110	0.000029	0.009988	0.003247	0.000044	0.000033	3.265341	0.866255	2.278	0.604	73	
YP079	0.074846	0.000638	0.016316	0.000280	0.000264	0.000037	0.015956	0.003239	0.000073	0.000024	3.266797	0.435529	2.279	0.304	71	
YP079	0.075207	0.000792	0.013254	0.000228	0.000193	0.000052	0.017848	0.002221	0.000100	0.000024	3.438629	0.533649	2.399	0.372	60	
YP079	0.070467	0.001158	0.010689	0.000249	0.000203	0.000041	0.016660	0.002230	0.000111	0.000033	3.535265	0.909732	2.466	0.634	53	
YP079	0.061750	0.000647	0.012843	0.000270	0.000172	0.000046	0.011056	0.003240	0.000054	0.000024	3.560850	0.553843	2.484	0.386	74	
YP079	0.051447	0.000516	0.008876	0.000085	0.000110	0.000037	0.017060	0.003242	0.000063	0.000033	3.711299	1.088083	2.589	0.759	64	
YP079	0.035987	0.000596	0.007143	0.000218	0.000091	0.000031	0.012251	0.002229	0.000032	0.000024	3.724409	0.987919	2.598	0.689	74	
YP079	0.032545	0.000610	0.006883	0.000219	0.000113	0.000021	0.012786	0.004339	0.000023	0.000022	3.779391	0.943415	2.637	0.658	79	
YP079	0.071337	0.000787	0.013925	0.000456	0.000182	0.000046	0.017610	0.003243	0.000052	0.000042	4.009469	0.902683	2.797	0.629	78	
YP079	0.076480	0.001054	0.013164	0.000239	0.000217	0.000034	0.004096	0.002113	0.000069	0.000027	4.262681	0.618116	2.974	0.431	73	
Background:	*0.007500*	*0.000349*	*0.000040*	*0.000020*	*0.000020*	*0.000010*	*0.000488*	*0.000050*	*0.000060*	*0.000010*						
J-value = 0.000388906 ± 0.0000019																
				Feldspar												
YP079	0.061016	0.000685	0.010633	0.000230	0.000167	0.000045	0.010744	0.000226	0.000115	0.000022	2.552079	0.607647	1.786	0.425	44	
YP079	0.084715	0.001055	0.014673	0.000240	0.000239	0.000035	0.013854	0.000227	0.000154	0.000013	2.675643	0.274829	1.872	0.192	46	
YP079	0.216401	0.001078	0.051880	0.000652	0.000712	0.000073	0.001770	0.000268	0.000236	0.000022	2.825818	0.132504	1.977	0.093	67	
YP079	0.282861	0.001939	0.054434	0.000435	0.000835	0.000073	0.001393	0.000268	0.000396	0.000031	3.045075	0.176092	2.131	0.124	58	
YP079	0.289358	0.001189	0.083961	0.000683	0.001159	0.000074	0.002863	0.000226	0.000107	0.000031	3.070659	0.113267	2.149	0.080	89	
YP079	0.208830	0.001512	0.055571	0.000631	0.000763	0.000073	0.001826	0.000268	0.000116	0.000022	3.140112	0.125867	2.197	0.089	83	
YP079	0.192402	0.000848	0.046407	0.000580	0.000617	0.000064	0.001005	0.000227	0.000157	0.000013	3.144810	0.093412	2.201	0.066	76	
YP079	0.047123	0.000577	0.008551	0.000219	0.000109	0.000025	0.009490	0.000268	0.000064	0.000022	3.293870	0.771703	2.305	0.540	59	
YP079	0.072369	0.000553	0.012711	0.000332	0.000157	0.000045	0.010536	0.000227	0.000095	0.000022	3.491758	0.513403	2.443	0.359	61	
YP079	2.539288	0.005160	0.034177	0.000189	0.002048	0.000084	0.000898	0.000226	0.008097	0.000120	4.287825	1.051174	3.000	0.735	5	*
YP079	0.039678	0.000993	0.009427	0.000199	0.000147	0.000035	0.021579	0.000227	0.000072	0.000031	7.263095	0.993273	5.078	0.694	76	◊
Background:	*0.001325*	*0.000158*	*0.000030*	*0.000020*	*0.000010*	*0.000010*	*0.000468*	*0.000050*	*0.000020*	*0.000010*						

Sample #	^{40}Ar	±1σ	^{39}Ar	±1σ	^{38}Ar	±1σ	^{37}Ar	±1σ	^{36}Ar	±1σ	$^{40}Ar^*/^{39}ArK$	±1σ	Age (Ma)	±1σ	% $^{40}Ar^*$
McM#65	Huckleberry Ridge Tuff - C														
J-value = 0.000389481 ± 0.0000019															
				Feldspar											
YP081	0.259764	0.000954	0.083896	0.000755	0.000968	0.000083	0.001401	0.000270	0.000056	0.000014	2.897987	0.056199	**2.031**	**0.041**	94
YP081	0.225191	0.001233	0.066850	0.000735	0.000794	0.000073	0.001077	0.000270	0.000096	0.000022	2.942576	0.104611	**2.062**	**0.074**	87
YP081	0.368575	0.001492	0.112406	0.000931	0.001417	0.000103	0.001502	0.000268	0.000116	0.000022	2.973300	0.054548	**2.084**	**0.047**	91
YP081	0.205738	0.001378	0.065526	0.000559	0.000784	0.000083	0.000748	0.000269	0.000036	0.000022	2.975316	0.105043	**2.085**	**0.074**	95
YP081	0.205367	0.001233	0.066250	0.000735	0.000814	0.000063	0.001291	0.000269	0.000026	0.000014	2.982470	0.072132	**2.090**	**0.052**	96
YP081	0.212178	0.001533	0.068380	0.000683	0.000845	0.000043	0.000804	0.000270	0.000026	0.000022	2.988617	0.102612	**2.094**	**0.073**	96
YP081	0.154638	0.000749	0.047002	0.000631	0.000487	0.000053	0.000800	0.000269	0.000046	0.000022	2.997986	0.145619	**2.101**	**0.103**	91
YP081	0.232107	0.001585	0.073765	0.000652	0.000845	0.000073	0.001071	0.000269	0.000026	0.000014	3.040874	0.064969	**2.131**	**0.047**	97
YP081	0.350803	0.001274	0.107496	0.000858	0.001387	0.000053	0.002271	0.000270	0.000066	0.000022	3.081807	0.066682	**2.160**	**0.048**	94
YP081	0.363721	0.002428	0.092568	0.000714	0.001203	0.000083	0.001938	0.000269	0.000256	0.000022	3.111512	0.079067	**2.180**	**0.057**	79
YP081	0.269446	0.001160	0.055354	0.000590	0.000702	0.000043	0.000962	0.000268	0.000316	0.000031	3.178557	0.172553	**2.227**	**0.121**	65
YP081	0.139935	0.000831	0.042185	0.000384	0.000497	0.000043	0.000260	0.000270	0.000007	0.000022	3.270970	0.158960	**2.292**	**0.112**	99
YP081	0.148995	0.001533	0.036375	0.000538	0.000457	0.000073	0.000962	0.000269	0.000096	0.000022	3.312909	0.190925	**2.322**	**0.134**	81
Background:	***0.001325***	***0.000158***	***0.000030***	***0.000020***	***0.000010***	***0.000010***	***0.000468***	***0.000050***	***0.000020***	***0.000010***					
J-value = 0.000390029 ± 0.0000019															
YP081	0.248382	0.001508	0.072681	0.000519	0.000953	0.000105	0.005084	0.001335	0.000143	0.000040	2.836280	0.165725	**1.990**	**0.117**	83
YP081	0.211439	0.001416	0.029686	0.000581	0.000514	0.000057	0.036065	0.001340	0.000425	0.000048	2.894715	0.484160	**2.031**	**0.340**	40
YP081	0.251768	0.000394	0.073546	0.000406	0.001025	0.000095	0.011242	0.001334	0.000131	0.000040	2.895699	0.162128	**2.032**	**0.114**	84
YP081	0.654773	0.003332	0.170960	0.001325	0.002384	0.000165	0.010806	0.001339	0.000521	0.000040	2.928718	0.075577	**2.055**	**0.054**	76
YP081	0.595003	0.002622	0.182421	0.001263	0.002472	0.000054	0.008498	0.001696	0.000201	0.000038	2.935978	0.066673	**2.060**	**0.048**	90
YP081	0.187091	0.001559	0.055309	0.000612	0.000739	0.000057	0.007949	0.001338	0.000082	0.000040	2.943578	0.218693	**2.066**	**0.154**	87
YP081	0.402738	0.001963	0.124387	0.001294	0.001577	0.000092	0.000391	0.004338	0.000116	0.000022	2.962443	0.061890	**2.079**	**0.045**	91
YP081	0.610454	0.002397	0.194808	0.001046	0.002527	0.000105	0.008435	0.001340	0.000102	0.000033	2.978827	0.054478	**2.090**	**0.040**	95
YP081	0.305370	0.001565	0.098945	0.000952	0.001368	0.000063	0.006163	0.001697	0.000032	0.000038	2.991593	0.118615	**2.099**	**0.084**	97
YP081	0.506685	0.001797	0.158807	0.001418	0.001973	0.000113	0.006253	0.004332	0.000104	0.000022	2.996416	0.049607	**2.103**	**0.037**	94
YP081	0.480882	0.002300	0.149701	0.001459	0.001716	0.000093	0.004282	0.001693	0.000102	0.000038	3.010552	0.082313	**2.113**	**0.059**	94
YP081	0.502475	0.002272	0.151997	0.001356	0.002211	0.000155	0.009349	0.001334	0.000152	0.000040	3.010685	0.083889	**2.113**	**0.060**	91
YP081	0.595989	0.002044	0.171906	0.000808	0.002303	0.000085	0.003189	0.001337	0.000263	0.000048	3.014101	0.084705	**2.115**	**0.061**	87
YP081	0.400389	0.002843	0.114890	0.000849	0.001352	0.000085	0.006517	0.001337	0.000183	0.000040	3.015433	0.108482	**2.116**	**0.077**	86
YP081	0.647767	0.001974	0.192695	0.000994	0.002198	0.000113	0.001695	0.004335	0.000226	0.000031	3.015730	0.051215	**2.116**	**0.038**	90
YP081	0.313486	0.001704	0.100642	0.000632	0.001247	0.000113	-0.000260	0.004329	0.000006	0.000013	3.097036	0.045783	**2.173**	**0.034**	99
YP081	0.341252	0.000870	0.103171	0.000591	0.001383	0.000085	0.013155	0.001336	0.000011	0.000033	3.125234	0.093000	**2.193**	**0.066**	99
YP081	0.322743	0.001486	0.101119	0.000756	0.001329	0.000072	-0.001562	0.004330	0.000006	0.000022	3.172977	0.068985	**2.227**	**0.050**	99
Background:	***0.007500***	***0.000349***	***0.000040***	***0.000020***	***0.000020***	***0.000010***	***0.000488***	***0.000050***	***0.000060***	***0.000010***					

Sample #	^{40}Ar	±1σ	^{39}Ar	±1σ	^{38}Ar	±1σ	^{37}Ar	±1σ	^{36}Ar	±1σ	$^{40}Ar^*/^{39}ArK$	±1σ	Age (Ma)	±1σ	% $^{40}Ar^*$
McM#70		Mesa Falls Tuff													
J-value = 0.000376604 ± 0.0000019															
				Feldspar											
CMW01	0.308415	0.000770	0.149528	0.000889	0.001910	0.000113	0.001747	0.000445	0.000138	0.000022	1.789655	0.045657	1.213	0.032	87
CMW01	0.257084	0.002143	0.130199	0.000920	0.001735	0.000092	0.001888	0.000224	0.000063	0.000022	1.831000	0.053640	1.241	0.037	93
CMW01	0.306374	0.001364	0.158324	0.000868	0.002204	0.000154	0.002938	0.000250	0.000053	0.000022	1.837024	0.043345	1.245	0.030	95
CMW01	0.293374	0.001593	0.147356	0.000589	0.001723	0.000092	0.003035	0.000251	0.000073	0.000014	1.845470	0.030511	1.251	0.022	93
CMW01	0.558189	0.001395	0.285778	0.000775	0.003522	0.000123	0.034546	0.000250	0.000104	0.000031	1.845500	0.033260	1.251	0.024	94
CMW01	0.251734	0.000702	0.126331	0.001675	0.001417	0.000022	0.003514	0.000251	0.000062	0.000022	1.846692	0.057490	1.252	0.040	93
CMW01	0.427074	0.002009	0.219331	0.000651	0.002510	0.000164	0.004725	0.000250	0.000072	0.000022	1.850049	0.031647	1.254	0.023	95
CMW01	0.695977	0.003594	0.288269	0.001468	0.003573	0.000194	0.003895	0.000251	0.000542	0.000041	1.858426	0.044941	1.260	0.031	77
CMW01	0.448520	0.001038	0.229536	0.001375	0.002564	0.000062	0.003020	0.000444	0.000068	0.000022	1.866779	0.031158	1.265	0.022	95
CMW01	0.553588	0.001810	0.283483	0.001034	0.003595	0.000184	0.004082	0.000226	0.000073	0.000022	1.877060	0.024537	1.272	0.018	96
CMW01	0.522365	0.002185	0.269032	0.001241	0.003472	0.000143	0.003704	0.000225	0.000053	0.000022	1.883685	0.026695	1.277	0.019	97
CMW01	0.603608	0.002279	0.302709	0.000755	0.003493	0.000184	0.005362	0.000225	0.000112	0.000022	1.884368	0.023020	1.277	0.017	94
CMW01	0.310597	0.001738	0.128326	0.000600	0.001641	0.000113	0.002850	0.000251	0.000233	0.000022	1.884812	0.053418	1.277	0.037	78
CMW01	0.514990	0.001811	0.260173	0.001954	0.003205	0.000082	0.003980	0.000251	0.000082	0.000022	1.885962	0.029660	1.278	0.021	95
CMW01	0.743615	0.001966	0.378261	0.000962	0.004658	0.000184	0.005796	0.000226	0.000102	0.000022	1.886028	0.018410	1.278	0.014	96
CMW01	0.713216	0.005201	0.365164	0.003070	0.004627	0.000154	0.004520	0.000224	0.000083	0.000022	1.886333	0.027648	1.279	0.020	97
CMW01	0.341153	0.001518	0.164206	0.000920	0.002205	0.000092	0.003192	0.000225	0.000103	0.000022	1.892407	0.041607	1.283	0.029	91
CMW01	0.288951	0.001125	0.138209	0.001013	0.001652	0.000123	0.002282	0.000251	0.000093	0.000022	1.892430	0.049936	1.283	0.035	90
CMW01	0.271987	0.001218	0.135366	0.000672	0.001754	0.000082	0.002098	0.000251	0.000053	0.000014	1.894056	0.032705	1.284	0.023	94
CMW01	0.689703	0.002562	0.348660	0.001303	0.004189	0.000123	0.004392	0.000444	0.000097	0.000014	1.895595	0.015696	1.285	0.013	96
CMW01	0.365444	0.002467	0.188404	0.000920	0.002236	0.000062	0.003786	0.000225	0.000023	0.000022	1.904001	0.037717	1.290	0.027	98
CMW01	0.401087	0.001447	0.200529	0.001065	0.002643	0.000123	0.004259	0.000250	0.000052	0.000022	1.923221	0.034900	1.304	0.025	96
CMW01	0.232878	0.001001	0.112542	0.000786	0.001611	0.000113	0.001671	0.000251	0.000053	0.000014	1.930377	0.039534	1.308	0.028	93
CMW01	0.581613	0.001570	0.259015	0.001158	0.003360	0.000103	0.004663	0.000225	0.000273	0.000022	1.934580	0.026977	1.311	0.020	86
CMW01	0.460098	0.002592	0.226403	0.001468	0.002726	0.000164	0.003524	0.000226	0.000073	0.000022	1.937168	0.033096	1.313	0.024	95
CMW01	0.645494	0.001935	0.318183	0.001571	0.003666	0.000164	0.005878	0.000225	0.000092	0.000031	1.943068	0.031123	1.317	0.022	96
CMW01	0.586764	0.001703	0.274243	0.001055	0.003596	0.000143	0.005870	0.000444	0.000167	0.000022	1.959619	0.025952	1.328	0.019	92
CMW01	0.123367	0.000878	0.059803	0.000610	0.000755	0.000082	0.000963	0.000446	0.000018	0.000022	1.972409	0.113044	1.337	0.077	96
CMW01	0.377895	0.001518	0.184146	0.000538	0.002307	0.000123	0.003003	0.000225	0.000043	0.000022	1.983219	0.036341	1.344	0.026	97
Background:	*0.002170*	*0.000190*	*0.000025*	*0.000030*	*0.000010*	*0.000010*	*0.000510*	*0.000050*	*0.000030*	*0.000010*					
J-value = 0.000375552 ± 0.0000019															
				Feldspar											
CMW01	0.108150	0.001306	0.041992	0.000517	0.000720	0.000072	0.001134	0.000263	0.000126	0.000021	1.686224	0.149353	1.140	0.101	65
CMW01	0.661371	0.002739	0.328152	0.001117	0.003760	0.000164	0.005314	0.000447	0.000217	0.000022	1.819888	0.022623	1.230	0.017	90
CMW01	0.408358	0.000998	0.207849	0.000672	0.002666	0.000113	0.004173	0.000447	0.000087	0.000022	1.840336	0.032634	1.244	0.023	94
CMW01	0.296922	0.001569	0.146695	0.000765	0.001746	0.000082	0.002644	0.000447	0.000088	0.000022	1.847065	0.047200	1.248	0.033	91
CMW01	0.650829	0.002075	0.299395	0.000806	0.003882	0.000215	0.003279	0.000446	0.000318	0.000032	1.850247	0.032331	1.257	0.023	85
CMW01	0.549521	0.002465	0.281461	0.001199	0.003684	0.000194	0.003832	0.000262	0.000076	0.000021	1.872959	0.024612	1.266	0.018	96
CMW01	0.294852	0.001569	0.148205	0.001334	0.001766	0.000154	0.002046	0.000446	0.000058	0.000022	1.873786	0.048745	1.266	0.034	94
CMW01	0.601954	0.001785	0.306526	0.001385	0.003463	0.000092	0.005600	0.000446	0.000087	0.000022	1.879839	0.023851	1.271	0.018	96
CMW01	0.561392	0.002489	0.288859	0.001086	0.003995	0.000123	0.006831	0.000446	0.000057	0.000014	1.885414	0.018211	1.274	0.014	97
CMW01	0.470328	0.002423	0.240010	0.001313	0.003040	0.000194	0.002483	0.000262	0.000056	0.000021	1.890659	0.029136	1.278	0.021	96
CMW01	0.521906	0.002054	0.251400	0.001272	0.003105	0.000082	0.002992	0.000447	0.000108	0.000022	1.949315	0.029189	1.317	0.021	94
CMW01	0.351488	0.002334	0.165343	0.000744	0.001981	0.000103	0.003477	0.000446	0.000098	0.000022	1.951293	0.043208	1.319	0.030	92
Background:	*0.002310*	*0.000210*	*0.000060*	*0.000030*	*0.000020*	*0.000010*	*0.000540*	*0.000060*	*0.000020*	*0.000010*					

Sample #	^{40}Ar	±1σ	^{39}Ar	±1σ	^{38}Ar	±1σ	^{37}Ar	±1σ	^{36}Ar	±1σ	$^{40}Ar^*/^{39}ArK$	±1σ	Age (Ma)	±1σ	% $^{40}Ar^*$	
McM#62	Sheridan Reservior															
J-value = 0.000392002 ± 0.0000019																
				Feldspar												
YR215	0.080921	0.000659	0.021644	0.000311	0.000245	0.000053	0.004417	0.000194	0.000069	0.000022	2.798957	0.299226	1.974	0.211	75	
YR215	0.076117	0.001050	0.015629	0.000249	0.000245	0.000053	0.004114	0.000194	0.000109	0.000022	2.811109	0.416375	1.983	0.294	57	
YR215	0.083952	0.000821	0.026254	0.000487	0.000337	0.000043	0.005226	0.000193	0.000029	0.000013	2.875587	0.157923	2.028	0.112	90	
YR215	0.097626	0.001218	0.026801	0.000322	0.000337	0.000053	0.006363	0.000193	0.000068	0.000031	2.889381	0.347542	2.038	0.245	79	
YR215	0.818853	0.004297	0.024578	0.000373	0.000797	0.000053	0.007238	0.000193	0.002518	0.000061	3.041682	0.750145	2.145	0.529	8	*
YR215	0.125821	0.001382	0.037293	0.000404	0.000592	0.000083	0.005573	0.000141	0.000032	0.000022	3.118125	0.183894	2.199	0.130	92	
YR215	0.127404	0.000915	0.039081	0.000455	0.000500	0.000053	0.005821	0.000141	0.000012	0.000014	3.167672	0.115172	2.234	0.082	97	
YR215	0.302469	0.001318	0.040556	0.000487	0.000644	0.000083	0.011778	0.000193	0.000587	0.000031	3.181932	0.232038	2.244	0.164	42	
YR215	0.118216	0.001351	0.032805	0.000342	0.000438	0.000034	0.008286	0.000141	0.000042	0.000022	3.229258	0.208042	2.278	0.147	89	
YR215	0.238059	0.001280	0.050777	0.000610	0.000622	0.000053	0.013086	0.000141	0.000250	0.000032	3.231773	0.189651	2.279	0.134	69	
YR215	0.109338	0.000893	0.030036	0.000354	0.000312	0.000033	0.009015	0.000137	0.000041	0.000023	3.237376	0.232307	2.283	0.164	89	
YR215	0.188377	0.001259	0.057000	0.000404	0.000704	0.000053	0.012422	0.000141	0.000011	0.000022	3.250619	0.120100	2.293	0.086	98	
YR215	0.217881	0.001631	0.061413	0.000755	0.000726	0.000093	0.015239	0.000193	0.000056	0.000022	3.278515	0.114647	2.312	0.082	92	
YR215	0.192655	0.001025	0.035295	0.000332	0.000489	0.000044	0.009375	0.000141	0.000251	0.000041	3.354679	0.347700	2.366	0.245	61	
YR215	0.355774	0.001423	0.046476	0.000714	0.000806	0.000053	0.014389	0.000141	0.000670	0.000051	3.395422	0.329708	2.395	0.233	44	
YR215	0.341328	0.001691	0.065438	0.000455	0.000888	0.000063	0.022670	0.000141	0.000358	0.000032	3.600555	0.147197	2.539	0.105	69	
YR215	0.181000	0.001560	0.040700	0.000507	0.000644	0.000063	0.011620	0.000193	0.000107	0.000022	3.670799	0.167846	2.589	0.119	82	
YR215	0.308393	0.001012	0.074537	0.000497	0.000991	0.000073	0.021049	0.000194	0.000114	0.000013	3.683815	0.058474	2.598	0.044	89	
YR215	0.506102	0.002063	0.073614	0.000435	0.001164	0.000053	0.023639	0.000141	0.000767	0.000032	3.794241	0.131868	2.676	0.094	55	
YR215	0.425927	0.002039	0.038686	0.000404	0.000644	0.000053	0.010165	0.000193	0.000927	0.000031	3.926677	0.246729	2.769	0.174	35	
YR215	0.018040	0.000439	0.001946	0.000106	0.000040	0.000034	0.000373	0.000141	0.000034	0.000022	4.161101	3.405939	2.934	2.400	44	*
YR215	0.027680	0.000598	0.004716	0.000130	0.000087	0.000024	0.002338	0.000137	0.000023	0.000023	4.445753	1.457641	3.135	1.027	76	*
YR215	0.264415	0.002132	0.038571	0.001168	0.000552	0.000083	0.011521	0.000193	0.000277	0.000031	4.733488	0.283495	3.338	0.201	69	
Background:	*0.002760*	*0.000194*	*0.000110*	*0.000030*	*0.000030*	*0.000020*	*0.000544*	*0.000050*	*0.000030*	*0.000010*						
McM#70	Sheridan Reservior															
J-value = 0.000380640 ± 0.00000188																
		HF		Feldspar												
YR215_MY29_1	0.187283	0.001056	0.056331	0.000579	0.000614	0.000051	0.011082	0.000098	0.000074	0.000021	2.936884	0.113456	2.011	0.078	88	
YR215_MY29_2	0.196286	0.001128	0.062110	0.000269	0.000798	0.000062	0.009262	0.000098	0.000064	0.000021	2.853838	0.100165	1.955	0.069	90	
YR215_MY29_3	0.104692	0.000701	0.023970	0.000383	0.000246	0.000041	0.005047	0.000116	0.000074	0.000021	3.458317	0.261626	2.368	0.180	79	
YR215_MY29_4	0.253231	0.001436	0.056436	0.000651	0.000746	0.000062	0.014276	0.000116	0.000101	0.000021	3.955710	0.119894	2.709	0.083	88	
YR215_MY29_5	0.310859	0.001301	0.083452	0.000600	0.001033	0.000062	0.012741	0.000116	0.000142	0.000021	3.222399	0.078129	2.207	0.055	86	
YR215_MY29_6	0.739950	0.003720	0.088306	0.000734	0.001196	0.000072	0.019238	0.000116	0.001420	0.000040	3.626723	0.144450	2.484	0.100	43	
YR215_MY29_7	0.162601	0.001135	0.046150	0.000651	0.000644	0.000072	0.003351	0.000117	0.000094	0.000030	2.919728	0.200501	2.000	0.138	83	
YR215_MY29_8	0.165806	0.001322	0.046194	0.000517	0.000542	0.000092	0.015100	0.000117	0.000051	0.000021	3.262006	0.139752	2.234	0.096	91	
YR215_MY29_9	0.311237	0.003918	0.097856	0.000920	0.001411	0.000113	0.033732	0.000117	0.000086	0.000021	2.919687	0.078918	2.000	0.055	92	
YR215_MY29_10	0.181432	0.001520	0.040700	0.000538	0.000501	0.000062	0.009040	0.000117	0.000153	0.000040	3.348693	0.298249	2.293	0.205	75	
YR215_MY29_11	0.168227	0.001301	0.040263	0.000589	0.000552	0.000072	0.013294	0.000117	0.000041	0.000021	3.872481	0.164720	2.652	0.114	93	
YR215_MY29_12	0.216953	0.001312	0.055589	0.000424	0.000685	0.000072	0.014474	0.000117	0.000081	0.000021	3.470190	0.115144	2.376	0.080	89	
YR215_MY29_13	0.225058	0.001353	0.061478	0.000527	0.000808	0.000051	0.016647	0.000117	0.000101	0.000011	3.176211	0.064126	2.175	0.045	87	
YR215_MY29_14	0.386830	0.001643	0.090921	0.000868	0.001211	0.000103	0.006276	0.000242	0.000489	0.000032	2.663752	0.109120	1.824	0.075	62	
YR215_MY29_15	0.507757	0.001622	0.044091	0.000310	0.000802	0.000093	0.009427	0.000242	0.001168	0.000051	3.684418	0.346895	2.523	0.238	31	
YR215_MY29_16	0.111111	0.000728	0.032681	0.000351	0.000434	0.000052	0.010328	0.000242	0.000018	0.000023	3.234912	0.213272	2.215	0.146	95	
YR215_MY29_17	0.157041	0.001424	0.047856	0.000630	0.000475	0.000052	0.005606	0.000242	0.000059	0.000023	2.913931	0.150914	1.996	0.104	89	
YR215_MY29_18	0.180456	0.000831	0.034925	0.000393	0.000516	0.000052	0.008898	0.000243	0.000228	0.000023	3.232557	0.200556	2.214	0.138	62	
YR215_MY29_19	0.214348	0.001008	0.059672	0.001612	0.000618	0.000093	0.015887	0.000243	0.000057	0.000015	3.310443	0.118595	2.267	0.082	92	
YR215_MY29_20	0.115762	0.001205	0.032198	0.000135	0.000362	0.000033	0.006132	0.000243	0.000029	0.000015	3.325831	0.146439	2.278	0.101	92	
YR215_MY30_1	0.185903	0.001616	0.056810	0.000372	0.000698	0.000082	0.016363	0.000103	0.000056	0.000024	2.978845	0.129104	2.040	0.089	91	
YR215_MY30_2	0.065686	0.000708	0.018880	0.000414	0.000228	0.000041	0.003899	0.000103	0.000039	0.000017	2.862441	0.268545	1.961	0.184	82	
YR215_MY30_3	0.094626	0.000597	0.029314	0.000372	0.000299	0.000051	0.009299	0.000103	-0.000002	0.000017	3.247223	0.172669	2.224	0.119	100	
YR215_MY30_4	0.404974	0.001057	0.031733	0.000496	0.000504	0.000051	0.008624	0.000103	0.000988	0.000042	3.558619	0.397112	2.437	0.272	27	
YR215_MY30_5	0.061224	0.000390	0.018062	0.000300	0.000207	0.000031	0.005538	0.000103	0.000019	0.000024	3.079188	0.395229	2.109	0.271	91	
YR215_MY30_6	0.071708	0.000557	0.022970	0.000197	0.000248	0.000051	0.007023	0.000103	0.000028	0.000024	2.753800	0.309552	1.886	0.212	88	
YR215_MY30_7	0.051578	0.000841	0.016658	0.000300	0.000187	0.000041	0.003632	0.000103	-0.000001	0.000024	3.105683	0.430929	2.127	0.295	100	

Sample #	^{40}Ar	±1σ	^{39}Ar	±1σ	^{38}Ar	±1σ	^{37}Ar	±1σ	^{36}Ar	±1σ	$^{40}Ar^*/^{39}ArK$	±1σ	Age (Ma)	±1σ	% $^{40}Ar^*$
McM#70	Sheridan Reservior														
J-value = 0.000380640 ± 0.00000188															
	HF			Feldspar											
YR215_MY30_8	0.063184	0.000426	0.018127	0.000300	0.000215	0.000041	0.005800	0.000097	0.000015	0.000021	3.236211	0.339746	2.216	0.233	93
YR215_MY30_9	0.066809	0.000839	0.016732	0.000321	0.000144	0.000041	0.006031	0.000098	0.000025	0.000021	3.547162	0.372290	2.429	0.255	89
YR215_MY30_10	0.075175	0.000565	0.018953	0.000310	0.000246	0.000051	0.007391	0.000098	0.000005	0.000021	3.889676	0.327721	2.664	0.225	98
YR215_MY30_11	0.025066	0.000368	0.007784	0.000197	0.000123	0.000021	0.002940	0.000098	-0.000004	0.000011	3.373363	0.430495	2.310	0.295	100
YR215_MY30_12	0.176852	0.000676	0.027966	0.000548	0.000430	0.000051	0.006400	0.000098	0.000315	0.000021	2.993255	0.226018	2.050	0.155	47
YR215_MY30_13	0.061330	0.000666	0.016309	0.000444	0.000154	0.000031	0.004762	0.000098	0.000035	0.000021	3.116392	0.383737	2.134	0.263	83
YR215_MY30_14	0.036323	0.000465	0.012631	0.000259	0.000113	0.000041	0.003304	0.000098	-0.000014	0.000021	3.205400	0.486171	2.195	0.333	100
YR215_MY30_15	0.087890	0.000666	0.025425	0.000486	0.000368	0.000031	0.003870	0.000098	0.000046	0.000021	2.923919	0.246464	2.003	0.169	84
YR215_MY30_16	0.057449	0.000676	0.017230	0.000217	0.000144	0.000051	0.003693	0.000098	0.000056	0.000011	2.377215	0.195768	1.628	0.134	71
YR215_MY30_17	0.035722	0.000406	0.010824	0.000248	0.000164	0.000041	0.000639	0.000098	0.000016	0.000021	2.847437	0.565531	1.950	0.387	86
YR215_MY30_18	0.064447	0.000768	0.018211	0.000166	0.000225	0.000031	0.003953	0.000098	0.000066	0.000021	2.472017	0.336540	1.693	0.231	70
YR215_MY30_19	0.053784	0.000942	0.014708	0.000259	0.000184	0.000041	0.003183	0.000098	0.000016	0.000021	3.336030	0.421512	2.285	0.289	91
YR215_MY30_20	0.080610	0.000768	0.024421	0.000269	0.000307	0.000041	0.006245	0.000098	0.000025	0.000011	2.995691	0.141207	2.052	0.097	91
Background:	***0.002640***	***0.000200***	***0.000020***	***0.000020***	***0.000010***	***0.000020***	***0.000390***	***0.000050***	***0.000020***	***0.000010***					
McM#62	Sheridan Reservior														
J-value = 0.000392002 ± 0.0000019															
				Glassy Groundmass											
YR215	2.402106	0.005564	0.108182	0.000776	0.002852	0.000133	0.000498	0.003628	0.007232	0.000071	2.451310	0.202169	1.720	0.142	10
YR215	1.167774	0.005377	0.061357	0.000776	0.001237	0.000123	0.006484	0.003631	0.003430	0.000071	2.513540	0.355747	1.764	0.250	12
YR215	0.205103	0.000865	0.068517	0.000332	0.000838	0.000092	0.007989	0.003635	0.000050	0.000024	2.779786	0.105650	1.951	0.075	93
YR215	0.349363	0.001499	0.117399	0.001252	0.001545	0.000072	0.011269	0.006029	0.000067	0.000027	2.807173	0.075118	1.970	0.054	94
YR215	0.280079	0.001135	0.095065	0.000333	0.001256	0.000099	0.005453	0.000239	0.000039	0.000020	2.826330	0.064113	1.983	0.046	96
YR215	0.174796	0.001047	0.059375	0.000570	0.000818	0.000072	-0.000250	0.003638	0.000022	0.000024	2.835766	0.124337	1.990	0.088	96
YR215	0.128567	0.001072	0.044967	0.000528	0.000582	0.000063	0.002754	0.000239	-0.000001	0.000010	2.863975	0.077621	2.010	0.056	100
YR215	0.317975	0.001573	0.105744	0.001066	0.001615	0.000103	0.010989	0.003636	0.000049	0.000024	2.870787	0.074870	2.015	0.054	95
YR215	0.353257	0.002238	0.121794	0.001179	0.001583	0.000080	0.007640	0.000239	-0.000002	0.000010	2.905362	0.041508	2.039	0.031	100
YR215	0.270296	0.001336	0.090042	0.000797	0.001155	0.000072	0.002742	0.003629	0.000021	0.000024	2.933164	0.084633	2.058	0.060	98
YR215	0.099456	0.000907	0.033866	0.000487	0.000520	0.000055	0.002192	0.000239	-0.000001	0.000020	2.941858	0.181570	2.064	0.128	100
YR215	0.235926	0.001284	0.079096	0.000870	0.001137	0.000082	0.007506	0.006024	0.000008	0.000027	2.952836	0.106809	2.072	0.076	99
YR215	0.369593	0.002139	0.119881	0.000725	0.001605	0.000092	0.006472	0.003624	0.000050	0.000024	2.959879	0.064634	2.077	0.047	96
YR215	0.125186	0.001093	0.042310	0.000559	0.000602	0.000063	0.002637	0.000239	-0.000001	0.000010	2.963647	0.084177	2.080	0.060	100
YR215	0.203885	0.002170	0.069329	0.000518	0.000879	0.000072	-0.000996	0.003625	-0.000008	0.000024	2.975212	0.109741	2.088	0.078	100
YR215	0.283511	0.001561	0.091081	0.000735	0.001321	0.000082	0.003006	0.006030	0.000039	0.000035	2.985535	0.117254	2.095	0.083	96
YR215	0.178357	0.001865	0.058042	0.000942	0.000726	0.000032	-0.002495	0.003632	0.000002	0.000024	3.061066	0.136302	2.148	0.096	100
YR215	0.276535	0.001315	0.085071	0.000663	0.001167	0.000062	0.001502	0.006025	0.000050	0.000027	3.078356	0.097655	2.160	0.069	95
YR215	0.156734	0.001095	0.051903	0.000704	0.000707	0.000112	-0.004315	0.001999	-0.000012	0.000024	3.089144	0.142204	2.168	0.100	100
YR215	0.103037	0.001085	0.035252	0.000549	0.000521	0.000042	0.005751	0.003641	-0.000050	0.000024	3.340799	0.211000	2.344	0.149	100
Background:	***0.007244***	***0.000323***	***0.000040***	***0.000020***	***0.000020***	***0.000010***	***0.000497***	***0.000050***	***0.000060***	***0.000010***					
J-value = 0.000385646 ± 0.0000019															
				Glassy Groundmass											
YR217	0.036280	0.000881	0.008596	0.000218	0.000184	0.000046	0.000410	0.003017	0.000076	0.000039	1.602841	1.343885	1.113	0.932	38
YR217	0.181942	0.000872	0.039346	0.000198	0.000603	0.000046	0.006619	0.003015	0.000264	0.000048	2.641757	0.357477	1.833	0.248	57
YR217	0.359796	0.003083	0.039222	0.000383	0.000797	0.000038	0.005670	0.003018	0.000864	0.000065	2.662319	0.498301	1.847	0.346	28
YR217	0.935273	0.001491	0.067017	0.000569	0.001318	0.000075	0.010430	0.003012	0.002553	0.000075	2.698951	0.330146	1.873	0.229	19
YR217	0.358797	0.002661	0.047607	0.000590	0.000714	0.000092	0.005443	0.007753	0.000776	0.000031	2.721795	0.202454	1.889	0.141	35
YR217	0.119954	0.001181	0.038819	0.000363	0.000531	0.000065	0.005665	0.003016	0.000044	0.000039	2.753550	0.302691	1.911	0.210	89
YR217	0.901336	0.006169	0.088315	0.000828	0.001573	0.000062	0.003883	0.007744	0.002216	0.000080	2.790851	0.278949	1.937	0.194	27
YR217	0.394318	0.002243	0.054822	0.000632	0.000845	0.000073	0.011366	0.006720	0.000815	0.000052	2.799769	0.283825	1.943	0.197	38
YR217	1.155118	0.004317	0.052634	0.000394	0.001377	0.000073	0.002149	0.006716	0.003407	0.000111	2.816085	0.627857	1.954	0.436	12
YR217	0.359405	0.002464	0.069400	0.000580	0.000867	0.000113	0.003887	0.007751	0.000546	0.000051	2.853451	0.219362	1.980	0.153	55
YR217	0.369967	0.002123	0.023179	0.000383	0.000521	0.000056	0.001839	0.003009	0.001025	0.000056	2.891130	0.723364	2.006	0.502	17
YR217	0.287426	0.002481	0.052411	0.000590	0.000856	0.000053	-0.004757	0.006713	0.000449	0.000042	2.951076	0.244750	2.048	0.170	53
YR217	0.251219	0.002151	0.038296	0.000311	0.000600	0.000063	0.013674	0.006722	0.000434	0.000033	3.208200	0.260940	2.226	0.181	48
Background:	***0.007244***	***0.000323***	***0.000040***	***0.000020***	***0.000020***	***0.000010***	***0.000497***	***0.000050***	***0.000060***	***0.000010***					

Sample #	^{40}Ar	± 1σ	^{39}Ar	± 1σ	^{38}Ar	± 1σ	^{37}Ar	± 1σ	^{36}Ar	± 1σ	$^{40}Ar^*/^{39}ArK$	± 1σ	Age (Ma)	± 1σ	% $^{40}Ar^*$	
McM#62	Snake River Butte															
J-value = 0.000388385 ± 0.0000019																
				Feldspar												
YR185	0.080669	0.000797	0.023046	0.000518	0.000187	0.000056	0.033682	0.006105	0.000093	0.000021	2.306954	0.281578	1.612	0.197	66	
YR185	0.257687	0.001415	0.040786	0.000351	0.000882	0.000084	0.002494	0.000135	0.000513	0.000031	2.603655	0.231552	1.820	0.162	41	•
YR185	0.407084	0.002264	0.122915	0.000507	0.001628	0.000104	0.003504	0.006093	0.000141	0.000031	2.972770	0.077681	2.077	0.055	90	
YR185	0.459374	0.002927	0.134025	0.000993	0.001703	0.000164	0.002590	0.002496	0.000193	0.000030	3.002783	0.073904	2.098	0.053	87	
YR185	1.365191	0.003722	0.437568	0.001924	0.005972	0.000085	0.004058	0.006103	0.000081	0.000031	3.065302	0.026377	2.142	0.022	98	
YR185	0.481700	0.002212	0.141291	0.000807	0.001618	0.000065	0.000767	0.006097	0.000162	0.000021	3.070893	0.050629	2.146	0.037	90	
YR185	0.574505	0.003232	0.177091	0.001386	0.002242	0.000104	-0.003611	0.006088	0.000103	0.000041	3.072325	0.074393	2.147	0.053	95	
YR185	0.319017	0.001061	0.096579	0.000738	0.001342	0.000074	0.002596	0.000135	0.000073	0.000022	3.080897	0.072503	2.153	0.052	93	
YR185	0.583034	0.002930	0.178523	0.000911	0.002262	0.000065	0.005700	0.006100	0.000110	0.000031	3.082986	0.056104	2.154	0.041	94	
YR185	0.525041	0.002503	0.164983	0.001024	0.002088	0.000135	0.000766	0.006092	0.000052	0.000021	3.089615	0.045541	2.159	0.034	97	
YR185	0.383206	0.001862	0.120693	0.000882	0.001455	0.000084	0.002242	0.000135	0.000033	0.000014	3.094886	0.043437	2.163	0.033	97	
YR185	0.418058	0.001051	0.127060	0.000564	0.001649	0.000074	0.002486	0.000135	0.000083	0.000022	3.097975	0.053910	2.165	0.039	94	
YR185	0.366077	0.001508	0.102853	0.000944	0.001383	0.000064	0.002166	0.000135	0.000143	0.000022	3.149060	0.071348	2.201	0.051	88	
YR185	0.736751	0.003399	0.230739	0.001035	0.002886	0.000175	0.005687	0.006086	0.000020	0.000021	3.166758	0.034287	2.213	0.027	99	
YR185	0.098270	0.000771	0.025150	0.000503	0.000453	0.000045	0.030983	0.000135	0.000055	0.000022	3.259760	0.269600	2.278	0.189	83	
YR185	0.014242	0.000157	0.001087	0.000148	0.000075	0.000027	0.000521	0.000136	0.000033	0.000014	4.079217	3.781247	2.850	2.640	30	•
Background:	*0.007244*	*0.000323*	*0.000040*	*0.000020*	*0.000020*	*0.000010*	*0.000497*	*0.000050*	*0.000060*	*0.000010*						
J-value = 0.000387289 ± 0.0000019																
YR185	0.083597	0.000585	0.021327	0.000163	0.000350	0.000041	0.026339	0.000245	0.000073	0.000011	2.908056	0.161034	2.027	0.113	74	
YR185	0.474326	0.002263	0.134190	0.000901	0.001751	0.000136	0.003172	0.000244	0.000229	0.000021	3.030100	0.052720	2.112	0.038	86	
YR185	0.334003	0.001588	0.095855	0.000345	0.001219	0.000076	0.002298	0.000244	0.000129	0.000021	3.085587	0.066886	2.150	0.048	88	
YR185	0.156233	0.001112	0.043320	0.000373	0.000499	0.000052	0.059237	0.007772	0.000071	0.000031	3.119157	0.213866	2.174	0.149	86	
YR185	0.808204	0.002703	0.239623	0.001138	0.002789	0.000103	0.004678	0.007774	0.000196	0.000031	3.131229	0.042443	2.182	0.032	93	
YR185	0.098111	0.001385	0.027782	0.000507	0.000356	0.000062	0.037390	0.007767	0.000037	0.000031	3.135430	0.337057	2.185	0.235	89	
YR185	0.709250	0.001968	0.198875	0.001014	0.002656	0.000194	0.005451	0.007765	0.000266	0.000031	3.171524	0.049673	2.210	0.037	89	
YR185	0.141654	0.001742	0.034951	0.000311	0.000499	0.000052	0.055391	0.007779	0.000102	0.000021	3.186617	0.188917	2.221	0.132	78	
YR185	0.408855	0.001526	0.109839	0.000643	0.001454	0.000058	0.002121	0.000245	0.000169	0.000021	3.266462	0.060529	2.276	0.044	88	
YR185	0.097716	0.001092	0.022666	0.000394	0.000234	0.000052	0.028795	0.007760	0.000060	0.000012	3.535326	0.179273	2.463	0.126	82	
Background:	*0.007244*	*0.000323*	*0.000040*	*0.000020*	*0.000020*	*0.000010*	*0.000497*	*0.000050*	*0.000060*	*0.000010*						
J-value = 0.000394285 ± 0.0000019																
YR185^	4.488546	0.031466	0.192729	0.001325	0.004950	0.000177	0.002920	0.000280	0.013468	0.000210	2.639251	0.361977	1.872	0.257	10	†
YR185^	2.827464	0.013274	0.242713	0.001366	0.004510	0.000127	0.004992	0.000281	0.006848	0.000141	3.312358	0.180645	2.350	0.129	28	†
YR185^	3.183489	0.006354	0.239674	0.001015	0.004684	0.000117	0.004804	0.000281	0.008538	0.000081	2.756108	0.103975	1.955	0.074	20	†
YR185^	5.639179	0.021998	0.253042	0.001253	0.006462	0.000268	0.004229	0.000281	0.016418	0.000180	3.112818	0.228478	2.208	0.162	13	†
YR185^	2.064505	0.011897	0.106975	0.000923	0.002691	0.000157	0.002873	0.000282	0.005788	0.000081	3.309695	0.251405	2.348	0.179	16	†
YR185^	0.071643	0.001049	0.019259	0.000364	0.000211	0.000054	0.000285	0.000230	0.000033	0.000022	3.209733	0.348955	2.277	0.248	86	†
YR185^	6.444530	0.016786	0.041471	0.000470	0.004695	0.000135	0.000817	0.000484	0.020991	0.000210	5.827756	1.553786	4.132	1.101	3	†
YR185^	0.900842	0.002308	0.098435	0.000552	0.001792	0.000105	0.001443	0.000484	0.001891	0.000051	3.475316	0.157160	2.465	0.112	37	†
YR185^	0.182915	0.001536	0.046536	0.000521	0.000668	0.000085	0.001584	0.000484	0.000121	0.000023	3.163367	0.154816	2.244	0.110	80	†
YR185^	7.286550	0.057901	0.137120	0.001088	0.005983	0.000075	0.002908	0.000485	0.023480	0.000150	2.538429	0.532775	1.801	0.378	4	†
YR185^	11.179006	0.046227	0.116102	0.001067	0.008364	0.000297	0.002492	0.000485	0.036551	0.000400	3.258405	1.093980	2.311	0.776	2	†
YR185^	1.423795	0.007375	0.127712	0.000665	0.002426	0.000145	0.002773	0.000486	0.003511	0.000091	3.025858	0.218372	2.147	0.155	26	†
YR185^	1.188019	0.004657	0.120642	0.000542	0.002068	0.000115	0.001379	0.000486	0.002591	0.000061	3.501393	0.155455	2.484	0.111	35	†
YR185^	1.295589	0.009168	0.098600	0.000943	0.001792	0.000105	0.001939	0.000486	0.003231	0.000051	3.457481	0.182837	2.453	0.130	26	†
YR185^	3.158262	0.011421	0.082627	0.000758	0.002508	0.000115	0.001520	0.000486	0.009841	0.000170	3.029172	0.625507	2.149	0.444	7	†
YR185^	0.646310	0.003287	0.143261	0.001191	0.001987	0.000065	0.002989	0.000487	0.000570	0.000051	3.334758	0.111907	2.366	0.080	74	†
YR185^	3.350446	0.015652	0.104407	0.000622	0.003352	0.000175	0.001489	0.000292	0.010225	0.000111	3.151862	0.347900	2.236	0.247	9	†
YR185^	0.978354	0.003154	0.054080	0.000519	0.001247	0.000054	0.000638	0.000292	0.002665	0.000101	3.529895	0.554852	2.504	0.394	19	†
YR185^	0.606950	0.002921	0.176763	0.000845	0.002149	0.000083	0.002544	0.000604	0.000136	0.000023	3.205799	0.044455	2.274	0.034	93	†
YR185^	2.606427	0.010522	0.101013	0.000747	0.002855	0.000073	0.001894	0.000604	0.007986	0.000140	2.439453	0.424207	1.731	0.301	9	†

Sample #	^{40}Ar	±1σ	^{39}Ar	±1σ	^{38}Ar	±1σ	^{37}Ar	±1σ	^{36}Ar	±1σ	$^{40}Ar^*/^{39}ArK$	±1σ	Age (Ma)	±1σ	% $^{40}Ar^*$	
McM#62	Snake River Butte															
J-value = 0.000394285 ± 0.0000019																
				Feldspar												
YR185^	1.344950	0.005669	0.122528	0.001388	0.002201	0.000114	0.001751	0.000604	0.003197	0.000091	3.267619	0.226582	2.318	0.161	29	†
YR185^	3.370604	0.013104	0.197802	0.001388	0.004143	0.000164	0.003561	0.000605	0.009396	0.000111	3.003373	0.179218	2.131	0.128	17	†
YR185^	4.164251	0.017023	0.114981	0.000502	0.003488	0.000164	0.002405	0.000605	0.012826	0.000101	3.253265	0.298300	2.308	0.212	8	†
YR185^	1.489330	0.004335	0.197048	0.000475	0.003059	0.000154	0.002406	0.000605	0.002976	0.000061	3.094771	0.094443	2.195	0.068	40	†
YR185^	2.127103	0.002488	0.099504	0.000660	0.002241	0.000094	0.001538	0.000606	0.006077	0.000101	3.331224	0.300645	2.363	0.214	15	†
J-value = 0.000393144 ± 0.0000019																
YR185^	0.049699	0.000720	0.012279	0.000375	0.000172	0.000034	0.014438	0.000510	0.000052	0.000021	2.798748	0.534342	1.980	0.378	69	
YR185^	0.286379	0.001583	0.088762	0.000620	0.001113	0.000073	0.001935	0.000507	0.000075	0.000021	2.975997	0.363011	2.105	0.257	92	
YR185^	0.389520	0.003856	0.121472	0.000611	0.001599	0.000113	0.001091	0.000477	0.000087	0.000022	2.995382	0.678201	2.119	0.480	93	
YR185^	0.231174	0.001537	0.071836	0.000683	0.001008	0.000074	0.001632	0.000774	0.000053	0.000018	2.998739	0.227304	2.121	0.161	93	
YR185^	0.368339	0.001364	0.119093	0.000690	0.001450	0.000073	0.002898	0.000508	0.000035	0.000021	3.006147	0.252195	2.126	0.179	97	
YR185^	0.295699	0.002406	0.087977	0.000944	0.001123	0.000073	0.001778	0.000508	0.000105	0.000012	3.007618	0.229164	2.128	0.162	89	
YR185^	0.443909	0.003094	0.141254	0.001913	0.001946	0.000103	0.002415	0.000476	0.000057	0.000013	3.024422	1.128380	2.139	0.798	96	
YR185^	0.247754	0.001926	0.075381	0.000761	0.000796	0.000083	0.000984	0.000509	0.000066	0.000021	3.030091	0.155320	2.143	0.110	92	
YR185^	0.618971	0.003854	0.196854	0.001614	0.002725	0.000084	0.004408	0.000774	0.000073	0.000025	3.035366	0.179726	2.147	0.128	96	
YR185^	0.427631	0.002236	0.133636	0.000890	0.001529	0.000084	0.004567	0.000774	0.000073	0.000025	3.039579	0.425443	2.150	0.301	95	
YR185^	0.286388	0.001768	0.087635	0.000984	0.001133	0.000063	0.002102	0.000509	0.000065	0.000021	3.048254	0.157801	2.156	0.112	93	
YR185^	0.236161	0.009313	0.071949	0.003086	0.000878	0.000093	-0.000137	0.000508	0.000056	0.000021	3.053390	0.104091	2.160	0.074	93	
YR185^	0.591610	0.001996	0.182520	0.001066	0.002193	0.000114	0.004068	0.000772	0.000113	0.000025	3.058923	0.112407	2.164	0.080	94	
YR185^	0.340417	0.001225	0.103584	0.000828	0.001243	0.000035	0.003261	0.000773	0.000073	0.000025	3.078451	0.044796	2.178	0.034	94	
YR185^	0.229889	0.002205	0.065734	0.000456	0.000742	0.000054	0.002452	0.000775	0.000093	0.000025	3.078725	0.094729	2.178	0.068	88	
YR185^	0.319516	0.001777	0.099540	0.000725	0.001191	0.000084	0.003088	0.000771	0.000043	0.000025	3.082460	0.156091	2.180	0.111	96	
YR185^	0.064291	0.000522	0.015902	0.000363	0.000158	0.000032	0.021294	0.000476	0.000052	0.000013	3.086002	0.897252	2.183	0.634	76	
YR185^	0.096711	0.000766	0.029666	0.000435	0.000413	0.000052	0.038628	0.000477	0.000017	0.000013	3.091619	0.609138	2.187	0.431	95	
YR185^	0.515417	0.003584	0.155619	0.001489	0.002089	0.000123	0.001754	0.000477	0.000107	0.000022	3.109472	0.768209	2.200	0.543	94	
YR185^	0.659736	0.003019	0.207775	0.001283	0.002633	0.000054	0.003416	0.000772	0.000043	0.000018	3.114314	0.627331	2.203	0.444	98	
YR185^	0.267155	0.001360	0.084277	0.000436	0.001069	0.000084	0.001951	0.000771	0.000013	0.000025	3.123562	0.183486	2.209	0.130	99	
YR185^	0.487902	0.001788	0.155652	0.000952	0.001846	0.000104	0.004870	0.000770	0.000002	0.000018	3.129893	1.097105	2.214	0.776	100	
YR185^	0.329656	0.001677	0.103228	0.000394	0.001405	0.000082	0.002744	0.000475	0.000016	0.000013	3.146481	0.301542	2.226	0.214	99	
YR185^	0.186209	0.000954	0.051299	0.000683	0.000711	0.000054	-0.000163	0.000772	0.000084	0.000025	3.147186	0.348909	2.226	0.247	87	
YR185^	0.314823	0.001573	0.091058	0.000670	0.001184	0.000073	0.001940	0.000508	0.000085	0.000021	3.180892	0.349969	2.250	0.248	92	
YR185^	0.321316	0.001854	0.089424	0.000508	0.001149	0.000082	0.000095	0.000476	0.000117	0.000022	3.206163	0.609623	2.268	0.431	89	
YR185^	0.335462	0.001204	0.104246	0.000745	0.001100	0.000054	0.002280	0.000773	0.000003	0.000025	3.209054	0.556437	2.270	0.394	100	
YR185^	0.326446	0.001527	0.095023	0.000797	0.001181	0.000074	0.000487	0.000770	0.000054	0.000025	3.268695	0.218942	2.312	0.155	95	
YR185^	0.321574	0.003146	0.093357	0.000807	0.001026	0.000082	0.011045	0.000476	0.000044	0.000013	3.304617	0.913359	2.337	0.646	96	
YR185^	0.295228	0.003068	0.084419	0.000660	0.000990	0.000043	0.002262	0.000509	0.000035	0.000012	3.374268	1.556977	2.387	1.101	96	
YR185^	0.241435	0.001554	0.062038	0.000680	0.000857	0.000093	0.021385	0.000507	0.000090	0.000021	3.462824	0.181112	2.449	0.129	89	
YR185^	0.117594	0.001423	0.031960	0.000580	0.000445	0.000054	0.001307	0.000775	0.000013	0.000018	3.555522	0.299118	2.515	0.212	97	
Background:	***0.001470***	***0.001940***	***0.000138***	***0.000040***	***0.000030***	***0.000020***	***0.000474***	***0.000050***	***0.000020***	***0.000010***						
McM#70	Snake River Butte															
J-value = 0.000381262 ± 0.00000188																
		HF		Feldspar												
MY25_1	0.299516	0.001018	0.093584	0.000517	0.001259	0.000061	0.000751	0.000727	0.000036	0.000021	3.086649	0.069862	2.117	0.049	96	
MY25_2	0.356155	0.002539	0.110323	0.000972	0.001208	0.000123	0.002060	0.000728	0.000036	0.000021	3.132665	0.067150	2.149	0.048	97	
MY25_3	0.445235	0.001872	0.139552	0.000786	0.001484	0.000102	0.001979	0.000731	0.000026	0.000021	3.135987	0.050027	2.151	0.036	98	
MY25_4	0.249562	0.002174	0.077620	0.000724	0.001014	0.000092	0.001712	0.000728	0.000016	0.000012	3.155039	0.061664	2.164	0.044	98	
MY25_5	0.371880	0.002081	0.112835	0.000807	0.001464	0.000051	0.001832	0.000727	0.000046	0.000012	3.175959	0.043286	2.179	0.032	96	
MY25_6	0.559935	0.003134	0.168046	0.001261	0.002108	0.000092	0.003291	0.000730	0.000085	0.000012	3.181901	0.037115	2.183	0.028	95	
MY25_7	0.782083	0.003573	0.235498	0.001261	0.003140	0.000133	0.004324	0.000728	0.000105	0.000031	3.189088	0.044892	2.188	0.033	96	
MY25_8	0.627783	0.003186	0.187980	0.001344	0.002343	0.000102	0.003618	0.000726	0.000075	0.000021	3.221279	0.043888	2.210	0.032	96	
MY25_9	0.494635	0.001622	0.148144	0.000941	0.001730	0.000082	0.002589	0.000730	0.000056	0.000021	3.228058	0.048215	2.214	0.035	97	
MY25_10	0.881631	0.001893	0.271520	0.000889	0.003815	0.000204	0.005387	0.000730	0.000015	0.000012	3.230891	0.018342	2.216	0.017	99	
MY25_11	0.096412	0.000502	0.027515	0.000455	0.000391	0.000031	0.034922	0.000726	0.000017	0.000012	3.321405	0.143094	2.278	0.099	95	
MY25_12	0.123928	0.001039	0.034581	0.000455	0.000564	0.000041	0.044972	0.000727	0.000024	0.000012	3.375800	0.117128	2.316	0.081	94	

Sample #	^{40}Ar	±1σ	^{39}Ar	±1σ	^{38}Ar	±1σ	^{37}Ar	±1σ	^{36}Ar	±1σ	$^{40}Ar^*/^{39}ArK$	±1σ	Age (Ma)	±1σ	% $^{40}Ar^*$	
McM#70	Snake River Butte															
J-value = 0.000381262 ± 0.00000188																
		HF		Feldspar												
MY25_13	0.101506	0.000694	0.028614	0.000559	0.000407	0.000032	0.035111	0.000906	0.000051	0.000013	3.023917	0.147854	2.074	0.102	85	
MY25_14	0.389236	0.001551	0.122261	0.000838	0.001563	0.000082	0.001228	0.000907	0.000015	0.000021	3.146458	0.057210	2.158	0.041	99	
MY25_15	0.563725	0.002580	0.178896	0.001220	0.002114	0.000133	0.002917	0.000905	-0.000001	0.000013	3.152417	0.033547	2.163	0.026	100	
MY25_16	0.611267	0.001610	0.189855	0.001065	0.002328	0.000103	0.003274	0.000906	0.000039	0.000013	3.158743	0.028107	2.167	0.023	98	
MY25_17	0.533612	0.003624	0.168991	0.001241	0.002032	0.000123	0.002738	0.000905	-0.000001	0.000022	3.158911	0.049246	2.167	0.036	100	
MY25_18	0.554432	0.003426	0.170241	0.001251	0.002083	0.000082	0.003181	0.000904	0.000049	0.000022	3.171418	0.048524	2.176	0.035	97	
MY25_19	0.361177	0.001819	0.113811	0.000735	0.001725	0.000113	0.001403	0.000903	0.000000	0.000013	3.174457	0.042417	2.178	0.031	100	
MY25_20	0.518795	0.003426	0.156727	0.000921	0.001991	0.000143	0.003889	0.000904	0.000069	0.000022	3.180136	0.049859	2.182	0.036	96	
MY25_21	0.388798	0.000691	0.111146	0.000931	0.001523	0.000113	0.001503	0.000909	0.000115	0.000021	3.191498	0.062898	2.189	0.045	91	
MY25_22	0.479444	0.001819	0.148880	0.001169	0.001889	0.000103	0.003812	0.000907	0.000009	0.000013	3.202495	0.037921	2.197	0.029	99	
MY25_23	0.966780	0.003459	0.210217	0.001334	0.002770	0.000133	0.002494	0.000907	0.000985	0.000051	3.214286	0.075708	2.205	0.053	70	•
MY25_24	0.342155	0.001152	0.103574	0.000445	0.001357	0.000062	0.001853	0.000906	0.000030	0.000022	3.219283	0.064143	2.208	0.046	97	
MY25_25	0.648968	0.002812	0.200178	0.000518	0.002637	0.000133	0.002226	0.000908	0.000015	0.000021	3.219636	0.035413	2.209	0.027	99	
MY25_26	0.386307	0.003363	0.111670	0.001334	0.001306	0.000093	0.002745	0.000907	0.000089	0.000022	3.223143	0.075219	2.211	0.053	93	
MY25_27	0.345659	0.002489	0.106731	0.000497	0.001267	0.000123	0.000595	0.000908	0.000006	0.000012	3.223199	0.044076	2.211	0.033	100	
MY25_28	0.685352	0.002374	0.124649	0.001386	0.001594	0.000113	0.001683	0.000909	0.000955	0.000041	3.233647	0.104621	2.218	0.073	58	•
MY25_29	0.514857	0.003008	0.152003	0.000766	0.001827	0.000072	0.002557	0.000904	0.000069	0.000022	3.252379	0.049234	2.231	0.036	96	
MY25_30	0.117680	0.000819	0.028623	0.000373	0.000448	0.000052	0.036591	0.000903	0.000070	0.000022	3.385577	0.229156	2.322	0.158	82	•
Background:	*0.001310*	*0.000140*	*0.000038*	*0.000031*	*0.000008*	*0.000014*	*0.000570*	*0.000057*	*0.000030*	*0.000010*						
J-value = 0.000381073 ± 0.00000188																
		HF		Feldspar												
MY26_1^	1.528206	0.004023	0.494492	0.002740	0.006316	0.000164	0.008425	0.000889	0.000064	0.000022	3.052198	0.023027	2.093	0.020	99	
MY26_2^	0.916637	0.002995	0.289842	0.001499	0.003349	0.000164	0.005867	0.000988	0.000085	0.000023	3.075769	0.030047	2.109	0.024	97	
MY26_3^	1.093978	0.002643	0.348889	0.001127	0.004361	0.000245	0.007251	0.000987	0.000065	0.000023	3.080764	0.023046	2.112	0.020	98	
MY26_4^	2.433186	0.004701	0.753882	0.002771	0.009566	0.000215	0.016355	0.000890	0.000362	0.000022	3.085682	0.015624	2.116	0.016	96	
MY26_5^	1.449572	0.004388	0.447551	0.001892	0.005979	0.000225	0.008377	0.000889	0.000224	0.000032	3.091065	0.026499	2.119	0.022	95	
MY26_6^	0.988406	0.001258	0.311545	0.001365	0.003881	0.000154	0.004476	0.000986	0.000075	0.000023	3.101002	0.025899	2.126	0.021	98	
MY26_7^	1.225891	0.004982	0.384208	0.001592	0.004555	0.000215	0.003723	0.000987	0.000094	0.000015	3.118126	0.021602	2.138	0.019	98	
MY26_8^	1.800091	0.004941	0.563950	0.002161	0.007185	0.000184	0.011677	0.000887	0.000123	0.000022	3.127404	0.018901	2.144	0.017	98	
MY26_9^	1.138813	0.004315	0.354008	0.001013	0.004351	0.000164	0.006501	0.000986	0.000095	0.000023	3.137664	0.024356	2.151	0.020	98	
MY26_10^	1.240027	0.002674	0.388044	0.002109	0.004791	0.000174	0.009021	0.000989	0.000074	0.000023	3.139023	0.025328	2.152	0.021	98	
MY26_11^	1.859046	0.005912	0.447117	0.003102	0.006234	0.000205	0.009235	0.000888	0.001524	0.000091	3.150772	0.065067	2.160	0.046	76	•
MY26_12^	1.867497	0.007144	0.560951	0.002440	0.007379	0.000225	0.011957	0.000888	0.000323	0.000032	3.158966	0.025062	2.166	0.021	95	
MY26_13^	1.696966	0.004336	0.522603	0.001148	0.006786	0.000245	0.011537	0.000890	0.000153	0.000022	3.160517	0.016625	2.167	0.016	97	
MY26_14^	1.580028	0.002615	0.495659	0.002006	0.006081	0.000184	0.011814	0.000891	0.000043	0.000022	3.162027	0.019203	2.168	0.018	99	
MY26_15^	2.115517	0.004670	0.658234	0.002295	0.008228	0.000184	0.013528	0.000889	0.000093	0.000022	3.172328	0.016528	2.175	0.016	99	
MY26_16^	1.593498	0.005044	0.493837	0.002264	0.006221	0.000092	0.007882	0.000985	0.000055	0.000023	3.194110	0.022491	2.190	0.020	99	
MY26_17^	1.457884	0.005922	0.449950	0.001551	0.005315	0.000266	0.008850	0.000887	0.000054	0.000022	3.204704	0.022590	2.197	0.020	99	
Background:	*0.001230*	*0.000140*	*0.000050*	*0.000030*	*0.000010*	*0.000010*	*0.000610*	*0.000060*	*0.000030*	*0.000020*						
J-value = 0.000380886 ± 0.00000188																
MY27_11^	1.364844	0.003431	0.422900	0.001654	0.005291	0.000215	0.007371	0.000991	0.000195	0.000023	3.091291	0.021612	2.119	0.019	96	
MY27_12^	1.559603	0.006837	0.491543	0.002544	0.006528	0.000164	0.007635	0.000989	0.000095	0.000023	3.115978	0.025342	2.135	0.021	98	
MY27_13^	1.605008	0.004555	0.506027	0.001975	0.006119	0.000297	0.009877	0.000991	0.000094	0.000032	3.118838	0.024037	2.137	0.020	98	
MY27_1^	0.912748	0.003021	0.284108	0.001758	0.003251	0.000194	0.007336	0.000993	0.000090	0.000028	3.119361	0.036470	2.138	0.028	97	
MY27_2^	1.187946	0.002167	0.364270	0.002513	0.004365	0.000143	0.007060	0.000694	0.000150	0.000036	3.139652	0.036703	2.152	0.028	96	
MY27_3^	1.147995	0.003462	0.357234	0.001344	0.005026	0.000154	0.007366	0.000990	0.000085	0.000032	3.143494	0.030551	2.154	0.024	98	
MY27_4^	1.962989	0.004085	0.594504	0.002967	0.007735	0.000204	0.011199	0.000563	0.000290	0.000031	3.157802	0.023024	2.164	0.020	96	
MY27_5^	1.038452	0.003856	0.324960	0.000580	0.003977	0.000143	0.006686	0.000694	0.000030	0.000028	3.168450	0.028605	2.171	0.023	99	
MY27_6^	1.100460	0.005149	0.339326	0.002409	0.004453	0.000113	0.007363	0.000990	0.000065	0.000023	3.186722	0.033737	2.184	0.026	98	
MY27_7^	2.811695	0.002782	0.528553	0.001406	0.007309	0.000174	0.009032	0.000693	0.003789	0.000112	3.201125	0.063255	2.194	0.045	60	•
MY27_8^	1.076264	0.003773	0.328414	0.002389	0.004171	0.000205	0.005842	0.000695	0.000080	0.000045	3.205070	0.047737	2.196	0.035	98	
MY27_9^	1.251560	0.003929	0.355487	0.001933	0.004311	0.000102	0.005339	0.000562	0.000371	0.000031	3.211930	0.032910	2.201	0.026	91	•
MY27_10^	1.112715	0.005567	0.336049	0.002605	0.004332	0.000235	0.006708	0.000562	0.000111	0.000031	3.213490	0.040361	2.202	0.030	97	
Background:	*0.001020*	*0.000140*	*0.000050*	*0.000030*	*0.000010*	*0.000010*	*0.000540*	*0.000060*	*0.000030*	*0.000020*						

Sample #	^{40}Ar	±1σ	^{39}Ar	±1σ	^{38}Ar	±1σ	^{37}Ar	±1σ	^{36}Ar	±1σ	$^{40}Ar^*/^{39}ArK$	±1σ	Age (Ma)	±1σ	% $^{40}Ar^*$
McM#62	Snake River Butte														
J-value = 0.000386742 ± 0.0000019															
				Glass											
YR185	0.278642	0.002680	0.039160	0.000540	0.000759	0.000049	0.004580	0.000245	0.000599	0.000030	2.597050	0.242569	1.807	0.169	36
YR185	0.663561	0.002663	0.035065	0.000332	0.000662	0.000083	0.010978	0.006613	0.001919	0.000081	2.753945	0.690192	1.916	0.480	14
YR185	0.241237	0.001126	0.039868	0.000497	0.000652	0.000093	0.007910	0.006609	0.000440	0.000043	2.792781	0.319109	1.943	0.222	46
YR185	0.474190	0.002295	0.073911	0.000828	0.001146	0.000093	0.002184	0.004540	0.000905	0.000075	2.796919	0.302733	1.946	0.211	43
YR185	0.115286	0.001297	0.021762	0.000373	0.000355	0.000043	0.006377	0.006607	0.000180	0.000025	2.853786	0.345991	1.986	0.241	53
YR185	0.263020	0.001837	0.044247	0.000499	0.000810	0.000076	0.002271	0.000245	0.000459	0.000040	2.876307	0.274614	2.002	0.191	48
YR185	0.226850	0.001086	0.044576	0.000446	0.000805	0.000063	0.007922	0.006620	0.000330	0.000033	2.904288	0.224775	2.021	0.157	57
YR185	0.372873	0.002358	0.063042	0.000600	0.001105	0.000073	-0.007733	0.004527	0.000638	0.000040	2.925241	0.193872	2.036	0.135	49
YR185	0.217534	0.002181	0.039423	0.000569	0.000583	0.000062	0.002180	0.004531	0.000345	0.000057	2.930903	0.430459	2.040	0.300	53
YR185	0.287119	0.001796	0.039430	0.000386	0.000739	0.000076	0.002713	0.000245	0.000579	0.000030	2.940419	0.234639	2.046	0.164	40
YR185	0.439836	0.002972	0.062895	0.000621	0.001217	0.000083	0.012096	0.004530	0.000853	0.000040	2.987848	0.196576	2.079	0.137	42
YR185	0.205466	0.001165	0.031754	0.000456	0.000481	0.000062	0.005999	0.004534	0.000374	0.000040	2.989018	0.377836	2.080	0.263	46
YR185	0.222215	0.001309	0.035472	0.000273	0.000626	0.000049	0.002197	0.000245	0.000389	0.000030	3.020501	0.257577	2.102	0.180	48
YR185	0.244418	0.001082	0.047327	0.000509	0.000769	0.000067	0.002056	0.000246	0.000339	0.000030	3.044947	0.194414	2.119	0.136	59
YR185	0.176299	0.001703	0.035793	0.000518	0.000665	0.000062	-0.000870	0.004523	0.000226	0.000040	3.060126	0.337740	2.129	0.235	62
YR185	0.176287	0.001705	0.035794	0.000518	0.000663	0.000062	-0.001143	0.004832	0.000224	0.000041	3.078820	0.345645	2.142	0.241	62
YR185	0.188939	0.001806	0.035630	0.000601	0.000662	0.000053	0.001789	0.006621	0.000261	0.000025	3.136588	0.218646	2.183	0.153	59
YR185	0.156823	0.001106	0.051898	0.000704	0.000693	0.000113	-0.007234	0.004831	-0.000025	0.000035	3.162666	0.202220	2.201	0.141	100
YR185	0.325358	0.003107	0.046365	0.000600	0.000727	0.000062	0.004473	0.004535	0.000605	0.000066	3.164468	0.425806	2.202	0.296	45
YR185	0.310990	0.000480	0.050081	0.000507	0.000767	0.000033	0.002950	0.004541	0.000515	0.000048	3.171447	0.285672	2.207	0.199	51
YR185	0.208791	0.001351	0.039748	0.000590	0.000655	0.000043	-0.003920	0.004526	0.000277	0.000040	3.195399	0.304108	2.223	0.212	60
YR185	0.397556	0.001408	0.070956	0.000735	0.001265	0.000053	0.000255	0.006616	0.000562	0.000033	3.264023	0.144609	2.271	0.101	58
Background:	***0.007244***	***0.000323***	***0.000040***	***0.000020***	***0.000020***	***0.000010***	***0.000497***	***0.000050***	***0.000060***	***0.000010***					
McM#70	Green Canyon Flow														
J-value = 0.000381637 ± 0.00000188															
				Feldspar											
YR242	0.049965	0.000452	0.022550	0.000352	0.000271	0.000041	0.020772	0.000646	0.000039	0.000022	1.705515	0.292394	1.171	0.201	77
YR242	0.201572	0.001596	0.103184	0.000786	0.001375	0.000062	0.001008	0.000643	0.000074	0.000022	1.741097	0.066673	1.196	0.046	89
YR242	0.269848	0.000997	0.117768	0.001024	0.001558	0.000113	0.001246	0.000419	0.000206	0.000022	1.773612	0.058203	1.218	0.041	77
YR242	0.496860	0.002153	0.187875	0.001055	0.002662	0.000092	0.002708	0.000418	0.000536	0.000022	1.801659	0.037989	1.237	0.027	68
YR242	0.290539	0.001058	0.145815	0.000993	0.001784	0.000092	0.000796	0.000644	0.000074	0.000022	1.842074	0.047201	1.265	0.033	92
YR242	0.277774	0.001455	0.145947	0.001065	0.001865	0.000174	0.001710	0.000417	0.000026	0.000022	1.850170	0.047812	1.271	0.034	97
YR242	0.378329	0.001700	0.175649	0.000889	0.002275	0.000102	0.001863	0.000646	0.000174	0.000022	1.861257	0.039664	1.278	0.028	86
YR242	0.267108	0.000718	0.132954	0.000941	0.001466	0.000103	0.001035	0.000418	0.000066	0.000022	1.861467	0.051165	1.279	0.036	93
YR242	0.474061	0.001382	0.233949	0.001034	0.002652	0.000052	0.002339	0.000418	0.000126	0.000022	1.867133	0.029716	1.282	0.022	92
YR242	0.455250	0.002210	0.239885	0.001323	0.002888	0.000102	0.001913	0.000644	0.000024	0.000022	1.868299	0.030606	1.283	0.022	98
YR242	0.242460	0.001430	0.124334	0.000455	0.001416	0.000072	0.001064	0.000645	0.000034	0.000022	1.868373	0.054358	1.284	0.038	96
YR242	0.259693	0.001213	0.128717	0.000693	0.001518	0.000072	0.001115	0.000644	0.000064	0.000022	1.870280	0.052726	1.285	0.037	93
YR242	0.306355	0.001382	0.152997	0.000817	0.001844	0.000123	0.002133	0.000418	0.000066	0.000022	1.874688	0.044784	1.288	0.032	94
YR242	0.233100	0.000759	0.116921	0.001076	0.001405	0.000092	0.001243	0.000418	0.000046	0.000022	1.876552	0.058847	1.289	0.041	94
YR242	0.381119	0.001327	0.180332	0.000858	0.002234	0.000102	0.001113	0.000643	0.000144	0.000022	1.877226	0.038124	1.289	0.027	89
YR242	0.232528	0.001410	0.024967	0.000507	0.000374	0.000041	0.023663	0.000645	0.000628	0.000031	1.878627	0.378844	1.290	0.260	19
YR242	0.561143	0.001862	0.270894	0.000817	0.003234	0.000174	0.002907	0.000417	0.000176	0.000031	1.879578	0.035441	1.291	0.025	91
YR242	0.539361	0.002320	0.277117	0.000983	0.003684	0.000113	0.003128	0.000419	0.000056	0.000022	1.886788	0.025899	1.296	0.019	97
YR242	0.289926	0.001596	0.146622	0.001354	0.001856	0.000072	0.000584	0.000644	0.000044	0.000022	1.888114	0.049180	1.297	0.035	95
YR242	0.412523	0.001254	0.215292	0.001551	0.002960	0.000102	0.001861	0.000645	-0.000006	0.000014	1.924409	0.024221	1.322	0.018	100
YR242	0.425190	0.001648	0.213969	0.000931	0.002479	0.000123	0.002237	0.000646	0.000044	0.000014	1.926594	0.022239	1.323	0.017	97
YR242	0.337320	0.001643	0.149989	0.001541	0.001732	0.000092	0.001816	0.000417	0.000156	0.000022	1.941251	0.049144	1.333	0.035	86
Background:	***0.001880***	***0.000180***	***0.000040***	***0.000030***	***0.000020***	***0.000020***	***0.000530***	***0.000060***	***0.000030***	***0.000020***					
J-value = 0.000381449 ± 0.00000188															
YR242	0.216951	0.001472	0.109519	0.000517	0.001590	0.000113	0.003309	0.000647	0.000064	0.000022	1.809426	0.061895	1.242	0.043	91
YR242	0.637559	0.000997	0.322541	0.001633	0.003716	0.000164	0.004691	0.000647	0.000133	0.000022	1.854641	0.022588	1.273	0.017	94
YR242	0.568428	0.001586	0.271806	0.001303	0.003583	0.000164	0.003415	0.000647	0.000214	0.000022	1.859144	0.026348	1.276	0.019	89
YR242	0.502515	0.002168	0.238064	0.001706	0.003154	0.000143	0.004959	0.000647	0.000143	0.000031	1.933176	0.042453	1.327	0.030	91

Sample #	^{40}Ar	±1σ	^{39}Ar	±1σ	^{38}Ar	±1σ	^{37}Ar	±1σ	^{36}Ar	±1σ	$^{40}Ar^*/^{39}ArK$	±1σ	Age (Ma)	±1σ	% $^{40}Ar^*$	
McM#70	Green Canyon Flow															
J-value = 0.000381449 ± 0.00000188																
				Feldspar												
YR242	0.345007	0.001180	0.152714	0.001117	0.001992	0.000143	0.001374	0.000117	0.000226	0.000032	1.822562	0.063217	1.251	0.044	80	
YR242	0.364228	0.001410	0.141855	0.001303	0.001937	0.000092	0.002403	0.000648	0.000354	0.000031	1.830582	0.068435	1.257	0.047	71	*
YR242	0.449780	0.001482	0.202959	0.001220	0.002714	0.000082	0.003846	0.000648	0.000263	0.000022	1.832575	0.034876	1.258	0.025	83	
YR242	0.286035	0.001097	0.137663	0.001117	0.001543	0.000113	0.001863	0.000117	0.000106	0.000022	1.851319	0.051101	1.271	0.036	89	
YR242	0.299465	0.001470	0.134913	0.000290	0.001941	0.000051	0.001869	0.000117	0.000166	0.000022	1.857185	0.050524	1.275	0.035	83	
YR242	0.677015	0.002501	0.304613	0.001437	0.004016	0.000133	0.002573	0.000117	0.000365	0.000014	1.868153	0.018359	1.282	0.014	84	
YR242	0.434819	0.001398	0.211296	0.001055	0.002534	0.000174	0.002354	0.000117	0.000135	0.000014	1.868539	0.023016	1.283	0.017	91	
YR242	0.266206	0.001709	0.135203	0.000962	0.001778	0.000062	0.000834	0.000117	0.000036	0.000022	1.890736	0.052423	1.298	0.037	96	
YR242	0.239968	0.001356	0.117784	0.000827	0.001543	0.000092	0.001810	0.000117	0.000056	0.000022	1.898067	0.059014	1.303	0.041	93	
YR242	0.294514	0.001605	0.141260	0.000900	0.001716	0.000102	0.001864	0.000117	0.000086	0.000022	1.906036	0.049820	1.308	0.035	91	
YR242	0.443690	0.001439	0.220497	0.001799	0.002810	0.000133	0.002077	0.000116	0.000075	0.000022	1.911113	0.034509	1.312	0.025	95	
Background:	*0.001890*	*0.000180*	*0.000040*	*0.000030*	*0.000020*	*0.000020*	*0.000530*	*0.000060*	*0.000030*	*0.000020*						
J-value = 0.000380698 ± 0.00000188																
		HF		Feldspar												
MY28_1	0.202131	0.001312	0.104843	0.000879	0.001126	0.000092	0.001027	0.000416	0.000066	0.000024	1.741081	0.069851	1.193	0.048	90	
MY28_2	0.313199	0.001840	0.146617	0.001344	0.001839	0.000123	0.000426	0.000665	0.000166	0.000030	1.801840	0.064684	1.235	0.045	84	
MY28_3	0.298483	0.001281	0.105391	0.000693	0.001413	0.000082	0.001264	0.000416	0.000366	0.000033	1.805281	0.093178	1.237	0.064	63	
MY28_4	0.306268	0.001582	0.149542	0.000972	0.001649	0.000133	0.001482	0.000543	0.000122	0.000023	1.806048	0.048349	1.237	0.034	88	
MY28_5	0.307450	0.001270	0.136355	0.001075	0.001893	0.000072	0.001338	0.000414	0.000206	0.000024	1.807871	0.054370	1.239	0.038	80	
MY28_6	0.294265	0.001997	0.102738	0.000827	0.001348	0.000082	0.002099	0.000664	0.000365	0.000030	1.813128	0.090749	1.242	0.063	63	*
MY28_7	0.204558	0.001301	0.072379	0.000806	0.001065	0.000062	0.000237	0.000416	0.000247	0.000024	1.819786	0.100978	1.247	0.069	64	*
MY28_8	0.438101	0.002259	0.215079	0.000993	0.002661	0.000133	0.002568	0.000544	0.000152	0.000023	1.827856	0.034509	1.252	0.025	90	
MY28_9	0.255850	0.002030	0.114597	0.001138	0.001476	0.000113	0.001794	0.000544	0.000152	0.000032	1.839679	0.086760	1.260	0.060	82	
MY28_10	0.306723	0.001426	0.152519	0.000952	0.001833	0.000093	0.002179	0.000543	0.000082	0.000023	1.851634	0.047202	1.269	0.033	92	
MY28_11	0.343216	0.001415	0.174789	0.001148	0.002273	0.000164	0.001248	0.000542	0.000063	0.000023	1.857838	0.041746	1.273	0.029	95	
MY28_12	0.391215	0.002572	0.179117	0.001034	0.002281	0.000102	0.001417	0.000414	0.000196	0.000016	1.860458	0.032405	1.275	0.023	85	
MY28_13	0.321662	0.001104	0.133770	0.001086	0.001709	0.000102	0.003162	0.000416	0.000246	0.000033	1.861767	0.074206	1.276	0.051	77	
MY28_14	0.393170	0.001509	0.178263	0.001158	0.002355	0.000103	0.001330	0.000545	0.000203	0.000023	1.869376	0.041092	1.281	0.029	85	
MY28_15	0.690850	0.002655	0.344427	0.002554	0.004399	0.000205	0.003725	0.000543	0.000152	0.000032	1.875501	0.031850	1.285	0.023	93	
MY28_16	0.381122	0.002050	0.190380	0.001158	0.002263	0.000103	0.001717	0.000544	0.000072	0.000023	1.889521	0.039197	1.295	0.028	94	
MY28_17	0.377568	0.002445	0.182729	0.002213	0.002330	0.000102	0.001263	0.000665	0.000106	0.000021	1.895396	0.042600	1.299	0.030	92	
MY28_18	0.423915	0.002144	0.199902	0.001127	0.002181	0.000093	0.001015	0.000542	0.000143	0.000023	1.909833	0.037409	1.308	0.027	90	
MY28_19	0.149448	0.001073	0.064851	0.000507	0.000769	0.000092	0.001974	0.000416	0.000086	0.000024	1.912385	0.110831	1.310	0.076	83	
MY28_20	0.286036	0.001499	0.123804	0.000383	0.001699	0.000113	0.001182	0.000415	0.000166	0.000016	1.913563	0.041310	1.311	0.029	83	
MY28_21	0.221178	0.001415	0.105459	0.001117	0.001353	0.000113	-0.000993	0.000542	0.000063	0.000015	1.920422	0.049362	1.316	0.035	91	
MY28_22	0.210376	0.001322	0.099177	0.001127	0.001321	0.000082	0.001979	0.000417	0.000066	0.000033	1.924439	0.100670	1.319	0.069	91	
MY28_23	0.187231	0.001343	0.092570	0.000558	0.001034	0.000041	0.001267	0.000417	0.000016	0.000024	1.970749	0.078335	1.350	0.054	97	
MY28_24	0.566026	0.001905	0.203592	0.001117	0.002733	0.000103	0.002095	0.000542	0.000532	0.000042	2.007593	0.062155	1.375	0.043	72	*
MY28_25	1.554292	0.002780	0.268572	0.001499	0.003908	0.000194	0.002331	0.000543	0.003432	0.000101	2.010879	0.111813	1.378	0.077	34	*
MY28_26	0.118774	0.000558	0.025102	0.000465	0.000390	0.000031	0.028519	0.000415	0.000209	0.000024	2.271159	0.284495	1.556	0.195	47	*
Background:	*0.000820*	*0.000140*	*0.000020*	*0.000030*	*0.000010*	*0.000010*	*0.000500*	*0.000060*	*0.000020*	*0.000010*						

Notes:

^ = Single feldspar crystals measure 1 - 2mm in diameter

HF = Feldspar crystals washed in weak (10 %) hydrofloric acid solution

* = Alteration product

◊ = Xenocryst

† = Suspected ^{36}Ar contamination during sample loading

A3.1.2.1 Bishop Tuff single-grain fusion Ar-Ar data

Sample #	^{40}Ar	±1σ	^{39}Ar	±1σ	^{38}Ar	±1σ	^{37}Ar	±1σ	^{36}Ar	±1σ	$^{40}Ar^*/^{39}ArK$	±1σ	Age (Ma)	±1σ	% $^{40}Ar^*$
McM#65		Bishop Tuff													
J-value = 0.000383903 ± 0.0000019															
		F5		Feldspar											
BP029	0.019805	0.000455	0.011338	0.000239	0.000267	0.000041	0.010298	0.000806	0.000059	0.000022	0.196258	0.587773	0.136	0.406	10
BP029	0.040176	0.000483	0.014939	0.000372	0.000228	0.000023	0.016610	0.000843	0.000104	0.000022	0.628843	0.442888	0.435	0.306	23
BP029	0.091848	0.001129	0.019350	0.000311	0.000236	0.000031	0.014452	0.000805	0.000268	0.000022	0.647958	0.348675	0.448	0.241	13
BP029	0.032327	0.000724	0.020980	0.000342	0.000297	0.000051	0.019176	0.000806	0.000047	0.000022	0.876847	0.319088	0.606	0.220	56
BP029	0.036033	0.001102	0.018410	0.000528	0.000238	0.000042	0.021732	0.000839	0.000063	0.000022	0.949031	0.364182	0.656	0.252	48
BP029	0.019442	0.000312	0.013206	0.000341	0.000146	0.000031	0.015043	0.000585	0.000022	0.000022	0.974061	0.488110	0.673	0.337	66
BP029	0.030897	0.000451	0.021018	0.000476	0.000257	0.000031	0.020001	0.001017	0.000035	0.000022	0.982211	0.305314	0.679	0.211	66
BP029	0.344147	0.002291	0.166913	0.000476	0.002160	0.000092	0.001473	0.000587	0.000576	0.000041	1.042340	0.073771	0.720	0.051	50
BP029	0.209266	0.001633	0.161480	0.001282	0.001843	0.000123	0.000550	0.000845	0.000138	0.000022	1.042615	0.042876	0.720	0.030	80
BP029	0.127009	0.001029	0.107481	0.000548	0.001330	0.000072	0.000569	0.001013	0.000050	0.000022	1.044637	0.060397	0.722	0.042	88
BP029	0.191473	0.002237	0.168904	0.001830	0.002047	0.000072	0.002060	0.000843	0.000048	0.000014	1.049601	0.030180	0.725	0.021	93
BP029	0.354845	0.002530	0.281745	0.001262	0.003621	0.000174	0.000962	0.000844	0.000198	0.000022	1.051459	0.025505	0.727	0.018	83
BP029	0.103802	0.001019	0.090543	0.000590	0.001097	0.000062	-0.001509	0.000842	0.000029	0.000022	1.051896	0.074014	0.727	0.051	92
BP029	0.155210	0.001341	0.124542	0.001210	0.001547	0.000082	0.000274	0.000840	0.000078	0.000014	1.059993	0.036560	0.732	0.026	85
BP029	0.255550	0.000970	0.163035	0.001148	0.002078	0.000092	0.001192	0.000587	0.000276	0.000031	1.067327	0.057356	0.738	0.040	68
BP029	0.045899	0.000842	0.039841	0.000331	0.000472	0.000041	-0.000143	0.001017	0.000010	0.000022	1.077600	0.161872	0.745	0.112	93
BP029	0.113979	0.001913	0.093689	0.001303	0.001330	0.000082	0.000060	0.000807	0.000042	0.000022	1.083445	0.075365	0.749	0.052	89
BP029	0.172527	0.000590	0.152125	0.001375	0.001741	0.000112	0.001472	0.000586	0.000026	0.000022	1.083831	0.043559	0.749	0.030	96
BP029	0.171690	0.001758	0.147561	0.001799	0.001700	0.000154	0.000683	0.000839	0.000038	0.000022	1.086642	0.048110	0.751	0.033	93
BP029	0.189929	0.001424	0.153126	0.001158	0.001892	0.000113	0.002431	0.001018	0.000079	0.000022	1.087210	0.043499	0.751	0.030	88
BP029	0.118012	0.000887	0.093068	0.000972	0.001138	0.000092	0.000772	0.000587	0.000056	0.000022	1.090064	0.070664	0.753	0.049	86
BP029	0.393991	0.001978	0.269318	0.002141	0.003110	0.000123	0.003012	0.000586	0.000325	0.000041	1.105830	0.046322	0.764	0.032	75
BP029	0.192305	0.002072	0.150801	0.002275	0.001904	0.000123	0.002166	0.000585	0.000086	0.000022	1.107336	0.047809	0.765	0.033	87
BP029	0.198209	0.002238	0.173754	0.002358	0.002150	0.000082	0.001099	0.000844	0.000018	0.000014	1.109652	0.031067	0.767	0.022	97
BP029	0.113733	0.001351	0.099436	0.000342	0.001310	0.000102	0.000711	0.001012	0.000010	0.000013	1.114628	0.040886	0.770	0.029	97
BP029	0.094143	0.001269	0.082021	0.000972	0.001046	0.000072	-0.000585	0.000841	0.000009	0.000014	1.116258	0.054628	0.771	0.038	97
BP029	0.184551	0.001570	0.161813	0.000972	0.001964	0.000102	0.000285	0.001014	0.000010	0.000022	1.122395	0.041182	0.776	0.029	98
BP029	0.149226	0.001648	0.118483	0.001365	0.001586	0.000102	0.001870	0.000508	0.000055	0.000021	1.123536	0.056674	0.776	0.039	89
BP029	0.173161	0.001281	0.136552	0.000424	0.001557	0.000082	0.000912	0.000587	0.000066	0.000022	1.125251	0.048138	0.778	0.034	89
BP029	0.030524	0.000815	0.018973	0.000414	0.000197	0.000031	0.020156	0.000584	0.000031	0.000013	1.127431	0.211015	0.779	0.146	70
BP029	0.177744	0.001343	0.150140	0.001231	0.001986	0.000102	-0.000070	0.000583	0.000026	0.000022	1.132151	0.044722	0.782	0.031	96
BP029	0.192169	0.001343	0.123781	0.001375	0.001628	0.000112	0.000768	0.000584	0.000176	0.000022	1.132219	0.054536	0.782	0.038	73
BP029	0.220837	0.001925	0.187177	0.001830	0.002548	0.000082	0.001650	0.000845	0.000028	0.000014	1.135414	0.026877	0.785	0.019	96
BP029	0.217505	0.001341	0.165464	0.000983	0.002219	0.000092	-0.000854	0.001013	0.000100	0.000022	1.135523	0.039995	0.785	0.028	86
BP029	0.265051	0.002402	0.227405	0.001562	0.002699	0.000092	0.001539	0.000805	0.000022	0.000014	1.137198	0.022816	0.786	0.016	98
BP029	0.133691	0.001208	0.113223	0.000755	0.001414	0.000082	0.000628	0.000584	0.000016	0.000022	1.138802	0.058279	0.787	0.040	96
BP029	0.109688	0.000604	0.096262	0.000879	0.001412	0.000092	-0.000143	0.001016	0.000000	0.000013	1.139359	0.041458	0.787	0.029	100
BP029	0.186961	0.002572	0.164039	0.001913	0.002006	0.000102	0.000490	0.000586	-0.000004	0.000013	1.146726	0.031424	0.792	0.022	100
BP029	0.050494	0.001027	0.018611	0.000445	0.000216	0.000041	0.020786	0.000805	0.000097	0.000022	1.177534	0.362563	0.814	0.251	43
BP029	0.123239	0.001030	0.088835	0.001303	0.001148	0.000062	-0.000137	0.000840	0.000059	0.000022	1.192316	0.077139	0.824	0.053	86
BP029	0.044564	0.000606	0.020861	0.000352	0.000249	0.000032	0.020964	0.000841	0.000063	0.000022	1.243566	0.318130	0.859	0.220	58
BP029	0.024290	0.000473	0.017885	0.000610	0.000259	0.000042	0.018110	0.000843	0.000004	0.000022	1.295811	0.372294	0.895	0.257	95
BP029	0.029683	0.000749	0.011603	0.000239	0.000165	0.000021	0.010696	0.001015	0.000047	0.000022	1.357013	0.554679	0.938	0.383	53
BP029	0.023148	0.000548	0.013704	0.000342	0.000236	0.000041	0.014209	0.000806	-0.000002	0.000014	1.722430	0.315176	1.190	0.218	100
Background:	*0.002280*	*0.000181*	*0.000020*	*0.000020*	*0.000010*	*0.000010*	*0.000448*	*0.000050*	*0.000020*	*0.000010*					
J-value = 0.000381511 ± 0.0000019															
		Ig1Eb		Feldspar		Pumice #1									
BP097	0.019014	0.000534	0.012823	0.000220	0.000141	0.000034	0.010918	0.000399	0.000021	0.000023	0.989810	0.522451	0.680	0.359	66
BP097	0.333319	0.002186	0.126005	0.001158	0.001737	0.000090	0.001391	0.000239	0.000670	0.000030	1.074904	0.073129	0.738	0.050	40
BP097	0.229971	0.001301	0.201635	0.000704	0.002400	0.000096	0.001148	0.000399	0.000024	0.000023	1.105384	0.033939	0.759	0.024	97
BP097	0.121957	0.000841	0.105227	0.000343	0.001316	0.000116	0.000697	0.000399	0.000004	0.000014	1.147464	0.041655	0.788	0.029	99
BP097	0.033627	0.000505	0.020862	0.000231	0.000274	0.000041	0.000123	0.000399	0.000024	0.000023	1.268352	0.321170	0.871	0.221	78
BP097	0.086577	0.000515	0.025742	0.000333	0.000315	0.000077	0.029241	0.000399	0.000177	0.000023	1.336715	0.260632	0.918	0.179	39

Sample #	^{40}Ar	±1σ	^{39}Ar	±1σ	^{38}Ar	±1σ	^{37}Ar	±1σ	^{36}Ar	±1σ	$^{40}Ar^*/^{39}ArK$	±1σ	Age (Ma)	±1σ	% $^{40}Ar^*$	
McM#65		Bishop Tuff														
J-value = 0.000381511 ± 0.0000019																
		Ig1Eb		Feldspar		Pumice #1										
BP097	0.244827	0.001989	0.018063	0.000487	0.000396	0.000052	0.017373	0.000988	0.000795	0.000041	0.541842	0.677041	**0.371**	**0.463**	3	•
BP097	0.083912	0.000324	0.030240	0.000497	0.000472	0.000051	0.021327	0.000506	0.000209	0.000021	0.729137	0.209823	**0.499**	**0.144**	26	
BP097	0.024080	0.000663	0.014317	0.000259	0.000140	0.000032	0.021616	0.000987	0.000044	0.000013	0.768136	0.270864	**0.526**	**0.185**	45	
BP097	0.032139	0.000740	0.020207	0.000292	0.000294	0.000049	0.021362	0.000399	0.000049	0.000023	0.879418	0.332584	**0.604**	**0.228**	55	
BP097	0.025581	0.000453	0.016081	0.000176	0.000201	0.000034	0.016403	0.000983	0.000030	0.000023	1.037668	0.417556	**0.710**	**0.286**	65	
BP097	0.175175	0.000745	0.126918	0.000724	0.001561	0.000072	0.002258	0.000986	0.000139	0.000031	1.055653	0.072874	**0.723**	**0.050**	76	
BP097	0.282846	0.001209	0.177634	0.001076	0.002184	0.000113	0.000290	0.000982	0.000320	0.000022	1.060095	0.037129	**0.726**	**0.026**	66	
BP097	0.339187	0.001438	0.267935	0.001551	0.003512	0.000154	0.002257	0.000985	0.000184	0.000023	1.063169	0.026283	**0.728**	**0.018**	84	
BP097	0.151837	0.001096	0.124831	0.001438	0.001386	0.000103	0.002255	0.000984	0.000064	0.000023	1.065203	0.055724	**0.729**	**0.038**	87	
BP097	0.295699	0.002031	0.267561	0.002730	0.003211	0.000092	0.000991	0.000505	0.000035	0.000013	1.066799	0.019199	**0.730**	**0.014**	96	
BP097	0.176807	0.001334	0.125617	0.001189	0.001591	0.000053	0.001948	0.000988	0.000144	0.000023	1.068930	0.055290	**0.732**	**0.038**	76	
BP097	0.154930	0.001220	0.105884	0.000600	0.001254	0.000133	0.001929	0.000985	0.000139	0.000031	1.073920	0.087741	**0.735**	**0.060**	73	
BP097	0.166690	0.000870	0.142645	0.000931	0.001840	0.000154	-0.000481	0.000961	0.000045	0.000011	1.075077	0.024948	**0.736**	**0.018**	92	
BP097	0.555270	0.003965	0.153126	0.000952	0.001943	0.000092	0.017705	0.000506	0.001320	0.000051	1.078323	0.101204	**0.738**	**0.069**	29	
BP097	0.161084	0.001210	0.136404	0.001024	0.001826	0.000134	-0.000105	0.000986	0.000044	0.000023	1.084585	0.050546	**0.742**	**0.035**	92	
BP097	0.178695	0.000983	0.147224	0.000714	0.001930	0.000116	0.001110	0.000400	0.000064	0.000014	1.085319	0.030310	**0.745**	**0.021**	89	
BP097	0.582568	0.002729	0.170123	0.000776	0.002544	0.000102	0.001915	0.000567	0.001341	0.000060	1.094832	0.106234	**0.749**	**0.073**	31	
BP097	0.184652	0.001365	0.161998	0.001551	0.002235	0.000083	0.001473	0.000987	0.000024	0.000023	1.095964	0.043469	**0.750**	**0.030**	96	
BP097	0.191320	0.001262	0.162577	0.001138	0.002071	0.000113	0.002102	0.000986	0.000044	0.000023	1.097024	0.042607	**0.751**	**0.029**	93	
BP097	0.188925	0.000674	0.143291	0.001293	0.001887	0.000063	0.000525	0.000985	0.000104	0.000023	1.103369	0.048010	**0.755**	**0.033**	84	
BP097	0.391605	0.003361	0.329088	0.002255	0.003998	0.000102	0.004477	0.000506	0.000094	0.000021	1.105729	0.023034	**0.757**	**0.016**	93	
BP097	0.267415	0.001229	0.198624	0.002193	0.002452	0.000123	0.002916	0.000567	0.000161	0.000021	1.106972	0.034305	**0.758**	**0.024**	82	
BP097	0.175120	0.001313	0.121087	0.001789	0.001408	0.000092	0.015006	0.000983	0.000136	0.000031	1.114276	0.078392	**0.763**	**0.054**	77	
BP097	0.070106	0.000298	0.046381	0.000642	0.000498	0.000052	0.029259	0.000984	0.000062	0.000022	1.114929	0.138649	**0.763**	**0.095**	73	
BP097	0.413020	0.002331	0.345181	0.001593	0.004028	0.000113	0.001717	0.000506	0.000095	0.000021	1.115593	0.020182	**0.764**	**0.014**	93	
BP097	0.164085	0.001230	0.130724	0.001283	0.001694	0.000143	0.002256	0.000985	0.000059	0.000022	1.120922	0.050928	**0.767**	**0.035**	89	
BP097	0.173339	0.001531	0.146309	0.000983	0.001694	0.000092	0.000781	0.000983	0.000030	0.000022	1.124571	0.045494	**0.770**	**0.031**	95	
BP097	0.289573	0.001313	0.257222	0.001045	0.003247	0.000154	0.001925	0.000983	-0.000001	0.000022	1.126358	0.025734	**0.771**	**0.018**	100	
BP097	0.141522	0.001438	0.093588	0.000611	0.001193	0.000062	0.000785	0.000988	0.000120	0.000022	1.133944	0.070307	**0.776**	**0.048**	75	
BP097	0.141632	0.001178	0.106485	0.001107	0.001234	0.000123	0.000291	0.000986	0.000070	0.000022	1.136033	0.062092	**0.778**	**0.043**	85	
BP097	0.130820	0.000832	0.108398	0.000209	0.001463	0.000102	0.005215	0.000507	0.000024	0.000013	1.142457	0.035210	**0.782**	**0.024**	95	
BP097	0.107895	0.000755	0.089337	0.000652	0.001070	0.000072	0.001436	0.000984	0.000020	0.000013	1.142825	0.044322	**0.782**	**0.031**	95	
BP097	0.126068	0.001636	0.107417	0.000734	0.001294	0.000123	0.000839	0.000984	0.000004	0.000015	1.162025	0.043715	**0.795**	**0.030**	99	
BP097	0.184821	0.001668	0.090298	0.000590	0.001218	0.000082	0.025852	0.000506	0.000268	0.000031	1.169271	0.103258	**0.800**	**0.071**	57	
BP097	0.884652	0.003229	0.189194	0.001572	0.002799	0.000082	0.000583	0.000567	0.002242	0.000031	1.174906	0.051929	**0.804**	**0.036**	24	
BP097	0.050158	0.000522	0.036107	0.000300	0.000415	0.000043	0.025931	0.000987	0.000008	0.000015	1.327177	0.120997	**0.908**	**0.083**	95	
BP097	0.094481	0.000653	0.001599	0.000066	0.000069	0.000023	0.002425	0.000987	0.000299	0.000022	3.765529	4.016143	**2.576**	**2.746**	5	•
Background:	***0.001325***	***0.000158***	***0.000030***	***0.000020***	***0.000010***	***0.000010***	***0.000468***	***0.000050***	***0.000020***	***0.000010***						
J-value = 0.000373263 ± 0.0000019																
		Ig1Eb		Feldspar		Pumice #2										
BP097	0.033746	0.007221	0.021444	0.000375	0.000311	0.000046	0.024913	0.003088	0.000062	0.000034	0.719721	0.577076	**0.484**	**0.388**	45	
BP097	0.019942	0.007206	0.015243	0.000293	0.000137	0.000037	0.014874	0.003093	0.000025	0.000034	0.830827	0.811225	**0.558**	**0.545**	63	
BP097	0.148282	0.007223	0.120792	0.000591	0.001578	0.000114	0.001998	0.003091	0.000078	0.000041	1.036666	0.116229	**0.697**	**0.078**	84	
BP097	0.237352	0.001466	0.198476	0.001004	0.002603	0.000113	0.001944	0.000228	0.000099	0.000020	1.047755	0.031106	**0.704**	**0.021**	87	
BP097	0.185552	0.007281	0.163347	0.001253	0.002028	0.000065	-0.001357	0.003087	0.000039	0.000041	1.065509	0.086431	**0.716**	**0.058**	94	
BP097	0.317563	0.001450	0.261189	0.000901	0.003233	0.000076	0.009884	0.002001	0.000127	0.000037	1.071899	0.042544	**0.720**	**0.029**	88	
BP097	0.165162	0.000987	0.137840	0.001314	0.001745	0.000073	0.001449	0.000228	0.000050	0.000020	1.091843	0.044677	**0.734**	**0.030**	91	
BP097	0.104771	0.000645	0.086953	0.000808	0.001172	0.000063	0.000770	0.000228	0.000030	0.000010	1.103663	0.036239	**0.742**	**0.025**	92	
BP097	0.027601	0.000697	0.017634	0.000488	0.000191	0.000043	0.016110	0.000228	0.000026	0.000020	1.134007	0.338917	**0.762**	**0.228**	72	
BP097	0.268617	0.007338	0.209938	0.000973	0.002355	0.000145	0.011505	0.003090	0.000096	0.000041	1.145052	0.067294	**0.769**	**0.045**	89	
BP097	0.324084	0.001977	0.162328	0.000529	0.002099	0.000096	0.006419	0.002000	0.000458	0.000046	1.162382	0.084003	**0.781**	**0.057**	58	
BP097	0.041402	0.000400	0.026632	0.000488	0.000253	0.000034	0.024566	0.000228	0.000033	0.000010	1.182970	0.114040	**0.795**	**0.077**	76	
BP097	0.017102	0.000440	0.010898	0.000232	0.000110	0.000034	0.010966	0.000228	-0.000003	0.000010	1.648022	0.276381	**1.107**	**0.186**	100	

Sample #	^{40}Ar	±1σ	^{39}Ar	±1σ	^{38}Ar	±1σ	^{37}Ar	±1σ	^{36}Ar	±1σ	$^{40}Ar^*/^{39}ArK$	±1σ	Age (Ma)	±1σ	% $^{40}Ar^*$	
McM#65		Bishop Tuff														
J-value = 0.000373263 ± 0.0000019																
		Ig1Eb		Feldspar		Pumice #2										
BP097	0.018214	0.000498	0.015099	0.000193	0.000193	0.000042	0.003879	0.001914	0.000019	0.000017	0.834962	0.340891	0.561	0.229	69	*
BP097	0.164403	0.001187	0.140798	0.001169	0.001801	0.000113	0.002932	0.005814	0.000097	0.000028	0.964657	0.059417	0.648	0.040	82	
BP097	0.268990	0.007401	0.220026	0.001201	0.002928	0.000114	0.009839	0.003094	0.000146	0.000041	1.026503	0.064404	0.690	0.043	84	
BP097	0.277583	0.007422	0.218840	0.001149	0.002519	0.000145	0.004803	0.003096	0.000157	0.000041	1.056031	0.064794	0.710	0.044	83	
BP097	0.224804	0.001715	0.188009	0.001087	0.002404	0.000083	0.002928	0.005805	0.000087	0.000028	1.059403	0.044987	0.712	0.030	88	
BP097	0.202637	0.007394	0.155763	0.001253	0.001742	0.000135	0.000320	0.003096	0.000098	0.000041	1.114091	0.091054	0.749	0.061	85	
BP097	0.029967	0.000619	0.022920	0.000373	0.000254	0.000042	0.022031	0.001915	0.000014	0.000033	1.124885	0.428896	0.756	0.288	86	
BP097	0.021030	0.001063	0.012851	0.000291	0.000166	0.000034	0.022064	0.005812	0.000012	0.000028	1.368434	0.644582	0.919	0.433	83	
Background:	*0.007500*	*0.000349*	*0.000040*	*0.000020*	*0.000020*	*0.000010*	*0.000488*	*0.000050*	*0.000060*	*0.000010*						
J-value = 0.000377924 ± 0.0000019																
		Ig2NWa		Feldspar												
BP113	0.141092	0.001206	0.121345	0.000941	0.001418	0.000123	-0.000292	0.001348	0.000043	0.000021	1.057017	0.052928	0.719	0.036	91	
BP113	0.224408	0.001508	0.145696	0.001489	0.001663	0.000092	0.036522	0.001349	0.000234	0.000021	1.066350	0.045317	0.725	0.031	69	*
BP113	0.259538	0.000892	0.222907	0.001665	0.002645	0.000156	0.002387	0.000400	0.000074	0.000023	1.066696	0.031226	0.726	0.022	92	
BP113	0.153661	0.000822	0.128986	0.000910	0.001541	0.000082	0.001865	0.001344	0.000053	0.000012	1.070252	0.029247	0.728	0.020	90	
BP113	0.143063	0.000770	0.125336	0.000931	0.001398	0.000052	0.001101	0.001351	0.000023	0.000012	1.087108	0.030091	0.740	0.021	95	
BP113	0.203168	0.001268	0.176576	0.001262	0.002083	0.000082	0.002636	0.001344	0.000033	0.000021	1.095983	0.036836	0.746	0.025	95	
BP113	0.272406	0.001237	0.234364	0.000827	0.003074	0.000103	0.002807	0.001352	0.000053	0.000012	1.096015	0.016480	0.746	0.012	94	
BP113	0.263424	0.000564	0.226040	0.000786	0.002726	0.000154	0.002033	0.001353	0.000053	0.000021	1.096372	0.027919	0.746	0.019	94	
BP113	0.143063	0.000892	0.115884	0.000848	0.001368	0.000116	0.001604	0.000400	0.000054	0.000023	1.097192	0.058654	0.746	0.040	89	
BP113	0.228018	0.001293	0.194997	0.001469	0.002766	0.000154	0.002566	0.000982	0.000044	0.000023	1.103022	0.035937	0.750	0.025	94	
BP113	0.303090	0.001927	0.263012	0.001696	0.003185	0.000103	0.002565	0.000982	0.000044	0.000015	1.103210	0.019310	0.750	0.014	96	
BP113	0.123039	0.001071	0.104012	0.001272	0.001296	0.000092	0.000791	0.001350	0.000023	0.000012	1.117234	0.038189	0.760	0.026	94	
BP113	0.251520	0.001480	0.218507	0.000972	0.002879	0.000083	0.000994	0.000981	0.000024	0.000015	1.117871	0.021442	0.760	0.015	97	
BP113	0.184927	0.001143	0.159306	0.001231	0.002021	0.000133	0.003736	0.001352	0.000022	0.000021	1.119386	0.040680	0.761	0.028	96	
BP113	0.369076	0.001241	0.328752	0.001489	0.004218	0.000215	0.003353	0.000983	0.000004	0.000015	1.119462	0.014541	0.762	0.011	100	
BP113	0.222562	0.001276	0.180844	0.001335	0.002154	0.000103	0.019591	0.000295	0.000065	0.000020	1.124787	0.034433	0.765	0.024	91	
BP113	0.247686	0.001997	0.214084	0.000796	0.002686	0.000092	0.002336	0.001349	0.000023	0.000021	1.125601	0.030829	0.766	0.021	97	
BP113	0.103470	0.000664	0.090540	0.000838	0.001162	0.000073	0.000052	0.000982	0.000004	0.000015	1.128350	0.049370	0.768	0.034	99	
BP113	0.202135	0.000977	0.172761	0.001448	0.002215	0.000103	0.002021	0.001345	0.000023	0.000021	1.131037	0.037701	0.769	0.026	97	
BP113	0.135666	0.000798	0.114537	0.001036	0.001469	0.000063	0.001298	0.000295	0.000020	0.000010	1.133765	0.028602	0.771	0.020	96	
BP113	0.169235	0.001414	0.145615	0.000765	0.001674	0.000143	0.000946	0.001351	0.000013	0.000021	1.135653	0.044267	0.773	0.030	98	
BP113	0.242022	0.001112	0.212109	0.001293	0.002634	0.000174	0.002335	0.001348	0.000003	0.000021	1.137245	0.030614	0.774	0.021	100	
BP113	0.183116	0.001339	0.145009	0.001139	0.001888	0.000124	0.001889	0.000295	0.000059	0.000010	1.141540	0.024078	0.777	0.017	90	
BP113	0.251281	0.001695	0.216112	0.000952	0.002532	0.000123	0.000943	0.001346	0.000013	0.000012	1.144846	0.018859	0.779	0.014	98	
BP113	0.180738	0.001591	0.155842	0.001531	0.002011	0.000082	0.002484	0.001345	0.000003	0.000021	1.154680	0.042779	0.785	0.029	100	
BP113	0.191458	0.000771	0.156682	0.000714	0.001889	0.000106	0.001605	0.000400	0.000034	0.000014	1.158091	0.028259	0.788	0.020	95	
BP113	0.213891	0.000787	0.122445	0.000953	0.001551	0.000053	0.001087	0.000294	0.000080	0.000020	1.554468	0.050153	1.057	0.035	89	◊
BP113	1.130165	0.003749	0.085030	0.000531	0.001224	0.000063	0.043567	0.000294	0.001108	0.000040	9.439232	0.157045	6.411	0.112	71	◊
Background:	*0.001325*	*0.000158*	*0.000030*	*0.000020*	*0.000010*	*0.000010*	*0.000468*	*0.000050*	*0.000020*	*0.000010*						
J-value = 0.000375533 ± 0.0000019																
		Ig2Nb		Feldspar												
BP168	0.253448	0.001520	0.196990	0.001045	0.002564	0.000133	0.002920	0.000568	0.000141	0.000021	1.075252	0.033121	0.727	0.023	83	
BP168	0.332009	0.001364	0.203297	0.001417	0.002564	0.000174	0.004758	0.000568	0.000380	0.000031	1.080190	0.045843	0.730	0.031	66	*
BP168	0.070278	0.001089	0.053459	0.000552	0.000713	0.000053	0.001429	0.000296	0.000040	0.000020	1.095605	0.112975	0.741	0.076	83	
BP168	0.172280	0.001304	0.143866	0.001055	0.001802	0.000097	0.011530	0.000278	0.000047	0.000012	1.101077	0.026615	0.744	0.018	92	
BP168	0.242501	0.001707	0.203568	0.001706	0.002789	0.000082	0.001924	0.000569	0.000061	0.000012	1.102477	0.021553	0.745	0.015	92	
BP168	0.512853	0.002103	0.274105	0.002699	0.003474	0.000164	0.006609	0.000569	0.000700	0.000041	1.116461	0.045745	0.755	0.031	59	*
BP168	0.366620	0.002478	0.256610	0.001531	0.003249	0.000266	0.002257	0.000569	0.000241	0.000021	1.151100	0.027053	0.778	0.019	80	*
BP168	0.368991	0.003220	0.265515	0.002037	0.003295	0.000097	0.002301	0.000278	0.000199	0.000021	1.167810	0.027611	0.789	0.019	84	
BP168	0.312549	0.003459	0.162383	0.001045	0.001879	0.000102	0.056113	0.000568	0.000407	0.000050	1.184486	0.094580	0.801	0.064	61	*
BP168	0.823546	0.004209	0.185652	0.000902	0.002798	0.000093	0.002522	0.000296	0.002009	0.000070	1.237737	0.113852	0.837	0.077	27	*
BP168	0.094419	0.000846	0.036189	0.000342	0.000479	0.000062	0.033337	0.000569	0.000163	0.000031	1.279464	0.252682	0.865	0.171	49	*

Sample #	^{40}Ar	±1σ	^{39}Ar	±1σ	^{38}Ar	±1σ	^{37}Ar	±1σ	^{36}Ar	±1σ	$^{40}Ar^*/^{39}ArK$	±1σ	Age (Ma)	±1σ	% $^{40}Ar^*$	
McM#65	Bishop Tuff															
J-value = 0.000375533 ± 0.0000019																
	Ig2Nb			Feldspar												
BP168	0.466543	0.001659	0.200798	0.001583	0.002402	0.000165	0.010321	0.000793	0.000860	0.000051	1.058193	0.075496	**0.715**	**0.051**	45	•
BP168	0.188561	0.001778	0.160848	0.000798	0.001762	0.000106	0.012750	0.001330	0.000059	0.000033	1.064595	0.062033	**0.720**	**0.042**	91	
BP168	0.255964	0.001500	0.221513	0.001635	0.002913	0.000175	0.011435	0.005397	0.000044	0.000034	1.096681	0.047000	**0.741**	**0.032**	95	
BP168	0.331073	0.002370	0.287945	0.001997	0.003271	0.000206	0.004427	0.000794	0.000051	0.000022	1.097105	0.024857	**0.742**	**0.017**	95	
BP168	0.331945	0.001725	0.291191	0.001242	0.003816	0.000196	0.005248	0.001329	0.000041	0.000028	1.098746	0.029588	**0.743**	**0.020**	96	
BP168	0.310994	0.000917	0.275360	0.001449	0.003291	0.000135	0.005899	0.005401	0.000026	0.000034	1.101959	0.037439	**0.745**	**0.026**	98	
BP168	0.394999	0.002909	0.341843	0.003269	0.004405	0.000145	0.011947	0.000794	0.000049	0.000022	1.112851	0.023119	**0.752**	**0.016**	96	
BP168	0.191439	0.001550	0.159616	0.000807	0.001830	0.000165	0.002813	0.005393	0.000046	0.000026	1.113476	0.049535	**0.753**	**0.034**	93	
BP168	0.254335	0.001517	0.212187	0.001656	0.002426	0.000156	0.009524	0.001328	0.000059	0.000033	1.115810	0.047447	**0.754**	**0.032**	93	
BP168	0.338760	0.002153	0.275161	0.001552	0.003301	0.000165	0.008975	0.005398	0.000105	0.000026	1.118625	0.029720	**0.756**	**0.021**	91	
BP168	0.192151	0.001242	0.149889	0.001685	0.001772	0.000068	0.001504	0.000278	0.000080	0.000021	1.125030	0.043718	**0.760**	**0.030**	83	
BP168	0.248866	0.001298	0.181237	0.001242	0.002539	0.000156	0.001499	0.001328	0.000152	0.000040	1.125969	0.065973	**0.761**	**0.045**	82	
BP168	0.233323	0.001211	0.199049	0.000745	0.002518	0.000087	0.003205	0.000279	0.000029	0.000012	1.128910	0.018632	**0.763**	**0.013**	96	
BP168	0.380795	0.002526	0.291875	0.001986	0.003782	0.000165	0.006572	0.000793	0.000171	0.000031	1.131768	0.033550	**0.765**	**0.023**	87	
BP168	0.307913	0.001540	0.243523	0.001966	0.003301	0.000185	0.007118	0.005391	0.000085	0.000026	1.160957	0.033568	**0.785**	**0.023**	92	
BP168	0.030869	0.000430	0.017669	0.000212	0.000334	0.000043	0.027303	0.000228	0.000033	0.000020	1.199139	0.335687	**0.811**	**0.227**	68	•
BP168	0.273245	0.002615	0.074524	0.001065	0.001107	0.000087	0.000526	0.000278	0.000620	0.000050	1.208689	0.203367	**0.817**	**0.138**	32	•
BP168	0.036050	0.000645	0.020607	0.000424	0.000317	0.000047	0.034438	0.000793	0.000033	0.000031	1.270782	0.448183	**0.859**	**0.303**	72	•
Background:	*0.007500*	*0.000349*	*0.000040*	*0.000020*	*0.000020*	*0.000010*	*0.000488*	*0.000050*	*0.000060*	*0.000010*						
J-value = 0.000373203 ± 0.0000019																
	Ig2Nb			Biotite												
BP168	0.083966	0.000625	0.007763	0.000143	0.000171	0.000025	0.000272	0.000229	0.000260	0.000020	0.921977	0.765756	**0.619**	**0.514**	8	
BP168	0.048675	0.000686	0.015605	0.000178	0.000187	0.000050	0.000304	0.000279	0.000090	0.000012	1.416494	0.223614	**0.951**	**0.150**	45	
BP168	0.016050	0.000416	0.002777	0.000301	0.000055	0.000050	0.000260	0.000279	0.000040	0.000021	1.530446	2.226384	**1.028**	**1.495**	26	•
BP168	0.135469	0.000387	0.025218	0.000383	0.000320	0.000059	0.000215	0.000279	0.000310	0.000040	1.740037	0.474551	**1.169**	**0.319**	32	
BP168	0.096732	0.000809	0.021280	0.000342	0.000371	0.000050	0.000171	0.000279	0.000190	0.000021	1.907929	0.293156	**1.281**	**0.197**	41	
BP168	0.014800	0.000430	0.005293	0.000162	0.000058	0.000034	-0.000091	0.000229	0.000010	0.000010	2.236747	0.568381	**1.502**	**0.382**	80	
Background:	*0.001325*	*0.000158*	*0.000030*	*0.000020*	*0.000010*	*0.000010*	*0.000468*	*0.000050*	*0.000020*	*0.000010*						
McM#70																
J-value = 0.000384126 ± 0.0000019																
	F7			Feldspar												
CMW12	0.242865	0.001382	0.201135	0.001385	0.002260	0.000072	0.001299	0.000214	0.000110	0.000012	1.046368	0.020565	**0.723**	**0.015**	87	
CMW12	0.236367	0.001174	0.215078	0.001034	0.002689	0.000153	0.000893	0.000213	0.000010	0.000021	1.085569	0.030108	**0.751**	**0.021**	99	
CMW12	0.366680	0.001288	0.299701	0.001354	0.003558	0.000102	0.001958	0.000213	0.000139	0.000021	1.085961	0.021910	**0.751**	**0.016**	89	
CMW12	0.111390	0.000828	0.098488	0.001209	0.001236	0.000092	0.000835	0.000110	0.000010	0.000018	1.099697	0.055729	**0.760**	**0.039**	97	
CMW12	0.174382	0.000662	0.136873	0.000920	0.001778	0.000082	0.000855	0.000109	0.000080	0.000025	1.100376	0.054345	**0.761**	**0.038**	86	
CMW12	0.191248	0.001026	0.158732	0.000930	0.001972	0.000112	0.000973	0.000109	0.000050	0.000025	1.111002	0.047139	**0.768**	**0.033**	92	
CMW12	0.097286	0.000789	0.079615	0.000445	0.001125	0.000113	0.000607	0.000214	0.000030	0.000012	1.111202	0.046940	**0.768**	**0.033**	91	
CMW12	0.261483	0.001161	0.214738	0.001168	0.002596	0.000123	0.001294	0.000109	0.000070	0.000025	1.120909	0.035137	**0.775**	**0.025**	92	
CMW12	0.171728	0.001464	0.153079	0.001096	0.002085	0.000092	0.000736	0.000109	0.000000	0.000018	1.120916	0.036560	**0.775**	**0.026**	100	
CMW12	0.324458	0.001288	0.275878	0.001127	0.003527	0.000082	0.002076	0.000213	0.000049	0.000021	1.123123	0.023646	**0.777**	**0.017**	95	
CMW12	0.161969	0.000901	0.140294	0.001292	0.001788	0.000143	0.000943	0.000109	0.000010	0.000018	1.132557	0.039445	**0.783**	**0.028**	98	
CMW12	0.164392	0.000810	0.142556	0.001189	0.001544	0.000092	0.000750	0.000214	0.000010	0.000021	1.132860	0.045333	**0.783**	**0.032**	98	
CMW12	0.223435	0.001330	0.193539	0.001034	0.002526	0.000082	0.001301	0.000214	0.000010	0.000012	1.139727	0.020832	**0.788**	**0.015**	99	
CMW12	0.210391	0.000904	0.184009	0.000734	0.002403	0.000113	0.002709	0.000213	-0.000001	0.000021	1.144525	0.034720	**0.791**	**0.024**	100	
CMW12	0.021420	0.000429	0.016538	0.000321	0.000246	0.000031	0.018697	0.000214	0.000005	0.000021	1.205037	0.380639	**0.833**	**0.263**	93	
CMW12	1.153847	0.001997	0.145067	0.000941	0.002474	0.000041	0.001012	0.000214	0.003250	0.000050	1.334215	0.104140	**0.922**	**0.072**	16	
CMW12	0.022210	0.000460	0.016982	0.000383	0.000246	0.000041	0.019501	0.000214	-0.000005	0.000012	1.397757	0.217130	**0.966**	**0.150**	100	
Background:	*0.000890*	*0.000150*	*0.000034*	*0.000020*	*0.000010*	*0.000016*	*0.000390*	*0.000050*	*0.000030*	*0.000010*						

Notes:

Sample picked from crushed pumice from 500 µm - 1 mm sieve fraction and washed in acetone

F5 = Fall Unit

Ig1Eb = Ignimbrite package

Ig2NWa = Ignimbrite package

Ig2Nb = Ignimbrite package

F7 = Fall unit

• = Alteration product

◊ = Xenocryst

A4. Chemical Data

A4.1 Introduction

Appendix A4 details all the chemical data collected on samples in this study for the purpose of sample characterisation and previously published XRF data referred to in the text. It is divided into sections based on analytical method used for data collection.

Section A4.1.1: XRF analyses

Tables show major element (wt. % concentration), and minor/trace element (ppm concentrations) determined by XRF analysis.

Section A4.1.2: Electron microprobe analyses

Tables detail all Electron microprobe data collected on samples in this study and are listed by sample and then by mineral phase. Tables display raw totals and concentrations in wt. %. The identity of any inclusions analysed (namely apatite and plagioclase) is also given.

A4.1.1 XRF Analyses

Sample:	YP127	YP079	YP081	CMW01
Formation:	HRT	HRT	HRT	MFT
Unit:	A	B	C	-
Major Elements (wt. %)				
SiO_2	73.62	73.08	73.29	76.01
TiO_2	0.152	0.265	0.102	0.153
Al_2O_3	12.57	12.22	12.20	11.80
Fe_2O_3	2.04	2.59	1.69	1.54
MnO	0.049	0.052	0.035	0.033
MgO	0.16	0.28	0.12	0.11
CaO	0.77	1.14	0.64	0.63
Na_2O	3.21	3.20	3.14	2.88
K_2O	5.42	4.98	5.08	5.59
P_2O_5	0.023	0.095	0.014	0.025
LOI	2.77	2.24	3.70	1.84
Total	100.78	100.15	100.02	100.61
Trace Elements (ppm)				
Rb	169	128	222	184
Sr	34	74	36	33
Y	74	53	90	62.2
Zr	261	315	221	207
Nb	52	35	62	38.4
Ba	776	1795	207	389
Pb	35	30	32	31
Th	28	20	34	26
U	6	4	8	6
Sc	2	2	0	1
V	4	12	6	0
Cr	4	2	1	4
Co	0	1	1	1
Ni	5	4	3	5
Cu	6	6	5	5
Zn	90	74	85	48
Ga	22	20	24	20
Mo	6	5	5	4
As	2	3	4	4
S	0	54	38	40

HRT = Huckleberry Ridge Tuff; MFT = Mesa Falls Tuff.

Sample:	YR215*	YR185*	YR242
Formation:	SRD	SRB	GCD
Unit:			
Major Elements (wt. %)			
SiO_2	75.51	75.15	77.33
TiO_2	0.28	0.18	0.072
Al_2O_3	12.10	12.84	11.95
Fe_2O_3	2.87	2.11	1.20
MnO	0.06	0.04	0.030
MgO	0.10	0.12	0.04
CaO	0.89	0.87	0.33
Na_2O	3.51	3.51	3.80
K_2O	4.65	5.16	4.78
P_2O_5	0.03	0.02	0.016
LOI	0.80	2.48	0.31
Total	99.79	100.26	99.84
Trace Elements (ppm)			
Rb	146	171	334
Sr	67	52	1
Y	57.4	59.8	44.8
Zr	488	267	128
Nb	37.8	39.4	65.3
Ba	2036	1028	10
Pb	30	27	44
Th	21	29	50
U	4	6	11
Sc	3	2	1
V	6	8	3
Cr	5	5	3
Co	0	0	0
Ni	4	5	3
Cu	6	4	5
Zn	84	60	40
Ga	20	20	23
Mo	7	3	6
As	1	4	5
S	0	0	4

SRD = Sheridan Reservoir dome; SRB = Snake River Butte dome; GCF = Green Canyon Flow dome
*XRF data collected by Bruce Charlier (2009).

Sample:	BP029	CMW12	BP079 #1	BP079 #2	BP113	BP168
Formation:	BT	BT	BT	BT	BT	BT
Unit:	F5	F7	Ig1Eb	Ig1Eb	Ig2NWa	Ig2Nb
Major Elements (wt. %)						
SiO_2	75.00	74.75	75.39	75.11	73.76	74.11
TiO_2	0.076	0.073	0.069	0.071	0.162	0.196
Al_2O_3	12.19	12.04	12.28	12.43	13.70	13.00
Fe_2O_3	0.87	0.82	0.80	0.81	1.04	1.21
MnO	0.037	0.035	0.035	0.034	0.020	0.026
MgO	0.07	0.08	0.05	0.06	0.15	0.22
CaO	0.56	0.49	0.45	0.46	0.69	0.88
Na_2O	3.65	3.10	3.36	3.43	2.84	3.28
K_2O	4.50	5.07	5.12	5.03	5.80	5.40
P_2O_5	0.018	0.013	0.010	0.014	0.028	0.047
LOI	3.24	3.84	2.61	2.73	2.23	1.89
Total	100.20	100.31	100.18	100.18	100.42	100.27
Trace Elements (ppm)						
Rb	171	172	180	178	95	87
Sr	13	8	4	4	80	112
Y	25.2	23.4	24.2	24.9	10.7	10.2
Zr	88	88	84	89	124	126
Nb	21.4	21.5	21.9	22.1	10.2	9.8
Ba	33	23	10	15	362	498
Pb	31	32	32	32	21	28
Th	20	19	21	22	11	13
U	8	7	8	7	4	2
Sc	1	3	1	3	1	2
V	1	4	0	0	5	3
Cr	2	2	2	2	3	3
Co	0	1	0	0	1	1
Ni	4	4	4	4	7	4
Cu	3	3	3	4	6	3
Zn	26	26	25	27	15	21
Ga	15	15	15	16	14	13
Mo	7	7	7	7	4	4
As	8	9	9	7	2	5
S	12	48	12	6	13	28

BT = Bishop Tuff

A4.1.2 Electron microprobe analyses

Electron microprobe (wt. %) analyses of all Fish Canyon magmatic system samples

Sample	Analysis	SiO_2	TiO_2	Al_2O_3	FeO	MnO	MgO	CaO	Na_2O	K_2O	BaO	SrO	F	Cl	Total	
Pagosa Peak Dacite		Biotite														
BFC83	Point #1	37.85	4.38	12.97	15.45	0.34	14.26	0.01	0.51	9.13	0.33	0.04	0.44	0.16	95.87	
BFC83	Point #2	37.91	4.55	13.07	15.62	0.31	14.33	0.01	0.42	9.22	0.36	0.12	0.32	0.15	96.39	
BFC83	Point #3	37.77	4.55	13.17	15.74	0.37	14.29	0.00	0.45	9.19	0.44	0.04	0.49	0.17	96.67	
BFC83	Point #4	37.93	4.51	13.24	15.74	0.40	14.21	0.01	0.46	9.17	0.26	0.00	0.51	0.15	96.59	
		Biotite														
BFC83	Point #1	37.87	4.54	13.08	15.65	0.32	14.56	0.01	0.40	9.22	0.35	0.03	0.70	0.15	96.87	
BFC83	Point #2	38.12	4.56	12.95	15.61	0.31	14.62	0.00	0.45	9.17	0.25	0.05	0.50	0.16	96.76	
BFC83	Point #3	38.29	4.56	13.15	15.56	0.35	14.71	0.01	0.43	9.30	0.16	0.03	0.52	0.15	97.22	
BFC83	Point #4	37.32	4.54	13.48	16.17	0.32	14.08	0.00	0.41	9.08	0.72	0.02	0.48	0.15	96.76	
BFC83	Point #5	37.54	4.59	13.49	16.05	0.35	14.11	0.00	0.39	9.12	0.69	0.00	0.43	0.16	96.92	
BFC83	Point #6	37.69	4.67	13.43	15.91	0.37	14.17	0.04	0.35	9.00	0.49	0.04	0.51	0.15	96.80	
BFC83	Point #7	37.74	4.67	13.82	15.63	0.31	13.95	0.02	0.39	8.89	0.50	0.00	0.60	0.15	96.66	
BFC83	Point #8	37.97	4.40	13.17	15.42	0.33	14.41	0.02	0.42	9.08	0.21	0.00	0.56	0.15	96.15	
BFC83	Point #9	38.08	4.44	13.20	15.56	0.36	14.15	0.04	0.40	9.08	0.24	0.02	0.60	0.16	96.32	
BFC83	Point #10	38.14	4.11	13.15	15.72	0.36	14.47	0.01	0.40	9.27	0.23	0.00	0.62	0.14	96.63	
BFC83	Point #11	37.90	4.39	13.25	15.82	0.35	14.44	0.01	0.45	9.25	0.19	0.01	0.43	0.16	96.64	
BFC83	Inclusion	0.36	0.02	0.00	0.41	0.19	0.16	52.22	0.31	0.05	0.00	0.03	4.69	0.77	59.22	^
BFC83	Inclusion	67.11	0.13	10.70	1.31	0.03	0.23	0.73	1.50	5.11	0.05	0.00	0.01	0.22	87.12	#
		Biotite														
BFC83	Point #1	37.76	4.53	13.33	15.69	0.37	14.48	0.01	0.39	9.24	0.28	0.00	0.56	0.17	96.82	
BFC83	Point #2	37.80	4.56	13.34	15.74	0.37	14.49	0.01	0.49	9.17	0.27	0.00	0.57	0.17	96.96	
BFC83	Point #3	37.83	4.47	13.34	15.69	0.35	14.43	0.01	0.43	9.25	0.27	0.03	0.42	0.18	96.69	
BFC83	Point #4	37.80	4.48	13.17	15.82	0.32	14.45	0.00	0.50	9.12	0.29	0.04	0.57	0.17	96.73	
BFC83	Point #5	37.78	4.44	13.25	15.71	0.38	14.43	0.01	0.41	9.28	0.40	0.09	0.55	0.16	96.90	
BFC83	Point #6	37.69	4.61	13.40	15.88	0.33	14.45	0.01	0.38	9.10	0.29	0.05	0.39	0.16	96.76	
BFC83	Point #7	37.78	4.41	13.19	15.57	0.32	14.38	0.02	0.43	9.16	0.29	0.06	0.56	0.17	96.34	
BFC83	Inclusion	0.34	0.01	0.00	0.31	0.20	0.15	52.54	0.17	0.04	0.00	0.06	4.84	0.73	59.40	^
BFC83	Inclusion	0.38	0.00	0.00	0.47	0.21	0.15	52.35	0.08	0.11	0.00	0.00	5.37	0.71	59.82	^
		Biotite														
BFC83	Point #1	37.83	4.57	13.00	15.70	0.33	14.27	0.02	0.46	9.23	0.22	0.00	0.49	0.15	96.28	
BFC83	Point #2	37.85	4.56	13.08	15.65	0.37	14.19	0.04	0.41	9.09	0.33	0.00	0.59	0.16	96.31	
BFC83	Point #3	37.89	4.36	13.04	15.85	0.37	14.19	0.03	0.45	9.26	0.16	0.02	0.59	0.16	96.37	
BFC83	Point #4	37.90	4.54	13.01	15.80	0.34	14.17	0.02	0.41	9.22	0.23	0.00	0.58	0.16	96.38	
BFC83	Point #5	38.04	4.54	12.96	15.84	0.36	14.37	0.05	0.44	9.14	0.21	0.02	0.44	0.17	96.58	
BFC83	Point #6	37.96	4.46	13.01	15.77	0.36	14.23	0.03	0.41	9.21	0.27	0.05	0.48	0.18	96.41	
BFC83	Point #7	37.84	4.53	12.99	15.80	0.36	14.29	0.04	0.46	9.26	0.18	0.05	0.44	0.16	96.40	
BFC83	Point #8	37.97	4.41	13.20	15.50	0.36	14.12	0.04	0.43	9.14	0.29	0.03	0.55	0.16	96.22	
BFC83	Inclusion	0.39	0.02	0.00	0.31	0.24	0.14	52.56	0.04	0.02	0.00	0.02	4.64	0.73	59.12	^
BFC83	Inclusion	0.43	0.05	0.00	0.32	0.19	0.16	52.44	0.09	0.02	0.00	0.00	4.09	0.73	58.51	^
		Biotite														
BFC83	Point #1	37.82	4.39	13.15	15.73	0.34	14.40	0.01	0.48	9.10	0.17	0.01	0.58	0.17	96.34	
BFC83	Point #2	37.90	4.51	13.10	15.66	0.30	14.21	0.00	0.43	9.12	0.38	0.01	0.59	0.17	96.36	
BFC83	Point #3	37.98	4.61	13.20	16.08	0.33	14.15	0.01	0.51	9.22	0.28	0.02	0.73	0.16	97.29	
BFC83	Point #4	38.02	4.63	13.11	16.12	0.33	13.97	0.01	0.49	9.11	0.26	0.02	0.44	0.16	96.67	
BFC83	Point #5	38.04	4.43	12.99	16.04	0.35	14.20	0.01	0.45	9.21	0.27	0.00	0.47	0.16	96.61	
BFC83	Point #6	38.06	4.37	12.96	15.94	0.36	14.15	0.01	0.47	9.16	0.23	0.04	0.63	0.17	96.56	
BFC83	Point #7	37.88	4.62	13.04	16.07	0.33	14.22	0.01	0.48	9.21	0.33	0.00	0.59	0.17	96.94	
BFC83	Point #8	37.88	4.35	13.20	15.86	0.37	14.08	0.02	0.39	9.29	0.19	0.01	0.47	0.16	96.26	
BFC83	Point #9	37.83	4.44	13.10	15.46	0.31	14.32	0.05	0.40	9.20	0.23	0.03	0.51	0.16	96.04	
BFC83	Inclusion	60.54	0.04	24.15	0.49	0.01	0.01	6.56	7.22	0.95	0.01	0.19	0.00	0.00	100.17	#
		Sanidine														
BFC83	Point #1	65.74	0.05	18.35	0.10	0.01	0.00	0.15	2.82	12.47	0.37	0.13	0.03	0.01	100.24	
BFC83	Point #2	65.52	0.00	18.45	0.12	0.00	0.00	0.19	2.64	12.50	0.33	0.08	0.00	0.01	99.84	
BFC83	Point #3	65.63	0.01	18.26	0.11	0.00	0.00	0.17	2.87	12.43	0.37	0.09	0.01	0.00	99.96	
BFC83	Point #4	65.61	0.00	18.36	0.13	0.01	0.00	0.19	2.63	12.42	0.40	0.10	0.00	0.00	99.86	
BFC83	Point #5	65.62	0.00	18.38	0.12	0.00	0.00	0.19	2.79	12.51	0.29	0.06	0.00	0.00	99.96	
BFC83	Point #6	65.58	0.01	18.30	0.12	0.02	0.00	0.17	2.69	12.57	0.29	0.15	0.00	0.00	99.90	
BFC83	Point #7	65.67	0.00	18.35	0.11	0.00	0.00	0.19	2.77	12.46	0.31	0.14	0.00	0.00	100.00	
BFC83	Point #8	65.42	0.00	18.30	0.12	0.00	0.00	0.16	2.67	12.42	0.60	0.11	0.00	0.01	99.80	
BFC83	Point #9	65.61	0.00	18.18	0.14	0.00	0.00	0.19	2.59	12.63	0.38	0.14	0.02	0.00	99.88	
BFC83	Point #10	65.66	0.01	18.29	0.13	0.01	0.00	0.16	2.74	12.53	0.28	0.07	0.00	0.00	99.88	

Sample	Analysis	SiO_2	TiO_2	Al_2O_3	FeO	MnO	MgO	CaO	Na_2O	K_2O	BaO	SrO	F	Cl	Total
Pagosa Peak Dacite		**Sanidine**													
BFC83	Point #1	65.59	0.00	18.30	0.14	0.00	0.00	0.21	2.75	12.58	0.37	0.08	0.00	0.00	100.00
BFC83	Point #2	65.72	0.00	18.42	0.13	0.02	0.00	0.18	2.80	12.64	0.22	0.07	0.00	0.00	100.21
BFC83	Point #3	65.74	0.00	18.39	0.13	0.00	0.00	0.20	2.79	12.58	0.26	0.04	0.00	0.00	100.15
BFC83	Point #4	65.67	0.00	18.32	0.12	0.00	0.00	0.18	2.65	12.56	0.35	0.05	0.01	0.00	99.90
BFC83	Point #5	65.68	0.00	18.40	0.14	0.00	0.00	0.19	2.68	12.51	0.31	0.06	0.02	0.00	99.99
BFC83	Point #6	65.57	0.02	18.42	0.12	0.01	0.00	0.19	2.73	12.54	0.30	0.06	0.00	0.00	99.94
BFC83	Point #7	65.70	0.01	18.43	0.13	0.01	0.00	0.18	2.75	12.58	0.32	0.06	0.00	0.01	100.17
BFC83	Point #8	65.46	0.01	18.38	0.12	0.01	0.00	0.17	2.64	12.68	0.43	0.16	0.00	0.00	100.07
BFC83	Point #9	65.49	0.01	18.34	0.14	0.00	0.00	0.19	2.60	12.51	0.21	0.13	0.00	0.01	99.62
BFC83	Point #10	65.75	0.00	18.39	0.13	0.02	0.00	0.17	2.66	12.59	0.25	0.13	0.00	0.00	100.09
BFC83	Point #11	65.76	0.00	18.42	0.13	0.01	0.00	0.19	2.82	12.56	0.15	0.07	0.00	0.01	100.12
BFC83	Point #12	65.70	0.00	18.38	0.13	0.00	0.00	0.18	2.61	12.60	0.27	0.08	0.00	0.00	99.96
		Sanidine													
BFC83	Point #1	64.15	0.00	18.73	0.12	0.00	0.00	0.20	2.64	12.01	1.62	0.18	0.00	0.00	99.65
BFC83	Point #2	64.38	0.05	18.74	0.11	0.01	0.00	0.21	2.70	12.15	1.51	0.21	0.06	0.00	100.13
BFC83	Point #3	64.66	0.01	18.62	0.10	0.00	0.00	0.17	2.58	12.28	1.17	0.16	0.06	0.00	99.82
BFC83	Point #4	64.47	0.03	18.54	0.10	0.00	0.00	0.18	2.59	12.26	1.03	0.14	0.00	0.01	99.35
BFC83	Point #5	64.88	0.03	18.48	0.09	0.00	0.00	0.17	2.60	12.22	0.99	0.17	0.00	0.00	99.63
BFC83	Point #6	64.19	0.00	18.66	0.11	0.00	0.00	0.20	2.60	12.22	1.41	0.15	0.03	0.00	99.56
BFC83	Point #7	64.46	0.04	18.62	0.10	0.01	0.00	0.18	2.65	12.21	1.26	0.11	0.00	0.00	99.64
BFC83	Point #8	64.96	0.03	18.47	0.11	0.01	0.00	0.16	2.68	12.14	0.87	0.12	0.00	0.00	99.55
		Plagioclase													
BFC83	Point #1	60.23	0.00	23.84	0.23	0.02	0.01	6.77	7.13	0.83	0.02	0.17	0.05	0.01	99.31
BFC83	Point #2	60.61	0.00	23.87	0.25	0.00	0.01	6.57	7.37	0.85	0.03	0.12	0.03	0.00	99.70
BFC83	Point #3	61.65	0.00	23.41	0.25	0.00	0.02	5.80	7.55	1.02	0.09	0.14	0.06	0.00	99.98
BFC83	Point #4	61.44	0.02	23.38	0.24	0.00	0.02	5.93	7.68	0.98	0.02	0.15	0.04	0.00	99.89
BFC83	Point #5	61.71	0.03	23.22	0.22	0.01	0.01	5.73	7.67	1.03	0.00	0.17	0.00	0.00	99.79
BFC83	Point #6	62.13	0.02	23.15	0.22	0.00	0.01	5.58	7.82	0.95	0.09	0.13	0.01	0.00	100.11
BFC83	Point #7	59.51	0.00	24.57	0.25	0.00	0.01	7.32	6.76	0.70	0.05	0.22	0.04	0.01	99.43
BFC83	Point #8	61.51	0.02	23.28	0.24	0.00	0.00	5.82	7.66	0.99	0.03	0.10	0.02	0.00	99.68
		Plagioclase													
BFC83	Point #1	61.10	0.00	23.69	0.22	0.00	0.02	6.24	7.43	0.89	0.02	0.14	0.00	0.00	99.74
BFC83	Point #2	60.79	0.04	24.05	0.22	0.01	0.01	6.45	7.30	0.82	0.07	0.16	0.04	0.00	99.95
BFC83	Point #3	61.55	0.02	23.58	0.24	0.00	0.02	5.85	7.43	0.96	0.03	0.21	0.04	0.00	99.92
BFC83	Point #4	60.85	0.00	24.07	0.20	0.00	0.01	6.47	7.42	0.82	0.00	0.06	0.00	0.01	99.91
BFC83	Point #5	61.09	0.00	23.60	0.24	0.01	0.01	6.19	7.35	0.90	0.07	0.22	0.01	0.00	99.69
BFC83	Point #6	60.32	0.00	24.36	0.25	0.00	0.01	6.76	7.13	0.79	0.03	0.17	0.00	0.00	99.82
		Feldspar - Transect #1													
BFC83	Point #1	65.98	0.00	18.34	0.13	0.02	0.00	0.19	2.96	12.10	0.25	0.09	0.01	0.01	100.09
BFC83	Point #2	65.76	0.00	18.17	0.10	0.01	0.00	0.21	3.02	12.02	0.22	0.15	0.02	0.00	99.67
BFC83	Point #3	61.52	0.01	23.50	0.20	0.00	0.00	5.96	7.78	1.01	0.07	0.09	0.00	0.00	100.13
BFC83	Point #4	61.55	0.00	23.62	0.18	0.00	0.00	5.89	7.73	0.96	0.00	0.14	0.07	0.00	100.15
BFC83	Point #5	61.21	0.02	23.64	0.18	0.01	0.00	6.11	7.41	0.95	0.00	0.10	0.00	0.00	99.63
BFC83	Point #6	65.69	0.00	18.49	0.08	0.00	0.00	0.29	3.11	11.75	0.31	0.04	0.00	0.00	99.76
BFC83	Point #7	65.79	0.00	18.33	0.13	0.00	0.00	0.18	2.86	12.37	0.24	0.05	0.00	0.00	99.96
BFC83	Point #8	65.70	0.00	18.37	0.12	0.01	0.00	0.20	2.76	12.62	0.26	0.12	0.04	0.01	100.22
BFC83	Point #9	65.61	0.01	18.27	0.12	0.00	0.00	0.19	2.76	12.63	0.17	0.18	0.00	0.01	99.97
		Feldspar - Transect #2													
BFC83	Point #1	64.65	0.00	18.74	0.10	0.00	0.00	0.18	2.71	12.05	1.55	0.15	0.03	0.01	100.17
BFC83	Point #2	64.55	0.03	18.61	0.12	0.00	0.00	0.17	2.77	12.03	1.34	0.14	0.04	0.00	99.81
BFC83	Point #3	64.51	0.02	18.82	0.13	0.01	0.00	0.17	2.51	12.24	1.34	0.12	0.14	0.01	100.00
BFC83	Point #4	61.09	0.02	24.12	0.21	0.01	0.02	6.25	7.69	0.97	0.08	0.25	0.02	0.00	100.74
BFC83	Point #5	60.94	0.00	24.12	0.24	0.00	0.01	6.21	7.54	0.90	0.06	0.06	0.00	0.00	100.08
BFC83	Point #6	61.29	0.01	23.87	0.22	0.00	0.02	6.01	7.59	0.98	0.03	0.09	0.00	0.00	100.11
BFC83	Point #7	60.54	0.01	24.28	0.23	0.00	0.00	6.49	7.09	0.89	0.05	0.23	0.00	0.00	99.81
BFC83	Point #8	65.41	0.02	18.42	0.12	0.00	0.00	0.13	2.68	12.58	0.52	0.05	0.00	0.01	99.95
BFC83	Point #9	65.42	0.04	18.40	0.12	0.00	0.00	0.16	2.72	12.47	0.31	0.07	0.06	0.00	99.76
BFC83	Point #10	65.54	0.04	18.29	0.10	0.00	0.00	0.17	2.67	12.53	0.18	0.14	0.05	0.00	99.72
BFC83	Point #11	64.32	0.00	18.79	0.11	0.01	0.00	0.20	2.76	12.02	1.54	0.14	0.00	0.00	99.90
BFC83	Point #12	60.31	0.02	24.42	0.26	0.00	0.01	6.55	7.20	0.90	0.04	0.16	0.00	0.00	99.88
BFC83	Point #13	61.33	0.01	23.72	0.26	0.00	0.01	5.79	7.55	1.07	0.04	0.23	0.00	0.01	100.01
BFC83	Point #14	59.93	0.00	24.81	0.25	0.00	0.03	6.86	7.01	0.82	0.04	0.24	0.06	0.00	100.06
BFC83	Point #15	64.22	0.03	21.86	0.33	0.00	0.02	5.24	6.82	1.67	0.10	0.12	0.06	0.05	100.52
BFC83	Point #16	60.85	0.03	24.43	0.33	0.01	0.02	6.40	7.24	1.04	0.12	0.16	0.02	0.01	100.65

Sample	Analysis	SiO_2	TiO_2	Al_2O_3	FeO	MnO	MgO	CaO	Na_2O	K_2O	BaO	SrO	F	Cl	Total	
Pagosa Peak Dacite		**Biotite**														
BFC196	Point #1	37.91	4.34	13.46	15.62	0.40	14.28	0.02	0.45	9.21	0.25	0.01	0.45	0.16	96.54	
BFC196	Point #2	37.72	4.61	13.17	16.01	0.35	14.28	0.02	0.41	9.26	0.29	0.04	0.44	0.16	96.76	
BFC196	Point #3	37.80	4.43	13.12	16.00	0.33	14.25	0.01	0.43	9.25	0.33	0.03	0.41	0.18	96.55	
BFC196	Point #4	37.82	4.48	13.14	15.89	0.37	14.28	0.00	0.43	9.29	0.37	0.04	0.58	0.17	96.86	
BFC196	Point #5	37.93	4.24	13.24	15.76	0.35	14.19	0.01	0.44	9.15	0.22	0.00	0.52	0.17	96.22	
BFC196	Inclusion	0.47	0.00	0.00	0.23	0.19	0.13	51.99	0.04	0.00	0.00	0.06	5.31	0.71	59.14	^
BFC196	Inclusion	0.42	0.01	0.00	0.34	0.21	0.14	51.88	0.22	0.06	0.00	0.02	4.47	0.74	58.51	^
BFC196	Inclusion	0.22	0.03	0.00	0.20	0.21	0.15	52.22	0.24	0.00	0.00	0.05	5.05	0.75	59.10	^
BFC196	Inclusion	0.36	0.00	0.00	0.21	0.16	0.14	52.28	0.08	0.01	0.00	0.04	5.23	0.72	59.23	^
		Biotite														
BFC196	Point #1	37.12	4.48	13.10	15.74	0.34	14.55	0.09	0.43	9.12	0.33	0.00	0.49	0.16	95.97	
BFC196	Point #2	37.10	4.57	13.02	15.56	0.32	14.42	0.04	0.33	9.10	0.29	0.05	0.73	0.15	95.69	
BFC196	Point #3	36.93	4.52	13.10	15.73	0.33	14.48	0.02	0.42	9.21	0.27	0.00	0.46	0.16	95.64	
BFC196	Point #4	36.80	4.61	13.05	16.03	0.31	14.34	0.03	0.40	9.17	0.26	0.04	0.61	0.16	95.80	
BFC196	Point #5	36.76	4.32	12.98	15.92	0.30	14.26	0.05	0.40	9.18	0.16	0.00	0.54	0.16	95.02	
BFC196	Point #6	36.95	4.37	13.14	16.04	0.34	14.36	0.01	0.43	9.27	0.24	0.00	0.44	0.16	95.75	
BFC196	Point #7	36.88	4.51	12.97	16.03	0.32	14.43	0.10	0.42	9.15	0.29	0.00	0.70	0.17	95.97	
BFC196	Point #8	36.98	4.53	12.98	15.82	0.38	14.55	0.02	0.40	9.17	0.14	0.06	0.43	0.16	95.62	
BFC196	Point #10	36.90	4.38	12.83	15.82	0.36	14.49	0.02	0.37	9.10	0.28	0.01	0.61	0.16	95.31	
BFC196	Point #11	36.83	4.51	13.08	15.92	0.35	14.22	0.02	0.44	9.25	0.26	0.00	0.44	0.16	95.48	
BFC196	Point #12	36.82	4.42	13.18	15.97	0.36	14.28	0.03	0.39	9.21	0.25	0.01	0.51	0.16	95.59	
BFC196	Inclusion	2.25	0.35	0.67	1.39	0.24	0.91	49.08	0.07	0.60	0.00	0.01	4.36	0.69	60.61	^
BFC196	Inclusion	0.66	0.01	0.00	0.31	0.25	0.16	51.54	0.47	0.01	0.00	0.01	4.58	0.86	58.86	^
BFC196	Inclusion	0.49	0.00	0.01	0.37	0.20	0.15	52.18	0.13	0.03	0.00	0.08	5.09	0.74	59.46	^
		Biotite														
BFC196	Point #1	37.12	4.39	12.89	15.81	0.34	14.20	0.05	0.41	9.15	0.11	0.00	0.49	0.17	95.13	
BFC196	Point #2	36.94	4.59	13.09	15.94	0.37	14.24	0.05	0.40	9.16	0.24	0.00	0.50	0.17	95.69	
BFC196	Point #3	37.12	4.43	13.31	15.78	0.39	14.23	0.04	0.42	9.02	0.28	0.01	0.59	0.17	95.78	
BFC196	Point #4	36.88	4.60	13.21	16.33	0.33	13.91	0.02	0.44	9.21	0.30	0.00	0.57	0.17	95.97	
BFC196	Point #5	37.23	4.42	13.02	16.26	0.34	14.26	0.03	0.43	9.12	0.23	0.00	0.43	0.17	95.95	
BFC196	Point #6	37.48	4.23	12.96	15.97	0.34	14.34	0.03	0.42	9.15	0.22	0.02	0.39	0.16	95.70	
BFC196	Point #7	37.11	4.34	13.34	15.90	0.33	14.28	0.00	0.35	9.10	0.33	0.03	0.58	0.17	95.87	
BFC196	Point #8	36.77	4.52	13.30	16.55	0.36	13.90	0.02	0.38	9.16	0.38	0.08	0.41	0.17	95.99	
BFC196	Point #9	37.34	4.34	13.06	15.84	0.35	14.46	0.00	0.41	9.17	0.25	0.00	0.43	0.18	95.85	
BFC196	Point #10	37.20	4.34	13.23	16.12	0.36	14.08	0.01	0.44	9.23	0.27	0.04	0.57	0.17	96.05	
		Plagioclase														
BFC196	Point #1	60.16	0.03	24.34	0.23	0.01	0.02	6.36	7.22	0.86	0.06	0.20	0.00	0.00	99.49	
BFC196	Point #2	59.50	0.01	24.57	0.23	0.00	0.01	6.78	6.82	0.85	0.07	0.18	0.00	0.00	99.02	
BFC196	Point #3	61.02	0.00	23.75	0.23	0.00	0.00	5.70	7.26	1.05	0.02	0.13	0.00	0.00	99.16	
BFC196	Point #4	59.89	0.00	24.43	0.25	0.00	0.01	6.63	6.80	0.85	0.02	0.17	0.00	0.00	99.05	
BFC196	Point #5	60.47	0.00	24.24	0.23	0.00	0.00	6.17	7.03	0.89	0.06	0.23	0.00	0.00	99.31	
BFC196	Point #6	59.79	0.02	24.56	0.23	0.02	0.00	6.60	7.18	0.79	0.03	0.20	0.00	0.00	99.41	
BFC196	Point #7	59.92	0.01	24.32	0.25	0.00	0.02	6.34	7.04	0.88	0.04	0.24	0.00	0.00	99.05	
		Plagioclase														
BFC196	Point #1	60.49	0.00	24.02	0.24	0.00	0.00	5.93	7.35	0.91	0.06	0.24	0.00	0.00	99.25	
BFC196	Point #2	60.71	0.01	23.84	0.24	0.00	0.02	5.69	7.42	1.01	0.05	0.18	0.03	0.00	99.20	
BFC196	Point #3	59.72	0.05	24.41	0.24	0.00	0.02	6.50	7.11	0.88	0.05	0.17	0.00	0.01	99.14	
BFC196	Point #4	59.53	0.00	24.74	0.22	0.02	0.01	6.70	7.14	0.82	0.02	0.12	0.00	0.00	99.33	
		Feldspar - Transect														
BFC196	Point #1	60.19	0.01	24.37	0.22	0.00	0.01	6.32	7.20	0.87	0.01	0.12	0.02	0.00	99.34	
BFC196	Point #2	60.00	0.03	24.39	0.21	0.00	0.02	6.28	7.01	0.87	0.04	0.19	0.00	0.00	99.03	
BFC196	Point #3	63.77	0.00	19.08	0.09	0.00	0.00	0.19	2.55	12.10	1.31	0.09	0.02	0.01	99.21	
BFC196	Point #4	63.48	0.04	19.06	0.11	0.00	0.00	0.17	2.46	12.16	1.68	0.16	0.00	0.00	99.31	
BFC196	Point #5	63.61	0.06	19.05	0.11	0.00	0.00	0.19	2.51	12.14	1.28	0.26	0.04	0.00	99.24	
BFC196	Point #6	64.12	0.03	19.02	0.11	0.00	0.00	0.20	2.52	12.26	1.03	0.12	0.01	0.00	99.41	
BFC196	Point #7	63.56	0.03	19.33	0.11	0.00	0.00	0.23	2.57	12.01	1.59	0.17	0.06	0.00	99.67	
		Feldspar														
BFC196	Point #1	59.69	0.03	24.49	0.23	0.00	0.01	6.53	6.94	0.86	0.07	0.16	0.04	0.00	99.05	
BFC196	Point #2	60.41	0.01	24.17	0.23	0.00	0.02	6.18	7.20	0.96	0.08	0.19	0.00	0.00	99.45	
BFC196	Point #3	63.57	0.06	19.09	0.10	0.00	0.00	0.19	2.58	11.99	1.63	0.14	0.08	0.00	99.43	
BFC196	Point #4	59.51	0.02	24.74	0.23	0.00	0.02	6.75	6.80	0.83	0.02	0.22	0.00	0.00	99.16	
BFC196	Point #5	60.08	0.00	24.26	0.22	0.00	0.00	6.25	7.24	0.91	0.03	0.26	0.00	0.00	99.26	

Sample	Analysis	SiO_2	TiO_2	Al_2O_3	FeO	MnO	MgO	CaO	Na_2O	K_2O	BaO	SrO	F	Cl	Total
Pagosa Peak Dacite		**Feldspar**													
BFC196	Point #1	59.96	0.01	24.32	0.24	0.00	0.01	6.39	7.23	0.90	0.05	0.10	0.04	0.00	99.24
BFC196	Point #2	63.72	0.02	19.14	0.10	0.00	0.00	0.22	2.59	12.00	1.54	0.08	0.00	0.00	99.40
BFC196	Point #3	63.77	0.06	19.21	0.09	0.00	0.00	0.17	2.42	12.02	1.55	0.18	0.01	0.00	99.46
BFC196	Point #4	60.13	0.00	24.35	0.24	0.00	0.02	6.52	6.89	1.07	0.08	0.15	0.00	0.00	99.45
		Feldspar													
BFC196	Point #1	63.93	0.00	19.25	0.08	0.01	0.00	0.19	2.67	12.08	1.48	0.16	0.00	0.00	99.85
BFC196	Point #2	60.04	0.03	24.33	0.21	0.00	0.00	6.46	7.07	0.93	0.08	0.20	0.00	0.00	99.35
BFC196	Point #3	63.91	0.00	19.11	0.12	0.01	0.00	0.21	2.48	11.96	1.67	0.19	0.00	0.00	99.66
BFC196	Point #4	63.77	0.01	19.13	0.10	0.00	0.00	0.19	2.58	12.20	1.33	0.19	0.08	0.00	99.59
		Biotite													
BFC171	Point #1	37.86	4.32	13.06	15.95	0.36	14.36	0.02	0.31	8.40	0.26	0.06	1.02	0.15	96.15
BFC171	Point #2	37.78	4.13	12.37	16.37	0.34	14.13	0.02	0.41	9.23	0.39	0.00	1.07	0.16	96.40
BFC171	Point #3	38.20	4.03	13.17	15.14	0.35	14.37	0.04	0.39	9.30	0.30	0.02	1.00	0.15	96.45
		Biotite													
BFC171	Point #1	37.95	4.02	13.38	15.87	0.30	14.26	0.08	0.42	9.17	0.14	0.01	0.64	0.17	96.41
BFC171	Point #2	37.74	4.07	13.38	15.55	0.34	14.24	0.07	0.40	9.06	0.59	0.05	0.59	0.18	96.26
BFC171	Point #3	37.70	4.37	13.25	14.98	0.33	14.23	0.07	0.24	9.55	0.27	0.06	0.95	0.18	96.16
		Biotite													
BFC171	Point #1	38.34	4.21	13.32	15.80	0.33	14.64	0.06	0.40	9.01	0.30	0.00	0.54	0.17	97.15
BFC171	Point #2	37.87	4.98	12.23	15.86	0.29	14.35	0.05	0.41	9.16	0.12	0.02	0.66	0.18	96.19
BFC171	Point #3	38.22	4.40	12.24	15.76	0.37	14.41	0.08	0.38	9.14	0.25	0.02	0.77	0.15	98.18
BFC171	Point #4	37.79	4.20	13.21	15.91	0.32	14.38	0.07	0.41	9.09	0.37	0.03	0.65	0.17	96.61
		Biotite													
BFC171	Point #1	38.68	4.04	13.12	15.53	0.31	14.62	0.05	0.46	8.89	0.18	0.00	0.54	0.17	96.58
BFC171	Point #2	38.07	4.82	13.16	15.68	0.32	14.50	0.04	0.40	9.06	0.42	0.02	0.49	0.19	97.15
		Biotite													
BFC171	Point #1	38.26	4.03	13.09	15.85	0.35	14.59	0.04	0.41	8.19	0.24	0.00	0.60	0.16	95.82
BFC171	Point #2	38.03	4.72	12.91	15.90	0.30	14.21	0.05	0.39	9.12	0.12	0.01	0.83	0.15	96.76
BFC171	Point #3	37.99	4.37	12.98	15.67	0.28	14.52	0.06	0.45	9.05	0.23	0.08	0.70	0.16	96.55
		Plagioclase													
BFC171	Point #1	60.61	0.02	24.22	0.22	0.00	0.01	6.30	7.65	0.87	0.02	0.14	0.00	0.00	100.06
BFC171	Point #2	59.38	0.01	24.94	0.23	0.00	0.02	7.10	7.14	0.71	0.03	0.20	0.01	0.00	99.78
BFC171	Point #3	61.34	0.00	24.02	0.22	0.02	0.00	6.00	7.49	0.95	0.07	0.18	0.00	0.00	100.30
		Plagioclase													
BFC171	Point #1	60.24	0.05	24.57	0.23	0.00	0.00	6.59	7.38	0.81	0.03	0.19	0.00	0.00	100.11
BFC171	Point #2	60.10	0.03	24.71	0.27	0.00	0.02	6.82	7.33	0.79	0.08	0.17	0.05	0.00	100.38
BFC171	Point #3	60.54	0.02	24.15	0.22	0.01	0.01	6.35	7.62	0.89	0.03	0.12	0.02	0.00	99.97
		Plagioclase													
BFC171	Point #1	60.64	0.00	24.45	0.23	0.01	0.01	6.52	7.43	0.85	0.03	0.19	0.01	0.00	100.36
BFC171	Point #2	61.58	0.02	23.81	0.23	0.00	0.00	5.77	7.69	0.98	0.00	0.17	0.00	0.01	100.25
BFC171	Point #3	61.29	0.02	24.02	0.23	0.00	0.01	6.05	7.52	0.87	0.03	0.15	0.00	0.00	100.22
		Plagioclase													
BFC171	Point #1	61.61	0.04	23.53	0.21	0.01	0.01	5.62	7.92	0.85	0.06	0.13	0.00	0.01	99.99
BFC171	Point #2	60.63	0.00	24.49	0.23	0.00	0.00	6.44	7.58	0.85	0.01	0.20	0.06	0.00	100.48
BFC171	Point #3	62.11	0.00	23.81	0.24	0.03	0.00	5.54	7.85	1.04	0.07	0.17	0.00	0.00	100.85
BFC171	Point #4	61.24	0.00	24.04	0.22	0.00	0.01	6.04	7.46	0.90	0.01	0.15	0.03	0.00	100.10
		Plagioclase													
BFC171	Point #1	61.06	0.01	24.26	0.21	0.00	0.01	6.16	7.60	0.90	0.04	0.19	0.00	0.00	100.45
BFC171	Point #2	60.53	0.03	24.42	0.19	0.00	0.01	6.50	7.43	0.84	0.00	0.13	0.05	0.00	100.13
BFC171	Point #3	60.57	0.01	24.45	0.22	0.00	0.02	6.54	7.44	0.82	0.04	0.16	0.00	0.00	100.28
		Plagioclase													
PCB1	Point #1	60.66	0.02	24.36	0.24	0.00	0.02	6.64	7.31	0.68	0.00	0.22	0.05	0.00	100.20
PCB1	Point #2	60.98	0.00	24.14	0.22	0.00	0.00	6.31	7.22	0.78	0.00	0.16	0.00	0.00	99.81
PCB1	Point #3	61.26	0.00	23.82	0.25	0.00	0.02	5.94	7.63	0.91	0.02	0.10	0.01	0.00	99.96
PCB1	Point #4	61.49	0.00	23.74	0.21	0.00	0.01	5.78	7.67	0.96	0.01	0.18	0.01	0.00	100.05
PCB1	Point #5	60.97	0.01	23.96	0.22	0.00	0.00	6.21	7.63	0.95	0.00	0.21	0.02	0.00	100.17

Sample	Analysis	SiO_2	TiO_2	Al_2O_3	FeO	MnO	MgO	CaO	Na_2O	K_2O	BaO	SrO	F	Cl	Total
Pagosa Peak Dacite		Plagioclase													
PCB1	Point #6	60.07	0.02	24.68	0.24	0.00	0.01	6.94	7.23	0.76	0.03	0.13	0.00	0.00	100.12
PCB1	Point #7	61.28	0.01	23.92	0.22	0.00	0.01	6.09	7.33	0.85	0.00	0.13	0.04	0.00	99.88
PCB1	Point #8	60.98	0.00	24.09	0.21	0.00	0.01	6.18	7.59	0.83	0.04	0.14	0.00	0.00	100.07
		Plagioclase													
PCB1	Point #1	60.51	0.00	24.15	0.24	0.00	0.01	6.52	7.30	0.76	0.02	0.15	0.00	0.00	99.68
PCB1	Point #2	61.47	0.02	23.54	0.21	0.00	0.02	6.02	7.74	0.95	0.00	0.13	0.12	0.00	100.21
PCB1	Point #3	61.00	0.00	23.78	0.22	0.02	0.02	6.21	7.39	0.84	0.04	0.21	0.00	0.00	99.72
PCB1	Point #4	60.41	0.02	24.21	0.20	0.00	0.00	6.69	7.28	0.72	0.03	0.17	0.00	0.00	99.74
PCB1	Point #5	99.78	0.02	0.28	0.05	0.00	0.01	0.07	0.05	0.07	0.04	0.05	0.00	0.00	100.43
PCB1	Point #6	65.81	0.13	20.09	2.08	0.02	0.03	3.38	7.94	1.10	0.00	0.15	0.00	0.00	100.74
PCB1	Point #7	61.33	0.00	23.76	0.20	0.00	0.01	6.05	7.43	0.99	0.02	0.12	0.00	0.00	99.91
PCB1	Point #8	61.18	0.01	23.89	0.23	0.00	0.00	6.12	7.49	0.98	0.03	0.13	0.07	0.00	100.13
PCB1	Point #9	61.11	0.03	24.00	0.22	0.00	0.01	6.07	7.59	0.95	0.00	0.15	0.00	0.00	100.13
PCB1	Point #10	61.09	0.00	23.99	0.22	0.00	0.02	6.09	7.54	0.86	0.04	0.12	0.14	0.00	100.12
		Plagioclase													
PCB1	Point #1	60.91	0.00	23.87	0.22	0.00	0.01	6.36	7.53	0.91	0.07	0.18	0.02	0.00	100.07
PCB1	Point #2	61.50	0.00	23.49	0.23	0.00	0.00	5.73	7.61	1.01	0.06	0.14	0.07	0.00	99.83
PCB1	Point #3	61.43	0.00	23.42	0.22	0.00	0.01	5.69	7.55	1.03	0.06	0.14	0.02	0.00	99.57
PCB1	Point #4	61.64	0.00	23.56	0.26	0.00	0.01	5.71	7.51	1.01	0.02	0.18	0.00	0.00	99.90
PCB1	Point #5	61.12	0.01	23.68	0.25	0.00	0.00	6.16	7.43	0.92	0.03	0.18	0.09	0.00	99.87
		Plagioclase													
PCB1	Point #1	61.21	0.00	23.35	0.19	0.01	0.00	6.11	7.53	0.95	0.04	0.11	0.00	0.00	99.54
PCB1	Point #2	60.49	0.03	23.64	0.19	0.00	0.01	6.53	7.21	0.86	0.04	0.21	0.07	0.00	99.29
PCB1	Point #3	61.79	0.00	22.95	0.22	0.01	0.00	5.57	7.75	1.03	0.02	0.13	0.05	0.00	99.53
PCB1	Point #4	61.37	0.02	23.12	0.22	0.02	0.01	5.83	7.75	1.01	0.06	0.12	0.00	0.00	99.52
		Sanidine													
PCB1	Point #1	65.36	0.04	18.60	0.12	0.00	0.00	0.22	3.30	11.54	0.73	0.11	0.00	0.00	100.00
PCB1	Point #2	65.47	0.02	18.49	0.13	0.00	0.00	0.19	3.27	11.53	0.75	0.10	0.00	0.00	99.95
PCB1	Point #3	65.48	0.00	18.38	0.13	0.00	0.00	0.15	3.27	11.64	0.59	0.12	0.00	0.01	99.76
PCB1	Point #4	65.34	0.01	18.57	0.12	0.00	0.00	0.19	3.20	11.78	0.44	0.17	0.00	0.00	99.81
PCB1	Point #5	65.47	0.03	18.56	0.13	0.00	0.00	0.18	3.23	11.62	0.41	0.15	0.07	0.00	99.85
PCB1	Point #6	65.53	0.05	18.51	0.12	0.00	0.00	0.17	3.28	11.69	0.40	0.14	0.00	0.00	99.89
PCB1	Point #7	65.48	0.07	18.59	0.13	0.00	0.00	0.19	3.37	11.69	0.37	0.14	0.12	0.00	100.14
PCB1	Point #8	65.56	0.00	18.51	0.12	0.01	0.00	0.19	3.13	11.69	0.39	0.14	0.00	0.00	99.75
PCB1	Point #9	65.66	0.02	18.59	0.13	0.01	0.00	0.24	3.41	11.51	0.33	0.11	0.00	0.00	100.00
PCB1	Point #10	65.57	0.00	18.56	0.17	0.01	0.01	0.19	3.35	11.63	0.51	0.13	0.00	0.00	100.12
PCB1	Point #11	65.16	0.00	18.35	0.12	0.01	0.00	0.22	3.21	11.51	0.65	0.18	0.08	0.00	99.49
PCB1	Point #12	65.33	0.03	18.43	0.12	0.00	0.00	0.21	3.11	11.50	0.65	0.11	0.00	0.00	99.47
		Sanidine													
PCB1	Point #1	65.40	0.01	18.42	0.12	0.00	0.00	0.23	3.27	11.27	0.94	0.21	0.00	0.00	99.89
PCB1	Point #2	65.46	0.03	18.50	0.12	0.01	0.00	0.22	3.41	11.24	0.96	0.12	0.00	0.00	100.09
PCB1	Point #3	65.35	0.04	18.47	0.11	0.00	0.00	0.20	3.20	11.48	1.00	0.20	0.00	0.01	100.06
PCB1	Point #4	65.24	0.04	18.24	0.10	0.00	0.00	0.18	3.33	11.33	0.97	0.13	0.00	0.00	99.56
PCB1	Point #5	65.32	0.02	18.49	0.11	0.00	0.00	0.19	3.31	11.49	1.00	0.08	0.07	0.00	100.07
PCB1	Point #6	65.25	0.03	18.33	0.11	0.00	0.00	0.20	3.15	11.50	0.95	0.12	0.00	0.00	99.64
PCB1	Point #7	65.30	0.01	18.48	0.10	0.00	0.00	0.18	3.22	11.51	1.00	0.11	0.06	0.00	99.99
PCB1	Point #8	65.17	0.03	18.27	0.11	0.00	0.00	0.20	3.19	11.59	0.94	0.22	0.05	0.01	99.78
PCB1	Point #9	65.45	0.02	18.48	0.11	0.00	0.00	0.23	3.36	11.29	1.02	0.18	0.00	0.01	100.14
PCB1	Point #10	65.13	0.04	18.55	0.09	0.00	0.00	0.25	3.45	11.14	0.99	0.16	0.00	0.01	99.80
		Sanidine													
PCB1	Point #1	65.26	0.00	18.50	0.10	0.01	0.00	0.25	3.28	11.49	0.84	0.15	0.09	0.00	99.97
PCB1	Point #2	65.37	0.02	18.05	0.10	0.00	0.00	0.26	3.14	11.63	0.81	0.09	0.00	0.00	99.48
PCB1	Point #3	65.38	0.03	18.24	0.09	0.00	0.00	0.26	3.01	11.52	0.81	0.09	0.01	0.00	99.43
PCB1	Point #4	65.34	0.00	18.28	0.11	0.00	0.00	0.25	3.17	11.61	0.85	0.16	0.00	0.01	99.76
PCB1	Point #5	64.64	0.00	18.59	0.11	0.00	0.00	0.30	3.39	11.18	1.30	0.13	0.08	0.00	99.71
PCB1	Point #6	64.91	0.00	18.61	0.10	0.00	0.00	0.25	3.32	11.37	1.17	0.19	0.00	0.00	99.93
PCB1	Point #7	64.84	0.02	18.45	0.12	0.00	0.00	0.28	3.21	11.26	1.22	0.16	0.04	0.00	99.60
PCB1	Point #8	65.10	0.07	18.43	0.12	0.00	0.00	0.30	3.25	11.22	0.88	0.13	0.00	0.00	99.50
PCB1	Point #9	65.27	0.03	18.38	0.11	0.01	0.00	0.26	3.25	11.29	0.89	0.16	0.05	0.00	99.69
PCB1	Point #10	65.22	0.02	18.49	0.13	0.00	0.00	0.28	3.30	11.36	0.89	0.12	0.00	0.01	99.83
PCB1	Point #11	65.47	0.00	18.40	0.20	0.00	0.00	0.26	3.22	11.26	0.91	0.13	0.00	0.00	99.85
PCB1	Point #12	64.94	0.04	18.60	0.15	0.00	0.00	0.33	3.54	10.71	1.26	0.16	0.00	0.00	99.74

Sample	Analysis	SiO_2	TiO_2	Al_2O_3	FeO	MnO	MgO	CaO	Na_2O	K_2O	BaO	SrO	F	Cl	Total
Pagosa Peak Dacite		**Sanidine - Transect**													
PCB1	Point #1	64.79	0.01	18.90	0.10	0.01	0.00	0.22	3.24	11.42	1.14	0.14	0.00	0.00	99.98
PCB1	Point #2	64.79	0.04	18.81	0.12	0.00	0.00	0.19	3.20	11.64	1.08	0.18	0.00	0.00	100.06
PCB1	Point #3	64.92	0.02	18.84	0.10	0.00	0.00	0.20	3.11	11.68	1.05	0.08	0.00	0.00	100.02
PCB1	Point #4	64.71	0.03	18.78	0.11	0.00	0.00	0.17	3.02	11.82	1.01	0.08	0.01	0.00	99.72
PCB1	Point #5	64.87	0.02	18.68	0.11	0.01	0.00	0.16	3.01	11.86	0.99	0.14	0.00	0.00	99.84
PCB1	Point #6	64.95	0.00	18.83	0.10	0.01	0.00	0.17	2.95	11.96	1.02	0.17	0.01	0.00	100.18
PCB1	Point #7	65.01	0.05	18.64	0.11	0.00	0.00	0.15	2.96	11.77	1.06	0.16	0.03	0.00	99.95
PCB1	Point #8	64.24	0.03	18.95	0.09	0.01	0.00	0.28	3.09	11.41	1.53	0.18	0.00	0.00	99.82
PCB1	Point #9	64.36	0.00	18.99	0.10	0.01	0.00	0.30	3.09	11.42	1.40	0.14	0.02	0.00	99.84
PCB1	Point #10	64.61	0.01	18.88	0.12	0.00	0.00	0.29	3.17	11.21	1.30	0.12	0.01	0.00	99.73
PCB1	Point #11	64.49	0.03	18.80	0.11	0.00	0.00	0.30	3.23	11.12	1.26	0.18	0.00	0.01	99.53
Fish Canyon Tuff		**Biotite**													
BFC129	Point #1	37.39	4.13	13.05	16.48	0.36	13.81	0.02	0.47	9.42	0.32	0.00	1.06	0.17	96.68
BFC129	Point #2	37.82	4.21	13.13	16.23	0.40	14.01	0.03	0.53	9.14	0.40	0.03	0.67	0.17	96.76
BFC129	Point #3	37.64	3.88	13.08	16.79	0.33	13.56	0.02	0.54	9.17	0.26	0.04	1.35	0.19	96.83
		Biotite													
BFC129	Point #1	37.49	4.21	13.13	16.72	0.35	13.60	0.02	0.54	9.20	0.29	0.05	1.04	0.17	96.80
BFC129	Point #2	37.45	4.18	13.12	16.52	0.34	13.73	0.03	0.47	9.17	0.25	0.12	1.15	0.17	96.70
BFC129	Point #3	37.81	4.37	13.10	16.28	0.32	13.94	0.02	0.47	9.27	0.35	0.00	1.48	0.16	97.56
		Biotite													
BFC129	Point #1	37.25	4.37	12.89	16.31	0.37	13.73	0.03	0.51	9.16	0.29	0.12	0.68	0.17	95.87
BFC129	Point #2	37.68	4.99	12.94	16.26	0.31	14.13	0.02	0.51	9.21	0.35	0.00	0.54	0.18	97.11
BFC129	Point #3	37.68	4.25	13.14	16.34	0.31	13.84	0.04	0.64	9.13	0.24	0.00	0.89	0.17	96.68
		Biotite													
BFC129	Point #1	37.24	4.78	13.02	16.08	0.34	13.94	0.04	0.50	9.15	0.16	0.00	0.59	0.15	95.99
BFC129	Point #2	36.89	4.95	12.86	15.94	0.35	13.93	0.03	0.50	9.00	0.27	0.00	0.60	0.17	95.51
BFC129	Point #3	37.17	4.94	12.85	16.17	0.33	13.76	0.03	0.54	9.03	0.34	0.03	0.55	0.17	95.90
		Biotite													
BFC129	Point #1	36.75	4.90	12.93	16.20	0.30	13.66	0.07	0.59	9.15	0.16	0.00	0.89	0.16	95.74
BFC129	Point #2	37.52	4.76	13.11	15.88	0.34	14.13	0.04	0.52	9.23	0.16	0.01	0.45	0.15	96.31
BFC129	Point #3	37.63	4.45	13.18	15.99	0.37	14.07	0.04	0.53	9.17	0.11	0.00	0.70	0.17	96.40
		Plagioclase													
BFC129	Point #1	60.86	0.03	24.13	0.22	0.00	0.01	6.19	7.41	0.92	0.03	0.14	0.00	0.00	99.97
BFC129	Point #2	61.26	0.00	23.94	0.21	0.00	0.00	6.01	7.73	0.89	0.01	0.12	0.00	0.00	100.16
BFC129	Point #3	61.54	0.10	23.62	0.22	0.00	0.00	5.66	7.52	1.04	0.07	0.16	0.01	0.00	99.96
		Plagioclase													
BFC129	Point #1	60.12	0.01	24.07	0.22	0.00	0.00	6.34	7.40	0.85	0.03	0.17	0.05	0.00	99.27
BFC129	Point #2	60.85	0.02	23.84	0.24	0.02	0.01	5.92	7.45	0.96	0.08	0.20	0.08	0.00	99.66
BFC129	Point #3	59.95	0.03	24.38	0.24	0.00	0.01	6.63	7.19	0.84	0.00	0.17	0.04	0.00	99.48
		Plagioclase													
BFC129	Point #1	61.07	0.02	23.73	0.22	0.00	0.01	5.92	7.57	1.01	0.00	0.20	0.00	0.00	99.76
BFC129	Point #2	61.77	0.00	23.35	0.22	0.00	0.00	5.42	7.80	1.14	0.01	0.17	0.03	0.01	99.93
BFC129	Point #3	61.10	0.03	23.79	0.20	0.00	0.01	5.92	7.63	0.96	0.04	0.21	0.05	0.00	99.94
		Plagioclase													
BFC129	Point #1	60.51	0.02	24.02	0.22	0.01	0.01	6.21	7.53	0.93	0.06	0.12	0.00	0.00	99.65
BFC129	Point #2	60.76	0.01	23.84	0.23	0.01	0.01	6.03	7.61	0.89	0.05	0.11	0.00	0.00	99.57
BFC129	Point #3	60.05	0.00	24.06	0.24	0.00	0.01	6.31	7.37	0.90	0.01	0.18	0.00	0.01	99.13
		Biotite													
BFC191	Point #1	37.97	4.13	13.26	16.99	0.32	13.12	0.01	0.44	9.29	0.33	0.00	0.52	0.19	96.57
BFC191	Point #2	37.69	4.32	13.16	16.46	0.32	13.39	0.02	0.41	9.29	0.19	0.02	0.47	0.18	95.90
BFC191	Point #3	37.65	4.03	13.23	17.03	0.33	13.69	0.01	0.37	9.21	0.25	0.00	0.32	0.18	96.30
		Biotite													
BFC191	Point #1	38.05	4.96	13.28	15.11	0.26	14.64	0.07	0.48	9.02	0.25	0.00	0.48	0.16	96.75
BFC191	Point #2	37.70	4.38	13.32	15.29	0.37	14.80	0.06	0.55	9.12	0.27	0.01	0.47	0.15	96.49

Sample	Analysis	SiO_2	TiO_2	Al_2O_3	FeO	MnO	MgO	CaO	Na_2O	K_2O	BaO	SrO	F	Cl	Total
Fish Canyon Tuff			**Biotite**												
BFC191	Point #1	37.29	4.09	13.18	16.65	0.33	13.52	0.03	0.43	9.18	0.25	0.02	0.44	0.18	95.59
BFC191	Point #2	37.31	4.66	13.12	16.92	0.30	13.35	0.02	0.39	9.24	0.29	0.06	0.38	0.17	96.21
BFC191	Point #3	37.45	4.32	13.22	16.16	0.28	13.91	0.03	0.40	9.16	0.27	0.00	0.41	0.17	95.77
			Biotite												
BFC191	Point #1	37.59	4.37	13.06	15.54	0.30	14.68	0.03	0.51	9.18	0.33	0.00	1.02	0.14	96.74
BFC191	Point #2	37.36	4.20	13.24	15.73	0.31	14.35	0.02	0.51	8.98	0.52	0.00	0.45	0.17	95.85
BFC191	Point #3	37.50	4.36	12.23	15.81	0.35	14.53	0.01	0.47	9.19	0.34	0.07	0.52	0.17	95.56
			Biotite												
BFC191	Point #1	37.47	4.22	12.21	14.63	0.26	14.65	0.06	0.48	8.95	0.58	0.00	0.48	0.12	94.08
BFC191	Point #2	37.63	4.13	12.30	14.73	0.28	14.87	0.03	0.50	9.04	0.51	0.04	0.33	0.11	94.50
BFC191	Point #3	37.45	4.91	13.22	14.71	0.28	14.60	0.03	0.44	8.98	0.63	0.00	0.35	0.11	95.72
			Plagioclase												
BFC191	Point #2	59.92	0.00	23.93	0.22	0.00	0.02	6.46	7.42	0.86	0.03	0.16	0.01	0.01	99.03
BFC191	Point #3	60.46	0.00	23.65	0.20	0.00	0.01	5.95	7.75	0.98	0.03	0.22	0.05	0.00	99.32
BFC191	Point #1	60.48	0.01	24.40	0.24	0.00	0.00	6.37	7.40	0.90	0.05	0.16	0.05	0.00	100.05
BFC191	Point #2	61.43	0.02	23.69	0.21	0.02	0.01	5.68	7.66	1.06	0.05	0.27	0.00	0.00	100.11
BFC191	Point #3	60.49	0.00	24.23	0.21	0.00	0.01	6.20	7.89	0.92	0.02	0.17	0.01	0.00	100.15
			Plagioclase												
BFC191	Point #1	60.67	0.00	24.27	0.20	0.01	0.01	6.22	7.62	0.94	0.04	0.16	0.01	0.00	100.16
BFC191	Point #2	60.49	0.02	24.37	0.22	0.02	0.02	6.41	7.60	0.86	0.02	0.16	0.00	0.00	100.17
BFC191	Point #3	60.22	0.01	24.51	0.22	0.00	0.02	6.59	7.40	0.82	0.04	0.17	0.00	0.00	100.01
			Plagioclase												
BFC191	Point #1	60.29	0.03	23.75	0.22	0.01	0.01	6.18	7.49	0.95	0.04	0.23	0.03	0.00	99.22
BFC191	Point #2	59.92	0.02	24.08	0.23	0.01	0.01	6.47	7.43	0.88	0.01	0.15	0.00	0.00	99.23
BFC191	Point #3	60.21	0.02	24.17	0.21	0.00	0.01	6.31	7.83	0.89	0.02	0.25	0.00	0.00	99.92
			Plagioclase												
BFC191	Point #1	60.83	0.05	23.58	0.21	0.00	0.00	5.81	7.69	0.98	0.03	0.15	0.00	0.00	99.31
BFC191	Point #2	60.89	0.04	23.83	0.23	0.02	0.01	5.91	7.66	0.85	0.00	0.19	0.00	0.00	99.63
BFC191	Point #3	60.11	0.05	24.33	0.22	0.00	0.01	6.53	7.45	0.87	0.00	0.14	0.02	0.00	99.74
Nutras Creek Dacite			**Biotite**												
BFC115	Point #1	37.77	4.33	13.29	17.27	0.36	13.41	0.00	0.38	9.31	0.31	0.08	0.45	0.17	97.13
BFC115	Point #2	37.71	4.22	13.26	17.39	0.41	13.40	0.01	0.42	9.35	0.17	0.04	0.52	0.17	97.06
BFC115	Point #3	38.37	4.14	13.40	16.95	0.18	12.94	0.08	0.28	9.10	0.37	0.02	2.06	0.18	98.09
BFC115	Point #4	37.97	3.13	13.33	17.59	0.32	13.39	0.02	0.33	9.26	0.39	0.00	1.69	0.18	97.59
BFC115	Point #5	37.79	4.88	13.06	17.86	0.34	12.91	0.05	0.38	9.32	0.17	0.00	0.89	0.17	97.83
BFC115	Point #6	37.93	4.60	13.16	17.06	0.35	13.35	0.02	0.34	9.30	0.30	0.02	0.37	0.17	96.97
BFC115	Inclusion	0.34	0.02	0.00	0.56	0.26	0.19	52.10	0.17	0.12	0.00	0.03	5.79	0.68	60.27 ^
BFC115	Inclusion	59.89	0.00	24.69	0.75	0.00	0.05	6.54	7.43	0.93	0.04	0.13	0.03	0.00	100.48 ¤
			Biotite												
BFC115	Point #1	37.94	4.11	13.29	16.11	0.25	14.08	0.05	0.49	9.09	0.27	0.03	0.81	0.16	96.68
BFC115	Point #2	38.12	4.03	13.21	16.58	0.26	14.02	0.03	0.46	9.33	0.28	0.03	1.21	0.16	97.72
BFC115	Point #3	38.41	3.99	13.07	15.61	0.30	14.44	0.04	0.53	9.20	0.13	0.00	0.77	0.17	96.68
BFC115	Point #4	38.27	4.00	13.10	15.46	0.35	14.47	0.04	0.45	9.10	0.16	0.00	0.60	0.15	96.15
BFC115	Point #5	38.04	4.15	12.98	15.76	0.37	14.33	0.04	0.45	9.14	0.22	0.05	0.78	0.17	96.50
BFC115	Point #6	37.92	4.15	13.18	16.53	0.33	14.36	0.03	0.54	9.09	0.38	0.01	0.63	0.16	97.32
			Biotite												
BFC115	Point #1	37.40	4.21	12.15	17.37	0.34	13.28	0.02	0.42	9.22	0.38	0.00	1.15	0.17	96.10
BFC115	Point #2	37.94	4.00	13.21	16.32	0.35	13.89	0.01	0.46	9.10	0.21	0.01	0.48	0.16	96.14
BFC115	Point #3	38.10	4.04	13.10	16.39	0.34	13.82	0.03	0.36	9.14	0.26	0.04	0.47	0.17	96.26
BFC115	Point #4	37.82	4.37	12.08	16.49	0.37	13.87	0.01	0.42	9.25	0.23	0.01	0.60	0.16	95.68
BFC115	Point #5	38.10	4.29	13.07	16.43	0.37	13.95	0.02	0.39	9.19	0.16	0.04	0.45	0.17	96.64
BFC115	Point #6	38.17	4.04	13.21	16.84	0.33	13.72	0.04	0.44	9.15	0.27	0.02	0.76	0.17	97.15
BFC115	Point #7	37.89	4.23	13.36	16.99	0.28	13.65	0.04	0.40	9.08	0.35	0.01	1.57	0.17	98.02
BFC115	Point #8	37.87	4.22	13.23	17.13	0.34	13.62	0.01	0.42	9.23	0.33	0.03	0.91	0.17	97.50
			Biotite												
BFC115	Point #1	37.59	4.22	13.33	17.11	0.38	13.48	0.01	0.47	9.24	0.29	0.00	0.60	0.16	96.88
BFC115	Point #2	37.63	4.03	13.16	16.96	0.36	13.59	0.00	0.39	9.43	0.19	0.02	0.50	0.17	96.45
BFC115	Point #3	37.82	4.12	12.27	16.75	0.35	13.62	0.01	0.42	9.29	0.23	0.04	0.43	0.16	95.52
BFC115	Point #4	37.88	4.24	13.19	16.64	0.33	13.69	0.02	0.42	9.21	0.18	0.05	0.38	0.16	96.40

Sample	Analysis	SiO_2	TiO_2	Al_2O_3	FeO	MnO	MgO	CaO	Na_2O	K_2O	BaO	SrO	F	Cl	Total
Nutras Creek Dacite		Biotite													
BFC115	Point #5	37.80	4.37	13.43	16.90	0.36	13.74	0.03	0.42	9.27	0.37	0.06	0.36	0.18	97.27
BFC115	Point #6	37.65	4.20	13.30	16.90	0.31	13.56	0.02	0.47	9.34	0.21	0.02	0.54	0.16	96.69
BFC115	Point #7	37.77	4.02	13.33	16.62	0.38	13.74	0.01	0.44	9.17	0.38	0.00	0.43	0.17	96.45
BFC115	Point #8	37.68	4.13	12.16	17.47	0.36	13.37	0.01	0.41	9.41	0.35	0.03	0.74	0.16	96.28
BFC115	Point #9	37.79	4.13	13.22	16.30	0.36	13.76	0.01	0.41	9.25	0.28	0.00	0.46	0.17	96.15
		Biotite													
BFC115	Point #1	37.44	4.01	12.31	18.43	0.36	12.60	0.00	0.42	9.39	0.20	0.01	1.08	0.18	96.45
BFC115	Point #2	37.66	4.33	13.20	17.74	0.37	12.97	0.01	0.42	9.15	0.38	0.00	0.43	0.16	96.81
BFC115	Point #3	38.10	4.03	12.92	16.60	0.37	12.98	0.09	0.50	8.86	0.32	0.04	0.41	0.16	95.37
BFC115	Point #4	37.78	4.37	13.32	17.55	0.38	12.98	0.00	0.45	9.23	0.26	0.08	0.46	0.17	97.03
BFC115	Point #5	37.65	4.00	13.25	17.53	0.38	13.14	0.01	0.48	9.13	0.36	0.00	0.43	0.17	96.53
BFC115	Point #6	37.51	4.02	13.28	18.39	0.42	12.74	0.03	0.35	9.32	0.31	0.00	1.36	0.16	97.91
BFC115	Point #7	37.55	4.33	13.37	18.54	0.38	12.58	0.02	0.40	9.18	0.30	0.03	0.94	0.16	97.76
		Sanidine													
BFC115	Point #1	64.81	0.00	18.77	0.11	0.00	0.00	0.19	2.81	11.91	1.29	0.10	0.07	0.00	100.06
BFC115	Point #2	64.70	0.00	18.75	0.10	0.00	0.01	0.18	2.80	11.76	1.34	0.10	0.04	0.00	99.78
BFC115	Point #3	65.49	0.02	18.66	0.11	0.00	0.00	0.15	2.97	11.93	0.88	0.16	0.00	0.00	100.37
BFC115	Point #4	65.24	0.02	18.60	0.10	0.02	0.00	0.13	2.99	12.00	0.82	0.12	0.00	0.00	100.01
BFC115	Point #5	65.04	0.00	18.64	0.10	0.00	0.00	0.20	2.73	11.94	0.85	0.21	0.06	0.00	99.78
BFC115	Point #6	64.95	0.04	18.68	0.08	0.02	0.00	0.15	2.76	12.21	1.02	0.11	0.00	0.00	100.02
BFC115	Point #7	65.40	0.00	18.77	0.10	0.00	0.00	0.18	2.98	11.99	0.72	0.16	0.00	0.00	100.30
BFC115	Point #8	64.77	0.00	18.61	0.09	0.00	0.00	0.16	2.68	11.90	1.21	0.12	0.00	0.00	99.55
BFC115	Point #9	64.83	0.02	18.67	0.09	0.00	0.00	0.16	2.83	12.12	1.11	0.06	0.05	0.00	99.94
BFC115	Point #10	64.65	0.02	18.64	0.12	0.00	0.00	0.19	2.97	11.64	1.00	0.15	0.00	0.00	99.37
BFC115	Point #11	64.68	0.01	18.68	0.10	0.00	0.00	0.19	3.05	11.59	0.98	0.13	0.00	0.01	99.42
		Sanidine													
BFC115	Point #1	65.12	0.01	18.67	0.12	0.00	0.00	0.20	2.97	11.88	0.80	0.15	0.01	0.01	99.92
BFC115	Point #2	64.73	0.01	18.80	0.12	0.00	0.00	0.19	2.87	11.91	1.38	0.10	0.00	0.01	100.11
BFC115	Point #3	64.28	0.00	18.73	0.10	0.00	0.00	0.16	2.76	11.96	1.72	0.20	0.03	0.00	99.95
BFC115	Point #4	65.14	0.04	18.59	0.12	0.01	0.00	0.13	2.69	12.33	0.93	0.09	0.07	0.00	100.14
BFC115	Point #5	64.65	0.02	18.82	0.11	0.00	0.00	0.19	2.82	11.90	1.20	0.13	0.00	0.00	99.85
BFC115	Point #6	64.48	0.00	18.79	0.10	0.00	0.00	0.20	2.99	11.67	1.45	0.21	0.08	0.00	99.97
BFC115	Point #7	65.34	0.00	18.63	0.10	0.00	0.00	0.12	2.79	12.09	0.93	0.09	0.02	0.00	100.14
BFC115	Point #8	64.47	0.04	18.79	0.10	0.01	0.00	0.25	2.86	11.80	1.38	0.12	0.00	0.00	99.83
BFC115	Point #9	65.38	0.00	18.57	0.13	0.01	0.02	0.16	2.76	12.22	0.77	0.11	0.03	0.00	100.15
BFC115	Point #10	65.60	0.00	18.67	0.10	0.00	0.00	0.23	3.21	11.53	0.53	0.12	0.00	0.00	99.99
BFC115	Point #11	64.56	0.00	18.72	0.12	0.01	0.00	0.18	2.83	11.98	1.28	0.12	0.01	0.00	99.81
		Sanidine													
BFC115	Point #1	64.91	0.03	18.85	0.10	0.00	0.00	0.24	3.08	11.54	1.45	0.16	0.08	0.01	100.45
BFC115	Point #2	64.34	0.00	18.96	0.11	0.01	0.00	0.21	2.87	11.57	1.79	0.09	0.00	0.00	99.94
BFC115	Point #3	65.25	0.00	18.74	0.10	0.01	0.00	0.19	2.75	12.00	0.74	0.17	0.02	0.01	99.99
BFC115	Point #4	64.62	0.01	18.65	0.10	0.00	0.00	0.20	2.90	11.80	1.12	0.15	0.02	0.01	99.58
BFC115	Point #5	64.95	0.04	18.70	0.10	0.00	0.00	0.21	2.97	11.78	1.11	0.20	0.00	0.00	100.04
BFC115	Point #6	65.02	0.00	18.75	0.11	0.00	0.00	0.16	2.75	12.03	1.10	0.11	0.02	0.00	100.05
BFC115	Point #7	64.90	0.02	18.63	0.11	0.00	0.00	0.20	2.81	11.89	1.11	0.21	0.04	0.00	99.91
BFC115	Point #8	65.18	0.02	18.65	0.11	0.02	0.00	0.18	2.69	12.19	0.98	0.10	0.00	0.01	100.13
BFC115	Point #9	64.69	0.02	18.74	0.09	0.01	0.00	0.20	2.73	11.96	1.02	0.19	0.00	0.00	99.66
BFC115	Point #10	64.70	0.00	18.74	0.10	0.00	0.00	0.21	3.00	11.52	1.52	0.13	0.10	0.00	100.02
		Sanidine													
BFC115	Point #1	64.65	0.00	18.69	0.10	0.00	0.00	0.29	2.80	11.84	1.06	0.22	0.09	0.00	99.75
BFC115	Point #2	65.17	0.02	18.56	0.09	0.00	0.00	0.23	2.83	12.19	0.51	0.16	0.00	0.00	99.75
BFC115	Point #3	64.51	0.00	18.51	0.10	0.00	0.00	0.26	2.63	12.21	1.03	0.21	0.07	0.00	99.55
BFC115	Point #5	64.59	0.00	18.60	0.11	0.01	0.00	0.24	2.71	12.06	1.01	0.15	0.00	0.00	99.48
BFC115	Point #6	64.87	0.01	18.49	0.10	0.00	0.00	0.28	2.82	11.80	1.06	0.17	0.03	0.01	99.63
BFC115	Point #7	64.61	0.00	18.53	0.13	0.00	0.00	0.32	2.92	11.69	0.99	0.16	0.00	0.01	99.36
BFC115	Point #8	65.10	0.03	18.33	0.10	0.01	0.01	0.20	2.65	12.18	0.63	0.11	0.00	0.00	99.36
BFC115	Point #9	64.55	0.02	18.51	0.11	0.00	0.00	0.26	2.71	12.06	1.07	0.15	0.00	0.00	99.44
BFC115	Point #1	64.11	0.00	18.70	0.12	0.01	0.00	0.24	2.40	12.29	1.38	0.12	0.06	0.00	99.44
BFC115	Point #2	64.45	0.00	18.57	0.16	0.00	0.03	0.24	2.66	11.85	1.35	0.10	0.00	0.00	99.42
BFC115	Point #3	64.44	0.02	18.88	0.13	0.00	0.00	0.20	2.69	11.97	1.49	0.16	0.00	0.00	99.99
BFC115	Point #4	64.85	0.35	18.69	0.10	0.00	0.00	0.17	2.72	12.39	1.13	0.16	0.00	0.00	100.57
BFC115	Point #5	64.85	0.00	18.59	0.11	0.00	0.00	0.19	2.56	12.49	0.80	0.11	0.05	0.01	99.75

Sample	Analysis	SiO_2	TiO_2	Al_2O_3	FeO	MnO	MgO	CaO	Na_2O	K_2O	BaO	SrO	F	Cl	Total
Nutras Creek Dacite		Sanidine													
BFC115	Point #6	64.41	0.01	18.99	0.10	0.01	0.00	0.24	2.54	11.88	1.40	0.17	0.00	0.00	99.77
BFC115	Point #7	64.94	0.02	18.69	0.11	0.00	0.00	0.24	2.62	12.27	0.97	0.22	0.00	0.00	100.08
BFC115	Point #8	65.20	0.00	18.47	0.09	0.00	0.00	0.19	2.66	12.50	0.79	0.14	0.00	0.00	100.04
		Plagioclase													
BFC115	Point #1	60.27	0.00	24.62	0.20	0.00	0.00	6.75	7.09	0.85	0.02	0.26	0.00	0.00	100.06
BFC115	Point #2	60.16	0.00	24.65	0.23	0.00	0.01	6.79	7.36	0.78	0.04	0.20	0.05	0.00	100.28
BFC115	Point #3	58.22	0.00	25.99	0.24	0.00	0.02	8.32	6.50	0.59	0.05	0.22	0.00	0.00	100.16
BFC115	Point #4	61.51	0.02	23.66	0.21	0.00	0.00	5.76	7.41	0.96	0.02	0.19	0.01	0.00	99.75
BFC115	Point #5	60.60	0.00	24.49	0.23	0.01	0.02	6.61	7.37	0.87	0.04	0.18	0.00	0.00	100.41
BFC115	Point #6	60.38	0.01	24.58	0.21	0.00	0.01	6.73	7.07	0.82	0.00	0.14	0.08	0.00	100.04
BFC115	Point #7	60.58	0.10	24.39	0.25	0.00	0.01	6.50	7.23	0.84	0.03	0.17	0.00	0.00	100.08
BFC115	Point #8	60.68	0.02	24.27	0.23	0.02	0.01	6.37	7.32	0.87	0.04	0.12	0.05	0.00	100.00
BFC115	Point #9	60.88	0.00	23.93	0.23	0.01	0.00	6.00	7.31	0.95	0.07	0.16	0.00	0.01	99.55
BFC115	Point #12	60.69	0.02	24.35	0.23	0.00	0.02	6.46	7.29	0.88	0.02	0.22	0.00	0.01	100.18
BFC115	Point #13	60.74	0.01	24.29	0.23	0.00	0.01	6.38	7.37	0.89	0.05	0.12	0.00	0.00	100.09
BFC115	Point #14	60.77	0.01	24.16	0.24	0.00	0.02	6.29	7.39	0.82	0.06	0.14	0.00	0.00	99.90
		Plagioclase													
BFC115	Point #1	61.25	0.00	23.98	0.21	0.01	0.01	5.92	7.43	1.04	0.05	0.21	0.08	0.00	100.21
BFC115	Point #2	60.24	0.01	24.49	0.24	0.00	0.00	6.63	7.30	0.84	0.04	0.22	0.00	0.01	100.04
BFC115	Point #3	60.35	0.00	24.74	0.23	0.00	0.02	6.77	7.33	0.82	0.04	0.20	0.05	0.00	100.54
BFC115	Point #5	60.45	0.03	24.37	0.23	0.00	0.02	6.57	7.08	0.88	0.00	0.15	0.00	0.00	99.78
BFC115	Point #6	61.23	0.00	24.18	0.23	0.00	0.01	6.13	7.45	0.93	0.04	0.08	0.05	0.00	100.32
		Plagioclase													
BFC115	Point #1	60.62	0.00	24.38	0.22	0.00	0.01	6.54	7.05	0.87	0.03	0.14	0.02	0.00	99.89
BFC115	Point #2	60.42	0.01	24.44	0.23	0.00	0.00	6.64	7.07	0.89	0.00	0.13	0.08	0.00	99.91
BFC115	Point #3	60.15	0.00	24.69	0.21	0.00	0.01	6.78	7.17	0.82	0.03	0.19	0.00	0.00	100.05
BFC115	Point #4	61.95	0.00	23.50	0.24	0.00	0.01	5.65	7.40	0.89	0.00	0.14	0.00	0.01	99.79
BFC115	Point #5	60.42	0.00	24.38	0.22	0.01	0.00	6.54	7.08	0.89	0.02	0.18	0.00	0.00	99.75
BFC115	Point #6	60.31	0.02	24.29	0.23	0.01	0.01	6.74	6.93	0.82	0.05	0.13	0.02	0.00	99.56
BFC115	Point #7	61.10	0.03	23.79	0.23	0.00	0.01	6.01	7.54	0.98	0.04	0.23	0.01	0.00	99.98
BFC115	Point #8	60.68	0.00	24.29	0.22	0.02	0.01	6.43	7.43	0.88	0.04	0.18	0.03	0.00	100.21

^ = Apatite inclusion

¤ = Plagioclase inclusion

Feldspar = crystals contain both Ca- and K-rich zones

Transect = data displayed in Figure 2.4

Electron microprobe (wt. %) analysis of all Yellowstone tuff and dome samples by phase

Sample	Analysis	SiO_2	TiO_2	Al_2O_3	FeO	MnO	MgO	CaO	Na_2O	K_2O	BaO	SrO	F	Cl	Total
Huckleberry Ridge Tuff - A			Pumice		Sanidine										
YP127	Point	66.18	0.00	18.81	0.10	0.00	0.00	0.47	4.70	9.30	0.50	0.06	0.02	0.00	100.14
YP127	Point	65.71	0.00	18.80	0.07	0.00	0.00	0.48	4.62	9.24	0.51	0.06	0.00	0.00	99.49
YP127	Point	65.69	0.01	18.75	0.05	0.00	0.00	0.46	4.65	9.45	0.52	0.01	0.04	0.00	99.63
YP127	Point	65.78	0.02	18.75	0.10	0.00	0.00	0.46	4.70	9.34	0.52	0.02	0.00	0.01	99.69
YP127	Point	65.49	0.00	18.70	0.10	0.00	0.00	0.46	4.70	9.29	0.50	0.03	0.04	0.00	99.30
YP127	Point	65.82	0.04	18.75	0.13	0.00	0.00	0.44	4.50	9.24	0.52	0.02	0.07	0.00	99.50
YP127	Point	65.43	0.04	18.74	0.12	0.00	0.00	0.43	4.43	9.49	0.52	0.03	0.01	0.00	99.23
YP127	Point	65.61	0.02	18.76	0.10	0.00	0.00	0.45	4.64	9.50	0.55	0.03	0.06	0.01	99.70
YP127	Point	65.58	0.00	18.74	0.10	0.00	0.00	0.46	4.54	9.43	0.54	0.03	0.05	0.00	99.45
YP127	Point	65.55	0.01	18.87	0.12	0.01	0.00	0.45	4.76	9.42	0.56	0.02	0.00	0.00	99.75
YP127	Point	65.45	0.04	18.67	0.08	0.00	0.00	0.43	4.46	9.39	0.53	0.06	0.12	0.00	99.18
YP127	Point	65.46	0.03	18.73	0.12	0.00	0.00	0.47	4.65	9.40	0.55	0.07	0.03	0.00	99.50
YP127	Point	65.32	0.00	18.82	0.09	0.00	0.00	0.48	4.56	9.34	0.54	0.02	0.14	0.01	99.25
YP127	Point	65.40	0.00	18.80	0.10	0.01	0.00	0.45	4.76	9.25	0.57	0.02	0.01	0.00	99.37
YP127	Point	65.85	0.00	19.11	0.13	0.00	0.00	0.43	4.69	9.49	0.65	0.02	0.03	0.00	100.42
YP127	Point	65.93	0.00	18.97	0.12	0.01	0.00	0.41	4.45	9.40	0.59	0.05	0.02	0.00	99.95
YP127	Point	65.78	0.03	18.95	0.11	0.00	0.00	0.43	4.71	9.46	0.57	0.03	0.00	0.01	100.08
YP127	Point	65.54	0.01	19.00	0.13	0.00	0.00	0.44	4.46	9.43	0.63	0.06	0.03	0.00	99.72
YP127	Point	65.47	0.00	19.01	0.10	0.00	0.00	0.42	4.48	9.36	0.65	0.07	0.00	0.00	99.57
YP127	Point	65.82	0.00	18.98	0.10	0.00	0.00	0.44	4.76	9.57	0.59	0.03	0.00	0.00	100.29
YP127	Point	65.92	0.02	18.86	0.06	0.00	0.00	0.43	4.61	9.47	0.61	0.04	0.00	0.00	100.02
YP127	Point	65.50	0.01	18.89	0.08	0.00	0.00	0.43	4.69	9.42	0.61	0.06	0.00	0.00	99.68
YP127	Point	65.54	0.02	18.87	0.13	0.00	0.00	0.43	4.67	9.44	0.64	0.04	0.06	0.00	99.83
YP127	Point	65.71	0.00	18.88	0.11	0.00	0.00	0.41	4.48	9.39	0.61	0.06	0.11	0.01	99.77
YP127	Point	65.61	0.02	18.87	0.12	0.01	0.00	0.43	4.62	9.45	0.59	0.02	0.09	0.00	99.84
YP127	Point	65.65	0.00	18.89	0.16	0.00	0.00	0.44	4.54	9.45	0.62	0.05	0.12	0.00	99.91
YP127	Point	65.40	0.03	18.82	0.11	0.00	0.00	0.43	4.64	9.45	0.59	0.05	0.01	0.00	99.54
YP127	Point	65.73	0.00	19.02	0.09	0.00	0.00	0.42	4.56	9.37	0.61	0.05	0.02	0.00	99.87
YP127	Point	65.57	0.02	18.94	0.10	0.00	0.00	0.43	4.69	9.41	0.62	0.03	0.09	0.00	99.90
YP127	Point	65.47	0.00	18.93	0.07	0.01	0.01	0.44	4.75	9.54	0.61	0.03	0.00	0.00	99.85
YP127	Point	65.51	0.01	19.00	0.09	0.00	0.00	0.43	4.70	9.53	0.58	0.06	0.00	0.00	99.91
YP127	Point	65.45	0.05	18.89	0.09	0.00	0.00	0.44	4.57	9.41	0.55	0.04	0.00	0.00	99.50
YP127	Point	65.77	0.02	18.92	0.09	0.00	0.01	0.42	4.60	9.45	0.59	0.04	0.00	0.00	99.92
YP127	Point	65.45	0.02	18.85	0.12	0.00	0.00	0.44	4.62	9.54	0.55	0.05	0.08	0.00	99.72
YP127	Point	65.58	0.00	18.86	0.10	0.00	0.00	0.42	4.54	9.55	0.57	0.04	0.00	0.00	99.66
YP127	Point	65.56	0.00	18.81	0.09	0.01	0.00	0.41	4.46	9.52	0.56	0.07	0.04	0.00	99.52
YP127	Point	65.55	0.00	18.72	0.14	0.00	0.00	0.41	4.53	9.49	0.53	0.03	0.00	0.00	99.41
YP127	Point	65.64	0.00	18.79	0.12	0.00	0.00	0.39	4.54	9.49	0.52	0.07	0.06	0.00	99.61
YP127	Point	65.25	0.00	18.85	0.10	0.00	0.00	0.37	4.35	9.60	0.96	0.08	0.00	0.01	99.56
YP127	Point	65.21	0.00	18.76	0.11	0.00	0.00	0.38	4.40	9.54	0.92	0.05	0.00	0.00	99.38
YP127	Point	65.40	0.04	18.89	0.11	0.00	0.00	0.38	4.38	9.54	0.96	0.02	0.00	0.00	99.74
YP127	Point	65.09	0.00	18.91	0.10	0.00	0.00	0.42	4.44	9.54	1.01	0.05	0.00	0.00	99.56
YP127	Point	65.06	0.01	18.85	0.09	0.00	0.00	0.44	4.37	9.46	1.01	0.06	0.01	0.00	99.37
YP127	Point	65.06	0.05	19.02	0.12	0.00	0.00	0.46	4.44	9.45	1.09	0.10	0.03	0.00	99.81
YP127	Point	65.20	0.02	18.97	0.10	0.00	0.00	0.45	4.50	9.42	1.03	0.10	0.02	0.00	99.82
YP127	Point	65.24	0.00	18.99	0.13	0.00	0.00	0.44	4.40	9.48	1.04	0.06	0.05	0.00	99.82
YP127	Point	65.42	0.00	18.71	0.15	0.00	0.01	0.37	4.60	9.56	0.89	0.06	0.00	0.01	99.79
YP127	Point	65.30	0.04	18.87	0.07	0.01	0.00	0.37	4.42	9.60	0.88	0.07	0.12	0.00	99.76
YP127	Point	65.44	0.00	18.57	0.11	0.01	0.00	0.35	4.43	9.67	0.85	0.04	0.00	0.00	99.47
YP127	Point	65.19	0.06	18.74	0.09	0.00	0.00	0.36	4.46	9.63	0.89	0.04	0.01	0.00	99.47
YP127	Point	65.51	0.02	18.84	0.13	0.01	0.00	0.36	4.51	9.62	0.85	0.07	0.14	0.00	100.05
YP127	Point	65.34	0.00	18.77	0.11	0.01	0.00	0.36	4.43	9.53	0.88	0.09	0.04	0.00	99.56
YP127	Point	65.30	0.00	18.61	0.09	0.00	0.00	0.33	4.38	9.61	0.88	0.06	0.08	0.00	99.34
YP127	Point	65.40	0.04	18.79	0.11	0.01	0.00	0.34	4.44	9.61	0.86	0.04	0.05	0.00	99.70
YP127	Point	65.39	0.00	18.73	0.12	0.00	0.00	0.35	4.22	9.67	0.85	0.03	0.00	0.00	99.36
YP127	Point	65.36	0.06	18.63	0.12	0.01	0.00	0.33	4.29	9.55	0.85	0.00	0.02	0.00	99.21
YP127	Point	65.47	0.00	18.79	0.10	0.00	0.00	0.34	4.45	9.75	0.88	0.03	0.13	0.00	99.96
YP127	Point	65.34	0.03	18.66	0.09	0.02	0.00	0.35	4.50	9.74	0.84	0.02	0.02	0.01	99.61
YP127	Point	65.51	0.00	18.82	0.10	0.00	0.00	0.34	4.54	9.73	0.86	0.03	0.00	0.00	99.93
YP127	Point	65.48	0.01	18.83	0.12	0.00	0.00	0.34	4.46	9.68	0.85	0.06	0.00	0.00	99.83
YP127	Point	65.30	0.03	18.75	0.10	0.00	0.00	0.35	4.46	9.65	0.86	0.05	0.00	0.00	99.56
YP127	Point	65.36	0.00	18.63	0.08	0.00	0.00	0.36	4.33	9.61	0.86	0.03	0.00	0.00	99.27
YP127	Point	65.37	0.03	18.74	0.09	0.00	0.00	0.33	4.65	9.63	0.88	0.04	0.00	0.00	99.76
YP127	Point	65.44	0.00	18.72	0.10	0.00	0.00	0.35	4.41	9.71	0.83	0.04	0.08	0.01	99.69
YP127	Point	64.85	0.01	18.74	0.08	0.00	0.00	0.40	4.48	9.54	1.09	0.05	0.00	0.00	99.25

Sample	Analysis	SiO_2	TiO_2	Al_2O_3	FeO	MnO	MgO	CaO	Na_2O	K_2O	BaO	SrO	F	Cl	Total
Huckleberry Ridge Tuff - A			Pumice		Sanidine										
YP127	Point	64.96	0.01	18.76	0.14	0.00	0.00	0.41	4.23	9.56	1.06	0.08	0.00	0.00	99.22
YP127	Point	64.82	0.00	18.80	0.07	0.00	0.00	0.41	4.53	9.61	1.03	0.03	0.04	0.00	99.33
YP127	Point	64.78	0.03	18.83	0.09	0.00	0.00	0.43	4.31	9.62	1.04	0.05	0.00	0.00	99.17
YP127	Point	64.99	0.02	18.89	0.12	0.00	0.00	0.41	4.32	9.70	1.09	0.06	0.00	0.00	99.61
YP127	Point	65.04	0.05	18.85	0.08	0.00	0.00	0.41	4.49	9.66	1.11	0.05	0.00	0.00	99.75
YP127	Point	64.74	0.01	18.80	0.11	0.00	0.00	0.42	4.39	9.48	1.14	0.05	0.00	0.01	99.15
YP127	Point	64.80	0.05	18.82	0.08	0.00	0.00	0.43	4.49	9.62	1.07	0.04	0.00	0.00	99.41
YP127	Point	64.74	0.05	18.85	0.10	0.00	0.00	0.42	4.34	9.49	1.15	0.05	0.00	0.00	99.20
YP127	Point	64.85	0.02	18.82	0.09	0.00	0.00	0.44	4.38	9.56	1.15	0.07	0.07	0.00	99.47
YP127	Point	64.74	0.01	18.74	0.12	0.00	0.00	0.42	4.30	9.66	1.12	0.06	0.00	0.00	99.17
YP127	Point	64.91	0.01	18.78	0.08	0.01	0.00	0.45	4.38	9.57	1.17	0.03	0.00	0.00	99.40
YP127	Point	64.78	0.05	18.89	0.14	0.00	0.00	0.41	4.47	9.57	1.14	0.04	0.06	0.00	99.54
YP127	Point	65.05	0.00	18.79	0.14	0.00	0.00	0.44	4.49	9.44	1.13	0.02	0.10	0.00	99.59
YP127	Point	65.08	0.01	18.85	0.10	0.00	0.00	0.44	4.44	9.55	1.13	0.05	0.00	0.00	99.66
YP127	Point	64.78	0.00	18.78	0.12	0.00	0.00	0.43	4.27	9.55	1.18	0.11	0.03	0.00	99.26
YP127	Point	64.95	0.03	18.67	0.09	0.00	0.00	0.42	4.29	9.61	1.17	0.06	0.00	0.00	99.30
YP127	Point	64.73	0.03	18.76	0.11	0.00	0.00	0.44	4.43	9.50	1.12	0.02	0.00	0.00	99.15
YP127	Point	64.76	0.03	18.79	0.10	0.01	0.00	0.43	4.26	9.46	1.18	0.05	0.01	0.00	99.07
YP127	Point	64.72	0.05	18.86	0.12	0.01	0.00	0.44	4.42	9.55	1.12	0.04	0.00	0.00	99.32
YP127	Point	64.72	0.05	18.86	0.09	0.00	0.00	0.44	4.52	9.45	1.16	0.07	0.00	0.00	99.37
YP127	Point	64.71	0.00	18.77	0.09	0.00	0.00	0.44	4.48	9.46	1.18	0.07	0.00	0.00	99.21
YP127	Point	64.67	0.02	18.82	0.12	0.00	0.00	0.46	4.55	9.38	1.21	0.03	0.06	0.00	99.32
YP127	Point	65.25	0.01	19.09	0.12	0.00	0.00	0.47	4.41	9.33	1.29	0.04	0.00	0.00	100.01
YP127	Point	64.91	0.00	18.97	0.08	0.00	0.00	0.48	4.47	9.24	1.22	0.09	0.10	0.00	99.58
YP127	Point	64.84	0.00	18.99	0.13	0.00	0.00	0.47	4.54	9.28	1.22	0.07	0.00	0.00	99.53
YP127	Point	65.83	0.03	18.95	0.12	0.00	0.00	0.40	4.54	9.55	0.88	0.08	0.03	0.00	100.40
YP127	Point	65.89	0.00	19.04	0.13	0.01	0.00	0.41	4.39	9.70	0.60	0.02	0.00	0.01	100.21
YP127	Point	64.82	0.01	18.96	0.14	0.00	0.00	0.45	4.29	9.36	1.16	0.05	0.03	0.00	99.28
YP127	Point	65.93	0.07	19.08	0.12	0.00	0.01	0.50	4.60	9.00	1.06	0.06	0.04	0.00	100.48
YP127	Point	65.45	0.03	18.93	0.08	0.01	0.00	0.49	4.65	9.06	1.10	0.02	0.09	0.00	99.90
YP127	Point	65.14	0.00	19.17	0.09	0.00	0.00	0.48	4.52	9.15	1.15	0.08	0.09	0.00	99.88
YP127	Point	65.81	0.00	19.06	0.12	0.01	0.00	0.46	4.47	9.22	1.16	0.09	0.00	0.00	100.40
YP127	Point	65.65	0.05	18.97	0.09	0.00	0.00	0.45	4.42	9.17	1.05	0.05	0.03	0.00	99.94
YP127	Point	64.39	0.02	19.49	0.12	0.00	0.00	0.89	4.68	8.25	1.85	0.04	0.00	0.00	99.73
YP127	Point	65.13	0.06	18.91	0.15	0.00	0.00	0.47	4.52	9.13	1.34	0.03	0.00	0.00	99.74
YP127	Point	64.89	0.00	19.07	0.12	0.00	0.00	0.50	4.48	9.14	1.38	0.07	0.00	0.00	99.66
YP127	Point	65.17	0.01	19.11	0.14	0.00	0.00	0.53	4.61	9.14	1.37	0.06	0.01	0.00	100.17
YP127	Point	64.93	0.00	19.19	0.10	0.00	0.00	0.51	4.39	9.17	1.41	0.08	0.01	0.00	99.80
YP127	Point	64.79	0.00	19.20	0.12	0.00	0.00	0.51	4.22	9.21	1.53	0.06	0.00	0.01	99.64
YP127	Point	64.64	0.00	19.30	0.10	0.00	0.00	0.55	4.68	8.98	1.63	0.06	0.08	0.00	100.02
YP127	Point	64.76	0.01	19.33	0.10	0.00	0.00	0.56	4.56	9.13	1.62	0.07	0.02	0.00	100.17
YP127	Point	65.30	0.00	19.07	0.11	0.00	0.00	0.44	4.49	9.20	1.33	0.02	0.00	0.01	99.96
YP127	Point	65.28	0.01	19.07	0.10	0.00	0.00	0.44	4.74	9.34	1.30	0.06	0.03	0.00	100.37
YP127	Point	65.47	0.00	19.18	0.06	0.00	0.00	0.43	4.48	9.13	1.39	0.10	0.00	0.00	100.23
YP127	Point	65.13	0.00	18.98	0.14	0.00	0.00	0.45	4.43	9.23	1.37	0.09	0.04	0.00	99.87
YP127	Point	64.86	0.01	19.19	0.10	0.00	0.00	0.50	4.42	9.24	1.47	0.05	0.01	0.01	99.86
YP127	Point	64.84	0.02	19.21	0.09	0.00	0.00	0.49	4.40	9.16	1.54	0.06	0.00	0.00	99.81
YP127	Point	65.10	0.00	19.07	0.12	0.00	0.00	0.48	4.40	9.14	1.45	0.09	0.02	0.00	99.86
YP127	Point	65.21	0.00	18.96	0.11	0.01	0.00	0.46	4.43	9.27	1.37	0.04	0.00	0.00	99.85
YP127	Point	65.12	0.01	19.21	0.11	0.00	0.00	0.45	4.39	9.34	1.38	0.05	0.06	0.00	100.12
YP127	Point	65.06	0.01	19.22	0.08	0.01	0.00	0.49	4.54	9.13	1.54	0.04	0.01	0.00	100.13
YP127	Point	65.34	0.03	19.12	0.12	0.00	0.00	0.44	4.47	9.22	1.30	0.06	0.00	0.00	100.11
YP127	Point	65.42	0.03	19.03	0.10	0.00	0.00	0.44	4.46	9.26	1.22	0.08	0.04	0.00	100.08
YP127	Point	65.16	0.02	19.18	0.11	0.00	0.00	0.48	4.47	9.22	1.32	0.06	0.02	0.00	100.05
YP127	Point	65.34	0.00	19.27	0.13	0.00	0.00	0.53	4.45	9.02	1.35	0.07	0.02	0.00	100.20
YP127	Point	64.58	0.06	18.93	0.09	0.00	0.00	0.60	4.53	8.97	1.44	0.06	0.02	0.00	99.27
YP127	Point	64.95	0.06	18.57	0.08	0.00	0.00	0.36	4.67	9.47	0.95	0.05	0.00	0.00	99.17
YP127	Point	65.12	0.00	18.75	0.13	0.00	0.00	0.40	4.66	9.45	1.06	0.07	0.00	0.00	99.64
YP127	Point	64.84	0.03	18.90	0.15	0.00	0.00	0.50	4.52	9.17	1.21	0.06	0.00	0.00	99.38
YP127	Point	65.35	0.04	18.75	0.10	0.00	0.00	0.39	4.28	9.45	1.04	0.07	0.00	0.01	99.48

Sample	Analysis	SiO_2	TiO_2	Al_2O_3	FeO	MnO	MgO	CaO	Na_2O	K_2O	BaO	SrO	F	Cl	Total
Huckleberry Ridge Tuff - B			Pumice		Sanidine										
YP079	Point	65.98	0.04	18.60	0.11	0.00	0.00	0.45	4.90	9.35	0.21	0.07	0.06	0.00	99.77
YP079	Point	66.23	0.01	18.66	0.12	0.00	0.00	0.43	4.91	9.42	0.29	0.10	0.06	0.00	100.24
YP079	Point	65.47	0.00	18.47	0.11	0.00	0.00	0.45	4.67	9.44	0.36	0.04	0.05	0.00	99.06
YP079	Point	66.05	0.01	18.72	0.09	0.01	0.00	0.44	4.80	9.42	0.46	0.03	0.00	0.00	100.03
YP079	Point	65.49	0.00	18.56	0.09	0.00	0.00	0.46	4.68	9.36	0.66	0.05	0.04	0.00	99.38
YP079	Point	64.89	0.00	18.59	0.13	0.00	0.01	0.54	4.87	8.77	1.31	0.00	0.01	0.01	99.11
YP079	Point	64.72	0.00	18.78	0.15	0.00	0.00	0.40	4.32	9.65	1.07	0.05	0.00	0.00	99.15
YP079	Point	65.00	0.04	18.73	0.13	0.01	0.00	0.41	4.32	9.74	1.02	0.03	0.00	0.00	99.43
YP079	Point	65.05	0.00	18.96	0.10	0.00	0.00	0.42	4.35	9.60	1.11	0.07	0.00	0.00	99.66
YP079	Point	64.99	0.03	18.77	0.08	0.00	0.00	0.39	4.33	9.69	1.07	0.06	0.00	0.00	99.41
YP079	Point	65.06	0.00	18.84	0.13	0.00	0.00	0.42	4.37	9.67	1.11	0.08	0.01	0.00	99.68
YP079	Point	65.17	0.01	18.89	0.10	0.00	0.00	0.41	4.35	9.59	1.13	0.06	0.00	0.00	99.71
YP079	Point	64.70	0.02	18.75	0.10	0.00	0.00	0.42	4.34	9.62	1.11	0.04	0.00	0.01	99.11
YP079	Point	64.90	0.01	18.73	0.13	0.00	0.00	0.45	4.29	9.54	1.14	0.07	0.00	0.00	99.26
YP079	Point	64.84	0.04	18.77	0.07	0.00	0.00	0.45	4.42	9.63	1.13	0.07	0.00	0.00	99.44
YP079	Point	65.18	0.03	18.98	0.08	0.00	0.00	0.47	4.60	9.55	1.08	0.07	0.01	0.00	100.05
YP079	Point	65.24	0.02	18.95	0.09	0.00	0.00	0.44	4.38	9.35	1.05	0.03	0.00	0.00	99.56
YP079	Point	64.77	0.03	18.98	0.09	0.00	0.00	0.47	4.27	9.50	1.06	0.06	0.00	0.00	99.22
YP079	Point	65.10	0.02	18.84	0.10	0.00	0.00	0.42	4.53	9.37	1.02	0.07	0.01	0.00	99.49
YP079	Point	65.32	0.00	19.00	0.10	0.01	0.00	0.44	4.32	9.46	1.01	0.06	0.00	0.00	99.73
YP079	Point	65.17	0.03	18.78	0.09	0.00	0.00	0.42	4.50	9.58	0.97	0.10	0.08	0.00	99.71
YP079	Point	65.25	0.02	18.90	0.09	0.00	0.00	0.40	4.39	9.52	0.97	0.04	0.04	0.00	99.61
YP079	Point	65.19	0.01	18.84	0.10	0.01	0.00	0.40	4.34	9.57	0.92	0.07	0.06	0.00	99.50
YP079	Point	65.21	0.02	18.78	0.13	0.00	0.00	0.37	4.40	9.64	0.90	0.06	0.00	0.00	99.52
YP079	Point	65.26	0.04	18.78	0.07	0.01	0.00	0.39	4.47	9.64	0.92	0.05	0.03	0.01	99.65
YP079	Point	65.27	0.01	18.80	0.08	0.01	0.00	0.37	4.49	9.52	0.92	0.04	0.01	0.00	99.52
YP079	Point	65.69	0.00	18.66	0.11	0.00	0.01	0.42	4.69	9.38	0.43	0.07	0.04	0.01	99.50
YP079	Point	65.94	0.01	18.76	0.13	0.00	0.00	0.46	4.59	9.36	0.43	0.05	0.00	0.01	99.74
YP079	Point	65.92	0.02	18.78	0.09	0.01	0.00	0.47	4.60	9.33	0.36	0.06	0.00	0.01	99.64
YP079	Point	66.04	0.05	18.80	0.07	0.00	0.00	0.46	4.59	9.27	0.35	0.01	0.05	0.01	99.70
YP079	Point	66.33	0.02	18.85	0.10	0.00	0.00	0.46	4.59	9.32	0.28	0.02	0.02	0.00	100.00
YP079	Point	66.43	0.03	18.84	0.12	0.01	0.00	0.43	5.01	9.42	0.19	0.06	0.00	0.00	100.52
YP079	Point	66.16	0.00	18.74	0.07	0.00	0.00	0.45	4.56	9.34	0.31	0.06	0.05	0.00	99.76
YP079	Point	65.33	0.00	18.74	0.12	0.01	0.00	0.46	4.72	9.23	0.55	0.06	0.01	0.00	99.23
					Plagioclase										
YP079	Point	64.48	0.01	21.96	0.20	0.00	0.00	3.65	8.20	1.85	0.03	0.05	0.02	0.00	100.44
YP079	Point	64.52	0.00	21.80	0.13	0.00	0.00	3.65	8.00	1.82	0.06	0.05	0.04	0.00	100.07
YP079	Point	63.19	0.04	21.65	0.22	0.00	0.00	3.96	8.31	1.56	0.12	0.08	0.00	0.00	99.13
YP079	Point	63.51	0.00	22.19	0.20	0.00	0.01	4.09	7.95	1.70	0.12	0.03	0.00	0.01	99.81
YP079	Point	63.70	0.01	22.27	0.23	0.00	0.00	4.01	7.95	1.69	0.14	0.01	0.03	0.01	100.05
YP079	Point	63.65	0.03	22.11	0.20	0.01	0.00	4.07	8.19	1.72	0.18	0.04	0.00	0.00	100.20
YP079	Point	62.90	0.06	22.12	0.26	0.00	0.00	4.14	8.01	1.69	0.16	0.02	0.02	0.00	99.37
YP079	Point	63.08	0.01	21.97	0.20	0.00	0.01	3.99	8.15	1.70	0.07	0.08	0.00	0.01	99.26
Huckleberry Ridge Tuff - C			Pumice		Sanidine										
YP081	Point	66.65	0.04	18.94	0.11	0.00	0.00	0.34	4.58	9.79	0.16	0.02	0.00	0.00	100.63
YP081	Point	66.58	0.03	18.91	0.11	0.00	0.00	0.34	4.76	9.87	0.17	0.05	0.00	0.00	100.82
YP081	Point	66.31	0.02	18.90	0.11	0.00	0.00	0.30	4.53	9.94	0.26	0.02	0.00	0.00	100.40
YP081	Point	66.61	0.00	19.01	0.12	0.01	0.00	0.32	4.76	9.91	0.16	0.04	0.02	0.00	100.96
YP081	Point	66.43	0.04	18.91	0.10	0.00	0.00	0.32	4.64	9.90	0.17	0.05	0.00	0.00	100.55
YP081	Point	66.84	0.00	18.84	0.10	0.00	0.00	0.29	4.73	10.02	0.08	0.03	0.00	0.00	100.94
YP081	Point	66.30	0.00	18.87	0.11	0.00	0.00	0.33	4.58	9.94	0.14	0.01	0.00	0.00	100.28
YP081	Point	66.56	0.02	18.83	0.11	0.03	0.01	0.33	4.64	9.85	0.17	0.11	0.00	0.00	100.67
YP081	Point	66.35	0.02	18.87	0.12	0.00	0.00	0.38	4.46	9.69	0.37	0.00	0.00	0.00	100.27
YP081	Point	66.12	0.02	19.02	0.10	0.00	0.00	0.40	4.60	9.76	0.47	0.05	0.01	0.00	100.54
YP081	Point	66.78	0.00	18.91	0.10	0.00	0.00	0.33	4.62	9.91	0.09	0.07	0.03	0.00	100.83
YP081	Point	66.61	0.03	18.78	0.09	0.00	0.00	0.30	4.46	9.92	0.06	0.05	0.04	0.00	100.35
YP081	Point	66.46	0.01	18.80	0.11	0.00	0.00	0.32	4.62	9.97	0.20	0.00	0.00	0.00	100.49
YP081	Point	66.31	0.00	18.82	0.09	0.00	0.00	0.34	4.52	9.90	0.21	0.00	0.02	0.00	100.20
YP081	Point	66.48	0.00	18.87	0.10	0.00	0.00	0.30	4.40	10.06	0.14	0.00	0.13	0.00	100.48
YP081	Point	66.62	0.02	19.05	0.10	0.00	0.00	0.34	4.59	9.92	0.19	0.08	0.00	0.00	100.90
YP081	Point	66.58	0.01	18.87	0.10	0.00	0.00	0.30	4.50	9.90	0.16	0.04	0.00	0.00	100.47
YP081	Point	66.68	0.03	18.86	0.10	0.00	0.00	0.31	4.59	9.92	0.03	0.07	0.03	0.00	100.62
YP081	Point	66.33	0.03	18.83	0.09	0.00	0.00	0.32	4.55	9.99	0.08	0.03	0.06	0.01	100.32

Sample	Analysis	SiO_2	TiO_2	Al_2O_3	FeO	MnO	MgO	CaO	Na_2O	K_2O	BaO	SrO	F	Cl	Total
Huckleberry Ridge Tuff - C			Pumice		Sanidine										
YP081	Point	66.20	0.00	19.02	0.12	0.00	0.00	0.43	4.62	9.60	0.41	0.07	0.00	0.00	100.48
YP081	Point	66.64	0.00	18.91	0.10	0.00	0.00	0.31	4.64	9.80	0.10	0.00	0.00	0.00	100.51
YP081	Point	66.37	0.02	18.98	0.10	0.01	0.00	0.37	4.70	9.71	0.24	0.00	0.02	0.00	100.52
YP081	Point	66.15	0.00	18.90	0.10	0.02	0.00	0.33	4.48	9.91	0.38	0.02	0.08	0.00	100.36
YP081	Point	66.29	0.01	18.82	0.10	0.02	0.00	0.35	4.56	9.88	0.23	0.02	0.04	0.00	100.32
YP081	Point	66.32	0.00	18.96	0.09	0.01	0.00	0.36	4.51	9.73	0.58	0.00	0.00	0.00	100.56
YP081	Point	66.38	0.01	18.84	0.10	0.00	0.00	0.30	4.55	10.08	0.10	0.01	0.07	0.00	100.44
YP081	Point	66.44	0.00	18.97	0.09	0.00	0.01	0.29	4.52	10.08	0.11	0.03	0.03	0.00	100.58
YP081	Point	66.39	0.00	18.82	0.10	0.00	0.00	0.29	4.58	10.04	0.09	0.00	0.00	0.00	100.31
YP081	Point	66.36	0.06	18.87	0.11	0.00	0.00	0.32	4.57	9.91	0.38	0.01	0.00	0.00	100.61
YP081	Point	66.51	0.00	18.84	0.10	0.00	0.00	0.30	4.50	9.99	0.15	0.02	0.11	0.00	100.52
YP081	Point	66.51	0.03	18.97	0.10	0.01	0.00	0.37	4.64	9.77	0.26	0.01	0.00	0.00	100.67
YP081	Point	66.27	0.00	19.06	0.11	0.03	0.00	0.38	4.54	9.75	0.42	0.04	0.10	0.00	100.70
YP081	Point	66.43	0.00	18.89	0.10	0.02	0.00	0.33	4.63	9.94	0.17	0.01	0.05	0.00	100.58
YP081	Point	66.83	0.02	19.02	0.08	0.01	0.00	0.31	4.53	9.88	0.13	0.05	0.00	0.00	100.85
YP081	Point	66.83	0.01	18.93	0.07	0.00	0.00	0.30	4.68	9.98	0.03	0.00	0.00	0.00	100.83
YP081	Point	66.68	0.02	18.76	0.10	0.00	0.00	0.27	4.54	10.03	0.04	0.01	0.00	0.00	100.46
YP081	Point	66.47	0.02	18.73	0.09	0.00	0.00	0.29	4.66	9.99	0.10	0.02	0.02	0.00	100.40
YP081	Point	65.78	0.01	18.81	0.13	0.00	0.00	0.34	4.57	9.74	0.43	0.01	0.05	0.00	99.88
YP081	Point	66.42	0.00	18.74	0.10	0.00	0.00	0.29	4.52	9.80	0.07	0.00	0.04	0.00	99.99
YP081	Point	66.56	0.00	18.83	0.10	0.00	0.00	0.28	4.59	9.97	0.19	0.00	0.00	0.01	100.52
YP081	Point	66.28	0.01	18.83	0.10	0.00	0.00	0.35	4.58	9.79	0.17	0.02	0.02	0.00	100.15
YP081	Point	66.81	0.03	18.88	0.11	0.01	0.00	0.32	4.68	10.04	0.07	0.03	0.01	0.00	100.98
YP081	Point	66.72	0.02	18.97	0.11	0.00	0.00	0.33	4.56	9.86	0.05	0.01	0.00	0.00	100.63
YP081	Point	66.60	0.01	18.63	0.09	0.00	0.00	0.29	4.42	9.98	0.04	0.05	0.00	0.00	100.10
YP081	Point	66.42	0.01	18.88	0.09	0.00	0.00	0.32	4.84	9.66	0.16	0.00	0.00	0.00	100.38
YP081	Point	66.63	0.00	18.80	0.09	0.01	0.00	0.29	4.57	10.02	0.15	0.04	0.03	0.00	100.65
YP081	Point	66.32	0.03	18.86	0.09	0.00	0.00	0.36	4.75	9.74	0.17	0.04	0.05	0.00	100.41
YP081	Point	66.52	0.05	18.82	0.08	0.00	0.00	0.31	4.47	10.05	0.12	0.06	0.00	0.00	100.48
YP081	Point	66.67	0.00	18.90	0.09	0.02	0.00	0.35	4.51	9.82	0.12	0.05	0.00	0.00	100.54
Mesa Falls Tuff			Pumice		Sanidine										
CMW01	Point	65.59	0.00	18.93	0.10	0.00	0.00	0.32	4.22	10.16	0.74	0.06	0.00	0.01	100.14
CMW01	Point	65.30	0.02	18.63	0.10	0.00	0.00	0.29	4.21	10.39	0.09	0.06	0.01	0.00	99.11
CMW01	Point	65.25	0.02	18.58	0.11	0.00	0.00	0.37	4.16	10.14	0.92	0.02	0.14	0.01	99.73
CMW01	Point	65.45	0.00	18.50	0.10	0.00	0.00	0.35	4.19	10.17	0.78	0.04	0.00	0.00	99.58
CMW01	Point	65.35	0.02	18.47	0.10	0.00	0.00	0.36	4.25	10.10	0.90	0.00	0.00	0.01	99.55
CMW01	Point	65.35	0.01	18.51	0.11	0.00	0.00	0.37	4.13	10.13	1.02	0.06	0.07	0.01	99.76
CMW01	Point	65.74	0.02	18.63	0.08	0.01	0.00	0.32	4.06	10.25	0.12	0.08	0.00	0.01	99.32
CMW01	Point	65.32	0.00	18.59	0.11	0.00	0.00	0.29	4.36	10.19	0.59	0.10	0.02	0.01	99.57
CMW01	Point	65.11	0.01	18.41	0.09	0.00	0.00	0.37	4.12	10.12	1.42	0.09	0.00	0.01	99.76
CMW01	Point	65.35	0.03	18.53	0.11	0.00	0.00	0.37	4.29	10.14	0.33	0.02	0.06	0.01	99.22
CMW01	Point	65.44	0.00	18.83	0.10	0.00	0.00	0.40	4.18	10.16	0.49	0.01	0.00	0.01	99.62
CMW01	Point	65.55	0.00	18.32	0.10	0.01	0.00	0.34	4.13	10.25	0.43	0.03	0.00	0.01	99.16
CMW01	Point	65.33	0.03	18.34	0.10	0.00	0.00	0.31	4.26	10.14	1.12	0.10	0.04	0.00	99.78
CMW01	Point	65.66	0.02	18.40	0.09	0.00	0.00	0.29	4.16	10.29	0.10	0.08	0.00	0.01	99.09
CMW01	Point	65.73	0.00	18.58	0.08	0.00	0.01	0.34	4.06	10.23	1.37	0.06	0.00	0.00	100.45
CMW01	Point	64.96	0.01	18.18	0.11	0.00	0.00	0.38	4.51	10.05	0.85	0.03	0.18	0.00	99.27
CMW01	Point	65.01	0.00	18.14	0.10	0.02	0.00	0.36	4.09	10.14	1.22	0.05	0.05	0.00	99.18
CMW01	Point	65.40	0.01	18.36	0.11	0.00	0.00	0.34	4.25	10.20	0.68	0.03	0.00	0.00	99.37
CMW01	Point	65.72	0.02	18.47	0.09	0.00	0.00	0.33	4.24	10.19	1.31	0.08	0.03	0.00	100.49
CMW01	Point	64.94	0.05	18.13	0.12	0.00	0.00	0.36	4.17	10.11	1.19	0.00	0.00	0.01	99.06
					Plagioclase										
CMW01	Point	62.61	0.00	22.28	0.21	0.00	0.00	4.24	7.98	1.55	1.00	0.05	0.00	0.01	99.94
CMW01	Point	62.31	0.04	21.97	0.19	0.00	0.01	4.39	8.26	1.42	0.62	0.07	0.02	0.00	99.29
CMW01	Point	61.58	0.00	22.62	0.23	0.00	0.01	4.93	7.97	1.13	0.51	0.06	0.00	0.01	99.05
Sheridan Reservior			Rhyolite		Anorthoclase										
YR215	Point	63.84	0.05	20.93	0.22	0.00	0.00	2.54	7.39	3.67	1.40	0.17	0.07	0.00	100.28
YR215	Point	63.85	0.01	20.73	0.20	0.00	0.01	2.64	7.57	3.38	0.79	0.06	0.00	0.00	99.23
YR215	Point	64.32	0.06	20.98	0.21	0.00	0.00	2.50	7.34	3.64	1.03	0.16	0.00	0.00	100.24
YR215	Point	63.48	0.04	21.05	0.21	0.00	0.00	2.89	7.55	3.14	1.01	0.03	0.10	0.00	99.50
YR215	Point	64.35	0.00	20.14	0.20	0.00	0.00	1.77	7.04	4.64	1.49	0.12	0.00	0.00	99.75

Sample	Analysis	SiO_2	TiO_2	Al_2O_3	FeO	MnO	MgO	CaO	Na_2O	K_2O	BaO	SrO	F	Cl	Total
Sheridan Reservior			Rhyolite		Anorthoclase										
YR215	Point	63.75	0.02	20.71	0.24	0.00	0.00	2.54	7.20	3.50	1.23	0.14	0.00	0.00	99.32
YR215	Point	64.14	0.04	20.67	0.21	0.00	0.00	2.24	7.34	3.91	1.25	0.14	0.01	0.00	99.97
YR215	Point	63.64	0.04	20.55	0.23	0.00	0.00	2.54	7.36	3.51	1.08	0.11	0.01	0.00	99.08
YR215	Point	63.97	0.00	20.34	0.19	0.00	0.00	1.92	6.62	4.70	1.53	0.11	0.00	0.00	99.40
YR215	Point	63.56	0.03	19.42	0.17	0.00	0.00	0.77	5.42	6.99	2.58	0.08	0.00	0.00	99.01
YR215	Point	64.01	0.03	20.69	0.22	0.01	0.00	2.43	7.13	3.86	1.17	0.12	0.00	0.00	99.66
YR215	Point	63.28	0.00	20.95	0.24	0.00	0.00	2.78	7.32	3.36	1.23	0.05	0.00	0.00	99.21
YR215	Point	63.46	0.02	20.69	0.23	0.01	0.00	2.38	7.17	3.83	1.37	0.17	0.00	0.00	99.34
YR215	Point	63.60	0.02	21.17	0.20	0.00	0.00	2.91	7.50	3.11	1.00	0.12	0.06	0.00	99.70
YR215	Point	64.13	0.01	21.11	0.21	0.00	0.00	2.64	7.53	3.46	1.15	0.07	0.04	0.00	100.35
YR215	Point	63.44	0.00	20.58	0.20	0.00	0.00	2.30	7.12	3.93	1.32	0.12	0.00	0.00	99.01
YR215	Point	64.45	0.01	19.68	0.17	0.00	0.00	1.17	6.32	5.97	1.89	0.05	0.00	0.00	99.73
YR215	Point	63.63	0.05	21.13	0.21	0.01	0.00	2.79	7.42	3.27	1.05	0.08	0.03	0.00	99.67
YR215	Point	63.89	0.05	20.83	0.23	0.00	0.00	2.46	7.48	3.52	1.18	0.10	0.00	0.00	99.74
YR215	Point	63.81	0.05	20.67	0.23	0.00	0.00	2.42	7.25	3.81	1.24	0.10	0.02	0.00	99.60
YR215	Point	64.22	0.04	20.52	0.22	0.00	0.00	2.25	7.40	3.82	1.20	0.08	0.00	0.00	99.74
YR215	Point	63.84	0.02	21.23	0.23	0.00	0.00	2.66	7.46	3.45	1.10	0.06	0.11	0.00	100.16
YR215	Point	64.11	0.01	21.06	0.19	0.00	0.01	2.71	7.48	3.29	0.85	0.09	0.00	0.00	99.80
YR215	Point	63.89	0.03	20.59	0.22	0.00	0.00	2.26	7.25	3.91	1.24	0.14	0.00	0.00	99.52
YR215	Point	64.01	0.01	20.68	0.19	0.00	0.00	2.32	7.21	3.86	1.24	0.04	0.00	0.00	99.58
YR215	Point	64.22	0.00	20.70	0.23	0.01	0.00	2.35	7.15	3.83	1.20	0.10	0.08	0.00	99.86
YR215	Point	64.57	0.06	21.02	0.21	0.00	0.00	2.54	7.64	3.51	0.89	0.04	0.00	0.00	100.47
YR215	Point	64.11	0.04	20.69	0.21	0.00	0.00	2.70	7.76	3.26	0.64	0.08	0.00	0.00	99.48
YR215	Point	64.36	0.06	20.82	0.22	0.00	0.01	2.55	7.61	3.41	0.73	0.10	0.02	0.00	99.90
YR215	Point	63.95	0.06	20.71	0.22	0.00	0.00	2.45	7.38	3.65	1.17	0.12	0.03	0.00	99.74
YR215	Point	64.01	0.02	20.95	0.19	0.00	0.00	2.66	7.39	3.42	0.80	0.08	0.07	0.00	99.59
YR215	Point	63.97	0.03	20.39	0.21	0.00	0.00	2.54	7.60	3.43	0.62	0.07	0.05	0.00	98.90
YR215	Point	63.68	0.02	21.20	0.21	0.00	0.00	3.17	7.49	2.82	0.68	0.11	0.00	0.01	99.39
YR215	Point	64.41	0.04	20.77	0.19	0.00	0.00	2.55	7.57	3.43	0.61	0.09	0.01	0.00	99.68
YR215	Point	63.49	0.04	21.33	0.25	0.01	0.00	3.22	7.44	2.78	0.90	0.04	0.00	0.01	99.51
YR215	Point	63.69	0.01	20.36	0.21	0.01	0.00	1.89	7.00	4.57	1.51	0.10	0.01	0.00	99.34
YR215	Transect 1	64.16	0.01	20.73	0.24	0.01	0.00	2.13	6.62	4.38	1.53	0.14	0.00	0.01	99.96
YR215	Transect 1	63.83	0.00	20.41	0.19	0.00	0.00	2.03	6.93	4.11	1.50	0.08	0.03	0.02	99.13
YR215	Transect 1	64.07	0.03	20.33	0.22	0.00	0.00	1.93	6.81	4.39	1.47	0.11	0.00	0.02	99.39
YR215	Transect 1	64.26	0.02	20.75	0.25	0.00	0.00	2.11	7.17	3.96	1.40	0.12	0.01	0.00	100.06
YR215	Transect 1	64.50	0.00	20.70	0.19	0.02	0.00	2.25	7.15	3.84	1.10	0.11	0.00	0.00	99.85
YR215	Transect 1	64.69	0.01	20.35	0.18	0.00	0.01	1.77	6.77	4.83	1.33	0.11	0.00	0.00	100.05
YR215	Transect 1	63.83	0.01	20.50	0.15	0.00	0.00	2.07	6.71	4.32	1.27	0.09	0.00	0.00	98.95
YR215	Transect 1	64.80	0.00	20.78	0.20	0.00	0.00	2.32	7.16	3.95	1.10	0.10	0.00	0.00	100.41
YR215	Transect 1	64.58	0.03	20.53	0.18	0.00	0.00	1.94	6.79	4.45	1.26	0.12	0.04	0.00	99.92
YR215	Transect 1	63.97	0.06	20.50	0.19	0.00	0.00	2.12	6.90	4.22	1.10	0.07	0.03	0.00	99.15
YR215	Transect 1	62.95	0.00	21.24	0.23	0.00	0.01	2.85	7.20	3.42	1.04	0.08	0.04	0.00	99.06
YR215	Transect 1	64.22	0.06	20.57	0.25	0.00	0.00	2.16	6.85	4.28	1.19	0.08	0.00	0.00	99.67
YR215	Transect 2	64.02	0.03	21.13	0.25	0.00	0.00	2.63	7.19	3.50	1.00	0.09	0.02	0.00	99.85
YR215	Transect 2	64.31	0.07	20.76	0.22	0.00	0.00	2.28	6.85	4.03	1.09	0.07	0.00	0.00	99.70
YR215	Transect 2	64.08	0.02	21.23	0.23	0.00	0.00	2.73	7.16	3.59	0.97	0.11	0.02	0.00	100.13
YR215	Transect 2	63.72	0.03	21.31	0.25	0.01	0.00	2.96	7.13	3.21	0.90	0.12	0.04	0.00	99.67
YR215	Transect 2	64.54	0.02	20.37	0.24	0.01	0.00	2.08	6.65	4.31	1.17	0.08	0.07	0.01	99.55
YR215	Transect 2	63.85	0.03	20.61	0.22	0.00	0.00	2.32	6.99	3.95	1.09	0.12	0.00	0.00	99.18
YR215	Transect 2	64.22	0.04	20.52	0.21	0.00	0.02	2.10	6.63	4.33	1.19	0.08	0.01	0.00	99.33
YR215	Transect 2	62.80	0.01	21.82	0.25	0.00	0.01	3.60	7.18	2.58	0.74	0.10	0.00	0.01	99.10
YR215	Transect 2	62.92	0.00	21.76	0.29	0.01	0.03	3.60	7.25	2.82	0.82	0.05	0.04	0.01	99.61
YR215	Transect 2	64.08	0.03	20.57	0.23	0.01	0.00	2.12	7.01	4.32	1.44	0.09	0.02	0.00	99.93
YR215	Transect 2	63.98	0.00	20.67	0.25	0.01	0.00	2.16	6.87	4.18	1.41	0.10	0.00	0.01	99.63

Sample	Analysis	SiO_2	TiO_2	Al_2O_3	FeO	MnO	MgO	CaO	Na_2O	K_2O	BaO	SrO	F	Cl	Total
Sheridan Reservior			Rhyolite		Anorthoclase										
YR215	Transect 2	63.90	0.01	20.46	0.25	0.00	0.00	2.18	7.02	4.06	1.43	0.07	0.06	0.00	99.44
YR215	Transect 2	63.97	0.02	20.51	0.23	0.00	0.00	2.23	7.03	3.93	1.32	0.09	0.00	0.00	99.35
YR215	Transect 2	64.17	0.00	20.64	0.25	0.00	0.00	2.22	7.05	4.07	1.32	0.09	0.00	0.00	99.83
YR215	Transect 3	63.97	0.03	20.69	0.24	0.00	0.01	2.28	6.91	3.95	1.30	0.13	0.01	0.00	99.53
YR215	Transect 3	63.78	0.05	20.76	0.23	0.00	0.00	2.44	7.25	3.74	1.22	0.11	0.00	0.00	99.60
YR215	Transect 3	63.74	0.01	20.68	0.22	0.00	0.00	2.31	7.01	3.96	1.28	0.12	0.04	0.00	99.37
YR215	Transect 3	63.93	0.00	20.42	0.24	0.00	0.01	2.13	7.01	4.35	1.42	0.09	0.00	0.00	99.61
YR215	Transect 3	63.69	0.01	20.58	0.25	0.01	0.00	2.20	7.08	4.13	1.38	0.10	0.04	0.00	99.48
YR215	Transect 3	63.68	0.00	20.55	0.19	0.00	0.00	2.28	7.01	4.02	1.38	0.08	0.00	0.00	99.20
YR215	Transect 3	63.35	0.00	20.81	0.24	0.00	0.00	2.48	7.08	3.82	1.35	0.07	0.01	0.00	99.20
YR215	Transect 3	63.68	0.04	20.81	0.24	0.00	0.01	2.46	7.27	3.70	1.23	0.09	0.02	0.00	99.56
YR215	Transect 3	63.81	0.02	20.36	0.20	0.00	0.00	1.96	6.87	4.53	1.48	0.10	0.07	0.01	99.39
YR215	Transect 3	64.08	0.03	20.43	0.20	0.00	0.00	2.03	6.72	4.50	1.44	0.08	0.03	0.01	99.54
YR215	Transect 3	64.22	0.02	20.74	0.23	0.00	0.00	2.22	6.98	4.09	1.45	0.12	0.00	0.01	100.09
YR215	Transect 3	64.01	0.05	20.95	0.19	0.01	0.00	2.49	7.17	3.76	1.31	0.09	0.03	0.00	100.05
YR215	Point	64.60	0.01	20.27	0.30	0.00	0.00	2.14	6.94	4.17	1.34	0.12	0.00	0.00	99.91
YR215	Point	64.22	0.01	20.82	0.18	0.01	0.00	2.42	7.05	3.91	1.28	0.11	0.01	0.00	100.01
YR215	Point	64.02	0.06	20.80	0.24	0.00	0.00	2.30	6.94	3.95	1.41	0.08	0.00	0.00	99.81
YR215	Point	64.05	0.01	20.68	0.25	0.00	0.00	2.25	6.81	4.00	1.47	0.09	0.07	0.00	99.69
YR215	Point	68.96	0.12	16.44	1.17	0.01	0.02	1.47	5.34	4.95	0.71	0.08	0.00	0.03	99.32
YR215	Point	63.79	0.04	20.81	0.21	0.00	0.02	2.49	7.03	3.76	1.29	0.13	0.00	0.00	99.57
YR215	Point	63.87	0.06	20.69	0.22	0.00	0.00	2.39	6.96	3.99	1.40	0.07	0.00	0.00	99.65
YR215	Point	63.97	0.03	20.29	0.20	0.00	0.00	2.05	6.75	4.41	1.44	0.08	0.00	0.00	99.22
YR215	Point	64.01	0.03	20.69	0.18	0.00	0.01	2.27	7.01	4.06	1.28	0.08	0.09	0.00	99.71
YR215	Point	64.01	0.03	20.49	0.21	0.00	0.00	2.21	6.89	4.28	1.33	0.15	0.00	0.00	99.60
YR215	Point	63.73	0.00	20.66	0.19	0.00	0.00	2.44	7.10	3.73	1.19	0.11	0.07	0.01	99.24
YR215	Point	63.70	0.05	20.72	0.23	0.00	0.00	2.56	7.18	3.60	1.04	0.10	0.02	0.00	99.22
YR215	Point	63.72	0.00	20.81	0.22	0.00	0.00	2.58	7.29	3.51	1.02	0.14	0.00	0.00	99.28
YR215	Point	63.87	0.07	20.68	0.26	0.00	0.00	2.61	7.44	3.58	1.02	0.07	0.00	0.00	99.60
YR215	Point	63.88	0.01	20.70	0.23	0.00	0.00	2.55	7.19	3.57	0.96	0.07	0.00	0.00	99.16
YR215	Point	63.93	0.00	20.50	0.22	0.00	0.01	2.40	7.10	3.85	1.07	0.12	0.00	0.00	99.20
YR215	Point	63.57	0.00	20.54	0.25	0.00	0.00	2.36	7.38	3.83	1.03	0.07	0.00	0.00	99.04
YR215	Point	63.83	0.03	20.58	0.22	0.00	0.00	2.44	7.16	3.65	0.96	0.11	0.07	0.00	99.03
YR215	Point	63.53	0.02	20.79	0.25	0.01	0.00	2.66	7.34	3.42	0.92	0.08	0.00	0.00	99.01
YR215	Point	63.47	0.04	20.68	0.23	0.00	0.00	2.55	7.53	3.55	0.92	0.07	0.00	0.00	99.03
YR215	Point	63.62	0.03	20.82	0.23	0.01	0.00	2.62	7.19	3.45	0.93	0.09	0.07	0.00	99.07
YR215	Point	65.54	0.01	19.56	0.44	0.00	0.00	1.90	6.63	4.37	1.19	0.11	0.00	0.01	99.75
YR215	Point	65.19	0.00	19.62	0.30	0.00	0.00	1.73	6.67	4.65	1.38	0.08	0.06	0.01	99.69
YR215	Point	64.16	0.01	20.84	0.19	0.00	0.00	2.39	7.05	3.90	1.24	0.08	0.03	0.00	99.88
YR215	Point	64.39	0.00	20.78	0.23	0.00	0.01	2.51	7.11	3.70	1.11	0.10	0.00	0.00	99.95
YR215	Point	64.16	0.03	20.90	0.20	0.00	0.00	2.40	7.09	3.78	1.15	0.10	0.00	0.00	99.80
YR215	Point	64.09	0.03	20.81	0.23	0.01	0.00	2.52	7.00	3.68	1.06	0.11	0.00	0.00	99.54
YR215	Point	64.25	0.01	20.96	0.26	0.00	0.00	2.52	7.33	3.62	1.08	0.13	0.02	0.00	100.18
YR215	Point	64.57	0.03	20.94	0.23	0.01	0.01	2.55	7.24	3.65	1.01	0.11	0.03	0.00	100.37
YR215	Point	63.97	0.04	20.87	0.23	0.00	0.00	2.57	7.14	3.61	0.97	0.10	0.00	0.00	99.49
YR215	Point	64.26	0.02	20.87	0.23	0.00	0.00	2.54	7.26	3.65	0.99	0.11	0.07	0.00	100.00
YR215	Point	64.55	0.00	20.90	0.23	0.00	0.00	2.54	7.22	3.58	1.01	0.08	0.03	0.00	100.14
YR215	Point	64.12	0.00	20.96	0.25	0.00	0.00	2.61	7.13	3.52	0.97	0.12	0.00	0.00	99.69
YR215	Point	64.18	0.02	21.11	0.22	0.00	0.01	2.80	7.30	3.38	0.90	0.08	0.00	0.00	100.01
YR215	Point	63.91	0.01	21.29	0.24	0.00	0.00	2.81	7.54	3.37	0.96	0.11	0.00	0.00	100.24
YR215	Point	64.16	0.00	21.08	0.25	0.00	0.00	2.64	7.27	3.52	0.96	0.08	0.04	0.00	99.98
YR215	Point	64.36	0.01	20.94	0.21	0.00	0.00	2.51	7.30	3.70	1.11	0.10	0.04	0.00	100.28
YR215	Point	64.05	0.00	20.97	0.23	0.00	0.00	2.69	7.11	3.50	1.01	0.11	0.00	0.00	99.68
YR215	Point	64.07	0.06	21.10	0.20	0.00	0.00	2.74	7.45	3.34	1.00	0.08	0.00	0.00	100.06
YR215	Point	64.12	0.03	21.02	0.19	0.00	0.00	2.77	7.41	3.45	0.99	0.10	0.00	0.00	100.09
YR215	Point	64.14	0.01	21.10	0.21	0.01	0.02	2.75	7.30	3.41	1.03	0.07	0.00	0.00	100.05
YR215	Point	64.34	0.01	21.16	0.22	0.00	0.00	2.68	7.44	3.45	1.07	0.11	0.00	0.00	100.49
YR215	Point	63.59	0.05	20.53	0.22	0.02	0.00	2.13	6.67	4.30	1.54	0.12	0.00	0.00	99.17
YR215	Point	64.09	0.01	20.76	0.21	0.00	0.00	2.10	6.75	4.31	1.53	0.10	0.05	0.00	99.90
YR215	Point	63.98	0.05	20.77	0.23	0.00	0.00	2.26	6.88	4.10	1.47	0.09	0.00	0.00	99.84
YR215	Point	64.21	0.05	20.65	0.22	0.00	0.00	2.18	6.79	4.22	1.48	0.07	0.00	0.00	99.87
YR215	Point	63.61	0.06	20.44	0.18	0.01	0.01	2.18	6.80	4.26	1.53	0.11	0.00	0.00	99.18
YR215	Point	64.05	0.00	20.95	0.22	0.00	0.00	2.42	7.08	4.00	1.46	0.10	0.00	0.01	100.29
YR215	Point	63.91	0.04	20.70	0.24	0.00	0.01	2.27	6.86	4.08	1.42	0.10	0.00	0.00	99.63
YR215	Point	64.33	0.01	20.80	0.22	0.01	0.00	2.37	7.21	3.87	1.06	0.10	0.00	0.00	99.98
YR215	Point	64.23	0.00	20.56	0.18	0.00	0.00	2.32	6.89	3.95	1.15	0.06	0.00	0.01	99.37
YR215	Point	64.08	0.01	20.90	0.23	0.01	0.00	2.64	7.32	3.39	0.97	0.06	0.03	0.00	99.64
YR215	Point	63.98	0.02	20.60	0.22	0.00	0.00	2.52	7.25	3.67	1.02	0.09	0.06	0.00	99.41
YR215	Point	63.87	0.00	20.69	0.24	0.00	0.00	2.68	7.23	3.49	0.92	0.08	0.00	0.00	99.22
YR215	Point	64.22	0.04	20.56	0.21	0.00	0.00	2.41	7.18	3.93	1.09	0.07	0.01	0.00	99.70
YR215	Point	63.74	0.02	20.32	0.24	0.01	0.00	2.16	6.93	4.28	1.38	0.12	0.02	0.00	99.22
YR215	Point	64.42	0.00	20.15	0.21	0.00	0.00	1.93	6.83	4.56	1.38	0.11	0.01	0.01	99.61
YR215	Point	64.11	0.02	20.66	0.25	0.00	0.00	2.16	6.90	4.24	1.46	0.12	0.02	0.00	99.92

Sample	Analysis	SiO_2	TiO_2	Al_2O_3	FeO	MnO	MgO	CaO	Na_2O	K_2O	BaO	SrO	F	Cl	Total
Sheridan Reservior			Rhyolite		Sanidine										
YR215	Point	64.21	0.03	19.27	0.17	0.02	0.00	0.99	6.07	6.35	1.85	0.03	0.01	0.00	99.01
YR215	Point	64.90	0.03	19.44	0.13	0.01	0.00	0.89	5.85	6.72	1.59	0.06	0.03	0.00	99.65
YR215	Point	64.17	0.00	19.79	0.20	0.00	0.00	1.31	6.24	5.82	1.73	0.16	0.01	0.00	99.44
YR215	Point	64.59	0.09	19.33	0.17	0.00	0.00	0.85	5.79	6.82	1.79	0.05	0.00	0.00	99.49
YR215	Point	64.66	0.02	19.49	0.17	0.01	0.00	0.95	5.77	6.70	1.90	0.04	0.00	0.00	99.71
YR215	Point	64.88	0.01	18.89	0.12	0.01	0.00	0.65	5.70	7.18	1.56	0.06	0.00	0.00	99.08
					Plagioclase										
YR215	Point	63.04	0.04	22.58	0.28	0.00	0.00	4.28	7.70	1.85	0.55	0.12	0.02	0.00	100.46
YR215	Point	62.34	0.01	22.67	0.23	0.00	0.00	4.81	7.81	1.36	0.25	0.05	0.00	0.00	99.54
YR215	Point	61.99	0.02	22.92	0.29	0.00	0.03	4.99	7.69	1.23	0.29	0.07	0.00	0.00	99.53
YR215	Point	61.80	0.05	22.73	0.29	0.00	0.05	4.95	7.57	1.26	0.29	0.09	0.04	0.00	99.11
YR215	Point	62.09	0.04	23.07	0.24	0.00	0.00	5.18	7.66	1.31	0.29	0.10	0.07	0.00	100.04
YR215	Point	62.21	0.04	22.73	0.26	0.00	0.00	4.59	7.89	1.54	0.48	0.07	0.00	0.00	99.81
			Rhyolite		Glass										
YR215	Point	77.60	0.06	11.47	2.07	0.04	0.04	0.63	3.53	4.90	0.13	0.04	0.05	0.05	100.62
YR215	Point	75.51	0.02	11.31	2.11	0.04	0.04	0.64	3.59	4.88	0.13	0.07	0.15	0.05	98.53
YR215	Point	77.86	0.07	11.40	2.12	0.03	0.04	0.62	3.70	4.91	0.18	0.01	0.08	0.05	101.08
YR215	Point	77.35	0.07	11.50	2.09	0.03	0.03	0.65	3.53	4.98	0.21	0.09	0.00	0.05	100.57
YR215	Point	76.86	0.09	11.32	2.15	0.03	0.02	0.61	3.55	4.89	0.19	0.03	0.13	0.05	99.93
YR215	Point	76.98	0.01	11.39	2.22	0.03	0.04	0.63	3.61	4.92	0.12	0.06	0.10	0.04	100.15
YR215	Point	77.82	0.05	11.27	2.11	0.06	0.03	0.61	3.77	4.93	0.16	0.08	0.12	0.05	101.05
YR215	Point	75.40	0.05	11.26	2.05	0.04	0.03	0.63	3.62	4.88	0.16	0.00	0.23	0.05	98.41
YR215	Point	77.72	0.03	11.53	2.18	0.05	0.03	0.61	3.66	4.97	0.13	0.00	0.12	0.05	101.09
YR215	Point	76.16	0.06	11.35	2.01	0.05	0.01	0.61	3.71	4.79	0.16	0.06	0.09	0.05	99.11
YR215	Point	76.20	0.02	11.23	2.07	0.04	0.03	0.64	3.54	4.94	0.16	0.01	0.07	0.05	99.00
YR215	Point	77.25	0.09	11.45	2.07	0.01	0.04	0.62	3.70	4.83	0.20	0.07	0.08	0.05	100.45
YR215	Point	77.27	0.00	11.62	1.97	0.04	0.03	0.62	3.81	4.91	0.13	0.02	0.12	0.04	100.57
YR215	Point	77.57	0.05	11.47	2.30	0.05	0.05	0.68	3.61	4.88	0.15	0.09	0.06	0.04	100.98
YR215	Point	75.57	0.08	11.60	2.08	0.04	0.03	0.63	3.64	4.89	0.08	0.08	0.22	0.05	98.97
YR215	Point	76.91	0.02	11.46	2.07	0.06	0.04	0.63	3.69	4.90	0.15	0.04	0.10	0.05	100.12
YR215	Point	75.55	0.02	11.28	2.13	0.07	0.03	0.63	3.48	4.87	0.12	0.01	0.16	0.04	98.39
YR215	Point	77.93	0.03	11.36	2.05	0.05	0.03	0.62	3.59	4.85	0.17	0.04	0.17	0.05	100.93
YR215	Point	77.45	0.08	11.30	2.20	0.06	0.03	0.64	3.79	4.85	0.18	0.02	0.16	0.04	100.80
YR215	Point	76.91	0.06	11.37	2.08	0.03	0.03	0.62	3.57	4.88	0.20	0.02	0.10	0.05	99.90
YR217	Point	76.45	0.03	11.64	2.17	0.03	0.03	0.65	3.70	4.95	0.14	0.04	0.12	0.05	99.98
YR217	Point	75.56	0.00	11.91	2.14	0.03	0.02	0.65	3.59	4.95	0.15	0.09	0.09	0.05	99.22
YR217	Point	77.64	0.00	12.03	2.13	0.04	0.04	0.65	3.43	5.00	0.10	0.08	0.01	0.06	101.21
YR217	Point	77.51	0.04	11.97	2.03	0.05	0.02	0.60	3.48	4.98	0.16	0.05	0.18	0.05	101.12
YR217	Point	77.73	0.02	12.04	2.06	0.03	0.03	0.63	3.53	4.99	0.16	0.06	0.06	0.05	101.40
YR217	Point	77.19	0.02	11.78	1.70	0.02	0.03	0.58	3.53	4.73	0.20	0.00	0.21	0.05	100.03
YR217	Point	77.52	0.00	11.96	2.15	0.04	0.03	0.63	3.62	4.99	0.20	0.00	0.10	0.05	101.28
YR217	Point	77.59	0.01	12.05	2.17	0.05	0.04	0.65	3.62	4.97	0.15	0.05	0.18	0.05	101.58
YR217	Point	77.34	0.00	11.88	2.14	0.05	0.04	0.64	3.74	4.94	0.18	0.00	0.03	0.04	101.01
YR217	Point	77.12	0.04	11.97	2.12	0.04	0.04	0.65	3.60	4.86	0.16	0.06	0.00	0.05	100.72
YR217	Point	76.44	0.00	11.68	2.13	0.06	0.03	0.63	3.46	4.88	0.17	0.04	0.01	0.04	99.56
YR217	Point	77.80	0.02	11.94	2.17	0.06	0.02	0.62	3.55	4.98	0.16	0.00	0.09	0.05	101.48
YR217	Point	77.66	0.01	11.99	2.13	0.03	0.02	0.64	3.59	5.03	0.19	0.13	0.00	0.05	101.49
YR217	Point	77.32	0.00	11.89	2.12	0.07	0.05	0.66	3.69	5.03	0.18	0.02	0.11	0.05	101.19
YR217	Point	77.80	0.01	11.99	2.04	0.02	0.04	0.62	3.72	5.00	0.19	0.05	0.16	0.06	101.70
YR217	Point	76.80	0.02	11.74	2.14	0.04	0.04	0.64	3.51	4.85	0.19	0.04	0.13	0.04	100.17
YR217	Point	77.39	0.03	12.05	2.17	0.04	0.04	0.64	3.68	4.99	0.18	0.03	0.06	0.06	101.36
YR217	Point	77.50	0.01	11.94	2.17	0.05	0.03	0.64	3.51	4.91	0.27	0.00	0.20	0.05	101.28
YR217	Point	76.27	0.01	11.67	2.11	0.03	0.03	0.64	3.67	4.77	0.15	0.03	0.11	0.05	99.57
YR217	Point	76.31	0.00	11.70	2.11	0.05	0.03	0.64	3.60	4.85	0.17	0.10	0.05	0.04	99.65
YR217	Point	77.84	0.00	12.05	1.62	0.05	0.03	0.56	3.66	4.99	0.18	0.00	0.11	0.04	101.14
YR217	Point	77.49	0.00	12.03	2.12	0.06	0.03	0.66	3.58	4.94	0.15	0.06	0.08	0.05	101.26
YR217	Point	77.88	0.01	12.04	1.83	0.05	0.03	0.59	3.59	5.02	0.13	0.06	0.16	0.05	101.44
YR217	Point	76.82	0.02	11.92	2.13	0.03	0.06	0.65	3.53	4.97	0.15	0.06	0.05	0.05	100.42
YR217	Point	77.65	0.03	12.00	2.14	0.04	0.04	0.64	3.60	4.95	0.19	0.06	0.14	0.05	101.52
YR217	Point	76.03	0.01	12.02	2.47	0.04	0.10	1.19	3.61	4.84	0.16	0.10	0.07	0.04	100.68
YR217	Point	76.49	0.03	11.73	2.12	0.07	0.05	0.65	3.55	4.85	0.15	0.00	0.08	0.04	99.79
YR217	Point	76.57	0.01	11.83	2.03	0.04	0.04	0.63	3.40	4.90	0.17	0.05	0.17	0.05	99.89
YR217	Point	77.02	0.05	11.82	2.10	0.04	0.03	0.64	3.52	4.88	0.10	0.01	0.06	0.06	100.31

Sample	Analysis	SiO_2	TiO_2	Al_2O_3	FeO	MnO	MgO	CaO	Na_2O	K_2O	BaO	SrO	F	Cl	Total
Sheridan Reservior			Rhyolite		Glass										
YR217	Point	76.56	0.03	11.73	2.14	0.04	0.04	0.61	3.53	4.87	0.20	0.03	0.26	0.04	100.06
YR217	Point	77.07	0.00	11.87	2.12	0.04	0.03	0.64	3.75	4.99	0.18	0.06	0.04	0.05	100.84
YR217	Point	76.37	0.00	11.79	2.10	0.02	0.03	0.65	3.48	4.90	0.20	0.02	0.05	0.06	99.65
YR217	Point	77.53	0.04	11.93	2.18	0.05	0.04	0.65	3.53	4.96	0.18	0.02	0.14	0.06	101.30
YR217	Point	77.16	0.02	11.90	2.17	0.05	0.02	0.64	3.50	4.94	0.21	0.08	0.11	0.05	100.86
YR217	Point	77.46	0.01	11.99	2.16	0.04	0.03	0.66	3.74	4.91	0.16	0.02	0.04	0.05	101.27
YR217	Point	77.81	0.00	12.07	2.10	0.04	0.03	0.63	3.66	5.03	0.17	0.02	0.09	0.05	101.69
YR217	Point	76.84	0.03	11.82	2.14	0.05	0.04	0.66	3.71	4.91	0.22	0.00	0.13	0.05	100.58
YR217	Point	77.30	0.02	11.89	2.12	0.05	0.02	0.62	3.60	5.01	0.15	0.02	0.09	0.05	100.94
YR217	Point	76.55	0.00	11.97	1.98	0.03	0.04	0.64	3.65	4.83	0.11	0.01	0.11	0.05	99.97
YR217	Point	76.42	0.00	11.83	2.09	0.05	0.04	0.63	3.48	4.87	0.18	0.04	0.06	0.05	99.72
YR217	Point	76.06	0.01	11.65	2.00	0.02	0.03	0.63	3.40	4.85	0.19	0.06	0.09	0.06	99.05
YR217	Point	77.23	0.00	12.02	2.10	0.05	0.04	0.65	3.74	4.99	0.17	0.04	0.13	0.05	101.21
YR217	Point	77.28	0.02	11.80	2.17	0.03	0.04	0.65	3.62	5.01	0.15	0.02	0.15	0.04	100.98
YR217	Point	77.44	0.00	12.06	2.13	0.05	0.04	0.65	3.63	4.97	0.15	0.00	0.08	0.05	101.25
YR217	Point	77.46	0.01	11.92	2.18	0.03	0.04	0.64	3.58	4.90	0.18	0.07	0.18	0.05	101.23
YR217	Point	77.69	0.02	11.98	2.10	0.07	0.04	0.64	3.62	4.97	0.17	0.00	0.09	0.05	101.43
YR217	Point	77.03	0.00	11.82	2.13	0.04	0.03	0.66	3.62	4.81	0.16	0.06	0.16	0.06	100.59
YR217	Point	77.02	0.04	11.84	2.13	0.06	0.03	0.63	3.67	4.90	0.12	0.05	0.05	0.06	100.59
YR217	Point	77.89	0.05	12.07	2.08	0.07	0.04	0.62	3.77	4.97	0.12	0.00	0.05	0.06	101.77
Snake Rive Butte			Rhyolite		Sanidine										
YR185	Point	65.16	0.00	18.64	0.10	0.01	0.00	0.35	4.35	9.83	1.04	0.02	0.07	0.00	99.57
YR185	Point	65.78	0.00	18.90	0.11	0.00	0.00	0.37	4.23	9.91	1.08	0.14	0.06	0.01	100.57
YR185	Point	65.47	0.03	18.89	0.11	0.00	0.00	0.37	4.45	9.64	1.22	0.09	0.00	0.00	100.27
YR185	Point	65.87	0.05	18.39	0.10	0.00	0.00	0.37	4.47	9.92	0.34	0.06	0.00	0.00	99.55
YR185	Point	65.48	0.02	18.89	0.09	0.00	0.00	0.42	4.35	9.64	1.21	0.08	0.01	0.00	100.20
YR185	Point	65.93	0.01	18.84	0.10	0.00	0.00	0.37	4.28	9.71	1.07	0.04	0.03	0.00	100.39
YR185	Point	65.50	0.03	18.69	0.11	0.01	0.00	0.40	4.50	9.50	0.98	0.03	0.01	0.00	99.76
YR185	Point	65.41	0.00	18.82	0.10	0.01	0.00	0.39	4.56	9.71	1.15	0.11	0.00	0.00	100.25
YR185	Point	65.00	0.05	18.72	0.09	0.00	0.00	0.41	4.48	9.62	1.29	0.06	0.08	0.00	99.80
YR185	Point	65.07	0.16	18.53	0.10	0.00	0.00	0.33	4.33	9.82	0.95	0.00	0.01	0.00	99.31
YR185	Point	66.00	0.00	18.60	0.10	0.01	0.00	0.30	4.42	9.80	0.86	0.04	0.02	0.00	100.16
YR185	Point	65.70	0.00	18.67	0.10	0.00	0.00	0.30	4.44	9.91	0.93	0.07	0.00	0.01	100.12
YR185	Point	65.21	0.28	18.31	0.10	0.01	0.00	0.32	4.35	9.75	0.87	0.04	0.00	0.00	99.25
YR185	Point	65.32	0.00	18.80	0.10	0.00	0.00	0.47	4.60	9.52	1.24	0.07	0.00	0.00	100.12
YR185	Point	65.88	0.02	18.84	0.10	0.00	0.00	0.35	4.26	9.81	1.00	0.07	0.00	0.00	100.33
YR185	Point	65.54	0.01	18.82	0.10	0.01	0.00	0.38	4.45	9.73	1.02	0.10	0.00	0.00	100.18
YR185	Point	65.09	0.00	18.71	0.08	0.00	0.00	0.42	4.24	9.52	1.33	0.07	0.00	0.01	99.47
YR185	Point	64.69	0.03	18.81	0.11	0.00	0.00	0.38	4.26	9.54	1.21	0.07	0.03	0.01	99.14
YR185	Point	65.15	0.02	18.71	0.09	0.00	0.00	0.37	4.31	9.69	1.31	0.00	0.00	0.00	99.66
YR185	Point	65.71	0.02	19.03	0.11	0.02	0.00	0.37	4.52	9.68	1.24	0.04	0.00	0.00	100.75
YR185	Point	65.67	0.03	18.57	0.11	0.00	0.00	0.37	4.41	9.71	0.97	0.04	0.00	0.00	99.87
YR185	Point	64.44	0.01	18.19	0.09	0.01	0.00	0.41	4.35	9.55	1.10	0.06	0.01	0.00	98.23
YR185	Point	65.14	0.02	18.68	0.10	0.00	0.00	0.35	4.56	9.70	1.13	0.02	0.00	0.01	99.71
YR185	Point	66.10	0.05	18.59	0.11	0.00	0.00	0.53	4.93	9.04	0.47	0.02	0.00	0.01	99.85
YR185	Point	65.19	0.02	18.47	0.10	0.00	0.00	0.37	4.37	9.72	0.90	0.09	0.01	0.00	99.22
YR185	Point	64.07	0.02	19.91	0.10	0.00	0.01	0.43	4.43	9.45	1.05	0.01	0.12	0.01	99.60
YR185	Point	65.99	0.00	18.12	0.10	0.00	0.00	0.33	4.35	9.93	0.33	0.09	0.00	0.00	99.23
YR185	Point	65.39	0.01	18.59	0.10	0.02	0.00	0.39	4.33	9.82	1.21	0.10	0.00	0.00	99.95
YR185	Point	65.82	0.05	18.26	0.10	0.02	0.00	0.32	4.37	9.80	1.07	0.06	0.00	0.00	99.88
YR185	Point	65.34	0.03	18.54	0.11	0.00	0.00	0.36	4.41	9.62	1.16	0.05	0.00	0.00	99.61
YR185	Point	65.23	0.08	18.49	0.12	0.01	0.00	0.37	4.29	9.66	1.17	0.07	0.00	0.00	99.48
YR185	Point	65.03	0.05	18.76	0.09	0.01	0.00	0.35	4.67	9.62	0.91	0.00	0.14	0.01	99.64
YR185	Point	65.38	0.03	18.60	0.10	0.01	0.00	0.36	4.40	9.78	1.11	0.00	0.00	0.00	99.79
YR185	Point	65.56	0.01	18.71	0.12	0.00	0.00	0.35	4.26	9.84	0.98	0.04	0.00	0.00	99.89
YR185	Point	65.20	0.04	18.52	0.11	0.00	0.00	0.43	4.30	9.42	1.13	0.04	0.04	0.00	99.23
YR185	Point	65.67	0.05	18.44	0.11	0.00	0.00	0.34	4.42	9.72	1.05	0.07	0.03	0.00	99.90
YR185	Point	65.53	0.01	18.72	0.09	0.01	0.00	0.38	4.40	9.56	1.15	0.06	0.00	0.01	99.92
YR185	Point	65.15	0.01	18.37	0.10	0.00	0.00	0.37	4.41	9.74	0.93	0.00	0.00	0.00	99.09
YR185	Point	65.30	0.03	18.23	0.10	0.00	0.00	0.35	4.55	9.76	0.91	0.05	0.00	0.00	99.30
YR185	Point	64.21	0.03	19.56	0.11	0.00	0.00	0.57	4.41	9.19	0.97	0.14	0.02	0.02	99.24

Sample	Analysis	SiO_2	TiO_2	Al_2O_3	FeO	MnO	MgO	CaO	Na_2O	K_2O	BaO	SrO	F	Cl	Total
Snake Rive Butte			Rhyolite		Sanidine										
YR185 •	Point	64.92	0.00	18.53	0.09	0.00	0.00	0.31	4.24	10.12	0.95	0.03	0.06	0.00	99.27
YR185 •	Point	64.92	0.06	18.46	0.10	0.01	0.00	0.31	4.15	10.05	0.94	0.07	0.00	0.00	99.08
YR185 •	Point	64.90	0.02	18.52	0.10	0.00	0.00	0.32	4.41	9.93	0.91	0.07	0.03	0.00	99.21
YR185 •	Point	64.98	0.04	18.50	0.07	0.01	0.00	0.31	4.11	10.04	0.93	0.04	0.06	0.00	99.09
YR185 •	Point	65.17	0.00	18.49	0.09	0.00	0.00	0.32	4.16	9.94	0.90	0.03	0.05	0.00	99.14
YR185 •	Point	64.98	0.02	18.55	0.11	0.00	0.00	0.32	4.24	10.02	0.96	0.07	0.00	0.00	99.28
YR185 •	Point	64.77	0.00	18.52	0.12	0.00	0.00	0.32	4.12	10.06	1.00	0.11	0.00	0.00	99.04
YR185 •	Point	64.90	0.00	18.55	0.11	0.00	0.00	0.31	4.26	9.93	0.97	0.05	0.00	0.00	99.08
YR185 •	Point	64.90	0.00	18.44	0.13	0.00	0.00	0.33	4.08	10.08	0.99	0.06	0.00	0.00	99.03
YR185 •	Point	65.15	0.02	18.56	0.12	0.00	0.01	0.32	4.19	10.02	0.98	0.06	0.00	0.01	99.44
YR185 •	Point	65.04	0.03	18.63	0.10	0.00	0.00	0.33	4.03	9.99	0.95	0.04	0.00	0.00	99.13
YR185 •	Point	65.16	0.00	18.59	0.11	0.00	0.00	0.33	4.18	9.89	0.98	0.03	0.00	0.00	99.27
YR185 •	Point	65.14	0.00	18.58	0.11	0.00	0.00	0.33	4.07	10.07	1.00	0.03	0.00	0.00	99.34
YR185 •	Point	65.17	0.03	18.59	0.10	0.00	0.00	0.34	4.18	10.00	0.97	0.05	0.02	0.00	99.45
YR185 •	Point	65.02	0.05	18.52	0.07	0.00	0.00	0.34	4.12	9.91	0.97	0.07	0.01	0.00	99.09
YR185 •	Point	64.96	0.00	18.65	0.10	0.00	0.00	0.35	4.17	9.91	0.98	0.07	0.01	0.00	99.21
YR185 •	Point	65.08	0.00	18.61	0.11	0.00	0.00	0.35	4.06	9.97	0.99	0.05	0.01	0.00	99.23
YR185 •	Point	64.94	0.02	18.63	0.10	0.00	0.00	0.36	4.28	9.86	1.00	0.05	0.05	0.00	99.30
YR185 •	Point	65.06	0.02	18.62	0.09	0.00	0.00	0.34	4.22	10.02	0.99	0.06	0.00	0.00	99.43
YR185 •	Point	65.07	0.00	18.68	0.08	0.00	0.00	0.36	4.08	9.89	1.00	0.05	0.01	0.00	99.22
YR185 •	Point	65.02	0.03	18.65	0.09	0.01	0.00	0.34	4.35	10.01	0.97	0.06	0.15	0.00	99.67
YR185 •	Point	65.32	0.03	18.73	0.10	0.00	0.00	0.34	4.21	9.97	1.01	0.03	0.00	0.00	99.73
YR185 •	Point	65.07	0.02	18.55	0.07	0.00	0.00	0.35	4.27	10.08	1.00	0.05	0.00	0.00	99.46
YR185 •	Point	65.17	0.00	18.69	0.09	0.01	0.00	0.35	4.28	9.99	0.97	0.08	0.06	0.01	99.69
YR185 •	Point	65.21	0.00	18.54	0.07	0.00	0.00	0.35	4.12	9.96	1.02	0.08	0.09	0.01	99.45
YR185 •	Point	65.19	0.04	18.57	0.08	0.00	0.00	0.36	4.19	10.07	1.00	0.06	0.02	0.00	99.57
YR185 •	Point	64.94	0.00	18.54	0.08	0.00	0.00	0.36	4.08	9.95	1.01	0.08	0.10	0.00	99.13
YR185 •	Point	65.06	0.02	18.74	0.13	0.00	0.00	0.34	4.21	9.84	0.94	0.05	0.12	0.00	99.46
YR185 •	Point	64.97	0.04	18.49	0.10	0.01	0.01	0.37	4.15	9.92	0.95	0.06	0.00	0.00	99.07
YR185 •	Point	65.06	0.01	18.68	0.07	0.00	0.00	0.34	4.11	10.05	0.92	0.06	0.04	0.00	99.36
YR185 •	Point	65.36	0.07	18.72	0.11	0.00	0.00	0.34	4.33	10.03	0.94	0.03	0.01	0.00	99.94
YR185 •	Point	65.26	0.03	18.74	0.08	0.00	0.00	0.35	4.25	9.98	0.92	0.06	0.03	0.00	99.70
YR185 •	Point	65.29	0.02	18.71	0.11	0.00	0.00	0.34	3.98	9.97	0.96	0.04	0.03	0.00	99.46
YR185 •	Point	65.31	0.02	18.71	0.09	0.00	0.00	0.34	4.09	10.01	0.93	0.10	0.07	0.00	99.68
YR185 •	Point	65.34	0.00	18.78	0.10	0.00	0.00	0.36	3.99	9.89	0.98	0.05	0.00	0.00	99.50
YR185 •	Point	65.02	0.02	18.73	0.07	0.00	0.00	0.36	4.23	9.92	0.98	0.05	0.13	0.00	99.51
YR185 •	Point	65.26	0.00	18.83	0.05	0.01	0.00	0.34	4.03	10.00	0.97	0.04	0.00	0.00	99.54
YR185 •	Point	65.15	0.00	18.75	0.11	0.00	0.00	0.34	4.16	10.00	0.96	0.06	0.08	0.00	99.61
YR185 •	Point	65.44	0.04	18.79	0.12	0.00	0.00	0.35	4.22	9.99	0.96	0.06	0.00	0.01	99.97
YR185 •	Point	65.38	0.04	18.74	0.10	0.00	0.00	0.34	4.21	10.08	0.97	0.07	0.00	0.00	99.93
YR185 •	Point	65.23	0.00	18.72	0.09	0.00	0.00	0.34	3.95	9.88	0.95	0.06	0.01	0.00	99.25
YR185 •	Point	65.14	0.01	18.57	0.09	0.00	0.00	0.35	4.16	10.00	0.97	0.09	0.00	0.00	99.37
YR185 •	Point	65.33	0.00	18.68	0.07	0.00	0.00	0.36	3.94	9.93	0.95	0.07	0.13	0.01	99.48
YR185 •	Point	65.16	0.04	18.61	0.10	0.00	0.01	0.38	4.15	9.89	0.92	0.04	0.05	0.02	99.36
YR185 •	Point	65.37	0.01	18.67	0.08	0.01	0.00	0.37	4.21	10.08	0.98	0.08	0.02	0.01	99.88
YR185 •	Point	65.27	0.01	18.71	0.10	0.00	0.01	0.40	4.20	10.08	0.96	0.03	0.05	0.01	99.83
YR185 •	Point	65.20	0.00	18.75	0.11	0.00	0.01	0.39	4.17	10.00	0.90	0.08	0.00	0.02	99.63
YR185 •	Point	65.02	0.02	18.70	0.08	0.00	0.00	0.36	4.16	10.05	0.97	0.07	0.07	0.01	99.51
YR185 •	Point	65.35	0.00	18.69	0.12	0.00	0.01	0.37	4.22	10.02	1.00	0.06	0.00	0.02	99.87
YR185 •	Point	65.20	0.04	18.76	0.12	0.00	0.01	0.38	4.15	9.94	0.96	0.06	0.00	0.01	99.61
Snake Rive Butte			Rhyolite		Glass										
YR185	Point	77.05	0.05	11.10	2.00	0.02	0.03	0.49	3.43	4.87	0.05	0.00	0.01	0.11	99.22
YR185	Point	77.49	0.05	11.32	1.25	0.02	0.02	0.53	3.48	4.96	0.03	0.02	0.06	0.10	99.34
YR185	Point	77.58	0.09	11.34	1.25	0.02	0.02	0.54	3.36	4.88	0.00	0.05	0.16	0.11	99.40
YR185	Point	77.46	0.06	11.37	1.18	0.05	0.03	0.54	3.26	5.20	0.04	0.00	0.12	0.12	99.42
YR185	Point	77.29	0.06	11.16	1.30	0.03	0.03	0.56	3.56	4.99	0.00	0.03	0.10	0.12	99.24
YR185	Point	77.20	0.08	11.26	1.29	0.03	0.02	0.53	3.49	4.97	0.04	0.02	0.18	0.12	99.23
YR185	Point	76.50	0.06	11.53	1.61	0.02	0.02	0.54	3.46	5.01	0.05	0.11	0.16	0.13	99.20
YR185	Point	77.42	0.03	11.48	1.31	0.03	0.01	0.54	3.63	5.08	0.04	0.03	0.13	0.11	99.85
YR185	Point	77.11	0.04	11.37	1.28	0.05	0.03	0.54	3.58	4.96	0.01	0.02	0.09	0.12	99.22
YR185	Point	77.96	0.08	11.47	1.29	0.04	0.02	0.54	3.50	5.00	0.00	0.02	0.14	0.12	100.20
YR185	Point	77.20	0.02	11.60	1.31	0.06	0.03	0.56	3.59	5.06	0.04	0.06	0.17	0.12	99.81
YR185	Point	77.37	0.02	11.35	1.30	0.03	0.03	0.55	3.49	4.91	0.07	0.01	0.06	0.13	99.31

Sample	Analysis	SiO_2	TiO_2	Al_2O_3	FeO	MnO	MgO	CaO	Na_2O	K_2O	BaO	SrO	F	Cl	Total
Snake Rive Butte			Rhyolite		Glass										
YR185	Point	76.98	0.01	11.43	1.85	0.04	0.01	0.54	3.21	4.79	0.05	0.00	0.11	0.12	99.14
YR185	Point	76.94	0.02	11.24	1.65	0.02	0.03	0.54	3.37	4.95	0.00	0.07	0.25	0.11	99.19
Green Canyon Dome			Rhyolite		Sanidine										
YR242	Point	66.19	0.01	18.54	0.10	0.00	0.00	0.25	4.44	10.24	0.00	0.02	0.00	0.00	99.79
YR242	Point	66.42	0.01	18.56	0.09	0.00	0.00	0.26	4.33	10.41	0.00	0.03	0.01	0.01	100.12
YR242	Point	65.93	0.00	18.37	0.06	0.01	0.00	0.27	4.36	10.38	0.00	0.05	0.00	0.00	99.44
YR242	Point	65.89	0.02	18.40	0.10	0.01	0.00	0.28	4.20	10.22	0.00	0.02	0.05	0.00	99.19
YR242	Point	66.11	0.00	18.43	0.14	0.00	0.00	0.27	4.40	10.22	0.00	0.00	0.00	0.00	99.57
YR242	Point	66.12	0.01	18.35	0.08	0.00	0.00	0.28	4.47	10.22	0.01	0.02	0.03	0.00	99.57
YR242	Point	66.39	0.04	18.57	0.13	0.00	0.00	0.28	4.40	10.20	0.01	0.03	0.04	0.01	100.11
YR242	Point	66.08	0.00	18.47	0.10	0.01	0.00	0.28	4.34	10.31	0.00	0.04	0.00	0.00	99.64
YR242	Point	66.15	0.00	18.34	0.11	0.00	0.00	0.29	4.23	10.22	0.00	0.04	0.00	0.01	99.40
YR242	Point	65.93	0.02	18.45	0.07	0.01	0.00	0.29	4.46	10.23	0.00	0.02	0.10	0.02	99.60
YR242	Point	66.02	0.04	18.50	0.08	0.00	0.00	0.33	4.43	10.30	0.00	0.03	0.00	0.01	99.75
YR242	Point	66.15	0.00	18.50	0.08	0.00	0.00	0.31	4.48	10.30	0.00	0.01	0.10	0.00	99.93
YR242	Point	65.97	0.02	18.38	0.10	0.00	0.00	0.31	4.35	10.24	0.00	0.04	0.03	0.01	99.45
YR242	Point	66.42	0.00	18.47	0.08	0.01	0.00	0.29	4.50	10.26	0.00	0.05	0.03	0.01	100.13
YR242	Point	66.16	0.01	18.47	0.11	0.00	0.00	0.29	4.46	10.35	0.00	0.06	0.01	0.01	99.94
YR242	Point	66.40	0.01	18.55	0.06	0.00	0.00	0.30	4.43	10.30	0.02	0.04	0.00	0.01	100.12
YR242	Point	66.15	0.00	18.46	0.10	0.01	0.00	0.31	4.35	10.28	0.01	0.03	0.01	0.02	99.74
YR242	Point	66.22	0.01	18.53	0.08	0.00	0.00	0.27	4.30	10.28	0.00	0.01	0.01	0.00	99.70
YR242	Point	66.28	0.02	18.37	0.10	0.01	0.00	0.29	4.38	10.27	0.00	0.05	0.00	0.02	99.79
YR242	Point	66.41	0.00	18.57	0.12	0.01	0.00	0.29	4.53	10.27	0.01	0.05	0.04	0.00	100.30
YR242	Point	66.36	0.04	18.51	0.09	0.01	0.00	0.30	4.37	10.35	0.00	0.07	0.05	0.01	100.15
YR242	Point	66.21	0.00	18.48	0.09	0.00	0.00	0.30	4.37	10.23	0.00	0.07	0.00	0.01	99.77
YR242	Point	66.39	0.00	18.40	0.09	0.00	0.00	0.32	4.56	10.32	0.03	0.03	0.00	0.00	100.15
YR242	Point	65.97	0.03	18.55	0.14	0.00	0.00	0.31	4.41	10.31	0.00	0.03	0.00	0.00	99.75
YR242	Point	66.13	0.03	18.47	0.07	0.00	0.00	0.27	4.37	10.28	0.00	0.05	0.02	0.01	99.71
YR242	Point	66.25	0.00	18.38	0.09	0.01	0.00	0.31	4.43	10.25	0.00	0.08	0.00	0.03	99.84
YR242	Point	66.29	0.03	18.39	0.10	0.00	0.00	0.25	4.20	10.32	0.00	0.02	0.00	0.03	99.65
YR242	Point	66.36	0.04	18.43	0.07	0.01	0.00	0.24	4.37	10.36	0.01	0.02	0.07	0.02	100.00
YR242	Point	66.27	0.00	18.50	0.07	0.00	0.00	0.26	4.31	10.35	0.01	0.00	0.04	0.00	99.84
YR242	Point	66.11	0.00	18.53	0.06	0.00	0.00	0.28	4.43	10.37	0.00	0.03	0.00	0.01	99.81
YR242	Point	66.45	0.01	18.57	0.12	0.00	0.01	0.27	4.25	10.36	0.00	0.06	0.04	0.00	100.14
YR242	Point	66.09	0.03	18.40	0.08	0.01	0.00	0.26	4.41	10.36	0.00	0.02	0.00	0.00	99.66
YR242	Point	66.04	0.01	18.43	0.11	0.01	0.00	0.27	4.46	10.34	0.02	0.04	0.00	0.02	99.78
YR242	Point	66.36	0.01	18.51	0.08	0.00	0.00	0.27	4.32	10.35	0.01	0.02	0.08	0.01	100.00
YR242	Point	66.46	0.02	18.50	0.12	0.00	0.00	0.27	4.36	10.41	0.02	0.02	0.00	0.01	100.17
YR242	Point	66.25	0.04	18.60	0.08	0.00	0.00	0.26	4.12	10.33	0.01	0.04	0.03	0.00	99.77
YR242	Point	66.22	0.01	18.43	0.10	0.00	0.00	0.28	4.29	10.34	0.01	0.01	0.00	0.00	99.71
YR242	Point	66.34	0.00	18.47	0.08	0.00	0.00	0.26	4.26	10.40	0.02	0.04	0.05	0.01	99.92
YR242	Point	66.02	0.00	18.43	0.06	0.00	0.00	0.26	4.25	10.44	0.00	0.00	0.00	0.00	99.46
YR242	Point	66.58	0.04	18.69	0.10	0.00	0.00	0.28	4.45	10.23	0.00	0.02	0.00	0.01	100.40
YR242	Point	66.21	0.02	18.52	0.12	0.00	0.00	0.28	4.18	10.32	0.00	0.02	0.00	0.00	99.68
YR242	Point	66.49	0.00	18.69	0.08	0.00	0.00	0.25	4.45	10.36	0.00	0.02	0.00	0.00	100.35
YR242	Point	66.17	0.00	18.58	0.10	0.00	0.00	0.25	4.36	10.40	0.00	0.00	0.00	0.00	99.86
YR242	Point	66.07	0.03	18.38	0.09	0.00	0.00	0.27	4.25	10.31	0.00	0.07	0.02	0.00	99.51
YR242	Point	66.08	0.01	18.53	0.11	0.00	0.00	0.25	4.48	10.32	0.01	0.05	0.00	0.00	99.84
YR242	Point	65.93	0.00	18.38	0.12	0.01	0.00	0.26	4.54	10.18	0.00	0.00	0.03	0.00	99.46
YR242	Point	65.92	0.00	18.31	0.09	0.00	0.00	0.24	4.50	10.29	0.01	0.03	0.00	0.01	99.41
YR242	Point	65.83	0.00	18.21	0.10	0.00	0.00	0.25	4.38	10.29	0.01	0.00	0.05	0.00	99.12
YR242	Point	65.91	0.00	18.31	0.10	0.00	0.00	0.25	4.49	10.36	0.01	0.04	0.00	0.00	99.48
YR242	Point	65.60	0.02	18.28	0.08	0.00	0.00	0.25	4.43	10.33	0.01	0.02	0.05	0.01	99.10
YR242	Point	65.66	0.00	18.31	0.09	0.00	0.00	0.25	4.33	10.47	0.00	0.04	0.08	0.00	99.23
YR242	Point	65.70	0.00	18.25	0.06	0.00	0.00	0.24	4.39	10.31	0.01	0.04	0.00	0.00	99.00
YR242	Point	65.67	0.02	18.20	0.10	0.00	0.00	0.28	4.32	10.39	0.02	0.04	0.02	0.00	99.07
YR242	Point	66.14	0.02	18.37	0.09	0.00	0.00	0.28	4.27	10.21	0.00	0.03	0.04	0.01	99.45
YR242	Point	66.04	0.03	18.48	0.05	0.00	0.00	0.28	4.31	10.44	0.01	0.05	0.02	0.00	99.72
YR242	Point	65.98	0.00	18.37	0.12	0.00	0.00	0.27	4.44	10.33	0.02	0.01	0.07	0.00	99.61
YR242	Point	65.97	0.01	18.46	0.11	0.01	0.00	0.30	4.22	10.26	0.00	0.06	0.05	0.01	99.47
YR242	Point	66.08	0.05	18.47	0.10	0.00	0.00	0.27	4.50	10.20	0.01	0.03	0.04	0.00	99.75
YR242	Point	66.12	0.04	18.53	0.07	0.00	0.00	0.29	4.46	10.36	0.00	0.03	0.01	0.00	99.92
YR242	Point	65.80	0.04	18.40	0.10	0.00	0.00	0.29	4.48	10.14	0.00	0.03	0.00	0.00	99.29

Sample	Analysis	SiO_2	TiO_2	Al_2O_3	FeO	MnO	MgO	CaO	Na_2O	K_2O	BaO	SrO	F	Cl	Total
Green Canyon Dome			Rhyolite		Sanidine										
YR242	Point	66.28	0.00	18.55	0.07	0.00	0.01	0.29	4.42	10.17	0.02	0.01	0.07	0.00	99.88
YR242	Point	65.95	0.00	18.45	0.11	0.00	0.00	0.28	4.56	10.23	0.02	0.02	0.09	0.00	99.70
YR242	Point	65.92	0.04	18.56	0.09	0.00	0.00	0.28	4.43	10.26	0.00	0.03	0.02	0.01	99.64
YR242	Point	66.02	0.04	18.44	0.10	0.00	0.00	0.30	4.45	10.14	0.03	0.03	0.00	0.00	99.54
YR242	Point	66.22	0.04	18.68	0.11	0.00	0.00	0.30	4.46	10.11	0.00	0.05	0.01	0.00	100.00
YR242	Point	65.70	0.00	18.47	0.08	0.00	0.00	0.30	4.36	10.10	0.00	0.03	0.12	0.00	99.16
YR242	Point	66.13	0.02	18.44	0.09	0.00	0.00	0.28	4.50	10.21	0.00	0.07	0.09	0.00	99.84
YR242	Point	65.83	0.00	18.22	0.08	0.00	0.00	0.23	4.24	10.34	0.00	0.02	0.06	0.00	99.02
YR242	Point	65.97	0.00	18.23	0.09	0.00	0.00	0.21	4.40	10.37	0.01	0.05	0.06	0.00	99.40
YR242	Point	65.66	0.02	18.28	0.10	0.01	0.00	0.23	4.34	10.39	0.00	0.04	0.00	0.00	99.07
YR242	Point	65.66	0.02	18.33	0.08	0.00	0.00	0.22	4.33	10.34	0.01	0.06	0.01	0.00	99.05
YR242	Point	65.82	0.01	18.35	0.10	0.00	0.00	0.24	4.53	10.31	0.00	0.00	0.00	0.00	99.35
YR242	Point	65.95	0.00	18.23	0.07	0.01	0.00	0.22	4.22	10.28	0.03	0.06	0.08	0.00	99.15
YR242	Point	65.97	0.01	18.33	0.06	0.00	0.00	0.23	4.33	10.26	0.00	0.04	0.01	0.01	99.25
YR242	Point	65.69	0.03	18.30	0.09	0.00	0.00	0.22	4.26	10.40	0.00	0.04	0.10	0.00	99.13
YR242	Point	65.72	0.04	18.30	0.07	0.00	0.00	0.22	4.32	10.39	0.00	0.01	0.14	0.01	99.22
YR242	Point	65.60	0.01	18.28	0.10	0.00	0.00	0.24	4.44	10.30	0.00	0.06	0.03	0.00	99.05
					Plagioclase										
YR242	Point	64.60	0.02	21.37	0.12	0.00	0.00	3.19	8.60	1.39	0.02	0.00	0.01	0.00	99.32
YR242	Point	64.84	0.00	21.33	0.13	0.00	0.01	3.09	8.72	1.41	0.01	0.00	0.01	0.01	99.57
YR242	Point	64.83	0.02	21.30	0.14	0.00	0.00	3.02	9.23	1.45	0.01	0.00	0.00	0.00	100.00
YR242	Point	64.82	0.00	21.25	0.17	0.00	0.00	3.06	9.00	1.42	0.00	0.00	0.00	0.01	99.73
YR242	Point	64.53	0.02	21.33	0.20	0.00	0.00	3.16	8.63	1.41	0.01	0.03	0.00	0.01	99.32
YR242	Point	64.52	0.02	21.46	0.15	0.00	0.00	3.19	8.95	1.39	0.00	0.05	0.00	0.00	99.73
YR242	Point	64.89	0.00	21.43	0.13	0.00	0.01	3.10	8.82	1.39	0.00	0.04	0.00	0.00	99.81
YR242	Point	64.33	0.02	21.45	0.14	0.01	0.00	3.31	8.80	1.36	0.01	0.00	0.00	0.00	99.43
YR242	Point	64.49	0.03	21.50	0.18	0.01	0.00	3.21	8.85	1.33	0.00	0.00	0.00	0.00	99.60
YR242	Point	64.76	0.01	21.46	0.17	0.00	0.01	3.17	8.70	1.40	0.02	0.03	0.00	0.00	99.74
YR242	Point	64.55	0.00	21.41	0.14	0.00	0.01	3.21	8.91	1.43	0.01	0.04	0.00	0.01	99.73
YR242	Point	64.47	0.00	21.40	0.17	0.00	0.00	3.19	8.64	1.41	0.00	0.05	0.00	0.00	99.34
YR242	Point	64.83	0.04	21.35	0.14	0.01	0.00	3.13	8.80	1.39	0.02	0.00	0.11	0.00	99.80
YR242	Point	64.62	0.00	21.19	0.15	0.00	0.00	3.10	8.68	1.45	0.01	0.07	0.05	0.01	99.33
YR242	Point	64.67	0.01	21.25	0.10	0.00	0.00	3.09	9.01	1.40	0.00	0.00	0.04	0.00	99.57
YR242	Point	64.62	0.01	21.21	0.13	0.01	0.00	3.09	8.91	1.43	0.00	0.02	0.00	0.00	99.43
YR242	Point	64.72	0.00	21.26	0.17	0.00	0.00	3.01	8.81	1.46	0.01	0.04	0.00	0.01	99.48
YR242	Point	64.48	0.00	21.08	0.13	0.00	0.00	3.08	8.72	1.47	0.01	0.03	0.00	0.00	99.01
YR242	Point	64.57	0.00	21.20	0.15	0.01	0.00	3.08	9.05	1.37	0.00	0.03	0.00	0.00	99.48
YR242	Point	64.23	0.03	21.22	0.13	0.01	0.00	3.21	8.96	1.46	0.03	0.03	0.04	0.01	99.36
YR242	Point	64.31	0.03	21.08	0.12	0.01	0.01	3.10	8.92	1.45	0.02	0.01	0.07	0.00	99.13
YR242	Point	64.60	0.02	20.93	0.18	0.00	0.00	2.91	9.00	1.51	0.00	0.01	0.00	0.01	99.18

Notes:

* = Single feldspar crystals measure 1 - 2mm in diameter

Transect = data displayed in Figure 3.9

Electron microprobe (wt. %) analysis of all Bishop Tuff samples by phase

Sample	Analysis	SiO_2	TiO_2	Al_2O_3	FeO	MnO	MgO	CaO	Na_2O	K_2O	BaO	SrO	F	Cl	Total
Bishop Tuff - F5			Pumice		Sanidine										
BP029	Point	66.16	0.00	17.93	0.11	0.00	0.00	0.14	3.81	11.11	0.00	0.02	0.03	0.00	99.31
BP029	Point	66.46	0.01	18.08	0.07	0.00	0.00	0.16	3.74	11.10	0.05	0.03	0.00	0.00	99.70
BP029	Point	66.51	0.00	18.48	0.06	0.01	0.00	0.17	3.87	11.09	0.03	0.07	0.00	0.00	100.29
BP029	Point	66.52	0.00	18.45	0.05	0.01	0.00	0.18	3.88	11.05	0.00	0.08	0.00	0.00	100.22
BP029	Point	66.36	0.00	18.23	0.08	0.01	0.00	0.15	4.03	11.05	0.03	0.03	0.06	0.00	100.03
BP029	Point	66.47	0.02	18.51	0.08	0.00	0.00	0.18	4.05	11.04	0.01	0.00	0.04	0.00	100.39
BP029	Point	66.24	0.03	18.05	0.07	0.00	0.00	0.18	4.01	11.04	0.00	0.06	0.03	0.00	99.70
BP029	Point	66.26	0.02	18.08	0.10	0.00	0.00	0.16	4.01	11.03	0.00	0.05	0.03	0.00	99.73
BP029	Point	66.16	0.03	17.90	0.08	0.00	0.00	0.14	3.93	11.03	0.00	0.00	0.06	0.00	99.33
BP029	Point	65.96	0.06	17.84	0.09	0.00	0.00	0.14	3.92	11.02	0.01	0.05	0.07	0.00	99.16
BP029	Point	66.28	0.02	18.07	0.07	0.00	0.00	0.14	3.93	11.02	0.00	0.02	0.01	0.00	99.55
BP029	Point	66.29	0.03	18.27	0.07	0.00	0.00	0.17	3.98	11.01	0.00	0.02	0.13	0.00	99.98
BP029	Point	66.15	0.02	17.91	0.06	0.03	0.00	0.14	3.89	11.00	0.00	0.03	0.00	0.00	99.23
BP029	Point	66.47	0.03	18.04	0.08	0.00	0.00	0.14	3.76	11.00	0.00	0.02	0.00	0.00	99.54
BP029	Point	66.49	0.01	18.38	0.07	0.01	0.00	0.16	3.88	11.00	0.00	0.02	0.04	0.00	100.07
BP029	Point	66.22	0.01	18.00	0.07	0.00	0.00	0.16	3.92	11.00	0.00	0.05	0.08	0.01	99.53
BP029	Point	66.28	0.03	18.14	0.08	0.00	0.00	0.15	4.04	10.98	0.04	0.01	0.09	0.00	99.86
BP029	Point	66.71	0.02	18.53	0.06	0.02	0.00	0.16	3.91	10.98	0.03	0.04	0.08	0.00	100.55
BP029	Point	66.16	0.04	18.18	0.07	0.00	0.00	0.17	3.91	10.98	0.04	0.04	0.00	0.00	99.58
BP029	Point	66.46	0.00	18.28	0.07	0.00	0.00	0.15	4.00	10.98	0.01	0.07	0.01	0.00	100.02
BP029	Point	66.30	0.00	18.24	0.08	0.01	0.00	0.15	3.94	10.97	0.01	0.08	0.00	0.00	99.77
BP029	Point	66.08	0.00	17.98	0.07	0.01	0.00	0.16	3.84	10.96	0.03	0.07	0.03	0.00	99.22
BP029	Point	66.40	0.00	18.25	0.07	0.00	0.00	0.16	4.10	10.96	0.03	0.03	0.04	0.00	100.04
BP029	Point	66.49	0.00	18.27	0.09	0.00	0.01	0.17	3.91	10.96	0.01	0.00	0.01	0.00	99.91
BP029	Point	66.25	0.00	18.00	0.08	0.01	0.00	0.17	3.96	10.95	0.00	0.02	0.00	0.00	99.43
BP029	Point	66.47	0.00	18.36	0.09	0.00	0.00	0.16	4.09	10.94	0.02	0.01	0.01	0.00	100.15
BP029	Point	66.44	0.02	18.28	0.06	0.00	0.00	0.18	3.69	10.93	0.00	0.07	0.02	0.00	99.69
BP029	Point	66.06	0.00	18.26	0.06	0.00	0.00	0.16	3.81	10.91	0.00	0.11	0.00	0.00	99.37
BP029	Point	65.91	0.01	17.99	0.06	0.00	0.00	0.16	3.97	10.91	0.02	0.10	0.05	0.00	99.19
BP029	Point	65.81	0.00	17.92	0.07	0.00	0.00	0.16	4.03	10.90	0.02	0.06	0.05	0.00	99.04
BP029	Point	66.18	0.01	18.10	0.08	0.00	0.00	0.17	3.80	10.89	0.00	0.00	0.00	0.00	99.24
BP029	Point	66.32	0.00	18.20	0.07	0.00	0.00	0.14	3.84	10.87	0.19	0.02	0.06	0.00	99.70
BP029	Point	66.30	0.00	18.32	0.08	0.00	0.00	0.18	4.09	10.84	0.03	0.00	0.01	0.00	99.86
					Plagioclase										
BP029	Point	78.97	0.00	12.19	0.66	0.05	0.03	0.41	3.85	4.24	0.02	0.00	0.02	0.08	100.52
BP029	Point	65.01	0.02	20.87	0.13	0.00	0.00	2.82	9.21	1.28	0.00	0.02	0.06	0.00	99.42
BP029	Point	65.18	0.00	21.27	0.12	0.00	0.00	3.04	9.33	1.22	0.02	0.00	0.01	0.00	100.21
BP029	Point	65.01	0.01	21.04	0.10	0.00	0.00	3.00	9.30	1.18	0.00	0.11	0.00	0.01	99.75
BP029	Point	64.87	0.01	21.41	0.13	0.00	0.00	3.29	9.12	1.17	0.01	0.05	0.00	0.00	100.07
BP029	Point	64.66	0.03	21.34	0.13	0.00	0.00	3.31	9.08	1.06	0.01	0.04	0.00	0.00	99.67
Bishop Tuff - F7			Pumice		Sanidine										
CMW12	Point	65.20	0.00	17.95	0.08	0.00	0.00	0.17	3.96	11.13	0.00	0.00	0.00	0.01	98.49
CMW12	Point	65.07	0.04	17.87	0.07	0.00	0.00	0.15	3.74	11.10	0.01	0.07	0.00	0.00	98.13
CMW12	Point	64.88	0.00	17.86	0.07	0.01	0.00	0.16	3.79	11.05	0.01	0.06	0.07	0.01	97.97
CMW12	Point	65.39	0.00	18.14	0.08	0.00	0.00	0.18	3.75	11.04	0.02	0.00	0.10	0.00	98.70
CMW12	Point	65.54	0.01	17.97	0.08	0.01	0.00	0.16	3.73	11.04	0.01	0.00	0.00	0.01	98.57
CMW12	Point	64.96	0.03	17.66	0.06	0.00	0.00	0.16	3.63	11.03	0.03	0.07	0.00	0.01	97.64
CMW12	Point	65.09	0.01	17.91	0.07	0.00	0.00	0.17	3.78	11.02	0.01	0.02	0.03	0.01	98.14
CMW12	Point	65.09	0.00	18.03	0.08	0.01	0.00	0.18	3.87	11.01	0.02	0.07	0.00	0.01	98.35
CMW12	Point	64.97	0.01	17.76	0.08	0.00	0.00	0.17	3.73	11.01	0.00	0.03	0.00	0.01	97.75
CMW12	Point	64.68	0.04	17.47	0.07	0.00	0.00	0.19	3.81	11.01	0.00	0.04	0.09	0.01	97.41
CMW12	Point	64.43	0.00	17.55	0.06	0.00	0.00	0.15	3.81	11.00	0.04	0.07	0.00	0.01	97.12
CMW12	Point	65.37	0.00	17.95	0.08	0.01	0.00	0.16	3.87	11.00	0.03	0.10	0.10	0.01	98.67
CMW12	Point	65.21	0.00	17.89	0.07	0.00	0.00	0.14	3.79	10.98	0.03	0.03	0.02	0.01	98.19
CMW12	Point	65.00	0.00	17.77	0.07	0.00	0.00	0.14	3.82	10.98	0.00	0.00	0.03	0.01	97.82
CMW12	Point	65.08	0.01	17.74	0.06	0.01	0.00	0.16	3.77	10.96	0.04	0.01	0.00	0.01	97.86
CMW12	Point	65.18	0.03	17.88	0.08	0.00	0.00	0.14	3.72	10.96	0.00	0.02	0.08	0.01	98.09
CMW12	Point	64.81	0.06	17.91	0.08	0.01	0.00	0.14	4.03	10.96	0.01	0.00	0.01	0.01	98.02
CMW12	Point	64.78	0.00	17.75	0.08	0.00	0.00	0.21	3.70	10.96	0.00	0.03	0.03	0.01	97.54
CMW12	Point	64.82	0.00	17.48	0.06	0.02	0.00	0.18	3.80	10.95	0.01	0.04	0.00	0.01	97.37
CMW12	Point	64.77	0.01	17.91	0.08	0.00	0.00	0.17	3.78	10.95	0.00	0.05	0.10	0.00	97.82
CMW12	Point	64.28	0.00	17.50	0.08	0.00	0.00	0.14	3.81	10.94	0.02	0.05	0.00	0.00	96.81
CMW12	Point	65.54	0.02	18.01	0.09	0.00	0.00	0.15	3.64	10.94	0.00	0.03	0.01	0.01	98.44
CMW12	Point	64.46	0.00	17.48	0.07	0.00	0.00	0.14	3.94	10.93	0.19	0.02	0.09	0.01	97.33

Sample	Analysis	SiO_2	TiO_2	Al_2O_3	FeO	MnO	MgO	CaO	Na_2O	K_2O	BaO	SrO	F	Cl	Total
Bishop Tuff - F7			**Pumice**		**Sanidine**										
CMW12	Point	64.96	0.02	17.83	0.08	0.00	0.00	0.20	3.85	10.92	0.02	0.07	0.03	0.01	98.00
CMW12	Point	65.06	0.00	17.80	0.05	0.00	0.00	0.17	3.78	10.92	0.03	0.05	0.00	0.00	97.87
CMW12	Point	65.49	0.00	18.06	0.08	0.00	0.00	0.16	3.83	10.92	0.00	0.01	0.00	0.01	98.55
CMW12	Point	64.69	0.03	17.55	0.07	0.00	0.00	0.15	3.65	10.91	0.01	0.00	0.00	0.01	97.08
CMW12	Point	64.86	0.00	17.79	0.07	0.01	0.00	0.16	3.76	10.91	0.00	0.04	0.07	0.01	97.68
CMW12	Point	64.98	0.00	17.68	0.10	0.01	0.00	0.17	3.85	10.88	0.03	0.00	0.00	0.01	97.70
CMW12	Point	65.36	0.01	18.23	0.07	0.00	0.00	0.15	3.91	10.88	0.00	0.04	0.03	0.01	98.69
CMW12	Point	64.52	0.02	17.46	0.08	0.00	0.00	0.21	3.72	10.86	0.00	0.11	0.00	0.01	96.99
CMW12	Point	64.54	0.01	17.38	0.08	0.03	0.00	0.16	3.70	10.86	0.00	0.08	0.00	0.01	96.83
CMW12	Point	64.87	0.01	17.72	0.07	0.00	0.00	0.16	3.94	10.84	0.00	0.00	0.00	0.01	97.61
CMW12	Point	65.06	0.03	17.58	0.09	0.00	0.00	0.18	3.82	10.83	0.02	0.05	0.01	0.01	97.66
CMW12	Point	65.06	0.02	17.65	0.08	0.02	0.00	0.14	3.78	10.83	0.00	0.02	0.00	0.00	97.59
CMW12	Point	63.42	0.00	16.97	0.07	0.03	0.00	0.17	4.04	10.83	0.00	0.03	0.01	0.01	95.55
CMW12	Point	65.34	0.03	17.92	0.09	0.00	0.00	0.15	3.79	10.82	0.02	0.02	0.00	0.00	98.17
CMW12	Point	64.32	0.02	17.31	0.08	0.00	0.01	0.18	3.83	10.80	0.00	0.05	0.00	0.00	96.59
CMW12	Point	64.59	0.02	17.55	0.08	0.03	0.00	0.17	3.84	10.79	0.00	0.03	0.00	0.01	97.11
CMW12	Point	63.87	0.00	16.98	0.06	0.00	0.00	0.16	3.87	10.69	0.02	0.05	0.00	0.01	95.72
					Plagioclase										
CMW12	Point	63.64	0.01	20.82	0.11	0.01	0.00	3.08	8.79	1.36	0.03	0.06	0.00	0.01	97.92
CMW12	Point	63.72	0.02	20.82	0.11	0.00	0.01	3.16	8.80	1.35	0.03	0.02	0.04	0.02	98.10
CMW12	Point	63.10	0.01	20.56	0.15	0.02	0.00	3.27	8.90	1.33	0.00	0.02	0.00	0.01	97.37
CMW12	Point	64.15	0.04	20.66	0.13	0.00	0.00	3.04	9.13	1.29	0.05	0.02	0.00	0.00	98.52
CMW12	Point	63.95	0.00	20.40	0.12	0.01	0.00	2.98	9.45	1.26	0.01	0.02	0.11	0.00	98.31
CMW12	Point	63.87	0.00	20.56	0.12	0.00	0.01	3.02	9.19	1.23	0.02	0.11	0.00	0.00	98.13
CMW12	Point	64.26	0.01	20.46	0.12	0.00	0.01	2.73	9.38	1.21	0.00	0.00	0.00	0.01	98.19
CMW12	Point	63.99	0.05	20.68	0.12	0.01	0.01	2.93	9.07	1.17	0.00	0.00	0.00	0.00	98.03
CMW12	Point	63.34	0.00	20.68	0.13	0.00	0.01	3.22	8.84	1.15	0.03	0.08	0.00	0.01	97.48
Bishop Tuff - lg1Eb			**Pumice #1**		**Sanidine**										
BP097	Point	65.41	0.03	18.31	0.08	0.00	0.00	0.16	3.77	11.04	0.02	0.01	0.04	0.00	98.87
BP097	Point	64.87	0.00	17.89	0.06	0.00	0.00	0.14	3.86	11.03	0.02	0.00	0.00	0.00	97.87
BP097	Point	65.15	0.00	17.94	0.07	0.00	0.00	0.15	3.95	11.02	0.04	0.02	0.02	0.00	98.37
BP097	Point	65.03	0.02	18.02	0.08	0.00	0.00	0.15	3.79	11.02	0.01	0.05	0.00	0.00	98.16
BP097	Point	64.92	0.03	17.72	0.07	0.01	0.00	0.15	3.76	11.02	0.03	0.07	0.00	0.01	97.78
BP097	Point	64.91	0.02	18.01	0.06	0.01	0.00	0.16	4.09	11.02	0.04	0.04	0.00	0.00	98.36
BP097	Point	65.33	0.01	18.14	0.07	0.00	0.00	0.15	3.93	11.01	0.00	0.04	0.00	0.00	98.68
BP097	Point	64.81	0.00	17.97	0.06	0.00	0.00	0.14	3.80	10.99	0.00	0.05	0.05	0.00	97.87
BP097	Point	64.92	0.00	17.98	0.07	0.00	0.00	0.17	3.91	10.94	0.00	0.00	0.04	0.00	98.02
BP097	Point	65.35	0.00	18.18	0.08	0.00	0.00	0.16	3.91	10.93	0.00	0.09	0.02	0.00	98.73
BP097	Point	64.96	0.00	17.91	0.08	0.00	0.00	0.17	3.94	10.93	0.00	0.00	0.07	0.00	98.06
BP097	Point	65.13	0.02	17.80	0.07	0.00	0.00	0.16	4.04	10.93	0.02	0.01	0.00	0.00	98.18
BP097	Point	65.06	0.00	18.19	0.08	0.00	0.00	0.15	3.97	10.93	0.04	0.00	0.07	0.00	98.49
BP097	Point	65.52	0.03	18.09	0.08	0.00	0.00	0.15	3.98	10.91	0.01	0.05	0.00	0.01	98.82
BP097	Point	64.23	0.02	17.51	0.07	0.00	0.01	0.15	4.02	10.91	0.00	0.00	0.00	0.00	96.92
BP097	Point	65.15	0.02	18.06	0.07	0.00	0.00	0.16	3.73	10.90	0.00	0.04	0.00	0.00	98.13
BP097	Point	64.27	0.04	17.48	0.09	0.00	0.00	0.15	3.84	10.89	0.01	0.07	0.00	0.00	96.84
BP097	Point	64.84	0.04	17.97	0.06	0.00	0.00	0.17	3.82	10.87	0.00	0.03	0.02	0.00	97.82
BP097	Point	65.33	0.00	18.00	0.09	0.02	0.00	0.16	3.90	10.86	0.03	0.06	0.00	0.00	98.45
BP097	Point	64.62	0.03	17.90	0.06	0.00	0.00	0.17	3.99	10.85	0.00	0.00	0.00	0.00	97.63
BP097	Point	64.72	0.01	17.83	0.07	0.02	0.00	0.17	4.03	10.83	0.06	0.06	0.05	0.00	97.85
BP097	Point	64.68	0.00	17.64	0.07	0.00	0.01	0.17	4.02	10.77	0.01	0.07	0.04	0.00	97.48
					Plagioclase										
BP097	Point	63.75	0.00	20.60	0.14	0.00	0.00	2.83	9.21	1.24	0.02	0.03	0.00	0.00	97.84
BP097	Point	62.32	0.05	20.15	0.12	0.00	0.00	2.95	9.15	1.21	0.00	0.02	0.05	0.00	96.03
BP097	Point	63.82	0.02	20.56	0.12	0.00	0.00	2.82	9.29	1.20	0.00	0.03	0.00	0.01	97.86
BP097	Point	63.65	0.01	20.56	0.12	0.00	0.00	2.88	9.46	1.19	0.01	0.05	0.01	0.00	97.95
BP097	Point	63.15	0.00	19.88	0.14	0.00	0.01	2.76	9.23	1.16	0.01	0.00	0.00	0.00	96.34
BP097	Point	63.51	0.00	20.92	0.11	0.00	0.00	3.16	9.26	1.15	0.00	0.02	0.00	0.01	98.13
BP097	Point	63.64	0.02	20.66	0.14	0.02	0.00	3.11	9.18	1.14	0.01	0.02	0.00	0.00	97.95
BP097	Point	62.63	0.00	20.07	0.10	0.00	0.00	2.94	9.23	1.13	0.00	0.04	0.00	0.00	96.15
BP097	Point	62.97	0.02	20.84	0.12	0.00	0.00	3.16	9.20	1.08	0.02	0.04	0.00	0.00	97.44
BP097	Point	61.81	0.00	20.28	0.14	0.01	0.00	3.25	9.11	1.08	0.04	0.00	0.00	0.00	95.71

Sample	Analysis	SiO_2	TiO_2	Al_2O_3	FeO	MnO	MgO	CaO	Na_2O	K_2O	BaO	SrO	F	Cl	Total
Bishop Tuff - F7		Pumice #2			Sanidine										
BP097	Point	66.35	0.00	18.39	0.08	0.00	0.00	0.16	3.82	11.18	0.00	0.03	0.00	0.00	100.00
BP097	Point	66.27	0.02	18.17	0.07	0.00	0.00	0.18	3.81	11.15	0.00	0.08	0.00	0.00	99.76
BP097	Point	66.13	0.00	18.24	0.07	0.00	0.00	0.14	3.78	11.10	0.00	0.03	0.01	0.00	99.50
BP097	Point	66.39	0.07	18.37	0.09	0.01	0.00	0.17	3.96	11.09	0.00	0.02	0.00	0.00	100.17
BP097	Point	66.11	0.00	17.99	0.08	0.01	0.00	0.14	3.79	11.09	0.00	0.09	0.00	0.00	99.31
BP097	Point	66.34	0.03	18.28	0.08	0.00	0.00	0.15	3.89	11.09	0.00	0.03	0.00	0.00	99.89
BP097	Point	66.17	0.01	18.19	0.08	0.00	0.00	0.15	3.84	11.06	0.06	0.02	0.02	0.00	99.61
BP097	Point	66.18	0.03	18.28	0.07	0.00	0.00	0.16	3.92	11.06	0.06	0.03	0.08	0.00	99.87
BP097	Point	66.23	0.02	18.24	0.05	0.00	0.00	0.16	4.05	11.04	0.04	0.08	0.04	0.00	99.95
BP097	Point	66.25	0.01	18.13	0.06	0.00	0.00	0.16	3.83	11.03	0.00	0.00	0.08	0.00	99.55
BP097	Point	66.18	0.00	18.28	0.07	0.00	0.00	0.12	3.78	11.02	0.02	0.01	0.00	0.00	99.49
BP097	Point	66.18	0.02	18.33	0.08	0.00	0.00	0.16	3.85	11.02	0.01	0.06	0.04	0.00	99.75
BP097	Point	66.41	0.01	18.39	0.08	0.00	0.00	0.17	4.00	11.01	0.00	0.00	0.00	0.00	100.07
BP097	Point	65.85	0.00	17.99	0.07	0.01	0.00	0.15	3.98	11.01	0.05	0.04	0.00	0.00	99.15
BP097	Point	66.19	0.02	18.15	0.08	0.00	0.00	0.15	3.93	11.01	0.00	0.05	0.06	0.00	99.64
BP097	Point	66.21	0.03	18.23	0.08	0.00	0.00	0.16	3.96	11.00	0.00	0.01	0.04	0.01	99.71
BP097	Point	66.40	0.00	18.27	0.08	0.00	0.00	0.14	3.76	10.99	0.00	0.05	0.00	0.00	99.70
BP097	Point	66.28	0.02	17.97	0.08	0.00	0.00	0.17	4.03	10.99	0.06	0.00	0.00	0.00	99.61
BP097	Point	66.22	0.03	18.24	0.07	0.00	0.00	0.16	4.00	10.98	0.03	0.02	0.05	0.00	99.80
BP097	Point	66.42	0.01	18.25	0.08	0.01	0.00	0.17	3.88	10.97	0.01	0.05	0.03	0.00	99.89
BP097	Point	66.43	0.00	18.22	0.05	0.00	0.00	0.15	3.91	10.96	0.02	0.00	0.00	0.00	99.75
BP097	Point	66.82	0.02	18.32	0.06	0.00	0.00	0.15	3.90	10.96	0.00	0.00	0.09	0.00	100.33
BP097	Point	66.31	0.00	18.03	0.07	0.00	0.00	0.15	3.91	10.95	0.04	0.02	0.00	0.00	99.48
BP097	Point	66.14	0.03	17.59	0.09	0.00	0.00	0.15	3.81	10.95	0.00	0.01	0.02	0.00	98.79
BP097	Point	66.21	0.02	17.98	0.08	0.00	0.00	0.17	3.96	10.94	0.00	0.01	0.00	0.00	99.38
BP097	Point	65.78	0.02	17.84	0.07	0.00	0.00	0.15	3.89	10.94	0.00	0.02	0.08	0.00	98.78
BP097	Point	66.23	0.03	17.85	0.10	0.00	0.00	0.16	3.77	10.91	0.02	0.02	0.02	0.01	99.11
BP097	Point	66.29	0.02	18.45	0.08	0.00	0.00	0.19	4.11	10.82	0.00	0.04	0.06	0.00	100.06
BP097	Point	66.69	0.01	17.07	0.14	0.00	0.00	0.15	3.93	9.73	0.05	0.04	0.00	0.00	97.81
					Plagioclase										
BP097	Point	65.23	0.01	20.39	0.13	0.00	0.00	2.68	9.07	1.29	0.00	0.01	0.00	0.00	98.81
BP097	Point	65.05	0.00	20.78	0.11	0.00	0.00	2.81	9.25	1.24	0.02	0.02	0.00	0.01	99.29
BP097	Point	65.50	0.01	21.00	0.11	0.00	0.00	2.98	9.28	1.24	0.00	0.07	0.08	0.00	100.25
BP097	Point	65.07	0.04	21.47	0.11	0.02	0.00	3.11	9.06	1.22	0.03	0.01	0.06	0.00	100.21
BP097	Point	64.84	0.00	20.95	0.12	0.00	0.00	2.94	9.35	1.20	0.00	0.00	0.03	0.00	99.45
BP097	Point	65.03	0.04	20.96	0.11	0.00	0.00	2.98	9.20	1.18	0.02	0.00	0.03	0.01	99.55
BP097	Point	64.99	0.00	21.22	0.12	0.00	0.00	3.08	9.33	1.18	0.01	0.00	0.00	0.00	99.94
BP097	Point	65.75	0.02	20.73	0.12	0.00	0.00	2.60	9.45	1.17	0.04	0.02	0.00	0.00	99.92
BP097	Point	65.00	0.00	21.38	0.13	0.00	0.00	3.11	8.88	1.17	0.00	0.00	0.00	0.01	99.68
BP097	Point	65.20	0.05	21.18	0.13	0.00	0.00	3.06	9.09	1.16	0.00	0.07	0.01	0.00	99.94
BP097	Point	65.46	0.02	21.24	0.11	0.01	0.00	2.98	9.14	1.16	0.00	0.03	0.03	0.00	100.19
BP097	Point	65.23	0.03	21.19	0.10	0.00	0.00	3.03	9.36	1.15	0.00	0.02	0.00	0.01	100.13
BP097	Point	65.10	0.00	21.18	0.11	0.00	0.00	3.02	9.04	1.14	0.00	0.06	0.07	0.00	99.73
BP097	Point	64.95	0.00	21.28	0.11	0.03	0.01	3.15	8.92	1.13	0.00	0.08	0.00	0.00	99.66
BP097	Point	64.72	0.00	20.95	0.12	0.01	0.00	3.12	9.19	1.13	0.00	0.00	0.04	0.00	99.28
BP097	Point	65.02	0.00	21.15	0.13	0.00	0.00	3.07	9.03	1.10	0.00	0.06	0.00	0.01	99.57
BP097	Point	64.58	0.00	21.09	0.12	0.00	0.00	3.19	8.96	1.09	0.00	0.02	0.00	0.00	99.06
BP097	Point	64.72	0.01	21.70	0.13	0.02	0.01	3.42	9.15	1.07	0.00	0.06	0.04	0.00	100.34

Sample	Analysis	SiO_2	TiO_2	Al_2O_3	FeO	MnO	MgO	CaO	Na_2O	K_2O	BaO	SrO	F	Cl	Total
Bishop Tuff - Ig2NWa			Pumice		Sanidine										
BP113	Point	65.80	0.03	18.82	0.11	0.00	0.00	0.27	3.77	10.81	0.79	0.09	0.08	0.00	100.56
BP113	Point	65.76	0.00	18.95	0.11	0.00	0.00	0.29	3.80	10.91	0.63	0.02	0.10	0.00	100.59
BP113	Point	66.43	0.00	18.62	0.08	0.01	0.00	0.23	3.54	11.23	0.10	0.09	0.00	0.01	100.34
BP113	Point	65.95	0.04	18.47	0.09	0.00	0.00	0.25	3.85	10.92	0.07	0.00	0.06	0.00	99.73
BP113	Point	66.59	0.28	18.73	0.08	0.02	0.00	0.22	3.97	11.03	0.07	0.04	0.03	0.00	101.05
BP113	Point	66.48	0.02	18.62	0.09	0.00	0.00	0.24	3.60	11.12	0.03	0.00	0.00	0.00	100.20
BP113	Point	65.97	0.00	18.47	0.07	0.00	0.00	0.23	3.92	11.03	0.06	0.04	0.05	0.00	99.84
BP113	Point	66.25	0.02	18.61	0.07	0.01	0.00	0.24	3.79	11.35	0.06	0.05	0.06	0.00	100.52
BP113	Point	65.91	0.03	18.59	0.08	0.01	0.00	0.25	3.78	10.95	0.38	0.08	0.00	0.00	100.07
BP113	Point	66.02	0.03	18.95	0.11	0.00	0.00	0.26	3.72	11.02	0.68	0.04	0.00	0.01	100.84
BP113	Point	66.45	0.03	18.66	0.08	0.00	0.00	0.22	3.66	11.08	0.08	0.04	0.01	0.00	100.33
BP113	Point	66.34	0.01	18.72	0.09	0.03	0.00	0.24	3.60	11.08	0.16	0.09	0.00	0.00	100.37
BP113	Point	65.85	0.01	18.71	0.11	0.00	0.00	0.26	3.82	10.84	0.58	0.00	0.00	0.00	100.19
BP113	Point	66.72	0.01	18.72	0.08	0.01	0.00	0.18	3.72	11.22	0.02	0.00	0.04	0.00	100.72
BP113	Point	66.52	0.00	18.66	0.08	0.01	0.00	0.22	3.76	11.31	0.04	0.02	0.06	0.00	100.69
BP113	Point	65.60	0.01	18.79	0.10	0.00	0.00	0.27	3.65	10.94	0.65	0.08	0.00	0.00	100.09
BP113	Point	66.01	0.03	18.66	0.09	0.00	0.00	0.28	3.65	10.86	0.47	0.06	0.07	0.00	100.18
BP113	Point	66.79	0.05	18.61	0.08	0.00	0.00	0.24	3.60	11.01	0.09	0.09	0.01	0.00	100.58
BP113	Point	66.38	0.00	18.32	0.07	0.00	0.00	0.25	3.71	11.08	0.05	0.06	0.04	0.00	99.97
BP113	Point	66.28	0.05	18.53	0.08	0.00	0.00	0.21	3.75	11.21	0.02	0.12	0.00	0.00	100.25
BP113	Point	66.63	0.01	18.76	0.09	0.00	0.00	0.23	3.69	11.26	0.00	0.04	0.00	0.00	100.71
BP113	Point	66.49	0.03	18.77	0.08	0.00	0.00	0.24	3.66	11.21	0.00	0.06	0.00	0.00	100.54
Bishop Tuff - Ig2Nb			Pumice		Sanidine										
BP168	Point	65.06	0.00	18.78	0.13	0.00	0.00	0.31	3.67	10.89	1.27	0.05	0.13	0.00	100.29
BP168	Point	66.03	0.03	18.61	0.10	0.00	0.00	0.30	3.53	11.04	0.35	0.04	0.09	0.01	100.13
BP168	Point	66.30	0.03	18.76	0.10	0.00	0.00	0.31	3.68	11.02	0.28	0.04	0.00	0.00	100.54
BP168	Point	66.43	0.02	18.54	0.09	0.00	0.00	0.22	3.66	11.35	0.07	0.07	0.06	0.00	100.51
BP168	Point	66.29	0.05	18.60	0.09	0.01	0.00	0.25	3.71	11.23	0.00	0.14	0.02	0.00	100.39
BP168	Point	65.04	0.02	18.85	0.13	0.00	0.00	0.31	3.72	10.73	1.27	0.12	0.09	0.00	100.28
BP168	Point	66.27	0.04	18.64	0.08	0.00	0.00	0.22	3.61	11.42	0.01	0.02	0.01	0.00	100.34
BP168	Point	66.05	0.02	18.62	0.08	0.02	0.00	0.24	3.61	11.13	0.24	0.07	0.02	0.00	100.09
BP168	Point	65.49	0.06	18.94	0.11	0.00	0.00	0.35	3.49	10.94	0.76	0.09	0.00	0.00	100.23
BP168	Point	66.41	0.04	18.67	0.08	0.00	0.00	0.25	3.73	11.32	0.08	0.07	0.00	0.00	100.66
BP168	Point	66.48	0.00	18.67	0.06	0.00	0.00	0.26	3.73	11.36	0.03	0.00	0.02	0.00	100.61
BP168	Point	65.36	0.00	18.76	0.11	0.00	0.00	0.32	3.72	10.95	0.69	0.03	0.00	0.00	99.94
BP168	Point	66.06	0.00	18.52	0.07	0.00	0.00	0.22	3.62	11.46	0.00	0.00	0.05	0.00	99.99
BP168	Point	65.98	0.02	18.68	0.08	0.00	0.00	0.26	3.58	11.33	0.28	0.13	0.09	0.00	100.42
BP168	Point	65.78	0.00	18.81	0.11	0.01	0.00	0.28	3.79	11.07	0.60	0.07	0.00	0.00	100.53
BP168	Point	65.48	0.03	18.89	0.11	0.00	0.00	0.29	3.69	10.96	1.09	0.08	0.00	0.00	100.63
BP168	Point	65.95	0.05	18.60	0.11	0.00	0.00	0.28	3.61	11.09	0.34	0.06	0.14	0.00	100.22
BP168	Point	65.94	0.00	18.72	0.08	0.01	0.00	0.25	3.56	11.20	0.55	0.06	0.01	0.00	100.39
BP168	Point	66.57	0.05	18.71	0.07	0.00	0.00	0.26	3.77	11.16	0.02	0.11	0.00	0.00	100.72
BP168	Point	65.78	0.04	18.69	0.11	0.01	0.00	0.26	3.69	11.08	0.48	0.09	0.02	0.00	100.25
BP168	Point	66.44	0.00	18.61	0.09	0.02	0.00	0.24	3.59	11.05	0.24	0.10	0.07	0.00	100.46
BP168	Point	66.42	0.03	18.56	0.08	0.00	0.00	0.25	3.56	11.28	0.03	0.04	0.00	0.00	100.25
BP168	Point	66.26	0.00	18.67	0.10	0.01	0.00	0.28	3.58	11.05	0.22	0.03	0.00	0.00	100.20
BP168	Point	65.49	0.01	18.74	0.10	0.00	0.00	0.33	3.78	10.72	0.98	0.11	0.09	0.01	100.36
BP168	Point	66.06	0.05	18.68	0.08	0.00	0.00	0.27	3.69	11.30	0.04	0.09	0.00	0.01	100.28
BP168	Point	66.19	0.03	18.57	0.10	0.00	0.00	0.27	3.70	11.14	0.04	0.02	0.00	0.00	100.06
BP168	Point	66.11	0.02	18.51	0.08	0.00	0.00	0.29	3.75	11.14	0.17	0.11	0.00	0.00	100.19
BP168	Point	65.18	0.03	18.71	0.13	0.01	0.00	0.29	3.57	10.82	0.97	0.12	0.00	0.00	99.82
BP168	Point	66.64	0.00	18.62	0.07	0.00	0.00	0.24	3.58	11.18	0.03	0.08	0.06	0.00	100.50
BP168	Point	64.83	0.02	18.99	0.13	0.00	0.00	0.35	3.59	10.87	1.09	0.07	0.00	0.00	99.93
BP168	Point	64.82	0.05	18.78	0.11	0.03	0.00	0.29	3.81	10.53	0.99	0.07	0.02	0.00	99.51

Sample	Analysis	SiO_2	TiO_2	Al_2O_3	FeO	MnO	MgO	CaO	Na_2O	K_2O	BaO	SrO	F	Cl	Total
Bishop Tuff - Ig2Nb			Pumice		Biotite										
BP168	Point	37.50	4.59	13.02	17.71	0.12	12.54	0.00	0.56	8.77	0.24	0.03	0.75	0.07	95.91
BP168	Point	37.68	4.67	13.10	17.82	0.10	12.71	0.00	0.54	8.91	0.22	0.00	0.20	0.08	96.04
BP168	Point	37.92	4.47	13.00	17.77	0.13	12.80	0.03	0.58	8.95	0.07	0.01	0.32	0.09	96.13
BP168	Point	37.77	4.53	12.91	17.60	0.10	12.66	0.01	0.59	8.86	0.15	0.00	0.16	0.09	95.43
BP168	Point	38.31	4.42	12.99	18.15	0.12	12.72	0.01	0.66	8.86	0.08	0.00	0.21	0.09	96.62
BP168	Point	37.54	4.56	13.00	18.70	0.14	12.22	0.01	0.60	8.96	0.17	0.01	0.13	0.08	96.12
BP168	Point	36.15	4.53	13.59	19.41	0.15	11.15	0.00	0.54	8.67	1.29	0.02	0.24	0.05	95.79
BP168	Point	37.49	4.57	12.95	18.12	0.11	12.52	0.01	0.63	9.07	0.26	0.07	0.12	0.07	95.98
BP168	Point	37.72	4.44	12.91	17.55	0.12	12.73	0.00	0.57	9.02	0.12	0.00	1.28	0.08	96.55
BP168	Point	37.66	4.67	12.94	17.62	0.10	12.69	0.00	0.57	9.07	0.16	0.04	0.35	0.08	95.94
BP168	Point	37.93	4.46	13.07	17.68	0.10	12.93	0.01	0.59	9.04	0.09	0.07	0.18	0.08	96.23
BP168	Point	38.10	4.39	13.03	17.65	0.10	12.96	0.01	0.62	8.94	0.10	0.03	0.26	0.09	96.28
BP168	Point	37.33	4.54	13.01	17.57	0.12	12.36	0.06	0.57	8.86	0.18	0.05	0.29	0.10	95.05
BP168	Point	37.72	4.61	12.97	17.89	0.14	12.68	0.01	0.56	8.89	0.15	0.01	0.20	0.08	95.89
BP168	Point	37.25	4.41	12.85	18.13	0.10	12.47	0.00	0.62	8.88	0.21	0.02	0.19	0.08	95.20
BP168	Point	37.62	4.57	12.87	17.89	0.12	12.60	0.00	0.58	9.04	0.18	0.06	0.29	0.08	95.90
BP168	Point	38.52	4.36	12.94	17.37	0.09	12.97	0.03	0.58	8.88	0.02	0.05	0.29	0.09	96.19
BP168	Point	37.33	4.59	12.87	18.27	0.12	12.18	0.01	0.58	8.89	0.21	0.00	0.24	0.09	95.36
BP168	Point	37.40	4.56	12.86	17.74	0.10	12.53	0.02	0.60	9.03	0.17	0.02	0.33	0.08	95.42

A5. Summary Tables

A5.1 Introduction

Appendix A5 is a collection of summary tables detailing previously published age determinations for geological units investigated in this study. Tables provide information on analytical technique, mineral used for geochronological study, age (Ma ± 1σ), reference and any additional information (e.g., Ar-Ar standard and/or ^{40}K decay constant used).

Table A5.1a: Fish Canyon Magmatic System age determinations.

Table A5.1b: Fish Canyon Tuff sanidine (FCs) and biotite age determinations.

Table A5.2: Yellowstone Volcanic Plateau Field - Huckleberry Ridge Tuff (HRT) and Mesa Falls Tuff (MFT) age determinations.

Table A5.3: Long Valley Volcanic Field – Bishop Tuff age determinations.

Table A5.1a: Fish Canyon Magmatic System age determinations.

Mineral	Analytical method	Additional notes	Age (Ma)	± 1σ	Age range (Ma)	Reference
Sanidine	K-Ar	Recalculated using decay constants of Steiger and Jäger (1977). Summit of Agua Ramon Mountain, ca. 7 km north-north-east of South Fork, Colorado, USA	27.9	0.4		Steven *et al.*, (1967) cited in Dazé *et al.*, (2003)
Sanidine	K-Ar		27.99	0.27		Hurford and Hammerschmidt, 1985
Biotite	K-Ar	Recalculated using decay constants of Steiger and Jäger (1977)	27.8	0.4		Steven *et al.*, (1967) cited in Dazé *et al.*, (2003)
Biotite	K-Ar		27.15	0.26		Hurford and Hammerschmidt, 1985
Biotite	K-Ar	All ages relative to SB-3 biotite primary standard with an age of 162.9 ± 0.9 Ma (dated by Lanphere and Dalrymple, 2000)	27.55	0.34		Lanphere and Baadsgaard, 2001
Hornblende	K-Ar	Recalculated using decay constants of Steiger and Jäger (1977)	26.6	0.95		Steven *et al.*, (1967) cited in Dazé *et al.*, (2003)
Hornblende	K-Ar		27.47	0.27		Hurford and Hammerschmidt, 1985
Hornblende	K-Ar		27.53	0.46		Lanphere and Baadsgaard, 2001
Plagioclase	K-Ar	Recalculated using decay constants of Steiger and Jäger (1977)	27.5	0.95		Steven *et al.*, (1967) cited in Dazé *et al.*, (2003)
Plagioclase	K-Ar		26.78	0.26		Hurford and Hammerschmidt, 1985
Sanidine, biotite, plagioclase, hornblende	K-Ar		27.9	0.7		Naeser *et al.*, (1981) cited in McDougall and Harrison, 1999
Sanidine, biotite, plagioclase, hornblende	K-Ar		27.9	0.7		Cebula *et al.*, (1986) cited in Dazé *et al.*, (2003)
Biotite and hornblende	K-Ar		27.5	0.2		Lanphere and Baadsgaard, 1997 cited in McDougall and Harrison, 1999
Sanidine, biotite, hornblende	K-Ar	K-Ar pooled age - from two samples of FCT collected at different times from same locality adjacent to US Highway 160. 9 km south-west of South Fork	28.4	0.1		Spell and McDougall (unpublished) cited in McDougall and Harrison, 1999
Apatite	Fission track		28	1.45		Cebula *et al.*, (1986) cited in Dazé *et al.*, (2003)
Apatite	Fission track		26.8	2.1		Carpena and Mailhe, 1987 cited in Spell and McDougall, 2003
Zircon	Fission track		27.79	1		Cebula *et al.*, (1986) cited in Dazé *et al.*, (2003)
Zircon	Fission track		27.9	1.1		Carpena and Mailhe, 1987 cited in Spell and McDougall, 2003
Zircon	U-Pb isotope dilution		28.41	0.03		Oberli *et al.*, (1990) cited in Dazé *et al.*, (2005)
Zircon	U-Pb isotope dilution		27.52	0.05		Lanphere and Baadsgaard, 2001
Zircon	U-Pb isotope dilution		28.48	0.03		Schmitz and Bowring, 2001 cited in Dazé *et al.*, (2003)
Titanite	U-Pb isotope dilution		28.4	0.04		Schmitz and Bowring, 2001 cited in Dazé *et al.*, (2003)
Zircon	U-Pb	Also identified a xenocrystic population 1442 ± 19 to 2350 ± 13 Ma	28.7	0.3		Lanphere and Baadsgaard, 2001
Zircon	U-Pb		28.36	0.03		Oberli *et al.*, (2002) cited in Spell and McDougall, 2003
Zircon	U-Pb	Range of precise ages	-	-	~ 28.67 Ma to ~ 28.03 Ma	Bachmann *et al.*, (2007b)
Zircon	U-Pb	Mean age from Chemical abrasion-treated *zircons*	28.61	0.08		Bachmann *et al.*, (2007b)
Titanite	U/Th-He		30.1	0.5		Reiners and Farley, 1999 cited in Spell and McDougall, 2003
Zircon	U/Th-He		27.3	1.1		Reiners *et al.*, (2002) cited in Spell and McDougall, 2003
Sanidine, plagioclase, biotite	Rb-Sr	Feldspar-biotite Rb/Sr isochron age	27.44	0.08		Lanphere and Baadsgaard, 2001

Table A5.1b: Fish Canyon Tuff sanidine (FCs) and biotite (Ar-Ar standard) age determinations.

Mineral	Analytical method	Additional notes	Age (Ma)	± 1σ	Age range (Ma)	Reference
Sanidine + biotite	Ar-Ar total fusion and step heating	Relative to Mmbh-1 with an age of 518.9 Ma	27.79			*Cebula et al., (1986) cited in Dazé et al.,* (2003)
Sanidine	Astronomical time scale APTS (weighted mean age)		28.03	0.18		Hilgen *et al.*, (1997) cited in Renne *et al.,* (1994)
Sanidine	Astronomical time scale APTS		28.15	0.19		*Dazé et al.,* (2003)
Sanidine	Historical [Vesuvius]	Age includes uncertainties in decay constants	28.04	0.23		Renne *et al.,* (1998)
Sanidine	Ar-Ar laser total fusion	Age refers to (Renne *et al.*, 1998) GA15-50 biotite of 98.8 ± 0.5 Ma. Not taking into account the external errors associated with measurement of decay constants for ^{40}K	28.02	0.16		Renne *et al.,* (1998)
Sanidine	Ar-Ar laser total fusion with U-Pb intercalibration		27.98	0.08		Villeneuve *et al.,* (2000)
Sanidine	Historical [Vesuvius]		~ 28.05	-		Min *et al.,* (2000)
Sanidine	Ar-Ar laser bulk fusion and incremental heating	All ages relative to secondary standard sanidine from Taylor Creek Rhyolite (age = 27.92 Ma) which was calibrated with SB-3 biotite primary standard			Range 27.46 ± 0.34 Ma to 27.76 ± 0.14 Ma	Lanphere and Baadsgaard, (2001)
Sanidine	Ar-Ar laser total fusion, bulk step heating	Relative to GA15-50 with an age of 98.5 ± 0.8 Ma	28.1	0.04		Spell and McDougall, (2003)
Sanidine	Ar-Ar total fusion and step heating	Biotite, hornblende and plagioclase, which are less readily set than sanidine, give mean ages that are somewhat older than sanidine so ages are bias corrected Ar-Ar age on sanidine	~ 28.03			Bachmann *et al.,* (2007b)
Sanidine	Ar-Ar step heating		28.04	0.18		Bachmann *et al.,* (2007b)
Sanidine	Astronomically tuned	Relative to ^{40}K decay constant of Min *et al.*, (2000)	28.201	0.023		Kuiper *et al.*, (2008)
Sanidine	Ar-Ar single grain fusion	Relative to ^{40}K decay constant of Renne *et al.*, (2010; 2011)	28.305	0.036		Renne *et al.*, (2010)
Sanidine	Astronomically tuned	Relative to ^{40}K decay constant of Min *et al.*, (2000)	~ 27.93	-		Channell *et al.*, (2010)
Sanidine	Ar-Ar single grain fusion	Relative to ^{40}K decay constant of Min *et al.*, (2000)	28.172	0.028		Rivera *et al.*, (2011)
Biotite	Ar-Ar		28.09	0.1		*Wijbrans et al., (1995) cited in Dazé et al.,* (2003)
Biotite	Ar-Ar bulk fusion	Relative to various primary standards	-	-	Range 27.90 ± 0.04 to 28.09 ± 0.09 Ma	Baksi *et al.*, (1996)
Biotite	Ar-Ar bulk fusion		27.72	0.21		Lanphere and Baadsgaard, 2001
Biotite	Ar-Ar bulk fusion	Relative to various primary standards	-	-	Range 27.41 ± 0.07 to 27.67 ± 0.08 Ma	Lanphere and Baadsgaard, 2001
Biotite	Ar-Ar incremental heating (furnace)		-	-	Range 27.35 ± 0.19 to 27.97 ± 0.14 Ma	Lanphere and Baadsgaard, 2001
Biotite	Ar-Ar laser fusion and laser incremental heating		28.13	0.24		*Dazé et al.,* (2003)
Biotite	Ar-Ar laser fusion	Fish Canyon Tuff and Pagosa Peak Dacite samples	28.25	0.1		Bachmann *et al.*, (2007b)

Table A5.2: Yellowstone Volcanic Plateau Field - Huckleberry Ridge Tuff (HRT) and Mesa Falls Tuff age determinations.

Unit	Mineral	Technique	Age (Ma)	± 1σ	Additional notes	Reference
HRT (Mt Everts)	Sanidine	Ar-Ar single-grain total fusion	2.01	0.16	Initial ages reported from three localities - Geological Society of America 1991 Abstracts with Programs	Obradovich and Izett, 1991
HRT (Huckleberry Ridge)			2.02	0.03		
HRT (Crown Butte)			2.05	0.02		
HRT	Sanidine	K-Ar	2.11	0.01	Preferred age from a regression of oldest and more precise ages - MSWD 4.46 large spread in data	Obradovich, 1992
HRT	Sanidine	K-Ar	2.02	0.01	Weighted mean age	Obradovich, 1992
HRT	Sanidine	K-Ar Isochron age (intercept of 304 ± 46.1)	1.99	0.01	Minimum age	Obradovich, 1992
HRT	sanidine	Ar-Ar single-grain fusion	2.00	0.01		Gansecki *et al*., (1998)
HRT	Sanidine	Ar-Ar single-grain fusion	2.10	0.01		Honey *et al*., (1998)
HRT	Zircon	^{238}U-^{206}Pb (Th-U corrected)	2.13	0.13	Age represents zircon crystallisation	Bindeman *et al*., (2001)
HRT A (Basal vitrophyre)	Sanidine	Ar-Ar single-grain fusion	2.09	0.01		Lanphere *et al*., (2002)
HRT B (Upper devitrified tuff)			2.05	0.01		
HRT C (Ash-fall from base of HRT on Mount Everts)			2.05	0.01		
HRT A (Basal vitrophyre)	Sanidine	Ar-Ar incremental heating - plateau age	2.05	0.01		Lanphere *et al*., (2002)
HRT B (Upper devitrified tuff)			2.06	0.01		
HRT C (Ash-fall from base of HRT on Mount Everts)			2.06	0.01		
HRT A	Sanidine	Ar-Ar single-grain fusion	2.123	0.003		Ellis *et al*., (2012)
HRT B			2.119	0.004		
HRT C			2.102	0.002		
HRT A	Sanidine	Ar-Ar single-grain total fusion	2.135	0.003	Relative to ^{40}K decay constant of Renne *et al*., (2010; 2011)	Ellis *et al*., (2012)
HRT B			2.131	0.004		
HRT C			2.113	0.002		
MFT (Ashton, Idaho)	Sanidine	K-Ar	1.26	0.01		Obradovich and Izett, 1991
MFT	Sanidine	Ar-Ar single-grain fusion	1.29	0.01		Obradovich and Izett, 1991
MFT (Basal pumice)	Sanidine	Ar-Ar single-grain fusion	1.29	0.01	Weighted average	Gansecki *et al*., (1998)
		Ar-Ar single-grain fusion				
MFT	Sanidine	Ar-Ar single-grain fusion	1.29	0.01		M. A. Lanphere (written communication, 2000) reported in Christiansen, 2001
MFT (Pumice)	Sanidine	Ar-Ar single-grain fusion	1.31	0.01		Lanphere *et al*., (2002)
MFT (Pumice)	Sanidine	Ar-Ar incremental heating - plateau age	1.29	0.01		
MFT (Pumice)	Sanidine	Ar-Ar	1.29	0.01	Weighted mean of plateau and isochron ages	
MFT	Zircon	U-Pb	1.46	0.3		Bindeman *et al*., (2007)

Table A5.3: Long Valley Volcanic Field – Bishop Tuff age determinations.

Unit	Fall or Flow	Mineral	Technique	Age (Ma)	± 1σ	Additional notes	Reference
-	-	Sanidine	K-Ar	0.870			Evernden *et al*., (1957) cited in Sarna-Wojcicki et al., (2000)
-	-	Sanidine	K-Ar	~ 1			Evernden *et al*., (1964) Sarna-Wojcicki *et al*., (2000)
-	-	Sanidine	K-Ar	0.700			Dalrymple *et al*., (1965)
-	-	Sanidine	Ar-Ar incremental heating	0.734	0.012		Hurford and Hammerschmidt, 1985
-	-	Sanidine	K-Ar	~ 0.730			Mankinen and Dalrymple, 1979; Dalrymple 1980 cited in Izett et al., (1988)
-	-	Sanidine, plagioclase, biotite, glass	K-Ar	0.736	0.003		Izett *et al*., (1988)
-	-	Sanidine	K-Ar	0.738	0.002		Izett *et al*., (1988)
-	Air fall pumice	Zircon	Fission Track	0.740	0.025		Naeser and Izett, 1976
Cowan Quarry	Air fall pumice	Zircon	Fission Track	0.750	0.025		Meyer *et al*., (1991) cited in Sarna-Wojcicki *et al*., (2000)
-	-	Sanidine	Ar-Ar	0.762	0.006		Obradovich and Izett, 1992 cited in Izett and Obradovich, 1994
-	-	Sanidine	Ar-Ar	0.759	0.003		Pringle *et al*., (1992)
-	Upper ash flow	Sanidine	Ar-Ar	0.757	0.005		Izett and Obradovich, 1994
-	Lower air fall pumice	Sanidine	Ar-Ar	0.764	0.003		Izett and Obradovich, 1994
-	Upper ash flow and lower air fall pumice	Sanidine	Ar-Ar	0.758	0.001		Sarna-Wojcicki and Pringle, 1992 cited in Sarna-Wojcicki *et al*., (2000)
-	-	Sanidine	Ar-Ar	0.761	0.001		van den Bogaard and Schirnick, 1995
-	-	Sanidine	Ar-Ar	0.768	0.002		Winick (MSc thesis), 2000
Various	Air fall pumice, ash bed & overlying ash flow tuff	Sanidine	Ar-Ar single-grain fusion	0.770	0.002	Recalculated by Crowley *et al*., (2007) based on Renne *et al*., (1998) age of Taylor Creek standard	Sarna-Wojcicki *et al*., (2000)
-	-	Sanidine	Ar-Ar	0.769		Relative to FCs standard age of 28.201 and decay constant of Min *et al*., (2000)	Kuiper *et al*., (2008)
-	-	Sanidine	Ar-Ar	0.762		Relative to FCs standard age of 27.93 Ma and decay constant of Min *et al*., 2000. Analytical uncertainty only.	Channell *et al*., (2010)
-	-	Sanidine (20 - 25 multi crystal total fusion)	Ar-Ar	0.767		Relative to A1 standard age of 6.943 Ma and decay constant of Min *et al*., (2000)	Rivera *et al*., (2011)
-	-	Sanidine (20 - 25 multi crystal total fusion)	Ar-Ar	0.768		Relative to FCs standard age of 28.172 Ma and decay constant of Min *et al*., (2000)	
-	-	Sanidine (20 - 25 multi crystal total fusion)	Ar-Ar	0.772	0.001	Relative to FCs standard age of 28.305 Ma and decay constant of Renne *et al*., (2010; 2011)	
-	-	Zircon	206Pb/238U (ID-TIMS)	0.767	0.001		Crowley *et al*., (2007)
-	Air fallout & intercalated ash-flow deposits of early BT	Zircon	238U-206Pb (ion microprobe)	0.823	0.006		Reid and Coath, 2000
Eastern Bishop Tuff	Late Bishop Tuff	Zircon crystallisation age	238U-206Pb (ion microprobe)	0.811	0.004	Ig2NW	Simon and Reid, 2005
Northern Bishop Tuff	Early Bishop tuff	Zircon crystallisation age	238U-206Pb (ion microprobe)	0.841	0.004	Ig1Eb	Simon and Reid, 2005
Northern Bishop Tuff	Early Bishop tuff	Zircon crystallisation age	238U-206Pb (ion microprobe)	0.823	0.007	Fall Unit 6	Simon and Reid, 2005